

Holocene Evolution of the Colima Volcanic Complex, Mexico

Julia Margaret Crummy

Submitted in accordance with the requirements for the degree of
Ph.D.

The University of Leeds
Institute of Geophysics and Tectonics
School of Earth and Environment

March 2013

The candidate confirms that the work submitted is her own and that appropriate credit has been given where reference has been made to the work of others.

This copy has been supplied on the understanding that it is copyright material and that no quotation from the thesis may be published without proper acknowledgement.

The right of Julia Margaret Crummy to be identified as Author of this work has been asserted by her in accordance with the Copyright, Designs and Patents Act 1988.

© 2013 The University of Leeds and Julia Margaret Crummy

Acknowledgements

None of this work would have been possible without the help and support of numerous people inside and outside the academic community. First and foremost I would like to thank my supervisors, Ivan Savov, Dan Morgan and Marjorie Wilson for their endless support and encouragement throughout my PhD. Thank you to Ivan for enabling me to visit some wonderful places, meet some wonderful people, and for introducing me to the incredibly beautiful Volcán de Colima! Thank you to Dan Morgan for putting up with my questions, frustrations and tears, without whose support I couldn't have done this. Marge with her red pen provided invaluable feedback in writing this thesis, and helped me see things clearer.

I am very grateful to Carlos Navarro-Ochoa for sharing his incredible knowledge on the Colima Volcanic Complex with me, and providing help and support during my field work in Mexico, that went above and beyond the call of duty. Thank you my friend!

I am eternally grateful to Jim Luhr for his samples and years of experience working on the CVC, without which, none of this work would have been possible.

A massive thank you goes to Chuck and Laura Connor who I met in my first two weeks of being a volcanologist, and as a result put up with endless questions! Chuck and Laura taught me how to use the *Tephra2* code, and provided invaluable feedback on my results.

Many people in the School of Earth and Environment helped make this an enjoyable time, so thank you all. In particular I would like to mention Hannah, Fran, Haggis, Meg and Fred who have provided entertainment over the last three and half years! A special thank you goes to Hannah not only for her ability to brighten up any situation, but also for the amazing support she has been through the tough times. You are my rock Hannah.

Finally, thank you to my parents, Janet and Mike, and to my wonderful fiancé, Steven, for always believing in me.

Abstract

Current activity at the Colima Volcanic Complex (CVC) is characterised by the andesitic lava dome growth and small Vulcanian style eruptions of Volcán de Colima; however, road cuts on the nearby Nevado de Colima, reveal a record of explosive eruptions spanning the Holocene and Late Pleistocene. New data presented here, in combination with published and unpublished datasets, reveal the majority of tephra fallout deposits spanning the last ~13,000 years, are medium-K sub-alkaline, ranging in composition from basaltic-andesite to high-silica andesite (50.7 - 60.4 wt.% SiO₂). These magmas display typical subduction-related trace element signatures with enriched fluid mobile elements (Rb, Ba, La, Ce, Sr) relative to high field strength elements (i.e. Nb, Ta).

Three units interbedded in the CVC stratigraphy, erupted at c.7000, 12,000 and 13,000 years before present (yrs B.P.), reveal pulses of alkaline magmatism which intersect the magmatic storage region of the CVC on timescales of thousands of years. These units are mineralogically and geochemically distinct from the typical sub-alkaline eruption deposits, characterised by the presence of phlogopite and elevated K₂O, P₂O₅ and incompatible trace element abundances. Through two-component mixing models, using whole-rock major and trace element geochemical data, and Sr-Nd isotopic data, after Langmuir et al. (1978), the alkaline component within these mixed magmas has been quantified to between 20 and 70%.

A new model defining the nature of the magmatic plumbing system of the CVC is presented, drawing on previously published models for alkaline magma petrogenesis, recent geophysical studies, and new petrological and geochemical data. Mineral compositions and textures reveal multiple phases of growth and destabilisation interpreted to reflect decompression and magma recharge events consistent with multiple levels of magma storage within the crust below the CVC.

Finally, initial volume estimates based on tephra modelling reveal these explosive eruptions were subplinian (0.03 to 0.3km³) events. These initial results reveal a link between magma composition and eruption volume, with the most evolved CVC magmas producing large volume eruptions.

Some Common Abbreviations used in the Text

AFC	Assimilation Fractional Crystallisation
a.s.l.	above sea-level
BSE	Backscatter Electron
CVC	Colima Volcanic Complex
E-MORB	Enriched Mid-Ocean Ridge Basalt
EPMA	Electron Probe Micro-analysis
FC	Fractional Crystallisation
FME	Fluid-mobile Elements
fO_2	Oxygen Fugacity
HFSE	High Field Strength Elements
HREE	Heavy Rare Earth Elements
ICP-AES	Inductively Coupled Plasma - Atomic Emission Spectrometry
ICP-MS	Inductively Coupled Plasma - Mass Spectrometry
INNA	Instrumental Neutron Activation Analysis
LAO	Low Amplitude Oscillations
LILE	Large Ion Lithophile Elements
LREE	Light Rare Earth Elements
MAT	Middle America Trench
MORB	Mid-Ocean Ridge Basalt
MREE	Middle Rare Earth Elements
N-MORB	Normal Mid-Ocean Ridge Basalt
OIB	Ocean Island Basalt
REE	Rare Earth Elements
SEM	Scanning Electron Microscope
STR	Saw-Tooth Resorption
TIMS	Thermal Ionisation Mass Spectrometer
TMVB	Trans-Mexican Volcanic Belt
TZR	Tepic-Zacoalco Rift
VEI	Volcanic Explosivity Index
XRF	X-Ray Fluorescence
yrs B.P.	years before present

Table of Contents

1	Introduction.....	- 1 -
1.1	The Colima Volcanic Complex.....	- 3 -
1.1.1	Volcán Cántaro.....	- 4 -
1.1.2	Nevado de Colima.....	- 5 -
1.1.3	Paleofuego de Colima	- 6 -
1.1.4	Volcán de Colima.....	- 7 -
1.1.5	Monogenetic Cinder Cones	- 7 -
1.2	Geological History of the Colima Volcanic Complex	- 8 -
1.2.1	The Basement Geology of the Trans-Mexican Volcanic Belt.....	- 8 -
1.2.2	Magmatic Evolution of the Trans-Mexican Volcanic Belt	- 10 -
1.2.3	The Tectonic Setting of the Western Trans-Mexican Volcanic Belt...-	- 12 -
1.3	Late Pleistocene and Holocene Eruption History of the Colima Volcanic Complex.....	- 16 -
1.3.1	Interplinian Activity	- 18 -
1.3.2	Plinian Activity	- 22 -
1.4	Modelling of Tephra Fallout at the Colima Volcanic Complex.....	- 29 -
1.5	Research Questions	- 30 -
2	Group I Basaltic-Andesites to Andesites.....	- 32 -
2.1	Stratigraphy.....	- 32 -
2.2	Petrology and Mineral Chemistry	- 36 -
2.2.1	Mineral Compositions	- 37 -
2.2.2	Textures and Mineral Zoning	- 48 -
2.2.3	Summary of Petrological Observations and Interpretations.....	- 64 -
2.3	Geothermometry and Hygrometry	- 66 -
2.3.1	Estimating Eruption Temperature and Magmatic Water Content for the CVC Magmas	- 68 -
2.4	Whole-rock Geochemistry	- 75 -
2.4.1	Major Elements	- 76 -
2.4.2	Trace Elements.....	- 80 -
2.5	Whole-rock Sr-Nd Isotopes.....	- 84 -
2.5.1	Isotopic Composition of the CVC Group I Magmas.....	- 86 -
2.6	Summary	- 90 -
3	Group II High-K Eruption Deposits	- 92 -
3.1	Stratigraphy.....	- 92 -
3.2	Petrology and Mineral Chemistry	- 95 -

3.2.1	Mineral Compositions	- 96 -
3.2.2	Petrological Textures and Mineral Zoning.....	- 106 -
3.3	Geothermometry and Hygrometry	- 121 -
3.3.1	Mineral-melt and Mineral-mineral Equilibrium Tests	- 121 -
3.3.2	Temperature and Water Content Estimates for the Group II CVC Magmas	- 123 -
3.4	Whole-Rock Geochemistry	- 125 -
3.4.1	Major Elements	- 126 -
3.4.2	Trace Elements	- 130 -
3.5	Sr-Nd Isotopes.....	- 132 -
3.6	Summary	- 135 -
4	Alkaline Cinder Cones.....	- 136 -
4.1	Petrology	- 137 -
4.2	Whole-rock Geochemistry	- 139 -
4.2.1	Major Elements	- 142 -
4.2.2	Trace Elements	- 142 -
4.3	Whole-rock Sr and Nd Isotopes	- 144 -
4.4	Models of Alkaline Cinder Cone Magma Source	- 145 -
4.4.1	Mantle Metasomatism	- 146 -
4.4.2	Subduction Erosion	- 149 -
4.5	Summary	- 151 -
5	Petrogenesis of the Colima Volcanic Complex Magmas	- 153 -
5.1	Source of the CVC Magmas	- 153 -
5.1.1	Mexican Mantle Wedge Composition.....	- 154 -
5.1.2	Sub-alkaline Arc Magma Source	- 155 -
5.1.3	Alkaline Magma Source	- 158 -
5.2	A Petrogenetic Link between the Sub-alkaline and Alkaline Magmas.....	- 163 -
5.3	Magmatic Plumbing System	- 169 -
5.3.1	Insights from Petrological Data.....	- 171 -
5.3.2	Geophysical Data	- 174 -
5.4	Petrogenesis of the CVC Magmas	- 177 -
6	Modelling of Tephra Fallout Deposits.....	- 181 -
6.1	Tephra Dispersal Modelling.....	- 181 -
6.1.1	The Tephra2 model	- 181 -
6.2	Modelling Tephra Dispersion at Volcán de Colima.....	- 189 -
6.2.1	Tephra Thickness Maps.....	- 193 -

6.3	Summary	- 194 -
7	Conclusions.....	- 196 -
7.1	Future Work	- 197 -
Appendix A: Stratigraphical Log.....		- 199 -
Appendix B: Group I Electron Microprobe Mineral Chemistry Data		- 208 -
Appendix C: Sample Preparation Procedure		- 264 -
Appendix D: Geochemical Analytical Methods		- 265 -
Appendix E: Group I Whole-rock Major and Trace Element Data		- 270 -
Appendix F: Sr and Nd Analytical Procedure		- 283 -
Appendix G: Group II Electron Microprobe Mineral Chemistry Data		- 286 -
Appendix H: Group II Whole-rock Major Element and Trace Element Geochemical Data		- 316 -
Appendix I: Cinder Cone Whole-rock Major and Trace Element Data		- 320 -
Appendix J: Granulometry Data		- 327 -
References.....		- 329 -

List of Tables

Table 1.1 Summary table of the characteristics of the CVC eruption deposits.	- 27 -
Table 2.1 Field characteristics of the Group I tephra fallout deposits.	- 33 -
Table 2.2 Mineralogy of pumice and scoria from the Group I plinian tephra fallout deposits observed at the CVC.	- 37 -
Table 2.3 Mineral chemistry of the Group I calc-alkaline basaltic-andesites to high- silica andesites based on EPMA analyses.	- 38 -
Table 2.4 Eruption temperature estimates from pressure and water-dependant thermometers	- 70 -
Table 2.5 Water content estimates for the Group I magmas.	- 71 -
Table 2.6 Ranges of whole-rock major element concentrations in weight % for Group I basalts to high-silica andesites.	- 77 -
Table 2.7 Ranges of whole-rock trace element concentrations in ppm for Group I basalts to high-silica andesites.	- 77 -
Table 2.8 $^{87}\text{Sr}/^{86}\text{Sr}$ and $^{143}\text{Nd}/^{144}\text{Nd}$ isotope ratio compositions for the Group I eruption deposits.	- 87 -
Table 3.1 Field characteristics of the Group II tephra fallout deposits.	- 92 -
Table 3.2 Mineralogy of scoria from the Group II tephra fallout deposits observed at the CVC.	- 96 -
Table 3.3 Mineral chemistry of scoria from the Group II eruption deposits.	- 97 -
Table 3.4 Eruption temperature estimates from pressure and water-dependent thermometers	- 122 -
Table 3.5 Water content estimates for the Group II magmas.	- 122 -
Table 3.6 Ranges of major element concentrations in weight % for Group II basalts to basaltic-andesites.	- 127 -
Table 3.7 Ranges of trace element concentrations in ppm for Group II basalts to basaltic-andesites.	- 127 -
Table 3.8 $^{87}\text{Sr}/^{86}\text{Sr}$ and $^{143}\text{Nd}/^{144}\text{Nd}$ isotope ratios for the Group II basalts to basaltic- andesites.	- 132 -
Table 4.1 Cinder cone composition and ages.	- 137 -
Table 4.2 A subset of whole-rock ICP-MS and XRF analyses for the alkaline cinder cones from Luhr and Carmichael (1981).	- 140 -
Table 4.3 $^{87}\text{Sr}/^{86}\text{Sr}$ and $^{143}\text{Nd}/^{144}\text{Nd}$ isotope data for the alkaline cinder cones (Cai, 2009).	- 144 -
Table 5.1 Comparison of the mineral assemblages of Group I, Group II and alkaline cinder cone pumice and scoria samples.	- 169 -
Table 6.1 Input parameters for the <i>Tephra2</i> inversion.	- 187 -
Table 6.2 Measured thickness and grain size range for units Y, W, U, S and P of the Group I eruption deposits.	- 190 -

Table 6.3 Granulometry data from section VF10-04 (VF95-06 of Luhr et al., 2010),
~10km from the vent. Data from units Y and W were collected by Jim Luhr..... - 190 -

Table 6.4 Input parameters for units Y, W, U, S and P of the Group I eruption
deposits. - 190 -

Table 6.5 Results of tephra dispersion modelling for units Y, W, U, S and P of the
Group I eruption deposits..... - 191 -

List of Figures

Figure 1.1 Schematic tectonic map of western Mexico showing the location of the Colima Volcanic Complex (CVC) modified from Maria and Luhr (2008).	1 -
Figure 1.2 Schematic diagram of the 100-year cyclic activity of Volcán de Colima after Luhr (2002).....	2 -
Figure 1.3 Landsat image of the Colima Volcanic Complex from the United States Geological Survey (USGS).....	4 -
Figure 1.4 Evolution of the CVC.....	6 -
Figure 1.5 Schematic terrane map of Mexico after Gómez-Tuena et al. (2007b).	9 -
Figure 1.6 Simplified schematic diagram of the magmatic evolution of the Trans-Mexican Volcanic Belt (TMVB) after Gómez-Tuena et al. (2007b) and Ferrari et al. (2012).....	11 -
Figure 1.7 Schematic tectonic map of western Mexico showing the location of the Colima Volcanic Complex (CVC) modified from Maria and Luhr (2008).	13 -
Figure 1.8 Simplified geological map of the CVC after Cortés et al. (2010).	14 -
Figure 1.9 Cartoon of the subducting Rivera and Cocos plates beneath the CVC after Yang et al. (2009).	15 -
Figure 1.10 Timeline of eruptions of Volcán de Colima and Paleofuego using data from Bretón González et al. (2002) and calibrated ^{14}C ages.....	17 -
Figure 1.11 Schematic diagram summarising volcanic activity at Volcán de Colima since records began in 1519, using the data from Bretón González et al. (2002)....	18 -
Figure 1.12 Classification of the CVC eruption deposits.	20 -
Figure 1.13 Whole-rock major element variation diagrams for interplinian and plinian eruption deposits of the CVC.....	21 -
Figure 1.14 Sample location map for the Holocene explosive eruption deposits.....	22 -
Figure 1.15 Uncalibrated radiocarbon ^{14}C ages for the explosive plinian CVC eruption deposits (Komorowski et al 1997; Luhr et al. 2010).	23 -
Figure 1.16 Composite stratigraphic section and field photographs of explosive eruption deposits exposed in road-cuts on the flanks of Nevado de Colima.	24 -
Figure 1.17 Classification of the interplinian and plinian CVC eruption deposits based on the classification of altered volcanic rocks of Hastie et al. (2007).	25 -
Figure 1.18 Time plots showing the variations in whole-rock major element geochemistry for the CVC eruption deposits over the past 30,000 years.	26 -
Figure 1.19 Incompatible whole-rock trace element abundances normalised to N-MORB and REE normalised to Chondrite for the CVC eruption deposits.	28 -
Figure 2.1 Location map for units U to Y and stratigraphic sections where units U to Y have been identified.	34 -
Figure 2.2 Field photograph and stratigraphic log of units U to Y from section VF10-01.	35 -
Figure 2.3 Feldspar ternary classification diagram after Deer et al. (1992).	39 -

Figure 2.4 Ranges of core and rim compositions of plagioclase from the Group I deposits versus eruption age in yrs B.P.	39 -
Figure 2.5 Optical microscope and SEM backscatter (BSE) images of clinopyroxene crystals in the Group I eruption deposits.	40 -
Figure 2.6 Classification of Ca-Mg-Fe clinopyroxenes after Morimoto (1988).....	40 -
Figure 2.7 Clinopyroxene core and rim Mg# for the Group I eruption deposits.	41 -
Figure 2.8 Classification of orthopyroxenes after Morimoto (1988).....	41 -
Figure 2.9 Range of core and rim Mg# in orthopyroxene for the Group I eruption deposits.	42 -
Figure 2.10 BSE images of hornblende phenocrysts.	43 -
Figure 2.11 Classification of calcic amphiboles after Leake et al. (1997).....	44 -
Figure 2.12 Backscatter SEM images of olivine.	45 -
Figure 2.13 Ranges of core and rim Mg# in olivine for the Group I eruption deposits...-	46 -
Figure 2.14 Range in SiO ₂ content of groundmass glass in scoria and pumice samples from the Group I eruption deposits versus eruption age in yrs B.P.	47 -
Figure 2.15 Scanned thin section of a streaky pumice clast from unit Y (VF97-06D). ...-	47 -
Figure 2.16 BSE images of types I, II and III plagioclase phenocrysts.	49 -
Figure 2.17 BSE images of types IV to VII of plagioclase present in Group I eruption deposits.	50 -
Figure 2.18 Oscillatory zoned plagioclase from Group I samples.....	51 -
Figure 2.19 Schematic diagram of the seven types of plagioclase identified in the Group I eruption deposits with descriptions and interpretations of their zoning patterns.....	53 -
Figure 2.20 Schematic diagram showing the possible crystallisation history of plagioclase phenocrysts.	54 -
Figure 2.21 BSE images and EPMA analyses of type I clinopyroxene.....	55 -
Figure 2.22 BSE images of type II clinopyroxene phenocrysts.....	56 -
Figure 2.23 Schematic diagram of the two types of clinopyroxene identified in the Group I eruption deposits with descriptions and interpretations of their zoning patterns.....	57 -
Figure 2.24 Cartoon of the crystallisation of clinopyroxene phenocrysts in the Group I magmas.....	58 -
Figure 2.25 BSE images and EPMA analyses of type I orthopyroxene.	59 -
Figure 2.26 BSE images and EPMA analyses of types II, III and IV orthopyroxene phenocrysts.	60 -
Figure 2.27 Schematic illustration of the four types of orthopyroxene phenocryst found in scoria and pumice from the Group I eruption deposits	61 -
Figure 2.28 Cartoon showing a possible crystallisation history of the types I to IV orthopyroxene phenocrysts.	62 -

Figure 2.29 BSE images and EPMA core-rim profile of hornblende from Group I samples.	- 63 -
Figure 2.30 Schematic diagram linking orthopyroxene (opx), clinopyroxene (cpx), plagioclase (plag) and hornblende (hbd) zoning patterns and textures.	- 65 -
Figure 2.31 Equilibrium tests for mineral-melt and mineral-mineral pairs.	- 73 -
Figure 2.32 Estimated eruption temperatures (a) and water contents (b) for the Group I eruption deposits.	- 74 -
Figure 2.33 Total Alkalis-Silica (TAS) diagram for the Group I eruption deposits, after Le Maitre et al. (2002).	- 76 -
Figure 2.34 Major element oxide variation diagrams.	- 78 -
Figure 2.35 Major element variation diagrams, with the main mineral phase compositions plotted based on average EPMA analyses.	- 79 -
Figure 2.36 Group I trace element concentrations (in ppm) against SiO ₂ content (in weight %).	- 80 -
Figure 2.37 Schematic N-MORB normalised multi-element plot for a typical subduction-related magma.	- 81 -
Figure 2.38 Cartoon of a cross-section of a subduction zone.	- 82 -
Figure 2.39 N-MORB normalised multi-element abundance plot for the Group I eruption deposits.	- 83 -
Figure 2.40 Chondrite normalised rare earth element (REE) abundance patterns for the Group I eruption deposits.	- 84 -
Figure 2.41 ¹⁴³ Nd/ ¹⁴⁴ Nd versus ⁸⁷ Sr/ ⁸⁶ Sr diagram showing the mantle reservoirs of Zindler and Hart (1986).	- 86 -
Figure 2.42 Variation of ⁸⁷ Sr/ ⁸⁶ Sr (a) and ¹⁴³ Nd/ ¹⁴⁴ Nd (b) with SiO ₂ content for the Group I eruption deposits.	- 88 -
Figure 2.43 ¹⁴³ Nd/ ¹⁴⁴ Nd versus ⁸⁷ Sr/ ⁸⁶ Sr diagram showing the relation of the Group I CVC magmas to the mantle reservoirs as defined by Zindler and Hart (1986).	- 89 -
Figure 2.44 ¹⁴³ Nd/ ¹⁴⁴ Nd versus ⁸⁷ Sr/ ⁸⁶ Sr diagram showing the CVC group I samples.	- 90 -
Figure 3.1 Google Earth map of the eastern side of Volcán de Colima and Nevado de Colima showing the section locations.	- 93 -
Figure 3.2 Stratigraphic log from section VF01-02.	- 94 -
Figure 3.3 Feldspar ternary classification diagram after Deer et al. (1992) for units N, F and D of the Group II eruption deposits.	- 98 -
Figure 3.4 Ranges of core and rim anorthite (An mol%) composition of plagioclase phenocrysts for the Group II eruption deposits.	- 99 -
Figure 3.5 Classification of clinopyroxenes in Group II scoria samples in the pyroxene quadrilateral after Morimoto (1988).	- 99 -
Figure 3.6 Ranges of Mg# in cores and rims of clinopyroxenes from the Group II eruption deposits.	- 100 -
Figure 3.7 Ca-Mg-Fe classification diagram for orthopyroxenes after Morimoto (1988).	- 100 -

Figure 3.8 Ranges of orthopyroxene core and rim Mg# for units N and D of Group II. -	101 -
Figure 3.9 Backscatter SEM images of hornblende from Group II samples.	102 -
Figure 3.10 Classification of calcic-amphiboles with $(Na+K)_A > 0.5$ after Leake et al. (1997).....	102 -
Figure 3.11 Backscatter SEM images of olivine phenocrysts from sample VF00-06O from unit D.	103 -
Figure 3.12 Ranges of olivine core and rim Mg# in the Group II eruption deposits.	103 -
Figure 3.13 Backscatter SEM images of fibrous phlogopite from the Group II samples.	104 -
Figure 3.14 Ranges of glass SiO ₂ content of the Group II scoria samples.	105 -
Figure 3.15 Backscatter SEM images of types I to III plagioclase phenocrysts observed in the Group II eruption deposits.....	107 -
Figure 3.16 Backscatter SEM images of types IV and V plagioclase from sample VF01-02Ns and VF00-06O from unit D.....	108 -
Figure 3.17 Backscatter SEM image and core-rim EPMA analyses for type VI and VII plagioclase from the Group II eruption deposits.	109 -
Figure 3.18 Schematic diagram of the seven types of plagioclase zoning observed in the Group II eruption deposits, including descriptions and interpretations.	110 -
Figure 3.19 Cartoon showing the possible crystallisation history of plagioclase phenocrysts within the Group II magmas involving multiple decompression and magma replenishment and mixing events	111 -
Figure 3.20 BSE images for types I and II clinopyroxene from the Group II eruption deposits.	112 -
Figure 3.21 BSE images and EPMA core-rim analyses of types III and IV clinopyroxene from Group II.	113 -
Figure 3.22 Backscatter SEM images of type V clinopyroxene phenocrysts from Group II.	113 -
Figure 3.23 Schematic diagram showing the five types of clinopyroxene phenocrysts observed in the Group II eruption deposits with descriptions and interpretations.	114 -
Figure 3.24 Cartoon showing the possible complex crystallisation history of clinopyroxene phenocrysts within the Group II magmas involving multiple magma replenishment and mixing events.....	115 -
Figure 3.25 Backscatter SEM images of the two types of hornblende phenocrysts from Group II.....	116 -
Figure 3.26 Core-rim variation in Mg# for type I and II hornblende phenocrysts from Group II.	117 -
Figure 3.27 BSE images of the groundmass glass from Group II scoria.....	118 -
Figure 3.28 Schematic diagram linking olivine (OL), clinopyroxene (CPX), plagioclase (PLAG) and hornblende (HBD) zoning patterns and mineral chemistry.....	120 -

Figure 3.29 Equilibrium tests for mineral-melt and mineral-mineral pairs.	123 -
Figure 3.30 Estimated eruption temperatures for the Group II deposits.	124 -
Figure 3.31 Estimated water contents for the Group II eruption deposits.	125 -
Figure 3.32 Total alkalis-silica (TAS) diagram after Le Maitre et al. (2002) for the Group II eruption deposits.	126 -
Figure 3.33 Major element variation diagrams for the Group II eruption deposits.	128 -
Figure 3.34 K ₂ O (a) and MgO (b) variation with SiO ₂ showing the control of the main mineral phases on the chemical trends.	129 -
Figure 3.35 Compatible trace element variations with SiO ₂ for the Group II eruption deposits.	130 -
Figure 3.36 N-MORB normalised trace element (a) and Chondrite normalised REE (b) abundance patterns for the Group II eruption deposits.	131 -
Figure 3.37 ⁸⁷ Sr/ ⁸⁶ Sr and ¹⁴³ Nd/ ¹⁴⁴ Nd versus SiO ₂ content (a and b) and 1/Sr (c) and 1/Nd (d) for the Group II eruption deposits.	133 -
Figure 3.38 ⁸⁷ Sr/ ⁸⁶ Sr versus ¹⁴³ Nd/ ¹⁴⁴ Nd for the CVC eruption deposits.	134 -
Figure 4.1 High resolution Landsat image of the CVC.	136 -
Figure 4.2 Total alkalis-silica (TAS) diagram after Le Maitre et al. (2002) for the cinder cone magmatic rocks.	138 -
Figure 4.3 Mineral assemblages of the basanite to minette series after Luhr and Carmichael (1981).	139 -
Figure 4.4 Whole-rock major element variation diagrams for the cinder cone magmatic rocks.	141 -
Figure 4.5 Compatible whole-rock trace elements, Cr and Ni versus SiO ₂ for the cinder cone magmas.	143 -
Figure 4.6 N-MORB normalised trace element and Chondrite-normalised REE abundance diagrams for the alkaline cinder cone magmas.	143 -
Figure 4.7 ⁸⁷ Sr/ ⁸⁶ Sr and ¹⁴³ Nd/ ¹⁴⁴ Nd versus SiO ₂ for the alkaline cinder cone magmas.	144 -
Figure 4.8 ⁸⁷ Sr/ ⁸⁶ Sr versus ¹⁴³ Nd/ ¹⁴⁴ Nd for the alkaline cinder cones.	145 -
Figure 4.9 La/K versus La (ppm) showing the control of residual phlogopite in the source during partial melting after Vigouroux et al. (2008).	146 -
Figure 4.10 Cartoon of a subduction zone showing the model for the formation of the alkaline cinder cones involving metasomatism of the mantle wedge.	147 -
Figure 4.11 Simplified map of the western TMVB.	148 -
Figure 4.12 Cartoon of the subduction erosion model after von Huene et al. (2004).	150 -
Figure 5.1 (a) ⁸⁷ Sr/ ⁸⁶ Sr versus ¹⁴³ Nd/ ¹⁴⁴ Nd isotope diagram and (b) ¹⁴³ Nd/ ¹⁴⁴ Nd versus SiO ₂ for the Group I samples and SAY-22E.	154 -
Figure 5.2 Trace element ratio plots showing source enrichments after Vigouroux et al. (2008).	155 -
Figure 5.3 Ti/Y versus Nb/Y variation diagram after Vigouroux et al. (2008) with the CVC Group I, Group II and alkaline cinder cone data.	156 -

Figure 5.4 Incompatible trace element ratio plots for the CVC magmas.	157 -
Figure 5.5 $^{87}\text{Sr}/^{86}\text{Sr}$ versus $^{143}\text{Nd}/^{144}\text{Nd}$ isotope diagram showing simple mixing lines between the mantle wedge composition of Gomez-Tuena et al. (2007a) and orthogneiss and pyroxene granulite lower-crustal xenoliths.....	159 -
Figure 5.6 Trace elements ratio plots showing the control of residual garnet in the source.....	160 -
Figure 5.7 Cartoon of the formation of mélangé diapirs in subduction zones modified for the CVC after Marschall and Schumacher (2012).	162 -
Figure 5.8 Whole-rock major element K_2O (a) and P_2O_5 (b) variation with SiO_2 showing the relationship between the Group I and Group II eruption deposits and the alkaline cinder cone samples.....	164 -
Figure 5.9 Whole-rock major element K_2O (a) and P_2O_5 (b) variation with SiO_2 showing mixing lines between end-member compositions after Langmuir et al. (1978).....	165 -
Figure 5.10 (a) $^{87}\text{Sr}/^{86}\text{Sr}$ and (b) $^{143}\text{Nd}/^{144}\text{Nd}$ variation with SiO_2 showing possible mixing lines between calc-alkaline and alkaline end-member compositions.	166 -
Figure 5.11 A simple mixing between the end member magmas on a $^{87}\text{Sr}/^{86}\text{Sr}$ versus $^{143}\text{Nd}/^{144}\text{Nd}$ plot.....	167 -
Figure 5.12 An N-MORB normalised trace element abundance diagram showing trace element patterns produced by mixing between sub-alkaline (Group I; grey field) and alkaline magmas (pale yellow field).....	168 -
Figure 5.13 Cartoon of the hot zone model of Annen et al. (2006).....	171 -
Figure 5.14 Cartoon of the magmatic plumbing system of the CVC based on the interpretation of the petrological data.	172 -
Figure 5.15 2¾ dimension magnetic model along a section through the north-south trending anomalies beneath Volcán de Colima and Nevado de Colima modified from López-Loera (2012).	174 -
Figure 5.16 The low-velocity isosurface plot from the tomography results from Gardine (2010).....	176 -
Figure 5.17 Cartoon of the petrogenesis of the CVC magmas.	180 -
Figure 6.1 Schematic diagram of the mass conservation equation.....	182 -
Figure 6.2 Schematic diagram describing the distribution of tephra mass within the eruption column.	183 -
Figure 6.3 Schematic diagram showing particle fall and transport through the layers...-	184 -
Figure 6.4 Schematic diagram showing the Gaussian distribution of particles within each layer.	185 -
Figure 6.5 Grain size distribution for units Y, W, U, S and P at section VF10-04 using the data in Table 6.3.	190 -
Figure 6.6 Eruption column height box plot.....	192 -
Figure 6.7 Total erupted mass (kg) boxplot of the results of modelling for units Y, W, U, S and P of the Group I eruption deposits.	193 -

Figure 6.8 Tephra thickness maps for units Y, W and S of the Group I eruption
deposits. - 194 -

Figure 7.1 Petrogenesis of the CVC magmas. - 196 -

1 Introduction

Volcán de Colima, the youngest vent of the Colima Volcanic Complex (CVC) situated in western Mexico (Figure 1.1), is considered one of North America's most active volcanoes (Cortés et al., 2010; Luhr et al., 2010). Between 2009 and 2011, Volcán de Colima erupted up to 11 times per day, producing small (<200m high) gas and ash clouds (Navarro-Ochoa personal communication). Historical activity is characterised by andesitic lava dome growth with numerous small, degassing eruptions, punctuated by larger explosive events (ash clouds up to 600 m above the vent) causing partial dome collapse and block-and-ash flows (Luhr and Carmichael, 1980; Medina-Martínez, 1983; Robin et al., 1987; Luhr and Carmichael, 1990b). Approximately every decade Volcán de Colima experiences vulcanian-type eruptions, producing ash clouds up to 12 km above the vent, and pyroclastic block-and-ash flows that travel up to 5 km from the vent (Robin et al., 1991; Luhr, 2002; Savov et al., 2008).

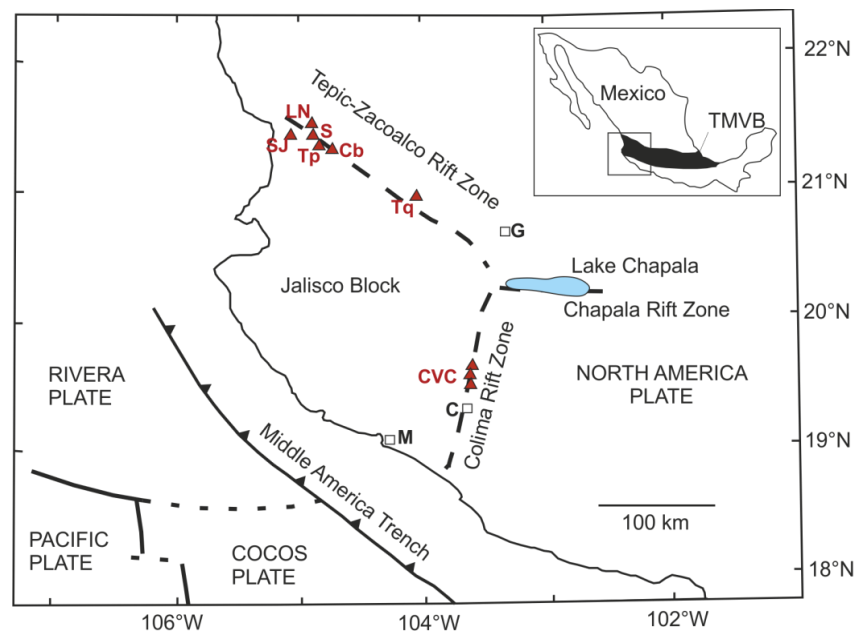


Figure 1.1 Schematic tectonic map of western Mexico showing the location of the Colima Volcanic Complex (CVC) modified from Maria and Luhr (2008).

CVC is located in the Trans-Mexican Volcanic Belt (TMVB) within the Colima Rift Zone. Also shown are the Chapala and Tepic-Zacoalco Rift (TZR) Zones. The volcanoes in the TZR are: Tq = Volcán Tequila; Cb = Volcán Ceboruco; Tp = Volcán Tepetitlic; S = Volcán Sanganguey; LN = Las Navajas; and SJ = Volcán San Juan. The cities are: G = Guadalajara; C = Colima; and M = Manzanillo.

An approximately 100-year cyclicity of highly explosive, sub-plinian to plinian, events has also been documented at Volcán de Colima (Luhr, 2002). The last of these occurred in 1913, and

prior to that, in 1818 (Bretón González et al., 2002). The cycle proposed by Luhr (2002) is shown in Figure 1.2, which begins with the destroyed cone, resulting from the explosive sub-plinian to plinian event (Stage 1). The cycle then proceeds through a ~50 year phase of apparent inactivity while magma rises within the conduit (Stage 2), followed by effusive lava dome growth and lava flows spilling down the flanks of Volcán de Colima (Stage 3). Activity then becomes more explosive with abundant vulcanian style explosions (stage 4), which lead up to the stage 5 highly explosive plinian eruption.

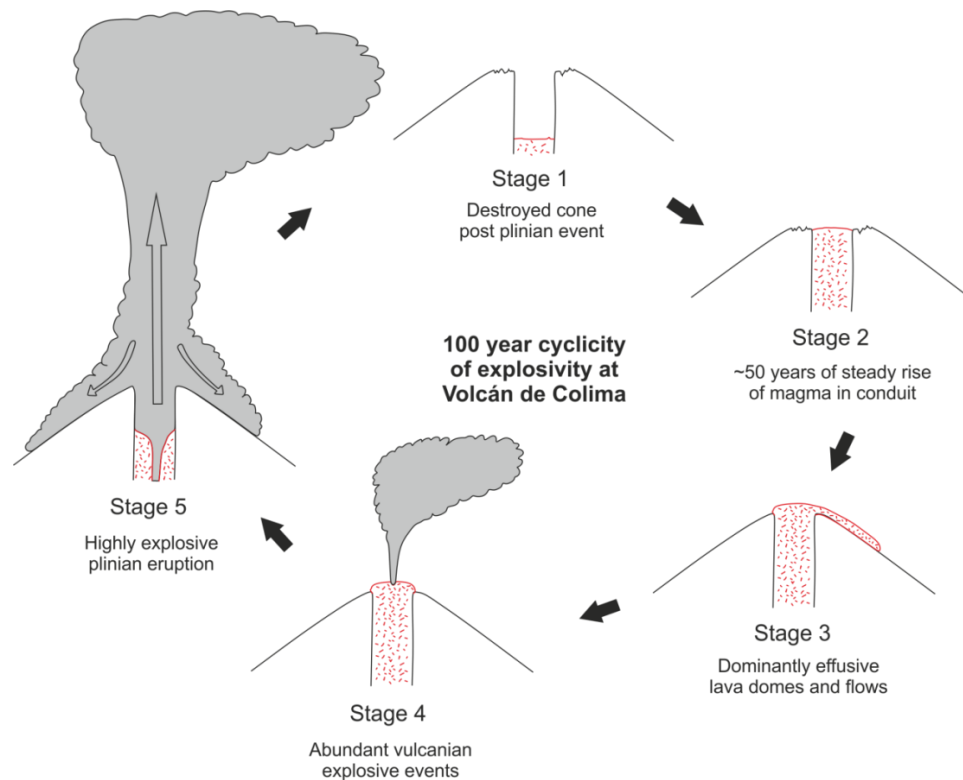


Figure 1.2 Schematic diagram of the 100-year cyclic activity of Volcán de Colima after Luhr (2002).

Stage 1 is the emptied conduit, post Plinian eruption and Stage 2 is the phase of magma growth within the conduit lasting ~50 years. During Stage 3, the magma rises and overflows the crater wall; Stage 4 represents the presence of a lava dome with abundant small vulcanian explosions; and stage 5 is the final, cycle ending, highly explosive phase

The majority of studies on Volcán de Colima have focused on the current phase of activity, with petrological and geochemical studies of the 1913 eruption deposit, and post-1913 effusive and vulcanian eruptive products (Thorpe et al., 1977; Luhr and Carmichael, 1980; Medina-Martínez, 1983; Robin et al., 1987; Luhr and Carmichael, 1990b; Robin et al., 1991; De la Cruz-Reyna, 1993; Luhr, 1993; Robin and Potrel, 1993; Richter, 2000; Luhr, 2002; Navarro-Ochoa et al., 2002; Saucedo et al., 2005; Atlas et al., 2006; Luhr et al., 2006; Reubi and Blundy, 2008; Savov et al., 2008; Saucedo et al., 2010). However, exposed in road cuts on the flanks of the nearby

extinct Nevado de Colima are deposits of numerous highly explosive eruptions comprising tephra fallout and ash-rich surges (Luhr et al., 2010). Radiocarbon dating of charcoal fragments found within these deposits reveals an explosive history of Volcán de Colima spanning the last 30,000 years (Komorowski et al., 1997; Luhr et al., 2010). These deposits are largely unstudied and poorly understood, with only two published papers, the first by Luhr and Carmichael (1982), and a second more detailed study by Luhr et al. (2010). Many of the current and recent studies on Volcán de Colima are concerned with forecasting future activity and monitoring current activity; however, few of these studies consider the volcano's explosive past, or patterns of activity which may emerge from a better understanding of the explosive Holocene (and late Pleistocene) eruption deposits.

This work incorporates, and expands upon the work of Luhr et al. (2010), focusing on the stratigraphic relationships of the Holocene eruption deposits, and the petrological and geochemical evolution of the erupted magmas during the past 13,000 years. Recent geophysical studies have imaged a potential magma storage region beneath Volcán de Colima at ~5 km depth and another potential deeper storage region at 15 to 30 km depth (Gardine, 2010; López-Loera, 2012). Detailed petrological and geochemical investigations of the erupted tephra fallout deposits are presented here, which, combined with the geophysical data, are used to define the nature of the magmatic plumbing system beneath the CVC.

1.1 The Colima Volcanic Complex

Since activity began at the CVC at approximately 1.7 Ma, volcanism has migrated south through four volcanic centres: Volcán Cántaro, Nevado de Colima, Paleofuego de Colima (Paleofuego) and Volcán de Colima (Figure 1.3; Luhr and Carmichael, 1990a). Magmatism has become less evolved with time, with Volcán Cántaro in the north comprising predominantly dacites, while the currently active Volcán de Colima is dominantly basaltic-andesite in composition (Luhr and Carmichael, 1990a).

The total estimated volume of the CVC volcanic apron is ~490 km³, comprising andesitic lava flows, debris avalanche deposits, lahar and pyroclastic flow and fall deposits (Cortés et al., 2005; Cortés et al., 2010). The evolution of the Nevado de Colima and Paleofuego volcanoes has been governed by numerous gravitational collapse events (Figure 1.4) partially destroying the edifices and leaving remnant caldera structures open to the south, southeast and southwest (Robin et al., 1987; Luhr and Prestegard, 1988; Luhr and Carmichael, 1990a; Stoopes and Sheridan, 1992; Komorowski et al., 1997; Cortés et al., 2005; Cortés et al., 2009; Cortés et al., 2010). The last of these events destroyed the Paleofuego edifice leaving a semicircular caldera in which the cone of the currently active Volcán de Colima resides (Cortés et al., 2010).

To the east and west of Volcán Cántaro are monogenetic cinder cones of alkaline lamprophyre (Figure 1.3; Luhr and Carmichael, 1981). These erupted contemporaneously with the andesites of Nevado de Colima (Figure 1.4; Allan and Carmichael, 1984; Allan, 1986; Robin et al., 1987; Luhr and Carmichael, 1990a).

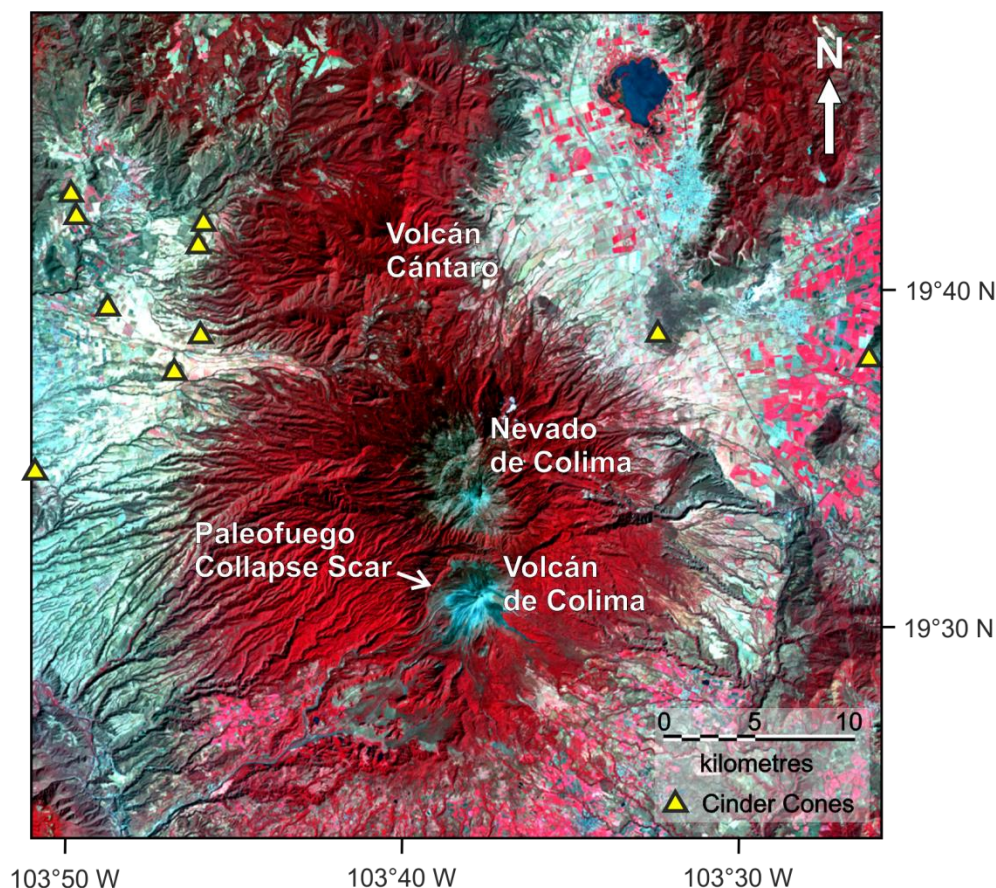


Figure 1.3 Landsat image of the Colima Volcanic Complex from the United States Geological Survey (USGS).

Red areas are forested areas, pink areas are farmland and blue areas are unvegetated. Volcán Cántaro in the north is the oldest volcanic centre, with Nevado, Paleofuego and Volcán de Colima to the south. The edge of the caldera wall of Paleofuego can be made out, in which Volcán de Colima resides (Luhr and Carmichael, 1990a; Komorowski et al., 1997).

1.1.1 *Volcán Cántaro*

An eroded composite volcano, Volcán Cántaro has an elevation of 2800m above sea-level (a.s.l.) and is characterised by prominent andesite to dacite domes in the northern part of the CVC (Figure 1.3; Luhr and Carmichael, 1990a). The stratigraphy of Volcán Cántaro comprises sequences of intercalated lava flows and pyroclastic flow and fall deposits (Luhr and Carmichael, 1990a; Cortés et al., 2010). These deposits are high-silica andesites and dacites, which are strongly porphyritic with biotite and plagioclase phenocrysts of up to 1cm (Luhr and

Carmichael 1990a). K-Ar dating of Volcán Cántaro rocks has yielded ages of 1.66 ± 0.24 Ma, 1.52 ± 0.20 Ma, 1.33 ± 0.20 Ma and 0.95 ± 0.17 Ma (Allan, 1986). The Volcán Cántaro sequences cover an area of 107 km^2 with an estimated volume of 71 km^3 (Cortés et al., 2010). Deposits from Volcán Cántaro are interfingering with Nevado de Colima deposits in the south indicating contemporaneous activity at these volcanic centres (Cortés et al., 2010).

1.1.2 Nevado de Colima

At approximately 0.53 Ma, activity began 15 km to the southeast of Volcán Cántaro at Nevado de Colima with the emission of andesitic lava flows (Robin et al., 1987; Luhr and Carmichael, 1990a; Cortés et al., 2005; Cortés et al., 2010). Activity continued throughout the Pleistocene, evolving through six eruptive episodes, represented by at least four sector collapse events, followed by the construction of new edifices (Figure 1.4; Cortés et al., 2010). The last of these occurred at ca. 18,500 years before present (yrs B.P.), which produced a debris avalanche deposit that is exposed at the Pacific coast, some 120 km from Nevado de Colima (Stoopes and Sheridan, 1992). Stoopes and Sheridan (1992) concluded that this was a huge debris avalanche that travelled the 120 km to the coast. However, later studies showed that it is more likely that the deposit travelled ~25 km to the Naranjo River where it dammed the river (Capra and Macias, 2002). This created a lake that eventually overflowed, bursting the dam, resulting in a giant debris flow (Capra and Macias, 2002). The final phase of activity at Nevado de Colima was the construction of the present summit dome, El Picacho, 4320m a.s.l. (Luhr and Carmichael, 1990a).

The stratigraphy of the Nevado de Colima deposits comprises a sequence of andesitic lava flows and pyroclastic flow and fall deposits, debris-flow deposits and debris avalanche deposits (Robin et al., 1987). Within these sequences a series of lahars and fluvial deposits, which make up the Atenquique Formation, were emplaced along ravines to the southeast and southwest of Volcán de Colima (Robin et al., 1987; Luhr and Carmichael, 1990a; Cortés et al., 2005). Robin et al. (1987) report maximum ages of 0.38 and 0.26 Ma for the Atenquique Formation, based on K-Ar dating of andesitic blocks from an overlying debris avalanche deposit. The Nevado de Colima deposits cover an area of approximately 300 km^2 and have a total estimated volume of 334 km^3 (Cortés et al., 2010). Luhr and Carmichael (1990) previously estimated a total volume of 450 km^3 .

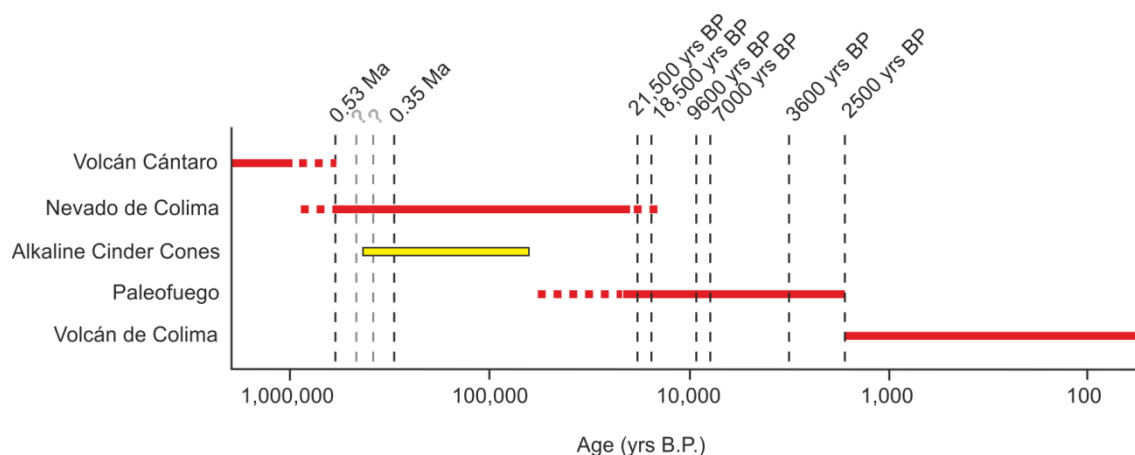


Figure 1.4 Evolution of the CVC.

Activity began at Volcán Cántaro at ~1.7 Ma, and continues today at Volcán de Colima. Nevado de Colima and Paleofuego each evolved through numerous edifice construction and gravitational collapse events, as shown by the dashed lines. Ages next to the dashed lines are debris avalanche deposits and lava flows that have been dated through ^{14}C techniques and K-Ar dating, respectively (Allan, 1986; Komorowski et al., 1997; Cortés et al., 2010). The ages of two of the collapse events of Nevado de Colima are unknown (grey dashed lines; Cortés et al., 2010).

1.1.3 *Paleofuego de Colima*

The formation of Paleofuego, ~5 km to the south of Nevado de Colima, began during the late Pleistocene, ~50,000 yrs B.P. (Figure 1.4; Robin et al., 1987; Cortés et al., 2005). Five collapse events have been associated with Paleofuego which have been dated at 2550 ± 110 , 3600 ± 120 , 7040 ± 160 , 9671 ± 88 and $18,520 \pm 260$ yrs B.P. (Luhr and Prestegard, 1988; Stoopes and Sheridan, 1992; Komorowski et al., 1997; Cortés et al., 2005; Cortés et al., 2009; Cortés et al., 2010). There is some discrepancy in the literature as to the source of the 18,500 yrs B.P. debris avalanche deposit. Stoopes and Sheridan (1992) associate the deposit with the last collapse event of Nevado de Colima, while Cortes et al. (2010) are not clear on the source as they discuss this event in relation to both the Nevado de Colima and Paleofuego volcanoes. Despite this confusion it is clear the two centres were contemporaneously active, with debris flow and yellow ash deposits from Nevado de Colima overlying 20 – 30m thick lava flows of Paleofuego (Cortés et al., 2010). To the southwest of Volcán de Colima, Paleofuego lavas are up to 20m thick with a 5m thick basal breccia (Luhr and Carmichael, 1990a; Cortés et al., 2005; Cortés et al., 2010). Underlying these lavas is a 20m thick debris avalanche deposit, interpreted as resulting from the fourth collapse of Nevado de Colima (Cortés et al., 2010).

The Paleofuego debris avalanche deposits contain angular blocks of porphyritic andesite, rich in plagioclase, and scoria with phlogopite phenocrysts hosted within a sandy-silty matrix (Cortés et al., 2010). The andesitic blocks are typically 10 to 30cm in diameter, but can reach up to 10m

in diameter (Cortés et al., 2010). The city of Colima is built on the c.7000 and c.18,500 yrs B.P. debris avalanche deposits (Cortés et al., 2005; Cortés et al., 2010).

The last collapse event of Paleofuego at ~2500 yrs B.P. produced a caldera 5 km in diameter, the escarpment of which forms a horseshoe shape open to the south (Allan, 1986; Luhr and Prestegard, 1988; Stoopes and Sheridan, 1992; Komorowski et al., 1997; Cortés et al., 2005; Cortés et al., 2010). The caldera wall exposes alternating andesitic lava flows and block-and-ash flow deposits with a total thickness of 350m (Cortés et al., 2010). The area covered by the Paleofuego lavas and block-and-ash flow deposits is estimated at ~70 km² with a volume of ~79 km³ (Cortés et al., 2010). It is estimated that the summit of Paleofuego was higher than Volcán de Colima with a height of ~4100 m a.s.l. (Luhr and Carmichael, 1990a).

1.1.4 Volcán de Colima

The currently active Volcán de Colima is situated inside the caldera left by the last collapse of Paleofuego (Figure 1.3). Luhr and Carmichael (1990) suggested that the cone is offset to the south of the presumed centre of the Paleofuego cone based on the presence of the prominent caldera wall to the north, which is buried in the south and east by young lava flows of Volcán de Colima. Volcán de Colima is a stratovolcano constructed of basaltic-andesite and andesite lava flows and pyroclastic flow and fall deposits, with a height of 3860m a.s.l. According to Cortes et al. (2010), the edifice currently covers an estimated area of 20 km² and has a volume of 9 km³. Luhr and Carmichael (1990) estimated a total volume of 10 km³.

1.1.5 Monogenetic Cinder Cones

To the east and west of Volcán Cántaro, eleven cinder cones erupted on the rift floor between 1.2 Ma and 62 Ka (Luhr and Carmichael, 1981; Allan and Carmichael, 1984; Carmichael et al., 2006). The two oldest cones erupted at 1.2 Ma and 0.5 Ma, producing <0.003 km³ of sub-alkaline basalt and basaltic-andesite (Luhr and Carmichael, 1981; Allan and Carmichael, 1984; Carmichael et al., 2006). Nine of the cinder cones are alkaline, producing ~1.3 km³ of magma between 450 ka and 62 ka (Figure 1.4; Luhr and Carmichael, 1981; Allan and Carmichael, 1984; Carmichael et al., 2006). The majority of the alkaline mafic magmas (>99%) erupted between 240 ka and 60 ka. During this time, volcanism was ongoing at the Nevado de Colima volcano (Robin et al., 1987; Luhr and Carmichael, 1990a; Cortés et al., 2005; Cortés et al., 2010).

The alkaline cinder cones were first described by Luhr and Carmichael (1981), who classified them as primitive basanites to minette lamprophyres with 47.6 – 50.3 wt.% SiO₂, 7.4 – 15.3 wt.% MgO and 2.5 – 4.4 wt.% K₂O. These distinctive high-K primitive magmas all have characteristic subduction-related trace element abundance patterns with enriched Large Ion Lithophile Elements (LILE: Ba, K, Sr) relative to High Field Strength Elements (HFSE: Ta, Nb,

Hf, Ti; Luhr and Carmichael, 1981; Carmichael et al., 2006; Maria and Luhr, 2008; Vigouroux et al., 2008; Cai, 2009). The occurrence and source of the alkaline magmas is discussed in detail in the geological literature (Luhr and Carmichael, 1981; Wallace and Carmichael, 1989; Lange and Carmichael, 1990; Luhr, 1997; Carmichael et al., 2006; Maria and Luhr, 2008; Vigouroux et al., 2008; Cai, 2009); however, the relationship between the sub-alkaline and the alkaline magmas is still poorly understood. A detailed review on the published geochemical and isotopic data for the alkaline cinder cones is presented in Chapter 4, along with a description of the models for the source of these distinct magmas.

1.2 Geological History of the Colima Volcanic Complex

The CVC is situated at the western end of the Trans-Mexican Volcanic Belt (TMVB), approximately 100 km from the Pacific coast (Figure 1.1). The TMVB is an ~1000 km long, ~80 to 230 km wide, continental magmatic arc comprising over 8000 volcanic centres stretching across central Mexico in an east-west orientation (Gómez-Tuena et al., 2007b). The arc has been described as one of the most complex and magmatically diverse convergent margins on the planet (Gómez-Tuena et al., 2007b). The TMVB has evolved through four stages of mafic, intermediate and silicic volcanism since the mid-Miocene, which have migrated away from, and later, towards the Middle America Trench (MAT; Gómez-Tuena et al., 2007b). This complexity is a result of a number of factors: the subduction of the Rivera and Cocos plates at different rates and varying angles; an extensional regime in the overriding plate; a continental basement of varying composition, age and thickness; and a heterogeneous mantle wedge that has been altered to varying degrees by subduction-related processes (Gómez-Tuena et al., 2007b).

1.2.1 The Basement Geology of the Trans-Mexican Volcanic Belt

The TMVB is superimposed on a basement of Precambrian and Palaeozoic terranes in the eastern part, and the Mesozoic Guerrero terrane in the western part of Mexico (Figure 1.5; Campa and Coney, 1983; Centeno-García et al., 1993; Mendoza and Suastegui, 2000; Dickinson and Lawton, 2001; Gómez-Tuena et al., 2007b). The Guerrero terrane comprises a series of Jurassic to Cretaceous volcanic arcs accreted to the Mexican mainland in the early Cretaceous (Campa and Coney, 1983; Mendoza and Suastegui, 2000; Dickinson and Lawton, 2001; Mukasa et al., 2007). The tectonostratigraphy of the Guerrero terrane was first described by Campa and Coney (1983), who divided it into three subterrane forming north-south trending belts (Figure 1.5): the easternmost Teloloapan subterrane comprising arc volcanics and related sedimentary rocks; the central Arcelia-Palmer Chico subterrane comprising pillow basalts overlain by sedimentary rocks; and the westernmost Zihuatanejo-Huetamo subterrane which lies

along the Pacific coast, underlying the CVC (Campa and Coney, 1983; Mendoza and Suastegui, 2000).

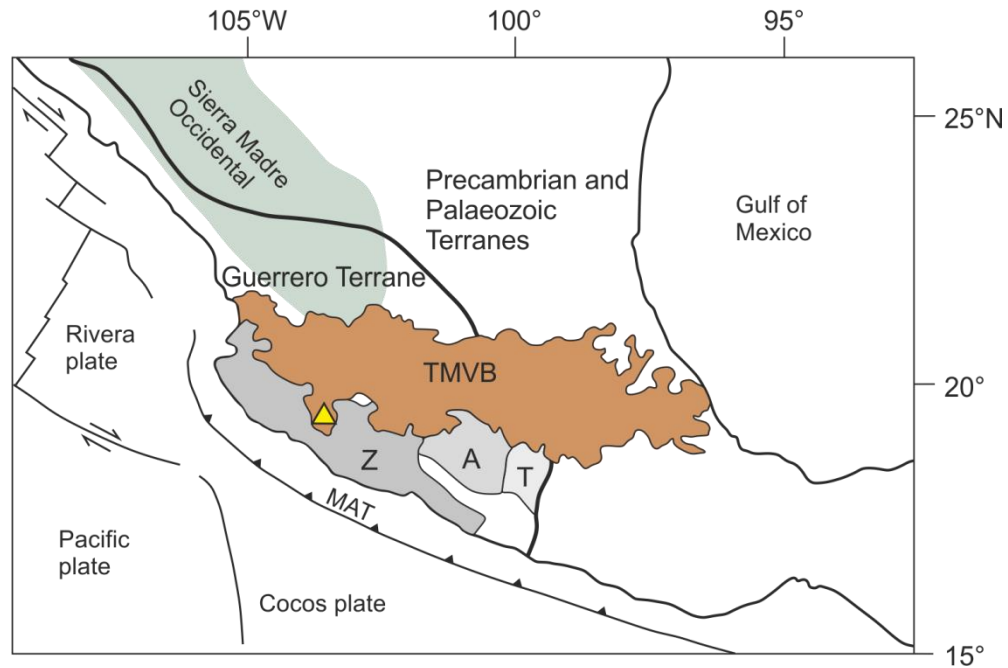


Figure 1.5 Schematic terrane map of Mexico after Gómez-Tuena et al. (2007b).

The Trans-Mexican Volcanic Belt (TMVB) crosses the Precambrian and Palaeozoic terranes of eastern Mexico and the Guerrero terrane of western Mexico. The Guerrero terrane comprises the Telaloapan (T), Arcelia-Palmer Chico (A) and Zihuatanejo-Huetamo (Z) subterrane. The yellow triangle marks the location of the CVC in the western end of the TMVB. MAT = Middle America Trench.

The Zihuatanejo-Huetamo subterrane comprises three sequences that represent an evolved island-arc and basin complex of late Jurassic to early Cretaceous age built on previously deformed basement (Mendoza and Suastegui, 2000). Underlying the CVC is the early Cretaceous Zihuatanejo sequence; a volcanic arc succession of >1500m of undeformed andesite to dacite lava flows interbedded with volcanoclastic turbidites and pyroclastic deposits overlain by ~500m of reefal limestones and red beds (Mendoza and Suastegui, 2000; Cortés et al., 2010). The Las Ollas complex of the Zihuatanejo-Huetamo subterrane underlies the Zihuatanejo sequence, and is part of a subduction zone complex comprising fault-bounded tectonic slices with blocks of tholeiitic arc-derived rocks preserving high temperature, low pressure metamorphism in a matrix of sheared flysch and serpentinite (Mendoza and Suastegui, 2000). The underlying Huetamo sequence comprises over 4500m of volcanoclastic turbidites of late Jurassic to late Cretaceous age representing accumulation in a back-arc basin (Mendoza and Suastegui, 2000).

The boundary between the Guerrero terrane and the Precambrian and Palaeozoic terranes of eastern Mexico is considered to represent the westernmost extent of Precambrian basement

(Figure 1.5; Ruiz et al., 1988; Urrutia-Fucugauchi and Uribe-Cifuentes, 1999). However, samples from the metamorphic basement underlying the Zihuatanejo-Huetamo subterrane have yielded Precambrian Sm-Nd model ages of ~1.2 Ga (Centeno-García et al., 1993). Granulitic and gabbroic lower-crustal xenoliths from the Michoacán-Guanajuato volcanic field, in the western-central TMVB, yield Sm-Nd model ages of ~1.5 Ga supporting the presence of Precambrian lower crust beneath the Guerrero Terrane (Urrutia-Fucugauchi and Uribe-Cifuentes, 1999). The Jalisco block, bound by the Colima graben to the east, and the Tepic-Zacoalco rift to the north (Figure 1.1), is the westernmost extent of the Guerrero terrane (Gómez-Tuena et al., 2007b; Ferrari et al., 2012). It is dominated by batholiths intruding mid- to late Jurassic schists, and overlain by late Cretaceous to Eocene subaerial ignimbrites and lavas (Ferrari et al., 2012). The majority of the batholiths are late Cretaceous to Palaeocene in age; however, some batholiths yield Precambrian Nd model ages (Ferrari et al., 2012).

1.2.2 Magmatic Evolution of the Trans-Mexican Volcanic Belt

Prior to the Miocene, the magmatic arc that forms the Sierra Madre Occidental had a north-northwest - south-southeast orientation (Figure 1.5; Ferrari et al., 2001; Gómez-Tuena et al., 2007b; Ferrari et al., 2012). Volcanism shifted through a counter-clockwise rotation during the Oligocene (~30 Ma), eventually forming the east-west trending TMVB (Ferrari et al., 2001; Gómez-Tuena et al., 2007b). Volcanism along the TMVB is a result of the subduction of the Cocos and Rivera plates beneath the North American plate. The oblique geometry of the TMVB with the Middle America Trench (MAT) has been attributed to variations in the dip angle of the subducting plates (Figure 1.5; Pardo and Suarez, 1995; Ferrari et al., 2001; Gómez-Tuena et al., 2007b).

Pardo and Suarez (1995) modelled the shape of the subducting plates using the hypocentres of local and teleseismic earthquakes. They found that the Cocos slab has an initial shallow dip of ~30° but dip varies laterally after ~30 km depth (Pardo and Suarez, 1995). Under central Mexico, the slab becomes subhorizontal at 110 to 275 km from the MAT, and then gradually steepens again to the southeast (Pardo and Suarez, 1993, 1995). Recent seismic tomography studies have shown that the Cocos plate has a shallower initial dip than previously modelled, of ~15° and then flattens out ~80 km from the trench (Soto et al., 2009; Yang et al., 2009; Ferrari et al., 2012). The sub-horizontal slab extends inland for ~200 km where it then abruptly plunges to 75° below the volcanic front (Perez-Campos et al., 2008).

Volcanism in the westernmost part of the TMVB is controlled by the Rivera plate, which is steeply dipping at an angle of 50° down to a depth of ~130 km (Pardo and Suarez, 1993, 1995). Yang et al. (2009) found that the down-going slab of the Rivera plate has a dip of ~40°, which steepens to ~70° beneath the TMVB.

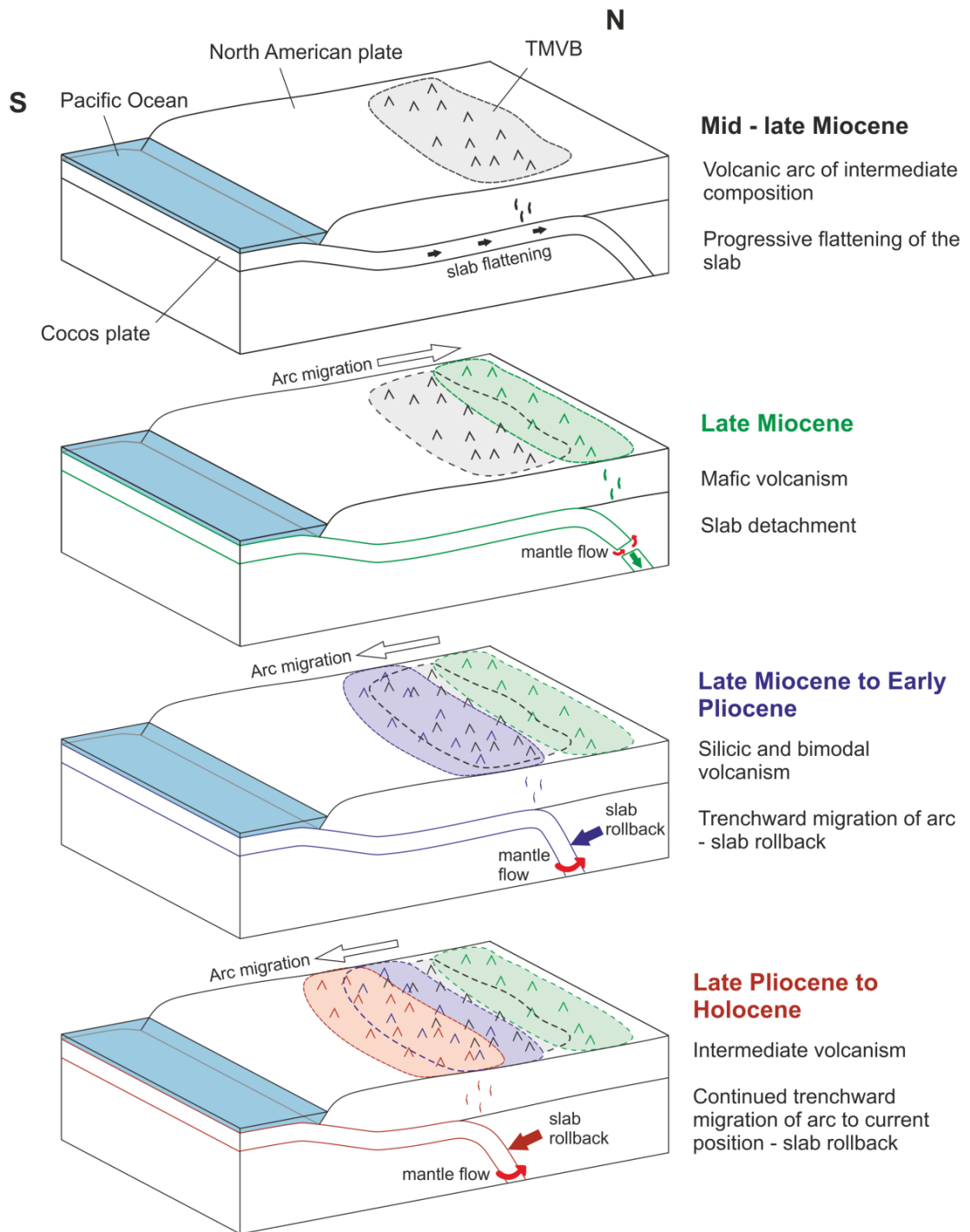


Figure 1.6 Simplified schematic diagram of the magmatic evolution of the Trans-Mexican Volcanic Belt (TMVB) after Gómez-Tuena et al. (2007b) and Ferrari et al. (2012).

During the mid-late Miocene, progressive flattening of the slab resulted in migration of the arc away from the trench. Mafic volcanism occurred in the late Miocene, as a result of slab detachment, and since the late Miocene, volcanism has migrated trenchwards as a result of slab rollback.

The geological evolution of the TMVB can be divided into four magmatic stages (Figure 1.6; Gómez-Tuena et al., 2007b; Ferrari et al., 2012). The first stage is a mid-late Miocene arc of intermediate composition characterised by basaltic-andesite lava flows (Gómez-Tuena et al., 2007b). During this period the volcanic arc migrated away from the trench and widened (Gómez-Tuena et al., 2007b). This migration and widening of the volcanic arc has been attributed to progressive flattening of the subducting slab between early and late Miocene times (Figure 1.6; Ferrari et al., 2012). In the late Miocene, there was a period of mafic volcanism, basaltic fissure eruptions and lava flows, which were emplaced to the north of the previous magmatic arc (Gómez-Tuena et al., 2007b; Ferrari et al., 2012). This phase of mafic volcanism has been related to slab-detachment allowing the influx of hot asthenosphere into the mantle wedge, promoting melting of the sub-continental mantle lithosphere (Ferrari, 2004). The third stage of TMVB evolution is characterised by silicic volcanism in the late Miocene and bimodal volcanism in the early Pliocene (Figure 1.6; Gómez-Tuena et al., 2007b). Dacite to rhyolite lava dome complexes were emplaced to the south of the mafic arc, and voluminous ignimbrites were deposited from caldera-forming eruptions (Gómez-Tuena et al., 2007b). During the Pliocene, small volume alkaline lava flows were emplaced in the northern part of the Colima graben, and along the TMVB, together with continued emplacement of silicic dome complexes (Gómez-Tuena et al., 2007b). The final phase of magmatism is represented by the current activity along the TMVB comprising basaltic to andesitic volcanism emplaced since the late Pliocene (Gómez-Tuena et al., 2007b; Ferrari et al., 2012).

Since the late Miocene, the volcanic front has migrated trenchward at an estimated rate of 7.5mm per year, to its present position ~150 km from the trench (Gómez-Tuena et al., 2007b; Ferrari et al., 2012). This trenchward migration has been attributed to rollback of the subducting Cocos slab (Figure 1.6; Ferrari et al., 2012 and references therein).

1.2.3 The Tectonic Setting of the Western Trans-Mexican Volcanic Belt

The CVC sits in the Colima Rift Zone, a ~190 km long, 50-65 km wide zone trending north-northeast – south-southwest from Lake Chapala to the Pacific coast (Figure 1.7; Allan, 1986). The Colima Rift Zone is well defined in the north by steeply dipping normal faults, but poorly constrained to the south (Allan, 1986). The northern and southern parts of the Colima rift are separated by the Tamazula fault zone (Figure 1.8) which has been interpreted as a basement structure which trends northeast-southwest extending for over 160 km crossing the Colima Rift at the CVC (Garduño et al., 1998; Cortés et al., 2010; Norini et al., 2010). Garduño et al. (1998) proposed that the volcanic activity and recent evolution of the CVC is controlled by the Tamazula fault, specifically the sector collapse events, which they suggest were triggered by displacement along this fault.

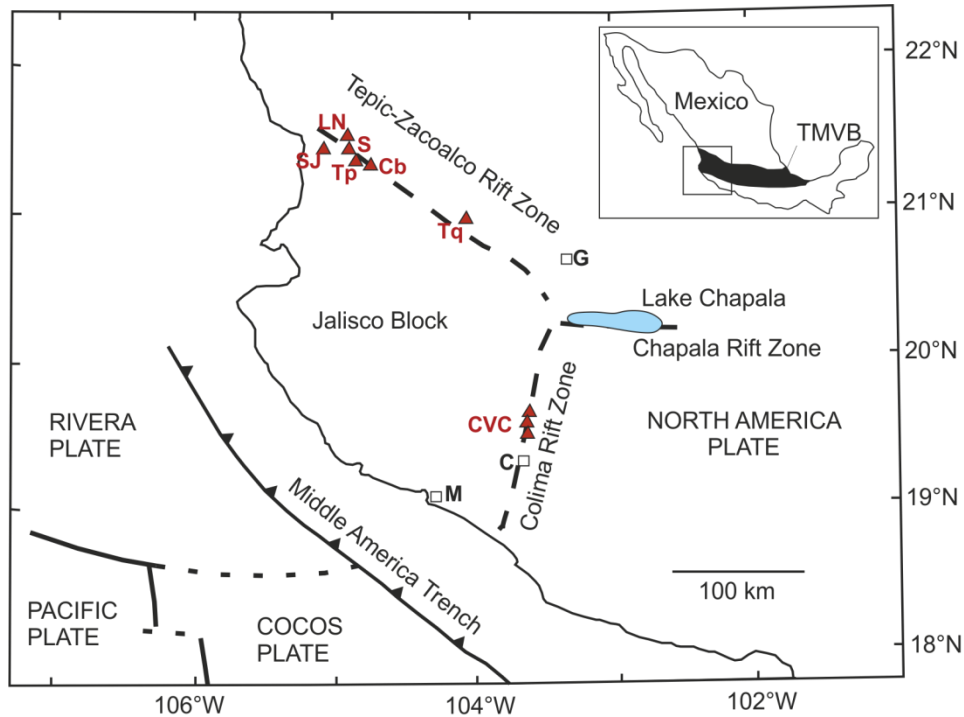


Figure 1.7 Schematic tectonic map of western Mexico showing the location of the Colima Volcanic Complex (CVC) modified from Maria and Luhr (2008).

CVC is located in the Trans-Mexican Volcanic Belt (TMVB) within the Colima Rift Zone. Also shown are the Chapala and Tepic-Zacoalco Rift (TZR) Zones. The volcanoes in the TZR are: Tq = Volcán Tequila; Cb = Volcán Ceboruco; Tp = Volcán Tepetiltic; S = Volcán Sanganguey; LN = Las Navajas; and SJ = Volcán San Juan. The cities are: G = Guadalajara; C = Colima; and M = Manzanillo.

Extending from the northern end of the Colima Rift Zone to the Gulf of California is the Tepic-Zacoalco Rift (TZR), a northwest-southeast trending series of grabens and half-grabens (Luhr et al., 1985; Allan, 1986; Ferrari and Rosas-Elguera, 2000; Ferrari et al., 2012). Volcanism in the TZR is represented by six volcanoes of andesite, dacite and rhyodacite composition; Tequila, Ceboruco, Tepetiltic, Sanganguey, Las Navajas and San Juan (Figure 1.7; Luhr et al., 1985). Volcán Ceboruco is the only currently active volcano along the TZR; the last eruption of which occurred in 1870 producing $\sim 1 \text{ km}^3$ rhyodacitic lava (Luhr et al., 1985). To the east of the TZR, is the Chapala Rift, which is approximately 110 km long with a width of 15 to over 60 km (Allan 1986). Few volcanic centres of Quaternary age are found in the Chapala Rift (Luhr et al. 1985).

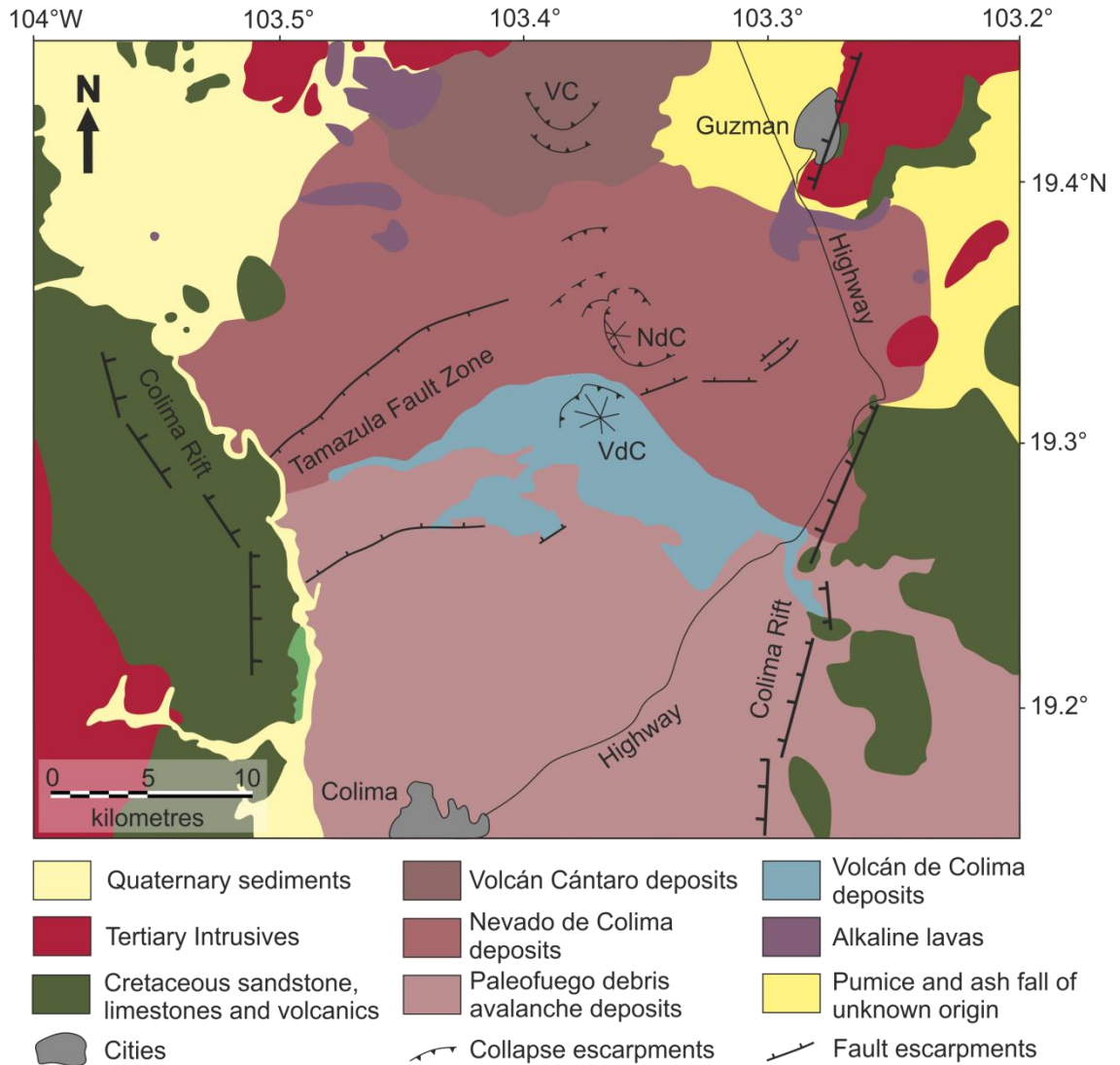


Figure 1.8 Simplified geological map of the CVC after Cortés et al. (2010).

The roughly north-south trending fault escarpments define the Colima Rift Zone. Much of the rift zone is filled with debris avalanche deposits to the south of the CVC, and lavas and pyroclastic flow and fall deposits of Volcán Cántaro (VC), Nevado de Colima (NdC), Paleofuego and Volcán de Colima (VdC). Numerous semi-circular escarpments resulting from sector collapse events are apparent on the CVC volcanoes. The northeast-southwest trending fault escarpments outline the Tamazula fault zone, though to have played a role in the evolution of the CVC (Garduño et al., 1998). The basement comprises Cretaceous volcanic rocks and sediments (see Section 1.2.1 for details).

The Colima Rift Zone and the TZR form the eastern and northern boundaries of the Jalisco block (Luhr et al., 1985; Allan, 1986; Ferrari and Rosas-Elguera, 2000; Ferrari et al., 2012). Together with the Chapala Rift, the Colima Rift Zone and the TZR form a rift-rift-rift triple junction (Figure 1.7), which has been described as resulting from the partial separation of the Jalisco block from the Mexican mainland (Luhr and Carmichael, 1981; Luhr et al., 1985; Allan, 1986; Gómez-Tuenca et al., 2007). Luhr et al. (1985) proposed that the Colima Rift is a continuation of the propagating East Pacific Rise. Other authors have attributed the rifting to

extension as a result of slab roll-back (Ferrari et al., 2001; Ferrari, 2004; Soto et al., 2009; Yang et al., 2009). Studies by Soto et al. (2009) and Yang et al. (2009) show that the Colima Rift Zone sits directly above the subducting boundary between the Rivera and Cocos plates (Figure 1.9). The plates separate at a depth of ~150 km as a result of the difference in rates and angles of subduction (Allan, 1986; Ferrari et al., 2001; Soto et al., 2009; Yang et al., 2009). The Rivera plate is subducting at ~20mm/year, while the Cocos plate is subducting at a rate of ~60mm/year (Pardo and Suarez, 1993, 1995). Soto et al. (2009) and Yang et al. (2009) proposed that the gap between the plates allows the flow of hot, more buoyant asthenosphere around the Rivera plate into the Cocos mantle wedge causing roll-back of the Cocos slab and resulting in extension on the overriding North American Plate (Figure 1.9). However, as presented in Section 1.2.2., roll-back of the Cocos slab commenced in the Late Miocene as a result of slab detachment (Figure 1.6; Ferrari, 2004; Gómez-Tuena et al. 2007b). Therefore, it is more likely that the flow of asthenosphere mantle around the Rivera plate is a consequence of slab-rollback rather than a cause.

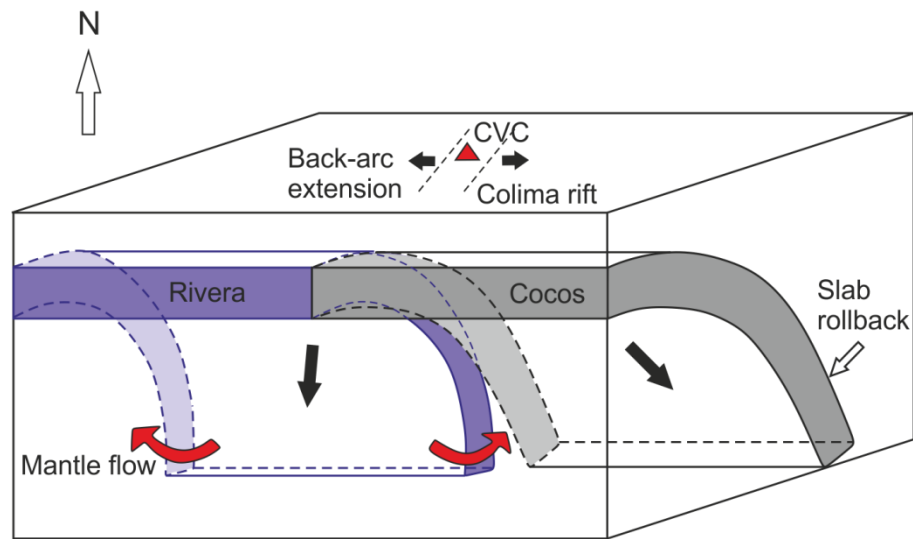


Figure 1.9 Cartoon of the subducting Rivera and Cocos plates beneath the CVC after Yang et al. (2009).

The plates subduct at different angles and directions resulting in a split between the slabs at depth (Pardo and Suarez, 1995; Soto et al., 2009; Yang et al., 2009). This allows flow of hot buoyant asthenosphere into the mantle wedge causing slab roll-back, resulting in back-arc extension of the overriding plate (Yang et al., 2009)

Recent structural and geodetic studies have shown that deformation along the TZR and Colima Rift Zone is dominantly extensional and that the Jalisco block is moving southwest with respect to North America (Norini et al., 2010; Selvans et al., 2011; Ferrari et al., 2012). Ferrari and Rosas-Elguera (2000) and Norini et al. (2010) proposed that the extension in the Colima Rift Zone and the TZR are a result of stress applied at the Rivera-Cocos-North America plate

boundary. Gómez-Tuena et al. (2007b) suggested that the whole TMVB is currently under an extensional tectonic regime based on a number of structural studies across the TMVB. They proposed that extension might be caused by the oblique convergence of the Cocos plate and deformation partitioning at the plate boundary, which produces a sinistral strike-slip component that is taken up along the TMVB (Ferrari and Rosas-Elguera, 2000; Ego and Ansan, 2002; Gómez-Tuena et al., 2007b).

1.3 Late Pleistocene and Holocene Eruption History of the Colima Volcanic Complex

Throughout the late Pleistocene and Holocene, the CVC has experienced periods of dominantly effusive activity (interplinian) punctuated by explosive sub-plinian to plinian eruptions. Since the mid-1990s, Volcán de Colima has been the focus of many studies investigating the geochemistry and petrology of the erupted deposits (Luhr and Carmichael, 1990b, a; Robin et al., 1991; Robin and Potrel, 1993; Komorowski et al., 1997; Righter, 2000; Luhr, 2002; Atlas et al., 2006; Luhr et al., 2006; Reubi and Blundy, 2008; Savov et al., 2008; Luhr et al., 2010; Saucedo et al., 2010; Verma and Luhr, 2010); the seismicity (De la Cruz-Reyna, 1993; Zobin et al., 2002; Zobin et al., 2008; Varley et al., 2010; Arámbula-Mendoza et al., 2011) and the resulting hazard assessment (Stoopes and Sheridan, 1992; Saucedo et al., 2005; Evans et al., 2009; Cortés et al., 2010; Connor et al., In Prep.).

The first studies from the early 1900s gave general descriptions of the CVC and detailed accounts of the 1913 sub-plinian to plinian eruption (Waitz, 1906, 1915, 1935). After ~50 years of apparent inactivity following the 1913 event, Volcán de Colima entered a phase of effusive activity with intermittent vulcanian eruptions (Luhr and Carmichael 1980). This new phase of activity led to studies of the morphology and evolution of the CVC (Mooser, 1961; Thorpe et al., 1977; Medina-Martínez, 1983). Medina-Martínez (1983) presented a study of the eruptive cyclicity at Volcán de Colima over the preceding ~400 years. The first detailed petrological and geochemical studies of CVC lavas and tephra deposits were presented by Luhr and Carmichael (1980; 1981; 1982; 1990a,b), and such studies continued throughout the 1990s and 2000s (Robin et al., 1991; Robin and Potrel, 1993; Righter, 2000; Luhr, 2002; Atlas et al., 2006; Luhr et al., 2006; Reubi and Blundy, 2008; Savov et al., 2008; Luhr et al., 2010). Massive debris avalanche deposits to the south of the CVC, resulting from numerous gravitational sector collapse events, also became the focus of many studies during the last few decades (Robin et al., 1987; Luhr and Prestegard, 1988; Stoopes and Sheridan, 1992; Komorowski et al., 1997; Cortés et al., 2009). Cortés et al. (2005) published the first comprehensive geological map of the CVC which was updated in 2010 (Cortés et al., 2010; Figure 1.8).

Lava flows are not well preserved in the CVC, with only recent (post-1818) lava flows exposed on the flanks of the currently active Volcán de Colima (Figure 1.10). This could signify a switch in behaviour from dominantly explosive activity as preserved in the tephra record, or suggest that lava flows that erupted throughout the late Pleistocene and Holocene have been destroyed or buried by subsequent eruptions. Nevado de Colima and Paleofuego have experienced numerous sector collapse events that have partially destroyed the edifices and produced massive debris avalanche deposits (Luhr and Presteggaard, 1988; Stoopes and Sheridan, 1992; Komorowski et al., 1997; Cortés et al., 2005; Cortés et al., 2010). Such episodes might remove or bury lava flows. Therefore it is assumed that periods of effusive activity between plinian events have occurred throughout the eruptive history of the CVC, but are not preserved.

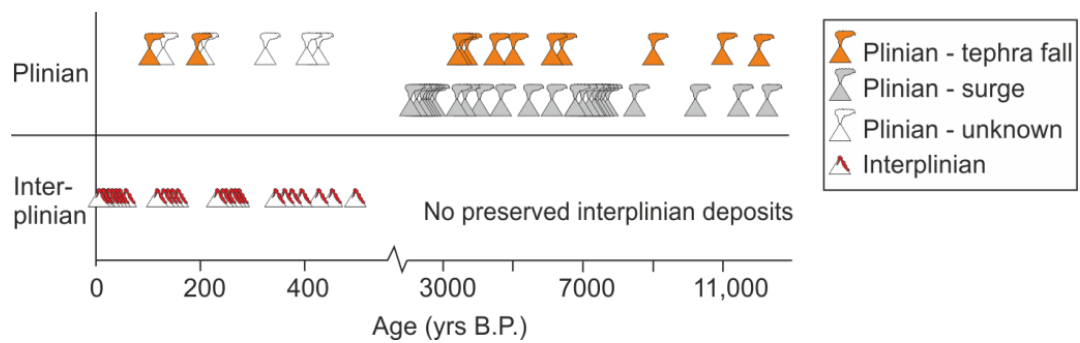


Figure 1.10 Timeline of eruptions of Volcán de Colima and Paleofuego using data from Bretón González et al. (2002) and calibrated ^{14}C ages.

Interplinian activity is poorly preserved due to erosion and burial by subsequent explosive and sector collapse events. Timing of historical interplinian and plinian activity is known largely from eye-witness accounts (Bretón González et al., 2002). Calibrated radiocarbon ages of the Holocene and late Pleistocene tephra fallout and surge deposits are from Luhr et al. (2010).

Historical records of activity at Volcán de Colima extend back to 1519 and the arrival of the Spanish conquistadors (Bretón González et al., 2002). Prior to the establishment of volcano observatories in the cities of Colima and Zapotlan in 1898, records of activity are from eyewitness accounts. Bretón González et al. (2002) presented a detailed history of volcanic activity since 1519, summarised here in Figure 1.11, in combination with reports from the Smithsonian Institute (Venzke et al., 2002-). Since 1519, there have been nine highly explosive, VEI=4 (Volcanic Explosivity Index after Newhall and Self, 1982) events; however, only the 1818 and 1913 eruptions are well-documented in the literature with detailed descriptions of thick ash-fall and pyroclastic flows (Bretón González et al., 2002; Luhr, 2002). Tephra fallout deposits from the 1818 and 1913 eruptions are the only historical fallout deposits preserved in the tephra record (Luhr et al., 2010). It is therefore assumed that these two events were larger

volume eruptions than the seven other reported VEI=4 historical events (Figure 1.11; Bretón González et al., 2002; Luhr et al., 2010).

The 1818 eruption produced a sustained ash column, which resulted in ash-fall in Mexico City ~470 km from the vent, and pyroclastic flows that travelled ~14 km along ravines (Bretón González et al., 2002). For 51 years after the 1818 eruption, activity at Volcán de Colima was restricted to the rise of the magma within the crater, and it was assumed that the volcano was inactive (Luhr and Carmichael, 1990b; Bretón González et al., 2002). In January of 1913, Volcán de Colima once again erupted explosively producing a sustained ash column that reached an estimated height of 20 km a.s.l. and pyroclastic flows that travelled up to 15 km from the vent (Luhr and Carmichael, 1980; Saucedo et al., 2010; Connor et al., In Prep.). Following the 1913 plinian eruption, the volcano again entered an effusive phase of activity while lava filled the ~350m deep crater (Luhr and Carmichael, 1980).

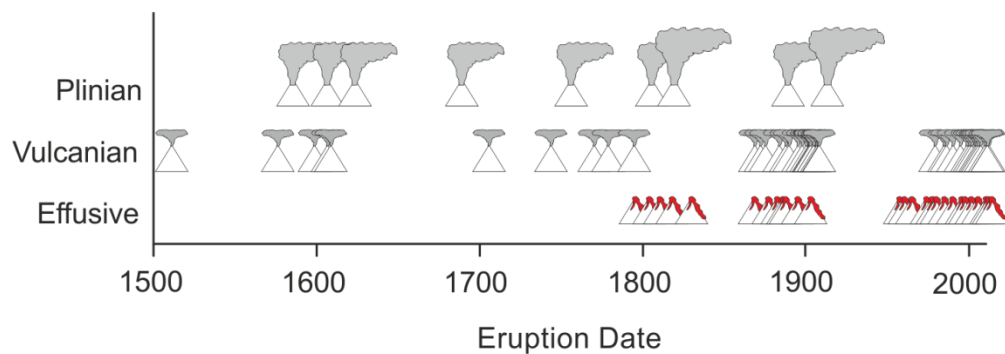


Figure 1.11 Schematic diagram summarising volcanic activity at Volcán de Colima since records began in 1519, using the data from Bretón González et al. (2002).

There is very little information in the records of lava flows from Volcán de Colima, and effusive deposits exposed on the flanks are all post-1818 lava flows (Bretón González et al., 2002). Numerous vulcanian-type eruptions have occurred throughout historical times, and up to nine VEI=4 eruptions have occurred since the 1500s. Tephra is only preserved from the 1818 and 1913 eruptions and there are numerous eye-witness accounts of these eruptions; therefore it is assumed these were larger eruptions than the other seven.

After the 1818 and 1913 plinian eruptions, the volcano entered phases of predominantly effusive activity punctuated by small vulcanian explosions (Robin et al., 1987; Bretón González et al., 2002; Luhr, 2002). This type of activity is termed here as interplinian and is described in further detail below.

1.3.1 *Interplinian Activity*

The nature of interplinian activity at the CVC is characterised by material erupted between 1869-1909 and 1957-present day. In 1869, the lava erupted on the northeast side of the Volcán

de Colima edifice forming the parasitic cone of Volcancito (Luhr and Carmichael, 1990b). Lava flowed into the northeast part of the caldera floor and along a ravine to the southeast. Activity continued at Volcancito until 1878 when activity in the main crater resumed (Bretón González et al., 2002). For the next 29 years, Volcán de Colima displayed effusive activity punctuated by small explosive eruptions that produced ash clouds above the vent and block-and-ash flows down the flanks of the volcano (Bretón González et al., 2002). Records of these eruptions are from eye-witness accounts and no details of column height or flow length were given. From 1904 to 1909 explosive activity decreased and the volcano entered a more fumarolic phase with occasional small explosions (Bretón González et al., 2002).

In 1957, the first activity from the summit of Volcán de Colima since the 1913 eruption was recorded with the extrusion of a new lava dome, followed by the production of lava flows and weak explosions in 1960 and 1961 (Bretón González et al., 2002; Luhr, 2002). For the next 30 years, activity was dominated by effusive lava dome extrusion and partial dome collapses, resulting in lava flows reaching up to 4 km in length (Luhr, 2002). A more explosive phase of activity commenced in 1999 with an explosion in February that sent ballistic projectiles up to 3.5 km away from the vent, and in July an eruption that produced an ash column 12 km a.s.l. and pyroclastic flows down the southern flank (Bretón González et al., 2002; Venzke et al., 2002-). This phase of activity continued until 2011, when an explosion resulting in partial dome collapse in July appears to have marked the end of this phase. Between July 2011 and January 2013, activity at Volcán de Colima decreased with little seismic activity and no eruptions (Carlos Navarro-Ochoa; personal communication). In January 2013, a small explosion occurred sending an ash cloud ~600m above the vent, resulting in the partial destruction of the lava dome (Carlos Navarro-Ochoa; personal communication). Activity has once again increased with two to three small explosions per day.

Luhr and Carmichael (1980) were the first to study the Colima andesites, describing the petrology and geochemistry of lava flows and ballistics erupted in 1869, 1913, 1961-1962 and 1975-1976. Further studies on interplinian activity focused on effusive and small explosive (VEI 2-3) deposits erupted between 1961 and 2005 (Robin et al., 1987; Luhr and Carmichael, 1990b; Robin et al., 1991; Luhr, 1993; Robin and Potrel, 1993; Luhr, 2002; Navarro-Ochoa et al., 2002; Savov et al., 2008).

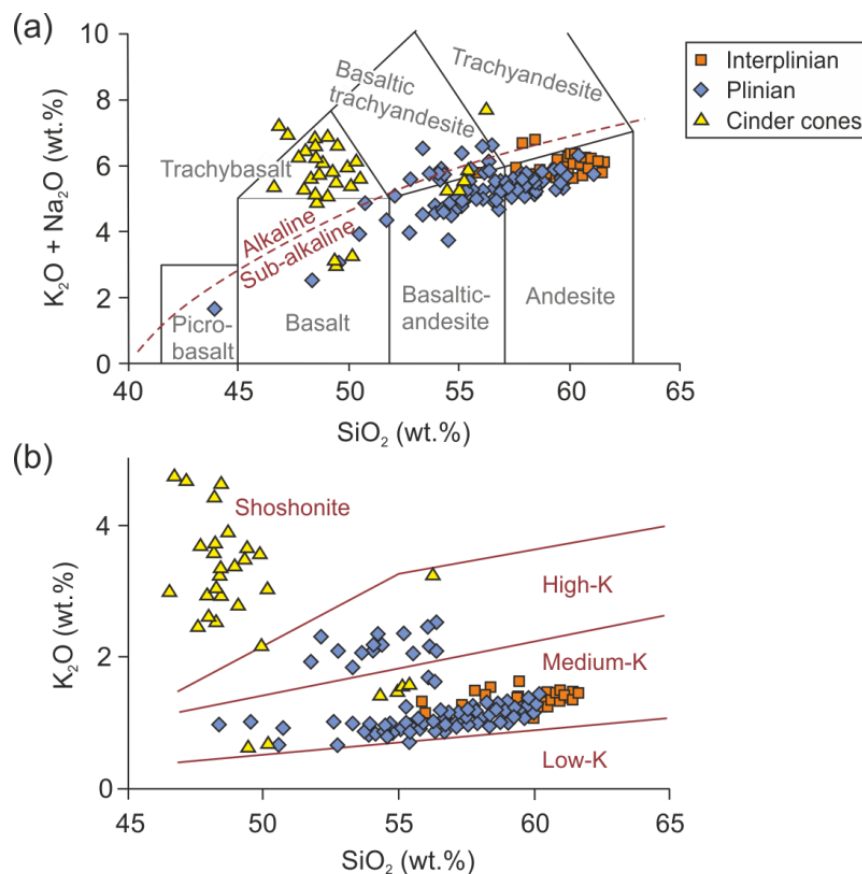


Figure 1.12 Classification of the CVC eruption deposits.

(a) Total alkalis-silica (TAS) classification diagram after Le Maitre et al. (2002) for CVC interplinian and plinian eruption deposits and the cinder cone magmas. (b) K_2O versus SiO_2 classification diagram after Le Maitre et al. (2002). Data sources for the interplinian and plinian deposits are given in the text. Plinian tephra fall deposits range in composition from picro-basalt to andesite. Interplinian deposits are typically andesitic in composition. The alkaline cinder cone magmas are high-K shoshonites (Luhr and Carmichael, 1981; Carmichael et al., 2006; Maria and Luhr, 2008; Vigouroux et al., 2008; Cai, 2009).

The majority of historical interplinian effusive deposits are medium-K sub-alkaline andesites with SiO_2 contents of 60 – 63 wt.% (Figure 1.12; Luhr and Carmichael, 1980; Luhr and Carmichael, 1990b, a; Robin et al., 1991; Luhr, 1993, 1997; Luhr, 2002; Savov et al., 2008). The lavas are typically highly crystalline and have up to 52 vol.% crystals with the mineral assemblage: plagioclase (40 vol.%) + orthopyroxene (6 vol.%) + clinopyroxene (3 vol.%) + titanomagnetite (2 vol.%) ± hornblende (1 vol.%; Luhr and Carmichael, 1980). The groundmass is crystalline, comprising glass and a mesostasis of the same mineral phases, with the exception of hornblende, which is not found in the groundmass (Luhr and Carmichael, 1980). Olivine xenocrysts occur in many samples, displaying pyroxene and oxide overgrowths. Hornblende crystals all display disequilibrium with breakdown rims of pyroxene and Fe-Ti oxides (Luhr and Carmichael, 1980; Luhr and Carmichael, 1990b; Luhr, 2002; Savov et al., 2008).

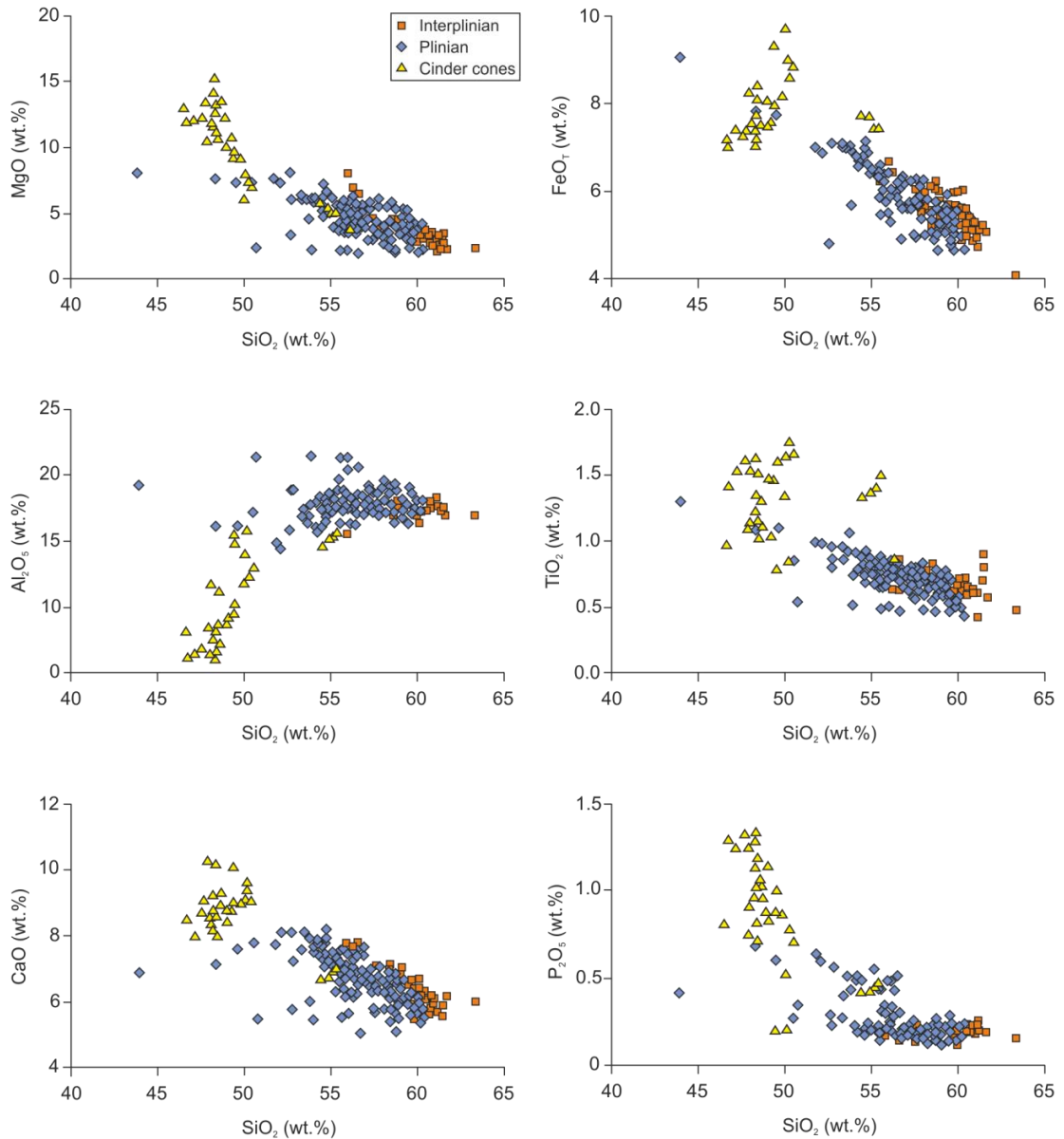


Figure 1.13 Whole-rock major element variation diagrams for interplinian and plinian eruption deposits of the CVC.

Also plotted are whole-rock major element compositions for the alkaline cinder cones (Luhr and Carmichael, 1981; Carmichael et al., 2006; Maria and Luhr, 2008; Vigouroux et al., 2008; Cai, 2009). The interplinian deposits are typically more evolved with higher SiO₂ and Al₂O₃, and lower MgO, FeO, TiO₂, CaO and P₂O₅ contents relative to the plinian deposits.

Geochemically, the interplinian deposits are typical medium-K, sub-alkaline subduction-related magmas showing enrichment in light rare earth elements (LREE: La, Ce, Pr, Nd) and fluid-mobile elements (FME: K, Rb, Cs, Ba); and relative depletions in high field strength elements (HFSE: Nb, Ta,). These deposits are andesitic to dacitic with high SiO₂, K₂O and Na₂O (Figure 1.12) and low MgO, FeO, TiO₂, CaO, and P₂O₅ (Figure 1.13). Their evolved nature is also apparent in their trace element characteristics with high Rb, Ba, Pb and U and low V, Cr, Co and Ni.

1.3.2 Plinian Activity

Throughout the 1990s and 2000s, Jim Luhr, Carlos Navarro-Ochoa and Ivan Savov sampled and described CVC eruption deposits preserved and exposed on the flanks of Nevado de Colima and in quarries and gullies on the rift floor (Figure 1.14; Luhr et al., 2010). Through detailed sampling of charcoal found within ash horizons and tephra fallout deposits, they were able to identify at least 25 deposits, erupted between 30,000 yrs B.P. and the present day (Figure 1.15; Luhr et al., 2010). Further field campaigns carried out as part of this study in January 2010 and February 2011 have built upon the work of Luhr et al. (2010) on the tephrochronology of the CVC. To date, eruption deposits have been described at 89 localities across an area of ~500 km², including exposures in quarries on the rift floor (Figure 1.14).

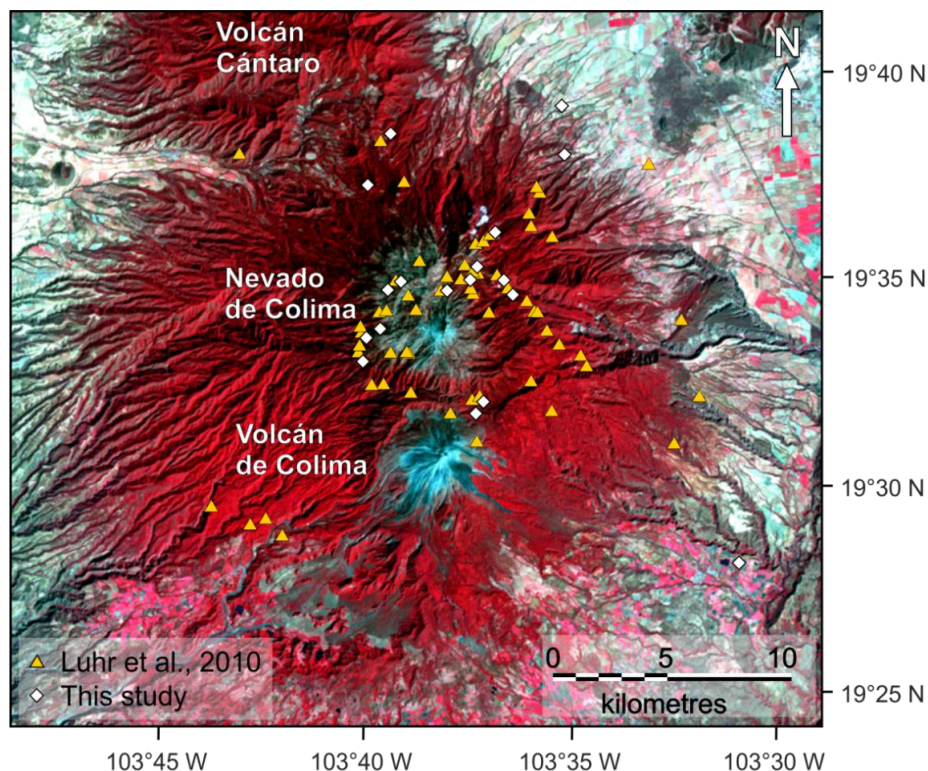


Figure 1.14 Sample location map for the Holocene explosive eruption deposits.

Locations are from Luhr et al. (2010) and new sites sampled in 2010 and 2011. The majority of samples are located in access roads on the upper slopes of Nevado de Colima. The lower slopes are densely vegetated therefore access is difficult.

In total, 181 radiocarbon ages have been obtained from the CVC eruptive stratigraphy, yielding uncalibrated ages from 80 ± 50 to $29,930 \pm 210$ yrs B.P. (Figure 1.15; Luhr et al., 2010). Of these, 143 ages represent the Holocene stratigraphy (0 to 9000 yrs B.P.). Nevado de Colima is densely vegetated; therefore the eruption deposits on the volcano's flanks are only exposed in road cuts.

Nevado de Colima is a national park which has one main access road on the northeast flank. Once inside the park entrance at 3480m a.s.l., there are numerous roads; therefore the majority of the deposits are exposed at high elevations, where the older units have been buried, eroded or destroyed by subsequent eruptions. There are a few roads on the lower slopes; however, the area is prone to landslides, and the roads are not well maintained. In the early 2000s, Luhr and Navarro-Ochoa collected samples for geochemical and petrological analysis from the older eruption deposits along roads on the lower slopes (Luhr et al., 2010). They also collected charcoal samples for radiocarbon dating. In an effort to re-sample some of these deposits, and to search for more charcoal samples to build on the tephrochronology of Luhr et al. (2010), these roads were re-visited in February 2011. Unfortunately, only one of the roads was passable, and no charcoal was found.

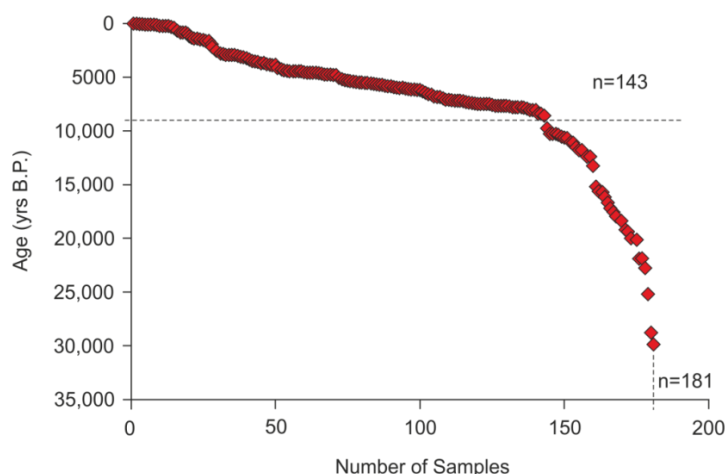


Figure 1.15 Uncalibrated radiocarbon ^{14}C ages for the explosive plinian CVC eruption deposits (Komorowski et al 1997; Luhr et al. 2010).

Out of a total of 181 dates, 143 of these were sampled between 9000 yrs B.P. and present. The younger eruption deposits are well exposed high on the flanks of Nevado de Colima, while the older eruption deposits are less well exposed, confined to lower elevations where the slopes are densely vegetated and access is difficult. Symbols are larger than analytical error (typically ± 60 years).

The stratigraphy of eruption deposits exposed on the flanks of Nevado de Colima comprise tephra fallout deposits varying in thickness from a few centimetres to over 1m (Figure 1.16). The fallout deposits comprise pumice or scoria, with clasts varying from <1cm to 17cm. Lithics are abundant in all the erupted units, typically occurring as angular fragments up to 2cm across (measured along the long-axis). Interbedded with the tephra layers are ash-rich surge or pyroclastic flow horizons (Figure 1.16). These ash beds are typically rich in charcoal fragments; however they commonly contained reworked pumice from the underlying fallout deposits. As a result, care must be taken when using the radiocarbon dating for tephrochronology.

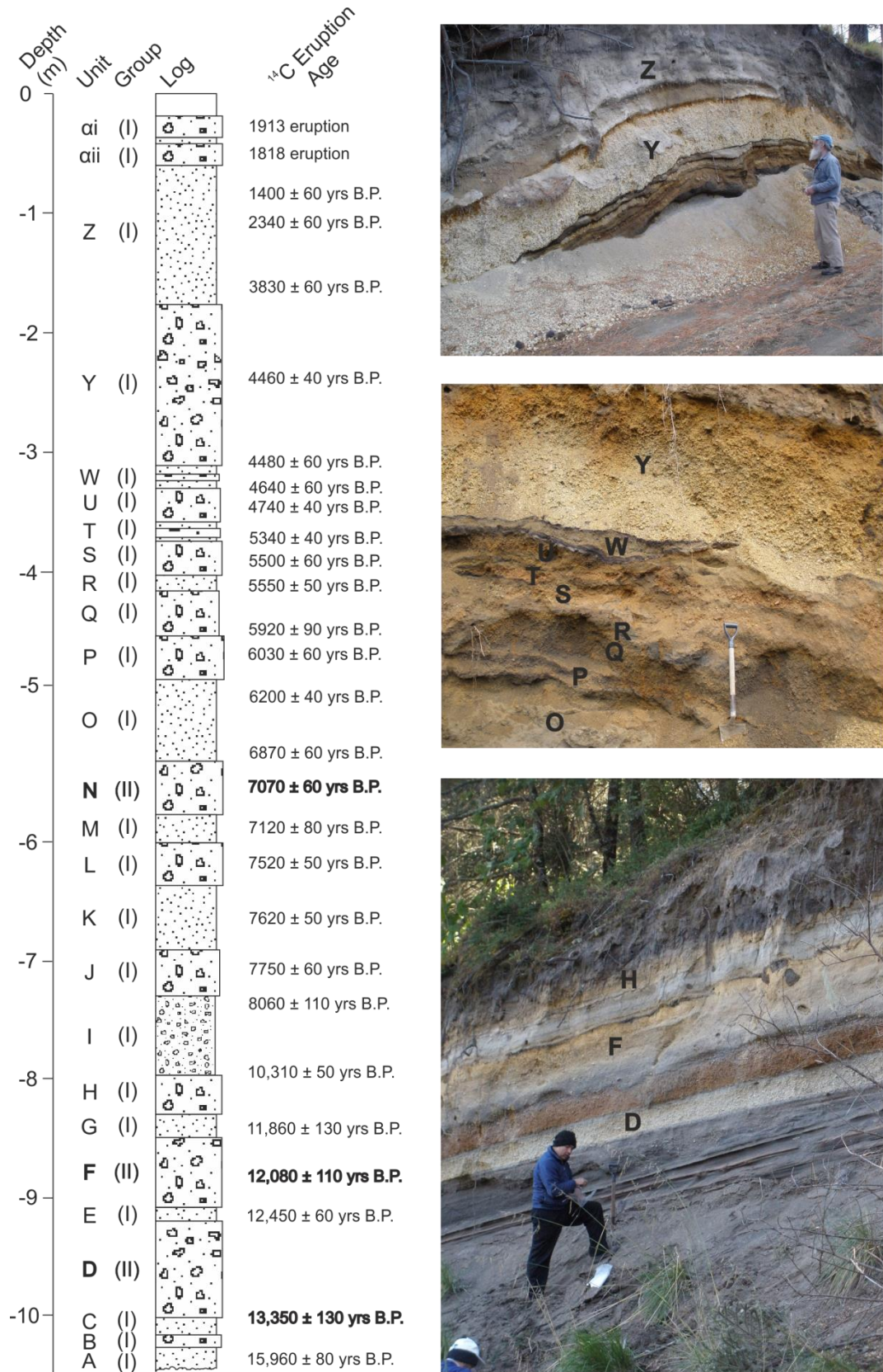


Figure 1.16 Composite stratigraphic section and field photographs of explosive eruption deposits exposed in road-cuts on the flanks of Nevado de Colima.

The unit names and uncalibrated ¹⁴C ages are as reported in Luhr et al (2010). The Group II eruption deposits (units N, F and D) are highlighted in bold.

Using a combination of radiocarbon dating, together with field mapping, petrology and geochemistry, a detailed stratigraphy of the CVC Holocene explosive eruption deposits has been compiled up to 13,000 yrs B.P. (Figure 1.16, Appendix A). Older eruption deposits are difficult to correlate due to poor exposure and a lack of detailed charcoal sampling for radiocarbon dating. Many of the units also show very similar petrological and geochemical characteristics; therefore correlating units based on these data alone is not possible.

The highly explosive (plinian) eruption deposits show a wide range in composition from basalt to andesite based on the TAS and K_2O vs. SiO_2 diagrams of Le Maitre et al. (2002; Figure 1.12). The samples are all pumice and scoria clasts exposed in road-cuts, therefore, the classification of altered volcanic rocks after Hastie et al. (2007) is also used (Figure 1.17). This classification uses the fluid immobile trace elements Co and Th in order to see through possible effects of post-eruption hydrothermal alteration. According to this classification, the plinian eruption deposits range in composition from basaltic-andesite to rhyolite (Figure 1.17). The majority of the deposits are medium-K; however, some samples appear to be trending towards the high-K alkaline cinder cone compositions (Figures 1.12 and 1.17).

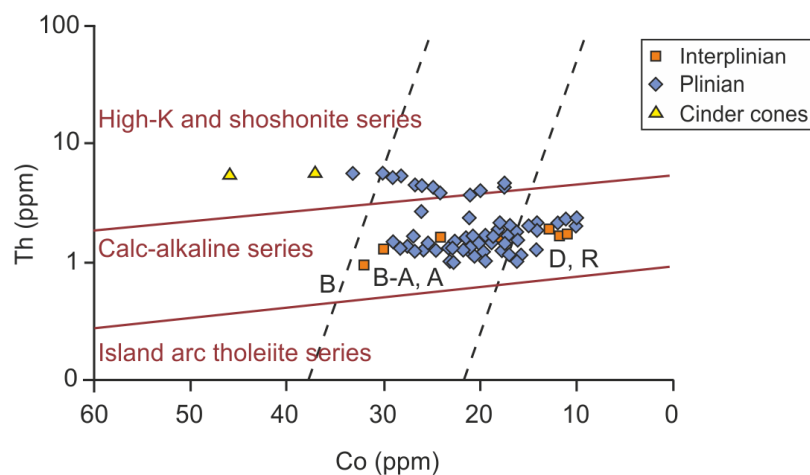


Figure 1.17 Classification of the interplinian and plinian CVC eruption deposits based on the classification of altered volcanic rocks of Hastie et al. (2007).

This classification uses immobile trace elements in place of the mobile elements in order to see through the effects of alteration.

The geochemical evolution of the CVC eruption deposits is shown on time series plots (Figure 1.18). The interplinian eruption deposits show little variation in whole-rock major element geochemistry, while the explosive (plinian) eruption deposits show a wide variation in SiO_2 , MgO , K_2O and P_2O_5 . Overall the SiO_2 content appears to decrease from 30,000 yrs B.P. to 12,000 yrs B.P., and then increases again from ~10,000 yrs B.P. to the present day. This pattern

is reflected in the MgO content, which shows the opposite trend. However, there are fewer samples from 10,000 to 30,000 yrs B.P., so it is difficult to draw concrete conclusions from the data.

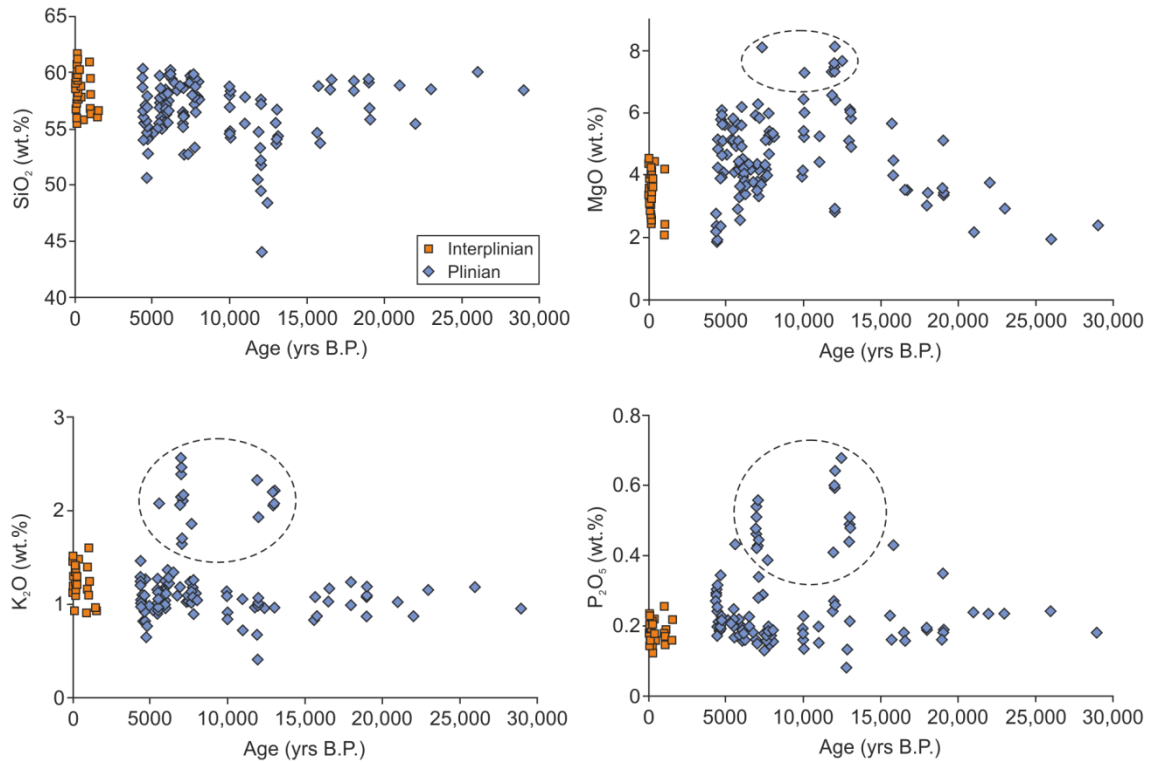


Figure 1.18 Time plots showing the variations in whole-rock major element geochemistry for the CVC eruption deposits over the past 30,000 years.

The deposits are divided into two groups based on the geochemical distinctions; the deposits with high MgO, K₂O and P₂O₅ (circled) form Group II.

The plots of K₂O and P₂O₅ against age reveal the majority of the eruption deposits show little compositional variation; however, some of the samples have distinctly high K₂O and P₂O₅ (Figure 1.18). Based on geochemistry and mineralogy, the plinian deposits can be divided into two groups. Group I represents the bulk of the tephra fallout deposits exposed on the flanks of Nevado de Colima, while Group II comprises three units with distinctive mineralogy and geochemistry (Figure 1.18). The main differences between the two groups are summarised in Table 1.1.

The Group I eruption deposits are medium-K, sub-alkaline basaltic-andesites to andesites (50.7 to 60.4 wt.% SiO₂) representing the products of differentiation from primitive mantle-derived melts. This evolutionary trend is shown by increasing whole-rock Al₂O₃, K₂O and Na₂O, and decreasing MgO, TiO₂, CaO and P₂O₅ with increasing SiO₂ (Figure 1.13).

Unit	Eruption Age (yrs B.P.)	Group	Composition	Crystallinity (vol.%)	Plag (vol.%)	Pyroxene (vol.%)	Hbd (vol.%)	Olivine (vol.%)	Phlog (vol.%)	SiO ₂ (wt.%)	MgO (wt.%)	K ₂ O (wt.%)
Y	4460±40	I	Andesite	10 - 15	5 - 10	< 1	2 - 4	-	-	53.9 – 60.4	1.8 – 2.3	1.0 – 1.5
W	4480±60 – 4540±60	I	Basaltic-Andesite	13 - 19	7 - 10	2 - 5	2 - 5	< 1	-	54.7 – 57.1	3.9 – 5.9	0.8 – 1.1
U	4740±40 – 4760±70	I	Basaltic-Andesite	20 - 25	12 - 15	3 - 6	2 - 5	1 - 2	-	50.7 – 56.8	2.3 – 6.1	0.7 – 1.3
S	5430±50 – 5500±60	I	Basaltic-Andesite	12 - 17	7 - 10	1 - 2	1 - 3	1 - 2	-	54.6 – 58.6	3.6 – 5.8	0.9 – 1.3
P	5980±50 – 6150±40	I	Basaltic-Andesite	14 - 22	10 - 15	1 - 2	1 - 3	< 1	-	55.4 – 59.7	2.6 – 6.2	1.0 – 1.3
N	6950±50 – 7070±60	II	Basaltic-Andesite	9 - 13	5 - 10	1 - 2	< 1	1	< 1	52.8 – 56.4	3.3 – 6.2	1.6 – 2.5
L	7520±50 – 7530±80	I	Andesite	11 - 19	5 - 10	< 1	1	3 - 5	-	58.0 – 59.9	3.9 – 5.1	1.0 – 1.2
J	7750±60 – 7760±50	I	Basaltic-Andesite	11 - 16	7 - 10	1	1 - 2	1	-	53.4 – 59.5	4.6 – 6.0	1.1 – 1.9
H	9770±60 – 10,310±50	I	Basaltic-Andesite	13 - 17	2 - 10	1 - 2	2 - 3	< 1 - 5	-	54.5 – 58.7	4.0 – 7.3	0.8 – 1.1
F	11,840±70 – 12,080±150	II	Basalt	7 - 12	< 1 - 1	2 - 5	< 1	1 - 3	1 - 2	43.9 – 53.3	6.4 – 8.1	0.4 – 2.3
D	12,460±60 – 13,350±130	II	Basalt	10 - 15	1 - 3	< 1 - 2	3 - 7	1	1	53.6 – 57.5	2.9 – 6.0	1.0 – 2.2

Table 1.1 Summary table of the characteristics of the CVC eruption deposits.

The Group II units, highlighted in bold, are distinguished by the presence of phlogopite, and their high K₂O contents. Mineral abbreviations are: Plag = plagioclase; Hbd = hornblende; Phlog = phlogopite.

The differentiation trend of the Group I eruption deposits is illustrated by units U, W and Y, which erupted sequentially between c.4700 to c.4400 yrs B.P. (Table 1.1; Luhr et al., 2010). These units vary in composition from basaltic (50.7 wt.% SiO₂) to high-silica andesite (60.3 wt.% SiO₂) from oldest (unit U) to youngest (unit Y). Pumice clasts from these units show a decrease in crystallinity over time, varying from 25 vol.% in unit U to 10 vol.% in unit Y. Similar trends are also observed in plagioclase, pyroxene and olivine abundances (Table 1.1). Accordingly olivine is not present in the more evolved unit Y, but here hornblende is common at up to 4 vol.%.

The Group I eruption deposits show very similar subduction-related trace element abundance patterns to the interplinian eruption deposits with enrichments in LREE and LILE relative to HFSE (Figure 1.19). Detailed petrological and geochemical analyses of the Group I eruption deposits is presented in Chapter 2.

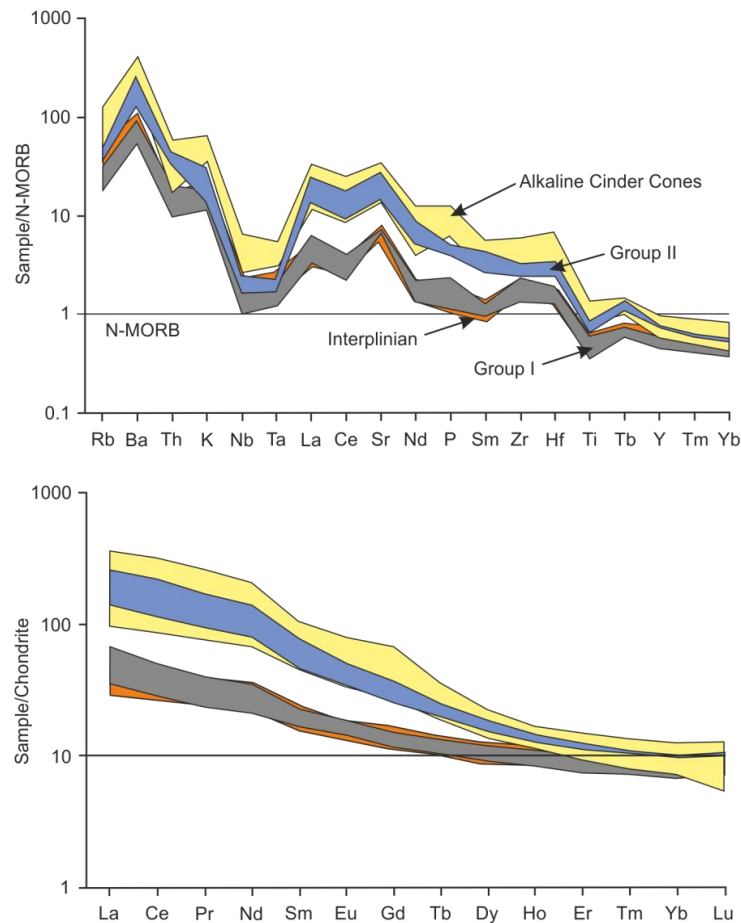


Figure 1.19 Incompatible whole-rock trace element abundances normalised to N-MORB and REE normalised to Chondrite for the CVC eruption deposits.

Normalising values are from Sun and McDonough (1989) and Nakamura (1974), respectively. All the CVC eruption deposits, including the alkaline cinder cones, have subduction-related trace element abundances characterised by depletions in the HFSE (Ta, Nb) relative to the LILE (Rb, Ba, K). The interplinian and Group I plinian samples have overlapping compositions, while the Group II samples show stronger enrichments in all the incompatible trace elements, partially overlapping the alkaline cinder cone compositions.

The Group II eruption deposits comprise units N, F and D of the Luhr et al. (2010) stratigraphy, which erupted c.7000, c.12,000 and c.13,000 yrs B.P. respectively (Figure 1.16). These units range in composition from basalt to basaltic-andesite (43.9 to 57.5 wt.% SiO₂; Table 1.1) but are geochemically distinct from the CVC sub-alkaline trend, distinguished by higher contents of K₂O (up to 2.5 wt.%), MgO (up to 8 wt.%) and P₂O₅ (up to 0.68 wt.%; Figure 1.18; Table 1.1). Scoria from these eruption deposits are petrologically distinct, characterised by the presence of phlogopite. Samples typically have low crystallinity of 10-15 vol.% and relatively low abundances of plagioclase and orthopyroxene and higher contents of clinopyroxene and olivine with respect to the Group I deposits (Table 1.1).

The three eruption deposits that form Group II display subduction-related trace element signatures; however, relative to Group I and the interplinian deposits, the Group II magmas display stronger enrichments in all of the incompatible trace elements, particularly in the LREE (La, Ce, Pr, Nd) and fluid mobile elements (Rb, Ba, K, Cs; Figure 1.19). The trace element abundance patterns of the Group II samples partially overlap the alkaline cinder cone field suggesting a petrogenetic link. The Group II eruptions deposits are discussed in detail in Chapter 3.

In the first study of the Holocene tephra deposits, Luhr and Carmichael (1982) discovered a scoria fallout deposit (unit N) exposed on the flanks of Nevado de Colima that was mineralogically and geochemically distinct from the rest of the fallout deposits. The authors proposed that this unit represented mixing between the medium-K, sub-alkaline CVC magma, and the alkaline magmas of the cinder cones. Based on morphology, the ages of the cinder cones were estimated at 1500 to >20,000 years old (Luhr and Carmichael, 1981) coinciding with the explosive eruptions that formed the Holocene CVC stratigraphy. Luhr and Carmichael (1982) therefore proposed that the geochemically distinct unit resulted from direct mixing between these two contemporaneously erupting magmas; however, this hypothesis was never fully explored. Allan and Carmichael (1984) and Carmichael et al. (2006) dated the cinder cones using K-Ar and ⁴⁰Ar/³⁹Ar techniques, which yielded ages of 450 ka to 62 ka; much older than the proposed mixed units of Luhr and Carmichael (1982). The relationship between the alkaline cinder cone magmas and the CVC magmas is explored throughout the thesis, and is discussed in detail in Chapter 5.

1.4 Modelling of Tephra Fallout at the Colima Volcanic Complex

The current hazard assessment maps at Volcán de Colima (Cortés et al., 2010) are based on various studies focusing on debris avalanche deposits from large sector collapse events (Luhr and Prestegard, 1988; Stoope and Sheridan, 1992; Komorowski et al., 1997; Cortés et al., 2009; Cortés et al., 2010); pyroclastic flows (Saucedo et al., 2005); and the 1913 plinian

eruption (Saucedo et al., 2010; Connor et al., In Prep.). No tephra dispersion modelling or eruption volume estimates have been carried out for the older plinian fallout deposits exposed on the flanks of Nevado de Colima. These deposits have average thicknesses of over 50cm, suggesting higher volume eruptions than that of the 1913 eruption which has an average tephra thickness of 30cm over the same area (Luhr et al., 2010).

Numerous towns and villages surround Volcán de Colima, including the cities of Colima and Ciudad Guzman, with populations of ~200,000 and ~150,000, respectively. Prevailing winds are from the southwest; therefore tephra is carried to the northeast, over the city of Ciudad Guzman. Ash from the 1913 plinian eruption reportedly fell in Guadalajara (~130 km to the north of Colima) and in Mexico City (~470 km northeast of Colima). These cities have two of Mexico's busiest international airports; therefore a highly explosive eruption, such as those which produced the Holocene tephra fallout deposits, could have a massive impact on the aviation industry, not only in Mexico, but globally. Chapter 6 presents the first tephra modelling for a large volume plinian eruption such as the one that produced the late Pleistocene and Holocene tephra fallout deposits observed at the CVC. Eruption column height and tephra dispersion modelling were carried out using *Tephra2* (Connor and Connor, 2006) for units Y, W, U, S and P of the Group I eruption deposits (Figure 1.16).

1.5 Research Questions

This Ph.D thesis examines the petrological and geochemical evolution of the CVC erupted magmas, with an emphasis on the Holocene eruptive stratigraphy. Mineralogical, geochemical and isotopic data is used to help constrain the crystallisation history of the CVC magmas (Group I and Group II), and to provide insights into the nature of the magmatic plumbing system. The relationship between the Group I magmas, the distinct Group II eruption deposits and the alkaline cinder cone magmas is investigated using petrological, geochemical and isotopic data, with an aim to quantitatively evaluate the possible mixing relationship between these magmas, as proposed by Luhr and Carmichael (1982). This research draws on new data presented here combined with published and unpublished datasets, and geophysical studies to present a model of CVC magma storage region.

The main research questions are:

1. How has the erupted magma composition evolved over the last ~13,000 yrs B.P.?
2. What is the nature of the magmatic plumbing system of the CVC, and, by drawing on petrological and geochemical data together with published geophysical data, can we define the nature of the plumbing system?

3. Is there a link between large volume medium-K, sub-alkaline and low volume high-K alkaline magmatism at the CVC, and what is the nature of this link?
4. How frequently do we observe alkaline magmatism at the CVC?
5. Is there a link between eruption volume and magma composition?

2 Group I Basaltic-Andesites to Andesites

The majority of the CVC Holocene tephra fallout deposits exposed on the flanks of Nevado de Colima are medium-K, sub-alkaline basaltic-andesite to andesite in composition. This chapter presents the results of field studies, petrological (optical microscopy, scanning electron microscopy and electron microprobe) and geochemical (whole-rock major and trace element, and whole-rock Sr and Nd isotope) analyses for the Group I eruption deposits. Initial results have shown that these deposits follow a fractional crystallisation trend, evolving from a primitive mantle-melt (see Section 1.3.2). Petrological and geochemical data are used here to investigate the evolution of the Group I deposits to help define the nature of the magmatic plumbing system, through which the magmas evolved.

Samples for petrological and geochemical analysis were collected during field campaigns in January 2010 and February 2011. Samples were also collected for granulometry, which are used for the tephra dispersion modelling presented and discussed in Chapter 6.

This work follows on from work carried out by Jim Luhr on the Holocene eruption deposits (Luhr and Carmichael, 1982, 1990b, a; Luhr et al., 2006; Luhr et al., 2010). Luhr worked on the CVC for over 20 years, publishing his first results with Ian Carmichael in 1980 (Luhr and Carmichael, 1980). Over the years he described and sampled Holocene eruption deposits at 71 localities; compiling a geochemical database of 196 whole-rock major and trace element analyses, and a polished thin section archive comprising over 100 samples. New geochemical analyses carried out as part of this work have been added to Luhr's database, together with published data from the literature (Luhr and Carmichael, 1980, 1981; Luhr and Carmichael, 1982; Allan and Carmichael, 1984; Robin et al., 1991; Luhr, 1993; Robin and Potrel, 1993; Komorowski et al., 1997; Luhr, 2002; Carmichael et al., 2006; Maria and Luhr, 2008; Savov et al., 2008; Luhr et al., 2010; Saucedo et al., 2010). All of these data are used here to investigate the Holocene explosive eruption deposits of the CVC.

2.1 Stratigraphy

The stratigraphy of the CVC deposits comprises pumice and scoria fall units separated by ash-rich surge and pyroclastic flow horizons (Figure 1.16). The tephra fallout deposits vary in thickness from 4cm to 1.4m and have distinctive colours including cream, orange and black (Figure 1.16; Table 2.1). The end-member units, U to Y, are used here to describe the stratigraphy and typical field characteristics of the Group I deposits, as they incorporate the entire range of magma compositions displayed by the Group I units from basaltic-andesite (unit U) to high-silica andesite (unit Y).

Unit	Eruption Age (yrs B.P.)	Number of localities	Deposit Type	Colour (dry)	Thickness (cm)	Max. Pumice size (cm)	Max. lithic size (cm)	Sorting	Composition
Y	4460±40	28	Pumice fall	Cream	48 - 140	17	7	Inverse	Andesitic
W	4480±60 – 4540±60	23	Scoria fall	Dark brown	8 - 28	6	5	Normal	Basaltic-Andesitic
U	4740±40 – 4790±100	30	Scoria fall	Dark orange	15 - 20	4	2	Normal	Basaltic-Andesitic
S	5430±50 – 5500±60	24	Scoria fall	Dark brown-orange	12 - 46	4.5	2	Normal	Basaltic-Andesitic
P	5980±50 – 6150±40	21	Pumice fall	Cream	6 - 40	9	6	Normal	Basaltic-Andesitic
L	7520±50 – 7530±80	16	Scoria fall	Dark brown	4 - 50	6	3	Inverse	Andesitic
J	7750±60 – 7760±50	8	Pumice fall	Pale orange - cream	7 - 15	6	3	Inverse	Basaltic-Andesitic
H	9770±60 – 10,310±50	9	Scoria fall	Dark grey / black	15 - 42	5	2	Inverse	Basaltic-Andesitic

Table 2.1 Field characteristics of the Group I tephra fallout deposits.

Eruption ages are from radiocarbon dating of charcoal found within or between tephra fallout deposits (Komorowski et al., 1997; Luhr et al., 2010). Maximum lithic fragment and pumice clast sizes, measured along the long-axis, are generally found in sections 4-5 km from the currently active vent. The older eruption deposits (i.e. unit H) are much less well exposed relative to the younger deposits (units U and Y). The deposits types have been divided into pumice and scoria fall based on chemical composition; pumice are more felsic, typically with a lower density, while scoria are more mafic with a higher density

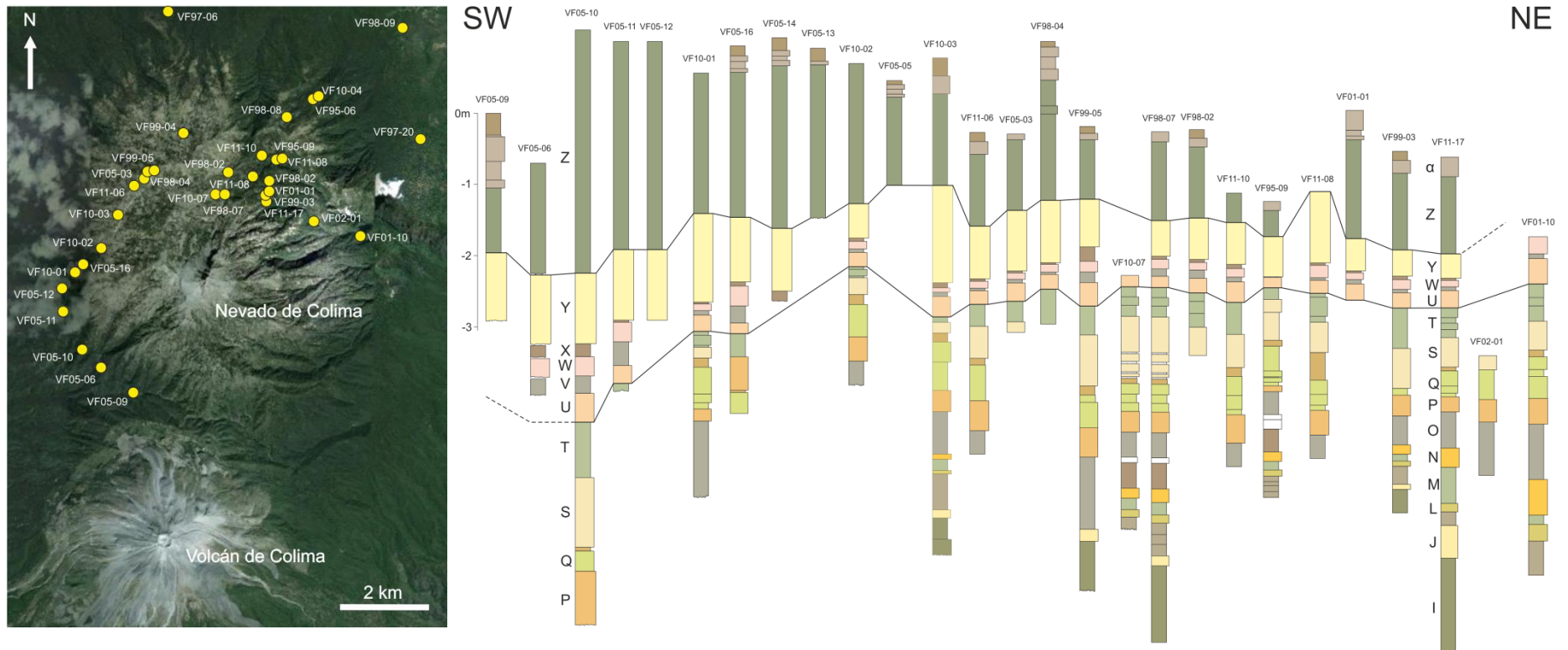


Figure 2.1 Location map for units U to Y and stratigraphic sections where units U to Y have been identified.

The black lines on the stratigraphy highlight the sequences of units U to Y. The stratigraphy is plotted in an arc from southwest to northeast.

Units U to Y erupted sequentially between ~4700 and ~4400 yrs B.P. and are well correlated across an area of ~100 km², from 4 to 11 km from the currently active vent of Volcán de Colima (Figure 2.1).

Units U to Y comprise tephra fallout deposits separated by 2 to 10cm thick ash horizons (Figure 2.2). The youngest unit in this sequence (unit Y) is a very distinct coarse, cream-coloured andesitic pumice-fall deposit that is easily recognisable across the area. It is inversely-graded and lithic rich, with lithic fragments up to 7cm, and pumice clasts ranging from 6cm up to 17cm. The largest pumice clasts are from section VF01-01, located on the north-northeast flank of Nevado de Colima, ~7.5 km from the vent (Figure 2.1). The thickness of unit Y has been measured at 28 localities, between 4 and 12 km from Volcán de Colima, varying from 48cm to 1.4m. Charcoal found within unit Y has yielded a radiocarbon age of 4460±40 yrs B.P. (Luhr et al., 2010), and ash layers above and below unit Y yielded ages of 4240±110 to 4450±60 yrs B.P. and 4480±60 to 4520±60 yrs B.P., respectively. Unit Y overlies a thin (2-10 cm) organic-rich ash horizon (unit X; Figure 2.2).

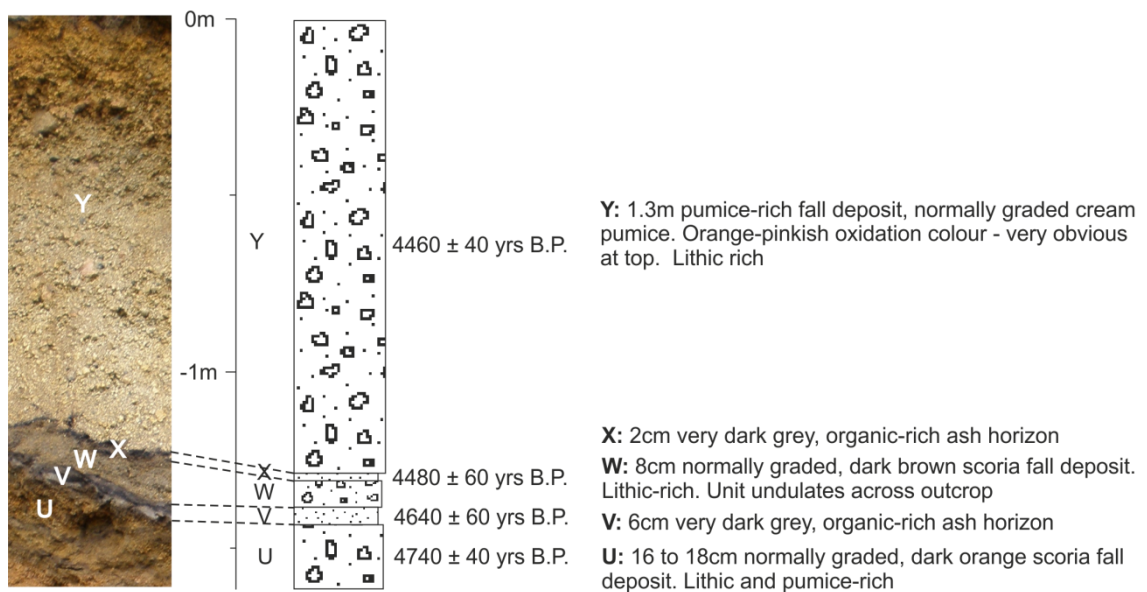


Figure 2.2 Field photograph and stratigraphic log of units U to Y from section VF10-01.

Ages are from sections VF01-01 and VF97-05, and are representative of this sequence. No ¹⁴C dates exist at this locality (VF10-01).

Underlying the ash horizon is the dark brown, basaltic-andesite, lithic-rich, scoria fall deposit of unit W. The average grain size of the scoria is less than 3cm, although scoria fragments up to 6cm are observed in localities more proximal to the vent. The maximum lithic fragment size is 5cm. Unit W is normally graded and varies in thickness from 8 to 28cm, measured at 23

localities (Table 2.1). Defining the base of the fall deposit is a very dark grey to black organic-rich ash horizon (unit V), which varies in thickness from 2 to 15cm (Figure 2.2). Unit W erupted approximately 4500 yrs B.P. based on dated charcoal from the binding ash horizons which yielded ages of 4480 ± 60 and 4540 ± 60 yrs B.P. (Luhr et al., 2010).

The oldest deposit in this sequence (unit U) is a distinctive dark orange, basaltic to basaltic-andesitic, scoria fall deposit with a fairly uniform thickness of 15 to 20cm across the area. Unit U is medium grained with scoria up to 4cm and lithic fragments up to 2cm. Radiocarbon dating of charcoal found within this layer yielded ages of 4740 ± 40 to 4790 ± 100 (Luhr et al., 2010). Unit U has been described at 30 localities (Table 2.1).

The field characteristics of the entire Group I eruption deposits are summarised in Table 2.1. The deposits are pumice and scoria fall deposits displaying characteristics similar to units U to Y described above. The younger eruption deposits, units P to Y (6000 - 4400 yrs B.P.), are well correlated across the CVC with good exposures high up on the flanks of Nevado de Colima (Figure 2.1). The older eruption deposits, however, are less well exposed, hence less-well correlated, as discussed in Section 1.3.2.

2.2 Petrology and Mineral Chemistry

Individual pumice and scoria samples from the Group I (and Group II; presented in Chapter 3) eruption deposits were collected during the 2010 and 2011 field seasons from various localities across Nevado de Colima. For each locality, clasts from each unit were selected for polished thin section preparation for optical microscope, scanning electron microscope (SEM) and electron microprobe (EPMA) work. Electron microscopy was carried out using a FEI Quanta 650 FEG-ESEM and mineral and glass compositions determined using a Jeol 8230 microprobe at the University of Leeds. Polished thin sections of samples collected by Jim Luhr, on loan from the Smithsonian Institution, Washington, USA, were also used alongside new samples for petrological investigation of the Group I (and Group II; Chapter 3) deposits.

The Group I eruption deposits are typical arc basaltic-andesites to andesites with the mineral assemblage: plagioclase + clinopyroxene + orthopyroxene + hornblende + Fe-Ti oxides \pm olivine in varying amounts (Table 2.2). Scoria and pumice are typically highly vesiculated with phenocryst and microphenocryst (<0.3mm after Wilcox, 1954) phases making up 15 – 25 vol.%. The groundmass comprises highly vesiculated glass with abundant microlites of the same mineral phases, with the exception of hornblende which is absent from the groundmass. Gabbroic glomerocrysts are present in all the samples (up to 2 vol. %), comprising plagioclase, clinopyroxene, orthopyroxene and commonly olivine and hornblende. The size of these vary from <1mm to 5mm.

Pumice from unit Y has a slightly different mineral assemblage from the other Group I eruption deposits in that the clasts are dominated by plagioclase and hornblende, with pyroxene present only in glomerocrysts and no olivine. These mineralogical differences are reflected in the whole-rock geochemistry, which is discussed in greater detail in Section 2.4.

Unit	Crystallinity (vol.%)	Plag (vol.%)	Opx (vol.%)	Cpx (vol.%)	Hbd (vol.%)	Olivine (vol.%)	Fe-Ti oxides (vol.%)
Y	10 - 15	5 - 10	0 - trace	0 - trace	2 - 4	-	Trace - 1
W	13 - 19	7 - 10	1 - 2	1 - 3	2 - 5	Trace - 1	1
U	20 - 25	12 - 15	1 - 2	3 - 4	2 - 5	1 - 2	1
S	12 - 17	7 - 10	1	1 - 2	1 - 3	1 - 2	1
P	14 - 22	10 - 15	1 - 2	1 - 3	Trace	Trace	1
L	11 - 19	5 - 10	Trace	1	3 - 5	-	1 - 2
J	11 - 16	7 - 10	1	1 - 2	1	-	1 - 2
H	13 - 17	2 - 10	1 - 2	2 - 3	Trace - 5	Trace - 2	1

Table 2.2 Mineralogy of pumice and scoria from the CVC Group I plinian tephra fallout deposits.

The mineral proportions are given as volume % of the whole sample, and were estimated from thin sections on the optical microscope. The mineral abbreviations are: Plag = plagioclase; Opx = orthopyroxene; Cpx = clinopyroxene; and Hbd = hornblende.

2.2.1 Mineral Compositions

Many of the mineral phases in the Group I tephra show large core-rim compositional variations. Plagioclase and pyroxene phenocrysts display strong zoning and resorption textures which are discussed in detail in Section 2.2.2.

Table 2.3 summarises the chemistry of the main phenocryst phases in the Group I explosive eruption deposits. The full mineral chemistry data tables are presented in Appendix B.

2.2.1.1 Plagioclase

The dominant mineral phase is plagioclase comprising 5-15 vol. % of the samples, occurring as euhedral to subhedral microphenocrysts (<0.3mm) and phenocrysts up to 3mm in length. Core and rim anorthite compositions vary from andesine (An₃₀) to bytownite (An₈₄; Figure 2.3).

Plagioclase phenocrysts are heterogeneous showing large variations (of up to 20 mol % An) in cores and in rims (Figure 2.4 and Table 2.3). Units Y, U, J and H all contain plagioclase phenocrysts with a similar range of core and rim compositions (Figure 2.4). Unit Y displays the widest variation in plagioclase anorthite content with cores and rims of An₂₈ to An₈₃ (Figure 2.4). Plagioclase in units S, P and L typically have more anorthitic cores than rims (Figure 2.4), while unit W contains plagioclase with a wide range of core compositions (An₃₈₋₈₄), and a narrow range of rim compositions (An₅₉₋₆₄).

Unit	Glass SiO ₂ (wt.%)	Plagioclase An (mol.%)		Clinopyroxene Mg#		Orthopyroxene Mg#		Olivine Mg#	
	Average	Cores	Rims	Cores	Rims	Cores	Rims	Cores	Rims
Y	65.4 (<i>n</i> =98; 54.2-73.9)	64 (<i>n</i> =36; 28-83)	57 (<i>n</i> =51; 29-83)	-	-	-	-	-	-
W	61.43 (<i>n</i> =37; 54.1-70.9)	57 (<i>n</i> =14; 38-84)	51 (<i>n</i> =13; 59-64)	0.80 (<i>n</i> =8; 0.76-0.83)	0.79 (<i>n</i> =7; 0.77-0.81)	0.76 (<i>n</i> =4; 0.75-0.77)	0.78 (<i>n</i> =2; 0.78)	0.78 (<i>n</i> =17; 0.76-0.80)	0.78 (<i>n</i> =16; 0.76-0.79)
U	60.4 (<i>n</i> =86; 52.8-70.1)	61 (<i>n</i> =23; 42-80)	59 (<i>n</i> =23; 41-79)	0.80 (<i>n</i> =18; 0.75-0.87)	0.79 (<i>n</i> =29; 0.75-0.83)	0.76 (<i>n</i> =13; 0.69-0.80)	0.77 (<i>n</i> =14; 0.69-0.80)	0.76 (<i>n</i> =17; 0.72-0.78)	0.77 (<i>n</i> =20; 0.61-0.78)
S	64.2 (<i>n</i> =9; 57.8-72.7)	57 (<i>n</i> =15; 51-69)	53 (<i>n</i> =15; 46-58)	0.78 (<i>n</i> =3; 0.75-0.81)	0.76 (<i>n</i> =3; 0.75-0.77)	0.78 (<i>n</i> =10; 0.73-0.85)	0.73 (<i>n</i> =11; 0.71-0.75)	-	-
P	67.0 (<i>n</i> =20; 62.9-68.9)	54 (<i>n</i> =9; 48-70)	50 (<i>n</i> =20; 45-55)	0.78 (<i>n</i> =6; 0.76-0.79)	0.76 (<i>n</i> =7; 0.75-0.79)	0.76 (<i>n</i> =6; 0.73-0.79)	0.74 (<i>n</i> =12; 0.72-0.77)	-	-
L	71.8 (<i>n</i> =37; 65.6-75.8)	64 (<i>n</i> =15; 64-80)	53 (<i>n</i> =16; 46-62)	0.75 (<i>n</i> =6; 0.73-0.77)	0.84 (<i>n</i> =2; 0.84)	0.78 (<i>n</i> =2; 0.74-0.81)	0.73 (<i>n</i> =4; 0.71-0.73)	-	-
J	62.5 (<i>n</i> =25; 54.5-68.7)	56 (<i>n</i> =15; 43-71)	53 (<i>n</i> =14; 39-71)	0.78 (<i>n</i> =7; 0.76-0.80)	0.79 (<i>n</i> =13; 0.75-0.84)	0.83 (<i>n</i> =3; 0.78-0.85)	0.77 (<i>n</i> =12; 0.72-0.81)	-	-
H	61.2 (<i>n</i> =31; 55.5-70.1)	47 (<i>n</i> =18; 31-69)	52 (<i>n</i> =17; 37-70)	0.83 (<i>n</i> =16; 0.76-0.88)	0.77 (<i>n</i> =15; 0.74-0.83)	0.72 (<i>n</i> =6; 0.69-0.75)	0.77 (<i>n</i> =7; 0.74-0.81)	0.83 (<i>n</i> =9; 0.80-0.87)	0.79 (<i>n</i> =8; 0.77-0.83)

Table 2.3 Mineral chemistry of the Group I basaltic-andesites to high-silica andesites based on EPMA analyses.

For each mineral, the average composition is given along with the number of analyses and the range of compositions. Analyses were carried out on the Jeol 8234 electron microprobe at the University of Leeds. Anorthite content is calculated as Ca/(Ca+Na+K), and Mg# is calculated as Mg/(Mg+Fe). Although olivine is present in units S and P, there is no microprobe data of olivine from these units. The full mineral chemistry dataset is presented in Appendix B.

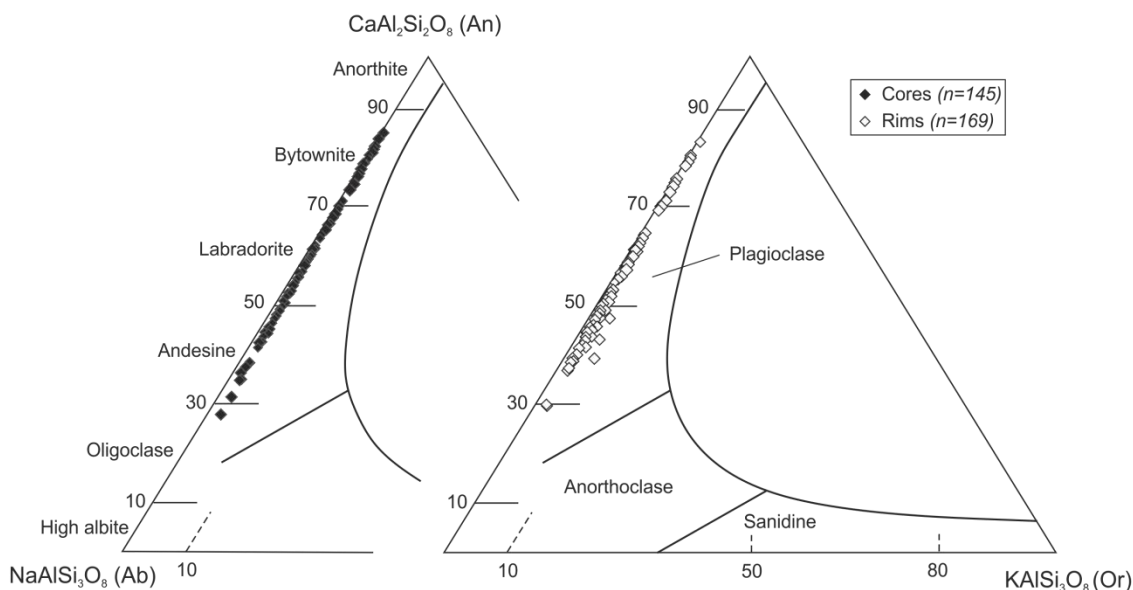


Figure 2.3 Feldspar ternary classification diagram after Deer et al. (1992).

Cores and rims span a wide range of plagioclase compositions from andesine (An_{30}) to bytownite (An_{84})

The heterogeneities in plagioclase compositions are reflected in the mineral textures and zoning patterns, which is discussed in detail in Section 2.2.2.

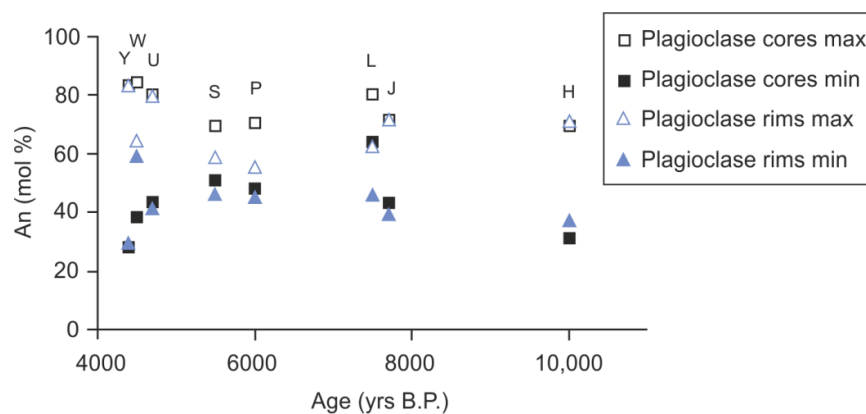


Figure 2.4 Ranges of core and rim compositions of plagioclase from the Group I deposits versus eruption age in yrs B.P.

An content is calculated as $An = Ca / (Ca + Na + K)$. Unit names (Y to H) are indicated. Unit Y plagioclase shows the widest range in An content, from An_{28} to An_{83} in core and rims

2.2.1.2 Clinopyroxene

Clinopyroxene is present in all samples with abundances varying from trace amounts to 4 vol.% (Table 2.2). The majority of clinopyroxene crystals occur in pairs or in glomerocrysts, suggesting they may be inherited (Figure 2.5a). Phenocrysts are commonly broken and rims are

embayed indicating they have undergone disequilibrium during growth (Figure 2.5b; see also Section 2.2.2.2).

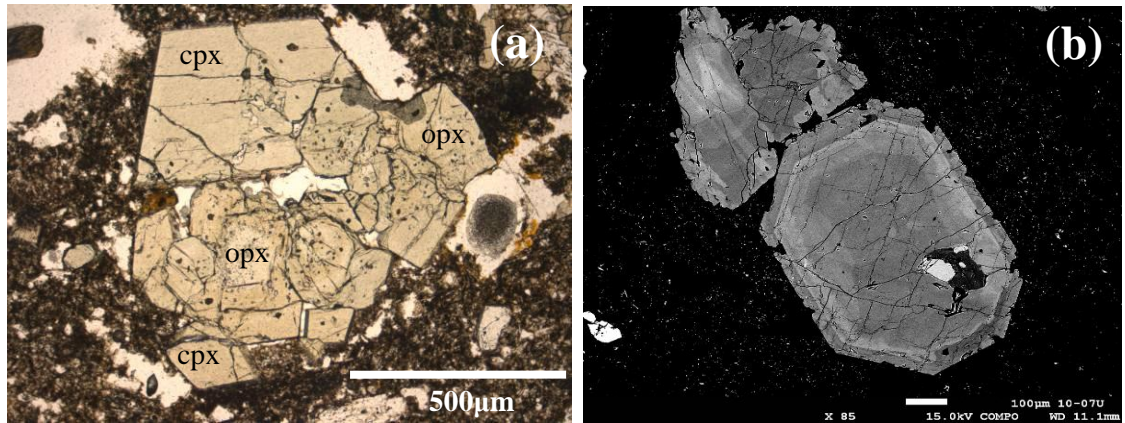


Figure 2.5 Optical microscope and SEM backscatter (BSE) images of clinopyroxene crystals in the Group I eruption deposits.

(a) shows a plane-polarised light image of a clinopyroxene (cpx) and orthopyroxene (opx) glomerocryst and (b) is a BSE image of clinopyroxene with an unstable, embayed rim. Images are from samples VF97-06B from unit W (a) and VF10-07U from unit U (b).

Clinopyroxene compositions vary in Mg# from 0.71 to 0.88 across the Group I eruption deposits (Table 2.3), and plot in the augite and diopside fields on the Ca-Mg-Fe classification diagram after Morimoto (1988; Figure 2.6). Typically, average core compositions are more magnesian (Mg# 0.78-0.84) compared with the average rim compositions (Mg# 0.74-0.79); however, cores and rims show wide variations in all the Group I eruption deposits (Figure 2.7).

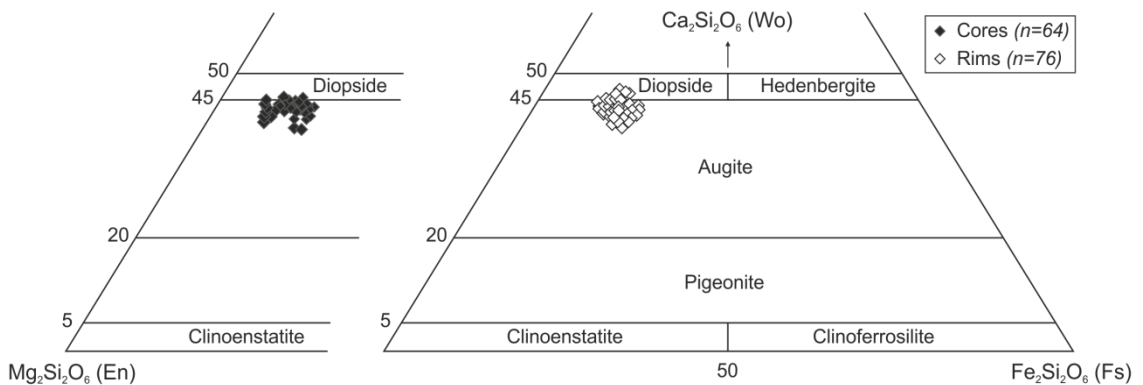


Figure 2.6 Classification of Ca-Mg-Fe clinopyroxenes after Morimoto (1988).

Clinopyroxenes plot in the augite and diopside fields. Cores (black diamonds) of clinopyroxene are more magnesian than the rims.

Clinopyroxene from units U and H have the most magnesian cores, while clinopyroxene from unit L has the least magnesian core (Figure 2.7). Unit H displays the widest variation in clinopyroxene Mg# in cores and rims (Figure 2.7). These variations in composition are explored further in Section 2.2.2.3.

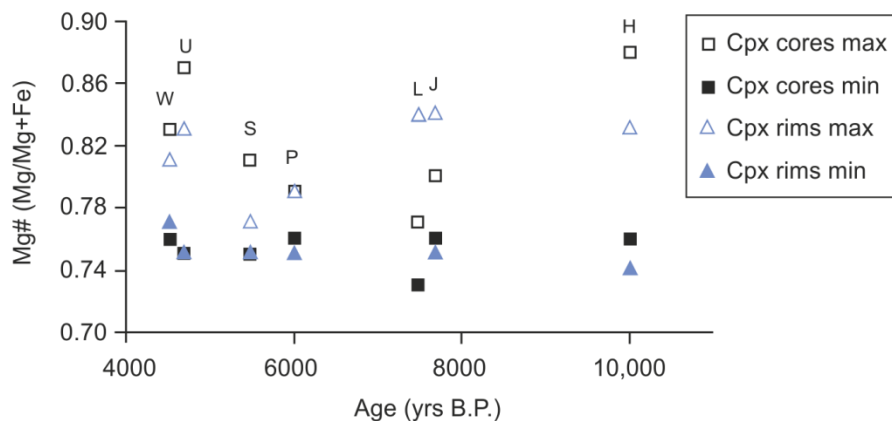


Figure 2.7 Clinopyroxene core and rim Mg# for the Group I eruption deposits.

Compositions are plotted versus eruption age in yrs B.P. to show differences between the units. Mg# = Mg/(Mg+Fe). Unit names (W to H) are indicated.

2.2.1.3 Orthopyroxene

Orthopyroxene is present in all of the Group I eruption deposits varying in abundance from trace to 2 vol. % (Table 2.2). Orthopyroxene typically occurs together with clinopyroxene in glomerocrysts (Figure 2.5a). Phenocrysts display strong zoning textures (see Section 2.2.2.5) and embayed rims.

Orthopyroxene phenocryst cores and rims occupy the enstatite field in the Ca-Mg-Fe classification diagram after Morimoto (1988; Figure 2.8). Mg# in phenocrysts varies from 0.69 to 0.85; average core compositions are more magnesian (Mg# 0.72 - 0.83) than average rim compositions (Mg# 0.72 - 0.78; Table 2.3).

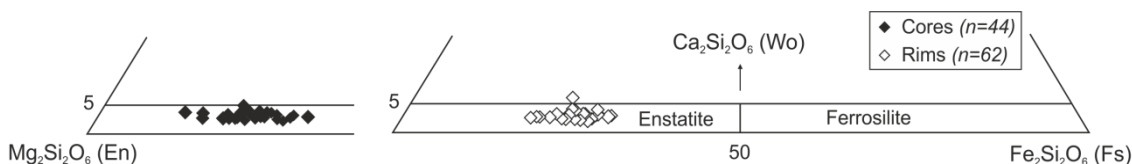


Figure 2.8 Classification of orthopyroxenes after Morimoto (1988).

Orthopyroxenes from the Group I eruption deposits are enstatite. Cores (black diamonds) are typically more magnesian than the rims (white diamonds).

Figure 2.9 shows the range of orthopyroxene core and rim Mg# in the Group I eruption deposits. Unit W shows the narrowest range in core and rim Mg# (0.75 - 0.77). Cores and rims in orthopyroxene from unit U show the same range in Mg# (0.69 - 0.80), while units S, P, L and J all display high magnesian cores relative to rims (Figure 2.9). Unit H orthopyroxene appear to be reversely zoned with more magnesian rims than cores (Figure 2.9). The variations in Mg# in orthopyroxene are discussed in more detail in relation to mineral textures in Section 2.2.2.5.

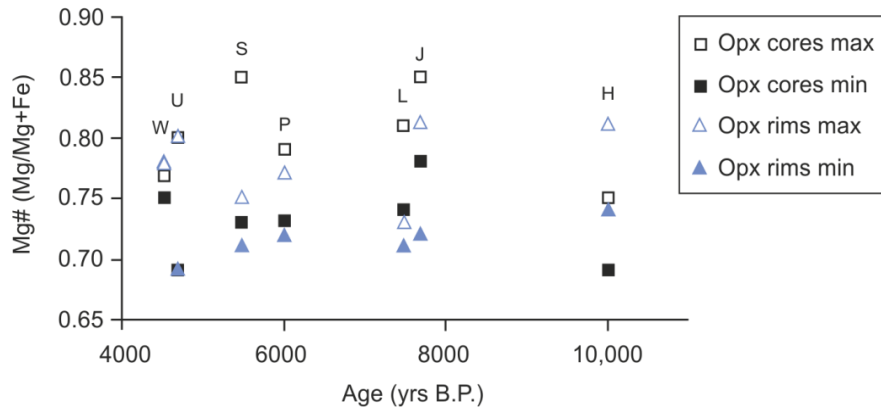


Figure 2.9 Range of core and rim Mg# in orthopyroxene for the Group I eruption deposits.

2.2.1.4 Hornblende

Hornblende phenocryst abundances vary from 1 to 4 vol.% (Table 2.2). Crystals are euhedral to subhedral with prismatic habit, typically up to 1.5mm in length. They commonly appear broken, and rims are generally sharp (Figure 2.10a); however hornblende with strong reaction rims of pyroxene, plagioclase and oxides are present in all units (Figure 2.10b). Ghost hornblende, having completely altered to oxides, pyroxene and plagioclase, is rare but does occur. Both altered and fresh crystals occur together in units S and L (Figure 2.10c). Many of the hornblende phenocrysts are weathered or altered, displaying a rusty appearance in plane-polarised light on the optical microscope (Figure 2.10d).

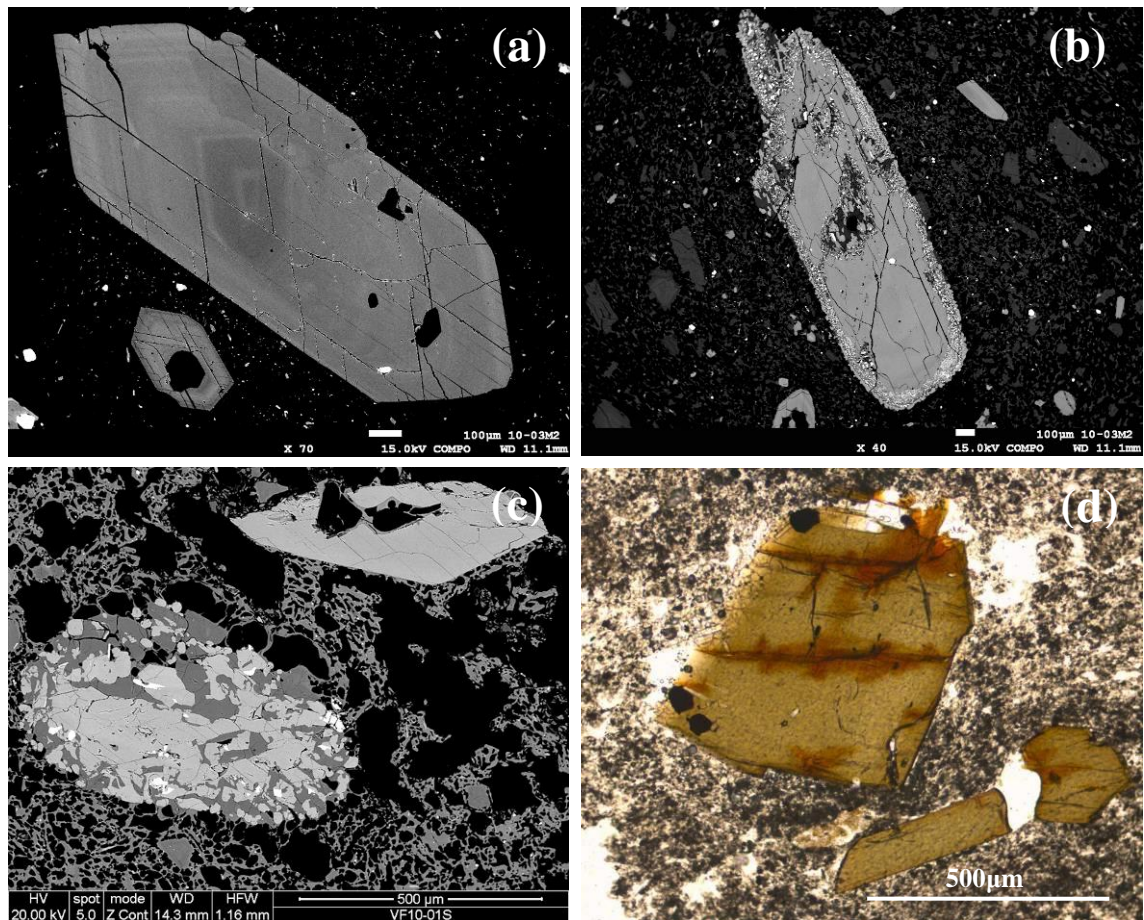


Figure 2.10 BSE images of hornblende phenocrysts.

Fresh, stable hornblende (a) and hornblende with a breakdown rim of Fe-Ti oxides (small white dots), pyroxene and plagioclase (b) from the same sample, VF10-03M2, from unit L. Image (c) shows two hornblende phenocrysts; one is stable with a sharp crystal rim, while the other is partially resorbed and overgrown by plagioclase, orthopyroxene and Fe-Ti oxides, from sample VF10-01S from unit S. (d) is an optical microscope photograph of a weathered or altered hornblende displaying a rusty appearance in plane-polarised light from sample VF97-05B from unit Y.

According to the classification of calcic amphiboles (≥ 1.5 Ca ions residing in the B site) after Leake et al (1997), the CVC Group I amphiboles are magnesiohastingsite and edenite (Figure 2.11a). Hornblende is the broad name given to coloured calcic-amphiboles, which Leake et al. (1997) reclassified based on the number of Na and K ions residing in the A site. Figure 2.11 shows the two classification diagrams for calcic-amphiboles of Leake et al. (1997). Amphiboles found in the Group I deposits have $(\text{Na}+\text{K})_A > 0.5$, therefore are classified according to Figure 2.11(a).

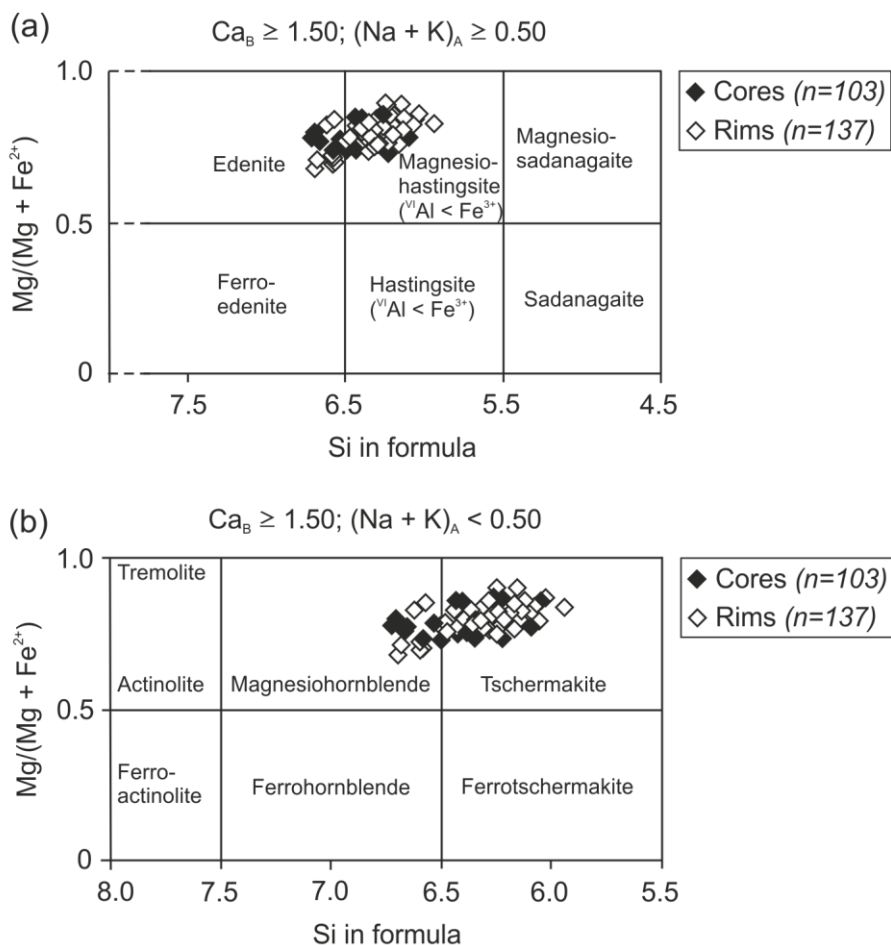


Figure 2.11 Classification of calcic amphiboles after Leake et al. (1997).

Plot (a) is used if the sum of the Na + K cations in the A site are more than 0.50; and plot (b) is used if $(Na+K)_A < 0.5$. The CVC Group I amphiboles have $(Na+K)_A > 0.5$, therefore can be classified as magnesiohastingsite and edenite.

2.2.1.5 Olivine

Olivine is present in all of the Group I eruption deposits except the more evolved units Y and L, and the intermediate unit J (Table 2.2). The abundance of olivine varies from trace amounts to 2 vol.%; and occurs as rounded and embayed phenocrysts up to 1mm across and microphenocrysts (Figure 2.12a and b). Olivine is also common in glomerocrysts (Figure 2.12c), occurring together with clinopyroxene and orthopyroxene (Figure 2.12d). Weak zonation from core to rim is common, with less magnesian rims, as revealed on the backscatter SEM images by a much lighter colour (Figure 2.12 c and d).

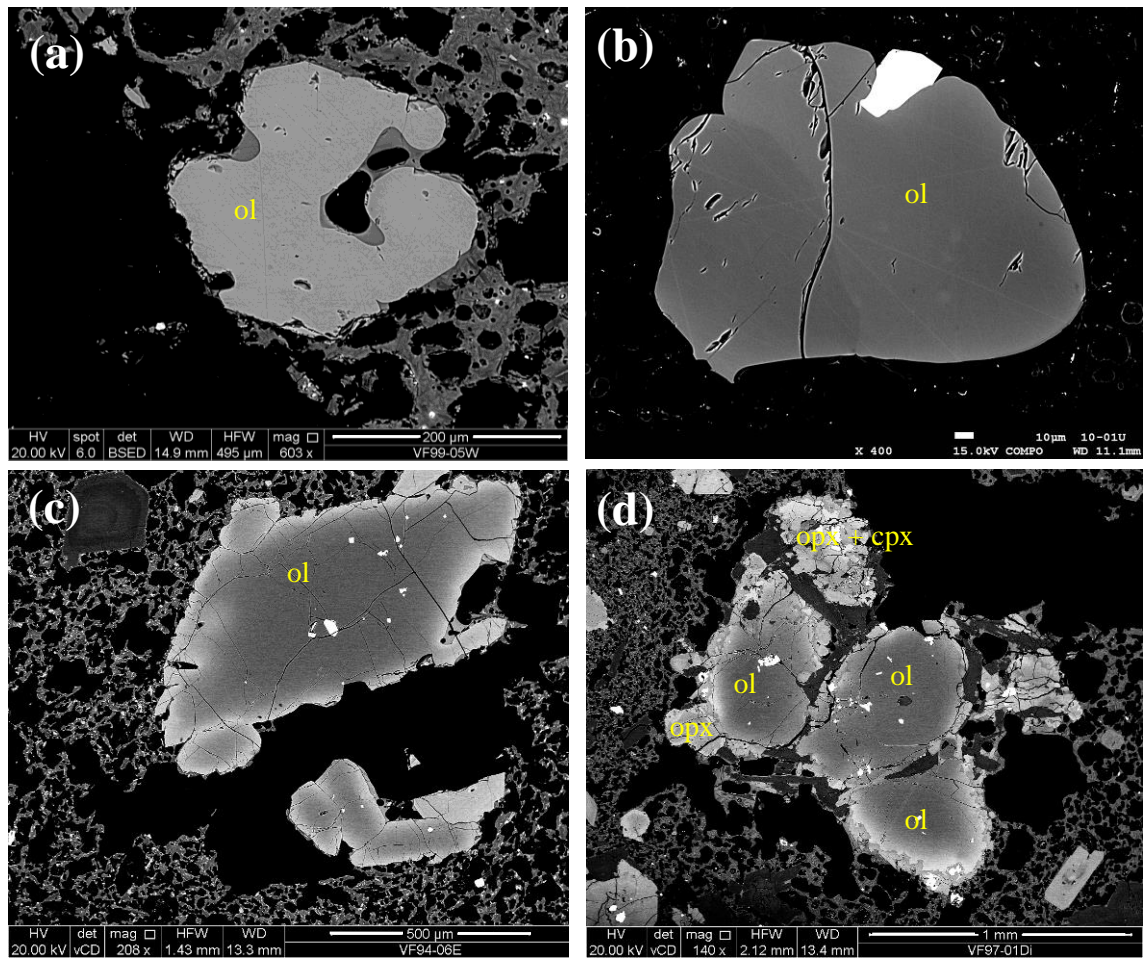


Figure 2.12 Backscatter SEM images of olivine.

Images are from units W, U and H from the Group I stratigraphy. Image (a) is an embayed microphenocryst from sample VF99-05W (unit W), (b) is a microphenocryst with an Fe-Ti oxide inclusion from VF10-01U (unit U), (c) is a phenocryst of a zoned olivine from VF94-06E (unit H), and (d) is a glomerocryst of olivine with orthopyroxene and clinopyroxene from VF97-01Di (unit H). The bright rims on (c) and (d) reflect Fe-rich olivine growth.

Core and rim compositions of phenocrysts and microphenocrysts vary between units, ranging from Mg# 0.78 to 0.87 and 0.61 to 0.80, respectively (Table 2.3 and Figure 2.13). Unit H has the most magnesian olivine with cores of Mg# 0.87 and rims of Mg# 0.78 (Table 2.3; Figure 2.13). Olivine crystals from units W and U are less magnesian with cores with maximum Mg# 0.80 and 0.78, respectively, and rims with Mg# as low as 0.76 and 0.61, respectively (Figure 2.13). The high-Mg cores (Mg# 0.87) indicate primitive mantle-derived melts (Deer et al., 1997).

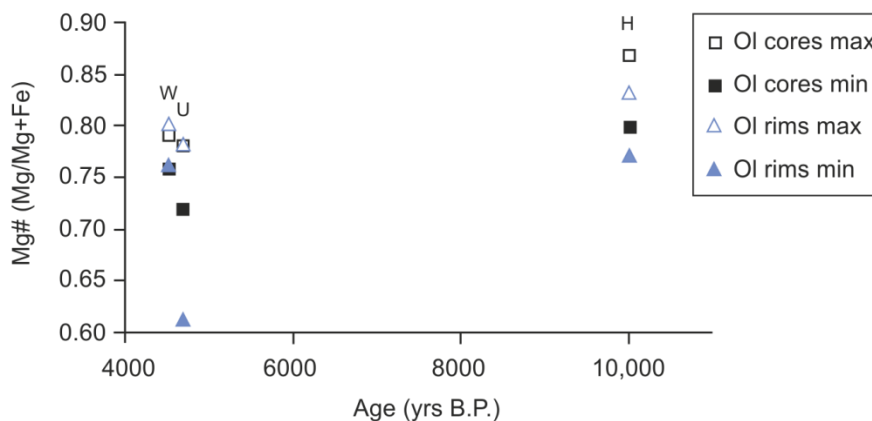


Figure 2.13 Ranges of core and rim Mg# in olivine for the Group I eruption deposits.

Unit names (W,U and H) are indicated. Unit H has the highest Mg core, with Mg# 0.87.

2.2.1.6 Fe-Ti oxides

Titanomagnetite and ilmenite commonly occur as microphenocrysts in the groundmass, in glomerocrysts and in reaction rims on hornblende crystals, varying in abundance from 1-2 vol.% (Table 2.2). No chemical analyses of the Fe-Ti oxides were collected. Fe-Ti oxides are also associated with pyroxene, olivine and hornblende phenocrysts.

2.2.1.7 Accessory minerals

The only observed accessory mineral in the Group I scoria and pumice samples is apatite, which commonly occurs as inclusions in hornblende phenocrysts and as microphenocrysts in the groundmass. Luhr and Carmichael (1982) report spinel inclusions in olivine and in the groundmass of scoria samples, however, no spinel was observed during this study.

2.2.1.8 Groundmass

The groundmass typically comprises intermediate to felsic glass (54 – 74 wt.% SiO₂; Figure 2.14) with abundant microlites of plagioclase and pyroxene. The groundmass glass composition reflects the whole-rock geochemistry, with the more evolved andesitic units (Y and L) having higher glass SiO₂ contents than the more basaltic unit U (Table 2.3, Figure 2.14).

Pumice and scoria clasts commonly display colour variations, reflected in the groundmass glass, which has a streaky appearance (Figure 2.15). These colour variations reflect heterogeneity of the glass with up to 20 wt.% variation in SiO₂ contents in a single clast (Table 2.3, Figure 2.14 and 2.15).

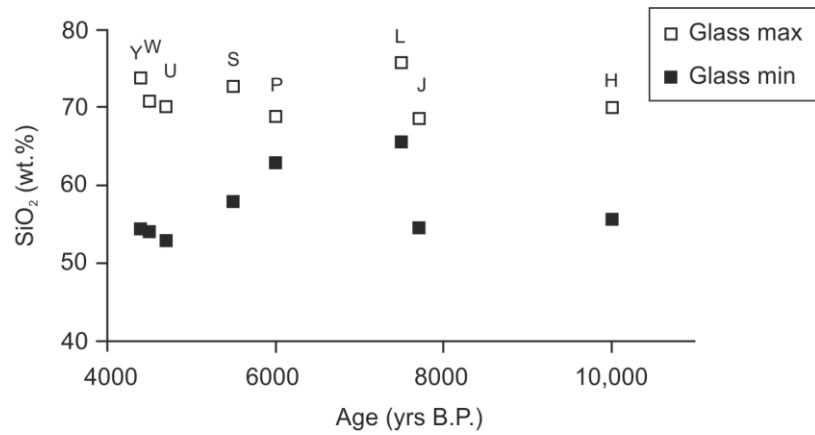


Figure 2.14 Range in SiO₂ content of groundmass glass in scoria and pumice samples from the Group I eruption deposits versus eruption age in yrs B.P.

Pumice and scoria clasts from all units display heterogeneities in glass SiO₂ contents (Figure 2.14). Unit Y displays the widest variation with 54.2 to 73.9 wt.% glass SiO₂ content, while unit P displays the narrowest range with only 62.9 to 68.9 wt.% SiO₂ (Figure 2.14 and Table 2.3).

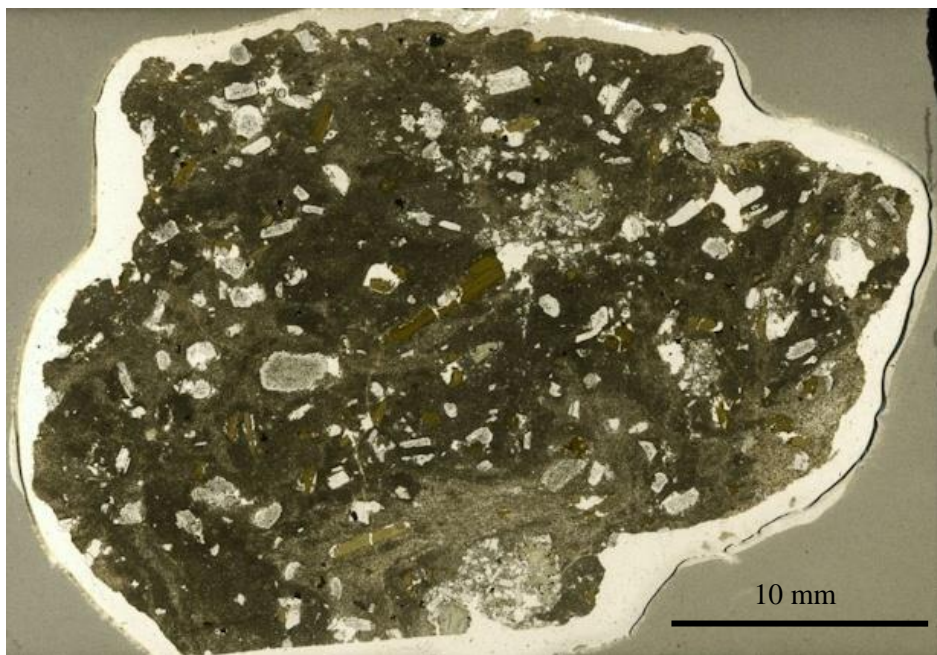


Figure 2.15 Scanned thin section of a streaky pumice clast from unit Y (VF97-06D).

Glass SiO₂ content varies from 54.2 to 73.9 wt.% between the light and dark areas.

Sources of heterogeneities in the SiO₂ content of glass can be the result of poor analyses, post-eruption alteration or magma mingling (Duzgoren-Aydin et al., 2002). Care was taken to

analyse glass free of microlites, using a 5µm beam on the electron microprobe, and any analyses with low totals were discarded eliminating analytical error. Post-eruption alteration results in the replacement of the groundmass and mineral phases by sericite, chlorite, clay minerals or sesquioxides (Fe, Mn oxides and hydroxides; Duzgoren-Aydin et al., 2002). No petrological evidence for this in the CVC pumice and scoria samples has been found; therefore, the source of the heterogeneities in the glass is assumed to be magma mingling.

2.2.2 Textures and Mineral Zoning

Mineral zoning and groundmass textures in scoria and pumice samples erupted from arc volcanoes can provide insights into the magmatic plumbing system of the volcano; compositional changes within mineral phases reflect a combination of changing pressure, temperature, water content and fO_2 within the magmatic storage region (Nelson and Montana, 1992; Ginibre et al., 2002a; Humphreys et al., 2006; Jerram and Kent, 2006; Davidson et al., 2007; Ginibre and Wörner, 2007; Streck, 2008; Crabtree and Lange, 2011), while groundmass textures can provide insights into magma ascent rates and late-stage crystallisation (Hammer et al., 1999; Szramek et al., 2006; Rutherford, 2008).

The main mineral phases of the Group I basaltic-andesites to andesites all display complex zoning textures. Plagioclase and pyroxene phenocrysts reveal crystallisation histories involving multiple phases of crystal growth, destabilisation, and, in many cases, regrowth.

2.2.2.1 Zoning in Plagioclase

Plagioclase crystals found in arc magmas commonly display complex zoning patterns and morphologies (Blundy and Cashman, 2001; Ginibre et al., 2002a; Ginibre et al., 2002b; Jerram and Kent, 2006; Ginibre and Wörner, 2007). The plagioclase textures observed in the Group I CVC eruption deposits have been characterised into seven types. No single eruption deposit contains all seven types, examined across multiple thin sections for each unit; however, there are types common to every unit.

Type I plagioclase are anhedral, displaying patchy zoning and sieve textures (Figure 2.16a and 2.16b). These phenocrysts have undergone pervasive resorption, leaving a porous, sieve texture, which was infilled by melt. The holes contain vesiculated glass, indicating the porosity of the crystal was open at the time of eruption. Recrystallisation gives the crystals a patchy appearance (Figure 2.16b). The anorthite content varies by up to 30 mol% between the light and dark patches. The cross-cutting relationship of the lighter, more anorthitic plagioclase, reveals this grew later, infilling the partially resorbed, more sodic plagioclase (Figure 2.16b; Ginibre and Wörner, 2007; Streck, 2008).

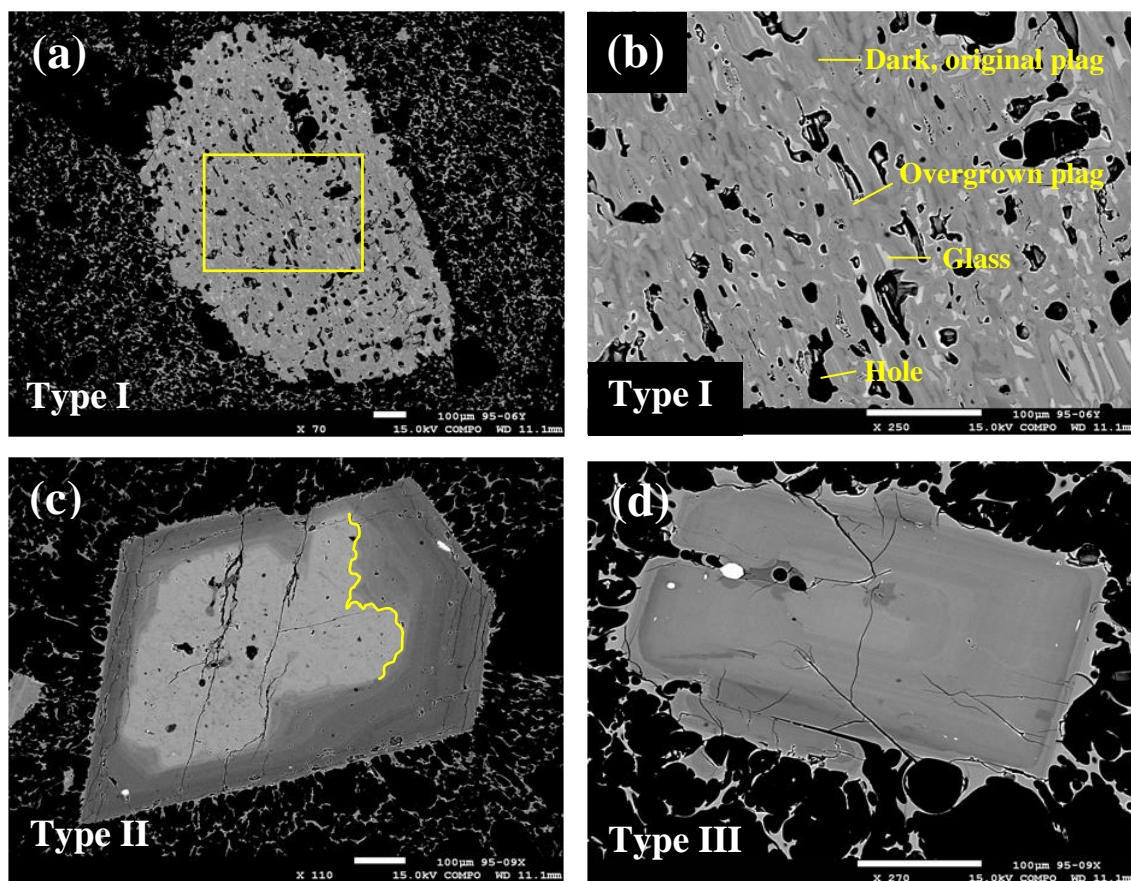


Figure 2.16 BSE images of types I, II and III plagioclase phenocrysts.

Type I (a) display pervasive resorption and recrystallisation from sample VF95-06Y from unit Y. (b) is a zoomed in image of (a) showing the patchy zonation: the dark grey patches are the original mineral, which is overgrown by more anorthitic plagioclase. The lightest patches are glass, and the black areas are holes. Type II (c) have a recrystallised core and normally zoned rim in equilibrium with the melt; and type III (d) are normally zoned plagioclase. Note the sharp dissolution surface surrounding the core in type II, as highlighted by the yellow line. Images (c) and (d) are from sample VF95-09X from unit U.

The second type, II, has a core of type I, surrounded by normally zoned plagioclase with a sharp dissolution surface along the core-rim boundary (Figure 2.16c). The composition from core to rim varies from An_{67-78} to An_{35-50} . This normal zoning pattern is also found in small (~0.5mm) euhedral phenocrysts and microphenocrysts (type III; Figure 2.16d) with similar compositions suggesting type III and the rim of type II plagioclase grew over similar time-scales in equilibrium with the same melt. Types I, II and III are observed in all Group I eruption deposits.

Oscillatory-zoned plagioclase (type IV; Figure 2.17a) is common in many of the units. These range from faint repeated variations which are termed low amplitude oscillations (LAO) after Ginibre et al. (2002a), to characteristic saw-tooth core-rim patterns with multiple resorption surfaces (STR; Ginibre et al. 2002a). Both small-scale (<10µm width and <5 mol. % An

amplitude) and large-scale (up to 100µm width and 20 mol. % An amplitude) STR type oscillatory zoning is present within the samples, often in the same crystal (Figure 2.18). Plagioclase displaying reversed zoning (type V; Figure 2.17b) with anorthite content varying by ~20% from the core to the rim is present only in unit W.

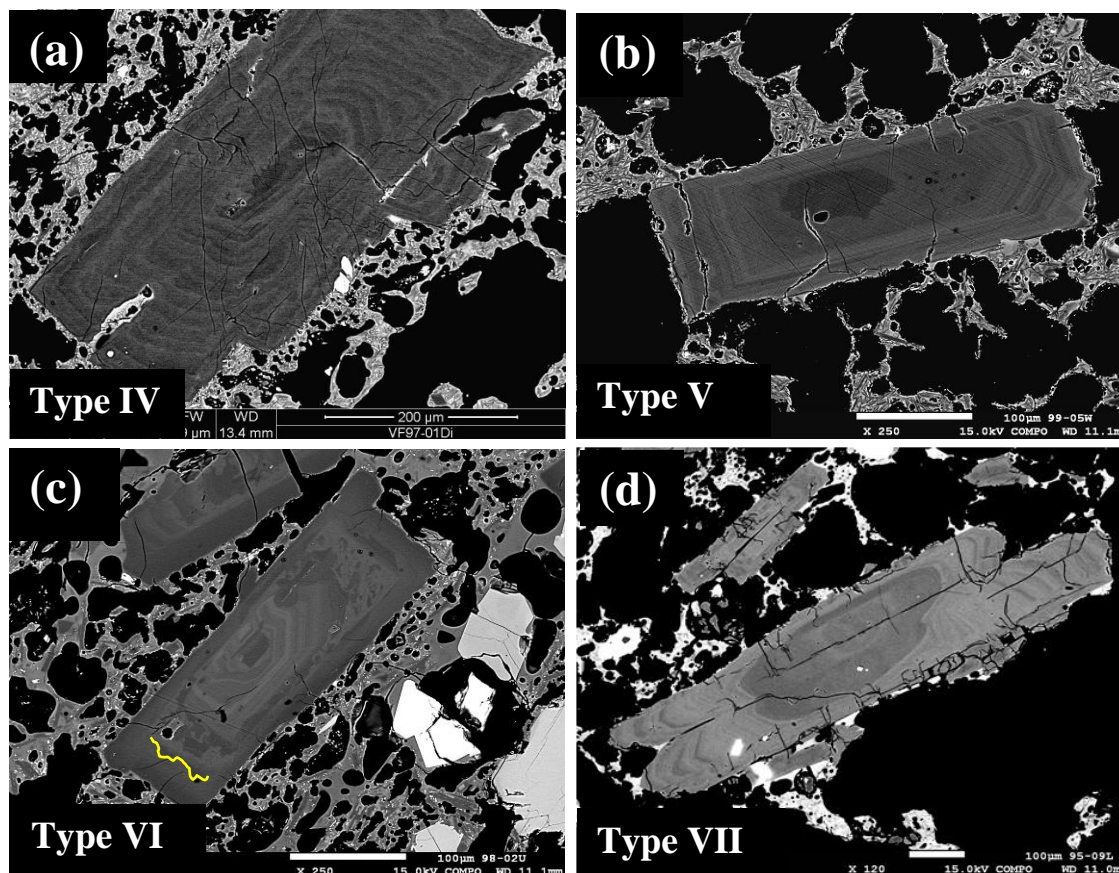


Figure 2.17 BSE images of types IV to VII of plagioclase present in Group I eruption deposits.

(a) type IV displays oscillatory zoning (sample VF97-01Di, unit H); (b) type V is reversely zoned (sample VF99-05W, unit W); (c) type VI displays a normally zoned core surrounded by a patchy sieve textured growth zone that is in turn surrounded by normally zoned plagioclase to the rim (sample VF98-02U, unit U); (d) type VII which has a normally zoned core surrounded by oscillatory zoning (sample VF95-09L, unit P). Note the sharp dissolution surface marking the edge of the patchy growth zone in type VI, part of which is picked out in yellow. See text for discussion on these textures.

Complex zoning, resorption, recrystallisation and equilibrium textures are displayed by type VI plagioclase (Figure 2.17c). The cores have a composition of ~An₆₀, and display growth rims with normal zoning. A zone of resorption and recrystallisation, and a sharp dissolution surface surrounds this sequence, which is then overgrown by normally zoned plagioclase to the rim. This type may be the equivalent of type II, but the core has not undergone such strong resorption as displayed by type I; alternatively it may represent an earlier phase of crystallisation which was overgrown by sodic plagioclase that later destabilised.

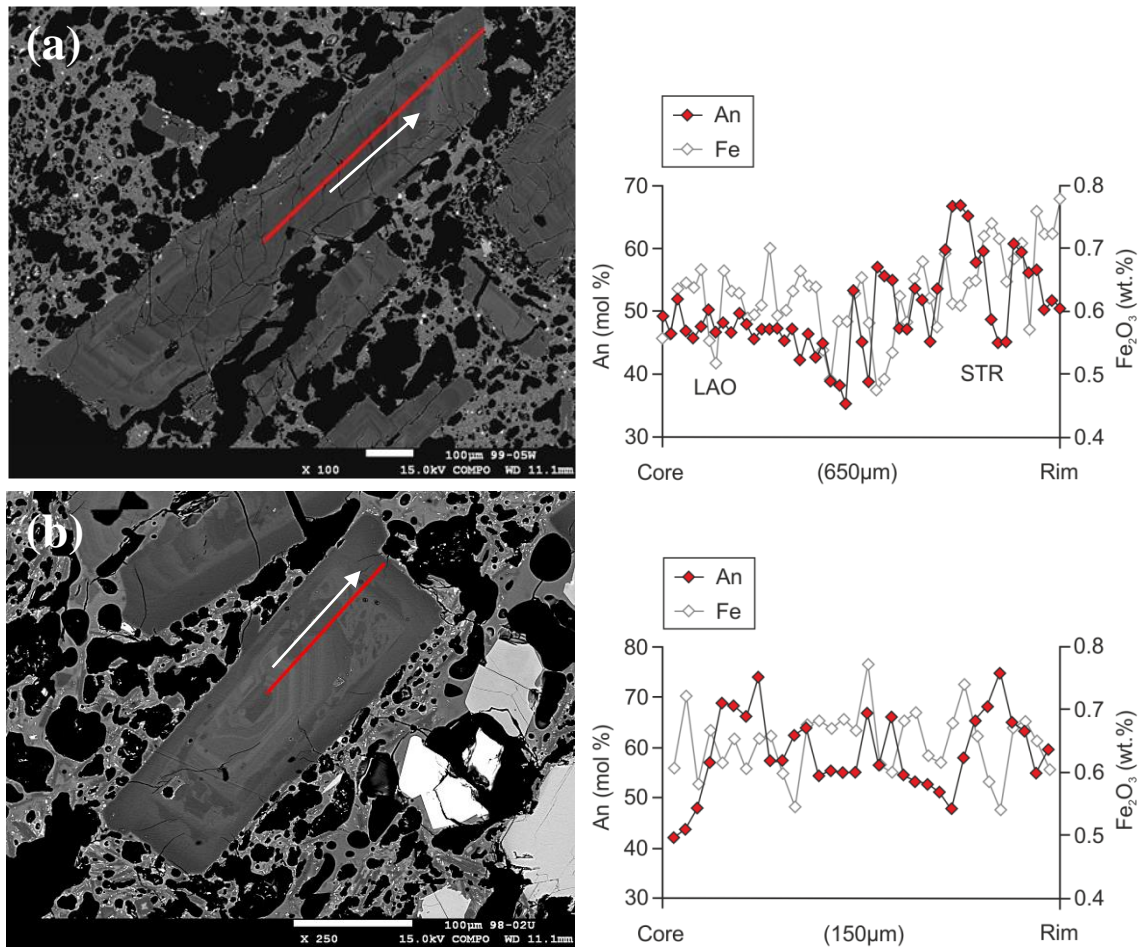


Figure 2.18 Oscillatory zoned plagioclase from Group I samples.

Plagioclase with characteristic saw-tooth core-rim anorthite content pattern from sample VF99-05W from unit W (a) and VF98-02U from unit U (b). The red lines represent the EPMA transects with analyses every 10µm. Both phenocrysts display the two types of oscillatory zoning discussed in the text: low-amplitude oscillations (LAO); and small- and large-scale resorption zones (STR).

The final type of plagioclase zoning is type VII, which has a normally zoned core showing no disequilibrium features. There is a sharp jump in anorthite content, followed by reverse and oscillatory zoning to the rim (Figure 2.17d). This type is only observed in unit P.

2.2.2.2 Interpretation of Plagioclase Zoning Patterns

The complex zoning patterns observed in the plagioclase phenocrysts and microphenocrysts imply a complex crystallisation history, involving multiple phases of plagioclase growth and continually changing conditions (pressure, temperature, H₂O content, *f*O₂, and melt composition) within the magmatic plumbing system. Such changes in conditions can be a result of local magma mixing due to convective overturn in a magma chamber, mafic magma recharge or depressurisation in water-undersaturated conditions (Nelson and Montana, 1992; Blundy and Cashman, 2001; Ginibre et al., 2002a; Ginibre et al., 2002b; Annen et al., 2006; Ginibre and

Wörner, 2007; Streck, 2008). The presence of multiple types of zoning and morphologies within a single eruption deposit can be attributed to crystal growth at different times and in different parts of the magmatic plumbing system, i.e. early, deep crystallisation versus late, shallow crystallisation.

Strong disequilibrium textures, such as sieve textures, patchy zoned phenocrysts and cores, and dissolution surfaces, indicate repeated destabilisation of plagioclase during crystallisation. The rounded and irregular rim displayed by type I plagioclase indicates that the mineral was not in equilibrium with the final melt composition. Sieve textures can be the result of rapid crystal growth which forms boxy, regular patterns (Streck, 2008); however, in this case the patchy zonation is irregular and displays cross-cutting relationships, suggesting that the phenocrysts have undergone pervasive resorption and recrystallisation (Ginibre and Wörner, 2007). The crystal morphology reveals that the more sodic plagioclase is the original mineral composition, which underwent dissolution, followed by precipitation of a more calcic composition infilling holes in the original crystal.

Pervasive resorption can result from temperature increase due to mafic magma recharge, which, if mechanical mixing occurred, would cause growth of more calcic plagioclase (Ginibre and Wörner, 2007); or from depressurisation in water-undersaturated conditions which would destabilise the plagioclase causing dissolution during which more calcic plagioclase would precipitate (Nelson and Montana, 1992; Ginibre and Wörner, 2007). The composition of plagioclase depends upon temperature, pressure, melt composition and water content. At a constant pressure and water content, the anorthite content of plagioclase will decrease with increasing magma differentiation and related decreasing temperature (Ginibre and Wörner, 2007). The solubility of water in magmas strongly depends on pressure; therefore, at a constant temperature and high pressure in water under-saturated conditions more sodic plagioclase will crystallise (Nelson and Montana, 1992; Ginibre and Wörner, 2007). With decreasing pressure, the plagioclase will become unstable, the melt will become water-saturated, and more calcic plagioclase will crystallise. Conversely, if the melt is water-saturated at high pressure, calcic plagioclase will be stable. Decreasing pressure will cause degassing, destabilisation of the calcic plagioclase, and decompression induced crystallisation of more sodic plagioclase (Nelson and Montana, 1992; Ginibre and Wörner, 2007).

If resorption and recrystallisation resulted from mafic magma recharge, differences in anorthite content between the original and overgrown plagioclase would be expected to correlate with changes in other elements such as Fe and Mg (e.g. Smith et al., 2009). In the analysed type I plagioclase, there is no major difference in Fe and Mg content between the original more sodic, albite-rich plagioclase and the overgrown more anorthitic plagioclase; indicating that this texture is not the result of magma mixing, but of depressurisation. The normal zoning

overgrowth is a later phase of crystallisation related to the renewed crystallisation of the magma at a shallower level in the system. The interpretation of the different zoning patterns displayed by the plagioclase phenocrysts is illustrated in Figure 2.19.

Phenocryst	Type	Description	Interpretation
	I	Patchy zoning and sieve texture - pervasive resorption and recrystallisation	Depressurisation in water-undersaturated conditions
	II	Core with patchy zoning and sieve texture surrounded by normally zoned plagioclase	Depressurisation followed by crystallisation in continually evolving magma, at shallower level
	III	Normally zoned plagioclase	Crystallisation in continually evolving magma
	IV	Oscillatory zoned plagioclase	Small-scale oscillations from thermal convection; Large-scale oscillations from magma recharge
	V	Reversely zoned plagioclase	Crystallisation in a progressively more mafic melt
	VI	Normally zoned core surrounded by patchy growth rim, surrounded by normal zoning to the rim	Crystallisation in continually evolving magma; mafic recharge and depressurisation; continued crystallisation in differentiating melt
	VII	Normally zoned core surrounded by reverse and oscillatory zoning to the rim	Crystallisation in continually evolving magma; magma replenishment and thermal convection causing reverse and oscillatory zoned rim

Figure 2.19 Schematic diagram of the seven types of plagioclase identified in the Group I eruption deposits with descriptions and interpretations of their zoning patterns

There are many kinetic models that describe the controls of crystal growth by diffusion across the crystal-melt boundary (Ginibre et al., 2002a and references therein). Although there is no definitive model, it is accepted that fine low amplitude oscillations are kinetically controlled, resulting from small-scale variations at the crystal-melt interface (Ginibre et al., 2002a). Small-scale oscillations with regular resorption surfaces (~10µm apart) occur as a result of thermal convection within the magma chamber, while slight compositional variations record heterogeneities within the storage system related to degassing as a result of crystallisation, and / or depressurisation, compositional differences as a result of crustal assimilation, thermal convection, or magma mixing (Ginibre et al., 2002a; Ginibre and Wörner, 2007).

The large-scale resorption events record variations of ~20 mol % An with dissolution surfaces cross-cutting multiple growth zones. Associated variations in Fe and Mg would suggest that these are major resorption events caused by magma replenishment (Ginibre et al., 2002a; Ginibre et al., 2002b). However, as observed in Figure 2.18, Fe₂O₃ displays an irregular pattern from core to rim that is not always associated with changes in An content. Step increases in An

content do not appear to be associated with step increases in Fe and Mg, therefore these large-scale resorption events are not associated with mafic magma recharge, but reflect increases in temperature and/or decompression.

A possible crystallisation history for the seven types of plagioclase phenocrysts in the Group I magmas is given in Figure 2.20. Initial plagioclase growth is in equilibrium with the melt, evolving as the melt differentiates. Mafic magma recharge then causes destabilisation of the plagioclase, and renewed crystal growth of a more anorthitic composition (Figure 2.20). Decompression in water-undersaturated conditions leads to pervasive resorption and precipitation of more calcic plagioclase (Type I). Continued crystallisation results in normally zoned overgrowths (Types II and VI), and normally zoned phenocrysts and microphenocrysts (Type III; Figure 2.20). Fresh input of mafic magma results in the reversely zoned Type V plagioclase; and thermal convection within the magma storage region results in oscillatory zoned plagioclase with regular resorption surfaces (Type IV) and oscillatory zoned overgrowths (Type VII; Figure 2.20). The presence of irregular type I phenocrysts, with no overgrowths, and with vesiculated glass inclusions, indicates magma ascended rapidly from depth. All Group I samples contain Types I, II and III indicating deeper magmas intercepted shallower magma bodies en route to the surface.

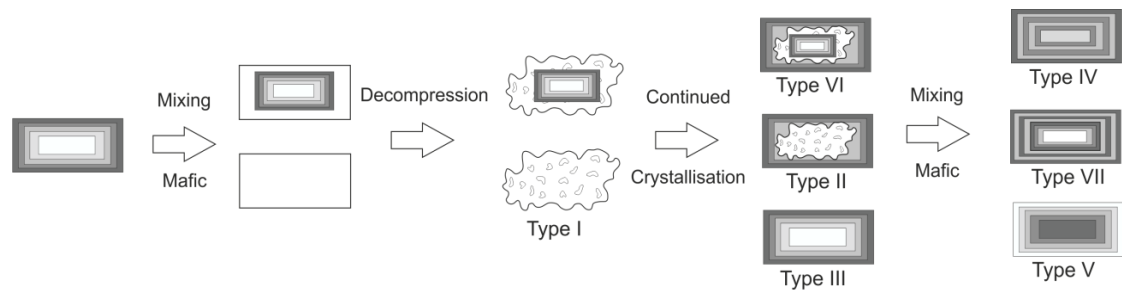


Figure 2.20 Schematic diagram showing the possible crystallisation history of plagioclase phenocrysts.

Phenocrysts record multiple phases of mafic magma replenishment, decompression and fluctuations in conditions within the magma storage region.

The wide ranges of core and rim compositions appear to reflect the complex crystallisation history of the magma prior to eruption. The presence of multiple types of phenocrysts results in wide ranges of core and rim compositions reflecting crystallisation at different stages of magma evolution.

2.2.2.3 Zoning in Clinopyroxene

Clinopyroxene phenocrysts in the Group I magmas display complex zoning patterns with large-scale resorption events and small-scale oscillations, supporting the evidence of decompression and heterogeneities in the magma storage region, as well as magma recharge as interpreted from the plagioclase zoning patterns (Section 2.2.2.2). The clinopyroxene phenocrysts can be classified into two types, both of which are found in all Group I scoria and pumice samples.

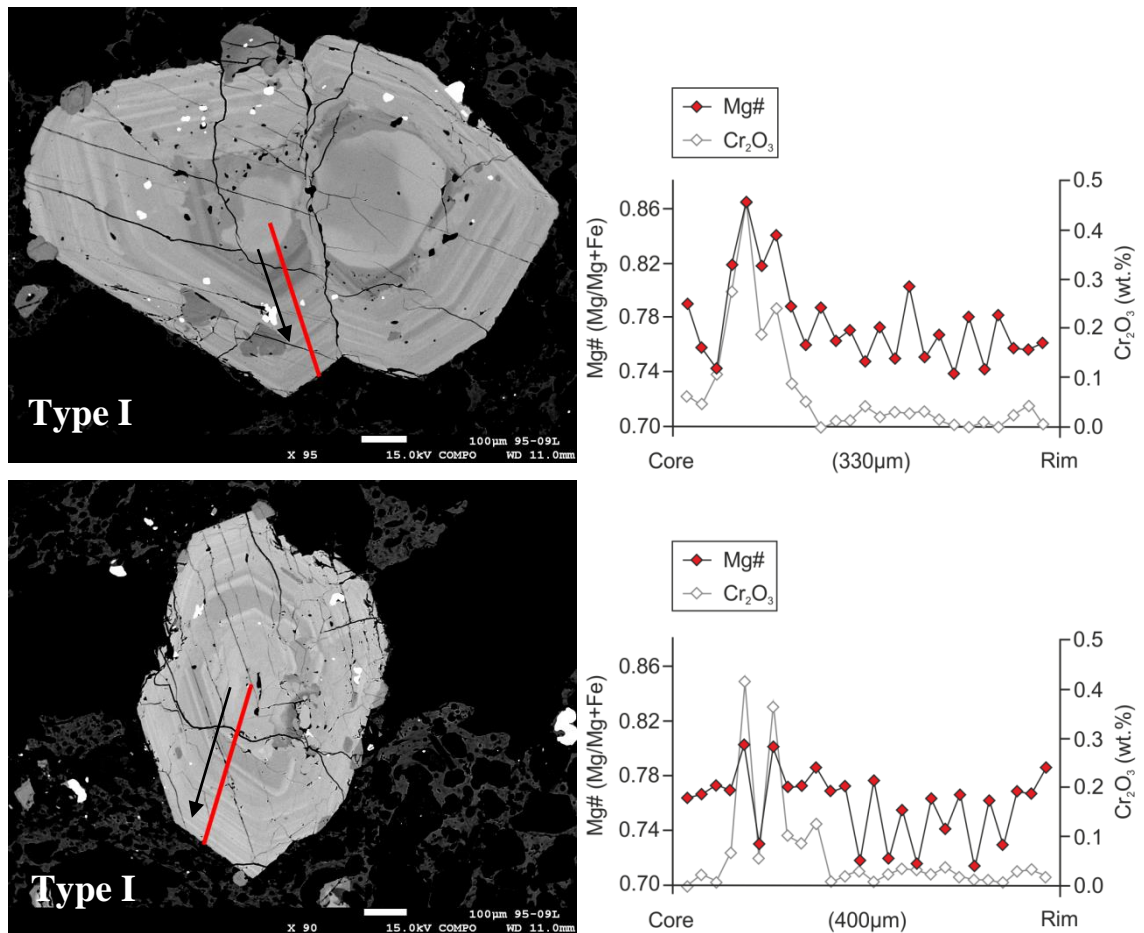


Figure 2.21 BSE images and EPMA analyses of type I clinopyroxene.

Images are from sample VF95-09L from unit P of the Group I eruption deposits. The strong correlation between spikes in Mg# and Cr₂O₃ indicating these events are caused by magma recharge (e.g. Streck, 2008). The spikes in Mg# and Cr correlate with dark grey growth zones in the clinopyroxene BSE images

Type I clinopyroxenes have low-Mg cores (Mg# 0.76), which are rounded and embayed, indicating resorption (Figure 2.21). Surrounding the core is a dark, high-Mg (Mg# 0.84-0.86) and high-Cr (0.46 wt.% Cr₂O₃) growth zone which has also undergone resorption indicated by rounded corners and dissolution surfaces cross-cutting multiple growth zones. Crystal growth in the high-Mg zone displays small-scale oscillatory zoning (Figure 2.21). The boundary between the core and the dark growth zone is sharp with a large compositional step from Mg#

0.76 to Mg# 0.84-0.86 (Figure 2.21). This is then overgrown by less magnesian clinopyroxene to the rim (Mg# 0.73-0.78). Again, there is a sharp compositional step at the boundary from Mg# 0.84-0.86 to Mg# 0.73-0.78, mirrored by a step decrease in Cr₂O₃ (Figure 2.21). This outermost growth zone typically displays oscillatory zoning with steps in the range of Mg# 0.74 to 0.78. Crystals are typically subhedral displaying embayed edges.

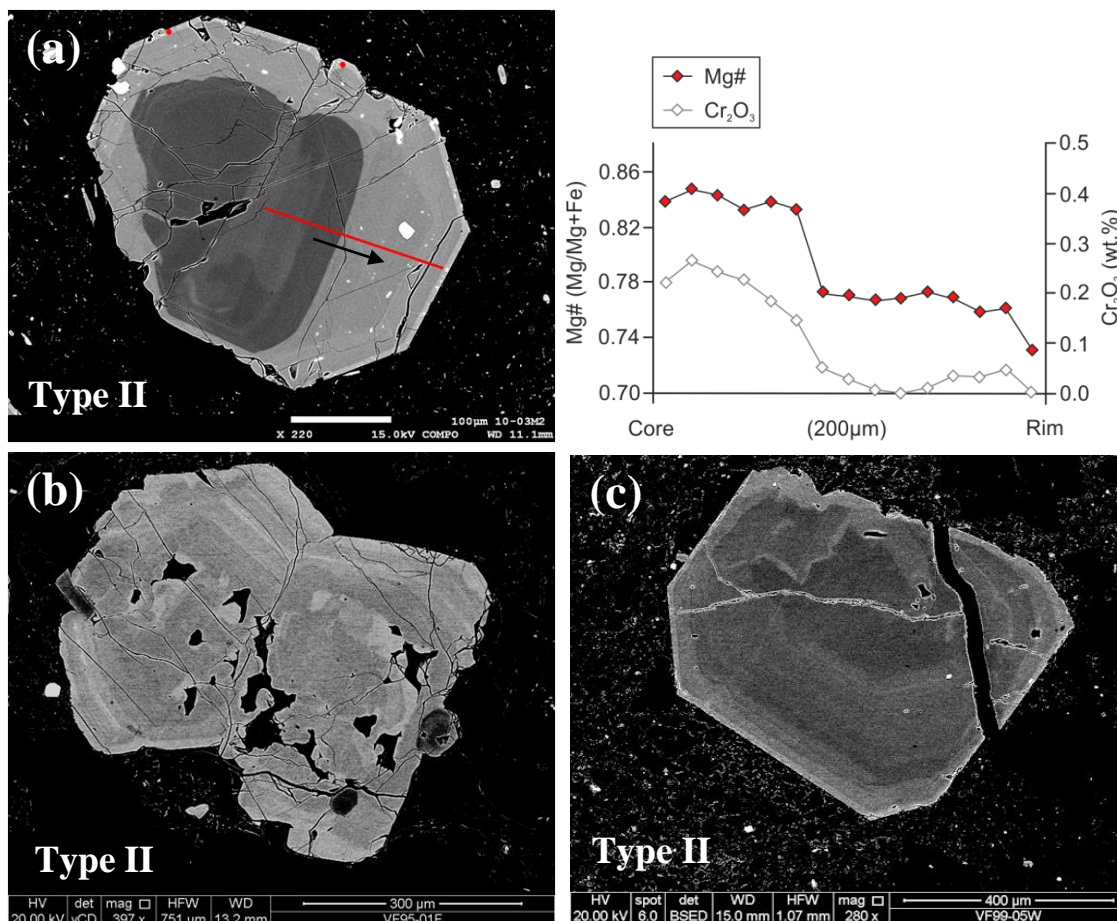


Figure 2.22 BSE images of type II clinopyroxene phenocrysts.

Images show clinopyroxene with a magnesian core displaying resorption and recrystallisation, surrounded by lighter, lower Mg clinopyroxene growth to the rim. Images are from samples VF10-03M2 (units L; a), VF95-01F (unit H; b) and VF99-05W (unit W; c). Also shown is a profile from EPMA analyses along the red line from core to rim (a). The step decrease in Mg# is coincident with a step decrease in Cr indicating mixing with a more evolved magma. This is reflected in the BSE image by a sharp colour change from dark to light grey.

Type II clinopyroxene phenocrysts have a core of similar composition to the high-Mg zone surrounding the core in type I crystals (Mg# 0.84-0.86; Figure 2.22). The core is partially resorbed, displaying rounded corners and sieve textures. Recrystallisation of the core forming less magnesian clinopyroxene (Mg# 0.76) gives it a patchy appearance (Figure 2.22). Surrounding the core is a low-Mg growth zone (Mg# 0.73-0.76) displaying oscillatory zoning, as observed in the type I crystals. The dissolution surface surrounding the core is accompanied

by a large step decrease in Mg# from ~0.84 to ~0.74, and a step decrease in Cr₂O₃ (Figure 2.22). Type II phenocrysts also display embayed edges.

2.2.2.4 Interpretation of Clinopyroxene Zoning Patterns

Destabilisation and resorption of clinopyroxene can result from mixing with either more mafic, or more evolved magma, large degrees of undercooling ($\Delta T = \text{liquidusT} - \text{magmaT}$) caused by depressurisation and degassing, or fluctuations in temperature, water content or fO_2 (Humphreys et al., 2006; Streck, 2008; Crabtree and Lange, 2011). Large-scale resorption and dissolution is commonly attributed to magma mixing; however, Crabtree and Lange (2011) show that such textures can also result from large undercoolings caused by degassing. At large undercoolings, crystal growth rates are higher, resulting in diffusion limited growth, producing crystals with skeletal, dendritic and hopper textures (Humphreys et al., 2006; Crabtree and Lange, 2011). Subsequent crystallisation can form patchy textures and reversed or normal zoning.

By investigating compositional changes in Mg# together with other elements such as Cr, (and Ti or Mn), it is possible to evaluate whether the process that resulted in the observed resorption and dissolution textures are linked to magma mixing or decompression-related degassing as proposed by Crabtree and Lange (2011). If a recharge event is the cause of the pyroxene destabilisation and recrystallisation, any change in Mg# will be correlated with equivalent changes in Cr and opposite changes in Ti and Mn (Streck, 2008).

EPMA analyses together with BSE images show that the strong resorption events with step increases in Mg# observed in the type I and II clinopyroxene phenocrysts coincide with increases in Cr (Figure 2.21), indicating that these events are linked to destabilisation and recrystallisation in a more mafic melt (Streck, 2008). Conversely, resorption events with step decreases in Mg# and coinciding decreases in Cr, as observed between the dark, high-Mg zone, and the low-Mg growth to the rim (Figure 2.22), indicate resorption and re-equilibration in a more evolved melt.

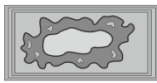
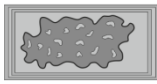
Phenocryst	Type	Description	Interpretation
	I	Partially resorbed low-Mg core surrounded by high-Mg zone showing strong resorption and dissolution; low-Mg growth to rim with small-scale oscillatory zoning	Mafic magma recharge followed by mixing with a more evolved melt; small-scale oscillations from decompression
	II	High-Mg zone showing strong resorption and dissolution, surrounded by low-Mg growth to rim with small-scale oscillatory zoning	Mixing with a more evolved melt; small-scale oscillations from decompression

Figure 2.23 Schematic diagram of the two types of clinopyroxene identified in the Group I eruption deposits with descriptions and interpretations of their zoning patterns

The oscillations observed in the clinopyroxene growth zones as revealed by fluctuations in Mg# are unrelated to changes in Cr, and therefore are interpreted as representing fluctuations in pressure, temperature, H₂O content or *f*O₂ in the magma chamber. Figure 2.23 summarises the observed zoning in clinopyroxene phenocrysts and the interpretations of their textures.

The type II phenocryst cores and rims have the same Mg# as the type I outer core growth zone and rims, suggesting these grew in the same melt (Figure 2.24). The cores of the type I clinopyroxene therefore represent an earlier phase of growth within a more evolved melt that subsequently mixed with a more mafic melt, destabilising the clinopyroxene and causing its partial resorption. Crystallisation then continued with more magnesian clinopyroxene (with high Cr) overgrowing the resorbed cores of type I and the formation of high-Mg crystals (cores of type II; Figure 2.24). Oscillations in the cores and the overgrowth of type I crystals indicate decompression and subsequent degassing as the melts ascended towards the surface.

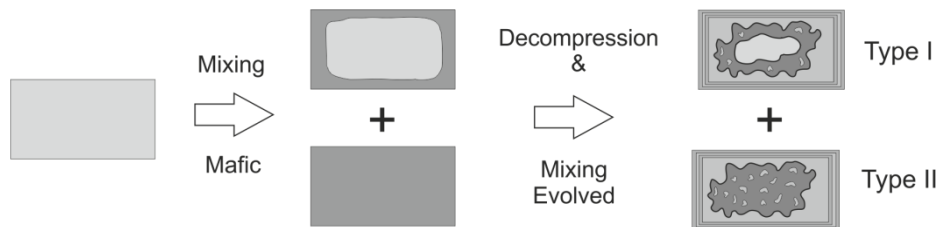


Figure 2.24 Cartoon of the crystallisation of clinopyroxene phenocrysts in the Group I magmas.

Strong resorption and recrystallisation reveal a complex history of multiple magma mixing events and decompression

Strong resorption of the more magnesian clinopyroxene and subsequent recrystallisation of less magnesian clinopyroxene indicates mixing with a more evolved magma, possibly in the storage region at shallower levels. The small-scale oscillations in Mg#, but not Cr, in the outer growth zone indicate fluctuations in pressure, temperature, volatile content and *f*O₂ (Streck, 2008). Embayed crystal edges indicate that the clinopyroxene phenocrysts were not in equilibrium with the final melt composition (Streck, 2008).

2.2.2.5 Orthopyroxene Zoning

Orthopyroxene phenocrysts display more complex zoning patterns than the clinopyroxenes and have been classified into four types. Not all units from the Group I eruption deposits have orthopyroxenes of all four types; however, all units have types III and IV.

Type I orthopyroxenes have a magnesian core (Mg# 0.78 - 0.81), displaying partial resorption, with rounded corners and sieve textures. Recrystallisation gives the core a patchy appearance (Figure 2.25). The dissolution surface surrounding the core is associated with a step decrease in

Mg# (to 0.74 - 0.78) and Cr. Crystals are then reversely zoned to the rim, which typically has a composition of Mg# 0.77 - 0.79 (Figure 2.25).

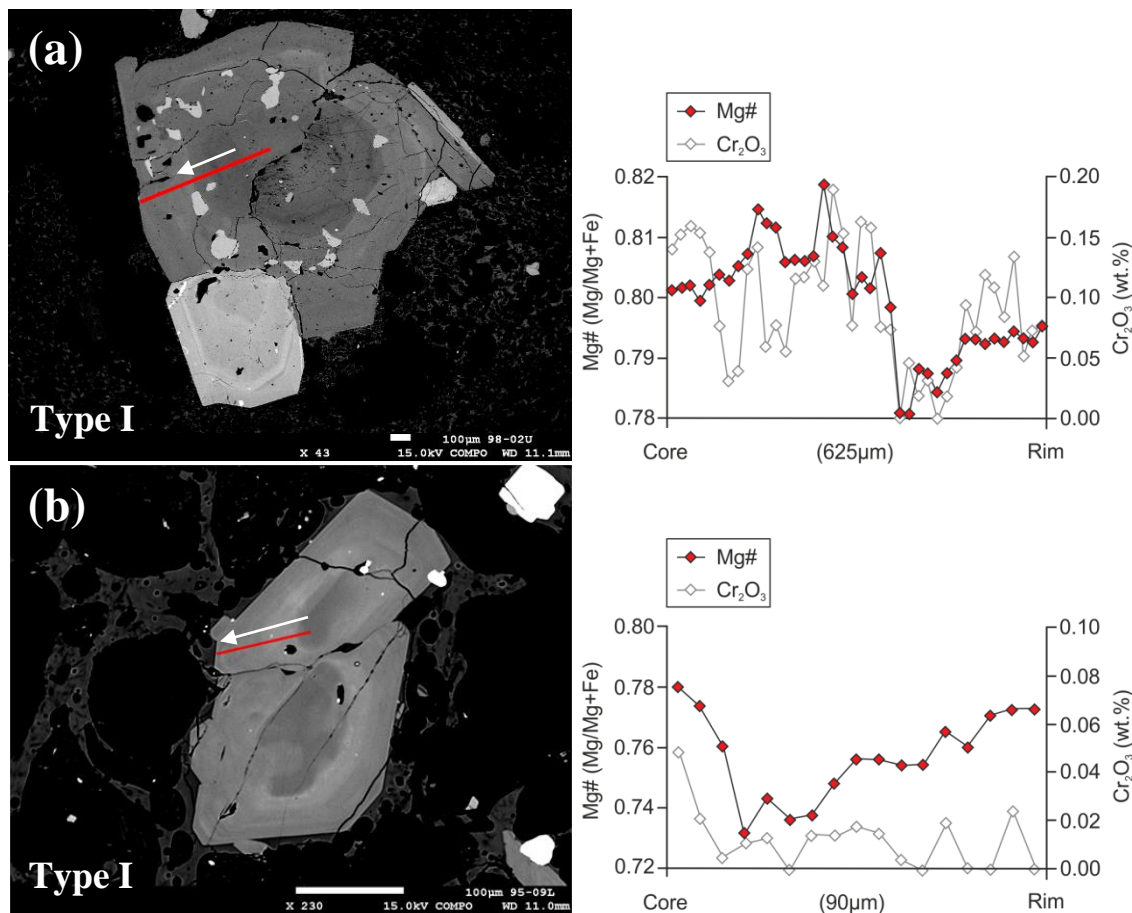


Figure 2.25 BSE images and EPMA analyses of type I orthopyroxene.

Type I phenocrysts display a high-Mg core, a step decrease in Mg#, coincident with Cr content and a dissolution surface, and reversed zoning to the rim. Image (a) is from sample VF98-02U from unit U, and image (b) is from sample VF95-09L from unit P.

Type II orthopyroxene phenocrysts also have a high-Mg core displaying partial resorption (Figure 2.26a). The core is then surrounded by a low-Mg growth zone (Mg# 0.70-0.74) which is strongly resorbed with a dissolution surface cross-cutting multiple growth zones. Associated with the dissolution surface is a step increase in Mg# (to 0.80) and Cr. This high-Mg growth zone also displays partial resorption, with rounded corners, and embayed edges. Overgrowing this is low-Mg orthopyroxene to the rim (Mg# 0.74).

Type III phenocrysts have low-Mg cores (Mg# 0.70-0.74) displaying strong resorption textures, with an associated step increase in Mg# to 0.80 (Figure 2.26b and c). This is then overgrown by low magnesian orthopyroxene growth to the rim (Mg#0.74). Type IV orthopyroxene have magnesian cores (Mg# 0.80-0.82) which are slightly rounded. These are overgrown by low-Mg growth to the rim (Mg# 0.72-0.74; Figure 2.26d).

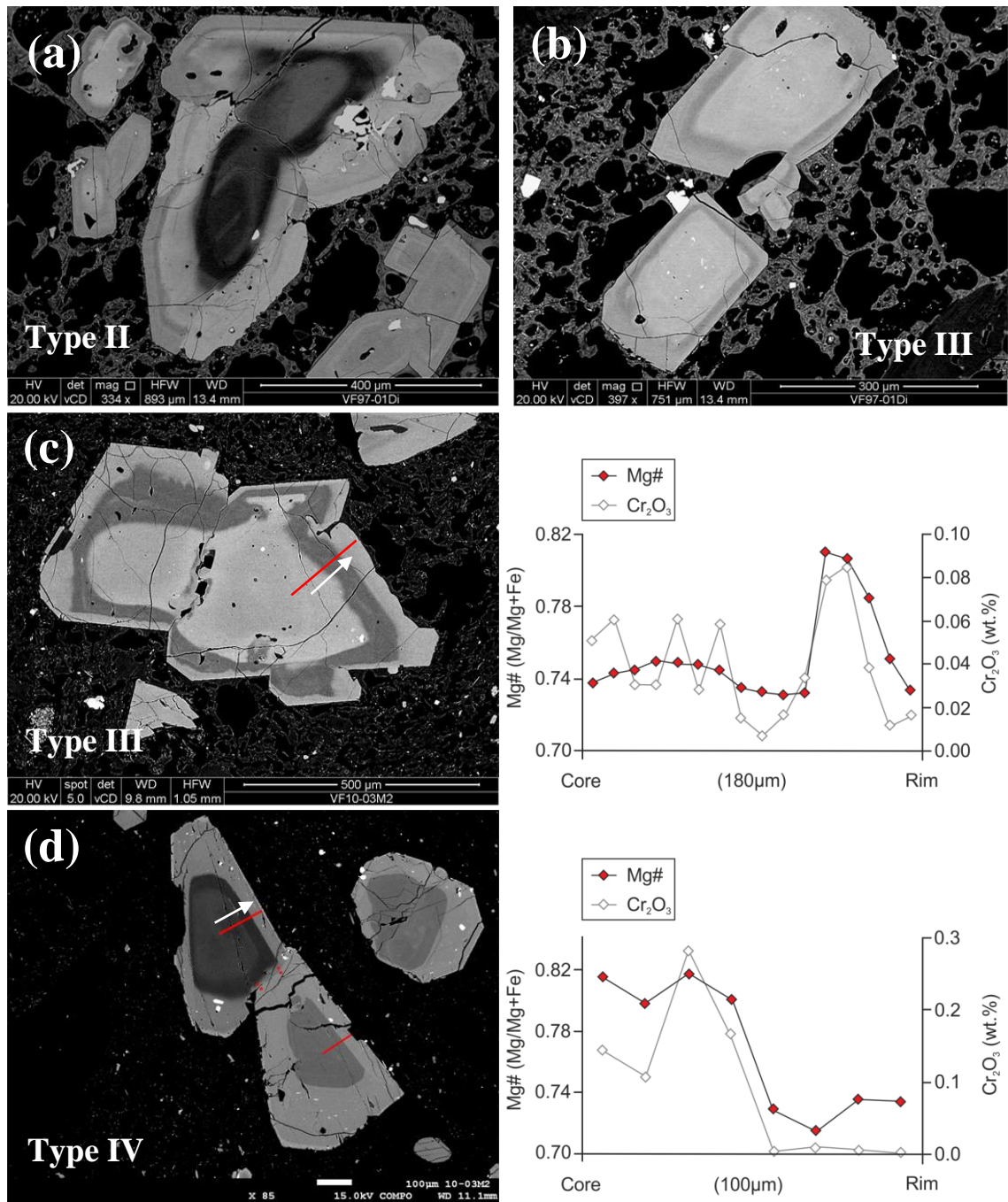


Figure 2.26 BSE images and EPMA analyses of types II, III and IV orthopyroxene phenocrysts.

Images are from sample VF97-01Di from unit H (a and b) and VF10-03M2 from unit L (c and d) of the Group I eruption deposits. Large step increases and decreases in Mg# are coincident with equivalent increases and decreases in Cr₂O₃, indicating magma replenishment events. The compositional changes are reflected on the BSE images by sharp colour changes; the darker grey reflects high-Mg.

2.2.2.6 Interpretation of Orthopyroxene Zoning Patterns

The majority of the orthopyroxene phenocryst cores and growth zones display strong or partial resorption. Examples of this are rounded corners and embayed crystal edges, sieve and patchy

textures, and dissolution surfaces cross-cutting multiple growth zones. Patchy textures are the result of resorption and subsequent recrystallisation of more or less magnesian orthopyroxene, equivalent in composition to that of the overgrowing orthopyroxene. Figure 2.27 summarises the four types of orthopyroxene phenocrysts and the interpretation of the zoning patterns.

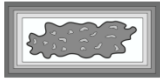



Phenocryst	Type	Description	Interpretation
	I	High-Mg core with resorption and recrystallisation with a step decrease in Mg# and reversed zoning to rim	Mixing with more evolved melt, followed by crystallisation in a progressively more mafic melt
	II	High-Mg core displaying resorption, followed by multiple growth zones with step decreases and increases in Mg#	Multiple mixing events: Mixing with more evolved magma; mafic magma recharge and mixing with more evolved magma
	III	Low-Mg core displaying resorption, followed by multiple growth zones with step increases and decreases in Mg#	Multiple mixing events: Mafic magma recharge and mixing with more evolved magma
	IV	High-Mg core displaying partial resorption with rounded corners, followed by step decrease in Mg# to rim	Mixing with more evolved magma

Figure 2.27 Schematic illustration of the four types of orthopyroxene phenocryst found in scoria and pumice from the Group I eruption deposits

As observed in the clinopyroxene phenocrysts, the large-scale resorption events with associated step increases or decreases in Mg# in orthopyroxenes are coincident with equivalent increases or decreases in Cr content (Figure 2.25 and 2.26), indicating that the destabilisation and re-equilibration is related to mixing with more mafic or more evolved magma, respectively. Type II and III phenocrysts record several large-scale resorption events, indicating crystallisation in an open system with multiple magma mixing events.

The cores of the type III crystals have the same Mg# as the high-Mg growth zone surrounding the cores of the type II phenocrysts, suggesting they grew from the same melt composition (Figure 2.28). The composition of subsequent growth zones of the type II and III crystals is equivalent to type IV crystals, again suggesting these grew in the same melt. The cores of the type II phenocrysts must therefore have crystallised first in a mafic melt prior to mixing with a more evolved melt. A possible crystallisation history of the orthopyroxene phenocrysts, involving multiple magma mixing events, is given in Figure 2.28.

The cores of type II phenocrysts crystallised first in a mafic magma, which then mixed with a more evolved magma resulting in destabilisation and partial resorption. Crystallisation continued, forming a lower Mg growth zone on type II crystals, and forming new, type III crystals with a low-Mg core. Subsequent mafic magma recharge resulted in another large-scale resorption event, forming a high-Mg growth zone on type II and III crystals, and forming new

type IV crystals with a high-Mg core. Further magma mixing with a more evolved magma destabilised the crystals once more, and resulted in a low-Mg rim on the type II, II and IV phenocrysts.

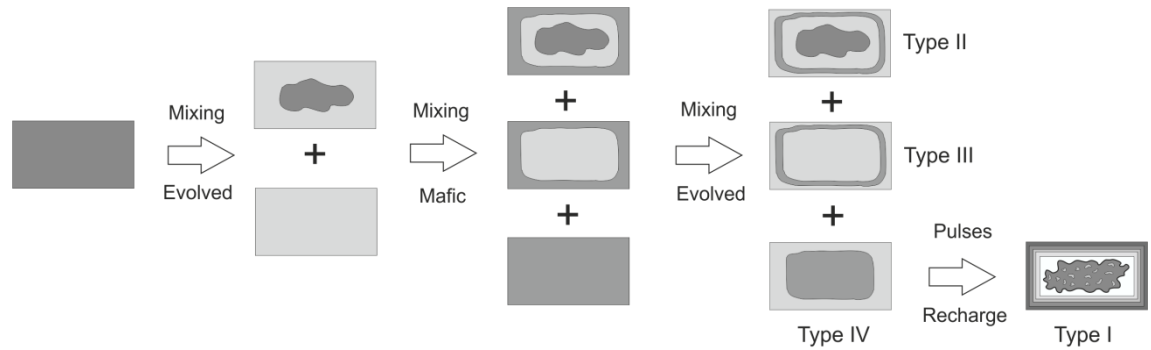


Figure 2.28 Cartoon showing a possible crystallisation history of the types I to IV orthopyroxene phenocrysts.

The crystals record magma mixing events, following a similar crystallisation history. The type I phenocrysts have oscillatory zoned rims suggesting pulses of magma recharge in the magma chamber.

Type I orthopyroxene is only found in units U, W and P. This type is similar to type IV, but with reverse zoning to the rim. Reverse zoning indicates crystallisation in a progressively more mafic melt; therefore these phenocrysts may have followed a similar crystallisation history as type IV, but remained in the more evolved melt in the magma chamber, which experienced pulses of mafic magma replenishment.

2.2.2.7 Hornblende zoning and textures

Hornblende phenocrysts commonly display weak normal zoning with a more Mg-rich core grading into a more Fe-rich rim. Variations in Mg# between cores and rims typically range from 0.72 to 0.68 (Figure 2.29), with small-scale oscillatory zoning reflected in fluctuations in Mg#. The composition of hornblende varies in response to changes in pressure, temperature, fO_2 and water content (Scaillet and Evans, 1999). Normal zoning indicates decreases in temperature and fO_2 , while small-scale oscillatory zoning suggests fluctuations in these parameters (Humphreys et al., 2006).

Two types of hornblende phenocryst are present in the Group I scoria and pumice samples: type I are fresh phenocrysts with sharp and unaltered rims (Figure 2.29a); and type II are crystals with breakdown rims of plagioclase, pyroxene and Fe-Ti oxides (Figure 2.29b and c). Type I hornblende phenocrysts are present in all Group I units, while the type II phenocrysts are not present in units Y, U and S. No unit contains only type II, broken down, phenocrysts.

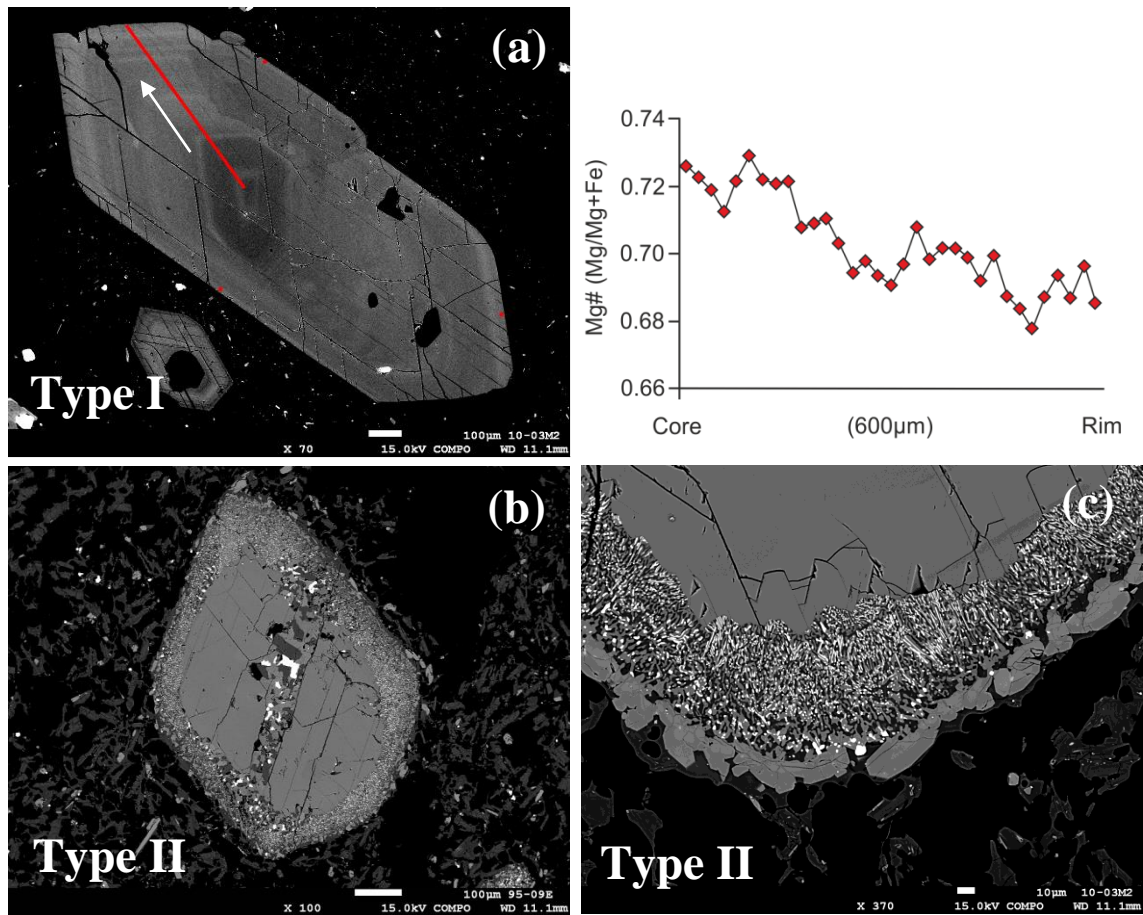


Figure 2.29 BSE images and EPMA core-rim profile of hornblende from Group I samples.

(a) BSE image and EPMA analysis of a type I hornblende phenocryst from VF10-03M2 from unit L: overall the phenocryst is normally zoned; however, the grey-scale contrast reflecting Mg and Fe content, and the EPMA analyses reveal oscillations in Mg#. Type II hornblendes with a strong reaction rim composed of Fe-Ti oxides, pyroxene and plagioclase are shown in (b) and (c). Image (b) is from sample VF95-09E (unit L) and image (c) is from VF10-03M2 (unit L).

Type I phenocrysts appear fresh with sharp edges; however, rims display slight rounding and embayments, and the crystals commonly contain holes in the centre (Figure 2.29a). These features are dissolution textures, analogous to the sieve textures observed in plagioclase and pyroxene phenocrysts, which may have resulted from increased temperature or compositional changes resulting from magma recharge (Streck, 2008).

Type II phenocrysts displaying reaction rims of pyroxene, plagioclase and Fe-Ti oxides are typically interpreted as resulting from depressurisation and related degassing (Figure 2.29b and c; Rutherford and Hill, 1993). Reaction rims begin to form on amphibole phenocrysts when the melt no longer contains sufficient dissolved water for the amphibole to remain stable (Rutherford, 2008). When this occurs, the amphiboles lose their H₂O and alkalis to the melt and begin to breakdown (Rutherford and Devine, 2003). The effusive eruption deposits of Volcán

de Colima contain amphiboles with very strong breakdown rims, commonly having a ghost appearance whereby the phenocryst has almost completely broken down as a result of a slow ascent rate and magma degassing (Savov et al., 2008). Reaction rims can also result from oxidation of the melt. In this case, the rims on amphibole are composed predominantly of Fe-Ti oxides with pyroxene and plagioclase (Rutherford and Devine, 2003). Such rims are observed in the effusive dome samples, but not in the explosive products of the CVC.

The juxtaposition of both fresh and altered hornblende phenocrysts within a single clast, suggests late-stage magma mixing (Rutherford, 2008). The type I hornblende may have formed in a batch of magma deeper in the system that intercepted the magma chamber during ascent to the surface. The phenocrysts display slight dissolution as a result of mixing with a more evolved magma. The type II crystals had long residence times in the shallow level magma chamber, where they destabilised, breaking down as a result of degassing. The absence of reaction rims on the type I phenocrysts implies the mixed magma must have been remobilised within a short timescale, rapidly ascending to the surface. Units Y, U and S do not contain hornblende phenocrysts with reaction rims, suggesting that the magmas which formed these units were erupted very rapidly to the surface, without long residence times in the magma storage region.

2.2.2.8 Groundmass textures

The groundmass of the Group I scoria and pumice samples comprises highly vesiculated glass dominated by small spherical bubbles. Such textures are indicative of rapid ascent rates which inhibit bubble coalescence (Szramek et al., 2006). The presence of abundant microlites in the groundmass glass indicates late-stage crystallisation which may be the result of rapid decompression, as demonstrated by isothermal decompression experiments on Mt Pinatubo dacites (Hammer et al., 1999; and references therein). Syn-eruptive devolatilisation of magma can occur within the conduit, resulting in a highly vesiculated groundmass with microlite crystallisation (Hammer et al., 1999; Szramek et al., 2006).

2.2.3 Summary of Petrological Observations and Interpretations

The mineral chemistry and textures observed in the Group I pumice and scoria samples reveal multiple phases of magma recharge and decompression. The schematic diagram in Figure 2.30 relates the observed zoning patterns in the main mineral phases and groundmass textures.

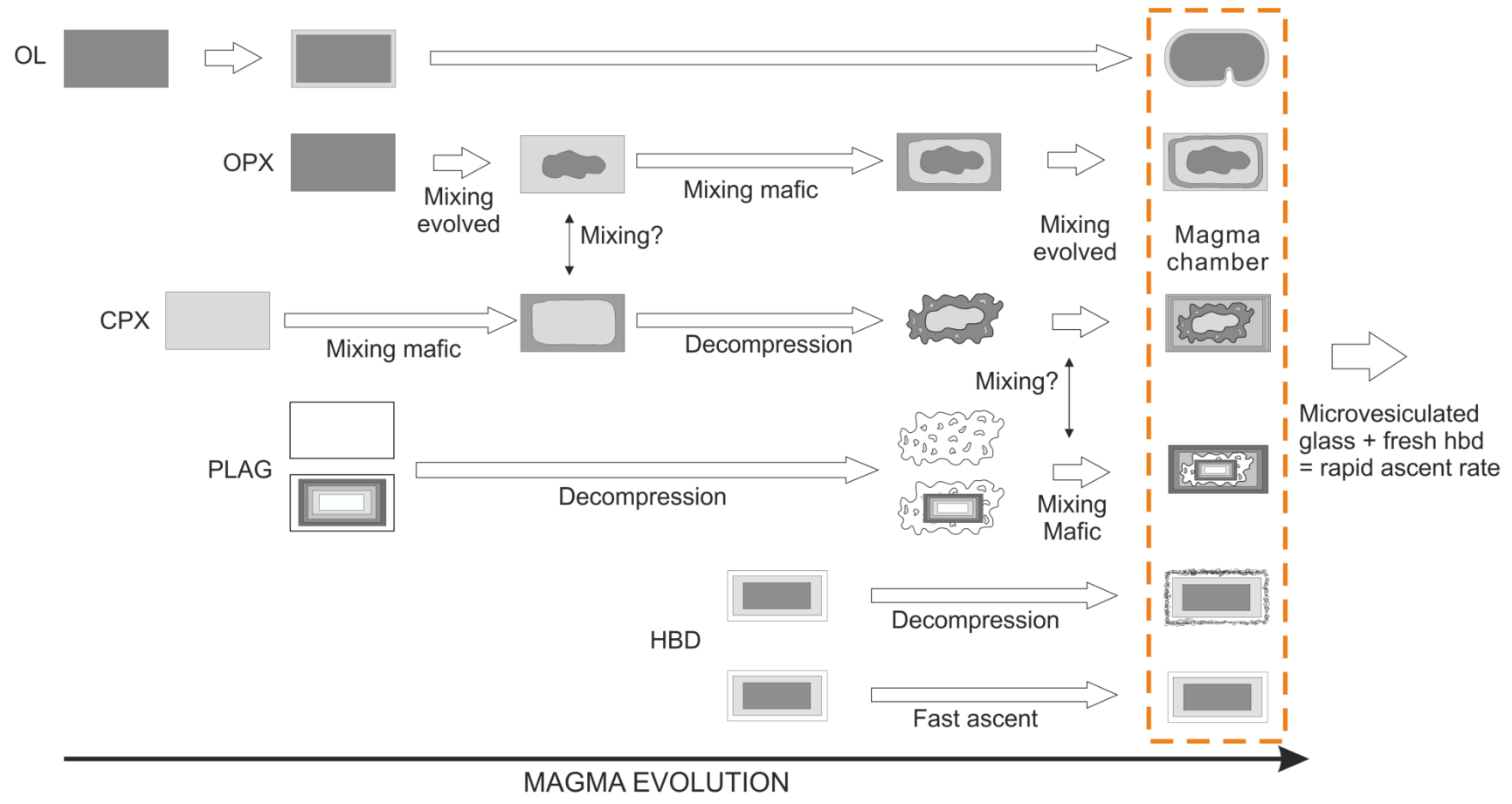


Figure 2.30 Schematic diagram linking orthopyroxene (opx), clinopyroxene (cpx), plagioclase (plag) and hornblende (hbd) zoning patterns and textures.

All phenocryst phases in the Group I pumice and scoria samples reveal complex crystallisation histories involving multiple phases of magma mixing and decompression events indicated by dissolution and recrystallisation textures.

EPMA analyses reveal some of the olivine phenocrysts have high Mg# of up to 0.87 indicating initial crystallisation from a primitive mafic melt. The cores of type I clinopyroxenes have lower Mg# of 0.78 but are overgrown by high-Mg clinopyroxene with Mg# 0.86, similar to the olivine composition. Cores of clinopyroxene crystals which grew from this mafic melt also have high-Mg, suggesting mixing between two batches of magma. Orthopyroxene phenocrysts also have cores ranging from Mg# 0.78 - 0.85, and display partial resorption, consistent with magma mixing. Further episodes of magma recharge are displayed by clinopyroxene and orthopyroxene phenocrysts; however some of the clinopyroxene phenocrysts display strong dissolution textures associated with decompression.

Plagioclase phenocrysts display very complex zoning patterns; however, many of the magma mixing events, and the decompression event, recorded by the pyroxene phenocrysts are also apparent in plagioclase phenocrysts. Oscillatory zoned rims and embayed crystal edges reveal thermal fluctuations in the magma chamber, probably as a result of continued mafic magma replenishment.

Hornblende phenocrysts with reaction rims indicate destabilisation associated with degassing (Rutherford and Hill, 1993), possibly as a result of long residence times in a shallow magma chamber. The occurrence of both altered and unaltered hornblende phenocrysts in individual pumice or scoria clasts suggests late-stage mixing. Unaltered hornblende phenocrysts together with the observed microvesiculated groundmass glass suggest very rapid magma ascent rates from the magma chamber to the surface.

2.3 Geothermometry and Hygrometry

Eruption temperature, pressure and magmatic water content can be calculated based on mineral-mineral and mineral-melt equilibria (e.g. Wood and Banno, 1973; Wells, 1977; Putirka, 2008). There is a specific temperature, pressure and water content at which the exact mineral composition is in equilibrium with the adjacent melt or mineral phase. This temperature can be calculated at a given pressure and water content based on the equilibrium partition coefficient, which controls the exchange of chemical components between the mineral (product) and the melt (reactant), or the mineral-mineral pair. In order for equilibrium to occur the energy flow across the reaction must be equal; if the temperature changes, the balance will be shifted and the products and reactants will not be in equilibrium (Putirka, 2008).

The eruption temperature and magmatic water content for the Group I CVC magmas have been estimated based on the clinopyroxene-orthopyroxene thermometers of Wood and Banno (1973) and Wells (1977), orthopyroxene-melt and clinopyroxene-melt thermometers of Putirka (2008), hornblende thermometer and hygrometer of Ridolfi et al. (2010), the plagioclase-glass thermometer and hygrometer of Putirka (2008) and the plagioclase-glass hygrometer of Lange

et al. (2009). The geothermometry and hygrometry results for the Group I magmas are presented in Tables 2.4 and 2.5, respectively.

Fe-Ti oxide geothermometry is considered one of the most accurate thermometers for calculating the eruption temperature of arc magmas, as Fe-Ti oxides re-equilibrate quickly in response to changes in temperature prior to the eruption (Ghiorso and Sack, 1991; Ghiorso and Evans, 2008). The temperature recorded by Fe-Ti oxide pairs should therefore closely reflect the eruption temperature. Unfortunately Fe-Ti oxide pairs were not found in the CVC eruption deposits.

The pyroxene thermometers are based on the exchange of Ca, Na, Mg, Fe and Al. For the clinopyroxene-melt thermometer (Putirka, 2008), the reaction involves jadeite ($\text{NaAlSi}_2\text{O}_6$) – diopside-hedenbergite [$\text{Ca}(\text{Mg,Fe})\text{Si}_2\text{O}_6$] exchange. In this reaction, Ca substitutes for Na, and Fm (Mg+Fe) substitutes for Al:

$$\begin{aligned} \frac{10^4}{T(K)} = & 7.53 - 0.14 \ln \left(\frac{X_{Jd}^{cpx} X_{CaO}^{liq} X_{Fm}^{liq}}{X_{DiHd}^{cpx} X_{Na}^{liq} X_{Al}^{liq}} \right) + 0.07(H_2O^{liq}) - 14.9 \left(X_{CaO}^{liq} X_{SiO_2}^{liq} \right) \\ & - 0.08 \ln \left(X_{TiO_2}^{liq} \right) - 3.62 \left(X_{NaO_{0.5}}^{liq} X_{KO_{0.5}}^{liq} \right) - 1.1(Mg\#^{liq}) - 0.18 \ln \left(X_{EnFs}^{cpx} \right) \\ & - 0.027P(kbar) \end{aligned}$$

Equation 2.1

where X_j^i is the cation fraction j in component i , e.g. $X_{NaO_{0.5}}^{liq}$ is the cation fraction of Na in the liquid, or melt. All mineral cation fractions are calculated on the basis of 6 oxygens, and liquid cation fractions are calculated on an anhydrous basis without re-normalisation (Putirka, 2008).

The first part of the equation; $0.14 \ln \left(\frac{X_{Jd}^{cpx} X_{CaO}^{liq} X_{Fm}^{liq}}{X_{DiHd}^{cpx} X_{Na}^{liq} X_{Al}^{liq}} \right)$, describes the equilibrium coefficient for jadeite – diopside-hedenbergite exchange. The second term, $0.07(H_2O^{liq})$, is the water content of the melt in wt.%. The third part accounts for the activity of Ca, Si, Ti, Na, K in the melt, and the Mg# of the melt, all of which can affect the equilibrium coefficient; $14.9 \left(X_{CaO}^{liq} X_{SiO_2}^{liq} \right) - 0.08 \ln \left(X_{TiO_2}^{liq} \right) - 3.62 \left(X_{NaO_{0.5}}^{liq} X_{KO_{0.5}}^{liq} \right) - 1.1(Mg\#^{liq})$. The term, $0.18 \ln \left(X_{EnFs}^{cpx} \right)$, accounts for Mg and Fe in enstatite, which is not considered in the equilibrium coefficient term. The final term (P) is the pressure in kbar.

The two-pyroxene thermometers are based on diopside-enstatite Mg-Fe interchange, and the orthopyroxene-melt thermometer is based on Mg-Fe exchange between orthopyroxene and melt. The single phase thermometer and hygrometer of Ridolfi et al. (2010) is based on the stability of amphibole within the melt. Amphibole crystallises over a wide range of P-T conditions,

following the liquid line of descent of the magma, therefore the exact composition of the amphibole is linked to a specific pressure, temperature, and water content (Ridolfi et al., 2010).

The plagioclase-glass hygrometer of Putirka (2008) is based on Ca, Na, Al and Si exchange:

$$H_2O \text{ (wt. \%)} = 25.95 - 0.0032T(^{\circ}\text{C}) \ln \left(\frac{X_{An}^{pl}}{X_{CaO}^{liq} (X_{AlO_{1.5}}^{liq})^2 (X_{SiO_2}^{liq})^2} \right) - 18.9(X_{K_{0.5}}^{liq}) \\ + 14.5(X_{MgO}^{liq}) - 40.3(X_{CaO}^{liq}) + 5.7(X_{An}^{pl})^2 + 0.108P(\text{kbar})$$

Equation 2.2

where all mineral components are cation fractions calculated on the basis of 8 oxygens and liquid components are cation fractions calculated on an anhydrous basis without re-normalisation.

2.3.1 *Estimating Eruption Temperature and Magmatic Water Content for the CVC Magmas*

A constraint of the mineral-melt geothermometers and hygrometers is that in order to calculate the eruption temperature, the pressure and melt water content must be known; and in order to calculate the water content, temperature and pressure must be known. However, the two-pyroxene thermometer of Putirka (2008) only requires the pressure to be constrained, while the two-pyroxene thermometers of Wood and Banno (1973) and Wells (1977) and the hornblende thermometer does not require any of the physical conditions to be known.

The eruption temperature, pressure and water content of the CVC lavas is quite well constrained by experimental petrology (Moore and Carmichael, 1998) and geophysical data (Gardine, 2010; López-Loera, 2012). Recent aeromagnetic and tomographic studies have imaged a shallow level magma chamber at 5 - 10 km depth under the CVC (Gardine, 2010; López-Loera, 2012). Geophysical studies on the CVC are discussed in detail in Chapter 5.

Moore and Carmichael (1998) estimated pre-eruption temperatures of 950 to 975°C, pressures of 750 to 1500 bars and water contents of 3 to 5 wt.% for Colima lavas based on high pressure water-saturated melting experiments on an andesite and basaltic-andesite from Volcán de Colima. The temperature, pressure and water contents were estimated by comparing the experimental mineral assemblage and compositions with the natural samples (Moore and Carmichael, 1998). However, caution must be used here as this is based on Colima andesites which do not contain olivine.

Based on these experimental petrology and geophysical studies, a pressure of 2 kbar (~6 km depth) is used here for estimating the eruption temperatures of the explosive CVC magmas.

The minimum estimated water content of 3 wt.% of Moore and Carmichael (1998) is used for the water-dependent thermometers (Table 2.4). The average temperatures calculated from the water-independent thermometers are used with the plagioclase-melt hygrometers of Putirka (2008) and Lange et al. (2009) to estimate the magmatic water content. These results, along with water content estimates from the hornblende hygrometer of Ridolfi et al. (2010) are given in Table 2.5.

2.3.1.1 Eruption Temperature Uncertainties

The relative errors of the geothermometers range from 34 to 87°C (Wood and Banno, 1973; Wells, 1977; Putirka, 2008; Ridolfi et al., 2010). The thermometers of Putirka (2008) are empirical, calibrated using regression of natural and experimental data. Regression analysis is used to determine the minimum number of parameters that explain the observed variability. All other parameters are discounted, therefore simplifying and minimising the errors of the geothermometers. Similarly, Wells (1977) and Wood and Banno (1973) used experimental data to empirically calibrate the effect of Fe solubility in the pyroxenes and are able to reproduce the experimental results to within 70°C and 60°C, respectively.

Amphibole composition is directly linked to the physical conditions of the system (i.e. pressure, temperature, water content and oxygen fugacity); therefore Ridolfi et al. (2010) calibrated the thermometer empirically for different components such as Si and Mg index, which gave uncertainties of 22°C.

The physical conditions of the storage region are fairly well constrained by the geophysical models and experimental petrology as described above. However, by varying the input pressure and water contents, the temperature can vary by up to 50°C. By using the maximum water content estimate of 5 wt.% of Moore and Carmichael (1998), the temperature decreases by 20°C for the clinopyroxene-melt thermometer, 30°C for the orthopyroxene-melt thermometer and 50°C for the plagioclase-melt thermometer. Pressure has a lesser effect on the eruption temperature. A pressure of 5 kbar (~15 km depth) yields an increase in eruption temperature of 10 to 15°C.

Sample	Unit	Water-dependent thermometers					Water-independent thermometers			
		P (kbar)	H ₂ O (wt.%)	Cpx-melt ^[1] T (°C) ± 45	Opx-melt ^[2] T (°C) ± 39	Plag-melt ^[3] T (°C) ± 36	2-px ^[4] T (°C) ± 56	2-px ^[5] T (°C) ± 70	2-px ^[6] T (°C) ± 60	Hbd ^[7] T (°C) ± 22
VF95-06Y	Y	2	3	-	-	1001	-	-	-	947
VF95-09X	Y	2	3	-	-	964	-	-	-	923
VF97-05B	Y	2	3	-	939	1044	-	-	-	927
VF97-06D	Y	2	3	-	-	956	-	-	-	950
VF99-05W	W	2	3	1020	-	1035	-	-	-	967
VF98-02W	W	2	3	-	988	1015	993	966	983	962
VF97-06B	W	2	3	1007	-	1035	-	-	-	972
VF98-02U	U	2	3	1008	1018	1055	959	982	1002	975
VF10-01U	U	2	3	1013	1050	993	977	1025	1022	-
VF10-07U	U	2	3	998	1042	946	960	1013	1016	-
VF95-06U	U	2	3	1015	990	1042	932	965	942	-
VF95-09T	S	2	3	958	944	1057	927	954	948	-
VF10-03Pi	P	2	3	969	982	991	933	974	964	-
VF10-03M2	L	2	3	912	977	910	927	954	948	-
VF95-09E	L	2	3	-	-	830	-	-	-	930
VF97-01F	J	2	3	978	1075	1027	965	1002	1024	-
VF10-03L	J	2	3	977	1006	991	936	969	972	-
VF95-01F	H	2	3	1001	1033	1014	970	1026	1007	949
VF94-06E	H	2	3	997	-	984	-	-	-	965
VF97-01Di	H	2	3	1004	-	1022	980	1039	1032	-

Table 2.4 Eruption temperature estimates from pressure and water-dependant thermometers

[1] clinopyroxene-melt (eq. 33; Putirka, 2008); [2] orthopyroxene-melt (eq. 38a; Putirka, 2008); and [3] plagioclase-melt (eq. 24a; Putirka, 2008); and water-independent thermometers: [4] two-pyroxene thermometers (Putirka, 2008); [5] (Wells, 1977); [6] (Wood and Banno, 1973); and [7] hornblende-only (Ridolfi et al., 2010).

Sample	Unit	Hbd ^[1]		Plag-melt		
		T (°C) ± 22	H ₂ O (wt.%)	T (°C)	H ₂ O (wt.%) ^[2]	H ₂ O (wt.%) ^[3]
VF95-06Y	Y	947	6.3 ± 0.7	947	4.8 ± 1.2	4.9 ± 0.9
VF95-09X	Y	923	5.8 ± 0.6	932	5.1 ± 0.5	4.6 ± 0.6
VF97-05B	Y	927	6.0 ± 0.6	927	5.7 ± 0.3	6.6 ± 1.0
VF97-06D	Y	950	6.3 ± 0.6	950	3.9 ± 1.4	5.2 ± 0.6
VF99-05W	W	967	6.0 ± 0.7	967	4.9 ± 0.3	4.1 ± 0.3
VF98-02W	W	962	6.3 ± 0.4	976	4.6 ± 1.6	4.8 ± 1.6
VF97-06B	W	972	5.9 ± 0.4	972	4.2 ± 0.6	4.7 ± 0.4
VF98-02U	U	975	6.5 ± 0.6	980	5.0 ± 1.0	5.4 ± 0.9
VF10-01U	U	-	-	1008	2.8 ± 0.4	3.7 ± 0.7
VF10-07U	U	-	-	996	1.6 ± 0.6	4.8 ± 1.0
VF95-06U	U	-	-	946	5.3 ± 1.1	4.8 ± 1.0
VF95-09T	S	-	-	943	5.9 ± 0.9	5.7 ± 0.7
VF10-03Pi	P	-	-	957	4.4 ± 1.3	4.5 ± 0.5
VF10-03M2	L	925	5.7 ± 0.6	940	3.0 ± 1.5	4.8 ± 0.6
VF95-09E	L	930	5.5 ± 0.4	930	0.3 ± 0.3	6.2 ± 0.6
VF97-01F	J	-	-	997	4.1 ± 1.3	4.2 ± 0.9
VF10-03L	J	-	-	959	3.8 ± 0.9	4.6 ± 0.6
VF95-01F	H	949	5.3 ± 1.0	988	3.7 ± 0.3	4.3 ± 0.8
VF94-06E	H	965	4.3 ± 1.0	965	5.1 ± 0.6	4.4 ± 0.6
VF97-01Di	H	-	-	1017	3.0 ± 1.0	4.0 ± 0.4

Table 2.5 Water content estimates for the Group I magmas.

Calculated using the hornblende hygrometer of [1] Ridolfi et al. (2010) and plagioclase-melt hygrometers of [2] Putirka (2008) and [3] Lange et al. (2009). The hornblende thermometer and hygrometer calculates the pressure, temperature and water content from the hornblende composition, while the plagioclase-melt hygrometers require the temperature and pressure to be constrained. A pressure of 2 kbar was used combined with the average temperature from the water-independent thermometers (Table 2.4)

2.3.1.2 Mineral-mineral and Mineral-melt Equilibria Tests

Mineral-mineral and mineral-melt geothermometers require the two phases to be in equilibrium with each other. Based on the mineral textures described in Section 2.2.2, the mineral phases in the Group I CVC eruption deposits have experienced multiple phases of disequilibrium during crystal growth. Mineral-mineral and mineral-melt pairs for geothermometry and hygrometry calculations were therefore analysed from shared crystal boundaries and sharp crystal edges adjacent to the glass. Minerals with embayments or displaying dissolution at the rims were not used for geothermometry or hygrometry.

Tests for equilibrium for the various thermometers are presented in Putirka (2008). These are based on the saturation level of the mineral phase in the melt, therefore calculating the temperature at which the mineral phase should form for a given melt composition at a given pressure. For example, the test for plagioclase-melt equilibrium is (eq. 26 from Putirka, 2008):

$$\begin{aligned} \frac{10^4}{T(K)} = & 10.86 - 9.7654(X_{SiO_2}^{liq}) + 4.241(X_{CaO}^{liq}) - 55.56(X_{CaO}^{liq}X_{AlO_{1.5}}^{liq}) \\ & + 37.50(X_{K_{0.5}}^{liq}X_{Al_{0.5}}^{liq}) + 11.206(X_{SiO_2}^{liq})^3 - 3.151 \times 10^{-2}(P(kbar)) \\ & + 0.1709(H_2O^{liq}) \end{aligned}$$

Equation 2.3

Comparisons between the calculated eruption temperatures from the plagioclase-melt thermometer and the temperature from the plagioclase-melt equilibrium test thermometer reveal the temperatures are within error, therefore the plagioclase-melt pairs are in equilibrium (Figure 2.31a).

The equilibrium of orthopyroxene and clinopyroxene with the melt, and between orthopyroxene-clinopyroxene pairs, can be calculated based on Fe-Mg partitioning between the mineral and the melt, or the two minerals (Rhodes et al., 1979):

$$K_D(Fe - Mg)^{opx-liq} = \frac{X_{Fe}^{opx} X_{Mg}^{liq}}{X_{Mg}^{opx} X_{Fe}^{liq}}$$

Equation 2.4

The equilibrium constant, or Fe-Mg exchange coefficient, $K_D(Fe - Mg)^{opx-liq}$, varies little with temperature or composition and remains constant at 0.29 ± 0.06 . For clinopyroxene-melt, the equilibrium constant is 0.28 ± 0.08 , and for clinopyroxene-orthopyroxene, it is 1.09 ± 0.14 (Putirka, 2008). Rhodes et al. (1979) developed a diagram to test for equilibrium by plotting the Mg# of the liquid versus the Mg# of the mineral with the equilibrium constant plotted as a solid line with the binding error envelope as dashed lines (Figure 2.31b, c and d). If the mineral and melt, or two minerals, are in equilibrium, the pair should plot on the solid line, or between the dashed lines.

The Rhodes diagrams for orthopyroxene-melt and clinopyroxene-melt (Figure 2.31b and c) reveal that the majority of the orthopyroxene and clinopyroxene crystals are not in equilibrium with the melt; therefore temperature estimates based on clinopyroxene- and orthopyroxene-melt equilibria do not reflect the exact magmatic conditions at the time of eruption. The majority of the analysed pyroxene pairs do, however, appear to be in equilibrium with each other, with an equilibrium constant of 1.09 ± 0.14 (Figure 2.31d; Putirka, 2008).

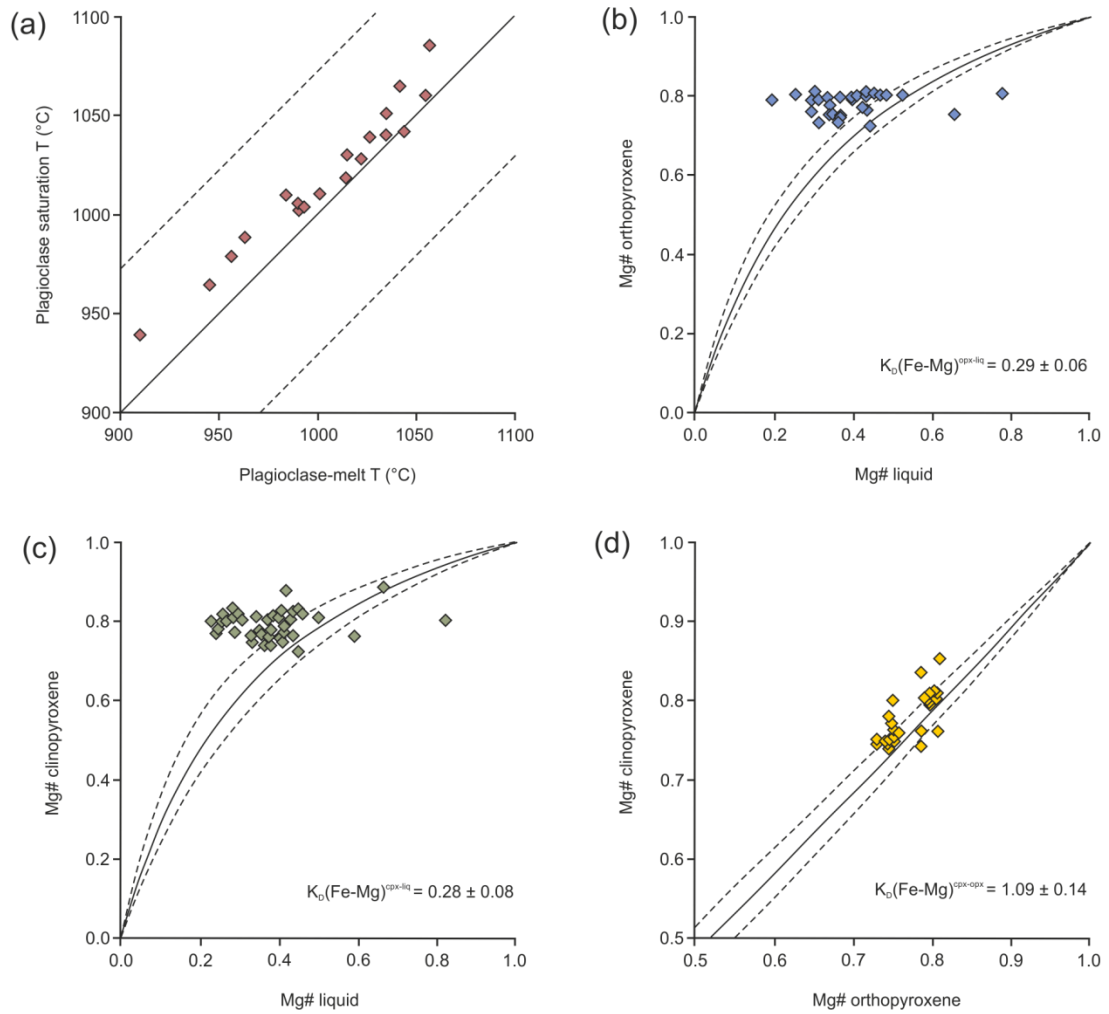


Figure 2.31 Equilibrium tests for mineral-melt and mineral-mineral pairs.

If pairs are in equilibrium, they should plot on the solid line, or within the error envelope defined by the dashed lines. The plagioclase-melt equilibrium test (a) compares the plagioclase-melt thermometry with the temperature at which plagioclase should become saturated and therefore crystallise (Putirka, 2008). Pyroxene-melt (b and c) and two-pyroxene (d) equilibrium is tested using the Rhodes diagram and the Fe-Mg exchange coefficient (Rhodes et al., 1979; Putirka, 2008).

The pyroxenes are not in equilibrium with the melt, therefore the temperature estimates from two-pyroxene thermometers must reflect that of another part of the system. Based on the plagioclase and pyroxene phenocryst textures, there have been multiple magma recharge events, and many of the pyroxene crystals occur in pairs or glomerocrysts (see Section 2.2.1.2), suggesting they may be inherited; therefore it is possible that the temperatures recorded are from another, hotter, batch of magma.

2.3.1.3 Eruption Temperatures and Water Contents for the CVC Group I Deposits

The equilibrium test for plagioclase-melt reveals that the two phases are in equilibrium, therefore it is possible to obtain good estimates of magmatic water contents using the

hygrometer of Putirka (2008). In order to calculate the water content from the Putirka (2008) hygrometer, the temperature must be well constrained.

Temperature estimates from the two-pyroxene and hornblende thermometers vary by up to 76°C (Figure 2.32a). In order to account for this variation the temperature results from these thermometers have been averaged, and this value used for the hygrometer calculations (Table 2.5). The water content estimates vary between the plagioclase-melt hygrometer and the hornblende hygrometer by up to 5 wt.%, with the hornblende hygrometer yielding higher water contents (Figure 2.32b). The water content recorded by the hornblende relates to the water content of the melt during crystallisation (Ridolfi et al., 2010). If growth is inhibited, subsequent water loss from the melt is not recorded by the hornblende phenocrysts.

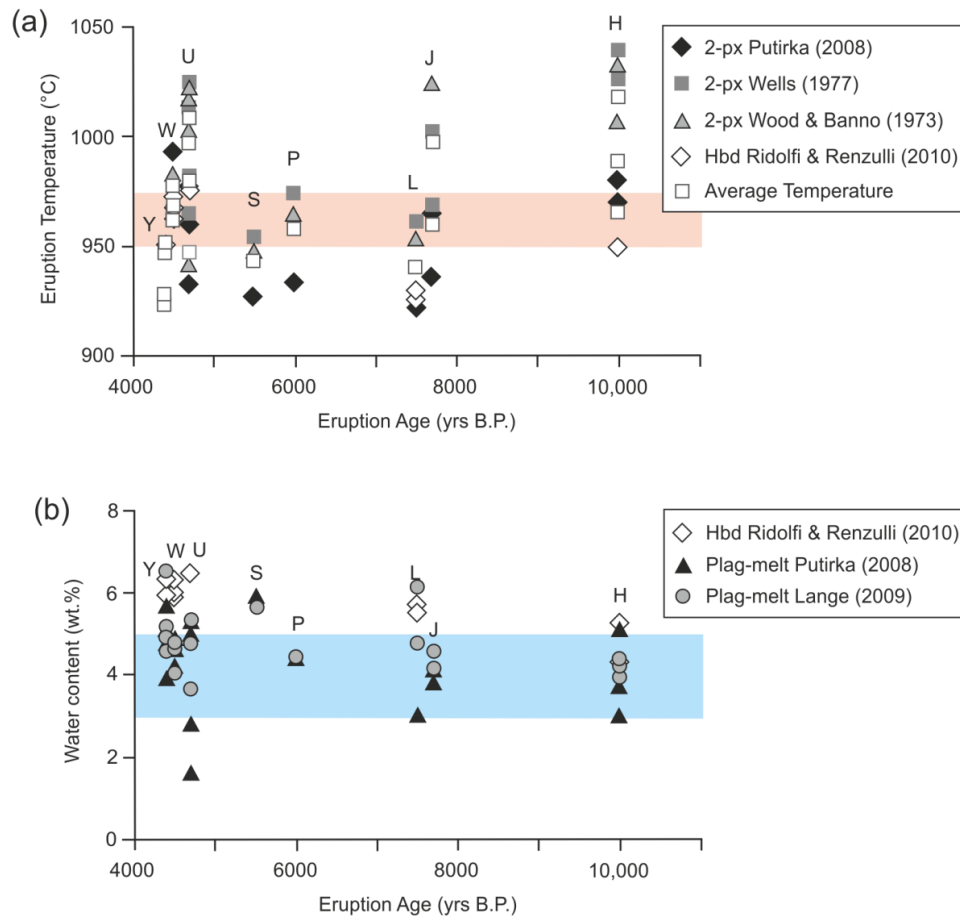


Figure 2.32 Estimated eruption temperatures (a) and water contents (b) for the Group I eruption deposits

Temperatures were estimated using the two-pyroxene thermometers of Putirka (2008), Wells (1977) and Wood and Banno (1973), the hornblende thermometer and hygrometer of Ridolfi et al. (2010), and the plagioclase-melt hygrometer of Putirka (2008). Also plotted is the average temperature of the results from the aforementioned thermometers, which was used for the plagioclase-melt hygrometer. The coloured blocks are the estimated temperature and water contents of Moore and Carmichael (1998) based on experimental studies of Colima lavas. The errors for the thermometers and hygrometers are reported in Tables 2.4 and 2.5

This method of using the average temperature from the two-pyroxene and hornblende thermometry does not yield absolute results, as the temperature estimates from the two-pyroxene geothermometry is not representative of the eruption temperature. As a result, it is difficult to draw any definitive conclusions from the eruption temperature and water content estimates for the explosive CVC Group I magmas. However, these estimated water contents of between 2 and 6 wt .% are consistent with water contents in arc magmas (i.e. Kelley and Cottrell, 2009). Overall the eruption temperatures and water contents do not appear to show any strong variations between eruption deposits, and hence do not correlate with magma composition.

2.4 Whole-rock Geochemistry

Whole-rock major and trace element analyses were carried out on 53 scoria and pumice samples from units U to H of the Colima stratigraphy, collected during the 2010 and 2011 field seasons. Scoria and pumice clasts were cleaned and prepared for analyses as outlined in Appendix C. The powdered samples were sent to Royal Holloway University of London (RHUL) for geochemical analysis. Major and selected trace elements were analysed by Inductively Coupled Plasma-Atomic Emission Spectrometry (ICP-AES) and the remaining trace and rare earth elements were analysed by Inductively Coupled Plasma-Mass Spectrometry (ICP-MS). Details of the analytical methods are given in Appendix D.

In addition to the analyses of this study, a database of whole-rock major and trace element data for the CVC has been compiled from published data (Luhr and Carmichael, 1980, 1981; Luhr and Carmichael, 1982; Allan and Carmichael, 1984; Robin et al., 1991; Luhr, 1993; Robin and Potrel, 1993; Komorowski et al., 1997; Luhr, 2002; Carmichael et al., 2006; Maria and Luhr, 2008; Savov et al., 2008; Vigouroux et al., 2008; Cai, 2009; Luhr et al., 2010; Saucedo et al., 2010) and unpublished data obtained by James Luhr and Ivan Savov. The full database comprises 398 samples from the CVC, including the alkaline cinder cones; of these 252 are from the Holocene and late Pleistocene explosive eruption deposits. Techniques used to analyse major and trace element compositions include X-ray Fluorescence (XRF), ICP-AES, ICP-MS and Instrumental Neutron Activation Analysis (INAA; see Appendix D for details of these analytical techniques, their limitations and a discussion of the compatibility of the various data).

The ranges of major and trace element abundances in the Group I eruption deposits are given in Tables 2.6 and 2.7, and Figures 2.33 to 2.40. The complete geochemical datasets can be found in Appendix E.

2.4.1 Major Elements

As discussed in Chapter 1, the Group I eruption deposits vary in composition from medium-K basaltic-andesites to high-silica andesites (Figure 2.33; and see Section 1.3.2), with SiO_2 contents ranging from 50.7 wt.% (in unit U) to 60.4 wt.% (in unit Y).

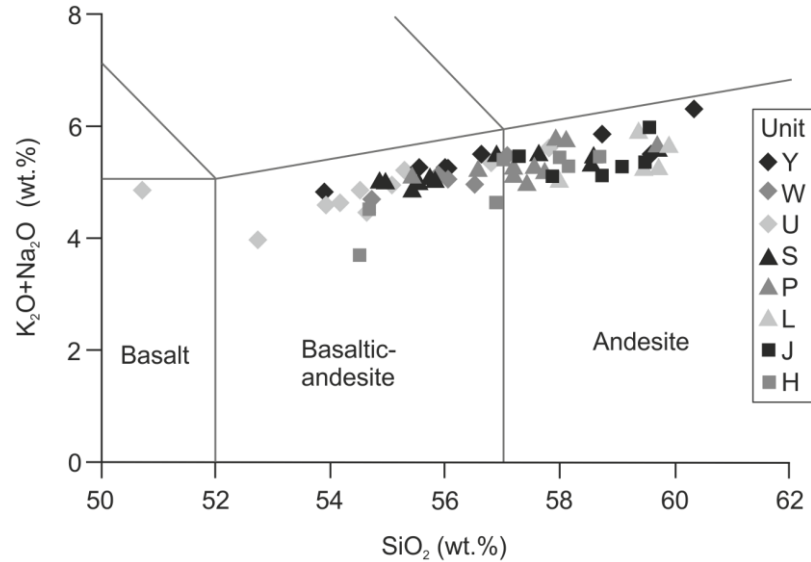


Figure 2.33 Total Alkalis-Silica (TAS) diagram for the Group I eruption deposits, after Le Maitre et al. (2002).

Magma compositions are predominantly basaltic-andesite and andesite. Unit U is the most mafic with the lowest SiO_2 content (50.7 wt.%), while unit Y has the most evolved pumice with up to 60.4 wt.% SiO_2 .

Overall the whole-rock major elements show an evolutionary trend toward increasing K_2O and Na_2O and decreasing MgO , CaO , FeO , TiO_2 , MnO and P_2O_5 with increasing SiO_2 (Figure 2.34). These trends are consistent with crystal fractionation from a mafic magma: as the ferromagnesian minerals, olivine, orthopyroxene, clinopyroxene, hornblende, and Ca-plagioclase crystallise the melt becomes depleted in the oxides of Mg, Fe, Ca, Mn and Ti, and enriched in SiO_2 , Na_2O and K_2O as the melt becomes more evolved (Figure 2.34).

Verma and Luhr (2010) suggested sample SAY-22E from Volcán Tezontal, a basaltic cinder cone to the east of the CVC, which erupted at 545 ka, could represent the parent magma composition for the basaltic-andesites to andesites (Luhr and Carmichael, 1981; Carmichael et al., 2006; Verma and Luhr, 2010). Trends on the whole-rock major element variation diagrams are consistent with a parent magma composition similar to SAY-22E; however, this is not true for unit Y which lies off the main differentiation trend. Unit Y is geochemically distinct from the rest of the Group I eruption deposits, with elevated Al_2O_3 and P_2O_5 , and depleted TiO_2 , MgO and CaO (Figure 2.34).

Unit	SiO ₂	TiO ₂	Al ₂ O ₃	FeOt	MnO	MgO	CaO	Na ₂ O	K ₂ O	P ₂ O ₅
Y	53.9 - 60.4	0.4 - 0.7	17.9 - 21.5	4.7 - 5.8	0.10 - 0.11	1.8 - 2.8	5.0 - 5.9	3.8 - 4.9	1.0 - 1.5	0.17 - 0.31
W	54.7 - 57.1	0.6 - 0.8	17.7 - 18.9	5.7 - 6.6	0.11 - 0.12	3.9 - 5.9	6.4 - 7.5	3.8 - 4.4	0.8 - 1.1	0.20 - 0.21
U	50.7 - 57.8	0.5 - 0.8	17.4 - 21.4	5.6 - 7.0	0.10 - 0.12	2.3 - 6.1	5.5 - 7.5	3.3 - 4.4	0.7 - 1.3	0.19 - 0.35
S	54.6 - 58.6	0.5 - 0.8	17.1 - 19.1	4.8 - 6.5	0.09 - 0.12	3.6 - 5.8	5.7 - 7.5	4.0 - 4.4	0.9 - 1.3	0.17 - 0.15
P	55.4 - 59.7	0.5 - 0.8	17.2 - 19.6	4.7 - 5.8	0.08 - 0.11	2.6 - 6.2	5.6 - 7.1	4.0 - 4.7	1.0 - 1.3	0.16 - 0.22
L	58.0 - 59.9	0.6 - 0.7	16.9 - 17.8	4.9 - 5.4	0.09 - 0.10	3.9 - 5.1	5.9 - 6.3	4.2 - 4.7	1.0 - 1.2	0.15 - 0.18
J	53.4 - 59.5	0.6 - 1.0	16.4 - 17.5	5.2 - 7.0	0.10 - 0.12	4.6 - 6.0	5.9 - 8.1	3.6 - 4.7	1.1 - 1.9	0.15 - 0.39
H	54.5 - 58.7	0.7 - 0.9	15.7 - 18.0	5.8 - 7.2	0.11 - 0.13	4.0 - 7.3	6.7 - 8.0	2.9 - 4.4	0.8 - 1.1	0.13 - 0.50

Table 2.6 Ranges of whole-rock major element concentrations in weight % for Group I basaltic-andesites to high-silica andesites.

Unit	V	Cr	Co	Ni	Cu	Zn	Rb	Sr	Y	Zr	Nb	Ba
Y	69 - 128	11 - 21	10 - 18	7 - 15	11 - 21	59 - 67	13 - 19	601 - 685	14 - 17	128 - 188	2 - 7	386 - 566
W	111 - 160	82 - 190	21 - 28	37 - 74	28 - 37	63 - 70	10 - 16	592 - 666	15 - 18	117 - 152	4 - 5	318 - 418
U	89 - 171	22 - 199	12 - 27	15 - 79	17 - 43	59 - 70	7 - 16	575 - 658	15 - 18	101 - 158	3 - 8	309 - 446
S	119 - 173	83 - 170	16 - 26	39 - 68	20 - 42	60 - 85	10 - 14	564 - 669	16 - 19	104 - 155	4 - 7	323 - 442
P	102 - 156	22 - 116	13 - 25	13 - 49	18 - 32	51 - 70	11 - 17	540 - 679	14 - 18	105 - 138	2 - 7	399 - 509
L	108 - 140	101 - 157	15 - 20	38 - 58	16 - 30	57 - 70	14 - 16	595 - 636	12 - 16	101 - 128	6 - 10	482 - 603
J	91 - 145	77 - 165	18 - 23	43 - 72	28 - 38	59 - 94	11 - 15	615 - 679	14 - 17	110 - 140	2 - 5	383 - 483
H	131 - 198	25 - 322	18 - 29	15 - 86	13 - 49	63 - 77	7 - 16	512 - 676	15 - 21	107 - 144	3 - 5	223 - 494

Table 2.7 Ranges of whole-rock trace element concentrations in ppm for Group I basaltic-andesites to high-silica andesites.

Full whole-rock major and trace element data tables are presented in Appendix E.

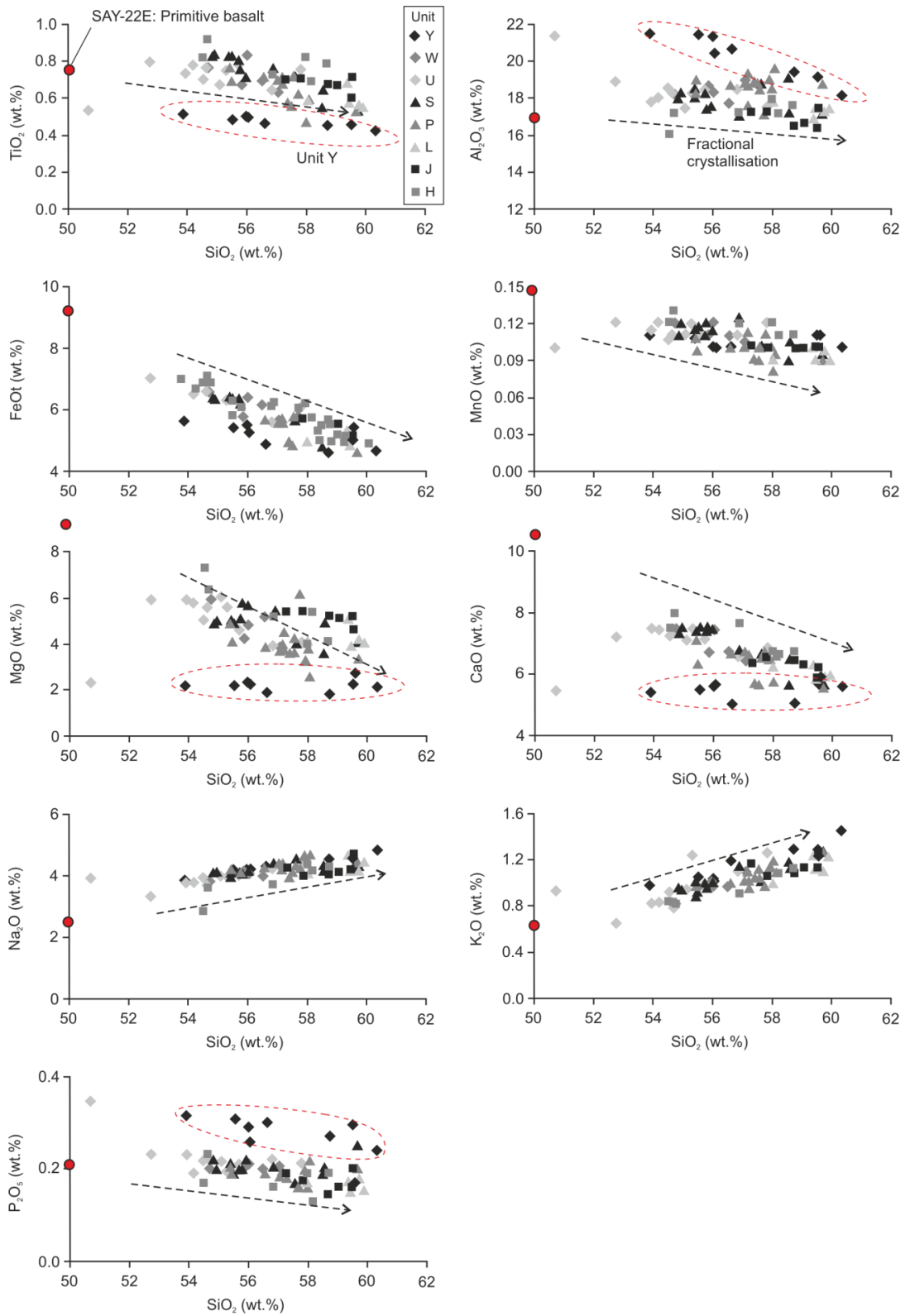


Figure 2.34 Major element oxide variation diagrams.

Trends in whole-rock major element abundances reflect fractional crystallisation of minerals from a mafic melt (dashed black arrow). Sample SAY-22E (red circle) from a basaltic cinder cone, east of the CVC is used to represent the parent basalt (Luhr and Carmichael, 1981; Luhr, 1997; Verma and Luhr, 2010). Unit Y lies off the main fractionation trend with marked differences in TiO₂, Al₂O₃, MgO, CaO and P₂O₅, as highlighted by the dashed red ellipse.

The typical mineral assemblage of the CVC Group I magmas is plagioclase + orthopyroxene + clinopyroxene + hornblende + Fe-Ti oxides ± olivine (see Section 2.2). Figure 2.35 shows the relationship of these mineral phases to the major element geochemistry with progressive differentiation of the melt. The majority of the Group I eruption deposits follow a trend defined by the extraction of plagioclase + orthopyroxene + hornblende + clinopyroxene. Assuming a parental mafic melt of a similar composition to SAY-22E, the proportion of extract removed to generate the evolved glass composition is ~80%, following the Lever Rule (Wilson, 1989).

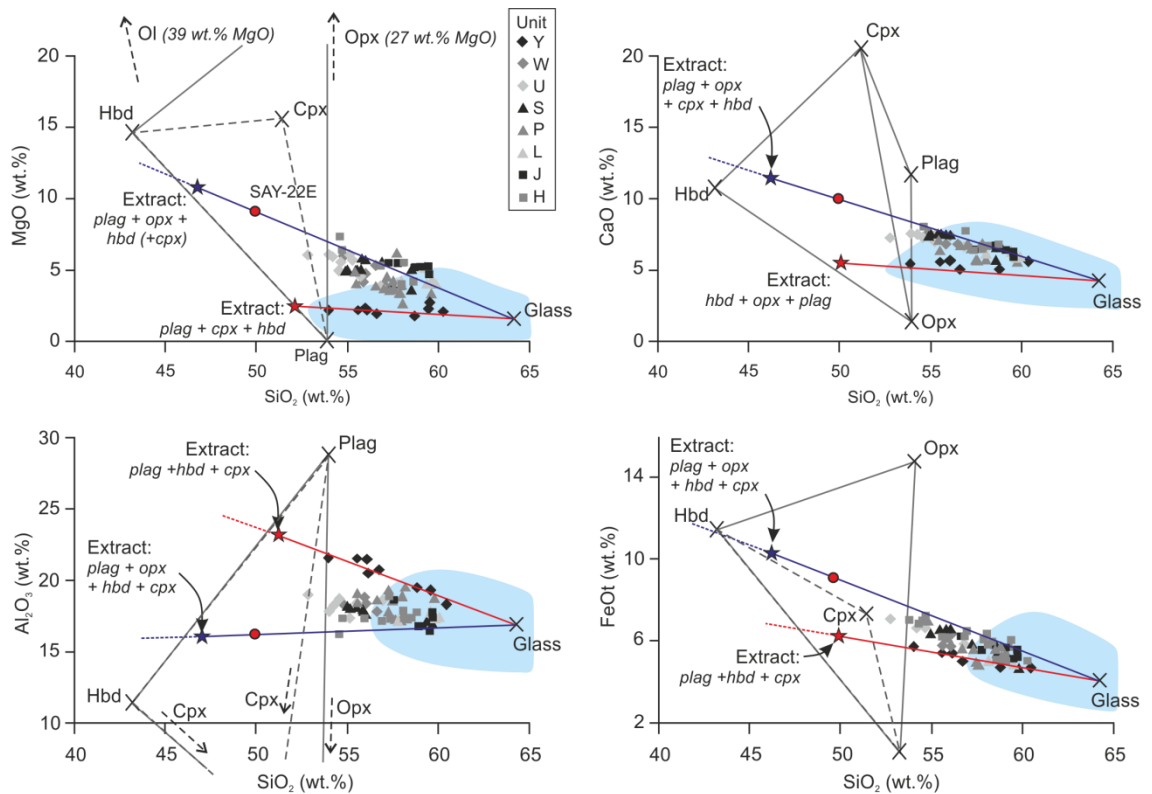


Figure 2.35 Major element variation diagrams, with the main mineral phase compositions plotted based on average EPMA analyses.

The majority of the Group I eruption deposits follow an evolutionary trend controlled by the fractionation of plagioclase, orthopyroxene, clinopyroxene and hornblende from a primitive magma (i.e. SAY-22E, red circle). Unit Y lies off this trend as discussed in the text. The glass composition is an average of glass EMPA analyses from Group I scoria (n=343), shown by the blue shaded area.

Unit Y, which does not follow this fractionation trend, is dominated by plagioclase with hornblende and trace amounts of clinopyroxene and orthopyroxene (Figure 2.35). The trend displayed by unit Y samples may be explained by the addition of plagioclase + hornblende + clinopyroxene to an evolved melt could also produce the trend displayed by the unit Y samples, driving the magma composition towards lower SiO₂ with low MgO and CaO, and high Al₂O₃

contents. Glomerocrysts comprising plagioclase + clinopyroxene + orthopyroxene ± hornblende ± olivine are present in all Group I pumice and scoria samples. The trend displayed by unit Y could represent the addition of these glomerocrysts to an evolved melt.

2.4.2 Trace Elements

The trends observed in the major element data are reflected in the abundances of the compatible trace elements Co, Ni, Cr and V, with less evolved samples containing higher concentrations (Figure 2.36). Co and Ni are preferentially incorporated into olivine during fractional crystallisation, resulting in a decrease in Co and Ni as olivine fractionation proceeds (Figure 2.36). Decreasing Cr with increasing SiO₂ suggests clinopyroxene or Cr-spinel fractionation. No spinel has been observed in the CVC eruption deposits; however, Luhr and Carmichael (1982) report spinel inclusions in olivine and in the groundmass. Parallel trends of decreasing Ti and V, as shown by the Group I deposits (Figures 2.34 and 2.36) is an indicator of Fe-Ti oxide fractionation. Again unit Y does not follow the differentiation trend of the Group I eruption deposits.

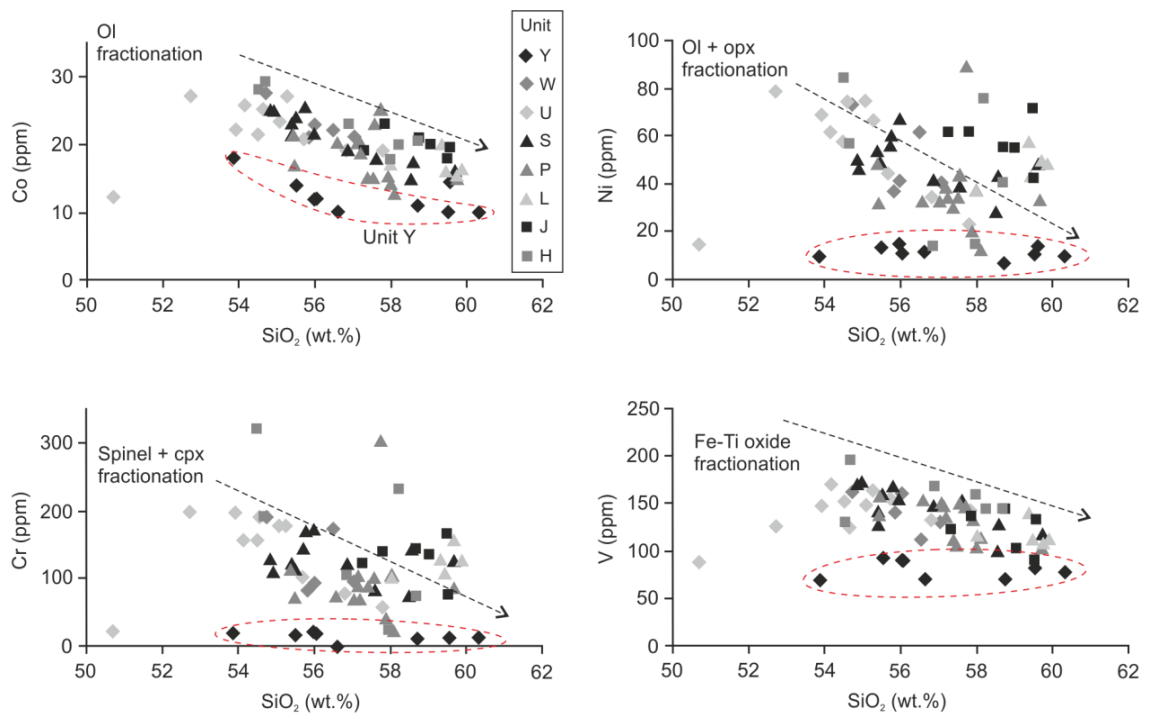


Figure 2.36 Group I trace element concentrations (in ppm) against SiO₂ content (in weight %)

The trends of decreasing Co, Ni, Cr and V with increasing SiO₂ content can be explained by fractionation of mafic minerals and Fe-Ti oxides.

2.4.2.1 Incompatible Trace Element Abundance Patterns in Subduction-related Magmas

The incompatible trace element abundances in a melt reflect the history of the melt i.e. composition of the parent magma and its source, and the extent and processes of melting and subsequent fractional crystallisation (Hanson, 1980).

Subduction-related magmas are typically enriched in large ion lithophile elements (LILE) and light rare earth elements (LREE) relative to high field strength elements (HFSE; Figure 2.37; e.g., Saunders et al., 1991; Sisson and Grove, 1993; Noll et al., 1996; Tatsumi and Kogiso, 1997; Gómez-Tuena et al., 2007a; Chauvel et al., 2009). The LILE, which include K, Rb, Ba, Cs and Sr (\pm Th), and the LREE (La and Ce) have large ionic radii and hence are water-soluble, readily entering a fluid phase (Pearce, 1982). Th behaves like a LILE as it is highly incompatible, readily entering the melt phase; however, it is also a HFSE, with an ionic charge of 3^+ (or 4^+), and an ionic potential (charge/size ratio) greater than 2.0 (Rollinson, 1993). As a result, Th was classified as a LILE in the early literature (e.g. Wilson, 1989; Saunders et al., 1991), and is typically grouped with the LILE (Figure 2.37).

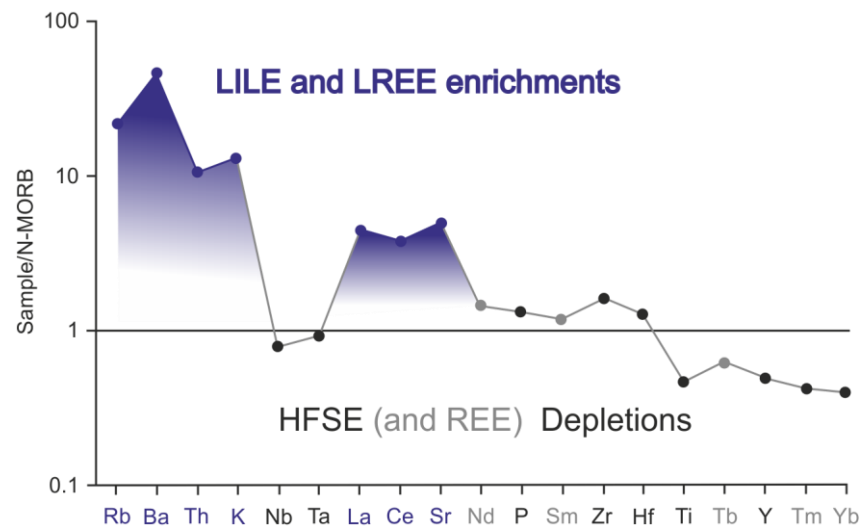


Figure 2.37 Schematic N-MORB normalised multi-element plot for a typical subduction-related magma.

Enrichments in the LILE and LREE are related to slab-derived fluids, while relative depletions in the HFSE (and heavy REE) are attributed to residual mineral phases in the source.

Dehydration of the subducting slab as a result of the breakdown of hydrous mineral phases releases volatiles, transporting the LILE and LREE into the overlying mantle wedge (Figure 2.38; Saunders et al., 1991; Noll et al., 1996; Tatsumi and Kogiso, 1997). Volatiles are released from the subducting slab at depths of ~20 km to > 100 km from serpentine minerals, chlorite, amphibole, and at greater depths, phlogopite (Saunders et al., 1991; Noll et al., 1996). It is widely accepted that by the time the slab has reached a depth of ~100 km it will have lost most

of its volatiles due to dehydration (Saunders et al., 1991; Noll et al., 1996; Tatsumi and Kogiso, 1997). Models of magma generation in subduction zone settings therefore propose that the fluids released from the slab at shallower depths react with peridotite at the base of the overlying mantle wedge, which is then dragged by slab-induced flow to a depth of ~100 km beneath the volcanic arc, where the hydrous minerals breakdown as result of increased pressure and temperature (Figure 2.38; Saunders et al., 1991; Noll et al., 1996).

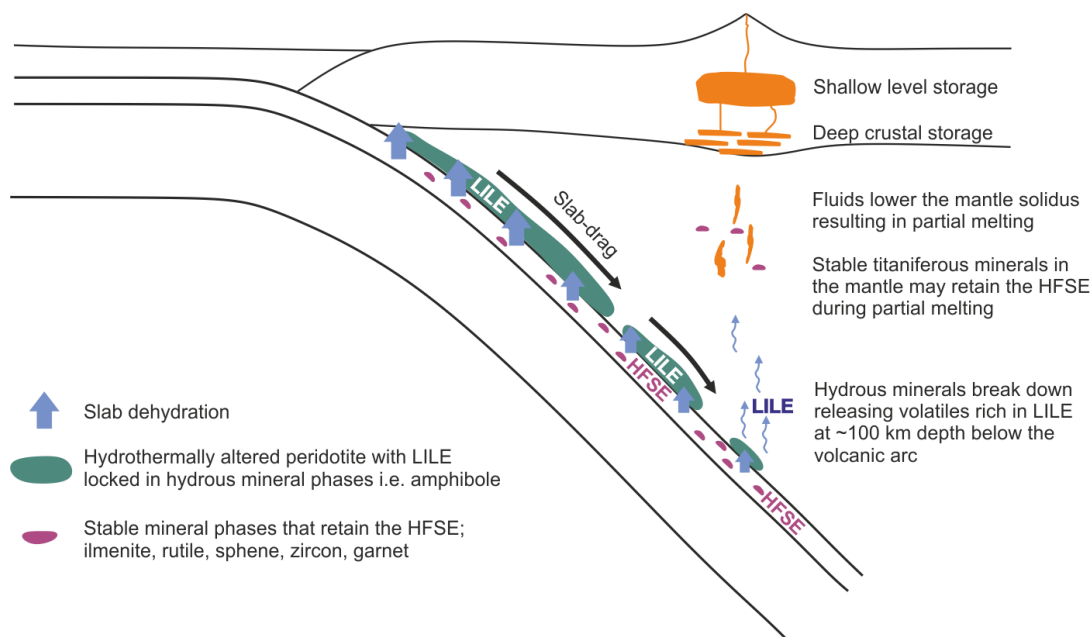


Figure 2.38 Cartoon of a cross-section of a subduction zone.

The decoupling of LILE and HFSE are the result of slab dehydration from the breakdown of hydrous mineral phases in the subducting slab.

There are various arguments for the relative depletions observed in the HFSE (Nb, Ta, Ti, Hf, Zr, Y \pm P). On one hand, the HFSE are insoluble in hydrous fluids and relatively insoluble in melts; therefore they likely remain in the subducting slab during dehydration and in the mantle during partial melting (Pearce, 1982; Saunders et al., 1991; Tatsumi and Kogiso, 1997). However, this is only true if there are stable mineral phases in the source into which the HFSE are preferentially incorporated (Saunders et al., 1991). Nb, Ta and Ti have high partition coefficients for titaniferous minerals such as ilmenite, titanite, rutile and perovskite (Saunders et al., 1991); while Zr and P are readily incorporated into zircon and apatite, respectively, and Zr, Hf and P into garnet and pyroxene at high pressures (Cox et al., 1979; Pearce, 1982; Saunders et al., 1991).

At high pressures, the LILE preferentially partition into the fluid phase, while HFSE do not; therefore decoupling of the LILE and HFSE is assumed to result from slab dehydration

(Saunders et al., 1991). However, if the mantle has a high enough abundance of residual titaniferous mineral phases, and a high water content, pressure and fO_2 , the HFSE can remain in the mantle during partial melting (Saunders et al., 1991).

Incompatible trace elements with respect to typical mantle mineralogies are normalised to N-MORB in order to compare deviations from melts derived from a depleted mantle source, and to remove the Oddo-Harkins effect in the REE: those with even numbers have higher abundance than those with odd numbers producing a zig-zag pattern on a composition-abundance diagram (Hanson, 1980). Typically REE are normalised to abundances in chondritic meteorites, as these are thought to represent the primordial earth (Nakamura, 1974).

2.4.2.2 Incompatible Trace Element Abundance Patterns in the CVC Group I Magmas

Multi-element plots of N-MORB normalised trace element abundances show the Group I CVC eruption deposits have a typical subduction-related magma signature with enrichments in the LILE and LREE relative to the HFSE as described above (Figure 2.39). The Group I magmas all display very similar trace element abundance patterns. Unit Y shows slight enrichments in Th, K, La, Ce, Nd, P, Zr and Hf and a greater depletion in Ti relative to the rest of the Group I deposits (Figure 2.39).

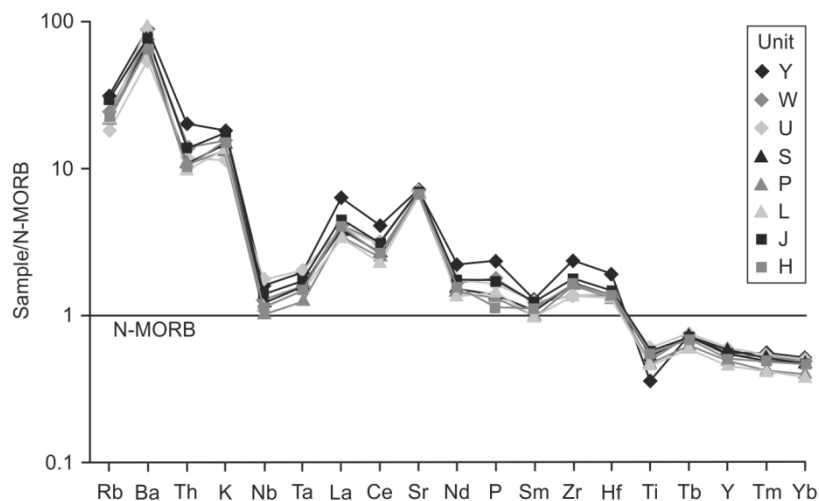


Figure 2.39 N-MORB normalised multi-element abundance plot for the Group I eruption deposits.

Normalisation values are from Sun and McDonough (1989). Enrichments and depletions are typical of subduction-related arc magmas, controlled by subduction zone fluids and mineral phases stable in the source region. A representative sample was chosen for each unit.

Chondrite-normalised REE patterns display strong enrichments in LREE (La, Ce, Pr, Nd) relative to MREE (Sm, Eu, Gd, Tb, Dy) and HREE (Er, Tm, Yb, Lu; Figure 2.40). Variations in the REE patterns predominantly reflect partial melting and / or fractionation of mineral

phases from the melt. Low percentages of partial melting will strongly enrich the LREE relative to the HREE, as the LREE preferentially enter the melt phase, while the middle to heavy REE are incorporated into residual minerals in the source, such as amphibole, clinopyroxene and garnet (Saunders et al., 1991). The fractionation of mineral phases from the melt will also strongly influence the REE pattern, dependant on their partition coefficients for the main mineralising phases. The fractionation of hornblende will result in depletion in the MREE (Eu, Gd, Tb, Dy) as they preferentially enter hornblende, while a pronounced depletion in the HREE is an indication of garnet in the source (Hanson, 1980). Clinopyroxene fractionation will form a similar pattern to hornblende fractionation; however, the partition coefficients of the MREE are lower for clinopyroxene than hornblende. The LREE have low partition coefficients for all of these minerals (Hanson, 1980).

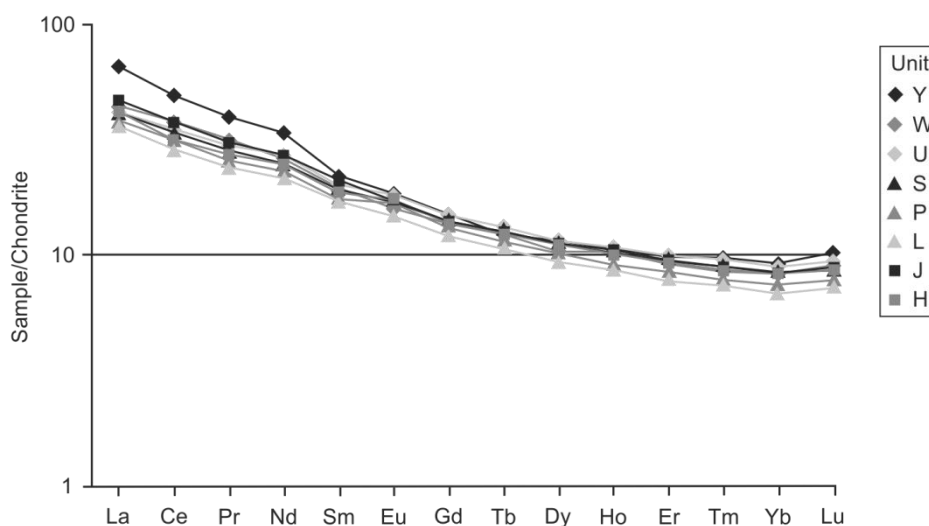


Figure 2.40 Chondrite normalised rare earth element (REE) abundance patterns for the Group I eruption deposits.

Normalising values are from Nakamura (1974). The LREE are strongly enriched relative to the MREE and HREE in all the Group I eruption deposits; this is more pronounced in unit Y.

The Chondrite-normalised REE patterns for the Group I CVC eruption deposits may therefore reflect low degrees of partial melting of a source containing residual amphibole, clinopyroxene and garnet, or fractionation of these minerals from the parental mafic melt. Either way, amphibole, clinopyroxene and garnet have a control on the REE patterns of the CVC magmas. The control of amphibole is consistent with the major element variations in Figure 2.35.

2.5 Whole-rock Sr-Nd Isotopes

The radiogenic isotopic composition of a magma is inherited from its source during partial melting and remains unchanged as fractional crystallisation progresses in the absence of

contamination by an isotopically distinct component (DePaolo and Wasserburg, 1976; Hawkesworth and van Calsteren, 1984). However, isotopic variations will occur if, during ascent, the magma interacts with other batches of magma or crystalline mush, or assimilates wall-rocks with isotopically distinct compositions (Hawkesworth and van Calsteren, 1984). Accordingly, the $^{87}\text{Sr}/^{86}\text{Sr}$ and $^{143}\text{Nd}/^{144}\text{Nd}$ isotopic ratios have been widely used to fingerprint magma source(s) and identify open- and closed-system processes occurring in the magma storage region such as magma mixing, crustal assimilation and fractional crystallisation (AFC; e.g. Kempton et al., 1991; Tatsumi et al., 1992; Straub et al., 2010; Verma and Luhr, 2010; Schmidt and Grunder, 2011).

The $^{87}\text{Sr}/^{86}\text{Sr}$ and $^{143}\text{Nd}/^{144}\text{Nd}$ isotopic ratios are controlled by the radioactive decay of ^{87}Rb to ^{87}Sr and ^{147}Sm to ^{143}Nd , respectively. The radioactive parent isotopes have long half-lives (48.8×10^9 for ^{87}Rb and 106×10^9 for ^{147}Sm) so when contrasted against a stable isotope of the same element (^{86}Sr and ^{144}Nd), the $^{87}\text{Sr}/^{86}\text{Sr}$ and $^{143}\text{Nd}/^{144}\text{Nd}$ ratios reflect the long-term evolution of the mantle reservoir (Hofmann, 1997). Young magmatic rocks therefore must record the radiogenic isotopic composition of their sources as there is insufficient time for the parent isotope in newly-formed magmas to decay and produce additional daughter isotopes to those inherited from the source (Hofmann, 1997).

Early studies of the radiogenic isotope systematics of MORB and OIB (e.g. DePaolo and Wasserburg, 1976; Richard et al., 1976; White and Bryan, 1977; Zindler et al., 1984) revealed a wide range of mantle-derived magma compositions and led Zindler and Hart (1986) to define end-member mantle reservoirs (Figure 2.41): depleted mantle (DM); enriched mantle (EM); HIMU; PREMA and Bulk Silicate Earth. Depleted mantle is characterised by low $^{87}\text{Sr}/^{86}\text{Sr}$ and high $^{143}\text{Nd}/^{144}\text{Nd}$, while enriched mantle has low $^{143}\text{Nd}/^{144}\text{Nd}$ and variable $^{87}\text{Sr}/^{86}\text{Sr}$. The enriched mantle reservoir has been proposed to represent mantle containing recycled crustal material via subduction, and can be sub-divided into EMI, which has low $^{143}\text{Nd}/^{144}\text{Nd}$ and low $^{87}\text{Sr}/^{86}\text{Sr}$ and EMII which is characterised by low $^{143}\text{Nd}/^{144}\text{Nd}$ and high $^{87}\text{Sr}/^{86}\text{Sr}$ (Figure 2.41; Zindler and Hart, 1986).

HIMU (high “ μ ”) is characterised by very high $^{206}\text{Pb}/^{204}\text{Pb}$ and $^{208}\text{Pb}/^{104}\text{Pb}$ ratios, low $^{87}\text{Sr}/^{86}\text{Sr}$ and intermediate $^{143}\text{Nd}/^{144}\text{Nd}$ and is thought to originate from a source enriched in U and Th relative to Pb with no associated increase in Rb/Sr (Zindler and Hart, 1986; Rollinson, 1993). The HIMU reservoir was originally defined based on highly radiogenic Pb isotope ratios in basalts from St Helena and the Cook Islands, but the definition and its use is debated in the geological literature (Stracke et al., 2005). The PREMA reservoir represents the PREvalent MAnTle composition with $^{87}\text{Sr}/^{86}\text{Sr} = 0.7033$ and $^{143}\text{Nd}/^{144}\text{Nd} = 0.5130$ derived from the occurrence of OIB with this isotopic composition (Zindler and Hart, 1986). These mantle

reservoirs lie along a linear trend of decreasing $^{143}\text{Nd}/^{144}\text{Nd}$ with increasing $^{87}\text{Sr}/^{86}\text{Sr}$, termed the Mantle Array (Zindler and Hart, 1986).

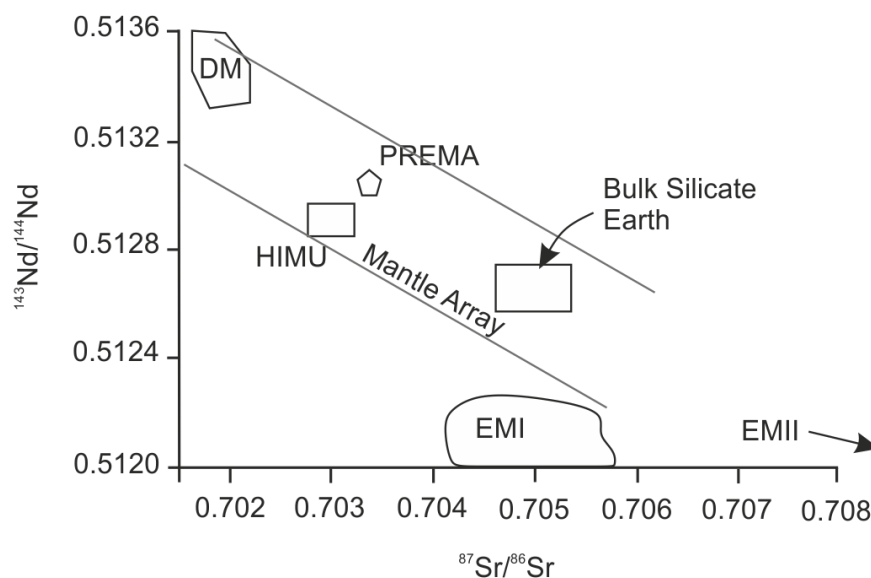


Figure 2.41 $^{143}\text{Nd}/^{144}\text{Nd}$ versus $^{87}\text{Sr}/^{86}\text{Sr}$ diagram showing the mantle reservoirs of Zindler and Hart (1986).

Another mantle reservoir defined by Zindler and Hart (1986) is the bulk silicate earth or primary uniform reservoir (Figure 2.41). The bulk silicate earth represents the composition of a homogenous primitive mantle formed during accretion, core formation and associated degassing prior to the formation of the continental crust (Zindler and Hart, 1986). Its $^{143}\text{Nd}/^{144}\text{Nd}$ composition is thought to approximate CI chondrite meteorites (0.51262), and from the negative correlation of $^{143}\text{Nd}/^{144}\text{Nd}$ with $^{87}\text{Sr}/^{86}\text{Sr}$, the $^{87}\text{Sr}/^{86}\text{Sr}$ ratio for bulk silicate earth is estimated as 0.7045 to 0.7055 (Zindler and Hart, 1986).

The definition of these reservoirs is highly debated in the geological literature (i.e. Hofmann, 1997; Stracke et al., 2005; Parai et al., 2009; Willbold and Stracke, 2010); however, they provide a base-line for mantle heterogeneity which aids interpretation of complex isotopic datasets.

2.5.1 Isotopic Composition of the CVC Group I Magmas

Powdered pumice and scoria whole-rock samples from the Group I eruption deposits were prepared as described in Appendix C and analysed for their $^{87}\text{Sr}/^{86}\text{Sr}$ and $^{143}\text{Nd}/^{144}\text{Nd}$ isotopic compositions on the TRITON thermal ionisation mass spectrometer (TIMS) at the University of Leeds, following standard column procedure outlined in Appendix F. A total of 55 $^{87}\text{Sr}/^{86}\text{Sr}$ and

31 $^{143}\text{Nd}/^{144}\text{Nd}$ analyses were made for the Group I and II eruption deposits. The $^{87}\text{Sr}/^{86}\text{Sr}$ and $^{143}\text{Nd}/^{144}\text{Nd}$ ratios for the Group I deposits are presented in Table 2.8.

Ratios are reported to an internal precision of 2σ error on the 6th decimal digit. All $^{87}\text{Sr}/^{86}\text{Sr}$ ratios are corrected for mass fractionation to $^{86}\text{Sr}/^{88}\text{Sr} = 0.1194$, and are corrected to the NBS987 standard (0.710248; Thirlwall, 1991) which averaged 0.710262 ± 5 over 58 runs between September 2010 and July 2012. The $^{143}\text{Nd}/^{144}\text{Nd}$ ratios were corrected to the La Jolla standard (0.51185; Thirlwall, 1991) which averaged 0.511842 ± 6 over 23 runs between August 2011 and July 2012. The analytical procedures are outlined in detail in Appendix F.

Sample	Unit	$^{87}\text{Sr}/^{86}\text{Sr}$	2σ error ($\times 10^{-6}$)	$^{143}\text{Nd}/^{144}\text{Nd}$	2σ error ($\times 10^{-6}$)
VF95-09X	Y	0.703627	± 4	0.512940	± 11
VF97-06D	Y	0.703633	± 6	0.512912	± 4
VF97-13B	Y	0.703623	± 6	0.512916	± 6
VF98-02W	W	0.703582	± 4	0.512916	± 6
VF95-06W	W	0.703574	± 6	0.512941	± 8
VF10-01U	U	0.703586	± 4	0.512924	± 6
VF10-02U	U	0.703593	± 4	0.512932	± 6
VF10-04U	U	0.703635	± 5	0.512921	± 7
VF10-07U	U	0.703594	± 4	0.512934	± 4
VF95-06P	S	0.703555	± 4	0.512953	± 3
VF95-09T	S	0.703592	± 4	0.512932	± 6
VF10-03Q	P	0.703577	± 13	0.512948	± 5
VF10-07M3	P	0.703604	± 4	0.512927	± 5
VF10-01P	P	0.703564	± 4	0.512948	± 7
VF10-03Pi	P	0.703557	± 10	0.512902	± 7
VF95-09E	L	0.703597	± 3	0.512909	± 5
VF10-03M2	L	0.703604	± 4	0.512932	± 8
VF10-03L	J	0.703610	± 4	0.512937	± 6
VF00-06R	H	0.703384	± 3	0.512952	± 5
VF94-06E	H	0.703705	± 5	0.512913	± 5
VF97-01Di	H	0.703689	± 5	0.512913	± 5

Table 2.8 $^{87}\text{Sr}/^{86}\text{Sr}$ and $^{143}\text{Nd}/^{144}\text{Nd}$ isotope ratio compositions for the Group I eruption deposits.

Values are reported to 2σ error on the 6th decimal digit, and have been normalised to the NBS-987 and La Jolla standards for Sr and Nd, respectively.

Within the Group I eruption deposits, $^{87}\text{Sr}/^{86}\text{Sr}$ and $^{143}\text{Nd}/^{144}\text{Nd}$ range from 0.703384 to 0.703705 and 0.512902 to 0.512952, respectively (Table 2.8). Unit H shows the widest variation, with both the most radiogenic and the least radiogenic Sr isotopic compositions (Figure 2.42). The rest of the Group I samples show a slight increase in $^{87}\text{Sr}/^{86}\text{Sr}$, and decrease

in $^{143}\text{Nd}/^{144}\text{Nd}$ with increasing SiO_2 , indicating assimilation and fractional crystallisation processes (AFC; Figure 2.42).

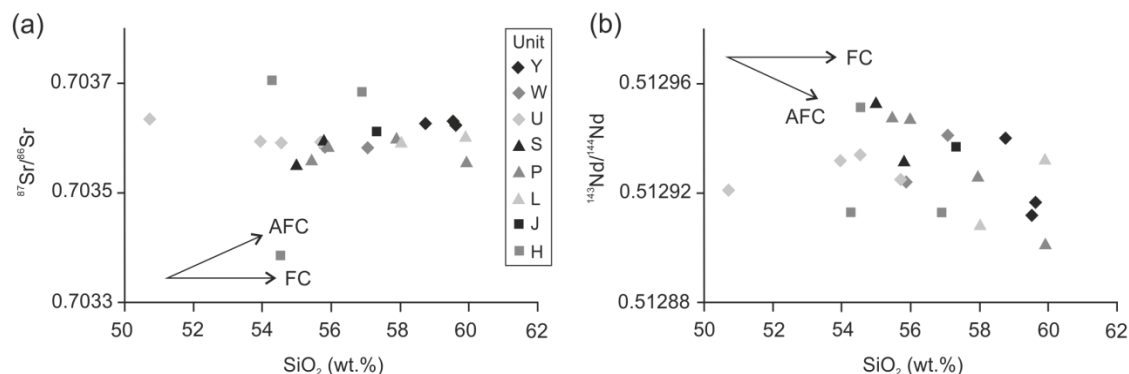


Figure 2.42 Variation of $^{87}\text{Sr}/^{86}\text{Sr}$ (a) and $^{143}\text{Nd}/^{144}\text{Nd}$ (b) with SiO_2 content for the Group I eruption deposits.

Analytical error is within symbol size. The arrows indicate trends for Fractional Crystallisation (FC) and Assimilation and Fractional Crystallisation (AFC).

The CVC Group I magmas lie along the mantle array trending away from the TMVB mantle wedge isotopic composition, towards a more enriched, or crustal source (Figure 2.43). Intra-plate type basalts found in the Michoacán-Guanajuato Volcanic Field in the central TMVB have been used as a proxy for the composition of the Mexican sub-arc mantle (Gómez-Tuena et al., 2007a; Vigouroux et al., 2008; Cai, 2009). These rocks represent primitive magmas with little evidence of slab contribution with low Ba/La and high Nb/La ratios, and no relative Nb-Ta depletion (Gómez-Tuena et al., 2007a). Gómez-Tuena et al. (2007a) estimated the composition of the mantle wedge underlying the TMVB by modelling the melting of a high-Mg basalt (sample ASC44 from the Sierra Chichinatzen Volcanic Field, central TMVB) to form a spinel peridotite comprising 53% olivine, 17% clinopyroxene, 28% orthopyroxene and 2% spinel. The authors applied a batch melting model at 5% melting to estimate the trace element concentrations in the mantle wedge. In order to estimate the Nd isotopic composition, the authors extrapolated the trend displayed by central TMVB rocks on a Pb/Nd versus $^{143}\text{Nd}/^{144}\text{Nd}$ diagram, and the Sr isotopic composition was assumed to be slightly more enriched than the East Pacific Rise MORB (Gómez-Tuena et al., 2007a). The $^{87}\text{Sr}/^{86}\text{Sr}$ and $^{143}\text{Nd}/^{144}\text{Nd}$ isotopic composition of such a source is 0.702900 and 0.513010 (Figure 2.44; Gómez-Tuena et al., 2007a).

No mantle xenoliths have been found at the CVC; however, they have been found in northern Mexico and the central TMVB (Liang and Elthon, 1990; Nimz et al., 1995; Mukasa et al., 2007). Nimz et al. (1995) report $^{87}\text{Sr}/^{86}\text{Sr}$ and $^{143}\text{Nd}/^{144}\text{Nd}$ isotope ratios of 0.702203 to

0.703276 and 0.512733 to 0.513320, respectively, for ten lherzolite, harzburgite and orthopyroxenite xenoliths found in northern Mexico (Figure 2.43). Mukasa et al. (2007) report $^{87}\text{Sr}/^{86}\text{Sr}$ and $^{143}\text{Nd}/^{144}\text{Nd}$ isotope ratios of 0.703642 and 0.70339, and 0.512858 and 0.512833, respectively, for two peridotite xenoliths from El Peñon in the central TMVB (Figure 2.43). The estimated mantle wedge composition of Gómez-Tuena et al. (2007a) lies within the mantle xenolith compositional field (Figure 2.43).

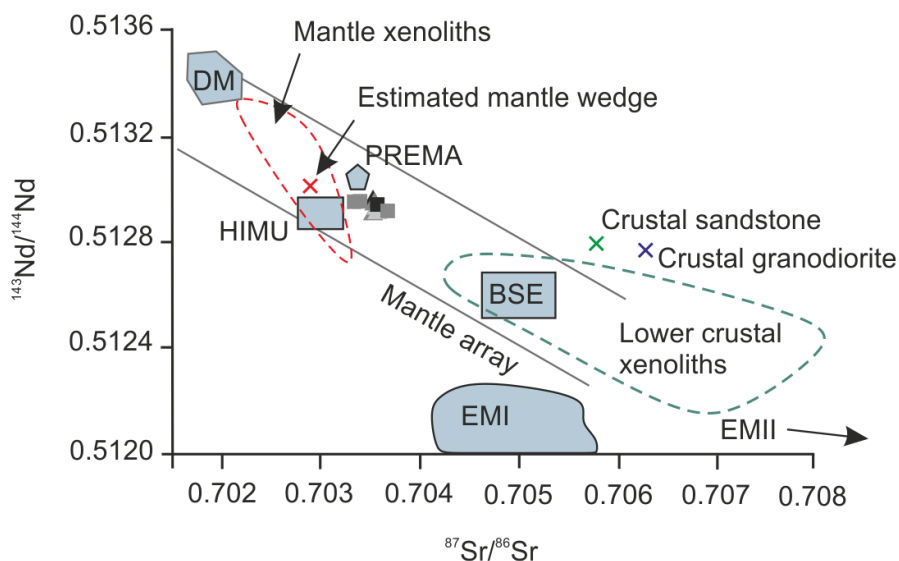


Figure 2.43 $^{143}\text{Nd}/^{144}\text{Nd}$ versus $^{87}\text{Sr}/^{86}\text{Sr}$ diagram showing the relation of the Group I CVC magmas to the mantle reservoirs as defined by Zindler and Hart (1986).

The Group I magmas lie along the mantle array trending away from the mantle xenolith compositions (defined by red dashed line after Nimz et al. 1995) and the estimated Mexican mantle wedge composition of Gómez-Tuena et al. (2007a). Also plotted are the compositions of granodiorite (Verma and Luhr, 2010) and sandstone (Centeno-García et al., 1993) crustal rocks, and lower crustal xenoliths (Ruiz et al., 1988; Cameron et al., 1992; Centeno-García et al., 1993; Mendoza and Suastegui, 2000). Figure 2.44 is a blow-up of the CVC Group I samples on a $^{143}\text{Nd}/^{144}\text{Nd}$ versus $^{87}\text{Sr}/^{86}\text{Sr}$ diagram.

Many isotopic and geochemical studies have been carried out on lower crustal xenoliths found throughout the TMVB, and basement rocks from the Zuahatanejo Subterranean of the Guerrero Terrane which underlies the CVC (see Section 1.2.1; Ruiz et al., 1988; Cameron et al., 1992; Centeno-García et al., 1993; Mendoza and Suastegui, 2000). Verma and Luhr (2010) proposed a crustal composition approximate to that of the La Huacana Granite (Michoacán), after Luhr and Carmichael (1985), and Centeno-García et al. (1993) measured the isotopic composition of the Cretaceous sandstone which forms part of the basement underlying the CVC. These two samples are used here to approximate the crust (Figure 2.43).

Figure 2.44 reveals the variations observed in the $^{87}\text{Sr}/^{86}\text{Sr}$ isotopic ratios of the Group I units. The majority of the Group I eruption deposits are isotopically homogenous; however, the samples from unit H of the Group I eruption deposits display a wide variation in $^{87}\text{Sr}/^{86}\text{Sr}$. Care was taken during the sample preparation and analytical steps (as described in Appendices C and F) to avoid contamination, therefore analytical error is an unlikely source for this variation.

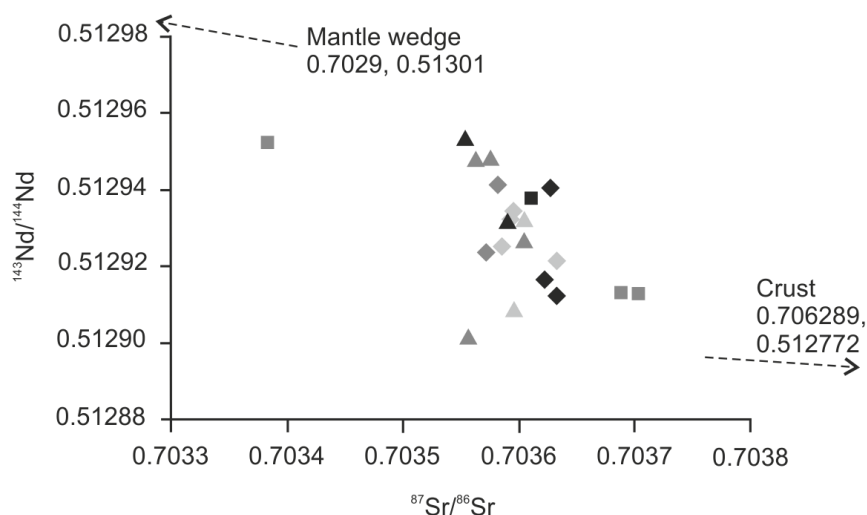


Figure 2.44 $^{143}\text{Nd}/^{144}\text{Nd}$ versus $^{87}\text{Sr}/^{86}\text{Sr}$ diagram showing the CVC group I samples.

The variation in the Sr isotope compositions may reflect the assimilation of crustal material as the Group I deposits appear to be trending towards the composition of the western TMVB crust as defined by Verma and Luhr (2010).

Another source of the variation may be from post-eruption alteration; however, there is no evidence for this in the mineralogy (see Section 2.2.1.8). The different isotopic compositions may also reflect mixing of an isotopically distinct magma batch which is recorded in the unit H eruption, but not in the rest of the Group I eruption deposits. In order to address this properly, further detailed investigation into the geochemical and isotopic composition from different horizons within the deposit would be needed.

2.6 Summary

The majority of the eruption deposits exposed on the flanks of Nevado de Colima belong to Group I. These deposits are pumice and scoria fall deposits, ranging in composition from medium-K, sub-alkaline basaltic-andesite to high-silica andesite, with the majority of units comprising basaltic-andesites. Mineral zoning reveals complex crystallisation histories involving multiple magma replenishment phases, decompression, and fluctuations in temperature, pressure, water contents and $f\text{O}_2$ in the magma storage region. Geothermometry and mineral textures reveal many of the pyroxene phenocrysts were not in equilibrium with the

final melt. Hornblende phenocryst and groundmass glass textures reveal very rapid ascent rates of the magma from the storage region to the surface.

Geochemical analyses reveal the Group I magmas evolved from mafic parental magmas, with subduction-related trace element signatures. However, the most evolved unit, Y, shows clear distinctions from the Group I fractionation trend, with low MgO, CaO, Co, Ni, Cr and V; elevated Al₂O₃ and P₂O₅; and enrichments in the LILE and LREE. Unit Y samples also show distinctions in mineralogy with only plagioclase and hornblende phenocryst phases.

Variations in ⁸⁷Sr/⁸⁶Sr and ¹⁴³Nd/¹⁴⁴Nd within the Group I eruption deposits follow a trend away from the inferred composition of the Mexican mantle wedge towards the composition of the local crust. Plots of ⁸⁷Sr/⁸⁶Sr and ¹⁴³Nd/¹⁴⁴Nd versus bulk-rock SiO₂ content indicate the Group I eruption deposits follow an AFC trend, which is supported by the ¹⁴³Nd/¹⁴⁴Nd versus ⁸⁷Sr/⁸⁶Sr diagram. The nature of the magma source and open-system processes will be explored further in the subsequent chapters.

3 Group II High-K Eruption Deposits

The majority of the CVC explosive eruption deposits are Group I medium-K basaltic-andesites and andesites as presented in Chapter 2. However, three of the tephra fallout deposits exposed on the flanks of Nevado de Colima are mineralogically and geochemically distinct from the Group I series, characterised by high K₂O and P₂O₅ and the presence of phlogopite. Luhr and Carmichael (1982) discovered phlogopite bearing scoria within a fall deposit exposed on the flanks of Nevado de Colima. They suggested this unit may have resulted from mixing between the magmas that produced the bulk of the Volcán de Colima eruption deposits and the alkaline magmas of cinder cones which erupted on the rift floor. This unit along with two others identified here, form the Group II eruption deposits which are interbedded within the Group I stratigraphy.

Following the structure of Chapter 2, this chapter presents the results of field studies and petrological and geochemical analyses of the Group II eruption deposits using new data collected as part of this study, and previously published (Luhr and Carmichael, 1982; Luhr et al., 2010) and unpublished data collected by Jim Luhr. These data are used to investigate the petrological and geochemical distinctions within the Group II units and to investigate their evolution within the CVC magmatic plumbing system.

3.1 Stratigraphy

Group II comprises units N, F and D of the CVC stratigraphy, which erupted approximately 7000, 12,000 and 13,000 yrs B.P., respectively (Table 3.1). Unit N is well correlated across the northern CVC, while units F and D are less well correlated with exposures limited to the lower flanks on the eastern side of Nevado de Colima (Figure 3.1).

Unit	Eruption Age (yrs B.P.)	Number of localities	Deposit Type	Colour (dry)	Thickness (cm)	Max. Scoria (cm)	Max. lithic (cm)	Sorting	Composition
N	6950±50 - 7070±60	16	Scoria fall	Orange	12-60	17	12	Inverse	Basaltic-andesite
F	11,840±70 - 12,080±150	6	Scoria fall	Yellow	13-90	5	8	Normal	Basaltic
D	12,460±60 - 13,350±130	9	Scoria fall	Grey	32-180	6.5	5	Inverse	Basaltic-andesite

Table 3.1 Field characteristics of the Group II tephra fallout deposits.

Eruption ages are from radiocarbon ¹⁴C dating of charcoal found in within or between tephra fallout deposits (Komorowski et al., 1997; Luhr et al., 2010). Maximum lithic fragment and pumice clast sizes, measured along the long-axis, are found in sections 4-5 km from the currently active vent.

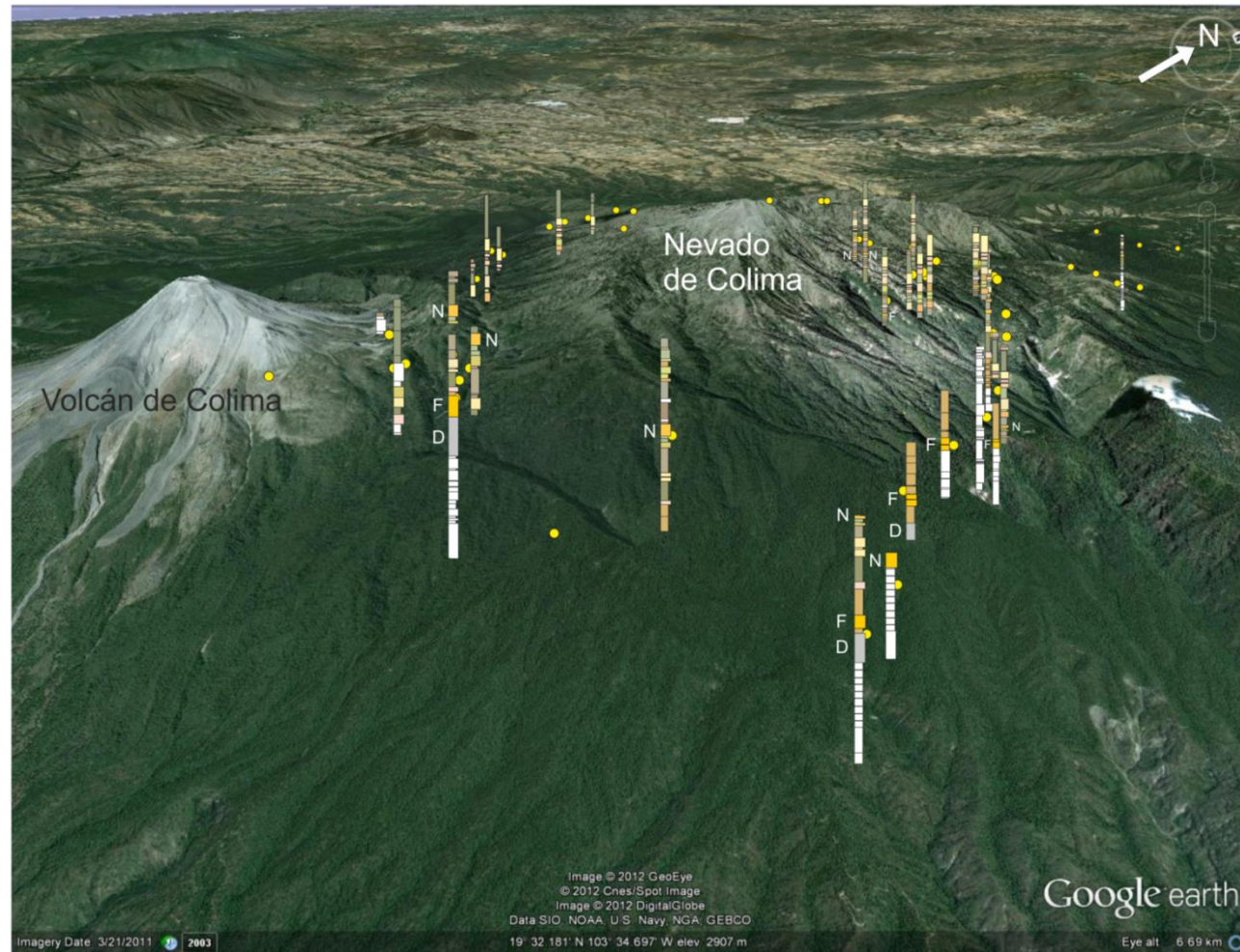
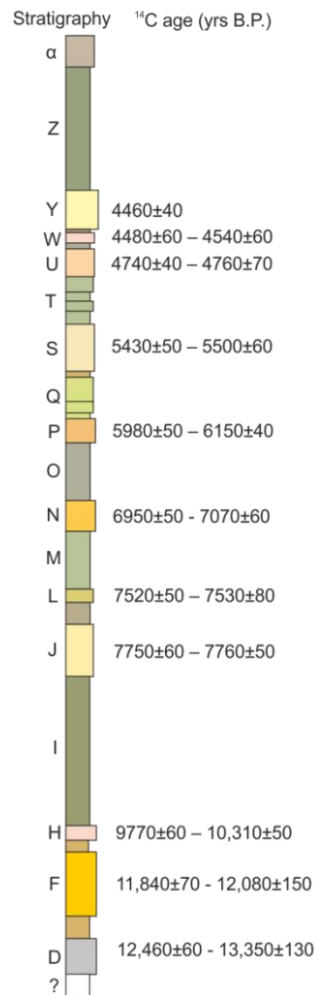


Figure 3.1 Google Earth map of the eastern side of Volcán de Colima and Nevado de Colima showing the section locations.

Where possible, the Group II eruption deposits, units N, F and D are indicated on the sections

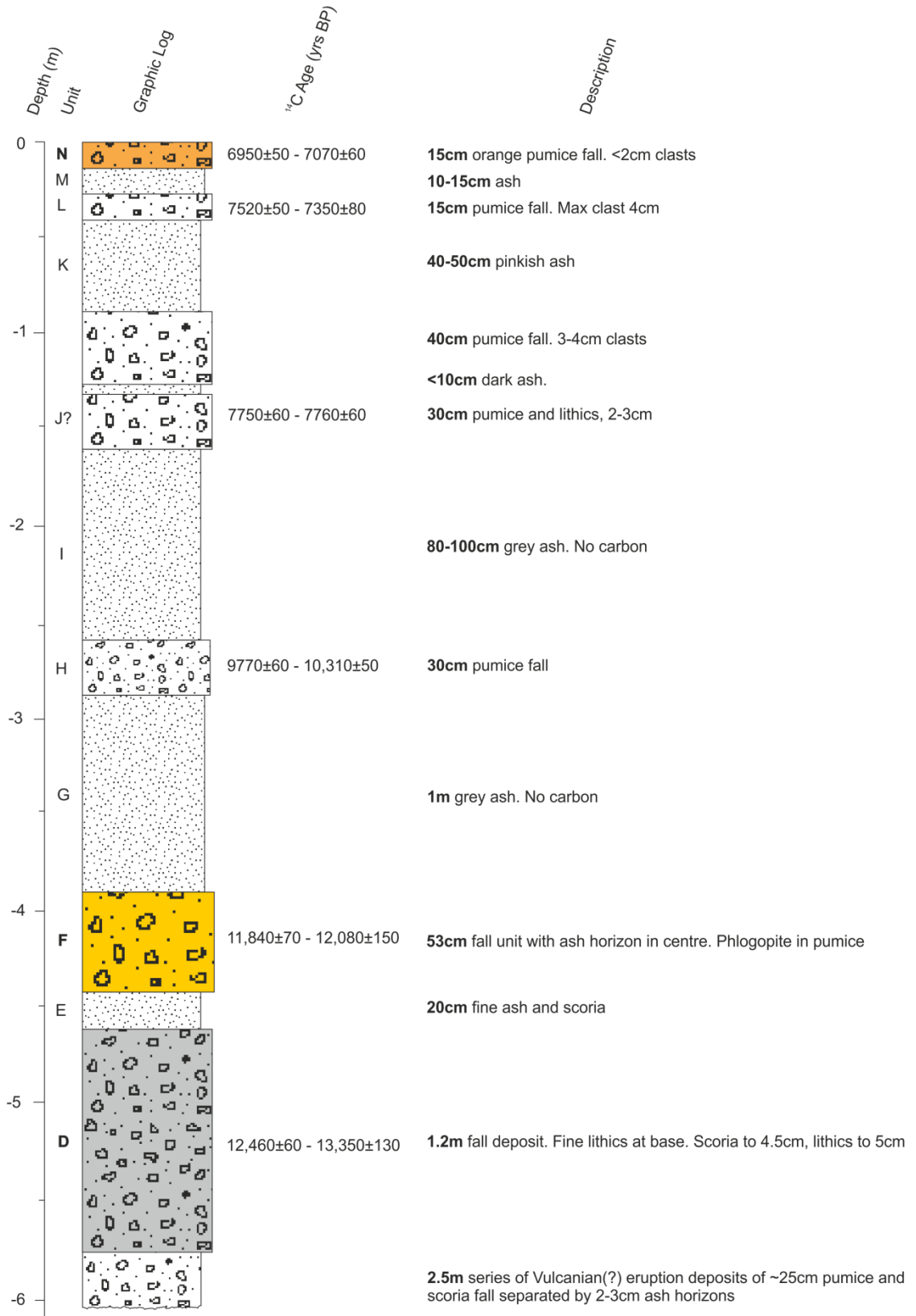


Figure 3.2 Stratigraphic log from section VF01-02.

This section is located 7 km from the vent, and shows the Group II deposits (units N, F and D) in the CVC stratigraphy, as described by Jim Luhr (unpublished). The ages shown are not obtained from this section, but have been added for reference from Tables 2.1 and 3.1.

Unit N is a distinctive orange coloured, inversely graded, basaltic-andesite scoria fall deposit (Table 3.1; Figure 3.2). It is typically medium-grained with scoria up to 3cm; however, scoria clasts up to 17cm and lithic fragments up to 12cm were found at localities more proximal to the vent (section VF97-01, 1.5 km from the vent). Unit N has been identified at 16 localities, varying in thickness from 12 to 60cm. Stratigraphically above and below the tephra fallout deposit of unit N are ash layers. Radiocarbon (^{14}C) ages of charcoal fragments found in these ash horizons constrain the age of unit N to between 6950 ± 50 and 7070 ± 60 yrs B.P. (Luhr et al., 2010). Above and below the ash horizons are the tephra fallout units P and L of the Group I eruption deposits, which are basaltic-andesites.

Unit F is a basaltic scoria fall deposit that is normally-graded with clasts up to 5cm, and lithic fragments up to 8cm (Table 3.1; Figure 3.2). The deposit shows a wide variation in thickness, from 3 to 90cm, measured at six localities 2.5 to 8 km from the vent. Unit F is a distinctive marker horizon as scoria clasts contain visible phlogopite phenocrysts. The age of this unit is approximately 12,000 yrs B.P. based on radiocarbon dating of charcoal found within the fall deposit which yielded ages of $11,840\pm 70$ and $12,080\pm 50$ yrs B.P. (Luhr et al., 2010).

Overlying unit F is a thick (up to 1m) ash layer, above which is the Group I eruption deposit, unit H. Below unit F, separating it from unit D, is a ~20cm thick pyroclastic flow deposit comprising ash and reworked scoria (Figure 3.2).

The oldest of the Group II deposits is unit D, which erupted ~13,000 yrs B.P. This unit is a grey basaltic-andesite scoria fall deposit (Table 3.1; Figure 3.2). It is inversely-graded with scoria clasts up to 6.5cm and lithic fragments to up to 5cm. The thickness of this unit ranges from 32 to 180cm, measured at 9 localities 2.5 to 10 km from the vent. Charcoal fragments from binding ash layers yielded radiocarbon ages of $12,460\pm 60$ and $13,350\pm 130$ yrs B.P. (Luhr et al., 2010).

3.2 Petrology and Mineral Chemistry

Scoria from the Group II eruption deposits are basalt to basaltic-andesite in composition with phenocryst and microphenocryst phases comprising plagioclase + clinopyroxene + hornblende + olivine + phlogopite + Fe-Ti oxides \pm orthopyroxene in varying amounts (Table 2.2). The groundmass is typically dark glass, which is highly vesiculated with abundant microlites of the mineral phases mentioned above. All three units also contain up to 1 vol.% glomerocrysts of predominantly clinopyroxene and olivine and, less commonly, orthopyroxene and phlogopite.

Unit	Crystallinity (vol.%)	Plag (vol.%)	Cpx (vol.%)	Opx (vol.%)	Hbd (vol.%)	Olivine (vol.%)	Phlogopite (vol.%)	Fe-Ti oxides (vol.%)
N	9-13	5-10	1-2	Trace	Trace	Trace-1	Trace	1
F	7-12	Trace-1	2-5	-	Trace	1-3	1-2	1-2
D	10-15	1-3	Trace-2	Trace	3-7	Trace-1	1	1-3

Table 3.2 Mineralogy of scoria from the Group II tephra fallout deposits observed at the CVC.

Abundances are given in volume % and were estimated from thin sections on the optical microscope. The mineral abbreviations are: Plag = plagioclase; Cpx = clinopyroxene; Opx = orthopyroxene; Hbd = hornblende.

Each of the three units that make up the Group II eruption deposits have phlogopite phenocrysts and / or microphenocrysts, which are not present in scoria and pumice from the Group I eruption deposits. The Group II units are, however, mineralogically distinct from each other. Unit N scoria phenocrysts comprise predominantly plagioclase and clinopyroxene, with up to 1 vol.% olivine, and trace abundances of hornblende and phlogopite (Table 2.2). Scoria from unit F has a lower degree of crystallinity than units N and D, and the mineral assemblage is dominated by clinopyroxene, olivine and phlogopite with up to 1 vol.% plagioclase and trace hornblende (Table 2.2). Unit D scoriae have the highest degree of crystallinity comprising predominantly hornblende and plagioclase, with clinopyroxene and up to 1 vol.% olivine and phlogopite. The groundmass also appears to be more crystalline in unit D, with abundant microlites. Fe-Ti oxides are present in all samples from 1 to 3 vol.%, and are most abundant in unit D (Table 2.2).

3.2.1 Mineral Compositions

The mineral phases in the Group II eruption deposits show a wide range of compositions with large core-rim variations, as well as large variations within cores and rims (Table 3.3; Appendix B). Complex zoning patterns and mineral textures are displayed by clinopyroxene and plagioclase phenocrysts, which are discussed in detail in Section 3.2.2.

3.2.1.1 Plagioclase

The abundance of plagioclase varies between units, from trace to 10 vol.% (Table 3.2). Unit N contains the highest abundance, while plagioclase phenocrysts in unit F are rare. Phenocrysts are typically euhedral to subhedral, up to 2mm in length, with a prismatic habit. Both fresh and altered, sieve textured, phenocrysts are present in all samples, commonly displaying complex zoning patterns. The Group II units have a high microphenocryst population relative to phenocrysts. Microphenocrysts (<0.3mm; Wilcox, 1954) are euhedral and prismatic, and have a fresh appearance.

Unit	Glass SiO ₂ (wt.%)	Plagioclase An (mol.%)		Clinopyroxene Mg#		Orthopyroxene Mg#		Olivine Mg#	
	Average	Cores	Rims	Cores	Rims	Cores	Rims	Cores	Rims
N	59.1 <i>(n=55; 49.5-64.8)</i>	57 <i>(n=12; 53-64)</i>	56 <i>(n=25; 47-65)</i>	0.81 <i>(n=12; 0.74-0.89)</i>	0.80 <i>(n=21; 0.72-0.82)</i>	0.87 <i>(n=2; 0.87)</i>	0.79 <i>(n=13; 0.76-0.81)</i>	0.80 <i>(n=8; 0.77-0.80)</i>	0.79 <i>(n=10; 0.77-0.80)</i>
F	58.5 <i>(n=5; 56.8-58.7)</i>	52 <i>(n=11; 42-62)</i>	52 <i>(n=10; 44-59)</i>	0.83 <i>(n=25; 0.70-0.90)</i>	0.81 <i>(n=22; 0.73-0.85)</i>	-	-	0.87 <i>(n=8; 0.86-0.88)</i>	0.81 <i>(n=9; 0.79-0.82)</i>
D	59.2 <i>(n=41; 54.4-66.9)</i>	54 <i>(n=33; 34-78)</i>	46 <i>(n=22; 24-74)</i>	0.82 <i>(n=37; 0.72-0.88)</i>	0.81 <i>(n=25; 0.75-0.83)</i>	0.86 <i>(n=2; 0.86)</i>	0.79 <i>(n=2; 0.78-0.81)</i>	0.86 <i>(n=14; 0.85-0.87)</i>	0.79 <i>(n=13; 0.79-0.81)</i>

Table 3.3 Mineral chemistry of scoria from the Group II eruption deposits.

For each mineral, the average composition is given with the number of analyses and the range of compositions in italics. Analyses were carried out on the Jeol 8234 electron microprobe at the University of Leeds. Anorthite content is calculated as $Ca/(Ca+Na+K)$, and Mg# is calculated as $Mg/(Mg+Fe)$. The full dataset is presented in Appendix B.

Cores and rims display a large variation in anorthite content ranging from andesine (An_{30}) to bytownite (An_{78} ; Figure 3.3). One plagioclase crystal from unit D has a rim composition of An_{24} (Table 3.3; Figure 3.3). The microphenocrysts have a narrower range in composition, varying from An_{48} to An_{65} .

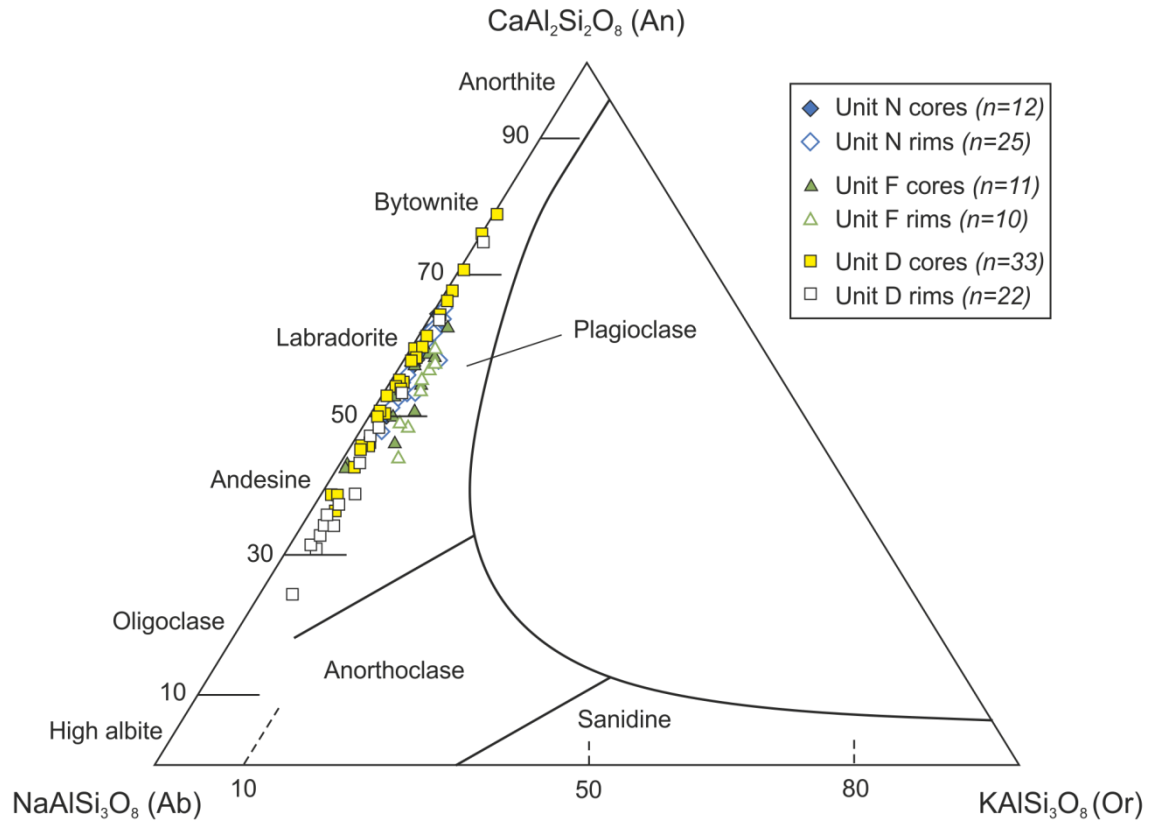


Figure 3.3 Feldspar ternary classification diagram after Deer et al. (1992) for units N, F and D of the Group II eruption deposits.

Figure 3.4 shows the range of core and rim anorthite contents in plagioclase phenocrysts from the Group II eruption deposits. Units N and F show similar ranges in core and rim compositions (10-20% An), while unit D shows a much wider range of anorthite contents from An_{34} to An_{78} in cores, and An_{24} to An_{74} in rims (Figure 3.4). These variations in plagioclase composition are reflected in the mineral textures as discussed in detail in Section 3.2.2.1.

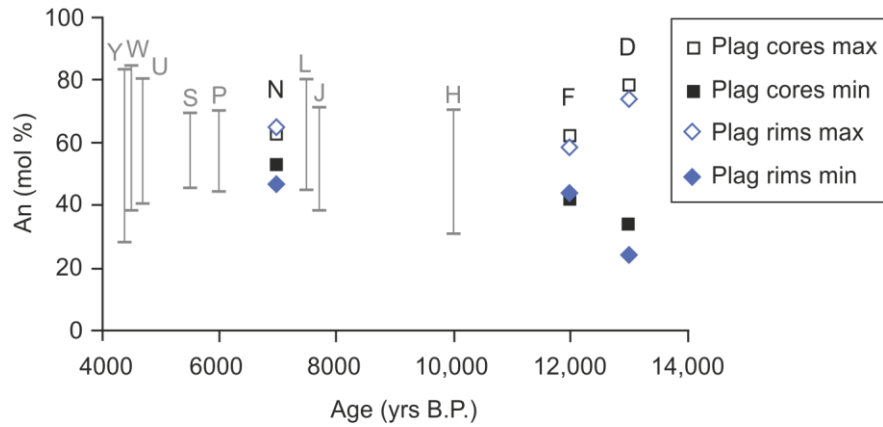


Figure 3.4 Ranges of core and rim anorthite (An mol%) composition of plagioclase phenocrysts for the Group II eruption deposits.

Also shown are the ranges of plagioclase compositions for the Group I units.

3.2.1.2 Clinopyroxene

Clinopyroxene is present in all units varying in abundance from trace to 5 vol.% (Table 3.2). As observed in the Group I eruption deposits, individual phenocrysts are rare, more commonly occurring in pairs or in glomerocrysts. Crystals are typically ~0.5mm across, but can reach up to 1.5mm, and are euhedral to subhedral with rounded corners suggesting some disequilibrium. Zoning is common, and sieve textured growth zones are present in many of the phenocrysts. These features are discussed in detail in Section 3.2.2.3.

Cores and rims cluster in the diopside and augite fields on the clinopyroxene Ca-Mg-Fe classification diagram of Morimoto (1988; Figure 3.5) showing little variation between core and rim compositions.

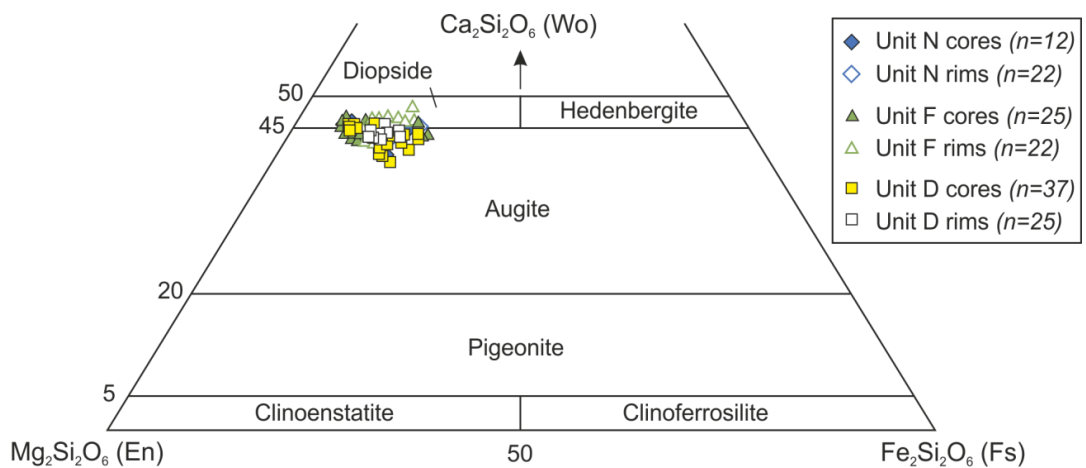


Figure 3.5 Classification of clinopyroxenes in Group II scoria samples in the pyroxene quadrilateral after Morimoto (1988).

The ranges of core and rim Mg# in clinopyroxene of the Group II deposits are shown in Figure 3.6. Clinopyroxenes from unit F show the widest range in Mg# with cores varying from Mg# 0.70 to 0.90 and rims ranging from Mg# 0.73 - 0.85. Core and rim compositions in units N and D typically display narrower ranges (Table 3.3). These variations in clinopyroxene Mg# are discussed in detail with respect to zoning patterns in Section 3.2.2.4.

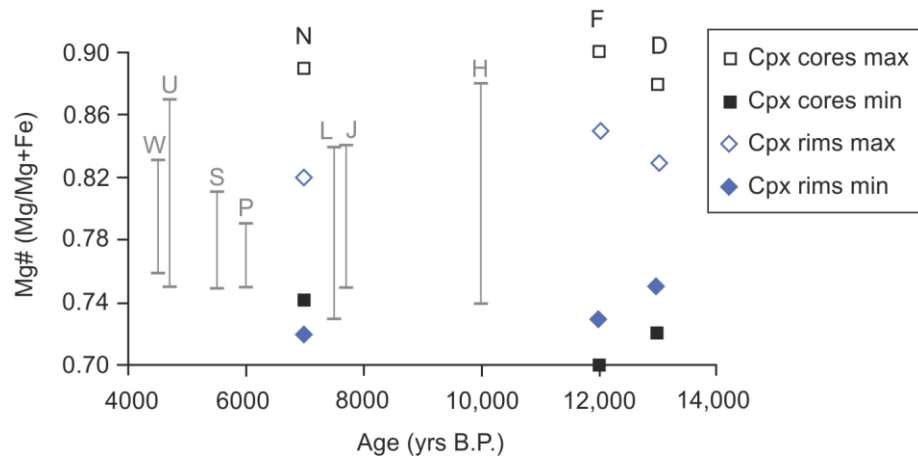


Figure 3.6 Ranges of Mg# in cores and rims of clinopyroxenes from the Group II eruption deposits.

Also shown are the range Group I clinopyroxene Mg#.

3.2.1.3 Orthopyroxene

Orthopyroxene crystals are rare in the Group II eruption deposits, with trace orthopyroxene present in units N and D, generally occurring together with clinopyroxene. Crystals are euhedral to subhedral, and show signs of disequilibrium with slightly embayed rims.

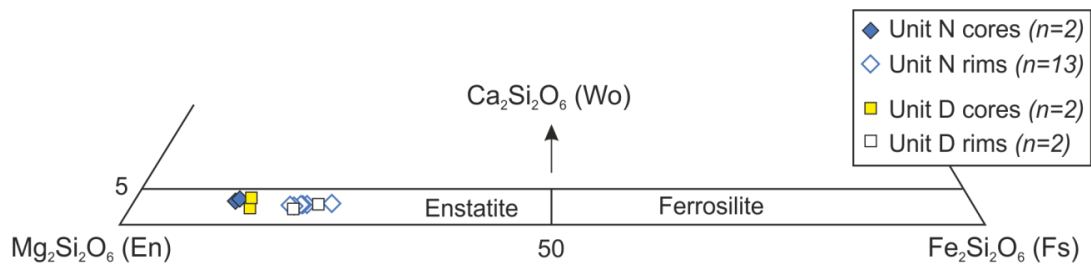


Figure 3.7 Ca-Mg-Fe classification diagram for orthopyroxenes after Morimoto (1988).

The rare orthopyroxene phenocrysts observed in the Group II eruption deposits, units N and D, lie in the enstatite field with clear differences in core and rim composition.

Cores and rims plot as enstatite on the orthopyroxene classification diagram of Morimoto (1988; Figure 3.7); cores are more magnesian (Mg# 0.86-0.87) than rims (Mg# 0.76-0.81; Table 3.3; Figure 3.8).

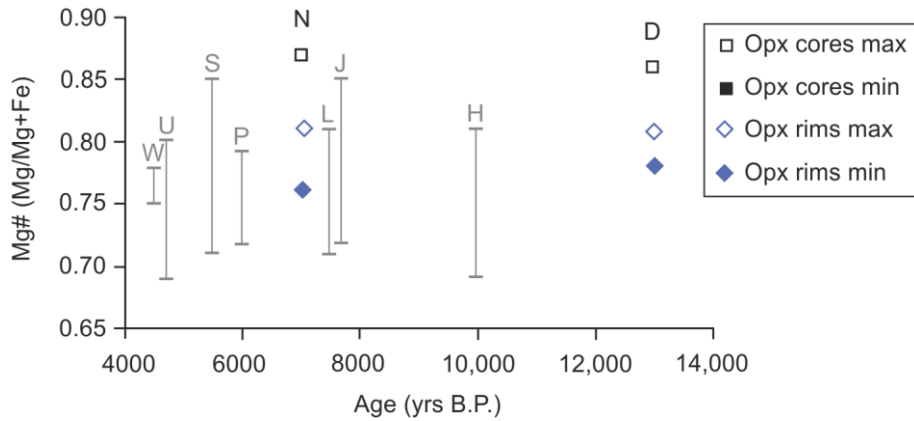


Figure 3.8 Ranges of orthopyroxene core and rim Mg# for units N and D of Group II.

Orthopyroxene is not present in unit F. Core compositions do not show any variation, while rim compositions range from 0.78-0.81 and 0.78-0.81 for units N and D, respectively. Also shown are the ranges of Mg# in orthopyroxenes from the Group I eruption deposits.

3.2.1.4 Hornblende

Hornblende phenocrysts and microphenocrysts are present in all three of the Group II eruption deposits. Hornblende is the dominant mineral phase in unit D, which has 3-7 vol.%, while units N and F have only trace abundances of hornblende (Table 3.2). Phenocrysts in unit D are typically up to 2mm in length and are subhedral with rounded edges (Figure 3.9a). Reaction rims of pyroxene, plagioclase and Fe-Ti oxides are rare; however, holes in the centre are common (Figure 3.9) and many phenocrysts appear broken. Hornblende in units N and F occurs as microphenocrysts with an anhedral, broken appearance (Figure 3.9d).

The Group II hornblende phenocrysts and microphenocrysts are calcic-amphiboles (i.e. $Ca_B \geq 1.50$; see Section 2.2.1.4) and according to the classification of Leake et al. (1997), are magnesiohastingsite. Core and rim compositions show little variation; however, backscatter SEM images reveal zoning textures which are discussed in detail in Section 3.2.2.5 (Figure 3.9c).

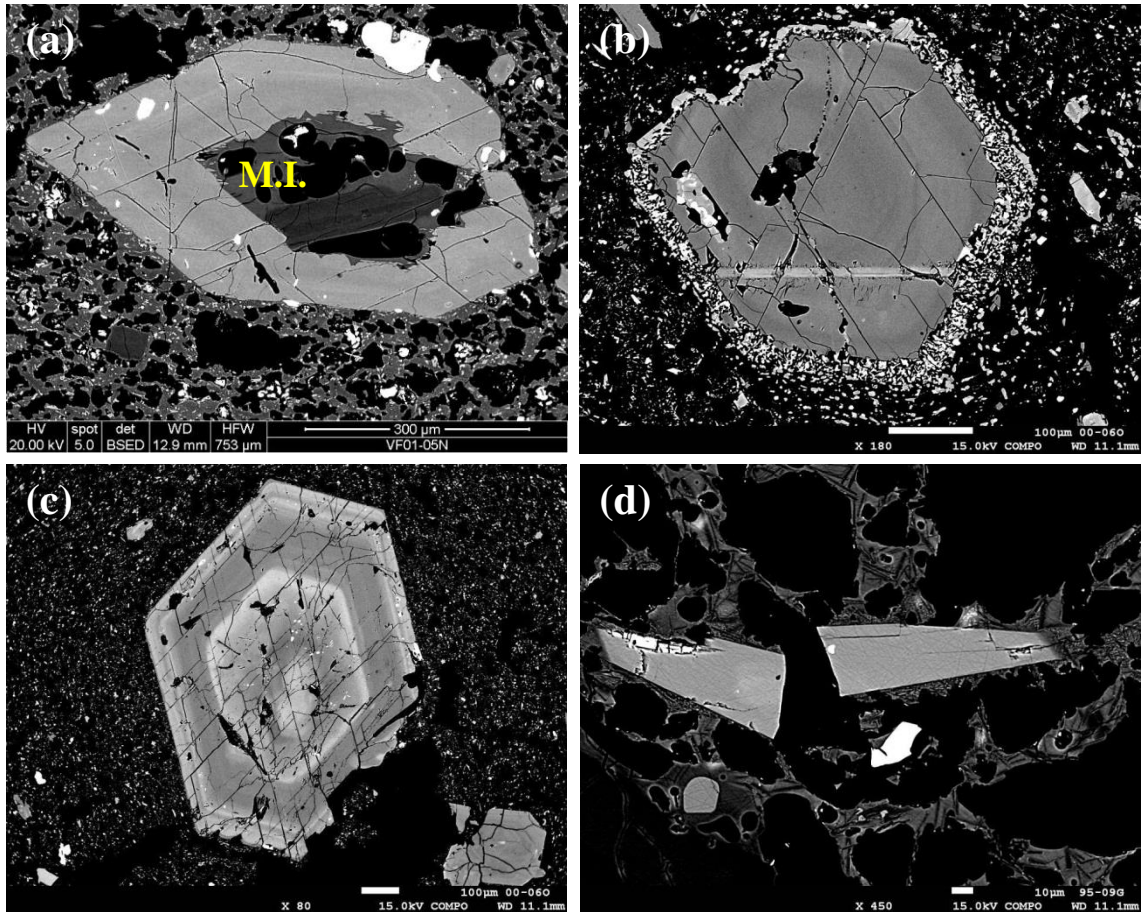


Figure 3.9 Backscatter SEM images of hornblende from Group II samples.

Images are from phenocrysts and microphenocrysts from samples VF01-05N and VF00-06O from unit D: (a) is a phenocryst with a large, vesiculated melt inclusion (M.I.); (b) is a phenocryst displaying a breakdown reaction rim of Fe-Ti oxides, pyroxene and plagioclase; (c) is a zoned hornblende with an embayed and partially broken rim; and (d) is an image of microphenocrysts from sample VF95-09G from unit N. All the phenocrysts contain holes.

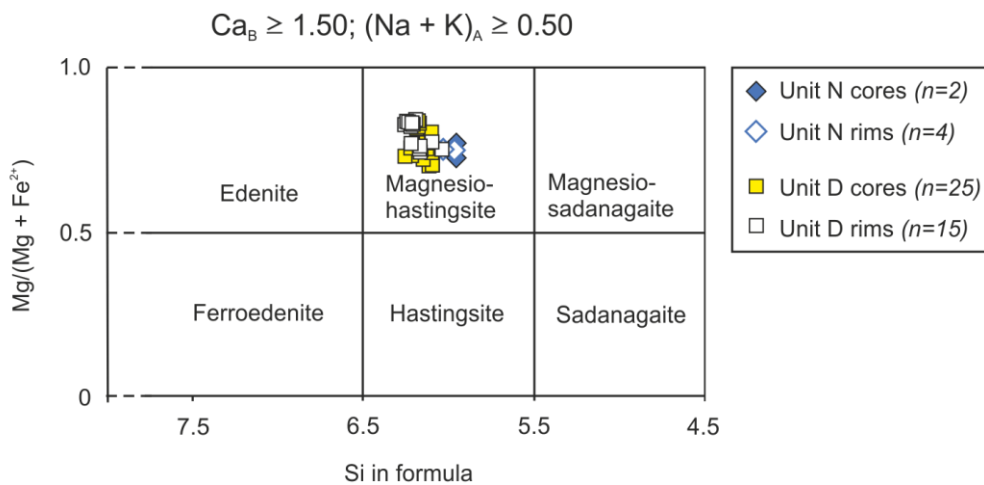


Figure 3.10 Classification of calcic-amphiboles with $(Na+K)_A > 0.5$ after Leake et al. (1997).

Core and rim phenocryst and microphenocryst compositions cluster in the magnesiohastingsite field.

3.2.1.5 Olivine

Olivine is present in all three units varying in abundance from trace to 3 vol.% (Table 3.2), occurring as rounded and embayed phenocrysts up to 1mm across and as microphenocrysts (Figure 3.11a). Olivine is also common in glomerocrysts with clinopyroxene and less commonly, orthopyroxene and phlogopite (Figure 3.11b).

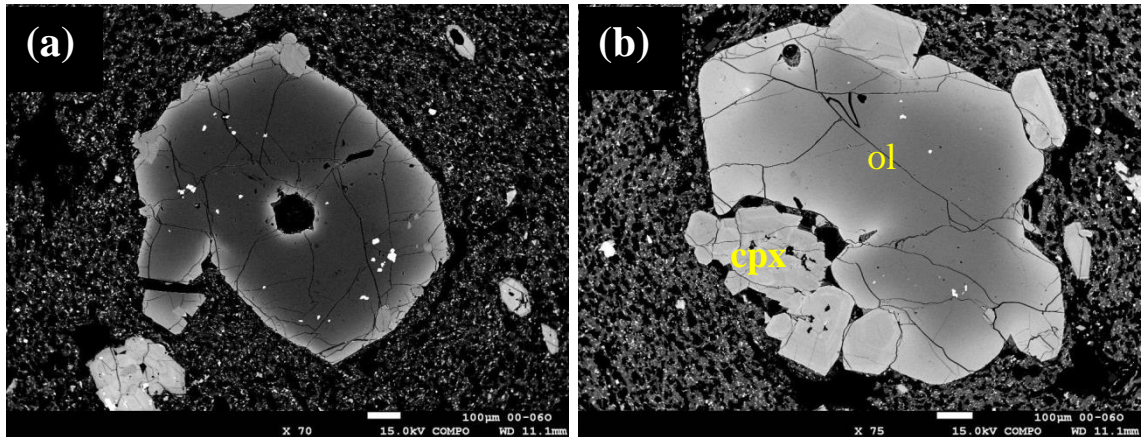


Figure 3.11 Backscatter SEM images of olivine phenocrysts from sample VF00-06O from unit D.

(a) is a rounded phenocryst with a hole in the centre; and (b) is an olivine (ol) and clinopyroxene (cpx) glomerocryst. Both olivines are zoned, with a more Fe-rich rim, as indicated by the light grey colour of these.

Core and rim Mg# of olivine phenocrysts from the Group II eruption deposits are typically more magnesian than olivines from the Group I units, with cores of up to Mg# 0.88 (Figure 3.12). The ranges of core and rim compositions are narrow; for example, unit D cores have Mg# 0.85-0.87 and rims have Mg# 0.79-0.81 (Figure 3.12; Table 3.3).

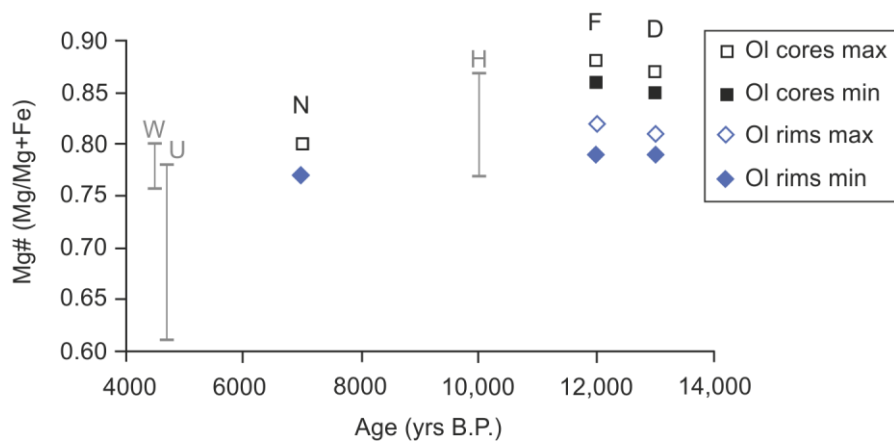


Figure 3.12 Ranges of olivine core and rim Mg# in the Group II eruption deposits.

Also shown are the ranges of olivine Mg# in the Group I deposits. The cores of the Group II olivines in units F and D are highly magnesian with Mg# up to 0.88.

3.2.1.6 *Phlogopite*

One of the distinguishing features between the Group I and Group II eruption deposits is the presence of phlogopite in the Group II tephra samples. Phlogopite varies in abundance from trace (in unit N) to 2 vol.% (in unit F; Table 3.2). Phlogopite occurs as microphenocrysts in units N and D, and phenocrysts up to 1mm in length in unit F. Phenocrysts are distinctive in thin section with a fibrous, sinuous texture (Figure 3.13), and commonly have a speckled appearance as a result of chloritisation along cleavage planes and crystal edges (Figure 3.13c). Phlogopite also occurs in glomerocrysts together with clinopyroxene, olivine and less commonly orthopyroxene (Figure 3.13d).

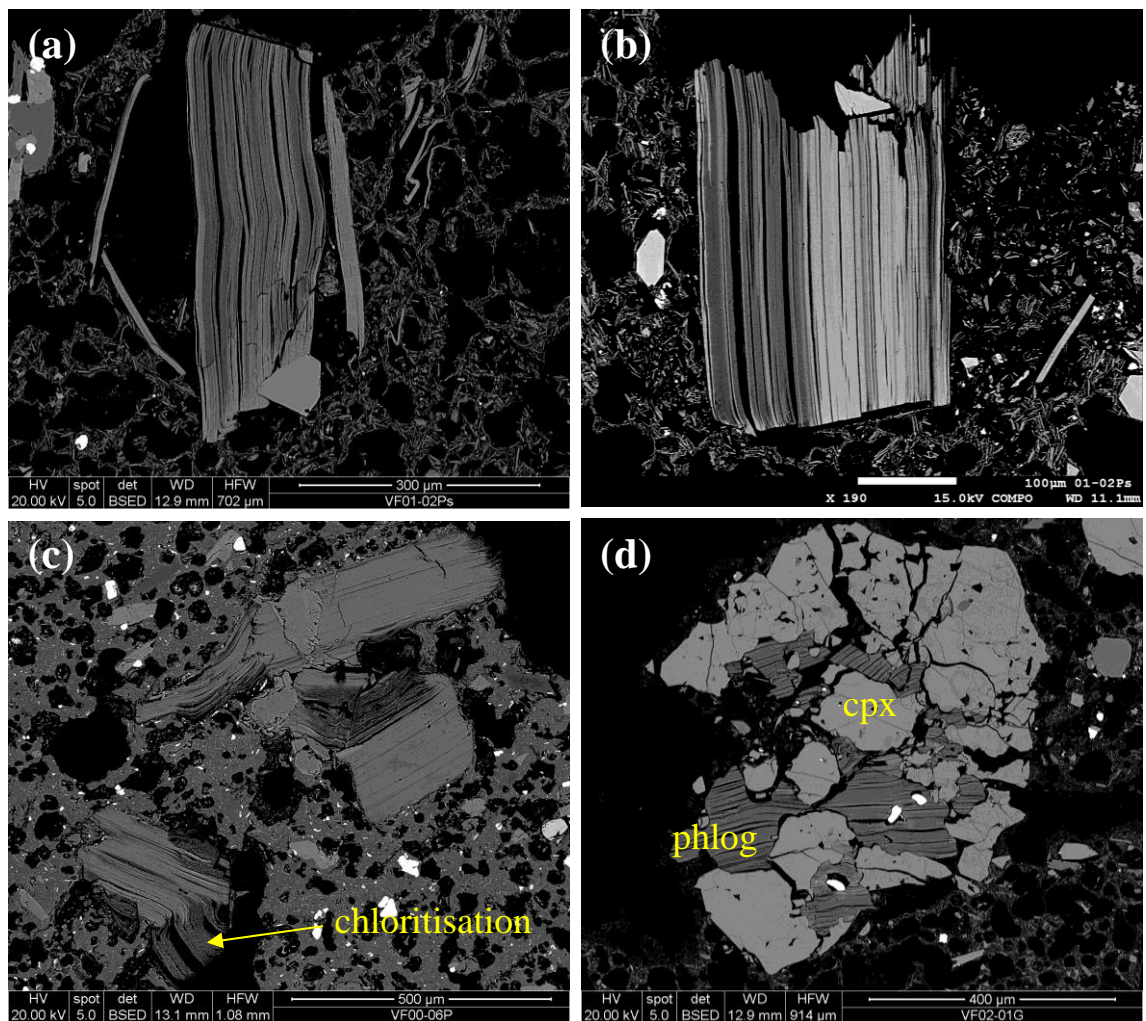


Figure 3.13 Backscatter SEM images of fibrous phlogopite from the Group II samples.

Phlogopite phenocrysts (a and b) from sample VF01-02Ps from unit F; (c) fibrous phlogopite displaying dark grey, speckled patches at the crystal edges and along the cleavage planes reflecting chloritisation from sample VF00-06P (unit F), and; (d) glomerocryst of phlogopite (phlog) and clinopyroxene (cpx) from sample VF02-01G (unit F).

3.2.1.7 Fe-Ti oxides

Fe-Ti oxides including titanomagnetite and ilmenite are common in the groundmass in all the Group II eruption deposits, with abundances varying from ~1 to 3 vol.% (Table 3.2). Unit D contains the highest abundance of Fe-Ti oxides. Fe-Ti oxides are also common in glomerocrysts and inclusions in olivine and clinopyroxene. Rare breakdown rims of hornblende phenocrysts in unit D also contain Fe-Ti oxides.

3.2.1.8 Accessory Minerals

The only accessory mineral observed in the Group II tephra is apatite, which occurs as inclusions in hornblende phenocrysts and as microphenocrysts in the groundmass. Luhr and Carmichael (1982) reported spinel inclusions in olivine and in the groundmass of scoria samples, however, no spinel was observed during this study.

3.2.1.9 Groundmass

The groundmass typically comprises mafic to felsic glass with 49.5 to 66.9 wt.% SiO₂ (Table 3.3) and commonly has a streaky appearance in units N and D. Units N and D show the widest range of glass SiO₂ contents within the Group II deposits, with variations of up to 15 wt.% (Figure 3.14). By contrast, the groundmass glass of unit F scoria shows very little variation in SiO₂ content (Figure 3.14) and does not have a streaky appearance. These variations in glass chemistry are also reflected in other elements such as TiO₂ and MgO.

The groundmass is typically highly vesiculated and contains abundant microlite crystal phases dominated by plagioclase and clinopyroxene. These textures are discussed in Section 3.2.2.7.

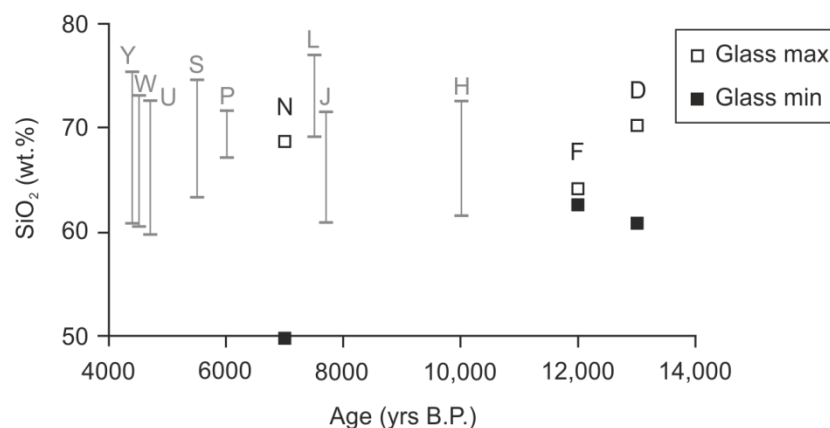


Figure 3.14 Ranges of glass SiO₂ content of the Group II scoria samples.

The ranges of the Group I glass compositions are also plotted in grey.

3.2.2 Petrological Textures and Mineral Zoning

The observed variations in composition of the main mineral phases in the Group II eruption deposits reflect complex mineral textures and zoning patterns. As discussed in Section 2.2.2., in relation to the Group I eruption deposits, zonation in minerals reflect variations in conditions within the magmatic plumbing system (i.e. pressure, temperature, H₂O content, fO_2 , and melt composition). The observed zoning patterns and compositional variations can therefore be used as a tool to investigate the crystallisation history of the magma.

3.2.2.1 Zoning in Plagioclase

As discussed in Section 2.2.2.1., the Group I plagioclase phenocrysts display complicated zoning patterns and textures that resulted from complex crystallisation histories involving decompression in water-undersaturated conditions, thermal convection within the magma storage region, changes in water content, and magma mixing. The plagioclase phenocrysts in the Group II eruption deposits display equally complex textures and zoning patterns, some of which have similar origins to those of the Group I deposits. The plagioclase phenocrysts from Group II have been divided into seven types. All seven types have been observed in unit D, while units N and F contain only types I to V.

Type I plagioclase crystals are anhedral, with irregular rims, and display sieve textures and patchy zonation (Figure 3.15a and b). The phenocrysts have undergone pervasive resorption leaving a porous sieve texture which was infilled by the melt. Recrystallisation of a more anorthitic, lighter grey, plagioclase gives the phenocrysts a patchy appearance. The cross-cutting relationship of the more anorthitic plagioclase reveals this grew later, infilling the pervasively resorbed more sodic, darker grey, plagioclase (Figure 3.15b).

Type II plagioclase phenocrysts have a dark grey, sodic core, which is surrounded by sieve textured plagioclase with patchy zonation (Figure 3.15c). The sieve textured and patchy outer growth zone is equivalent to type I plagioclase. The core of type II has the same composition as the dark patches in the sieve zone, and the original composition of type I; therefore these phenocrysts are interpreted to be equivalent to type I but with less pervasive resorption.

Plagioclase phenocrysts of type III have a sieve-textured and patchy core surrounded by normally-zoned plagioclase to the rim (Figure 3.15d). The core of these may well be equivalent to type I, which have continued to crystallise in the evolving magma.

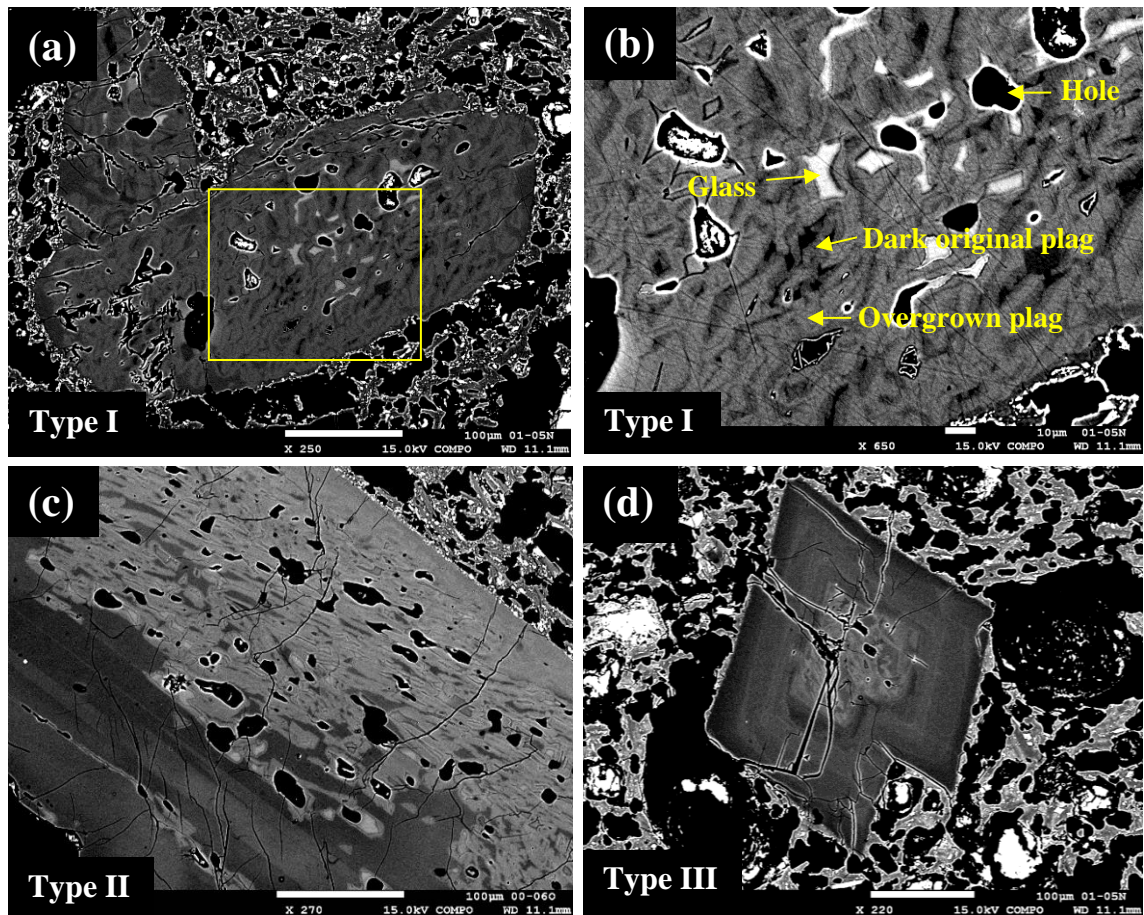


Figure 3.15 Backscatter SEM images of types I to III plagioclase phenocrysts observed in the Group II eruption deposits.

Type I (a) displays pervasive resorption and recrystallisation. Image (b) is a zoomed in image of (a), as shown by the yellow box; the black patches are holes, the very light grey patches are glass inclusions, the dark grey is the original sodic plagioclase which is infilled by the cross-cutting lighter grey, more calcic plagioclase. Type II plagioclase (c) is very similar to type I but with less pervasive resorption. Type III (d) has a strongly resorbed and recrystallised core, surrounded by normally zoned plagioclase to the rim. Images (a), (b) and (d) are from sample VF01-05N and image (c) is from VF00-06O from unit D.

Complex zoning patterns are displayed by type IV plagioclase (Figure 3.16a). These phenocrysts have a partially resorbed and recrystallised core, displaying a slightly patchy appearance and rounded, irregular edges. The dissolution surface, as indicated by the rounded core, is accompanied by a step decrease in anorthite content (from An_{54} to An_{40}) to a growth zone which displays sieve texture and patchy zonation (Figure 3.16a). The boundary of this layer is also rounded, and the dissolution surface is also accompanied by a step increase in anorthite content (from An_{40} to An_{54}). The changes in anorthite content are coincident with changes in Fe. The phenocrysts then display oscillatory zoning to the rim.

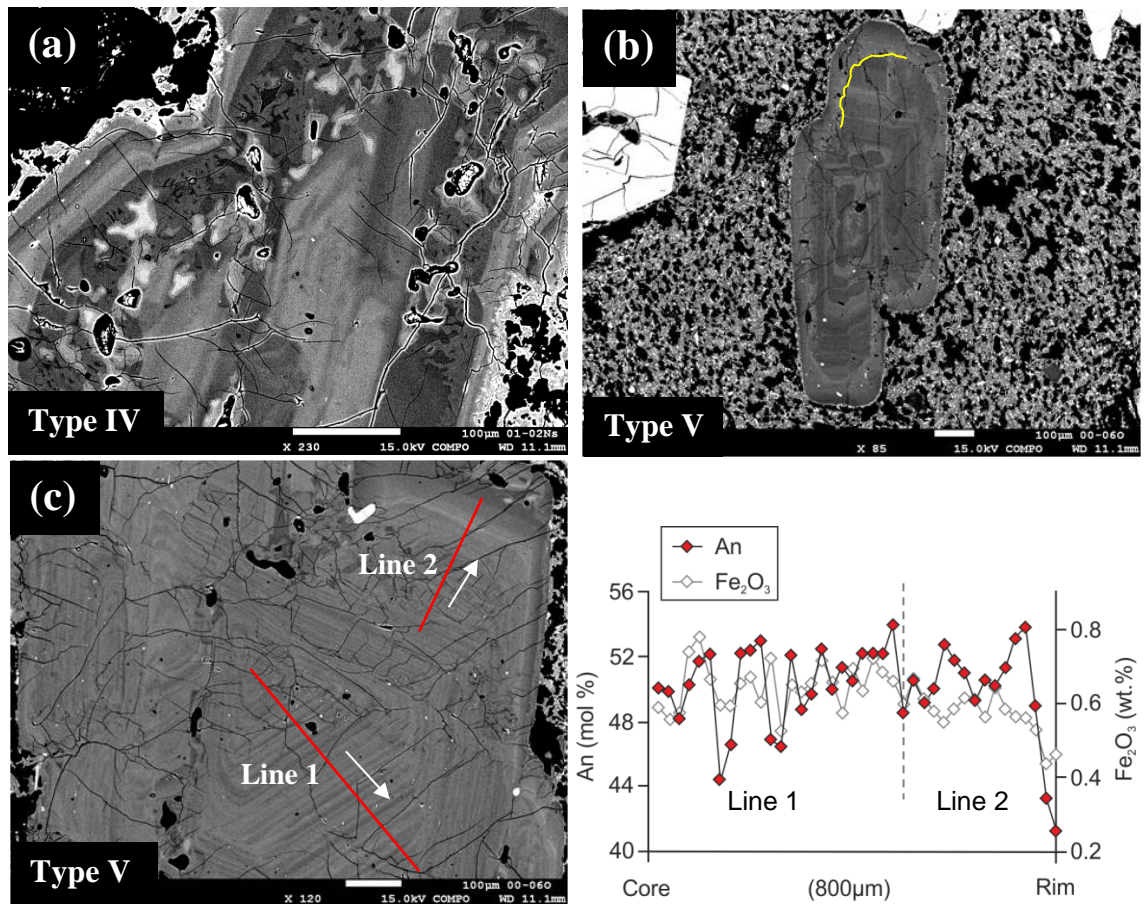


Figure 3.16 Backscatter SEM images of types IV and V plagioclase from sample VF01-02Ns and VF00-060 from unit D.

Type IV (a) displays complex zoning with a partially resorbed anorthitic core which is surrounded by a strongly resorbed and partially recrystallised growth zone, and an oscillatory zoned rim. Type V plagioclase (b and c) is oscillatory zoned with multiple low amplitude oscillations, and large-scale resorption surfaces (highlighted in yellow). Also shown is a core-rim EPMA profile of (c) along the red lines. The dashed line on the EPMA profile shows the join between the two red lines. All Fe analyses in plagioclase were recorded as Fe₂O₃.

Type V, oscillatory zoned, plagioclase phenocrysts are common in all three units (Figure 3.16b and c). Oscillations vary from low amplitude oscillations (LAO) to saw-tooth patterns with multiple resorption surfaces (STR; Ginibre et al., 2002a; see Section 2.2.2.1). Some of the oscillations are accompanied by large-scale resorption surfaces which cross-cut multiple growth zones (Figure 3.16b; yellow line). Fluctuations in anorthite content vary from <5 mol% to ~10 mol%, and commonly coincide with fluctuations in Fe (Figure 3.16). Oscillatory zoned phenocrysts with a sodic rim are observed in unit D (Figure 3.17a; Type VI).

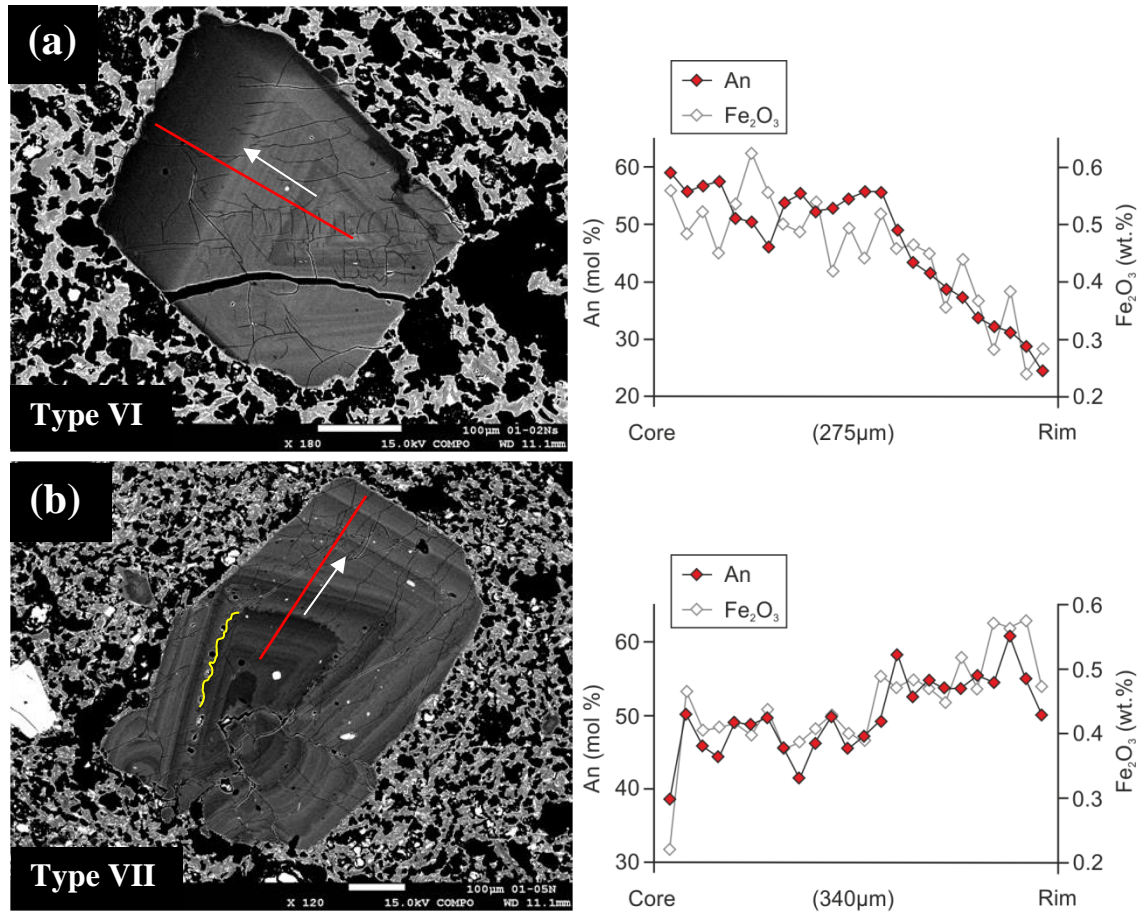


Figure 3.17 Backscatter SEM image and core-rim EPMA analyses for type VI and VII plagioclase from the Group II eruption deposits.

Images are from samples VF01-02Ns and VF01-05N from unit D of. Type VI (a) phenocrysts display oscillatory zoning similar to type V, but with a low anorthite rim of An₂₄. Type VII (b) plagioclase displays reverse oscillatory zoning to the rim, with resorbed, dissolution surface (yellow line) coincident with changes in An and Fe.

The final type, type VII, is oscillatory zoned, but displays overall reverse zoning with a more sodic core and anorthitic rim (Figure 3.17b). Again the oscillations vary from LAO to STR, commonly displaying large-scale dissolution surfaces with step increases and decreases in anorthite content (of up to 12 mol%), coincident with increases and decreases in Fe.

3.2.2.2 Interpretation of Plagioclase Zoning Patterns

The zoning patterns and textures observed in the plagioclase phenocrysts reveal a complex crystallisation history involving multiple phases of crystallisation and destabilisation during growth. Disequilibrium and recrystallisation of more or less calcic plagioclase can result from a number of factors including magma mixing, depressurisation in water-undersaturated conditions, and temperature and water content fluctuations within the magmatic plumbing system (see Section 2.2.2.2; Nelson and Montana, 1992; Blundy and Cashman, 2001; Ginibre et al., 2002a; Ginibre et al., 2002b; Annen et al., 2006; Ginibre and Wörner, 2007; Streck, 2008).

The descriptions and interpretations of the zoning patterns displayed by the seven types of plagioclase are summarised in Figure 3.18.

The type I (and II) phenocrysts are equivalent to the Group I type I phenocrysts which are interpreted as resulting from decompression in water-undersaturated conditions which caused destabilisation, followed by precipitation of more calcic plagioclase see Section 2.2.2.2 (Nelson and Montana, 1992; Ginibre and Wörner, 2007). The normal zoning overgrowth displayed by type III is a later phase of crystallisation related to differentiation of the magma at a shallower level in the system.




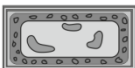

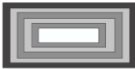

Phenocryst	Type	Description	Interpretation
	I	Patchy zonation and sieve texture - pervasive resorption and recrystallisation	Depressurisation in water-undersaturated conditions
	II	Patchy zonation and sieve texture - pervasive resorption and recrystallisation; sodic core	Depressurisation in water-undersaturated conditions, but less pervasive resorption
	III	Core with patchy zonation and sieve texture surrounded by normally zoned plagioclase	Depressurisation followed by crystallisation in continually evolving magma at shallower level
	IV	Partially resorbed and recrystallised core surrounded by pervasive resorbed growth zone, surrounded by oscillatory zoning	Multiple phases magma mixing; decompression and small-scale oscillations thermal convection
	V	Oscillatory zoned plagioclase	Small-scale oscillations from thermal convection; Large-scale oscillations from magma recharge
	VI	Oscillatory zoned plagioclase, with sodic rim	Thermal convection and magma recharge
	VII	Oscillatory zoned, but overall reverse zoning from core-rim; large scale resorption	Thermal convection and magma recharge in progressively mafic magma

Figure 3.18 Schematic diagram of the seven types of plagioclase zoning observed in the Group II eruption deposits, including descriptions and interpretations.

Step increases and decreases in anorthite content across dissolution surfaces coinciding with fluctuations in Fe (and Mg) are typically interpreted as resulting from mixing with either a more evolved or more mafic magma (e.g. Streck, 2008). Some of the large-scale step increases and decreases in anorthite content in the complex and oscillatory-zoned phenocrysts, types IV to VII, coincide with equivalent changes in Fe (Figure 3.16 and 3.17), indicating multiple mixing events during crystal growth.

A possible crystallisation history is given in Figure 3.19. The first plagioclase phenocrysts to crystallise formed in a differentiating magma at depth. Decompression in water-undersaturated conditions led to destabilisation of the original crystal, and precipitation of more calcic

plagioclase (Step 1). Continued crystallisation in an evolving magma led to normally-zoned overgrowths on some of the sieve textured plagioclases (Step 2; Figure 3.19).

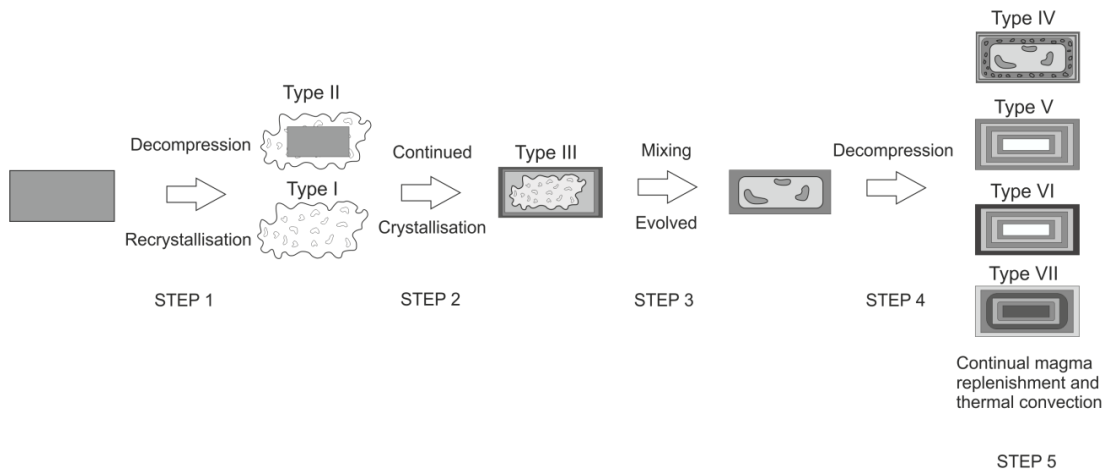


Figure 3.19 Cartoon showing the possible crystallisation history of plagioclase phenocrysts within the Group II magmas involving multiple decompression and magma replenishment and mixing events

Mixing with an evolved magma then resulted in destabilisation followed by crystallisation of more sodic plagioclase (Step 3). Decompression and associated degassing led to pervasive breakdown of the sodic plagioclase, and subsequent crystallisation of more calcic plagioclase (Step 4). Thermal convection and fluctuating water content within a shallower magma storage region, along with continual pulses of magma replenishment, resulted in the formation of oscillatory-zoned plagioclase (Step 5; Figure 3.19).

Plagioclase phenocrysts of types I to V occur in both Group I and Group II tephra samples. These phenocrysts are therefore interpreted as evolving within the same magmatic plumbing system. A test for this would be to analyse the trace elements within the phenocrysts and to microsample phenocrysts for Sr isotope analyses (i.e Davidson et al., 2007).

3.2.2.3 Zoning in Clinopyroxene

Clinopyroxene phenocrysts from Group II scoria display complex zoning patterns and textures supporting the evidence of disequilibrium and recrystallisation during growth as recorded by the plagioclase phenocrysts. The clinopyroxene phenocrysts in the Group II eruption deposits display more complex zoning patterns when compared with the Group I clinopyroxenes. Five general clinopyroxene types have been characterised in the Group II deposits; however, not all deposits contain all five types. Units N and F contain types I, II and V, while types I to IV are observed in unit D.

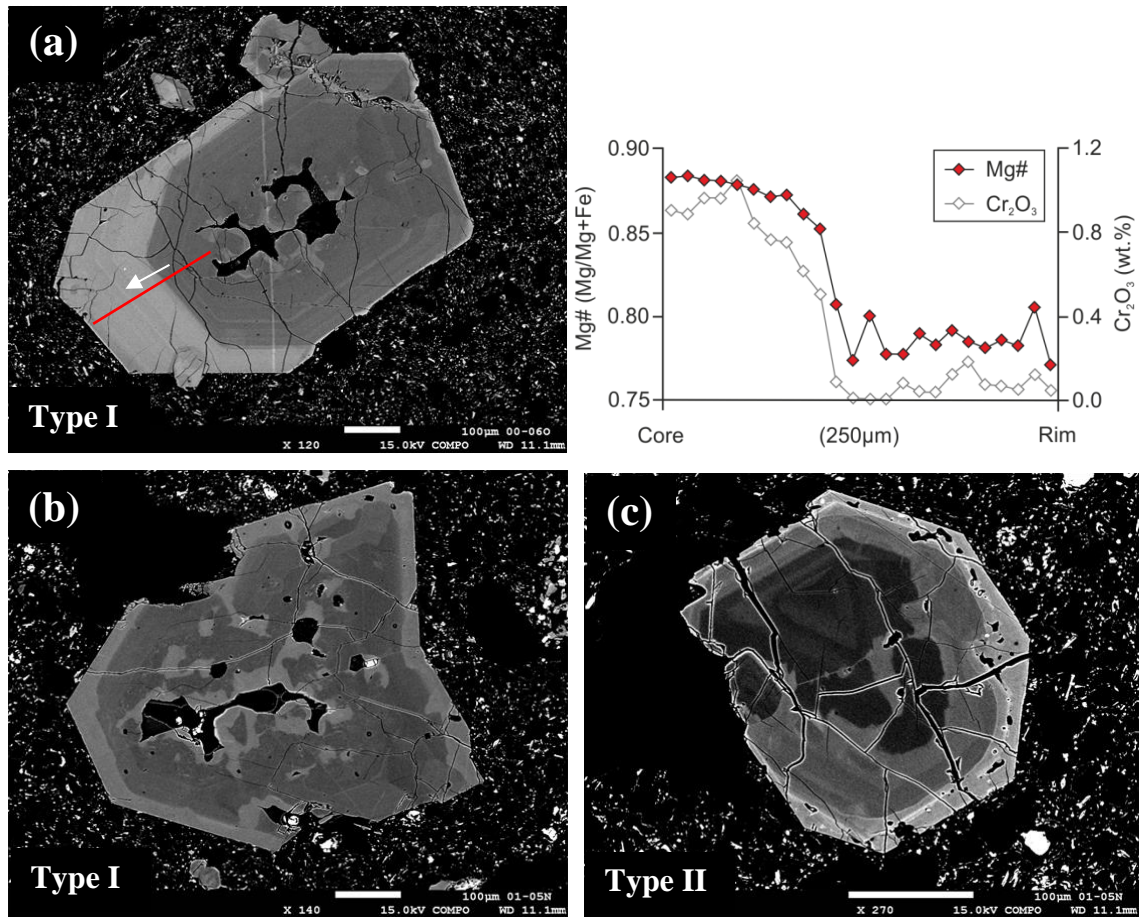


Figure 3.20 BSE images for types I and II clinopyroxene from the Group II eruption deposits.

Type I are shown in (a) and (b) and type II is shown by image (c) from sample VF00-06O and VF01-05N from unit D of the Group II eruption deposits. Also shown is a core-rim profile along the red line (a). The sharp colour change on the SEM image is reflected in the mineral chemistry with a step decrease in Mg# and Cr.

Type I clinopyroxenes have a high-Mg core (Mg# 0.88-0.90) that is resorbed and recrystallised (Figure 3.20a and b). The recrystallised clinopyroxene has the same Mg# as the rim (0.80-0.82). Type II phenocrysts are the same as type I but with a sharp step decrease in Mg# at the rim to 0.76 (Figure 3.20c). Types I and II are present as phenocrysts in unit D, but only in glomerocrysts in units N and F.

Type III clinopyroxene phenocrysts have a low-Mg core (Mg# 0.73-0.74) which is resorbed and recrystallised (Figure 3.21a). Surrounding this is a high-Mg zone (Mg# 0.85), overgrown by less magnesian clinopyroxene to the rim (Mg# 0.81). All zones display resorption textures with rounded crystal edges and corners. This type of zoning is only present in unit D.

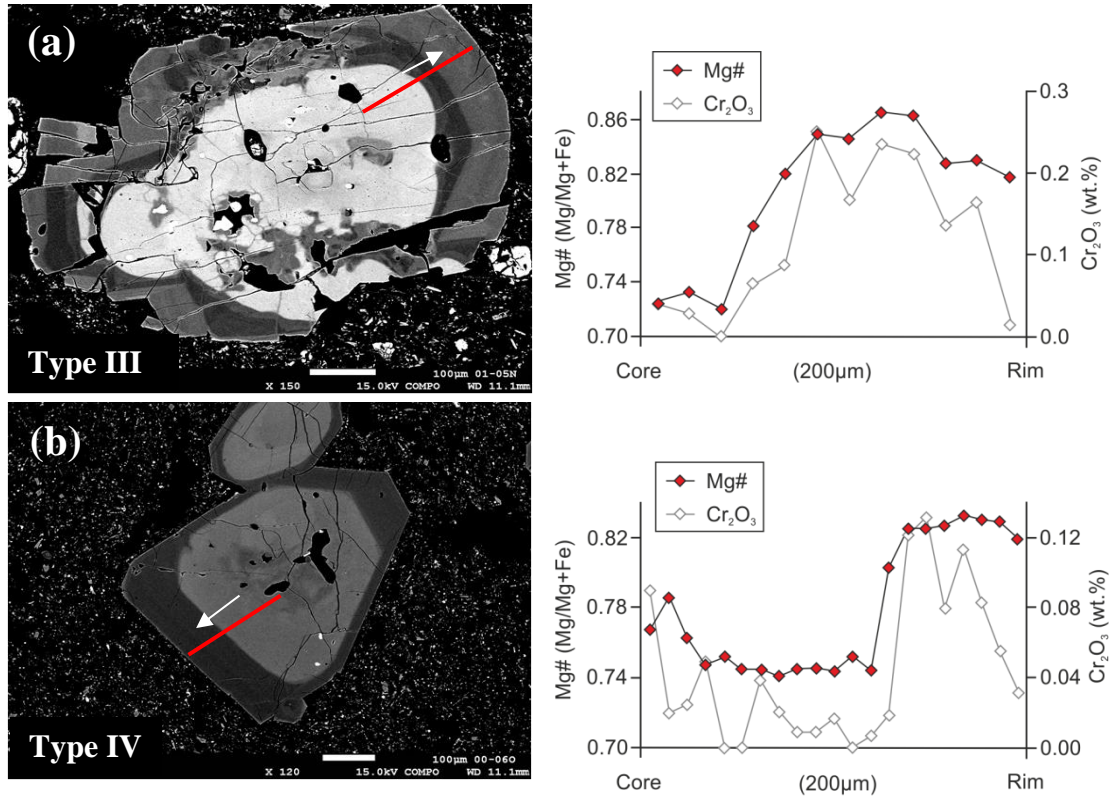


Figure 3.21 BSE images and EPMA core-rim analyses of types III and IV clinopyroxene from Group II.

(a) Type III and (b) type IV clinopyroxene phenocrysts from scoria from samples VF01-05N and VF00-06O from unit D. Both types display a low-Mg core surrounded by high-Mg clinopyroxene growth. Type III is then overgrown by a lower Mg rim.

Type IV clinopyroxenes have a normally zoned core varying from Mg# 0.80 in the centre to Mg# 0.75 at the edge (Figure 3.21b). The core displays dissolution and is surrounded by high-Mg growth to the rim (Mg# 0.84). The core-rim boundary is a sharp dissolution surface with a step increase in Mg# and corresponding increase in Cr (Figure 3.21b).

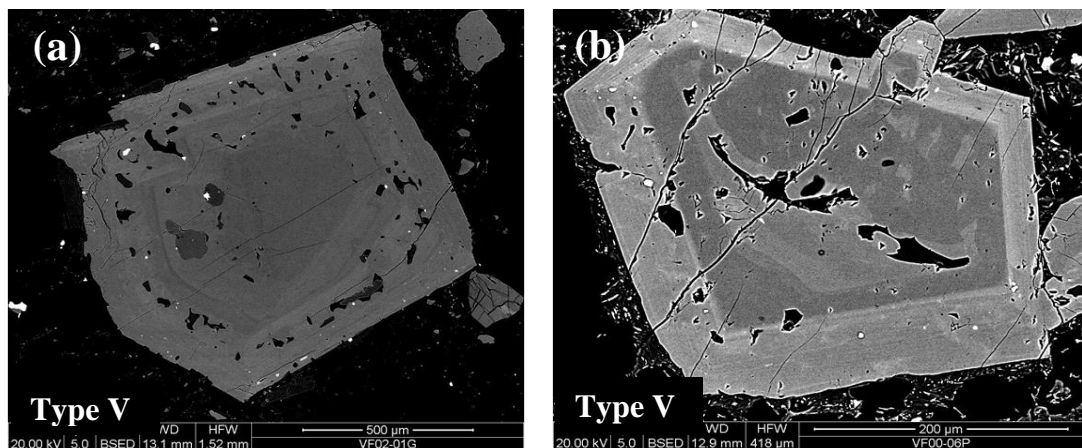


Figure 3.22 Backscatter SEM images of type V clinopyroxene phenocrysts from Group II.

Images are from units N (VF02-01G) and F (VF00-06P). Type V clinopyroxene displays strong sieve textures indicating pervasive resorption surrounded by oscillatory zoned rims. Interpretations of these textures are in the text.

Type V phenocrysts have a core of Mg# 0.82-0.85 that has a patchy appearance as a result of resorption and recrystallisation (Figure 3.22). Surrounding this is a lower-Mg growth zone which displays strong disequilibrium with a sieve texture (Figure 3.22a). Clinopyroxene growth is then oscillatory to the rim. This type of zoning is present in units N and F.

3.2.2.4 Interpretation of Clinopyroxene Zoning Patterns

The zoning patterns and textures observed in the clinopyroxene phenocrysts reveal multiple phases of magma mixing and decompression. The majority of clinopyroxene cores and growth zones display strong or partial resorption, such as sieve textures, rounded edges and dissolution surfaces cross-cutting multiple growth zones. Large step increases and decreases in Mg# associated with dissolution surfaces are coincident with equivalent changes in Cr, and opposite changes in Mn and Ti, indicating these events are the result of mixing with a more mafic or evolved magma (see Section 2.2.2.4; Streck, 2008). All five types of clinopyroxene phenocrysts reveal at least one magma mixing event (Figure 3.23).


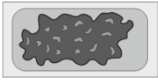


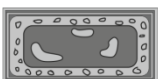
Phenocryst	Type	Description	Interpretation
	I	High-Mg core showing strong resorption and recrystallisation, surrounded by low-Mg growth to rim	Crystallisation in primitive melt, followed by decompression and mixing with a more evolved melt
	II	High-Mg core showing strong resorption and recrystallisation, surrounded by low-Mg growth zone, overgrown by lower Mg to rim	Crystallisation in primitive melt, followed by decompression and multiple mixing events with more evolved melt
	III	Low-Mg core showing partial resorption and recrystallisation, growth zones with step increases and decreases in Mg#	Multiple mixing events; mafic magma recharge followed by mixing with more evolved melt
	IV	Normally zoned core with high-Mg rim	Crystallisation in continually evolving magma; mafic magma recharge
	V	High-Mg core, resorbed and recrystallised, surrounded by low-Mg strong sieve textured zone and oscillatory zoning to rim	Crystallisation in mafic magma; mixing with evolved magma and thermal convection causing oscillatory zoned rim

Figure 3.23 Schematic diagram showing the five types of clinopyroxene phenocrysts observed in the Group II eruption deposits with descriptions and interpretations.

A possible crystallisation history for the clinopyroxene phenocrysts is given in Figure 3.24. The high-Mg cores of type I and II phenocrysts indicate they crystallised from a primitive mafic magma. Decompression and mixing with a more evolved magma, probably in a shallower level chamber, led to resorption and recrystallisation of a less magnesian clinopyroxene (Figure 3.24).

Further mixing with a more evolved magma led to a low-Mg overgrowth (Mg# 0.76; Type II). The cores of type III clinopyroxene have Mg# equivalent of the outer growth zone of the type II and the outer core of type IV phenocrysts, therefore these are likely to have crystallised from the same melt. Mafic magma replenishment then caused destabilisation resulting in partial resorption and rounded crystal edges, and crystallisation of more magnesian clinopyroxene (Mg# 0.85).

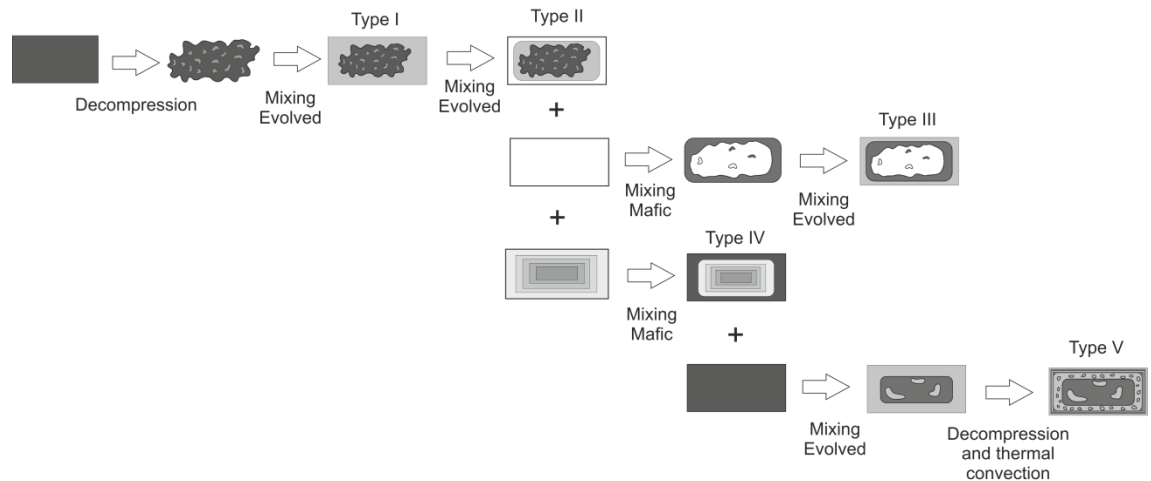


Figure 3.24 Cartoon showing the possible complex crystallisation history of clinopyroxene phenocrysts within the Group II magmas involving multiple magma replenishment and mixing events.

Type V clinopyroxene phenocrysts have cores of Mg# 0.82-0.85, and therefore are interpreted as forming in the same melt as the type III growth zone, and type IV rim (Figure 3.24). Another mixing event, this time with a more evolved magma, caused further destabilisation and crystallisation of less magnesian clinopyroxene (with an associated step decrease in Cr). This low-Mg zone in type V clinopyroxene displays strong resorption and recrystallisation, and the rim displays oscillatory zoning. Variations in Mg# in the oscillatory zoned rims are not reflected in Cr, Mn or Ti, and therefore are not related to magma mixing. These crystals are therefore interpreted to have undergone decompression followed by crystallisation in a shallow level storage region where thermal convection has resulted in oscillatory zoned rims.

3.2.2.5 Hornblende Zoning and Textures

Two populations of hornblende phenocrysts are observed in samples from unit D; those with reaction rims (type I); and those with sharp, unaltered rims (Type II; Figure 3.25). Where present in units N and F, hornblende occurs as broken microphenocrysts.

Type I phenocrysts with reaction rims of pyroxene, plagioclase and Fe-Ti oxides are rare, with rims varying in thickness from 40 μ m to almost entirely replacing the hornblende crystal (Figure

3.25a and b). The majority of the phenocrysts display unaltered rims; however, the rims are embayed and typically have rounded corners (Figure 3.25c and d).

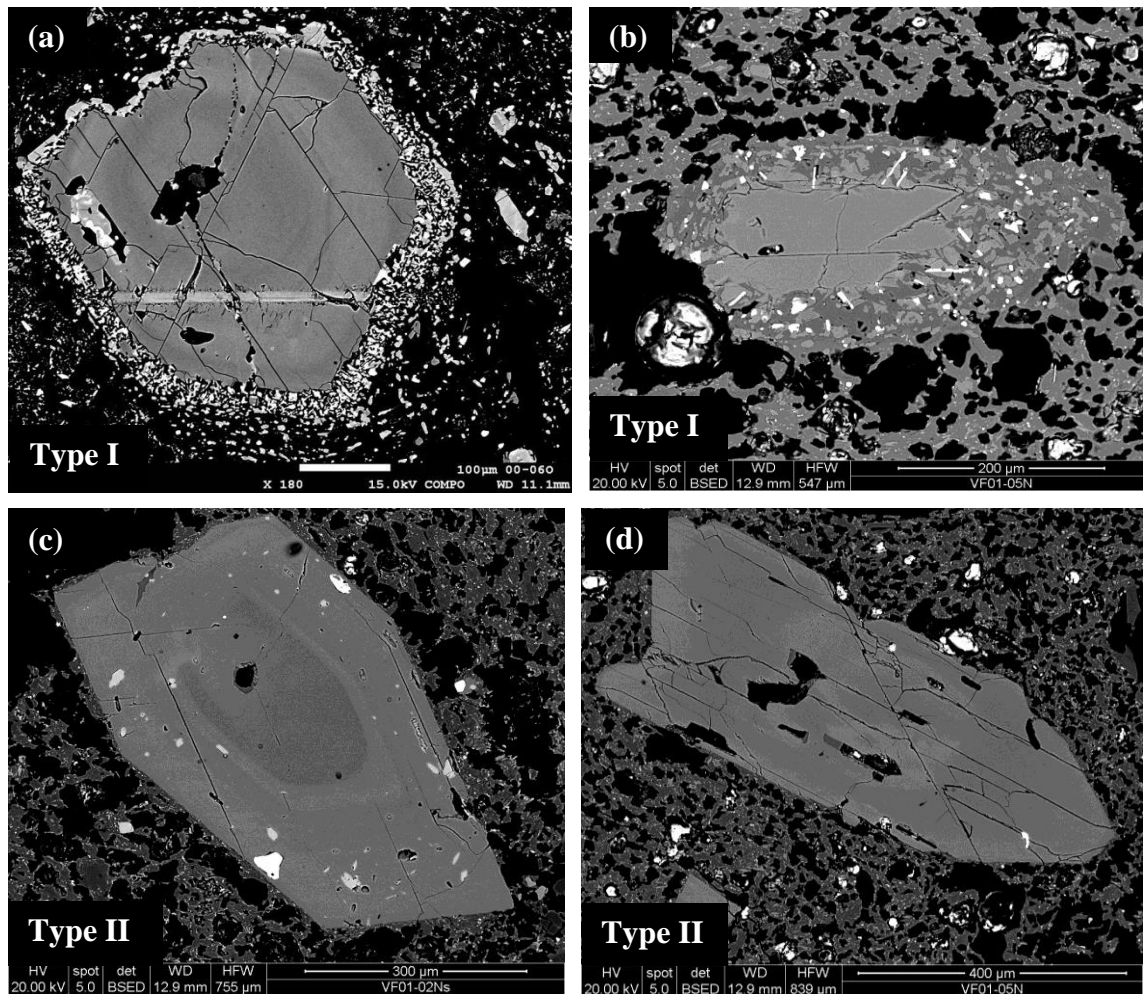


Figure 3.25 Backscatter SEM images of the two types of hornblende phenocrysts from Group II

Images are from samples VF00-06O, VF01-05N and VF01-02Ns from unit D. Type I phenocrysts display reaction rims of Fe-Ti oxides, pyroxene and plagioclase varying from ~40µm thick (a) to almost entirely replaced (b). Type II phenocrysts display unaltered rims (c); however, embayed rims and holes in the centre of crystals are common (d).

Both types of hornblende phenocryst display sieve-like textures with holes in the centre (Figure 3.25). As discussed in Section 2.2.2.7, these dissolution textures are likely to have resulted from increased temperature or compositional changes as a result of magma recharge (Streck, 2008).

Type I phenocrysts display weak zoning from core to rim, varying in Mg# from 0.74 to 0.75 (Figure 3.26a). Type II hornblende phenocrysts are less magnesian and typically display oscillatory zoning, with overall reverse zoning from core (Mg# 0.64) to rim (Mg# 0.68; Figure 3.26b).

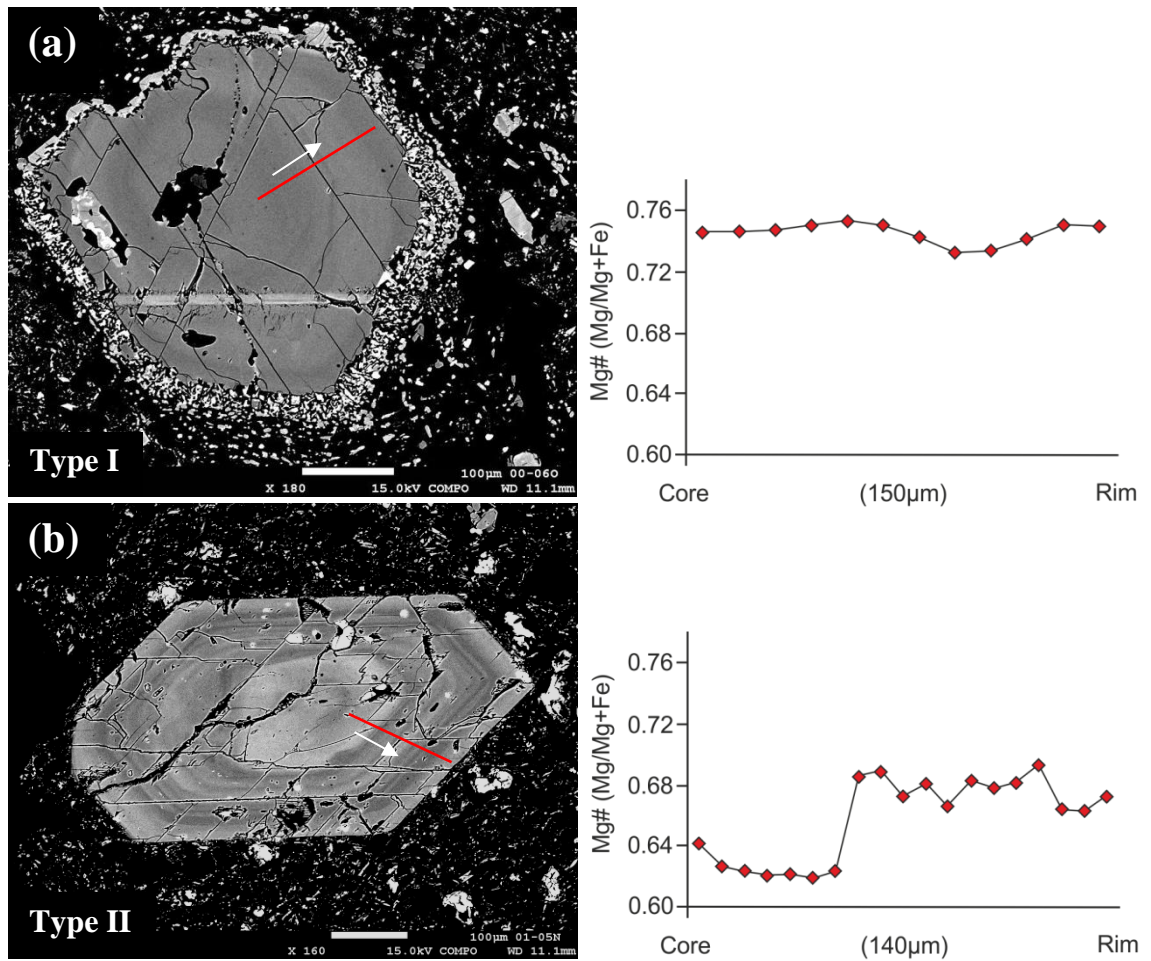


Figure 3.26 Core-rim variation in Mg# for type I and II hornblende phenocrysts from Group II.

Images are from samples VF00-06O and VF01-05N from unit D. Typically, type I hornblendes show little core-rim compositional variation (a), while type II display oscillatory zoning but with overall reverse zoning with low-Mg cores (b).

3.2.2.6 Interpretation of Hornblende Zoning Patterns

The presence of reaction rims on hornblende phenocrysts is typically interpreted as resulting from slow ascent rates or long residence times in the magma chamber (Rutherford and Devine, 2003; Browne and Gardner, 2006; Rutherford, 2008). The presence of hornblende phenocrysts with unaltered rims therefore suggests fast ascent rates and short residence times in a shallow level storage region. Samples from unit D have both stable and unstable phenocrysts indicating a late-stage magma mixing event (see Section 2.2.2.7; Rutherford, 2008). This is supported by the large-scale dissolution sieve textures. A magma body ascending rapidly would inhibit hornblende breakdown, and interception with the shallow-level storage region, could then trigger an explosive eruption (i.e. Sparks and Sigurdsson, 1977). The resulting tephra would then contain both types of hornblende phenocrysts.

The low-Mg cores of the type II hornblende phenocrysts indicate these crystallised in a more evolved melt, after the olivine and clinopyroxene phases. Oscillatory zoning and overall reversed zoning indicates pulses of magma mixing, as observed in the clinopyroxene and plagioclase phenocrysts. Type I phenocrysts show very little core-rim compositional variation and are more magnesian than type II, indicating they crystallised in a more mafic magma.

3.2.2.7 Groundmass Textures

The groundmass glass of scoria from the Group II eruption deposits is highly vesiculated with small spherical bubbles (Figure 3.27a) indicating rapid ascent rates from the storage region to the surface (Szramek et al., 2006; Savov et al., 2008). The glass, however, is less vesiculated than the scoria and pumice samples of the Group I eruption deposits.

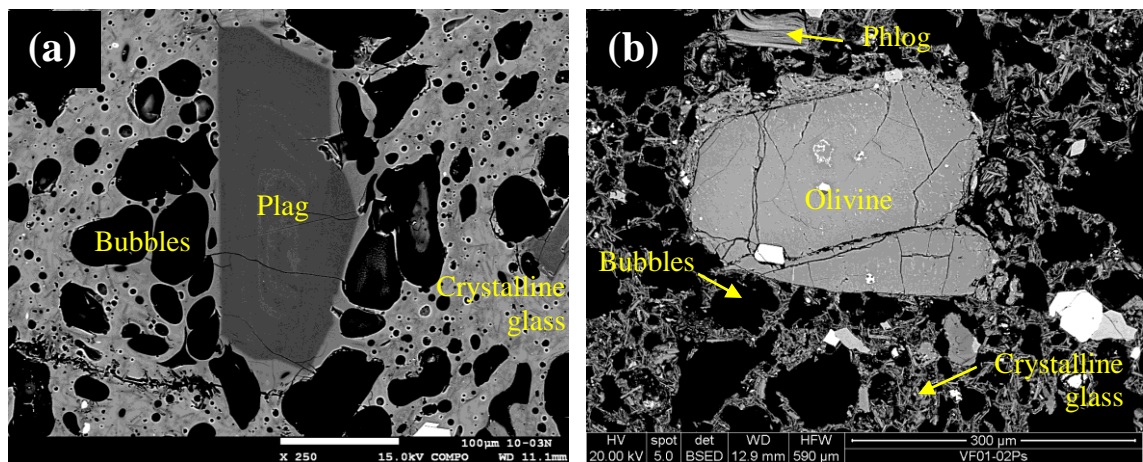


Figure 3.27 BSE images of the groundmass glass from Group II scoria.

Images are from sample VF10-03N from unit N (a) and sample VF01-02Ps from unit F (b) Group II deposits. Image (a) shows the highly vesiculated nature of the scoria, with abundant small spherical bubbles (black holes). Image (b) shows the highly crystalline glass with abundance microlite phases. Abbreviations are: Plag = plagioclase; Phlog = phlogopite.

The presence of abundant microlites in the glass (Figure 3.27) indicates late-stage crystallisation which may be the result of rapid decompression and syn-eruptive devolatilisation of the magma in the conduit (Hammer et al., 1999; Szramek et al., 2006). The groundmass glass of the Group II eruption deposits is highly crystalline relative to the glass of pumice and scoria samples from the Group I deposits.

3.2.2.8 Summary of Mineral Zoning Patterns and Textures

The zoning patterns, textures and chemistry of the main mineral phases present in the Group II eruption deposits reveal a complex crystallisation history involving multiple phases of magma mixing, decompression, thermal convection in a shallow level storage region, and rapid magma

ascent rates from the storage region to the surface. Figure 3.28 relates the observed textures and mineral chemistry in a schematic diagram to a possible crystallisation history for the Group II magmas.

Olivine and clinopyroxene (type I and II) cores have high Mg# (0.88-0.90) corresponding with high Cr₂O₃ (up to 1 wt.%) indicating crystallisation from a primitive mafic magma. Clinopyroxene phenocrysts reveal decompression followed by mixing with more evolved magmas, possibly as a result of intercepting sills at the base of the crust which is consistent with broad aspects of models such as the hot zone model of Annen et al. (2006), which will be explored further in Chapter 5.

Clinopyroxene crystallisation then continues through phases of mafic magma replenishment and mixing with more evolved magmas, before a final decompression phase as the magma rises to a shallow level storage region where thermal convection and pulses of magma recharge result in oscillatory zoning. Plagioclase crystallisation follows a similar path, with a decompression event followed by later magma mixing (Figure 3.28); however, earlier mixing events are not observed in the plagioclase phenocrysts.

Hornblende phenocrysts have cores with low Mg# (0.64-0.74) and therefore are interpreted to have crystallised later than the olivine and clinopyroxene phenocrysts, or in a different batch of magma. Oscillatory and reverse zoning in hornblende phenocrysts also reveal pulses of magma recharge. Hornblende phenocrysts are unstable at pressures of 100 to 10MPa (~4 to 0.4km depth; Browne and Gardner, 2006) therefore the formation of reaction rims is interpreted to result from long residence time in a shallow-level magma storage region. This is consistent with experimental petrology which showed that Colima magmas are stored at depths of 3 to 5 km prior to eruption (Moore and Carmichael, 1998), and geophysical data which reveal a magma storage region at ~5 km depth (Gardine, 2010; López-Loera, 2012).

The presence of hornblende phenocrysts with no reaction rims and the highly vesiculated groundmass textures indicate the magma was un-degassed, therefore ascended rapidly from the storage region to the surface. Samples containing both altered and unaltered hornblende phenocrysts indicate a late-stage mixing event during which rapidly ascending magma intercepted the shallow magma chamber en route to the surface, potentially triggering an explosive eruption (e.g. Sparks and Sigurdsson, 1977; Pallister et al., 1992; Pallister et al., 1996; Kent et al., 2010).

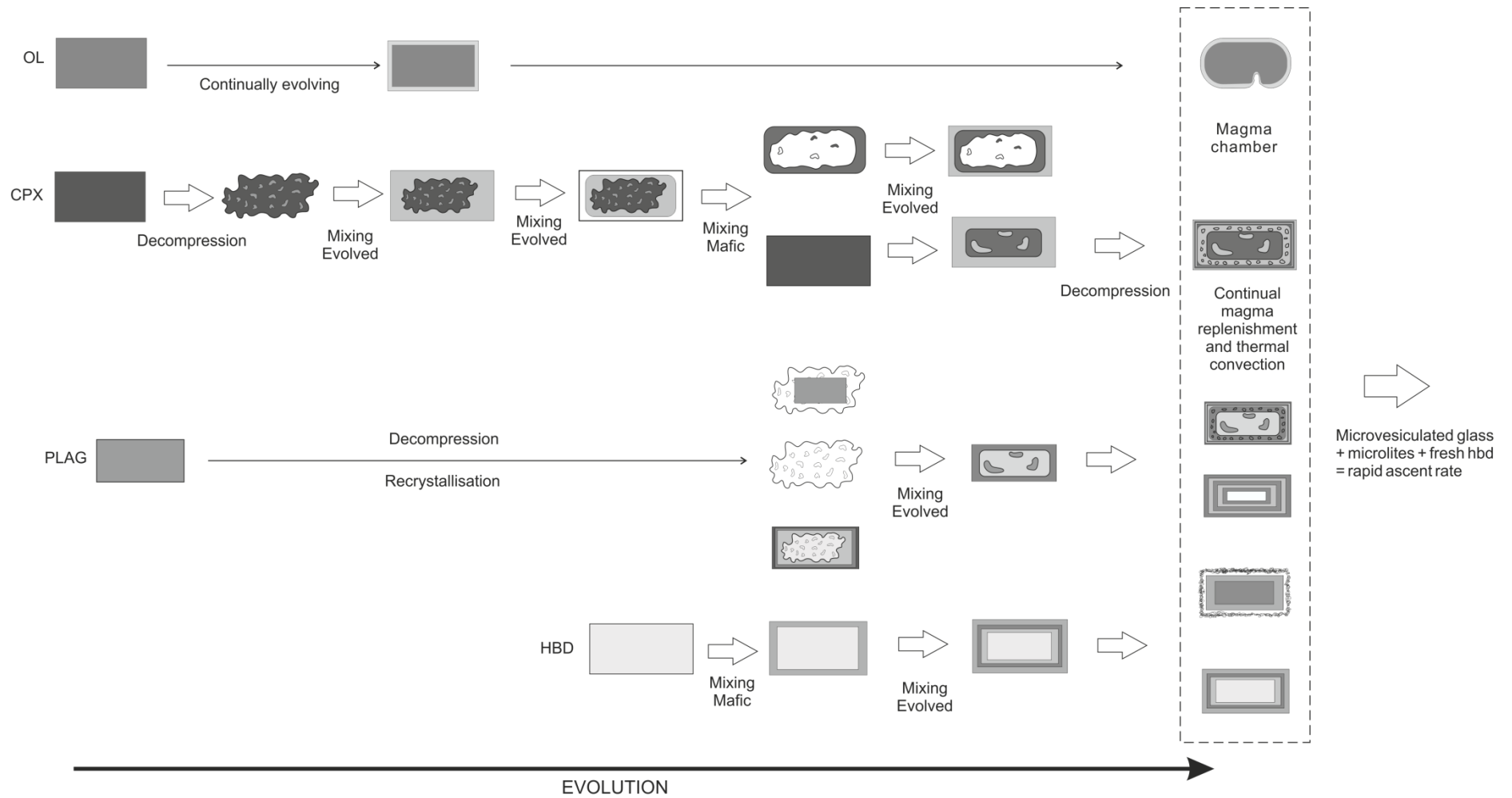


Figure 3.28 Schematic diagram linking olivine (OL), clinopyroxene (CPX), plagioclase (PLAG) and hornblende (HBD) zoning patterns and mineral chemistry

3.3 Geothermometry and Hygrometry

Eruption temperature and water contents for seven samples from the Group II eruption deposits have been estimated using the two-pyroxene thermometers of Wood and Banno (1973) and Wells (1977), the orthopyroxene-melt and clinopyroxene-melt thermometers of Putirka (2008), the hornblende thermometer and hygrometer of Ridolfi et al. (2010), and the plagioclase-melt thermometer and hygrometers of Putirka (2008) and Lange et al. (2009); as described in Section 2.3. The geothermometry and hygrometry results for the Group II magmas are presented in Tables 3.4 and 3.5, respectively.

Of the above mentioned geothermometers, only the clinopyroxene-melt and plagioclase-melt thermometers could be used for all three of the Group II eruption deposits. Orthopyroxene was only observed in trace amounts in some of the samples from units N and D. Hornblende is present as phenocrysts in all unit D samples; however, it is only present in trace amounts as microphenocrysts in units N and F.

The clinopyroxene-melt and plagioclase-melt thermometers require the pressure and water content to be constrained; a pressure of 2kbar (~6 km depth) and a water content of 3 wt.% was used for the CVC magmas based on experimental petrology and geophysical data (see Section 2.3; Moore and Carmichael, 1998; Gardine, 2010; López-Loera, 2012).

3.3.1 *Mineral-melt and Mineral-mineral Equilibrium Tests*

The equilibrium test for plagioclase-melt, based on an equation for calculating the temperature at which plagioclase will start crystallising from a specific melt composition (see section 2.3.1), reveals the analysed plagioclase-melt pairs for the Group II samples are in equilibrium with each other (Figure 3.29a). Rhodes diagrams for clinopyroxene-melt, orthopyroxene-melt and clinopyroxene-orthopyroxene equilibrium based on the Fe-Mg exchange coefficient between the mineral-melt and mineral-mineral phases (see section 2.3.1; Putirka 2008), reveal few of the clinopyroxene-melt pairs, and none of the orthopyroxene-melt pairs are in equilibrium (Figure 3.29b and c). However, as with the Group I samples, the two pyroxene phases are in equilibrium with each other (Figure 3.29d).

The majority of the pyroxene crystals occur in glomerocrysts and are not in equilibrium with the melt; therefore the temperatures estimates from the two-pyroxene thermometry must be for another part of the system, and probably reflect the temperature of another batch of magma, based on the mineral textures and zoning (see Section 2.3 and Section 3.2.2.8).

Sample	Unit	P (kbar)	H ₂ O (wt.%)	Water dependent thermometers			Water-independent thermometers			
				Cpx-melt ^[1] T (°C) ± 45	Opx-melt ^[2] T (°C) ± 39	Plag-melt ^[3] T (°C) ± 36	2-px ^[4] T (°C) ± 56	2-px ^[5] T (°C) ± 70	2-px ^[6] T (°C) ± 60	Hbd ^[7] T (°C) ± 34
VF95-09G	N	2	3	1023	1061	979	985	1030	1039	999
VF10-03N	N	2	3	1013	-	1019	-	-	-	-
VF10-07D	N	2	3	1023	1032	1029	968	995	1013	-
VF02-01G	F	2	3	988	-	991	-	-	-	-
VF01-05N	D	2	3	1000	-	1059	-	-	-	970
VF01-02Ns	D	2	3	987	974	996	924	948	943	970
VF00-06O	D	2	3	941	-	904	-	-	-	974

Table 3.4 Eruption temperature estimates from pressure and water-dependent thermometers

[1] clinopyroxene-melt (eq. 33; Putirka, 2008); [2] orthopyroxene-melt (eq. 38a; Putirka, 2008); and [3] plagioclase-melt (eq. 24a; Putirka, 2008); and water-independent thermometers: [4] two-pyroxene thermometers (Putirka, 2008); [5] (Wells, 1977); [6] (Wood and Banno, 1973); and [7] the hornblende-only (Ridolfi et al., 2010)

Sample	Unit	Hbd ^[1]		T (°C)	Plag-melt	
		T (°C) ± 34	H ₂ O (wt.%)		H ₂ O (wt.%) ^[2]	H ₂ O (wt.%) ^[3]
VF95-09G	N	999	5.2 ± 0.2	1013	2.9 ± 0.6	3.9 ± 0.2
VF10-03N	N	-	-	1014*	2.9 ± 0.3	4.3 ± 0.3
VF10-07D	N	-	-	992	3.4 ± 1.0	4.4 ± 0.6
VF02-01G	F	-	-	988*	3.1 ± 0.2	4.5 ± 0.2
VF01-05N	D	970	5.7 ± 1.0	970	5.2 ± 1.1	5.3 ± 1.9
VF01-02Ns	D	970	4.9 ± 1.4	946	4.9 ± 1.8	4.4 ± 0.9
VF00-06O	D	974	4.8 ± 1.0	974	1.6 ± 0.9	4.3 ± 0.1

Table 3.5 Water content estimates for the Group II magmas.

Estimated using the hornblende hygrometer of [1] Ridolfi et al. (2010) and plagioclase-melt hygrometers of [2] Putirka (2008) and [3] Lange et al. (2009). The hornblende thermometer and hygrometer calculates the pressure, temperature and water content from the hornblende composition, while the plagioclase-melt hygrometers require the temperature and pressure to be constrained. A pressure of 2 kbar was used, and the average temperature from the water-independent thermometers (Table 2.4). *The average temperatures for VF10-03N and VF02-01G are from the water-dependent thermometers as one or both pyroxene phases are absent from these samples

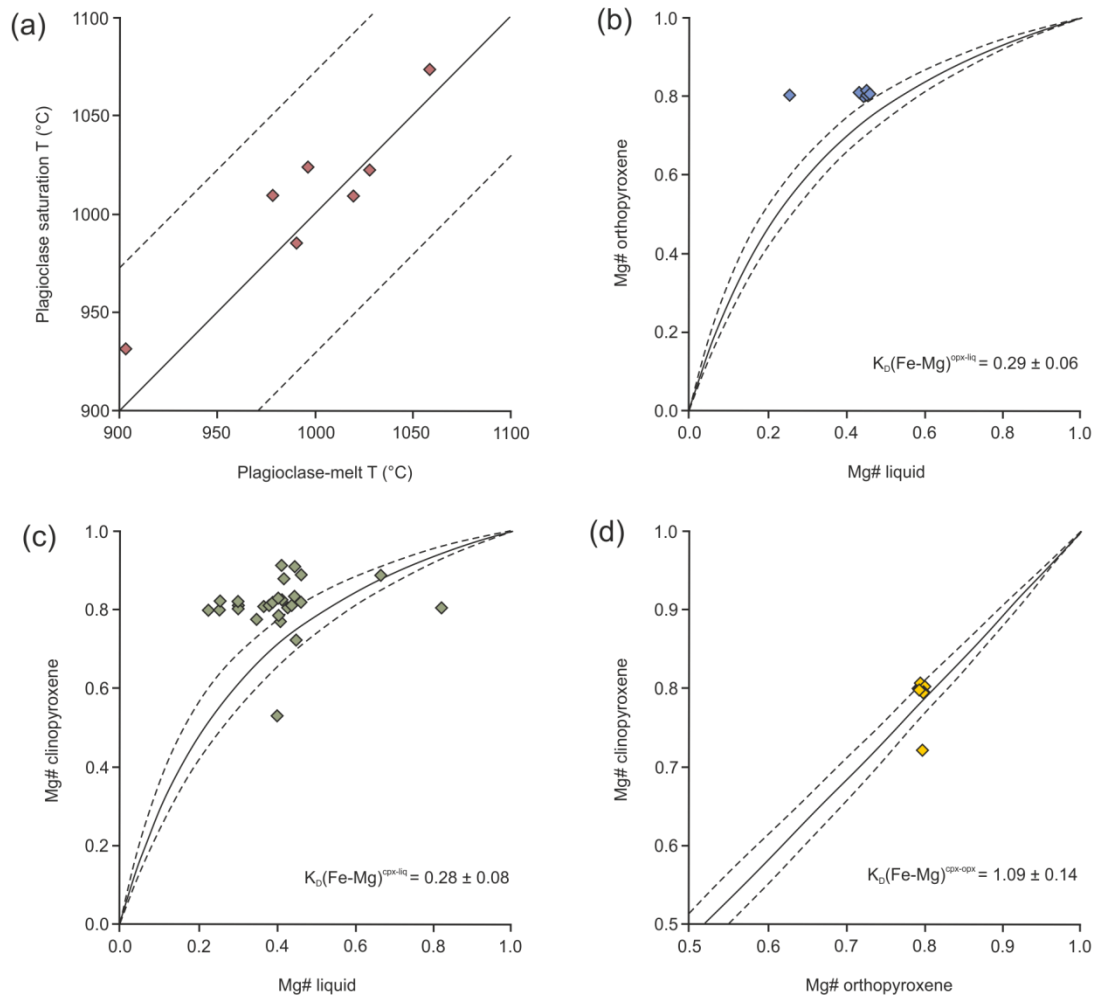


Figure 3.29 Equilibrium tests for mineral-melt and mineral-mineral pairs.

If pairs are in equilibrium, they should plot on the solid line, or within the error envelope defined by the dashed lines. The plagioclase-melt equilibrium test (a) compares the plagioclase-melt thermometry with the temperature at which plagioclase should become saturated and therefore crystallise (Putirka, 2008). Pyroxene-melt (b and c) and two-pyroxene (d) equilibrium is tested using the Rhodes diagram and the Fe-Mg exchange coefficient (Rhodes et al., 1979; Putirka, 2008)

3.3.2 Temperature and Water Content Estimates for the Group II CVC Magmas

Eruption temperatures have been estimated for units N and D based on the two-pyroxene thermometers of Wood and Banno (1973), Wells (1977) and Putirka (2008), and the hornblende thermometer of Ridolfi et al. (2010). The water-dependent mineral-melt thermometers were also used with a pressure of 2kbar and water content of 3 wt.% (Table 3.4). Unit F samples only contain one pyroxene phase, and the majority of glass analyses were poor due to the highly crystalline and vesiculated nature of the glass. As a result, temperature estimates were possible from only one unit F sample, VF02-01G (Table 3.4).

Figure 3.30 shows the results of the geothermometry for the Group II eruption deposits. Also shown on this plot is the estimated eruption temperature field (950-975°C) from the experimental petrology work of Moore and Carmichael (1998). Both the water-independent and water-dependent thermometer results are shown. Temperature estimates from the water-independent thermometers are highest for unit N (up to 1061°C), and show the widest range in eruption temperature from 968 to 1061°C (Figure 3.30a; Table 3.4). Eruption temperatures for unit D are much lower, ranging from 924 - 974°C, while no water-independent geothermometry was possible for unit F.

The water-dependent plagioclase-melt geothermometer yields temperature estimates of 979-1029°C for unit N, 991°C for unit F, and 904-1059°C for unit D (Figure 3.30). Also shown are the temperature estimates from the pyroxene-melt thermometry; however, the pairs are not in equilibrium and are therefore not considered here.

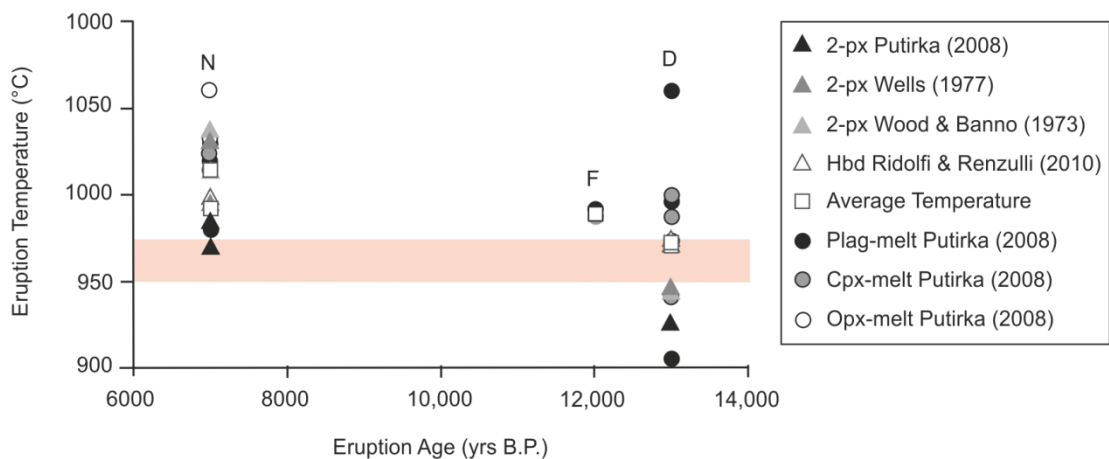


Figure 3.30 Estimated eruption temperatures for the Group II deposits.

Temperatures were estimated using the water-independent (triangle symbols) two-pyroxene thermometers of Putirka (2008), Wells (1977) and Wood and Banno (1973), and the hornblende thermometer of Ridolfi et al. (2010); and the water-dependent (circle symbols) plagioclase-melt, clinopyroxene-melt and orthopyroxene-melt thermometers of Putirka (2008). The coloured block is the estimated temperature by Moore and Carmichael (1998) based on experimental petrology for Colima lavas. The errors for the thermometers are reported in Table 3.4

Water contents have been estimated based on the hornblende hygrometer of Ridolfi et al. (2010) and the plagioclase-melt hygrometers of Putirka (2008) and Lange et al. (2009). The plagioclase-melt hygrometers require the temperature to be constrained; therefore the temperature from the water-independent thermometry was used for units N and D. Unfortunately the only usable temperature estimate obtained for unit F is from plagioclase-melt thermometry, for which the water content must be constrained. This temperature is used for the hygrometry; therefore the results for unit F are only relative to the experimental data of Moore

and Carmichael (1998). The results are shown in Table 3.5 and Figure 3.31. Unit D has the highest water content with up to 5.7 ± 1.1 wt.% H₂O. Water contents in unit N vary from 2.9 ± 0.6 to 4.4 ± 0.6 wt.% H₂O (Figure 3.31). Hornblende hygrometry yields higher water contents for the eruption deposits.

Melt inclusion studies of Colima lavas yielded water contents of 0.1 to 2.5 wt.% (Atlas et al., 2006; Reubi and Blundy, 2008), while melt inclusions from orthopyroxene phenocrysts in scoria from the 1913 eruption yielded higher water contents of 2.8 to 3.4 wt.% (Atlas et al., 2006) and 6.3 wt.% (unpublished dataset of Luhr). The high water contents of the Group II magmas are consistent with the high water content of the explosive 1913 eruption.

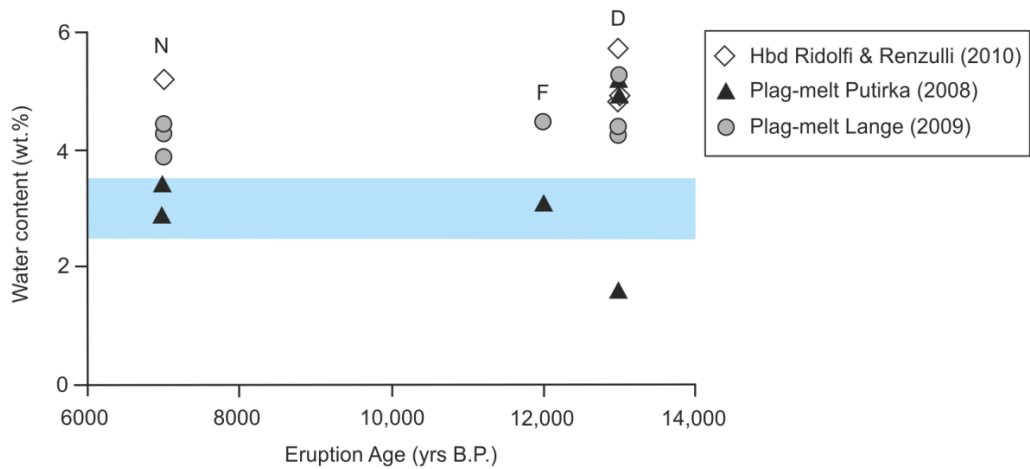


Figure 3.31 Estimated water contents for the Group II eruption deposits.

Water contents were estimated using the hornblende hygrometer of Ridolfi et al. (2010) and the plagioclase-melt hygrometers of Putirka (2008) and Lange et al. (2009). The coloured block is the estimated water contents of Moore and Carmichael (1998) based on experimental petrology for Colima lavas. The errors for the hygrometers are reported in Table 3.5

These results make it possible to draw comparisons between the eruption deposits; however, the equilibrium tests together with the mineral textures and zoning have shown that the magmas have complex crystallisation histories with many episodes of magma mixing and destabilisation of the crystallising phases. In order to accurately determine the eruption temperatures and water contents of the magmas, analyses of melt inclusions are necessary and more effort to find coexisting Fe-Ti oxide pairs is essential for immediate pre-eruption thermometry.

3.4 Whole-Rock Geochemistry

The majority of the whole-rock geochemical data for the Group II eruption deposits were collected and analysed by Jim Luhr during his 22 years working on the CVC (Luhr and Carmichael, 1982; Luhr et al., 2010). Much of these data are unpublished. Samples were

analysed by XRF at the Department of Mineral Sciences at the Smithsonian Institution, Washington D.C., USA, and by ICP-MS at Washington University. Details of these analytical techniques and their limitations are given in Appendix D. Three new samples, VF10-07D and VF10-03N from unit N, and VF10-04F from unit F were collected and analysed during the 2010 field season.

Through correlation in the field using Jim Luhr's stratigraphic logs, provided by Carlos Navarro-Ochoa, mineralogical distinctions and geochemistry, 20 samples analysed by Jim Luhr have been identified as belonging to units N, F and D. The ranges of major and trace element abundances in the Group II eruption deposits are given in Tables 3.6 and 3.7, and Figures 3.32 to 3.36. The complete geochemical dataset can be found in Appendix H.

This section presents the whole-rock geochemical data for the Group II units. Detailed discussion and interpretation of the datasets for the Group I and Group II eruption deposits is presented in Chapter 5.

3.4.1 Major Elements

Scoria samples from the Group II eruption deposits span a range of compositions from picro-basalt to basaltic trachyandesite (Figure 3.32). Overall, they can be considered basalt to basaltic-andesite in composition with SiO_2 contents ranging from 43.9 to 57.5 wt.% (Figure 3.32). Unit F is the most mafic and the most heterogeneous with 43.9 to 53.3 wt.% SiO_2 , while units N and D display variations of up to 4 wt.% SiO_2 .

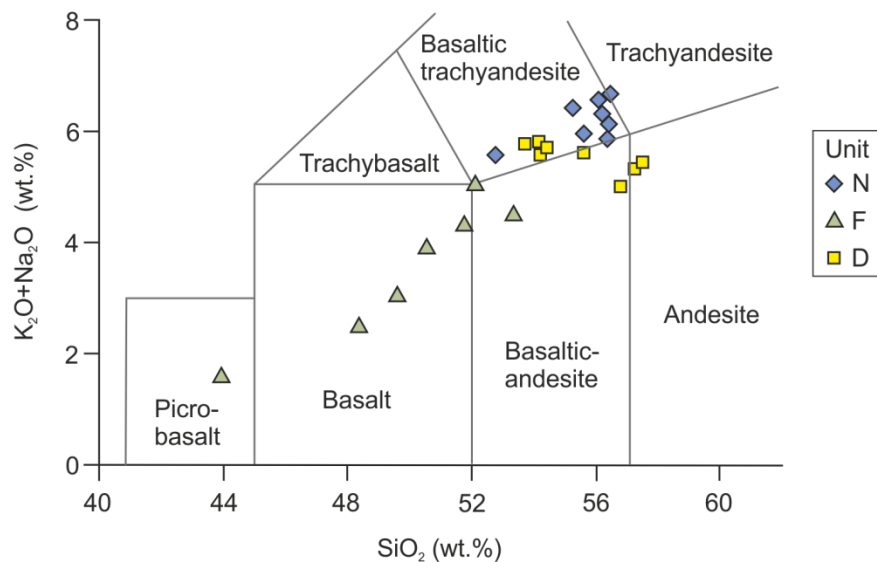


Figure 3.32 Total alkalis-silica (TAS) diagram after Le Maitre et al. (2002) for the Group II eruption deposits.

Units N, F and D range in composition from 43.9 to 57.5 wt.% SiO_2 .

Unit	SiO ₂	TiO ₂	Al ₂ O ₃	FeOt	MnO	MgO	CaO	Na ₂ O	K ₂ O	P ₂ O ₅
N	52.8 - 56.5	0.79 - 0.85	16.3 - 18.8	5.9 - 6.0	0.11 - 0.11	3.3 - 6.2	5.7 - 7.2	3.5 - 4.2	1.6 - 2.5	0.28 - 0.56
F	43.9 - 53.3	0.84 - 1.29	14.4 - 19.2	6.9 - 9.1	0.09 - 0.13	6.4 - 8.1	6.9 - 8.0	1.3 - 3.5	0.4 - 3.5	0.27 - 0.68
D	53.7 - 57.5	0.75 - 0.91	15.9 - 18.6	6.2 - 6.9	0.11 - 0.13	2.8 - 6.1	6.4 - 8.0	3.4 - 4.4	1.0 - 2.2	0.21 - 0.51

Table 3.6 Ranges of major element concentrations in weight % for Group II basalts to basaltic-andesites.

FeOt was calculated as $\text{FeOt} = \text{FeO} + (\text{Fe}_2\text{O}_3 * 0.899)$. Full data tables are in Appendix H

Unit	V	Cr	Co	Ni	Cu	Zn	Rb	Sr	Y	Zr	Nb	Ba
N	122 - 165	68 - 279	17 - 26	34 - 100	36 - 52	67 - 102	21 - 30	962 - 1466	18 - 22	177 - 281	2 - 8	677 - 1036
F	142 - 194	205 - 375	27 - 42	69 - 137	42 - 92	64 - 111	2 - 19	578 - 2540	17 - 21	125 - 433	2 - 9	539 - 1769
D	132 - 151	12 - 151	20 - 26	17 - 51	36 - 66	69 - 86	12 - 24	619 - 1398	17 - 22	137 - 288	3 - 7	395 - 812

Table 3.7 Ranges of trace element concentrations in ppm for Group II basalts to basaltic-andesites.

Full dataset is given in Appendix H.

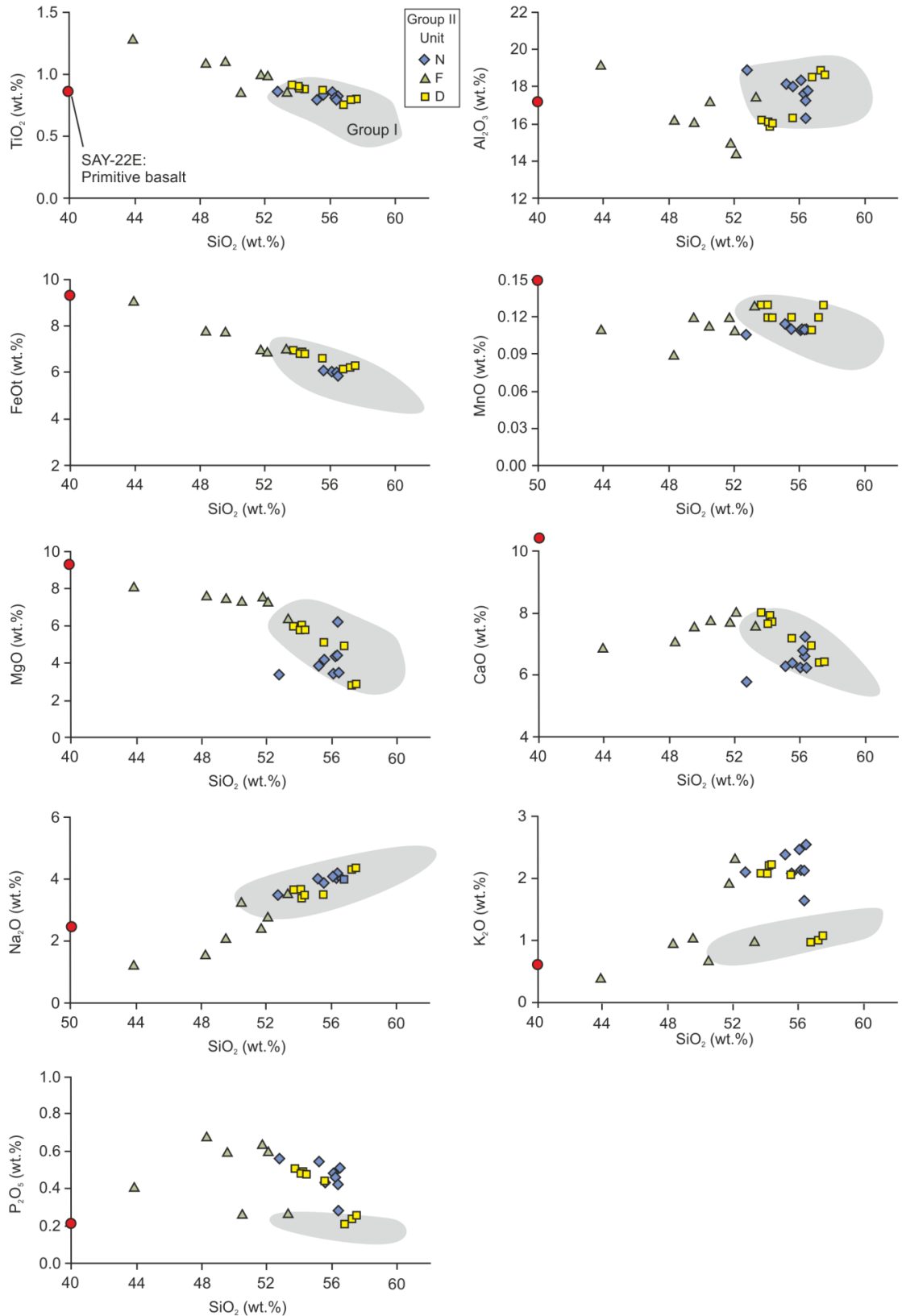


Figure 3.33 Major element variation diagrams for the Group II eruption deposits.

The Group I eruption deposits are represented by the grey shaded area. The Group II deposits generally follow a differentiation trend similar to the Group I deposits; however, the Group II units display elevated K_2O and P_2O_5 that is inconsistent with a fractional crystallisation trend from the proposed parental CVC magma; SAY-22E (red circle; Luhr, 1997).

Overall, the Group II eruption deposits follow a similar differentiation trend to the Group I medium-K series, with increasing K_2O and Na_2O and decreasing MgO , CaO , FeO , MnO and P_2O_5 with increasing SiO_2 (Figure 3.33). However, the Group II eruption deposits show geochemical distinctions with elevated K_2O (up to 3.5 wt.%) and P_2O_5 (up to 0.68 wt.%) relative to the Group I basaltic-andesites and andesites (Figure 3.33). Each of the three units that make up Group II are characterised by the presence of phlogopite, which is absent in scoria and pumice from the Group I eruption deposits. Figure 3.34 shows MgO and K_2O variation diagrams with the main mineral phases, averaged from Group I EPMA analyses.

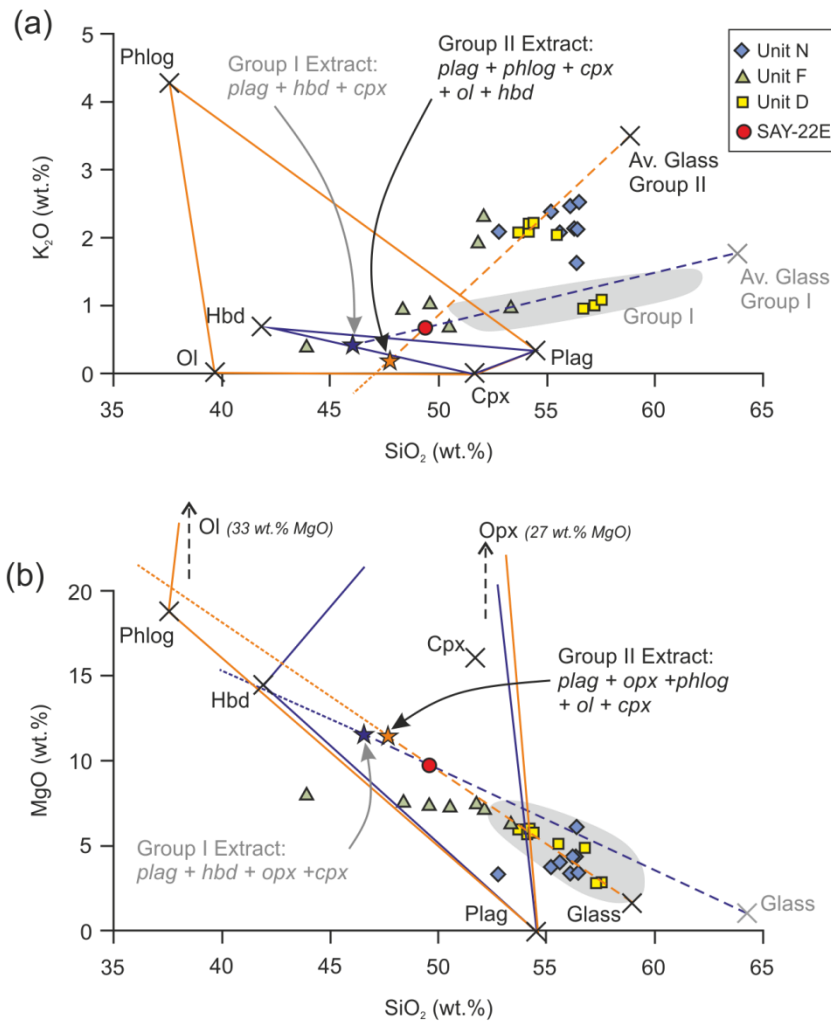


Figure 3.34 K_2O (a) and MgO (b) variation with SiO_2 showing the control of the main mineral phases on the chemical trends.

The Group I samples follow a trend of increasing K_2O and decreasing MgO with increasing SiO_2 reflecting the extraction of plagioclase (plag) + hornblende (hbd) + orthopyroxene (opx) + clinopyroxene (cpx) [+ olivine] from a mafic parental melt. Some of the Group II samples follow this same trend; however, some follow a trend reflecting the extraction of plagioclase + phlogopite (phlog) + clinopyroxene + orthopyroxene + olivine (ol) + hornblende.

The trend towards high K_2O with increasing SiO_2 displayed by the Group II eruption deposits could be explained by the fractionation (or extraction) of plagioclase + phlogopite + clinopyroxene + orthopyroxene + olivine + hornblende, from a mafic parent (i.e. sample SAY-22E). However, not all Group II samples follow this trend. Some of the samples follow the differentiation trend displayed by the Group I eruption deposits, as indicated by the blue dashed line (Figure 3.34), while others lie off the differentiation trends. These variation diagrams reveal that not all the Group II samples can be linked to the Group I magmas through fractional crystallisation from a common mafic parent. The wide range of K_2O (and P_2O_5 , CaO , Al_2O_3) within the Group II units suggests a magma mixing process between two compositionally distinct magma batches. The CVC magma sources are discussed in detail in Chapter 5.

3.4.2 Trace Elements

Compatible trace element variations are consistent with the overall differentiation trend displayed by the Group II eruption deposits (Figure 3.35). The trends reflect olivine + clinopyroxene + phlogopite + plagioclase + Fe-Ti oxide fractionation from a mafic parental magma. Again, olivine accumulation could explain the high Co and Cr, and low SiO_2 contents of the unit F samples.

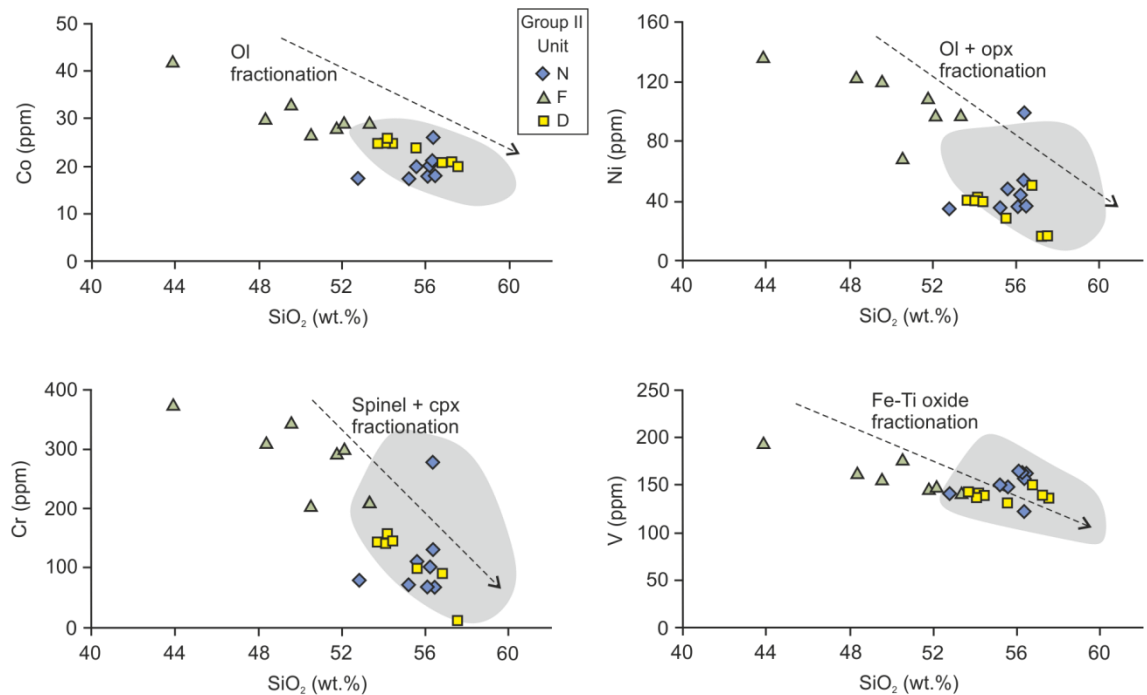


Figure 3.35 Compatible trace element variations with SiO_2 for the Group II eruption deposits.

The Group I eruption deposit compositions are defined by the shaded field. The Group II deposits follow similar trends to the Group I units. Unit F is strongly enriched in Co, Ni and Cr relative to the rest of the Group II and Group I units. This may reflect olivine accumulation.

Incompatible trace element abundance patterns in the Group II eruption deposits are consistent with those of typical subduction-related magmas; enrichments in LILE (Rb, Ba, K, Sr and Th) relative to HFSE (Nb, Ta, Ti, Hf, Zr, Y ± P) related to the addition of slab-derived fluids (see Section 2.4.2.1). The relative depletions in the HFSE reflect the presence of stable mineral phases in the subducting slab or mantle wedge (see Section 2.4.2.1).

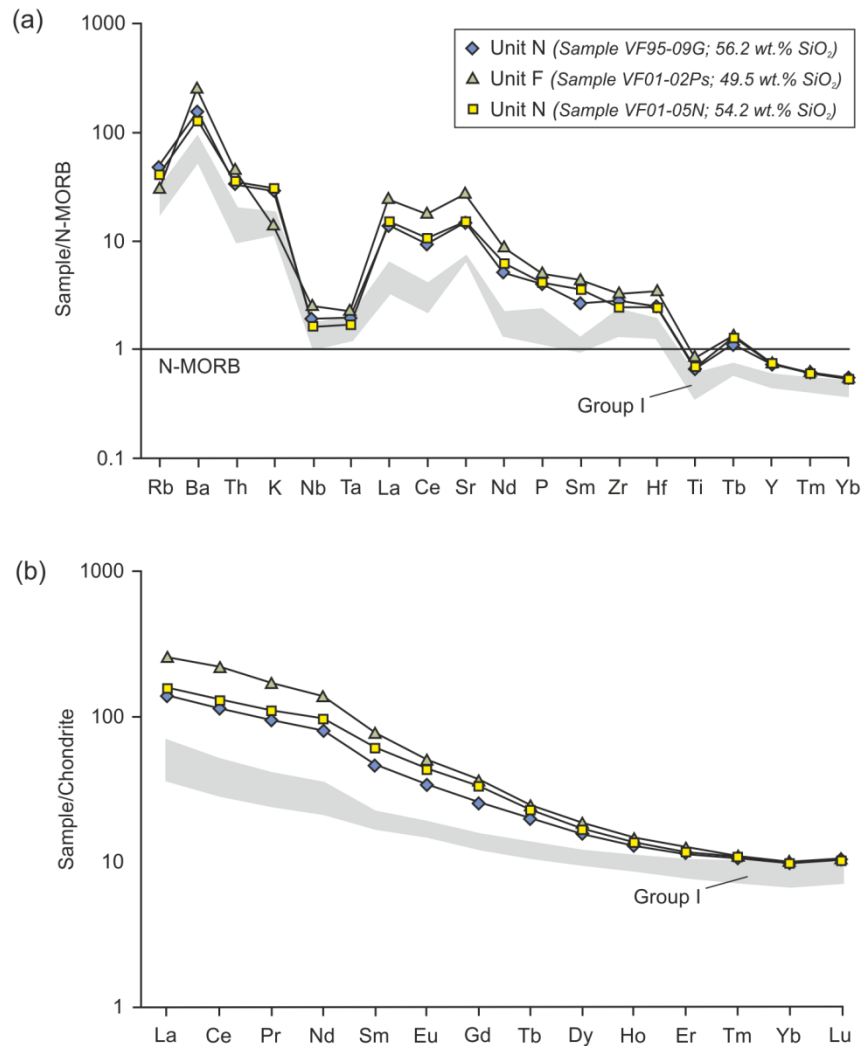


Figure 3.36 N-MORB normalised trace element (a) and Chondrite normalised REE (b) abundance patterns for the Group II eruption deposits.

N-MORB normalising values are from Sun and McDonough (1989) and Chondrite normalising values are from Nakamura (1974). The shaded area represents the Group I eruption deposits. The Group II units display stronger enrichments in the LILE and LREE relative to the Group I deposits. Unit F displays the strongest enrichments in the incompatible trace elements.

The Group II eruption deposits have elevated N-MORB normalised incompatible trace element abundances and chondrite-normalised REE abundances relative to the Group I eruption deposits (Figure 3.36). Unit F displays stronger enrichments in the LILE and LREE than units N and D,

possibly reflecting variations in partial melt extent and/or an increased fluid input from the subducting slab (Saunders et al., 1991)

The enrichments in the incompatible trace elements in the Group II eruption deposits relative to the Group I deposits are consistent with the observed concentrations of K₂O and P₂O₅ in the whole-rock major element geochemistry. Detailed interpretation and discussion of the major and trace element data will be presented in Chapter 5.

3.5 Sr-Nd Isotopes

Strontium (Sr) and Neodymium (Nd) isotope analyses were carried out for ten samples from the Group II eruption deposits: three from unit N, four from unit F and three from unit D (Table 3.8). The samples were prepared and analysed using the TIMS at the University of Leeds, as outlined in Appendix F. Ratios are reported to an internal precision of 2σ error on the 6th decimal digit. All ⁸⁷Sr/⁸⁶Sr ratios were corrected to the NBS987 standard (0.710248; Thirlwall, 1991) which averaged 0.710262±5 over 58 runs between September 2010 and July 2012. The ¹⁴³Nd/¹⁴⁴Nd ratios were corrected to the La Jolla standard (0.51185; Thirlwall, 1991) which averaged 0.511842±6 over 23 runs between August 2011 and July 2012. The analytical procedures are outlined in detail in Appendix F.

Sample	Unit	⁸⁷ Sr/ ⁸⁶ Sr	2σ error (10 ⁻⁶)	¹⁴³ Nd/ ¹⁴⁴ Nd	2σ error (10 ⁻⁶)
VF10-07D	N	0.703723	±3	0.512908	±6
VF95-09G	N	0.703711	±4	0.512916	±4
VF10-03N	N	0.703710	±5	0.512922	±4
VF95-06E	F	0.703576	±4	0.512927	±10
VF01-02Ps	F	0.704084	±4	0.512791	±4
VF01-05PA	F	0.704044	±4	0.512787	±5
VF10-04F	F	0.703681	±4	0.512913	±5
VF95-01B	D	0.703645	±5	0.512936	±5
VF01-02Ni	D	0.703696	±4	0.512920	±10
VF01-05N	D	0.703695	±4	0.512908	±5

Table 3.8 ⁸⁷Sr/⁸⁶Sr and ¹⁴³Nd/¹⁴⁴Nd isotope ratios for the Group II basalts to basaltic-andesites.

Ratios are reported to 2σ error on the 6th decimal place, and are normalised to the NBS-987 and La Jolla standards for Sr and Nd, respectively.

The isotopic ratios of ⁸⁷Sr/⁸⁶Sr and ¹⁴³Nd/¹⁴⁴Nd are commonly used in arc magmas to fingerprint the source and the nature of processes (open vs. closed system) occurring in the magmatic plumbing system (see Section 2.5; AFC; e.g. Kempton et al., 1991; Tatsumi et al., 1992; Straub

et al., 2010; Verma and Luhr, 2010; Schmidt and Grunder, 2011). A series of isotope ratio plots are shown in Figure 3.37, which show the ranges of $^{87}\text{Sr}/^{86}\text{Sr}$ and $^{143}\text{Nd}/^{144}\text{Nd}$ displayed by the Group II eruption deposits. The Group II units display slightly more radiogenic $^{87}\text{Sr}/^{86}\text{Sr}$ and less radiogenic $^{143}\text{Nd}/^{144}\text{Nd}$ than the majority of the Group I eruption deposits, represented by the grey area (Figure 3.37). Units N and D display a narrow range in $^{87}\text{Sr}/^{86}\text{Sr}$ and $^{143}\text{Nd}/^{144}\text{Nd}$, varying from 0.70365 to 0.70372 and 0.51291 to 0.51294, respectively (Table 3.8; Figure 3.37).

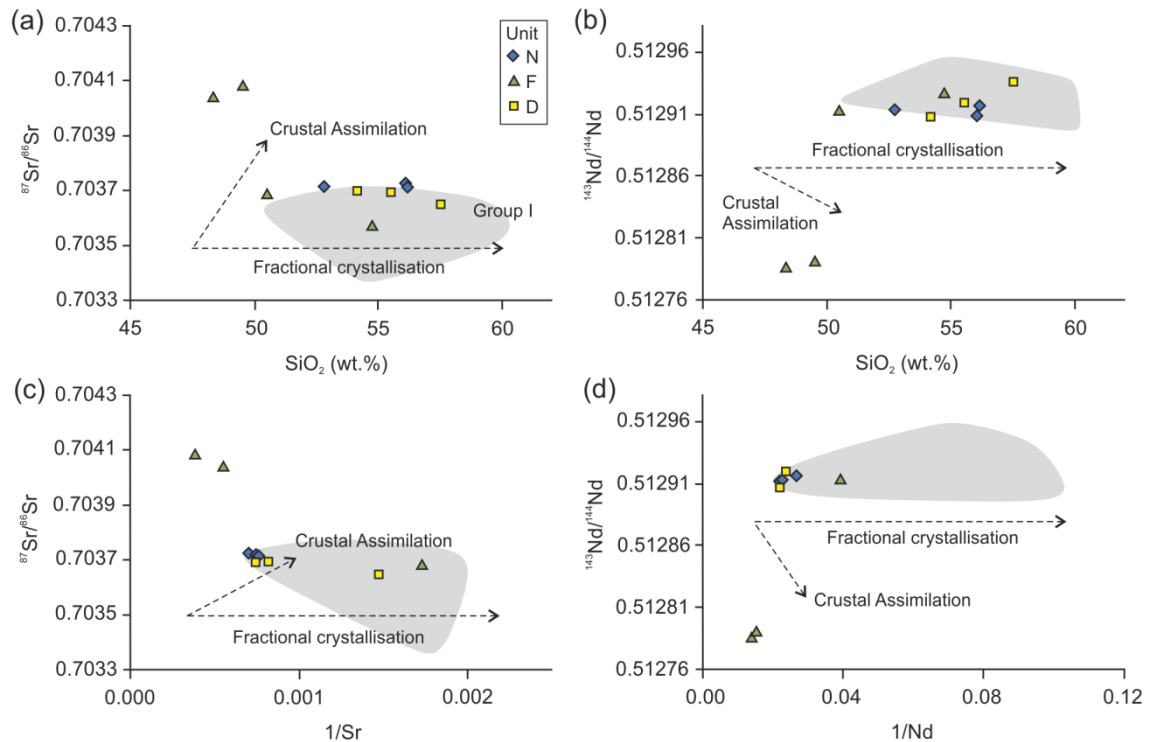


Figure 3.37 $^{87}\text{Sr}/^{86}\text{Sr}$ and $^{143}\text{Nd}/^{144}\text{Nd}$ versus SiO_2 content (a and b) and $1/\text{Sr}$ (c) and $1/\text{Nd}$ (d) for the Group II eruption deposits.

The isotopic composition of the Group I eruption deposits is represented by the shaded area. The Group II samples have more radiogenic $^{87}\text{Sr}/^{86}\text{Sr}$ and less radiogenic $^{143}\text{Nd}/^{144}\text{Nd}$ than the majority of the Group I samples, and two of the unit F samples have much higher $^{87}\text{Sr}/^{86}\text{Sr}$ and lower $^{143}\text{Nd}/^{144}\text{Nd}$ suggesting a different source composition.

Unit F displays a much wider range in $^{87}\text{Sr}/^{86}\text{Sr}$ (0.70358 - 0.70408) and $^{143}\text{Nd}/^{144}\text{Nd}$ (0.51279 - 0.51293; Table 3.8; Figure 3.37). However, there is a clear distinction within unit F samples; two of the samples have more radiogenic $^{87}\text{Sr}/^{86}\text{Sr}$ and less radiogenic $^{143}\text{Nd}/^{144}\text{Nd}$ corresponding with their lower SiO_2 content. Plots of $^{87}\text{Sr}/^{86}\text{Sr}$ against $1/\text{Sr}$ and $^{143}\text{Nd}/^{144}\text{Nd}$ against $1/\text{Nd}$ reveal the same pattern (Figure 3.37c and d). The clear separation of these two samples from the rest of the Group II eruption deposits suggests either a separate source, or contamination from a magma or crystalline mush with more radiogenic $^{87}\text{Sr}/^{86}\text{Sr}$ and less radiogenic $^{143}\text{Nd}/^{144}\text{Nd}$.

Figure 3.38 is a $^{87}\text{Sr}/^{86}\text{Sr}$ versus $^{143}\text{Nd}/^{144}\text{Nd}$ diagram showing various mantle reservoirs after Zindler and Hart (1986). The Group II eruption deposits lie along the mantle array, trending away from the Group I deposits towards a more enriched mantle component (Figure 3.38). The slightly more radiogenic $^{87}\text{Sr}/^{86}\text{Sr}$ and less radiogenic $^{143}\text{Nd}/^{144}\text{Nd}$ displayed by the Group II deposits, and the large variation displayed by unit F samples suggests mixing of two isotopically distinct magmas, such as the medium-K Group I magma and the high-K, alkaline cinder cone magmas.

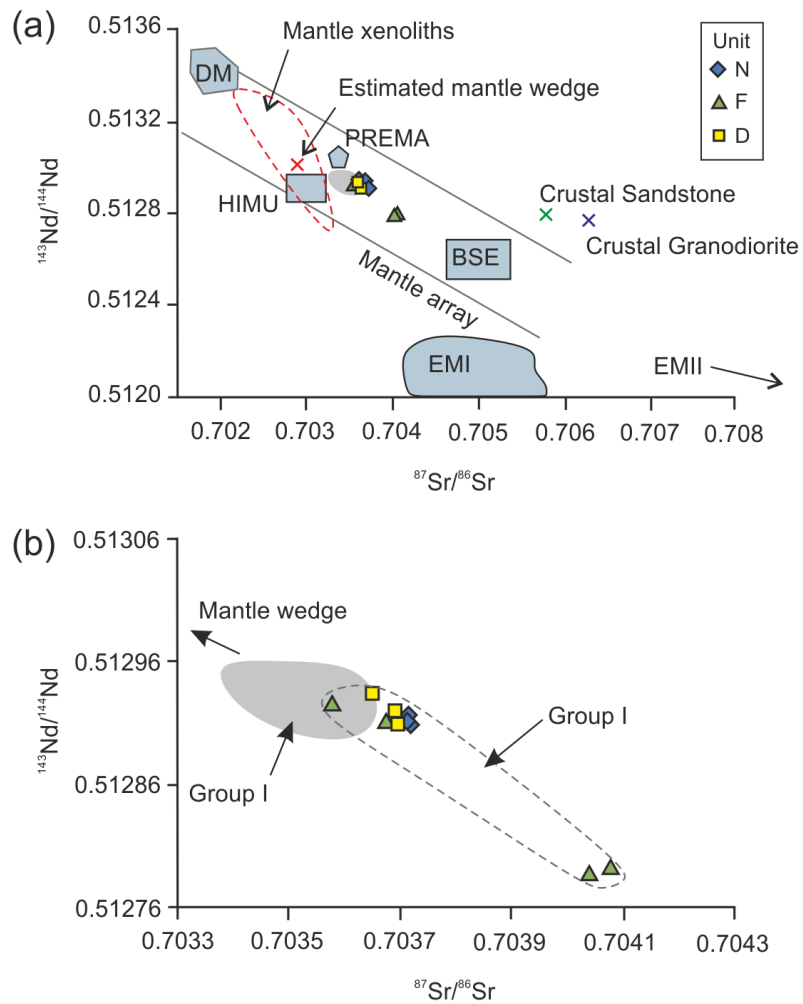


Figure 3.38 $^{87}\text{Sr}/^{86}\text{Sr}$ versus $^{143}\text{Nd}/^{144}\text{Nd}$ for the CVC eruption deposits.

(a) Fields for various mantle reservoirs after Zindler and Hart (1986) are plotted together with values for the estimated Mexican mantle wedge (Gómez-Tuena et al., 2007a) and the western Mexico crust (Verma and Luhr, 2010) and the Group I eruption deposits (light grey). (b) Blow-up of the CVC explosive eruption deposits showing the Group I units in grey, and the Group II eruption deposits. The Group II deposits trend away from the Mexican mantle wedge and the Group I eruption deposits, towards an enriched mantle component.

3.6 Summary

Within the Holocene explosive eruption deposits of the CVC, three mineralogically and geochemically distinct units (Group II) have been identified from the main CVC trend (Group I). The appearance of the Group II units in the stratigraphic record is sharp, with each eruption occurring as a single event within a predominantly sub-alkaline system.

Scoria from the Group II units contain phlogopite which is absent from the Group I eruption deposits. The Group II samples typically have the mineral assemblage plagioclase + clinopyroxene + hornblende + olivine + phlogopite + Fe-Ti oxides ± orthopyroxene in varying amounts. Although these three units (N, F and D) have been grouped together, they are mineralogically distinct from each other. Scoria from unit N comprises predominantly plagioclase and clinopyroxene, with up to 1 vol.% olivine, and trace abundances of hornblende and phlogopite. Unit F scoria is dominated by clinopyroxene, olivine and phlogopite with up to 1 vol.% plagioclase and trace hornblende, while unit D scoria comprise predominantly hornblende and plagioclase, with clinopyroxene and up to 1 vol.% olivine and phlogopite.

Mineral chemistry and backscatter SEM images reveal complex zoning patterns and textures that indicate crystallisation histories involving multiple phases of crystal destabilisation and recrystallisation related to decompression, magma mixing and thermal convection in the magmatic plumbing system.

Whole-rock major and trace element data reveal that the Group II eruption deposits have elevated K_2O and P_2O_5 and enriched LILE (K, Cs, Rb, Ba, Sr ± Th) and LREE (La, Ce, Pr, and Nd) relative to the Group I eruption deposits. The majority of whole-rock major and compatible trace elements reveal that the Group II units follow a similar differentiation trend to the Group I deposits; however, plots of K_2O and MgO versus SiO_2 reveal that the magmas of the Group II eruption deposits cannot have evolved through fractional crystallisation from the proposed basaltic parent magma of the CVC magmas alone.

Whole-rock $^{87}Sr/^{86}Sr$ and $^{143}Nd/^{144}Nd$ isotope ratios reveal the Group II deposits have slightly more radiogenic $^{87}Sr/^{86}Sr$ and slightly less radiogenic $^{143}Nd/^{144}Nd$ than the majority of the Group I units. Two of the samples from unit F have very different isotopic compositions from the remaining Group II samples. The clear separation of these two samples suggests either a separate source, or contamination from an isotopically distinct magma or crystalline mush, or crust. A literature review of the petrologically, geochemically and isotopically distinct alkaline cinder cone magmas is presented in the following chapter, and a discussion of the sources of the Group I and Group II magmas is presented in Chapter 5.

4 Alkaline Cinder Cones

In the northern part of the CVC, to the east and west of Volcán Cántaro, compositionally and isotopically distinct magmas erupted on the Colima Rift floor forming monogenetic cinder cones (Figure 4.1; Luhr and Carmichael, 1981; Carmichael et al., 2006). In total eleven cinder cones formed, nine of them are alkaline and two are sub-alkaline basalt and basaltic-andesite in composition (Figure 4.2; Luhr and Carmichael, 1981). Allan and Carmichael (1984) and Carmichael et al. (2006) dated these cones using $^{40}\text{Ar}/^{39}\text{Ar}$ techniques yielding ages ranging from 1217 ka to 62 ka (Table 4.1). The oldest dates belong to the sub-alkaline cones, while the alkaline cones erupted from 473 ka to 62 ka. During this time, volcanism was ongoing at the Nevado de Colima volcano (Luhr and Carmichael, 1990a; Cortés et al., 2005).

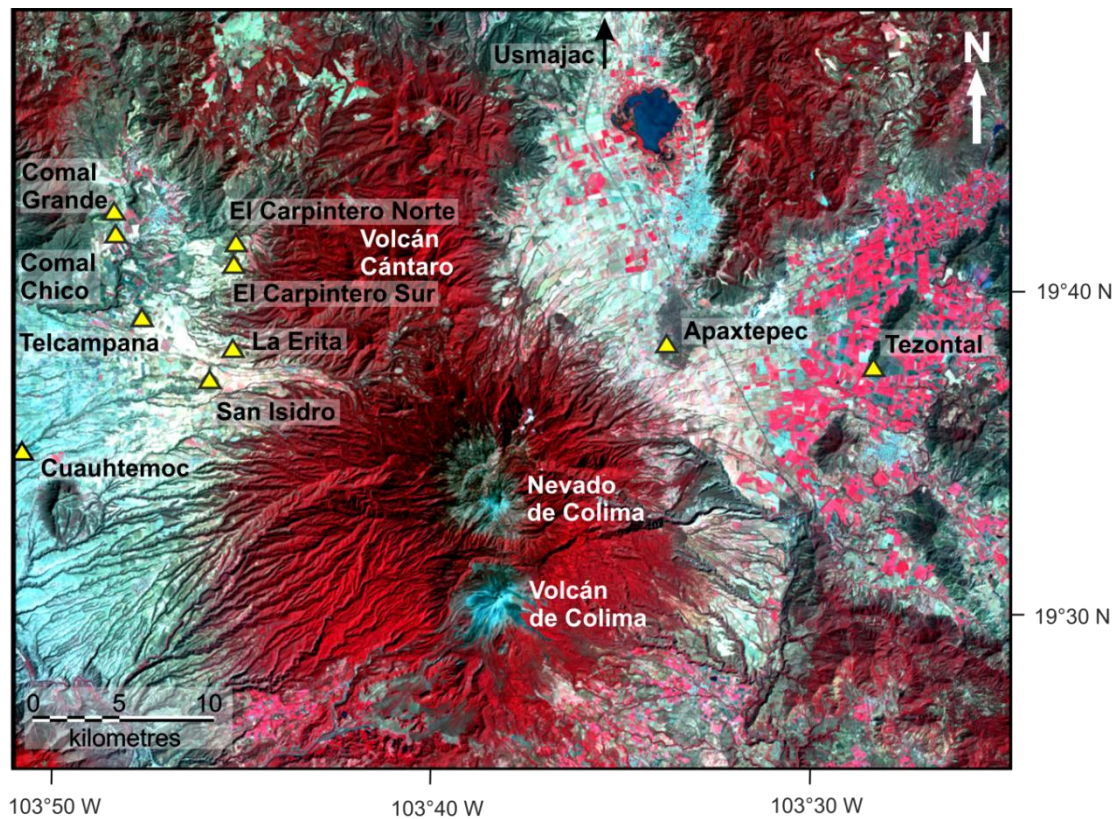


Figure 4.1 High resolution Landsat image of the CVC.

The locations of the alkaline and sub-alkaline cinder cones are indicated, to the east and west of the northern CVC. The cinder cones are basanite to minette, with exception of Tezontal and Usmajac which are basalt and basaltic-andesite, respectively.

This chapter is a review of previous work carried out on the alkaline cinder cone magmas. As presented in Chapter 3, the Group II units are high-K sub-alkaline magmas with geochemical

and isotopic signatures that appear to reflect mixing between two isotopically distinct magmas. Luhr and Carmichael (1982) suggested that distinct high-K tephra layers could result from direct mixing between magmas erupting through the CVC system, and alkaline magmas of the cinder cones. The alkaline magmas could therefore play an important role in the petrogenesis of CVC magmas.

The petrology and geochemistry of the cinder cone eruptive products were first studied by Luhr and Carmichael (1981). Later studies focused on their ages and eruptive volumes (Carmichael et al., 2006) and the petrogenesis of the magmas (Wallace and Carmichael, 1989; Luhr, 1997; Ferrari et al., 2001; Maria and Luhr, 2008; Vigouroux et al., 2008; Cai, 2009).

	Cone	Composition	Age (ka)
Alkaline	Apaxtepec	Basanite	62 ± 14
	Comal Chico	Basanite	137 ± 11
	Comal Grande	Basanite	137 ± 12
	Telcampana	Basanite	140 ± 13
	La Erita	Leucite-basanite	157 ± 20
	San Isidro	Minette	215 ± 18
	El Carpintero Norte	Minette	240 ± 27
	El Carpintero Sur	Minette	No analysis
	Cuauhtemoc	Basanite	473 ± 21
Sub-alkaline	Tezontal	Basalt	545 ± 144
	Usmajac	Basalt-andesite	1217 ± 92

Table 4.1 Cinder cone composition and ages.

Data are from Luhr and Carmichael (1981) and Carmichael et al. (2006). The ages were determined by $^{40}\text{Ar}/^{39}\text{Ar}$ techniques (Carmichael et al., 2006).

No new data have been obtained for the alkaline cinder cones as part of this study. All the petrological and geochemical data referred to here are collated from Luhr and Carmichael (1981), Carmichael et al. (2006), Maria and Luhr (2008) Vigouroux et al. (2008) and Cai (2009).

4.1 Petrology

Based on the total alkalis-silica (TAS) classification diagram after Le Maitre (2002), the alkaline cinder cone deposits are trachybasalts with 47.6 – 50.3 wt.% SiO_2 (Figure 4.2). Luhr and Carmichael (1981) termed these magmas basanites and minettes based on their mineralogy and chemical composition, and defined a transitional series from basanite to leucite-basanite to minette. Basanites are SiO_2 -undersaturated basalts with normative and modal nepheline, and

although the cinder cone deposits contain no modal nepheline, Luhr and Carmichael (1981) used the term basanite rather than trachybasalt. Minette is defined as mica-bearing lamprophyre which is characterised by Mg-rich biotite, clinopyroxene (augite) and olivine, with felsic phases restricted to the groundmass (Luhr and Carmichael, 1981). Subsequent studies on the alkaline magmas of the CVC adopted the terminology of Luhr and Carmichael (1981), which, for consistency, is also used here.

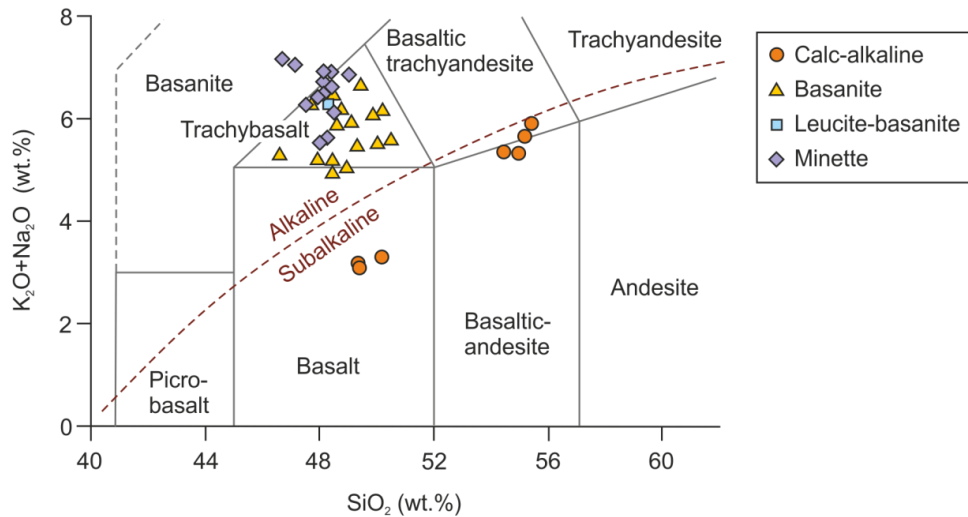


Figure 4.2 Total alkalis-silica (TAS) diagram after Le Maitre et al. (2002) for the cinder cone magmatic rocks.

Data are from Luhr and Carmichael (1981), Carmichael et al. (2006), Vigouroux et al. (2008), Maria and Luhr (2008) and Cai (2009). Two of the cinder cones are subalkaline, while the remainder are alkaline trachybasalts. The cinder cones are classified according to Luhr and Carmichael (1981).

The alkaline cinder cones form a transitional series from basanite to minette based on the appearance and increasing abundance of phlogopite, sanidine, leucite and apatite (Figure 4.3; Luhr and Carmichael, 1981). The typical mineral assemblage of the basanites, as defined by Luhr and Carmichael (1981), comprises phenocrysts and microphenocrysts of olivine + clinopyroxene + plagioclase (labradorite An_{50-70}) + titanomagnetite (Luhr and Carmichael, 1981). Titanomagnetite only occurs as microphenocrysts.

	Basanite	Leucite-basanite	Minette
Phenocrysts >0.3mm	olivine + chromite	olivine + chromite	olivine + chromite
Micro-phenocrysts 0.03 - 0.3mm	+ augite + plag	+ augite + san + leuc	+ augite + phlog + apatite + san + analc
Ground-mass <0.03mm	+ Ti-mt + glass	+ Ti-mt + apatite + phlog + glass	+ Ti-mt ± phlog + glass

Figure 4.3 Mineral assemblages of the basanite to minette series after Luhr and Carmichael (1981).

The series is characterised by the disappearance of plagioclase and the appearance of sanidine, leucite, apatite and phlogopite. The mineral abbreviations are: plag = plagioclase; san = sanidine; leuc = leucite; phlog = phlogopite; analc = analcime; and Ti-mt = titanomagnetite.

Leucite-basanites have the characteristic mineral assemblage of olivine + clinopyroxene phenocrysts, and microphenocrysts of sanidine + leucite + titanomagnetite + apatite + phlogopite (Luhr and Carmichael, 1981). The appearance of phlogopite, sanidine, leucite and apatite led Luhr and Carmichael (1981) to consider these magmas transitional between the basanites and minettes. The minettes comprise phenocrysts of olivine + clinopyroxene + phlogopite + apatite and microphenocrysts of sanidine, leucite, titanomagnetite, apatite and phlogopite (Luhr and Carmichael, 1981).

4.2 Whole-rock Geochemistry

The whole-rock major and trace element geochemical datasets of Luhr and Carmichael (1981), Carmichael et al. (2006), Maria and Luhr (2008), Vigouroux et al. (2008) and Cai (2009) are considered here. Luhr and Carmichael (1981) analysed 15 samples from the alkaline and sub-alkaline cinder cones by ICP-MS and XRF. The incompatible and rare-earth element abundances in ten of the samples were measured by INAA. Carmichael et al. (2006) re-sampled each of the cinder cones, and analysed them for whole-rock major and trace elements by XRF. No REE data were reported as part of their study. The focus of the work by Maria and Luhr (2008) was on melt inclusions from cinder cone magmas from the Colima and Mascota volcanic fields in the western TMVB. As part of their study, they analysed six samples from the Colima cinder cones for the full suite of major and trace element abundances by XRF and ICP-MS (Maria and Luhr, 2008). Similarly, Vigouroux et al. (2008) studied melt inclusions in the minettes and basanites of the CVC, but also analysed a suite of six whole-rock samples for their major and trace element abundances by XRF and ICP-MS. Cai (2009) re-analysed the trace element compositions of five of the cinder cones by ICP-MS as part of her PhD thesis at the University of Columbia.

Sample:	500	507	508	510	511	5A	6A	6D	7E	8G
Composition:	Basanite	Basanite	Basanite	Basanite	Minette	Leucite-basanite	Minette	Minette	Minette	Minette
Location:	Apaxtepec	Telcampana	Telcampana	Cuauhtemoc	La Erita	La Erita	San Isidro	San Isidro	El Carpintero Norte	Comal Chico
SiO₂	50.27	47.78	48.45	47.96	47.60	48.30	47.96	48.32	48.20	48.49
TiO₂	1.75	1.10	1.01	1.14	1.61	1.16	1.53	1.61	1.64	1.32
Al₂O₃	14.76	12.26	11.85	14.50	11.14	11.98	11.44	11.39	11.62	12.46
FeOt	8.60	7.35	7.47	8.23	7.21	7.37	7.49	7.47	7.06	7.67
MnO	0.15	0.14	0.14	0.16	0.13	0.13	0.13	0.13	0.11	0.15
MgO	7.41	13.40	15.25	10.44	12.35	13.27	12.21	11.65	11.81	11.07
CaO	9.39	9.11	8.86	10.29	8.78	9.25	8.57	8.64	8.32	8.84
Na₂O	3.20	2.60	2.12	2.63	3.83	3.85	3.45	3.51	3.28	3.23
K₂O	3.02	3.69	3.05	2.64	2.48	2.55	3.01	3.11	3.58	2.98
P₂O₅	0.76	0.91	0.71	0.74	1.31	1.02	1.23	1.27	1.32	1.05
L.O.I.	0.39	0.87	0.55	0.75	2.23	0.29	1.99	1.84	1.96	1.46
SUM	99.70	99.21	99.46	99.48	98.67	99.17	99.01	98.94	98.90	98.72
XRF (ppm)										
Cr	313	844	1280	580	805	755	655	658	265	700
Ni	82	449	506	192	506	392	344	406	436	272
Cu	50	62	39	74	50	71	82	100	90	41
Zn	84	81	74	69	83	72	84	85	80	83
Rb	38	32	21	16	62	37	51	49	73	31
Sr	1220	2142	1715	1464	1670	2308	2342	2456	3079	2273
Y	27	18	16	18	19	23	22	23	29	22
Zr	346	251	215	188	411	312	404	413	554	347
Nb	11	6	6	10	14	11	14	15	16	9
Ba	-	-	-	1117	-	2009	2425	-	-	2162

Table 4.2 A subset of whole-rock ICP-MS and XRF analyses for the alkaline cinder cones from Luhr and Carmichael (1981).

The full datasets for the cinder cones are given in Appendix I, and details of the analytical techniques are given in Appendix D.

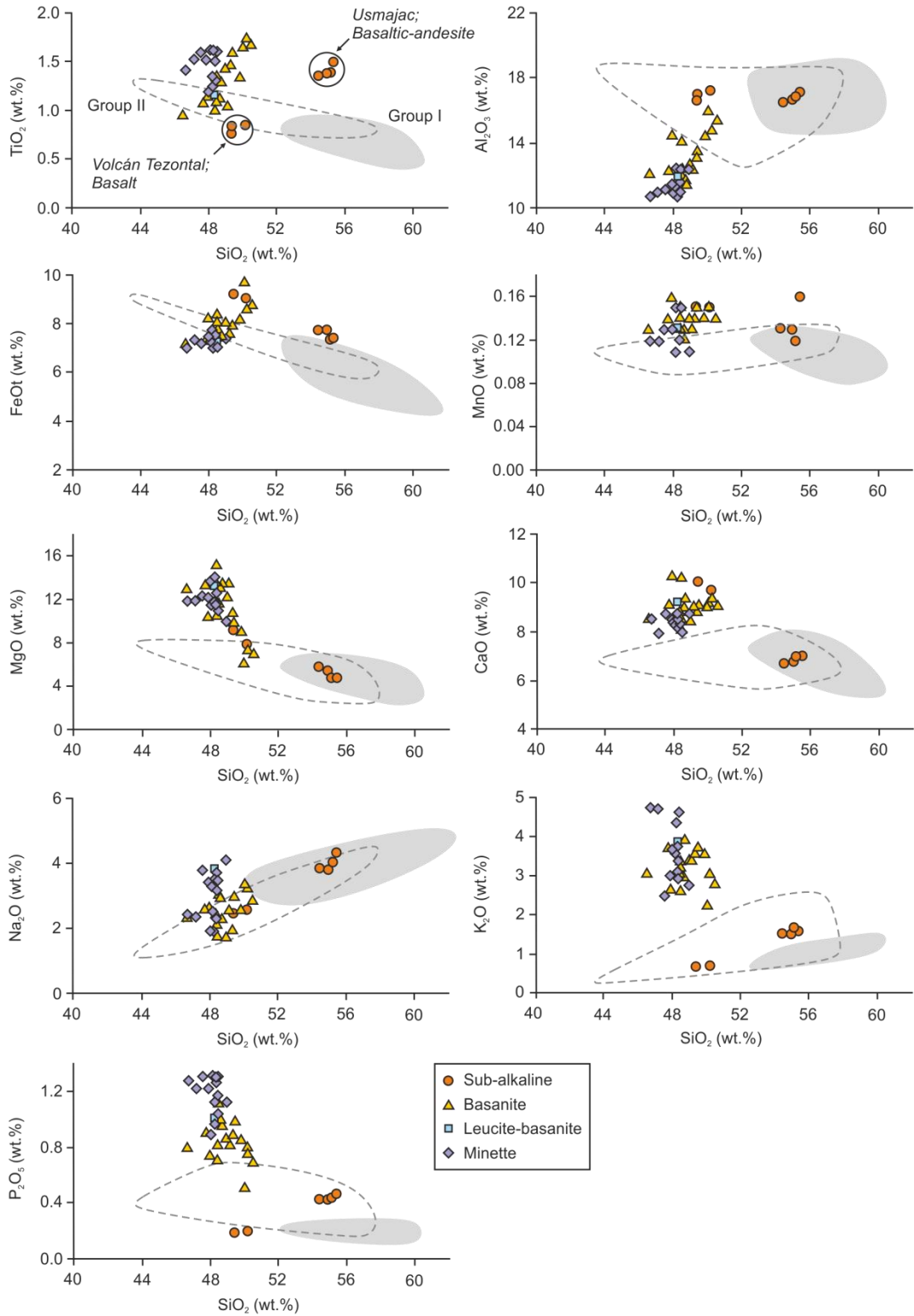


Figure 4.4 Whole-rock major element variation diagrams for the cinder cone magmatic rocks.

Compiled using data from Luhr and Carmichael (1981), Carmichael et al. (2006), Vigouroux et al. (2008), Maria and Luhr (2008) and Cai (2009). The grey shaded area represents the Group I deposits, and the field outlined by the dashed line represents the Group II eruption deposits. The sub-alkaline cinder cone samples lie within the compositional fields of the Group I and/or Group II eruption deposits. The alkaline magmas form a distinct group which do not lie on the same trend as the Group I and II deposits, indicating the alkaline and sub-alkaline magmas cannot be linked by fractional crystallisation.

The full geochemical datasets are given in Appendix I, and the analytical techniques are described in detail in Appendix D. Table 4.2 reports data for a subset of ten samples from Luhr and Carmichael (1981), spanning the series from basanite to minette.

4.2.1 Major Elements

The alkaline cinder cone deposits are characterised by low SiO₂ and Al₂O₃, and high TiO₂, MnO, MgO, CaO, K₂O and P₂O₅ (Figure 4.4). These magmatic rocks show relatively little variation in SiO₂ content (47.6 – 50.3 wt.%), but show large variations in MgO (7.4 – 15.3 wt.%), K₂O (2.5 – 4.4 wt.%) and P₂O₅ (0.7 – 1.3 wt.%; Figure 4.4). The high MgO, K₂O and P₂O₅ contents are reflected in the mineralogy, with mineral assemblages dominated by mafic minerals, and the presence of phlogopite, sanidine and apatite phenocrysts and microphenocrysts (Figure 4.3).

The major element geochemistry for the Group I and Group II eruption deposits shows overall differentiation trends from a mafic parent magma (see Sections 2.4 and 3.4). Samples from the two sub-alkaline cinder cones form two clusters, generally lying within the compositional fields of the Group I and II eruption deposits, suggesting a link between these magmas. The alkaline cinder cones, however, form a distinct group that lies off this trend indicating a separate source or fractionation trend (Figure 4.4). The major elements show the CVC Group I and Group II magmas and the alkaline cinder cone magmas cannot be linked by fractional crystallisation. However, the composition of the basaltic cinder cone, Volcán Tezontal, lies along the trend displayed by the alkaline cinder cones (Figure 4.4). This indicates there is a petrogenetic relationship between high-K alkaline and medium-K, sub-alkaline magmas at the CVC.

4.2.2 Trace Elements

The basanites to minettes are primitive magmas with high Cr and Ni contents of 195 – 1300 ppm and 200 – 500 ppm respectively (Figure 4.5). These abundances of Cr and Ni are significantly higher than in the basalts to andesites of the Group I and Group II eruption deposits. Again this is reflected in the mineralogy, with mafic minerals dominating the assemblage of the alkaline cinder cone scoria (see Section 4.1).

The N-MORB normalised trace element abundance patterns of the alkaline cinder cones reveal that these magmas have a typical subduction-related signature with elevated LILE (Rb, Ba, K, Sr ± Th) relative to HFSE (Nb, Ta, Ti, Hf, Zr, Y ± P; Figure 4.6a). The cinder cone deposits display strong enrichments in the majority of the incompatible elements relative to the Group I eruption deposits, and less so relative to the Group II units. The fluid mobile elements (Rb, Ba and K) show stronger enrichments than the less mobile elements (Figure 4.6a).

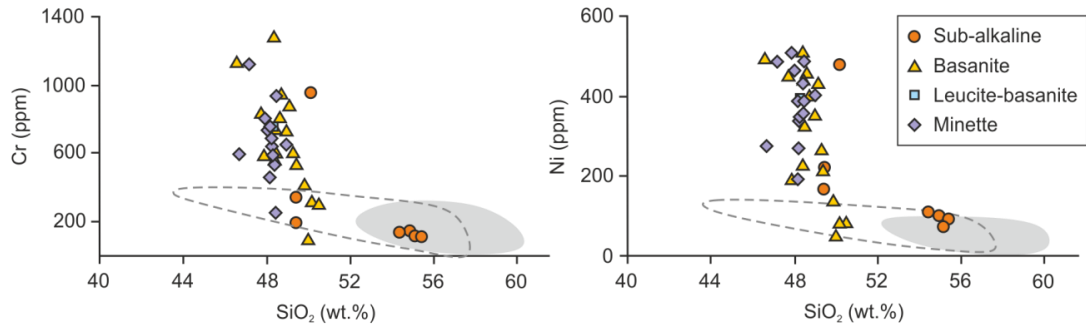


Figure 4.5 Compatible whole-rock trace elements, Cr and Ni versus SiO₂ for the cinder cone magmas.

The Group I and II eruption deposits are shown by the shaded area and dashed line, respectively. The alkaline cinder cones are primitive magmas indicated by their high Cr and Ni contents.

A Chondrite-normalised REE abundance plot reveals that the LREE (La, Ce, Pr and Nd) are strongly enriched relative to the MREE and HREE (Sm to Lu), and the Group I eruption deposits (Figure 4.6b). The abundances of the REE in the Group II eruption deposits overlap the abundances in the alkaline cinder cone magmas, and have similar patterns (Figure 4.6b).

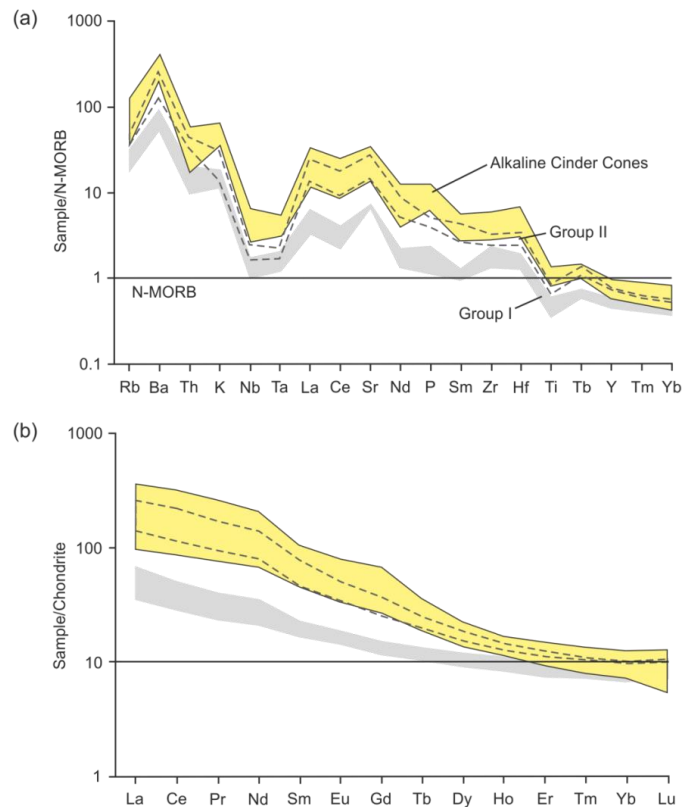


Figure 4.6 N-MORB normalised trace element and Chondrite-normalised REE abundance diagrams for the alkaline cinder cone magmas.

Normalising values are from Sun and McDonough (1989) and Nakamura (1974) for N-MORB and Chondrite, respectively. The fields for the Group I and Group II eruption deposits are indicated. The cinder cone magmas display characteristic subduction-related trace element abundances with enriched LILE relative to HFSE. Samples from Group II overlap the cinder cone magma field suggesting a link between the suites of samples.

4.3 Whole-rock Sr and Nd Isotopes

The $^{87}\text{Sr}/^{86}\text{Sr}$ and $^{143}\text{Nd}/^{144}\text{Nd}$ isotopic compositions of four of the alkaline cinder cones were analysed as part of Yue Cai's PhD at the Lamont-Doherty Earth Observatory of Columbia University (Cai, 2009). No new isotopic data for the alkaline cinder cones were analysed in this study.

Sample	Cone	Composition	$^{87}\text{Sr}/^{86}\text{Sr}$ (2σ error)	$^{143}\text{Nd}/^{144}\text{Nd}$ (2σ error)
1004-500	Apaxtepec	Basanite	0.70385 ± 3	0.51286 ± 1
SAY-101B	Telcampana	Basanite	0.70383 ± 3	0.51287 ± 1
SAY-7E	El Carpintero Norte	Minette	0.70417 ± 3	0.51277 ± 1
SAY-8H	Comal Chico	Minette	0.70381 ± 3	0.51283 ± 1

Table 4.3 $^{87}\text{Sr}/^{86}\text{Sr}$ and $^{143}\text{Nd}/^{144}\text{Nd}$ isotope data for the alkaline cinder cones (Cai, 2009).

Isotopic ratios are reported to a 2σ error of 3×10^{-5} for $^{87}\text{Sr}/^{86}\text{Sr}$ and 1×10^{-5} for $^{143}\text{Nd}/^{144}\text{Nd}$ (Cai, 2009).

The cinder cone magmas have more radiogenic $^{87}\text{Sr}/^{86}\text{Sr}$ (0.70381 to 0.70417) and less radiogenic $^{143}\text{Nd}/^{144}\text{Nd}$ (0.51277 to 0.51287; Table 4.3) relative to the Group I eruption deposits and the majority of the Group II units (Figure 4.7). The cinder cone samples display little variation in SiO_2 with $^{87}\text{Sr}/^{86}\text{Sr}$ and $^{143}\text{Nd}/^{144}\text{Nd}$ (Figure 4.7). The range of isotopic composition over a narrow whole-rock geochemical composition range indicates open-system processes such as mixing of isotopically distinct magmas or crustal contamination rather than fractional crystallisation.

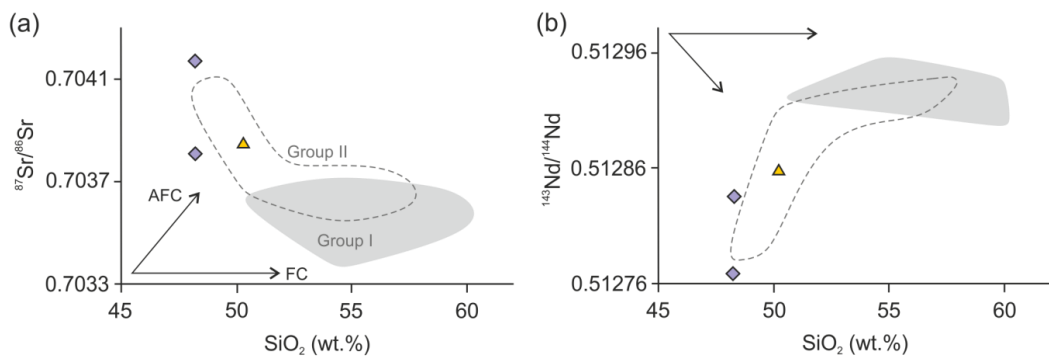


Figure 4.7 $^{87}\text{Sr}/^{86}\text{Sr}$ and $^{143}\text{Nd}/^{144}\text{Nd}$ versus SiO_2 for the alkaline cinder cone magmas.

The isotopic data are taken from Cai (2009). The fields for the Group I and Group II eruption deposits are indicated by the grey shaded area and the area defined by the dashed line, respectively. The cinder cone samples have more radiogenic Sr and less radiogenic Nd than the majority of the CVC explosive eruption deposits. No whole-rock major element data are available for one of the minettes (sample SAY-101B).

Two samples from unit F of the Group II eruption deposits have similar isotopic compositions to two of the alkaline magmas consistent with a common source or mixing event (Figure 4.7). This is supported by the whole-rock major element data, which shows that the Group I and Group II magmas, and the alkaline magmas cannot be linked by fractional crystallisation, and the incompatible trace element abundances which link the Group II eruption deposits and the cinder cones. The relationship between these deposits is examined in Chapter 5.

The variation of $^{87}\text{Sr}/^{86}\text{Sr}$ versus $^{143}\text{Nd}/^{144}\text{Nd}$ for the Group I and II eruption deposits, and the alkaline cinder cones shows all the CVC magmas fall within the mantle array (Zindler and Hart, 1986). Collectively, the CVC magmas appear to define a trend away from the estimated mantle wedge composition (Nimz et al., 1995; Gómez-Tuena et al., 2007a) towards a more enriched component (Figure 4.8), with the alkaline cinder cone magmas having a more enriched isotopic signature.

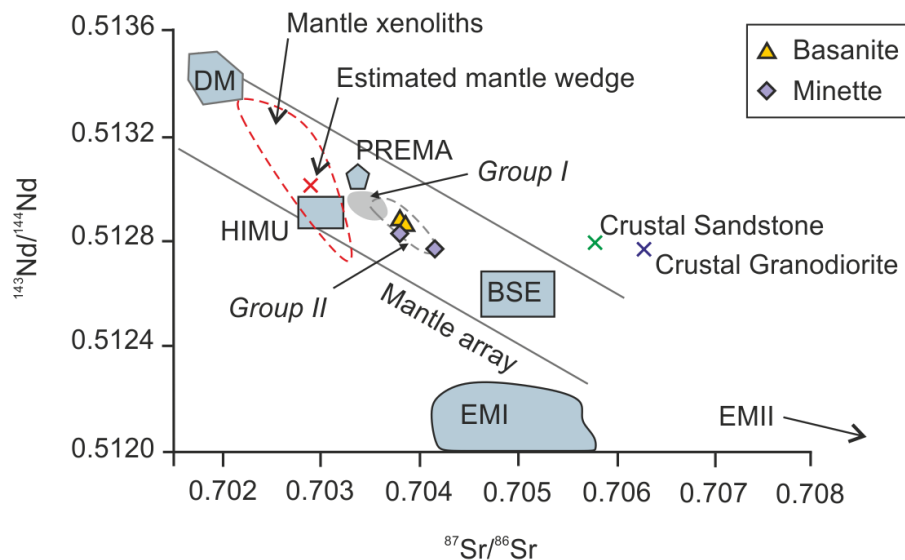


Figure 4.8 $^{87}\text{Sr}/^{86}\text{Sr}$ versus $^{143}\text{Nd}/^{144}\text{Nd}$ for the alkaline cinder cones.

The fields for the various mantle reservoirs after Zindler and Hart (1986) are also plotted together with values for the mantle wedge under the TMVB (Nimz et al., 1995; Gómez-Tuena et al., 2007a) and the western Mexico granodioritic crust (Verma and Luhr, 2010) and sandstone basement (Centeno-García et al., 1993). The isotopic compositions of the Group I (light grey area) and the Group II (area outlined by dashed line) eruption deposits are indicated. See Section 2.5 for a discussion of the mantle reservoirs.

4.4 Models of Alkaline Cinder Cone Magma Source

Various studies have proposed that the alkaline magmas are derived from an enriched mantle source associated with the subduction of the Rivera and Cocos plates beneath the North American plate (Wallace and Carmichael, 1989; Luhr, 1997; Ferrari et al., 2001; Carmichael et

al., 2006; Maria and Luhr, 2008; Vigouroux et al., 2008; Cai, 2009). However, the cause of the enrichment is debated in the geological literature. Cai (2009) proposed a source enriched by lower crustal material eroded off the continental crust after von Huene et al. (2004), while previous models suggested hydrous enrichment of the sub-arc mantle forming phlogopite-, amphibole-, apatite-bearing pyroxenite veins (Wallace and Carmichael, 1989; Luhr, 1997; Ferrari et al., 2001; Maria and Luhr, 2008; Vigouroux et al., 2008). These two models of mantle enrichment are described in this section, and are evaluated with respect to the collated cinder cone data presented here, and the Group I and Group II CVC eruption deposits in the following chapter.

4.4.1 Mantle Metasomatism

Studies of melt inclusions within olivine crystals from the alkaline and sub-alkaline cinder cones reveal H₂O contents of up to 7 wt.% and 5.5 wt.%, respectively (Maria and Luhr, 2008; Vigouroux et al., 2008). These high water contents led Vigouroux et al. (2008) to propose hydrous enrichment of the mantle wedge. Vigouroux et al. (2008) demonstrated that the presence of metasomatic minerals such as phlogopite, apatite and augite in the source buffered the concentrations of K, P, Ti, Nb and Ta during partial melting (Figure 4.9), while Wallace and Carmichael (1989) showed that the Colima minettes were generated at pressures of >15 kbar (>45km depth), from a source containing olivine, phlogopite and augite by comparing minette compositions with experimental phase equilibria.

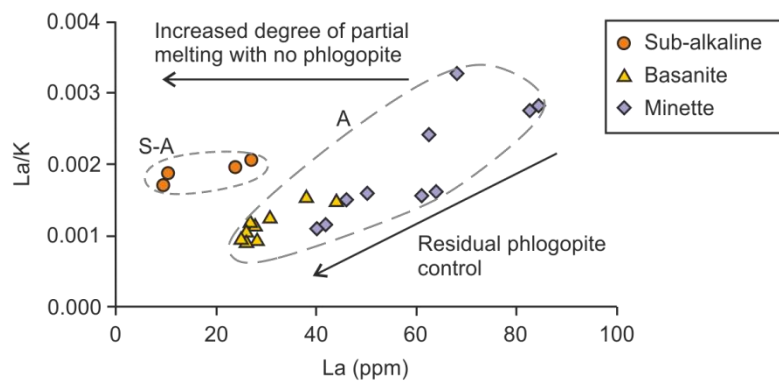


Figure 4.9 La/K versus La (ppm) showing the control of residual phlogopite in the source during partial melting after Vigouroux et al. (2008).

La is highly incompatible therefore readily enters the melt during partial melting. As melting increases, the concentration of La decreases in the melt as it becomes more diluted. The presence of residual phlogopite in the source buffers K resulting in a decrease in La/K. If there is no residual phlogopite in the source, both La and K decrease as melting increases thereby maintaining a constant La/K ratio. The sub-alkaline (S-A) cinder cones follow a trend consistent with no residual phlogopite in the source; while the alkaline (A) cinder cones follow a trend of residual phlogopite control.

Several models have been proposed whereby metasomatic veins are formed by fluids released from the dehydration of hydrous minerals within the subducting slab at shallow depths (Wallace and Carmichael, 1989; Luhr, 1997; Maria and Luhr, 2008; Vigouroux et al., 2008). Figure 4.10 is a cartoon of a subduction zone showing the formation of lamprophyric melts through hydrous enrichment of the mantle wedge, based on the aforementioned studies. The models propose that subduction-related fluids react with the mantle, forming enriched phlogopite-pyroxenite veins at shallow depths which are then advected by slab-drag or mantle corner flow to depths of 90 to 100 km. At these depths, the veins partially melt forming lamprophyric melts that rise and penetrate the overlying crust (Luhr, 1997; Maria and Luhr, 2008; Vigouroux et al., 2008).

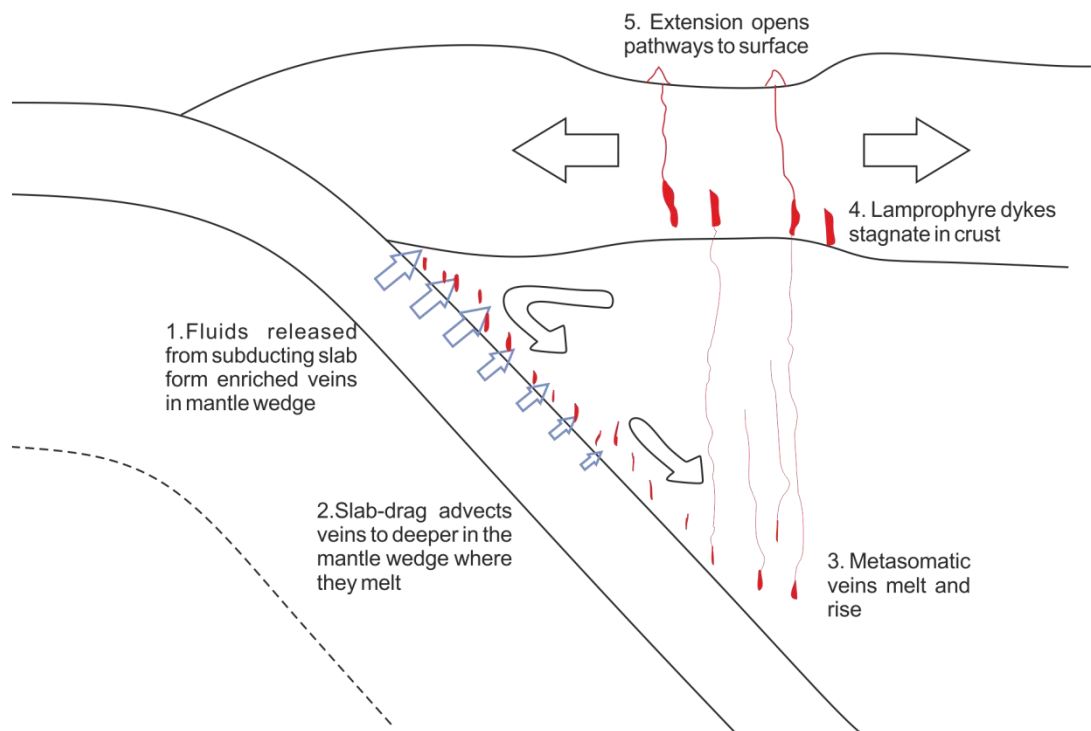


Figure 4.10 Cartoon of a subduction zone showing the model for the formation of the alkaline cinder cones involving metasomatism of the mantle wedge.

Based on the models of Wallace and Carmichael (1989), Luhr (1997), Maria and Luhr (2008) and Vigouroux et al. (2008) 1. Dehydration of hydrous minerals in the subducting slab at shallow levels releases water which reacts with the overlying mantle wedge, and forms enriched veins. 2. Flow caused by slab-drag advects the veins to deeper parts of the mantle wedge where they melt (3) and rise up through the mantle. The melts typically stagnate in the crust forming lamprophyre dykes (4); however, the extension at the CVC creates pathways to the surface, resulting in the formation of cinder cones.

Luhr (1997) proposed that lamprophyric melts, resulting from metasomatism of the sub-arc mantle, are common in subduction zone settings, but stagnate in the crust forming dykes. The back-arc extension that formed the Colima Rift is thought to have facilitated the rise of the

lamprophyric melts directly to the surface, by opening pathways through which the melt could rise (Luhr, 1997; Ferrari et al., 2001; Maria and Luhr, 2008; Vigouroux et al., 2008). In these models the minettes are direct metasomatic vein melts, with the transition to basanite resulting from a dilution of the vein melts by peridotite (wall-rock) mantle melts of more typical arc-type composition (Foley, 1992; Maria and Luhr, 2008).

Alkaline cinder cones and lavas are also found near the towns of Mascota, Los Volcanes, Ayutla and Tapalpa within grabens of the Jalisco Block (Figure 4.11; Wallace and Carmichael, 1989; Lange and Carmichael, 1990; Carmichael et al., 2006; Maria and Luhr, 2008). Alkaline lamprophyric lavas are also present in the Colima rift walls, which are older than the alkaline cinder cones, dated at 4.6 Ma to 0.6 Ma (Allan and Carmichael, 1984). Lavas with a geochemical signature similar to that of intra-plate basalts or ocean-island basalts (OIB) are also present in the western TMVB (Luhr, 1997; Ferrari et al., 2001; Maria and Luhr, 2008).

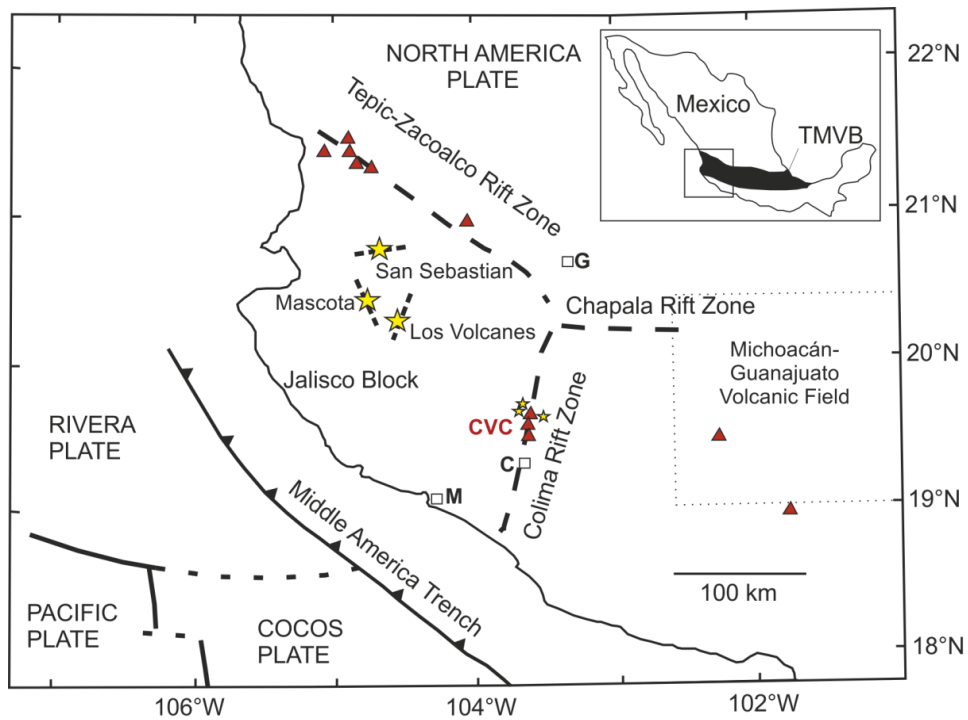


Figure 4.11 Simplified map of the western TMVB.

The map shows the location of the sub-alkaline volcanic centres (red triangles) and alkaline cinder cones and lavas (yellow stars) after Maria and Luhr (2008) and Lange and Carmichael (1990). Medium-K, sub-alkaline volcanism in the western TMVB is focused along the major rift zones (Colima and Tepic-Zacoalco Rifts). As well as in the CVC, alkaline cinder cones and lavas are found in graben within the Jalisco block at Los Volcanes, San Sebastian and Mascota.

During the last 8.5 Myr, the volcanic front has migrated ~80 km trenchward (Ferrari, 2004; Gómez-Tuena et al., 2007b; see Section 1.3.2). Intra-plate basalts were emplaced during a

period of stalled subduction of the Rivera plate 7.2 - 4.8 Ma (Ferrari et al., 2001). Ferrari et al. (2001) showed that these basalts have trace element abundances indicative of derivation from an enriched mantle source, but also have a subduction component revealed by high Ba/Zr and Ba/Ce ratios. The authors proposed a model whereby these intra-plate basalts were produced by small amounts of partial melting of a heterogeneous mantle, metasomatised to different extents by a fluid-rich subduction component, that can rise up through the crust fast enough not to freeze at depth. At the end of the Miocene, decreased convergence led to lateral flow of deep asthenosphere into the vertically opening mantle wedge, causing slab roll-back, the formation of heterogeneous mantle, and the migration of the volcanic front towards the trench (Ferrari et al., 2001; Ferrari, 2004).

Based on the work of Ferrari et al. (2001) and Ferrari (2004), Vigouroux et al. (2008) proposed a model for the formation of the alkaline magmas at the CVC, whereby metasomatic veins rich in phlogopite formed in the fore-arc mantle wedge and in deeper parts of the wedge when the plate was shallow dipping, and the volcanic front was further away. Slab dip increased at ~8.5Ma (Ferrari, 2004), advecting the veins downward and towards the trench by corner flow caused by slab roll-back (Luhr, 1997; Maria and Luhr, 2008; Vigouroux et al., 2008). Continued fluid-fluxing and melting of the veins and surrounding mantle by arc-parallel flow of hot mantle through the tear between the slabs (see Section 1.2.3) produced potassic melts beneath the entire western TMVB (Vigouroux et al., 2008). Extension associated with the upwelling hot mantle through the tear focused the potassic melts in the Colima and Tepic-Zacoalco grabens; therefore extension provided pathways for the melts rather than produced the melts by decompression melting (Luhr, 1997; Ferrari et al., 2001; Vigouroux et al., 2008).

4.4.2 Subduction Erosion

Cai (2009) favoured enrichment of the sub-arc mantle by lower crustal material eroded from the base of the overriding plate. Based on whole-rock trace element and Sr-Nd-Pb-Hf isotope data, she argued that the proposed hydrous enrichments are not enough to generate the lamprophyric alkaline magma compositions. Using an estimated residual mantle composition Cai (2009) modelled the composition of an enriched mantle source by the addition of 5% subduction zone fluid, and 5% composite slab melt involving altered oceanic crust (AOC) and subducted sediments. The residual mantle composition was estimated from mafic, high Nb magmas from the Sierra-Chichinatuzin Volcanic Field after Gómez-Tuena et al. (2007a; see Section 2.5.1). The fluid component was calculated at 90% altered oceanic crust (AOC) and 10% sediments, and the composite slab melt was calculated from 90% AOC melt and 10% sediment melt (Cai, 2009). The results revealed that the addition of subduction zone fluids could not reproduce the most primitive sub-alkaline or alkaline magmas, while 5% addition of slab melt could reproduce the proposed sub-alkaline source, but not the alkaline lamprophyric melts (Cai, 2009).

Similarly, Cai (2009) concluded, high degree melting of subducted sediments could not reproduce the Nd-Hf-Pb isotopic ratios of the alkaline magmas. The author therefore proposed that the enrichment cannot have come from the subducted slab, but rather lower crustal material eroded off the overlying continental crust, which Cai (2009) suggested would have similar Nd-Hf-Pb isotopic composition to the source of the alkaline magmas. Figure 4.12 is a cartoon of subduction erosion based on the model of von Huene et al. (2004) and Cai (2009).

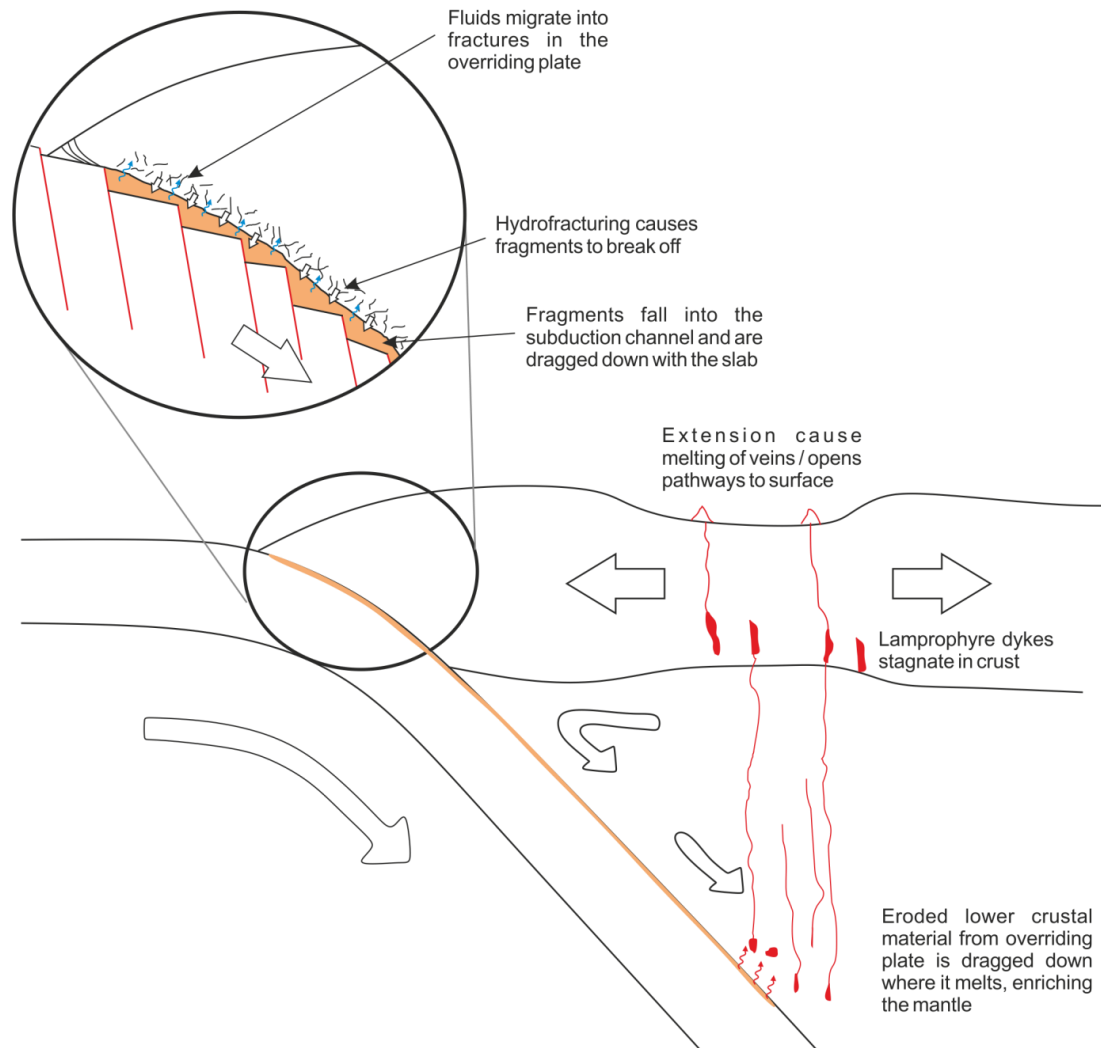


Figure 4.12 Cartoon of the subduction erosion model after von Huene et al. (2004).

Fluids released from subducting sediments migrate into fractures in the overriding plate. This causes pieces to break off and become incorporated into the subduction channel which carried sediments down into the mantle. Cai (2009) proposed the mantle becomes enriched by eroded lower crustal material from the overriding plate, and that this enriched mantle is the source of the alkaline cinder cones at the CVC.

Fluids released from subducting trench sediments migrate into fractures in the overriding plate, causing fragments to break off and become incorporated into the subduction channel, and are

dragged down with the slab (von Huene et al., 2004). The subduction channel is the zone at the interface between the two plates which comprises oceanic and terrigenous sediments which are carried down into the mantle by the subducting slab (Cloos and Shreve, 1988).

These sediments and eroded crustal material are carried down into the mantle where they melt and enrich the mantle. Cai (2009) proposed that mantle enrichment by lower crustal material can best explain the trace element abundances and isotopic compositions of the alkaline cinder cone magmas. The plausibility of these models with respect to the CVC data are tested in Chapter 5.

4.5 Summary

Located on the Colima Rift floor, to the east and west of Volcán Cántaro, are nine monogenetic alkaline cinder cones that erupted contemporaneously with the sub-alkaline volcanism of Nevado de Colima (473-62 ka). The alkaline magma compositions form a transitional series from basanite to minette characterised by the appearance and increasing abundance of phlogopite, sanidine, leucite and apatite. Two calc-alkaline cinder cones erupted 545 ka and 1.2 Ma. One of these is Volcán Tezontal, the proposed parent magma of the calc-alkaline CVC eruption deposits (see Section 2.4).

Whole-rock major element geochemical data reveal these are high-Mg, K₂O, P₂O₅ magmas reflected in their mineralogy by the presence of olivine, clinopyroxene, phlogopite, sanidine and apatite. Major element variation diagrams reveal that the calc-alkaline cinder cone samples lie within the CVC Group I and Group II compositional fields, while the alkaline cinder cone samples form their own distinct group which cannot be related to the medium-K sub-alkaline deposits through fractional crystallisation. The whole-rock trace element data reveal the alkaline magmas are primitive, subduction-related magmas with strong enrichments in the incompatible elements relative to the Group I magmas. The trace element abundance patterns partially overlap with the Group II eruption deposits with elevated LILE and LREE.

Radiogenic isotope data reveal variations in ⁸⁷Sr/⁸⁶Sr and ¹⁴³Nd/¹⁴⁴Nd over a narrow range of SiO₂ contents (and 1/Sr and 1/Nd), indicating a heterogeneous source, mixing of isotopically distinct magmas or crustal assimilation. The isotopic composition of the alkaline cinder cone magmas and the Group II eruption deposits overlap; they also have similar the incompatible trace element abundances. The whole-rock geochemistry reveals the high-K alkaline and medium-K sub-alkaline magmas cannot be linked by fractional crystallisation, therefore, the overlapping ⁸⁷Sr/⁸⁶Sr and ¹⁴³Nd/¹⁴⁴Nd ratios and trace element abundances are likely to reflect mixing.

Models for the petrogenesis of the alkaline magmas propose an enriched mantle source consisting of either phlogopite-pyroxenite veins within the sub-arc mantle wedge formed by hydrous enrichment from the subducting Rivera plate, or enrichment by eroded lower crustal material from the overriding continental plate. Whole-rock geochemistry reveals a mafic mantle-derived parental magma for the Group I and II eruption deposits; however, the mineralogy (the presence of phlogopite; see Section 3.2) and trace element and isotope geochemistry reveal distinctions in the Group II eruption deposits that can be linked to the alkaline cinder cone magmas. The relationship between the Group I and Group II Holocene explosive eruption deposits and the alkaline cinder cones is explored in the following chapter.

5 Petrogenesis of the Colima Volcanic Complex Magmas

The Holocene eruptive history of the CVC is dominated by medium-K, sub-alkaline volcanism from the Paleofuego and Volcán de Colima vents. In the previous Chapters, the explosive tephra fallout deposits have been described in detail, and based on mineralogy and whole-rock geochemistry, have been divided into two distinct groups, which although petrogenetically linked, cannot be related by simple differentiation from a common parental mantle melt (Section 3.4). Chapter 4 presents geochemical and petrological models for alkaline and calc-alkaline magmas which formed cinder cones on the Colima rift floor 1.2 Ma to 62 ka. The data for the alkaline magmas show a strong correlation with the Group II high-K sub-alkaline eruption deposits, with mineralogical, whole-rock major element, trace element and isotopic similarities.

This chapter considers the nature of the possible link between the CVC eruption deposits and the alkaline cinder cone magmas. In addition, it aims to investigate the open-system processes occurring in the magmatic plumbing system through mineral chemistry and zoning patterns (Sections 2.2 and 3.2). Geochemical modelling is used to explore magma mixing processes using the whole-rock geochemical and Sr-Nd isotope data, together with data from the literature.

The final part of this chapter brings together the modelling with the mineral chemistry and zoning patterns observed in Group I and Group II tephra (Chapters 2 and 3), and geophysical data to generate a schematic model of the origin of the CVC magmas, and the nature of the magmatic plumbing system beneath the CVC.

5.1 Source of the CVC Magmas

The magmatic activity of the CVC is controlled by the subduction of the oceanic Rivera and Cocos plates beneath the continental North American plate (Gómez-Tuena et al., 2007b; see Section 1.2). The tectonic setting of the western TMVB is complex with convergence and extensional regimes resulting in both sub-alkaline and alkaline magmatism, as discussed in Chapter 1 (Luhr and Carmichael, 1981; Luhr and Carmichael, 1985; Allan, 1986; Ferrari and Rosas-Elguera, 2000; Ferrari, 2004; Gómez-Tuena et al., 2007b; Soto et al., 2009; Yang et al., 2009; Ferrari et al., 2012).

The CVC is dominated by the stratovolcanoes of Volcán Cántaro, Nevado de Colima, Paleofuego and Volcán de Colima, with a total estimated erupted volume of $\sim 490 \text{ km}^3$ (Cortés et al., 2010). Alkaline magmas erupted as monogenetic cinder cones on the Colima Rift floor, to the east and west of Volcán Cántaro, with a much lower total estimated volume of $\sim 1.3 \text{ km}^3$ with respect to the main CVC sub-alkaline volcanism (Carmichael et al., 2006).

Both the medium-K sub-alkaline and high-K alkaline magmas are subduction-related, as revealed by the incompatible whole-rock trace element abundance patterns, which show coupled LILE enrichment and Nb-Ta depletions typical of hydrous slab components (see Sections 2.4 and 4.2). However, the alkaline magmas display much stronger enrichments in incompatible trace elements, such as the LREE, relative to the sub-alkaline erupted products, suggesting a highly enriched source, which is discussed in detail below (Luhr and Carmichael, 1981; Wallace and Carmichael, 1989; Lange and Carmichael, 1990; Luhr, 1997; Carmichael et al., 2006; Maria and Luhr, 2008; Vigouroux et al., 2008; Cai, 2009; see also Section 4.2). Whole-rock major element geochemistry also reveals distinctions between alkaline and sub-alkaline magmas, which cannot be explained solely by fractional crystallisation from a common parent magma.

5.1.1 Mexican Mantle Wedge Composition

Verma and Luhr (2010) proposed that the calc-alkaline basalt of Volcán Tezontal could represent the parent magma of the CVC magmas. Whole-rock major and compatible trace element data for the Group I CVC eruption deposits are in agreement with a mafic mantle-derived parent magma, such as sample SAY-22E from the basaltic Volcán Tezontal (see Section 2.4). However, the $^{87}\text{Sr}/^{86}\text{Sr}$ and $^{143}\text{Nd}/^{144}\text{Nd}$ isotopic data (Cai, 2009) reveal SAY-22E has a much lower radiogenic Nd isotopic composition relative to the Group I eruption deposits and cannot therefore be related by fractional crystallisation (Figure 5.1). In addition, SAY-22E lies outside the compositional field of the Mexican mantle xenoliths and the estimated mantle composition of Gómez-Tuena et al. (2007a).

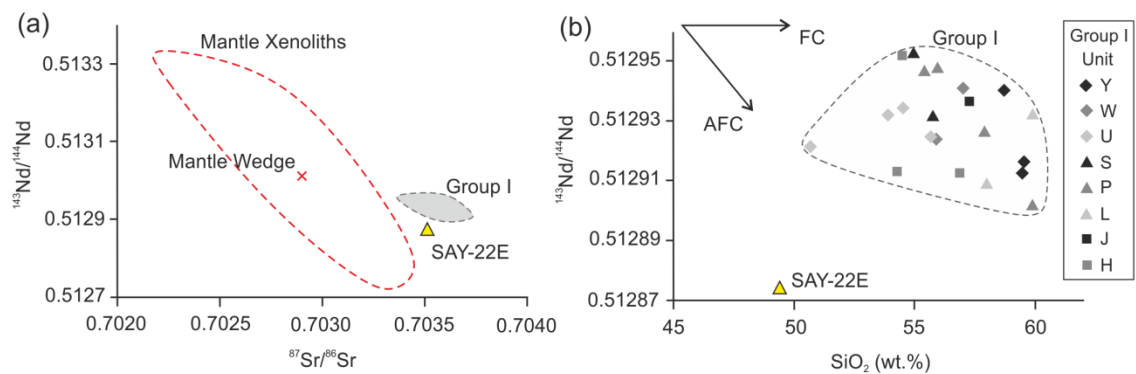


Figure 5.1 (a) $^{87}\text{Sr}/^{86}\text{Sr}$ versus $^{143}\text{Nd}/^{144}\text{Nd}$ isotope diagram and (b) $^{143}\text{Nd}/^{144}\text{Nd}$ versus SiO_2 for the Group I samples and SAY-22E.

The plots show the composition of the Group I CVC eruption deposits with respect to Mexican mantle xenolith data (Liang and Elthon, 1990; Nimz et al., 1995; Mukasa et al., 2007), the estimated Mexican mantle wedge composition of Gómez-Tuena et al. (2007a) and sample SAY-22E from Volcán Tezontal (Verma and Luhr, 2010). Sample SAY-22E lies outside the field of the mantle xenolith compositions. These plots show that SAY-22E cannot be linked to the Group I eruption deposits through fractional crystallisation; therefore SAY-22E cannot represent the mafic parental magma of the CVC sub-alkaline eruption deposits.

Although no mantle xenoliths have been found in the western TMVB, xenoliths of lherzolite, harzburgite, orthopyroxenite and peridotite have been found in other parts of the TMVB and in Northern Mexico (Liang and Elthon, 1990; Nimz et al., 1995; Mukasa et al., 2007). Gómez-Tuena et al. (2007a) also estimated the composition of the Mexican sub-arc mantle wedge based on the primitive, high-Mg, intra-plate type basalts from the central TMVB as described in Section 2.5.1. The estimated mantle composition correlates well with the xenolith data (Figure 5.1).

5.1.2 Sub-alkaline Arc Magma Source

The composition of the mantle underlying the CVC is heterogeneous, with erupted products ranging from typical calc-alkaline arc magmas to primitive alkaline magmas (Luhr and Carmichael, 1980, 1981; Allan and Carmichael, 1984; Lange and Carmichael, 1990; Luhr, 1997; Ferrari et al., 2001; Maria and Luhr, 2008; Vigouroux et al., 2008; Gómez-Tuena et al., 2011). The source of the sub-alkaline magmas is thought to be an originally depleted mantle source subsequently enriched by fluids from the dehydrating slab (Vigouroux et al., 2008; Cai, 2009).

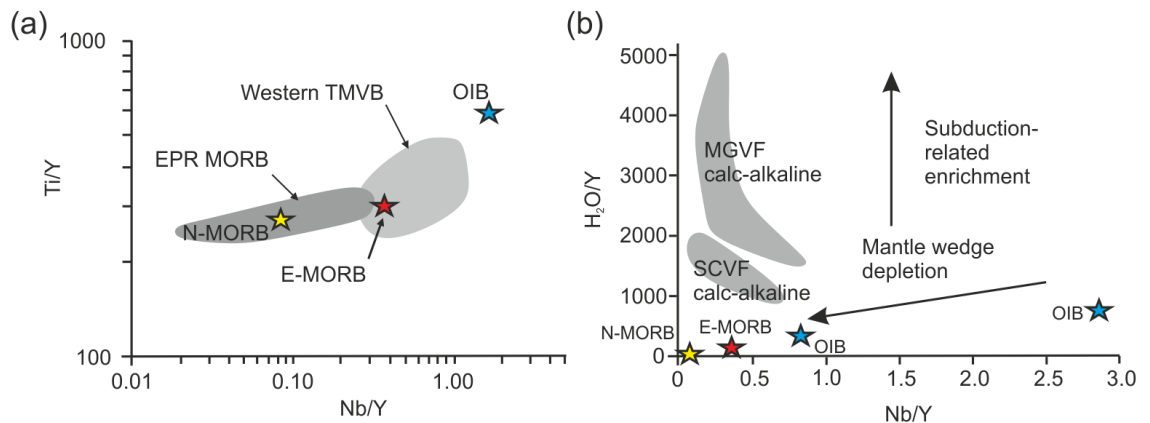


Figure 5.2 Trace element ratio plots showing source enrichments after Vigouroux et al. (2008).

(a) Ti/Y versus Nb/Y plot taken from Vigouroux et al. (2008) showing the composition of calc-alkaline magmas from the western TMVB (Righter et al., 1995; Righter and Rosas-Elguera, 2001; Petrone et al., 2006) along with N-MORB, E-MORB and OIB compositions from Sun and McDonough (1989). (b) Plot of H₂O/Y versus Nb/Y after Vigouroux et al. (2008). The calc-alkaline magmas are derived from a depleted mantle source residue left after the partial melt extraction of OIB, and then underwent subduction-related LILE, LREE and H₂O enrichment (Vigouroux et al., 2008). Vigouroux et al. (2008) took the data for the Michoacán-Guanajuato Volcanic Field (MGVF) from Johnson (2008) and the Sierra Chichinautzin Volcanic Field (SGVF) in central-eastern TMVB from Cervantes and Wallace (2002).

Using ratios of the fluid-immobile elements, Nb, Y and Ti, Vigouroux et al. (2008) showed that the mantle source of western TMVB magmas have a composition broadly similar to that of an

E-MORB mantle source (Figure 5.2a), and demonstrated a depleted mantle source for calc-alkaline magmas from the central TMVB, which was subsequently enriched in LILE and LREE through dehydration of the subducting slab (Figure 5.2b).

Figure 5.3 shows the Ti/Y versus Nb/Y plot of Vigouroux et al. (2008; Figure 5.2a) with the CVC Group I and Group II data and the alkaline cinder cone data. The CVC data points lie between the N-MORB and E-MORB compositions while the alkaline cinder cones lie within the field for the western TMVB magmas, trending towards the OIB composition. Vigouroux et al. (2008) used data from Righter et al. (1995), Righter and Rosas-Elguera (2001) and Petrone et al. (2006) to define the composition of magmas from the western TMVB, which include both alkaline and sub-alkaline erupted magmas.

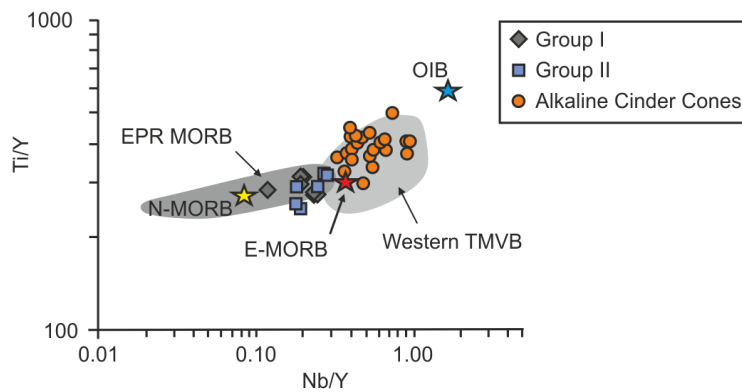


Figure 5.3 Ti/Y versus Nb/Y variation diagram after Vigouroux et al. (2008) with the CVC Group I, Group II and alkaline cinder cone data.

The Group I and Group II samples lie within the EPR-MORB field between the N-MORB and E-MORB compositions. The alkaline cinder cones lie within the compositional field of the western TMVB magmas as defined by Vigouroux et al. (2008).

Similarly, using Nb/Zr ratios, Cai (2009) concluded that the CVC magmas originated from a depleted mantle source, which underwent subduction-related incompatible element enrichment. Intra-plate type basalts, which represent primitive mafic magmas with little evidence of slab contribution, found in the Michoacán-Guanajuato Volcanic Field in the central TMVB, have commonly been used as a proxy to estimate the composition of the Mexican sub-arc mantle (see Section 2.5.1; Gómez-Tuena et al., 2007a; Vigouroux et al., 2008; Cai, 2009). The sub-alkaline magmas have much lower Nb/Zr ratios relative to the intra-plate basalts, reflecting a more depleted mantle source (Cai, 2009). Based on geochemical modelling, as previously discussed in Section 4.4.2, Cai (2009) proposed a depleted mantle source residue for the CVC sub-alkaline magmas left behind after the partial melting which formed the intra-plate basalts. Cai (2009) showed that this was then enriched by the addition of 5% composite slab melt made up of 90% altered oceanic crustal melt and 10% sediment melt.

Enrichments in fluid-mobile LILE (i.e. Rb, Cs, Ba, K, Sr) relative to LREE and HFSE (i.e. La, Ce, Th, Hf, Nb, Ta) are thought to reflect the addition of fluids derived from the subducting slab (Saunders et al., 1991), while high abundances of melt-mobile elements (e.g. Th, Be) are attributed to the addition of sediment melt (Schmidt and Poli, 2004). Depletions in the HREE (i.e. Y, Yb, Lu) reflect the presence of garnet in the source into which these elements are preferentially incorporated (Hanson, 1980; Defant and Drummond, 1990). Covariations of light and middle REE relative to the heavy REE (i.e. Dy/Yb, La/Yb and Sr/Y) are commonly used to trace metamorphosed slab or sediment melt (e.g. Defant and Drummond, 1993; Macpherson et al., 2006; Gómez-Tuena et al., 2007a; Moyen, 2009; Kirchenbaur et al., 2012).

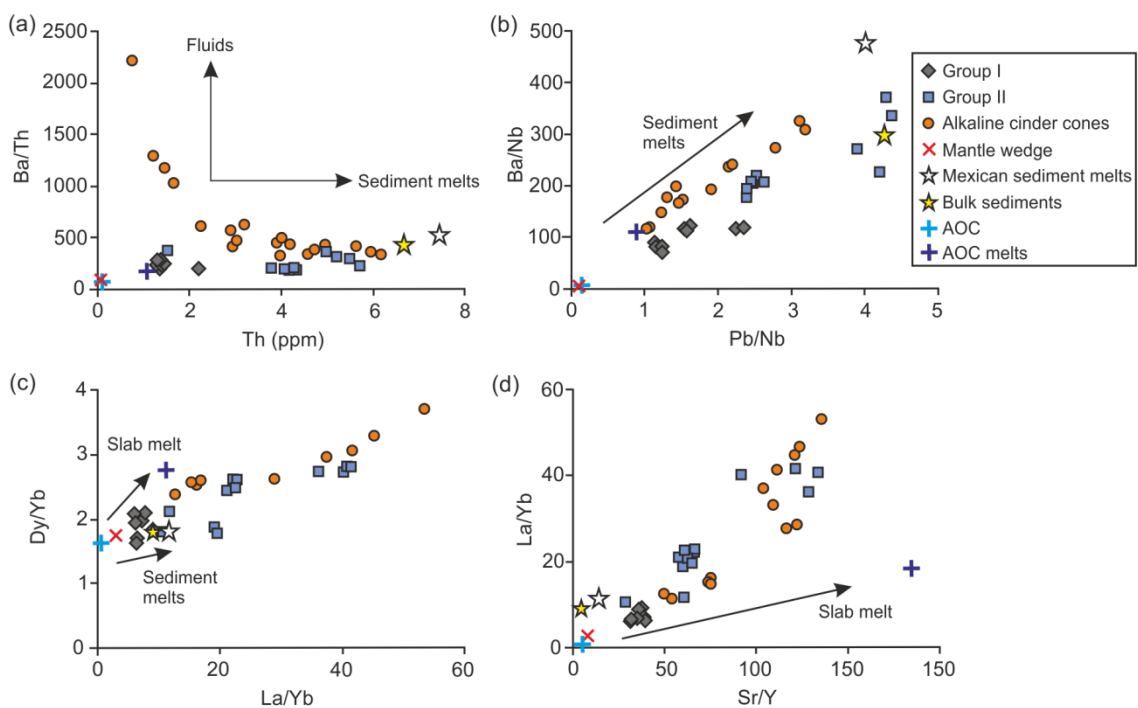


Figure 5.4 Incompatible trace element ratio plots for the CVC magmas.

The plots show the influence of subduction zone fluids, sediments and slab melts on the CVC magmas and the alkaline cinder cone magmas (Luhr and Carmichael, 1981; Carmichael et al., 2006; Maria and Luhr, 2008; Vigouroux et al., 2008; Cai, 2009). Only the mafic (<55 wt.% SiO₂) samples have been plotted to remove the effects of AFC. The Mexican mantle wedge composition is from Gómez-Tuena et al. (2007a). The bulk sediments are from DSDP Site 487 (Gómez-Tuena et al., 2003; LaGatta, 2003), and the sediment melt composition are from Gómez-Tuena et al. (2007a).

Incompatible trace element variation diagrams reveal that the CVC sub-alkaline (Group I) eruption deposits form a cluster with no strong slab-derived fluid or sediment melt component (high Ba/Th, Ba/Nb, Pb/Nb and Th), and no strong slab-melt, or residual garnet signature (high La/Yb and Sr/Y coupled with Dy/Yb; Figure 5.4). However, relative to the mantle wedge composition, these arc magmas are enriched in fluid- and melt-mobile elements (Figure 5.4).

Ratios of incompatible trace elements reveal an enriched source relative to the mantle wedge composition. Both fluid and sediment-melt signatures are displayed by the Group I magmas, which is supported by the characteristic subduction-related trace element signature on an N-MORB normalised multi-element diagram (see Section 2.4.22; Figure 2.39).

The sediment melt component was calculated by Gómez-Tuena et al. (2007a) assuming 5% batch melting of the bulk sediment composition from DSDP Site 487 located off the MAT trench of Acapulco, central Mexico (Gómez-Tuena et al., 2003; LaGatta, 2003). The sediment column in the trench consists of ~170m of hemipelagic, terrigenous sediments and pelagic, hydrothermal sediments (Plank and Langmuir, 1998; Gómez-Tuena et al., 2003; LaGatta, 2003). The bulk sediment composition is enriched in LILE (Rb, Ba, Sr), light and middle REE (La, Ce, Nd, Sm, Dy) and some of the HFSE (Th, Nb, Zr, Y, Yb). These elements are incompatible elements, therefore during melting they enter the melt phase, resulting in a melt highly enriched in these elements. The Mexican bulk sediments and sediment melts are strongly enriched in Th relative to the Mexican mantle wedge (Figure 5.4a). The sediments are also enriched in Ba, resulting in low Ba/Th ratios. Ba is a fluid mobile element, while Th is not, therefore a strong enrichment in Ba/Th ratios can be attributed to the addition of slab-derived fluids. The Ba/Th versus Th variation diagram reveals that the Group I magmas have higher Ba/Th and Th relative to the mantle wedge, trending towards the sediment melt composition (Figure 5.4a). The contribution of sediment to the enrichment of the Group I magmas is shown in Figure 5.4b. Sediments have high Pb and Ba and low Nb concentrations relative to the mantle wedge and altered oceanic crust (AOC; Gómez-Tuena et al., 2007), therefore ratios of these elements are high and can be used to identify a sediment melt signature. The CVC magmas all display enrichments in Ba/Nb and Pb/Nb (Figure 5.4b).

5.1.3 Alkaline Magma Source

There are two principal models for the source of the alkaline CVC magmas, as discussed in Chapter 4. The majority of studies propose a model involving the hydrous enrichment of the sub-arc mantle wedge by slab-derived fluids (Wallace and Carmichael, 1989; Luhr, 1997; Ferrari et al., 2001; Carmichael et al., 2006; Maria and Luhr, 2008; Vigouroux et al., 2008), while Cai (2009) argues against hydrous enrichment, favouring enrichment by the addition of lower crustal material eroded off the base of the overriding continental North American plate during subduction of the Rivera plate, as discussed in Section 4.4.

Cai's model can be tested by mixing the isotopic composition of the Mexican mantle wedge of Gómez-Tuena et al. (2007a) with the isotopic composition of lower crustal xenoliths, following the model of Langmuir et al. (1978; Figure 5.5). No lower-crustal xenoliths have been found in the CVC magmas; however, isotopic data for lower-crustal xenoliths, comprising mid-Cenozoic

(20-40 Ma) mafic (pyroxene) granulites, orthogneiss, paragneiss and scapolite-bearing xenoliths, from other parts of the TMVB and northern Mexico are available (Ruiz et al., 1988; Cameron et al., 1992). These materials have high $^{87}\text{Sr}/^{86}\text{Sr}$ ratios of 0.70493 to 0.70790 and low $^{143}\text{Nd}/^{144}\text{Nd}$ values of 0.51220 to 0.51278 (see Section 2.5.1). The Nd model ages of these xenoliths range from 557 Ma to 1318 Ma; however, through comparisons with Cenozoic volcanic rocks and cumulates from Mexican basalts, Cameron and Robinson (1990) concluded that these lower-crustal xenoliths are consistent with mid-Cenozoic crystallisation ages. The Nd model ages of the CVC eruption deposits range from 307 Ma to 585 Ma.

The alkaline cinder cone magmas have isotopic compositions which trend towards the composition of the lower crustal xenoliths, consistent with the model of Cai (2009). Figure 5.5 shows mixing lines between the estimated composition of the mantle wedge (Gómez-Tuena et al., 2007a) and a pyroxene-granulite xenolith (Cameron et al., 1992), and an orthogneiss xenolith (Cameron et al., 1992). Although the cinder cone magmas follow the mixing trend of the mantle-orthogneiss, only two of the samples lie along the mixing line. None of the CVC magmas lie along the mantle-pyroxene granulite mixing line (Figure 5.5). The strongly convex upwards shape of the line is consistent in all mantle-lower crustal xenolith mixing models bar the orthogneiss shown in Figure 5.5, due to the high Sr and low Nd contents of the xenoliths relative to the mantle wedge.

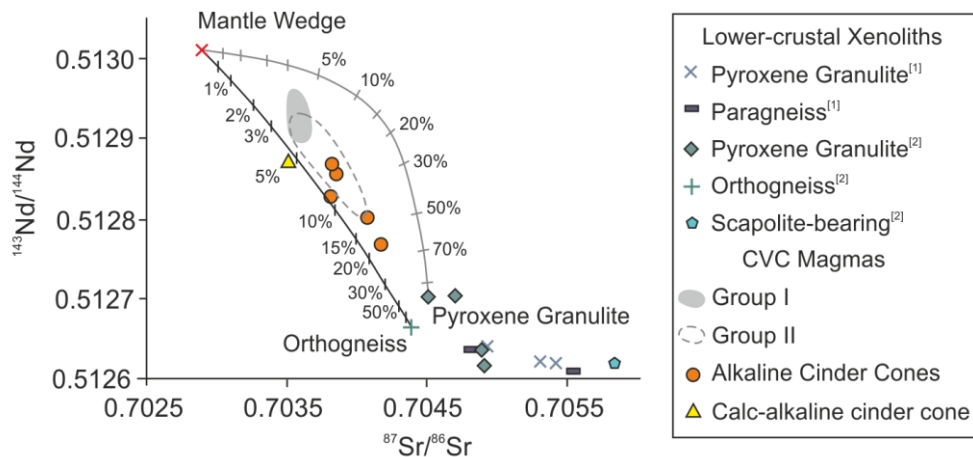


Figure 5.5 $^{87}\text{Sr}/^{86}\text{Sr}$ versus $^{143}\text{Nd}/^{144}\text{Nd}$ isotope diagram showing simple mixing lines between the mantle wedge composition of Gomez-Tuena et al. (2007a) and orthogneiss and pyroxene granulite lower-crustal xenoliths.

Xenolith data are from [1] Ruiz et al. (1988) and [2] Cameron et al. (1992). Although the alkaline cinder cone compositions trend towards the lower crustal xenoliths, only one of the alkaline magmas, and the sub-alkaline cinder cone lie along the mixing line with the orthogneiss xenolith, and none of the samples lie along the pyroxene granulite mixing line.

Based on the available lower-crustal xenolith Sr and Nd isotopic compositions, the alkaline cinder cone magmas are consistent with mantle source enrichment by eroded lower-crustal orthogneiss material; however, enrichment by other lower crustal xenolith compositions (i.e. pyroxene granulite) do not fit the data. Therefore, depending on the composition of the local lower crust this model may explain the enrichments observed in the alkaline cinder cone magmas; however, further information on the composition of the local lower crust is needed.

Trace element ratio plots reveal the alkaline magmas are heterogeneous, displaying fluid and sediment enrichment consistent with the models favouring hydrous enrichment and metasomatism of the mantle wedge (Figure 5.4). High La/Yb and Sr/Y are typically interpreted as “Adakites” resulting from melting of the eclogitised subducting slab leaving behind a garnet-bearing residue (e.g. Defant and Drummond, 1990; Defant and Drummond, 1993; Kelemen et al., 2004), or melting of a garnet-bearing mantle source (e.g. Castillo et al., 1999; Macpherson et al., 2006).

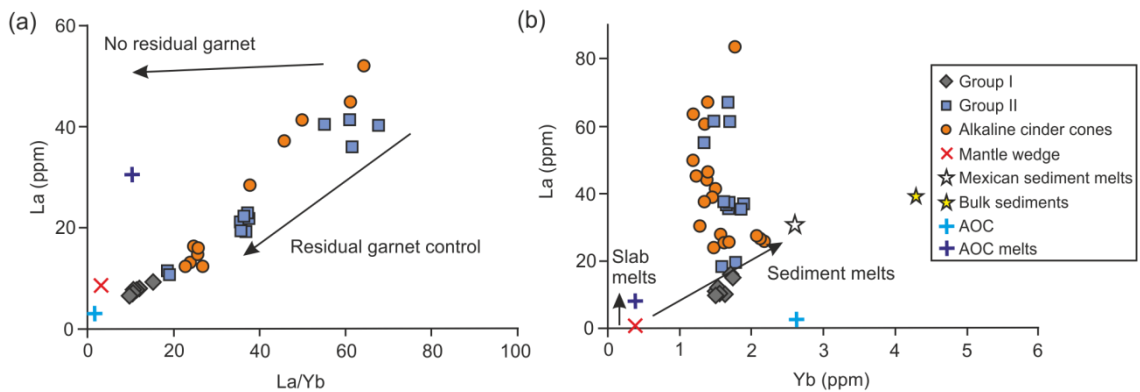


Figure 5.6 Trace elements ratio plots showing the control of residual garnet in the source.

(a) La versus La/Yb variation diagram after Vigouroux et al. (2008) demonstrating the control of residual garnet on the melt composition. As partial melting increases, La and La/Yb decrease as the concentration of La becomes diluted in the melt, and the concentration of Yb is buffered by the presence of garnet. The Group II calc-alkaline and the cinder cone alkaline magmas have these garnet-bearing signatures; however (b) is a plot of La vs. Yb showing a constant Yb in all CVC magmas and a strong enrichment in La in the cinder cones and Group II magmas.

Vigouroux et al. (2008) used a La versus La/Yb variation diagram to demonstrate the presence of residual garnet in the source (Figure 5.6a). La is incompatible in all likely residual mantle phases, therefore, at low degrees of partial melting La becomes concentrated in the melt. The concentration of Yb is buffered by garnet in the source, therefore as melting proceeds, La and La/Yb decrease (Figure 5.6a; Vigouroux et al., 2008). On this diagram, the Group II magmas and the alkaline cinder cones display signatures of a garnet-bearing source. However, high trace element ratios, such as La/Yb in the cinder cones and Group II magmas, can be achieved either

by a strong enrichment in La or by a depletion in Yb. A plot of La vs. Yb for the CVC magmas reveals that the alkaline cinder cones and the Group II magmas are strongly enriched in La relative to the Group I magmas and the mantle wedge, AOC and sediments (Figure 5.6b). The Yb contents show very little variation between all the CVC magmas, indicating the high La/Yb ratios are the result of La enrichment. These magmas do not display the Yb depletions characteristic of residual garnet in the source.

The trace elements reveal the alkaline magmas are highly enriched in incompatible elements related to slab-derived fluids (high Ba/Th) and sediment melts (high Th, Pb/Nb and Ba/Nb). However, some of these enrichments cannot be explained by the simple addition of sediment melts, AOC melts or slab-derived fluids. Very high Sr/Y and La/Yb ratios suggests low percentages of melting of an enriched mantle source as incompatible trace elements readily enter the melt phase and are therefore more concentrated in small percentages of melts.

5.1.3.1 Mantle Enrichment

Investigation into the source of mantle enrichment is beyond the scope of this work; however, it is worth noting the different mechanisms by which mantle enrichment can occur. Enrichment of the mantle may be related to the current subduction of the Rivera plate under the North American plate, resulting from the addition of slab-derived fluids and sediment melts (i.e. Vigouroux et al., 2008) or by subduction erosion (i.e. Cai, 2009), as previously discussed. Marschall and Schumacher (2012) proposed a model of mantle enrichment by the diapiric rise of *mélange* material into the arc magma source region in subduction zone settings. *Mélange* layers form at the slab-mantle interface by metasomatism and shearing, resulting in fragments of slab material mixing with serpentinitised peridotite mantle rocks (Savov et al., 2005; Marschall and Schumacher, 2012; Pabst et al., 2012). Studies of exhumed *mélange* zones (e.g. Sorenson and Barton, 1987; Cloos and Shreve, 1988; Bebout and Barton, 1989; Sorenson and Grossman, 1993; Miller et al., 2009) and seamounts in the Izu-Bonin-Marianas Arc (Savov et al., 2005; Savov et al., 2007; Pabst et al., 2012) reveal *mélanges* comprise predominantly serpentinitised muds or schists hosting blocks of serpentinitised mantle peridotite and fragments from the subducting slab metamorphosed to blueschist-facies. The *mélange* zones are low-density layers which, as the thickness increases, bulge upwards and eventually buoyantly rise as diapirs or plumes carrying enriched melts into the magmatic plumbing system (Savov et al., 2007; Marschall and Schumacher, 2012; Figure 5.7).

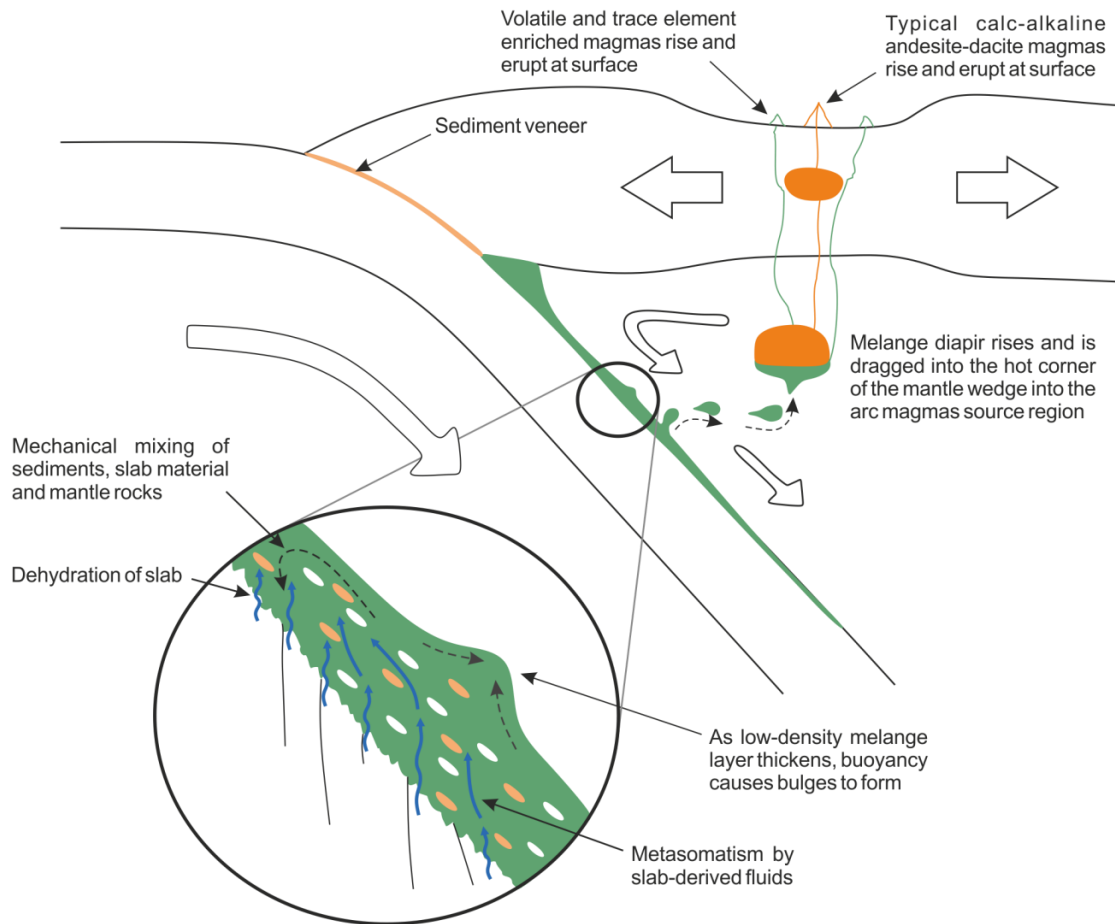


Figure 5.7 Cartoon of the formation of mélangé diapirs in subduction zones modified for the CVC after Marschall and Schumacher (2012).

In their model, the authors proposed intensely metamorphic mélanges form along the slab-mantle interface as a result of metasomatism, shearing and mixing of slab derived material (crust and sediments) and mantle rocks. They form a low-velocity zone which bulges and forms diapirs which are dragged by corner flow into the hot corner of the mantle wedge (Marschall and Schumacher, 2012). The diapirs carry volatile and trace element enriched melts into the arc magma source region. A wide range of magmas are then erupted at the surface, from highly enriched alkaline magmas to typical calc-alkaline basaltic-andesites to dacites.

The CVC alkaline cinder cone magmas are primitive, high-Mg magmas, highly enriched in the fluid mobile LILE, which can be attributed to hydrous fluids and sediment melts as shown in Figures 5.4 and 5.6. The principal argument against hydrous enrichment is based upon the inability to reproduce the trace element abundances and the Nd-Hf-Pb isotopic compositions of the alkaline magmas through the addition of slab-derived fluids and / or sediment melts (Cai, 2009; see Section 4.4.2). As described above, and in Section 4.4.2, this lead Cai (2009) to propose a model of subduction erosion, resulting in the enrichment of the mantle wedge by lower crustal material eroded off the overriding North American plate. However, as shown by Figure 5.7, based on the available data, the alkaline cinder cone magma Sr and Nd isotopic compositions are inconsistent with mantle source enrichment by eroded lower-crustal material.

The presence of a *mélange* layer along the slab-mantle interface of the subducting Rivera plate could provide the levels of enrichment required to reproduce the alkaline magma compositions. Such a scenario would satisfy both previous models: the *mélange* layer is formed through metasomatism by slab-derived fluids and shearing of fragments from the down-going slab and the mantle, and perhaps the overriding plate as well (Marschall and Schumacher, 2012).

Mantle enrichment, however, could also result from pockets of enriched mantle, unrelated to the current subduction, brought in to the system through mantle convection (Stracke et al., 2005; Woodhead et al., 2012). Woodhead et al. (2012) highlighted the importance of understanding the composition of the mantle prior to the onset of subduction. Based on Hf-Nd isotopes in basalts from the Mariana Trough, Woodhead et al. (2012) found that the ambient mantle is heterogeneous, with a more enriched end member than previously thought. The formation of a heterogeneous mantle with enriched blobs (the 'plum-pudding' model; Phipps Morgan and Morgan, 1999) or streaks (the 'marble-cake' model; Allegre and Turcotte, 1986) hosted within a largely depleted mantle is attributed to the recycling of subducted oceanic lithosphere or metasomatised mantle, which become incorporated into the mantle through convection (i.e. Allegre and Turcotte, 1986; Phipps Morgan and Morgan, 1999; Niu et al., 2002; Ulrich et al., 2012). Ulrich et al. (2012) recently proposed that recycling of OIB and seamounts on the ocean floor could provide the necessary mechanism to explain the mantle enrichments observed along the Mid-Atlantic Ridge.

5.2 A Petrogenetic Link between the Sub-alkaline and Alkaline Magmas

The Group II eruption deposits are high-K, sub-alkaline basalts to basaltic-andesites; however, they are distinct from the Group I units, characterised by the presence of phlogopite phenocrysts and microphenocrysts, and high MgO, K₂O and P₂O₅ and strongly enriched LILE and LREE abundances relative to the Group I deposits. The alkaline cinder cones are composed of primitive high- MgO magmas with high TiO₂, FeO, CaO, K₂O and P₂O₅ over a narrow range of SiO₂, forming a distinct group of CVC eruptive products (Figure 5.8).

Co-variations between K₂O and P₂O₅ with SiO₂ for the CVC erupted magmas show that the Group II eruption deposits lie compositionally between the Group I and alkaline cinder cone magmas (Figure 5.8). The sub-alkaline and alkaline magmas follow different differentiation trends, and therefore cannot be linked through fractional crystallisation from a common parental melt; however, they could represent a mixing relationship.

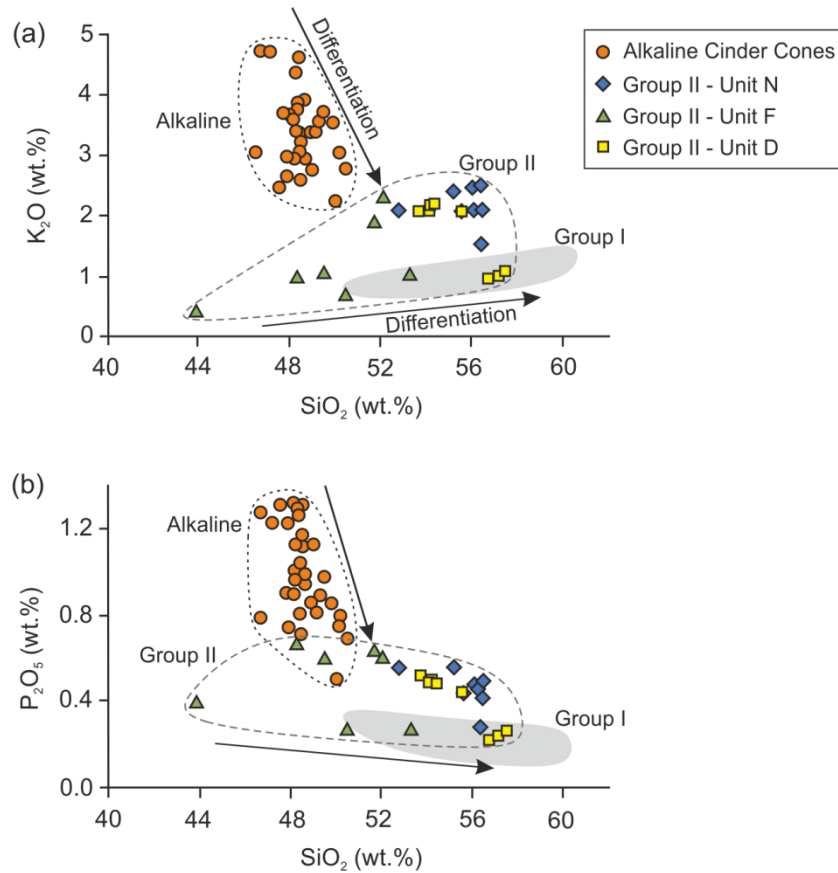


Figure 5.8 Whole-rock major element K₂O (a) and P₂O₅ (b) variation with SiO₂ showing the relationship between the Group I and Group II eruption deposits and the alkaline cinder cone samples.

The Group II samples lie off the fractionation trend of the majority of the CVC deposits (Group I), with higher K₂O and P₂O₅ concentrations trending towards the alkaline magmas, which may represent mixing between the two magma types.

Figure 5.9 shows the same whole-rock major element variation diagrams with mixing lines between end-member compositions following the model of Langmuir et al. (1978). Samples VF10-03M2, an andesite from unit L, and VF10-04U, a basalt from unit U, from the Group I eruption deposits were used for the sub-alkaline end-members. Sample SAY-7E from El Carpintero Norte was used as the alkaline end-member magma composition. The mixing lines reveal that the Group II eruption deposits could contain up to 50% alkaline magma component (Figure 5.9).

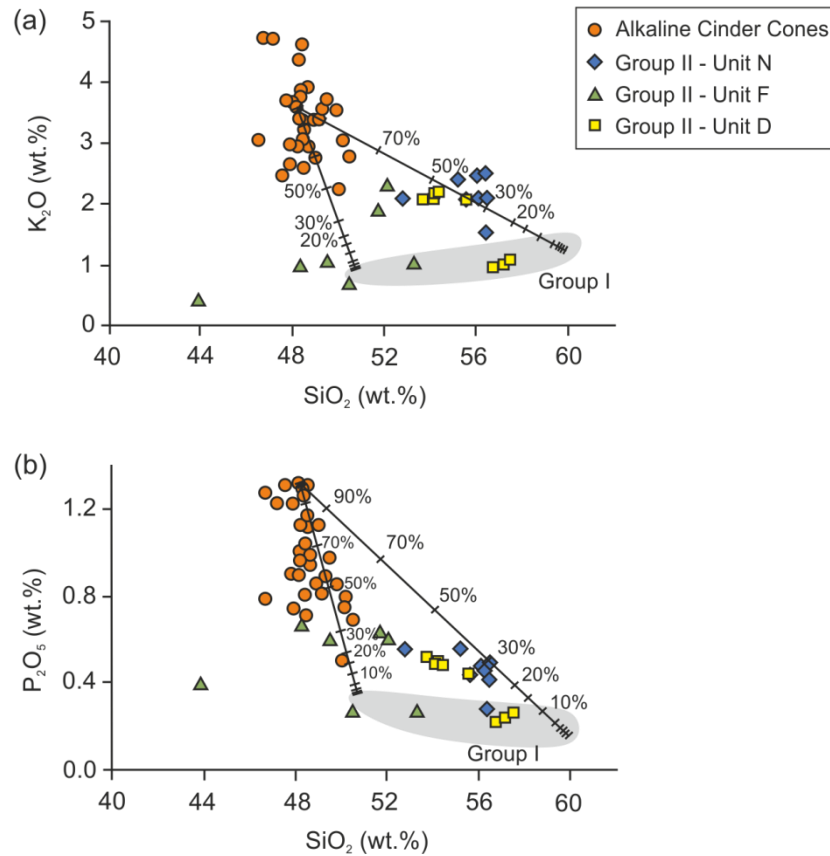


Figure 5.9 Whole-rock major element K₂O (a) and P₂O₅ (b) variation with SiO₂ showing mixing lines between end-member compositions after Langmuir et al. (1978).

Sub-alkaline end-members are sample VF10-03M2, an andesite from unit L of Group I, and VF10-04U, a basalt from unit U of Group I. Sample SAY-7E, a minette from El Carpintero Norte, was used for the alkaline end-member. The Group II eruption deposits lie compositionally between the sub-alkaline and alkaline magmas, with up to ~50% alkaline component.

As discussed in Chapters 2 and 3, the radiogenic isotopic ratios of ⁸⁷Sr/⁸⁶Sr and ¹⁴³Nd/¹⁴⁴Nd are commonly used to fingerprint magma sources and investigate open-system processes; therefore the isotopic compositions of the CVC magmas can be used to evaluate this potential mixing relationship between the high-K alkaline and medium-K sub-alkaline magmas. Overall, the Group I eruption deposits show little variation in isotopic composition with SiO₂, while Group II samples show a wide variation in both ⁸⁷Sr/⁸⁶Sr and ¹⁴³Nd/¹⁴⁴Nd (Figure 5.10). Unit H is shown separately from the rest of the Group I units as it is geochemically similar to, but isotopically distinct from the Group I deposits, with a wider range in ⁸⁷Sr/⁸⁶Sr and ¹⁴³Nd/¹⁴⁴Nd (see Section 2.5.1). The alkaline cinder cones have more radiogenic ⁸⁷Sr/⁸⁶Sr and less radiogenic ¹⁴³Nd/¹⁴⁴Nd than the Group I magmas; however, they show a wide variation in ⁸⁷Sr/⁸⁶Sr and ¹⁴³Nd/¹⁴⁴Nd over a narrow range of SiO₂ (Figure 5.10).

Mixing lines between the same end-member compositions used for the major elements reveal the Group II unit F samples may represent mixtures of sub-alkaline basalt with up to 90%

alkaline component. Samples from unit N and D of Group II have a much lower alkaline signature, and are more evolved. These samples may represent mixtures of basaltic-andesite or andesite with up to 30% alkaline component (Figure 5.10).

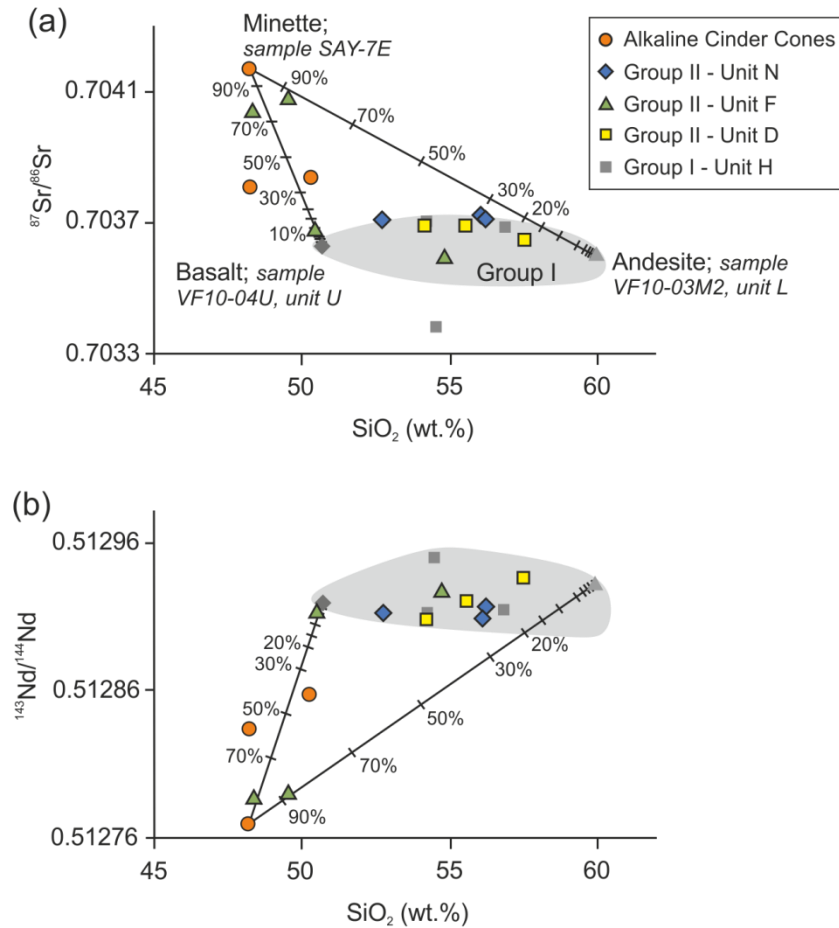


Figure 5.10 (a) $^{87}\text{Sr}/^{86}\text{Sr}$ and (b) $^{143}\text{Nd}/^{144}\text{Nd}$ variation with SiO_2 showing possible mixing lines between calc-alkaline and alkaline end-member compositions.

A calc-alkaline Group I andesite (sample VF10-03M2, unit L), a Group I basalt (sample VF10-04U, unit U) and a mafic alkaline minette (sample SAY-7E; Cai, 2009) were used as the end-member magmas. The Group II samples trend towards the compositions of the alkaline magmas. Unit F sample lie along the basalt-minette mixing line with between 10 and 80% alkaline component. Units N and D of Group II are more evolved and may represent mixtures of a basaltic-andesite or andesite end-member with lesser amounts (20-30%) of alkaline component.

This mixing relationship between the sub-alkaline and alkaline magmas to produce the Group II eruption deposits can also be explored using the same mixing model between end-member samples on a $^{87}\text{Sr}/^{86}\text{Sr}$ versus $^{143}\text{Nd}/^{144}\text{Nd}$ variation diagram (Figure 5.11). The Group II eruption deposits lie along the mixing line, supporting the models in Figures 5.9 and 5.10. However, on the $^{87}\text{Sr}/^{86}\text{Sr}$ versus $^{143}\text{Nd}/^{144}\text{Nd}$ variation diagram, the Group II magmas contain

between ~2 and 50% alkaline component. Two of the samples from unit H of the Group I eruption deposits also lie along the mixing line with up to 5% alkaline component.

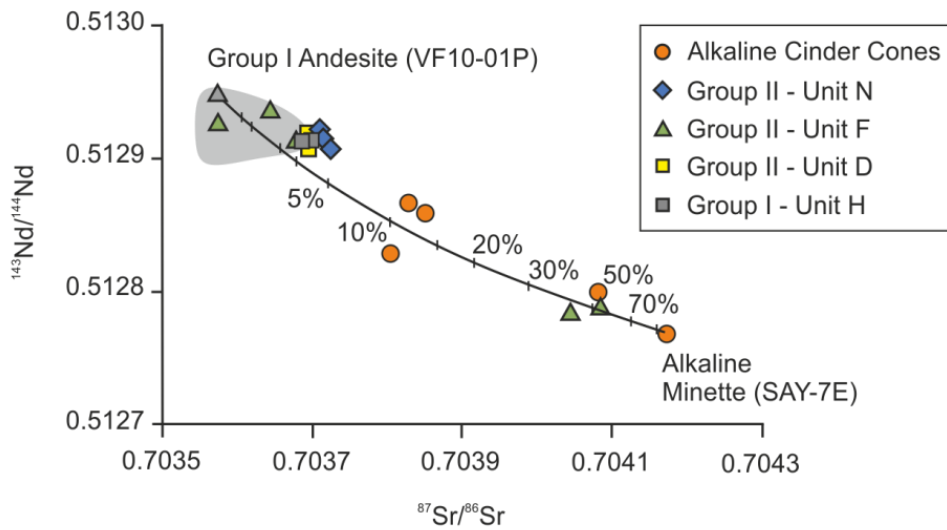


Figure 5.11 A simple mixing between the end member magmas on a $^{87}\text{Sr}/^{86}\text{Sr}$ versus $^{143}\text{Nd}/^{144}\text{Nd}$ plot.

The end-member compositions used were a Group I andesite (sample VF10-01P) and an alkaline minette (sample SAY-7E from El Carpintero Norte). The line shows the percentage of alkaline component. The Group II magmas lie along with ~2 to 50% alkaline magma component.

The presence of an alkaline component in the Group II magmas is supported by the whole-rock trace element data. The results of mixing calculations involving the trace elements are shown in Figure 5.12, with abundance patterns representing 5, 20 and 50% alkaline magma mixed with calc-alkaline Group I magma, using the same end-member compositions. The trace element abundance patterns for the mixed magmas do not agree perfectly with the Group II eruption deposits, for example, the abundances representing a 50% mixture agrees well with the majority of the elements with the exception of Rb, Ba, Nb, P, Zr and Hf which are all more enriched than in the Group II samples. This may reflect the presence of small amounts of accessory minerals in the alkaline melts, such as sphene, rutile, zircon or apatite which would result in relatively high abundances of Nb, P, Zr and Hf (see Section 2.4.2.1). Rb and Ba are highly mobile in fluids, therefore intense metasomatism causing enrichments in the alkaline parental melt, as proposed in the mélange diapir model (see Section 5.1.3.1), could account for the elevated Rb and Ba abundances.

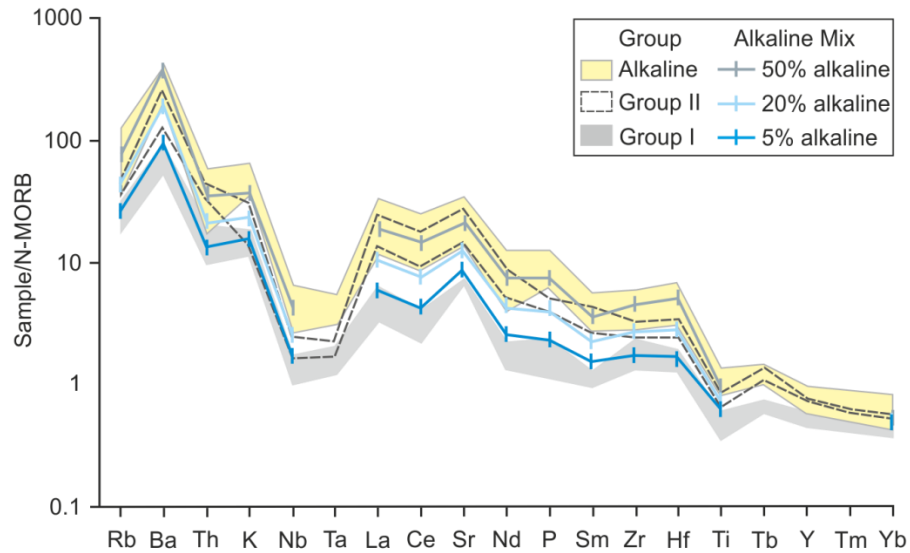


Figure 5.12 An N-MORB normalised trace element abundance diagram showing trace element patterns produced by mixing between sub-alkaline (Group I; grey field) and alkaline magmas (pale yellow field).

N-MORB normalising values are from Sun and McDonough (1989). The mixed compositions are calculated using the end-member andesite (VF10-01P) and alkaline minette (SAY-7E from El Carpintero Norte). The bright blue line represents compositions consisting of a mixture 95% sub-alkaline and 5% alkaline; the pale blue, 20% alkaline and the grey-blue, 50% alkaline. The Group II magmas (dashed outline) have between 20 and 50% alkaline component.

The abundances for the 5% alkaline mixture do not correlate with any of the Group II eruption deposits, but is better correlated with the most enriched Group I samples (Figure 5.12). The higher alkaline component required to reproduce the Group II trace element abundance patterns is consistent with the models involving Sr and Nd isotope variations with SiO₂ content (Figure 5.10).

The isotopic and whole-rock trace element data is in agreement with the whole-rock major element data, which reveals that the Group II eruption deposits lie compositionally between the Group I units and the alkaline cinder cone magmas. These geochemical plots also reveal that the alkaline magmas contain a sub-alkaline component.

The mixing relationship between the two magma types is also supported by the mineralogy of the different eruption deposits. The typical mineral assemblage of the Group I tephra is dominated by plagioclase, orthopyroxene, clinopyroxene and hornblende with olivine only present in the most mafic deposits (Table 5.1; see also Section 2.2). The Group II samples comprise clinopyroxene and olivine with varying amounts of plagioclase, hornblende and phlogopite (see Section 3.2), while the alkaline (minette) magmas predominantly comprise olivine and clinopyroxene with phlogopite, apatite and sanidine (Table 5.1; see also Section 4.1).

Deposit	Mineral Assemblage
Group I	plag + opx + cpx + hbd + Fe-Ti oxides ± ol
Group II	cpx + ol + hbd + plag + phlog + Fe-Ti oxides ± opx
Alkaline (minette)	ol + cpx + phlog + apatite + sanidine + Fe-Ti oxides

Table 5.1 Comparison of the mineral assemblages of Group I, Group II and alkaline cinder cone pumice and scoria samples.

A minette is used to represent the alkaline magma. The mineral abbreviations are: plag = plagioclase; opx = orthopyroxene; cpx = clinopyroxene; hbd = hornblende; phlog = phlogopite.

The Group II deposits are basalts and basaltic-andesites, yet comprise mineral assemblages dominated by clinopyroxene and olivine with phlogopite, that are more akin to the basanites and minettes of the alkaline cinder cones (Luhr and Carmichael, 1981). Plagioclase is absent, or present only in the groundmass, in the alkaline cinder cone magmas (Luhr and Carmichael, 1981). Unit F of Group II shows the strongest alkaline geochemical signature (Figure 5.11), which is consistent with its mineralogy, comprising a mineral assemblage dominated by clinopyroxene, olivine and phlogopite with minor plagioclase and trace hornblende (see Section 3.2). Units N and D show a weaker alkaline geochemical signature (Figure 5.11) which, again, is reflected in their mineralogy; unit N scoria comprises predominantly plagioclase and clinopyroxene, with up to 1 vol.% olivine, and trace abundances of hornblende and phlogopite, while Unit D scoria comprise predominantly hornblende and plagioclase, with clinopyroxene and up to 1 vol.% olivine and phlogopite (see Section 3.2).

These geochemical mixing models and mineralogical data reveal there is a petrogenetic relationship between the medium-K sub-alkaline and high-K alkaline erupted deposits of the CVC involving mixing between the two types of magmas. Evidence from the mineral compositions and zoning patterns of phenocrysts within the Group I and Group II eruption deposits reveal multiple magma mixing events in the magmatic plumbing system of the CVC (see Sections 2.2 and 3.2). Group II tephra contain phenocrysts that are also observed in the Group I samples, revealing a shared provenance of crystals. This suggests physical mixing between the alkaline and sub-alkaline magmas, and that the Group II magmas are evolving within the sub-alkaline magmatic storage region beneath the CVC.

5.3 Magmatic Plumbing System

Although the CVC has been the focus of numerous petrological and geochemical studies (Thorpe et al., 1977; Luhr and Carmichael, 1980; Medina-Martínez, 1983; Robin et al., 1987; Luhr and Carmichael, 1990b; Robin et al., 1991; De la Cruz-Reyna, 1993; Luhr, 1993; Robin

and Potrel, 1993; Righter, 2000; Luhr, 2002; Navarro-Ochoa et al., 2002; Saucedo et al., 2005; Atlas et al., 2006; Luhr et al., 2006; Reubi and Blundy, 2008; Savov et al., 2008; Saucedo et al., 2010), very few have attempted to define the nature of the magmatic plumbing system beneath the CVC.

Based on dissolved water in melt inclusions in plagioclase, pyroxene, olivine and hornblende phenocrysts within Colima lavas, Atlas et al. (2006), found that melt inclusions were trapped at depths of <12 km, and entrapment continued throughout the magmas ascent. The authors showed that water contents in the melt inclusions vary negatively with SiO₂ and K₂O, therefore, they concluded that crystallisation must have occurred during degassing under vapour-saturated conditions. Based on the lack of erupted rhyolitic magmas at the CVC, Atlas et al. (2006) suggested evolved, degassed magmas stagnate in sills, and are remobilised by a more mafic, less degassed magma en route to the surface. Atlas et al. (2006) therefore concluded that Colima magmas evolved in conduits or inter-fingered dykes in the upper crust, rather than in a large stratified magma chamber.

Reubi and Blundy (2008) also studied melt inclusions in plagioclase, orthopyroxene and clinopyroxene phenocrysts from andesitic lavas from Volcán de Colima, which erupted in 1998-2005. The authors similarly discarded the concept of a magma chamber beneath the CVC; however, they proposed a lower-crustal evolution of the Colima magmas rather than melt evolution in the upper crustal region, as proposed by Atlas et al. (2006). Reubi and Blundy (2008) concluded that the Colima andesites formed through the incorporation of mafic gabbroic clots into evolved dacitic melts following the hot zone model of Annen et al. (2006), whereby gabbroic sills are emplaced in the lower crust where the magma evolves through differentiation and crustal assimilation (Figure 5.13). Further magma emplacement eventually forms a hot zone of sills within the lower-crustal region, causing partial melting of the crustal rocks and older, crystallised sills. The partial melts rise in dykes, leaving behind cumulates of mafic material which are later assimilated by younger magmas (Annen et al., 2006). Based on the absence of intermediate glass compositions in their samples, Reubi and Blundy (2008) proposed that melts at the CVC are evolved, and become intermediate in composition through the assimilation of gabbroic cumulates.

This section presents a new model for the magmatic plumbing system of the CVC incorporating the petrological data presented in Chapters 2 and 3, and recent geophysical studies which imaged upper and lower crustal magma storage regions beneath Volcán de Colima (Gardine, 2010; López-Loera, 2012).

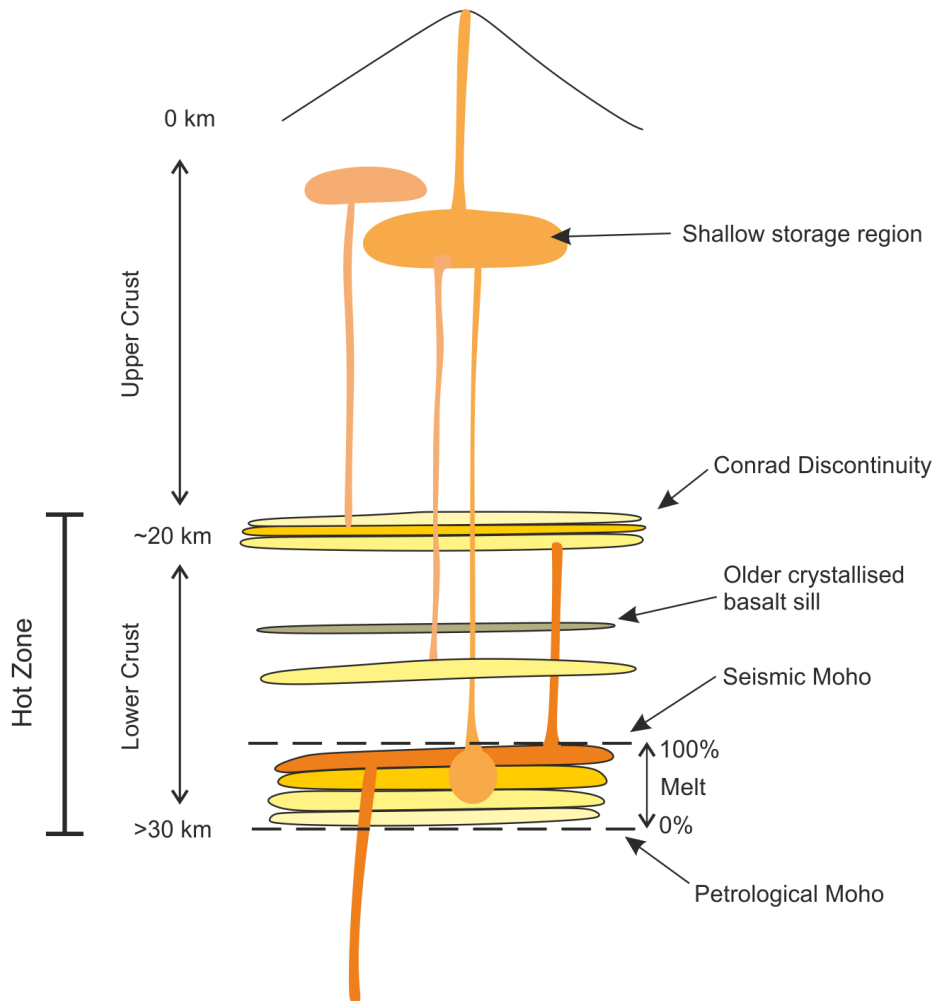


Figure 5.13 Cartoon of the hot zone model of Annen et al. (2006).

Magma is emplaced in a series of sills at the base of the crust, and in the lower crust. These sills form a hot zone which partially melts the crustal rocks, and older crystallised sills. Differentiated melts which have assimilated crustal rocks and mafic gabbroic cumulates rise and pond in shallow level storage region where further differentiation occurs. The colours reflect melting; orange = 100% melt and paler colours reflect lower percentages of melting,

5.3.1 Insights from Petrological Data

The mineral chemistry and zoning patterns and textures presented in Chapters 2 and 3 reveal a complex history of crystal growth and destabilisation within the Group I and Group II magmas (see Sections 2.2 and 3.2). Core-rim mineral chemistry profiles of clinopyroxene and orthopyroxene phenocrysts reveal step increases and decreases in Mg#, that correlate with Cr₂O₃ contents, and dissolution surfaces indicating mixing between more evolved and more mafic magmas. This is consistent with a magma plumbing system comprising multiple magma chambers or storage regions, broadly similar to the “hot zone” model of Annen et al. (2006). The presence of small-scale oscillations interpreted to reflect thermal convection, reveals the presence of a shallow-level magma chamber beneath Volcán de Colima.

Figure 5.14 is a cartoon of the CVC magmatic plumbing system based on the interpretation of the petrological data. Clinopyroxene, orthopyroxene and plagioclase phenocrysts record early decompression followed by mixing with a more evolved magma or melt.

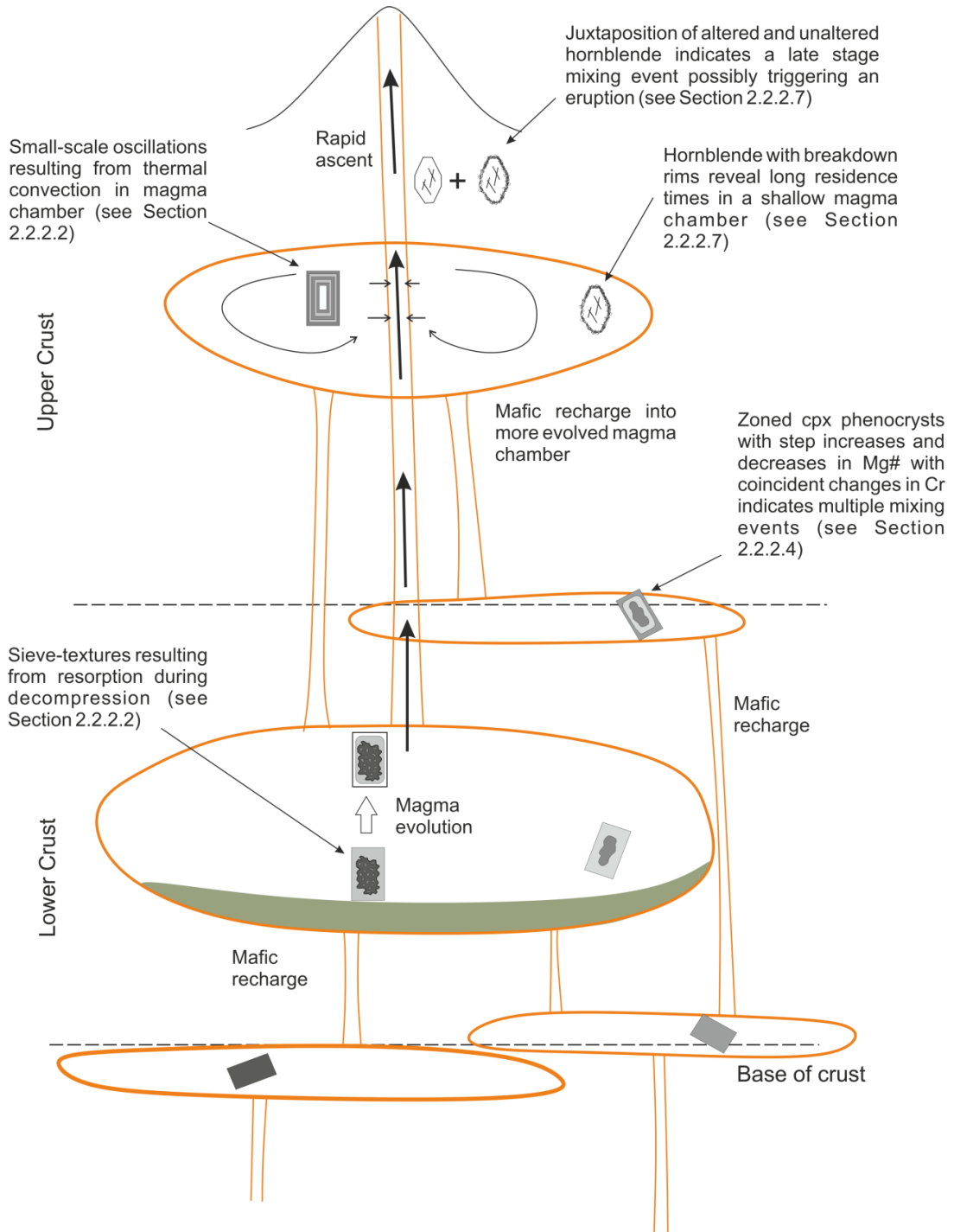


Figure 5.14 Cartoon of the magmatic plumbing system of the CVC based on the interpretation of the petrological data.

Plagioclase and pyroxene phenocrysts display complex zoning patterns interpreted to represent decompression and multiple magma mixing events.

The presence of sieve-textured cores and / or growth zones in plagioclase and pyroxene phenocrysts indicate destabilisation and resorption as a result of decompression, suggesting multiple levels of magma storage beneath the CVC (Figure 5.14). A shallow level storage region is indicated by the presence of plagioclase with small-scale oscillatory zoned and embayed rims which indicate thermal convection in a magma chamber. The presence of hornblende phenocrysts with breakdown rims of pyroxene, plagioclase and Fe-Ti oxides is indicative of slow-ascent rates or long residence times in a shallow magma chamber (Browne and Gardner, 2006; Rutherford, 2008).

Rapid ascent rates from the magma storage region for the CVC explosive eruption deposits are revealed by the highly vesiculated nature of the groundmass and the occurrence of hornblende phenocrysts with stable, sharp crystal edges. The presence of hornblende phenocrysts with breakdown rims is therefore attributed to long residence times in shallow level storage region (see Section 2.2.2.7).

Magma mixing in the magmatic plumbing system of the CVC is revealed by the 1913 erupted tephra (Robin and Potrel, 1993; Luhr, 2002; Luhr et al., 2006; Luhr et al., 2010; Saucedo et al., 2010). The more mafic nature of the 1913 eruption deposits compared to post-1913 lavas, lead Luhr (2002) to conclude that the proposed 100-year cycle of explosive activity at Volcán de Colima (see Chapter 1), ends with the injection of a mafic magma triggering an explosive plinian eruption.

The majority of scoria and pumice samples from the explosive eruption deposits studied here contain both stable and unstable hornblende phenocrysts with breakdown rims of pyroxene, plagioclase and Fe-Ti oxides (see Sections 2.2.2.7 and 3.2.2.5). The juxtaposition of stable and unstable hornblende phenocrysts suggests a late-stage magma mixing event (Rutherford, 2008; see also Section 2.2.2.7), which may have triggered the explosive eruptions.

The explosive CVC eruption deposits reveal a complex magmatic plumbing system beneath the CVC, involving multiple storage levels probably reflecting a system of sills and dykes at a deeper level (i.e. base of the crust) and a shallow-level magma chamber (Figure 5.14). Although such a plumbing system is similar to the hot zone model, based on the glass compositions, the model, as proposed by Reubi and Bluny (2008), does not work for the CVC. Their conclusions were based on a lack of intermediate glass compositions in Colima andesites. However, the explosive tephra samples have mafic to felsic (49.5 to 73.9 wt.% SiO₂; n=342) groundmass glass compositions, with the majority of analyses comprising intermediate glass compositions of 56 to 65 wt.% SiO₂ (n=228).

5.3.2 Geophysical Data

Recent geophysical studies have imaged two potential magma chambers, or magma storage regions, beneath Volcán de Colima (Gardine, 2010; López-Loera, 2012). Aeromagnetic data collected during three campaigns in 1963, 1983 and 1999 covering an area of 11,568 km³ over the CVC, reveals anomalies associated with Volcán de Colima and Nevado de Colima (López-Loera, 2012).

López-Loera (2012) modelled a 2¾ dimension section trending north-northeast – south-southwest along the magnetic anomalies (Figure 5.15). The 2¾ dimension model adds constraints on the shape of the modelled body, perpendicular to the 2D section. By using the magnetisation and magnetic susceptibility of local rocks (debris-avalanche deposits, andesitic lava flows, basement limestones and marine sediments), López-Loera (2012) interpreted one of the anomalies to represent a magma chamber 5.5 km thick, at a depth of 4.8 km beneath Volcán de Colima (Figure 5.15).

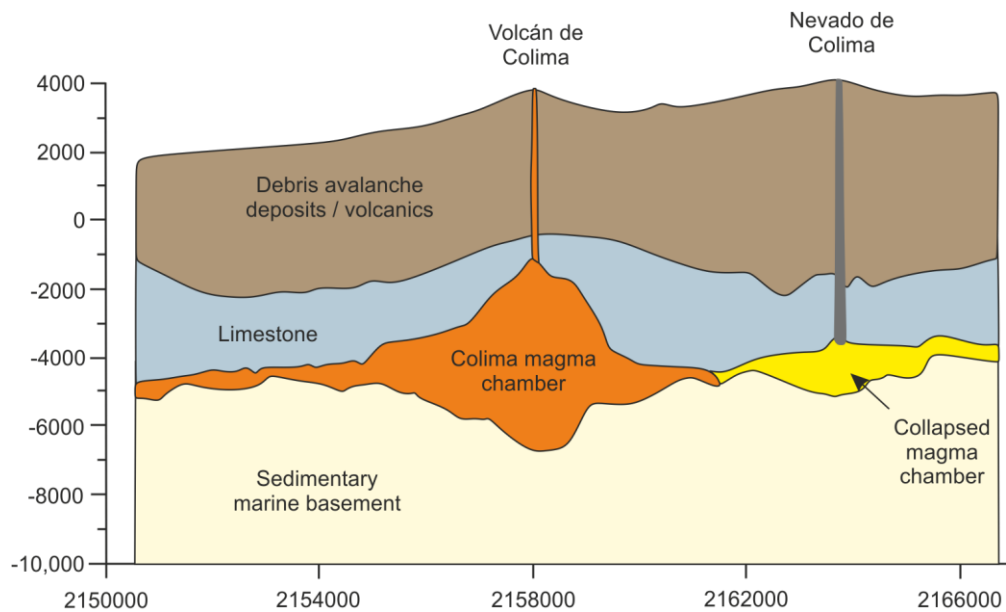


Figure 5.15 2¾ dimension magnetic model along a section through the north-south trending anomalies beneath Volcán de Colima and Nevado de Colima modified from López-Loera (2012).

The anomaly is defined by the contrast in magnetic susceptibility between the rock types (López-Loera, 2012). The body is elongated in a north-south direction with a length of over 6.8 km, extending 5.6 km to the south of the CVC with an average thickness of 0.54 km (López-Loera, 2012). In order to better constrain their model, the authors used a previous viscoelastic model by Cabrera-Gutiérrez and Espinolda (2010) who proposed the presence of a magma chamber of ~1.96 km in radius at ~5.6 km below the crater. This shallow magma chamber is

consistent with seismicity, which reveals a quiet zone at 3 to 7 km depth below the crater of Volcán de Colima (Nuñez-Cornú et al., 1994; Zobin et al., 2002; López-Loera, 2012).

Beneath Nevado de Colima, another anomaly exists which has been interpreted as representing a collapsed magma chamber (López-Loera, 2012). The anomaly extends >5.6 km in a north-south orientation, with a maximum thickness of 1.2 km, at a depth of 5.2 km below the remnant crater of Nevado de Colima (Figure 5.15).

Gardine (2010) carried out a P-wave tomographic study on the CVC using regional and local earthquakes ranging in magnitude from 1.5 to 5.1. Inversions were carried out on 8660 arrivals from 198 regional earthquakes associated with the subducting Rivera plate, and 101 shallow crustal earthquakes (Gardine, 2010). Two low-velocity zones were imaged, one at 4 to 10 km depth and a second at 15 to 30 km depth (Figure 5.16). Low-velocity zones have been imaged at other volcanoes (e.g. Husen et al., 2004; Waite and Moran, 2009), and are commonly interpreted as reflecting the presence of a magma chamber, as increased temperatures and partial melt slow down seismic waves (Husen et al., 2004; Waite and Moran, 2009; Gardine, 2010).

The shallow low-velocity zone imaged beneath Volcán de Colima covers an area of ~ 30×30 km, with a depth extending from just below sea-level (~4 km below the crater) to 10 km, giving a volume of ~9000 km³. The total estimated volume of erupted magmas from the CVC stratovolcanoes (Volcán Cántaro, Nevado, Paleofuego and Volcán de Colima) is ~490 km³, which is ~5% of the volume of the low-velocity zone. The magma chamber volume estimate at Soufriere Hills volcano, Montserrat, based on seismic tomography and thermal modelling is 13 km³ (Paulatto et al., 2012). Tomography studies at Mt St Helens volcano yielded magma chamber volume estimates of ~100 km³ (Lees, 1992; Waite and Moran, 2009). Larger magma chamber volumes of ~1200 km³ have been estimated for Teide volcano (De Barros et al., 2012) and 1000 to 1400 km³ for Los Hornos Caldera, Mexico (Verma and Gomez-Arias, 2013). In comparison to these magma chamber volume estimates at other volcanoes, and given the total estimated volume of erupted products, it seems unlikely that this anomaly represents a shallow-level magma chamber. Based on the large volume of this anomaly, Gardine (2010) concluded that it more likely reflects the regional geology, as the CVC sits in the Colima Rift, which is infilled by sediments which would have lower velocities than the basement rocks exposed in the graben walls (Gardine, 2010).

The second low-velocity zone is situated ~20 km southeast of Volcán de Colima (Gardine, 2010). Based on a lower-bound estimate of P-wave velocity changes in mantle olivine of 0.5 m/s/°C at temperatures below 700°C (Isaak, 1992), Gardine (2010) attributed the deeper low-velocity zone, with P-wave velocities 0.2 km/s slower than background, to a storage region with temperatures ~400°C above the background. Gardine (2010) used the Mexican subduction zone

thermal models of Currie (2002) to estimate a background temperature of $\sim 500^{\circ}\text{C}$ at ~ 25 km depth below the CVC. This is consistent with the new thermal models of Ferrari et al. (2012) which estimate the temperature at ~ 25 km depth to be between 500 and 600°C . The lower-velocity zone, therefore, has a temperature of $\sim 900^{\circ}\text{C}$.

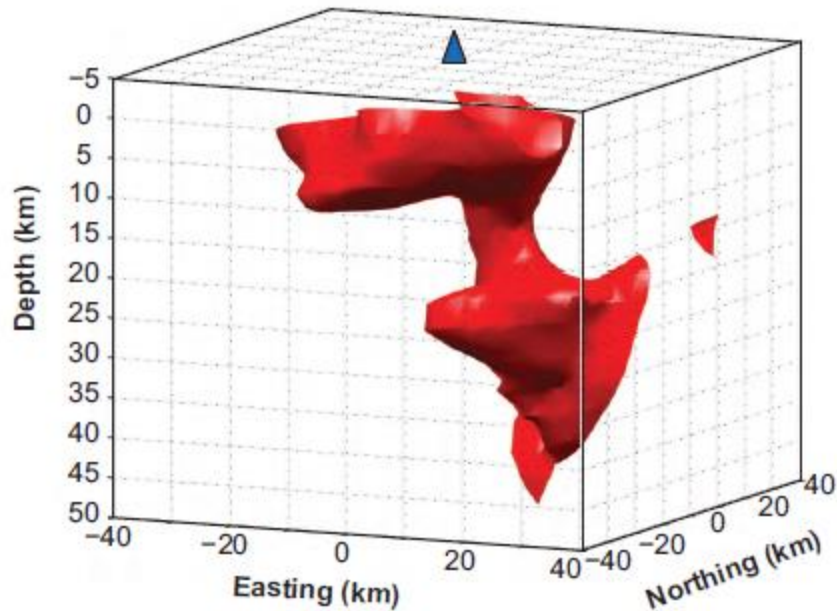


Figure 5.16 The low-velocity isosurface plot from the tomography results from Gardine (2010).

Volcán de Colima is indicated by the blue triangle at (0,0). The shallow low-velocity zone is under Volcán de Colima from 0 to 10 km depth. The deeper low-velocity zone is at 15-30 km depth, and is located ~ 20 km southeast of Volcán de Colima.

Partial melt also reduces the P-wave velocity; however, the velocity is reduced by 3.6% per 1% of partial melt (Hammond and Humphreys, 2000; Gardine, 2010). It is therefore unlikely that partial melt plays a strong role, given the small velocity anomaly displayed by the lower-velocity zone, although it may play a part. Gardine (2010) calculated an error of $\pm 200^{\circ}\text{C}$ on the temperature to account for up to 50% partial melt contributing to the reduced velocities.

This value of $900 \pm 200^{\circ}\text{C}$ is consistent with the estimated eruption temperatures for the Group I and Group II CVC magmas, which yielded 910 to 1050°C (see Sections 2.3 and 3.3); and with estimates from previous petrological studies (Savov et al., 2008; Luhr et al., 2010), and experimental petrology (Moore and Carmichael, 1998) which estimated eruption temperatures of $\sim 950^{\circ}\text{C}$.

The presence of shallow storage regions at ~ 5 km depth and another at ~ 15 to 30 km depth are consistent with the interpretation of the petrological data which reveal multiple magma storage regions at the CVC.

5.4 Petrogenesis of the CVC Magmas

The data presented here show Group I CVC magmas form from a depleted mantle source, which was subsequently enriched by fluids derived from dehydration of the subducting Rivera slab and sediment melts (Figure 5.17). Partial melts of the enriched peridotite mantle then evolve within the plumbing system of the CVC, undergoing magma differentiation and continued pulses of magma replenishment. The highly vesiculated nature of the groundmass glass, and the high water contents recorded by the plagioclase and hornblende phenocryst phases (see Section 2.3.1.3), indicate the magma arrived undegassed in the shallow level storage region, and ascended rapidly retaining its volatile content (Figure 5.14).

The alkaline magmas are derived from a highly enriched source region (Luhr, 1997; Maria and Luhr, 2008; Vigouroux et al., 2008; Cai, 2009). The source of the enrichment is debated in the geological literature with models favouring hydrous enrichment of the mantle wedge (e.g. Vigouroux et al., 2008), while others favour a subduction-erosion process (Cai, 2009). A recent study proposed the presence of a metamorphic *mélange* layer at the subducting slab-mantle interface, resulting in highly volatile and trace element enriched melts (Marschall and Schumacher, 2012). Such a model is plausible for the generation of the CVC alkaline magmas as they would introduce highly fluid and immobile element enriched melts into the CVC magmatic plumbing system. However, it should be noted that the source of mantle enrichment may be unrelated to the current subduction setting. This should be investigated in detail in follow up work.

Geochemical modelling has revealed that the Group II eruption deposits, which are petrologically and geochemically linked to both the sub-alkaline Group I and alkaline cinder cone magmas, are derived from mixing between the two magma types. The alkaline rocks are primitive magmas thought to represent direct melts of veined mantle with little differentiation during ascent (Luhr, 1997). The extensional setting in the western TMVB, which formed the Colima Rift Zone, provided pathways for the melts to reach the surface forming monogenetic cones (Figure 5.17). The appearance of the distinct Group II eruption deposits within the calc-alkaline stratigraphy suggests pulses of alkaline melts intercept and become incorporated into the magmatic plumbing system of the CVC, potentially triggering the eruption of more mafic, mixed eruption deposits.

These mixed units appear in the tephra record at ~7000, 12,000 and 13,000 yrs B.P., interbedded within the Group I stratigraphy, indicating that pulses of alkaline melts rise and intercept the magmatic plumbing system of the CVC on timescales of a few thousand years.

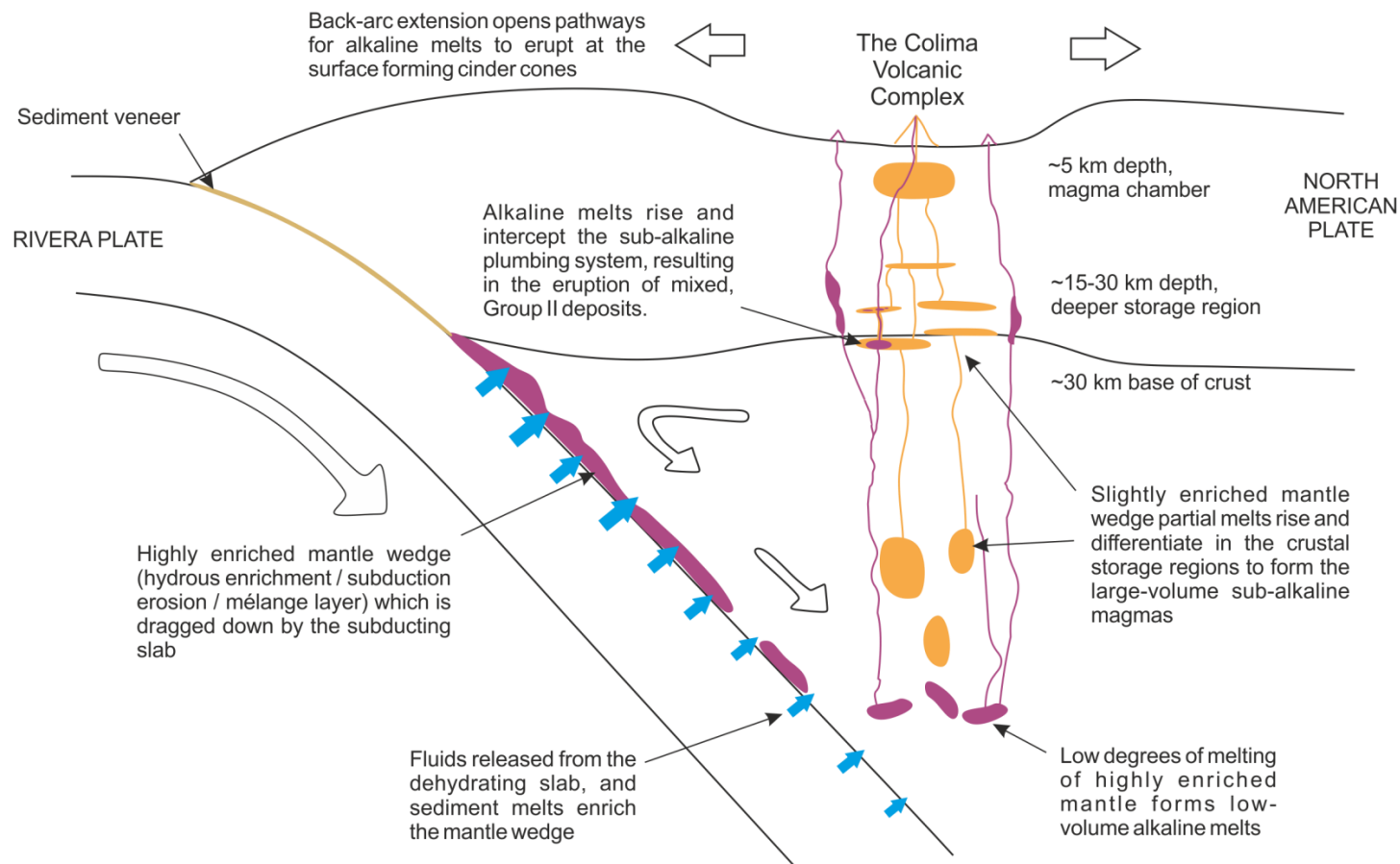


Figure 5.17 Cartoon of the petrogenesis of the CVC magmas.

Sub-alkaline magmas form from partial melts of the slightly enriched mantle wedge, which evolve through a complex crustal storage system. The alkaline magmas form from highly enriched mantle and rise through the crust forming cinder cones on the Colima Rift floor. The Group II mixed magmas result from the interception of alkaline magmas with the crustal magma chambers, or sills, through which the sub-alkaline magmas differentiate.

6 Modelling of Tephra Fallout Deposits

Throughout the Holocene, the CVC has experienced highly explosive eruptions producing thick (up to 1.4m) tephra fallout deposits up to 10 km away from the vent. Current hazard assessments and evacuation maps for the Colima area are based on the reported ash-fall distribution and pyroclastic flow-out length from the 1913 eruption (Cortés et al., 2005; Cortés et al., 2010). Surrounding the CVC are numerous towns and villages, including Ciudad Guzman, ~23 km to the northeast of Volcán de Colima, with a population of ~150,000, and the City of Colima, 30 km south of Volcán de Colima, with a population of ~200,000. New tephra dispersion modelling has been carried out for the 1913 eruption (Connor et al. *in prep*).

To put this into the context of earlier chapters, the Group I and Group II eruption deposits are typically thicker than the 1913 deposit (see Section 1.3.2), yet no hazard assessment work has been carried out for these eruptive units. This chapter presents the initial results of tephra dispersion modelling for units Y, W, U, S and P of the Group I eruption deposits, which includes eruption column height and volume estimates, and tephra dispersal maps. These units were chosen as they are well exposed across the CVC, and are well described in the stratigraphy.

6.1 Tephra Dispersal Modelling

There are numerous models to calculate the tephra dispersion from a given eruption based on field measurements such as deposit thickness and grain size distribution data (e.g. Suzuki, 1983; Carey and Sparks, 1986; Pyle, 1989; Fierstein and Nathenson, 1992; Connor et al., 2001; Bonadonna and Houghton, 2005). The aim of this work is not to assess the various models, but to present an initial tephra dispersion model of the fallout deposits of the CVC. Two weeks were spent at the University of South Florida, Tampa, learning how to use the *Tephra2* model, an updated version of *Tephra* (Connor et al., 2001; Bonadonna et al., 2005). *Tephra2* has been used here to calculate the tephra dispersal pattern, total erupted mass and maximum eruption column height of units Y, W, U, S and P of the Group I eruption deposits.

6.1.1 The *Tephra2* model

Tephra dispersal is affected by numerous parameters that describe an eruption and the atmosphere the erupting column penetrates (Connor et al., 2001). *Tephra2* is an advection-diffusion model based on the work of Suzuki (1983) that describes diffusion, transport and sedimentation of tephra particles released from an eruption column (Connor et al., 2001; Bonadonna et al., 2005). It calculates the total mass per unit area (kg m^{-2}) of tephra accumulation at individual grid locations by solving a simplified mass conservation equation

(Equation 6.1). The mass conservation equation takes into account the distribution of tephra mass in the eruption column and particle settling velocity, as well as horizontal diffusion within the eruption column and atmosphere after the particle has been ejected from the plume (Figure 6.1; Connor et al., 2001; Bonadonna et al., 2005; Connor and Connor, 2006; Connor et al., In Prep.).

$$M_{(x,y)} = \sum_{i=0}^{H_t} \sum_{j=\phi_{min}}^{\phi_{max}} M_{i,j}^o f_{i,j}(x, y)$$

Equation 6.1

The equation calculates the total mass per unit area, M (kg m^{-2}), of tephra accumulated at point (x,y) , from $M_{i,j}^o$: the total mass fraction of particles with size j (where ϕ_{min} and ϕ_{max} represent the minimum and maximum particle diameter) that fall from a point source, i , at a height ranging from 0 to H_t (where H_t is the total height of the volcanic plume); and $f_{i,j}(x, y)$: the diffusion of particles with size j in the atmosphere away from their source point i and the advection of these particles by wind (Figure 6.1; Connor et al., In Prep.).

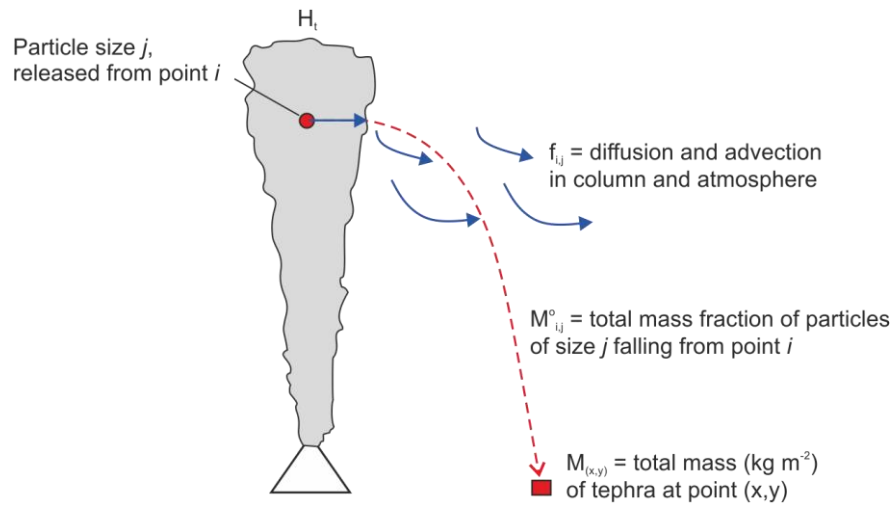


Figure 6.1 Schematic diagram of the mass conservation equation.

A mass of particles of size j are released from a point source ($M_{i,j}^o$) and are carried by diffusion and advection in the column and the atmosphere ($f_{i,j}$), and accumulated at point (x,y) on the ground.

$M_{i,j}^o$ describes the distribution of mass as a function of particle size and height in the eruption column. The eruption column height is controlled by the energy and mass flow of the eruption (Connor et al., 2001). Particles are carried upwards within a vertical column and assumed to be released from the centre as a result of decrease in upward velocity as a function of height and diffusion out of the column (Figure 6.2). The column is divided into horizontal layers, i , from the vent to the total eruption column height, H_t , each with its own uniform wind speed and

direction (Connor et al., 2001). The tephra mass can be distributed among these layers using a uniform random distribution reflecting the structure of a well-mixed strong plume (Sparks, 1986; Connor et al., In Prep.), or the mass can be distributed in, for example, the top 20% of the eruption column, using a probability density function of mass as a function of height, (Figure 6.2; Bonadonna et al., 2005).

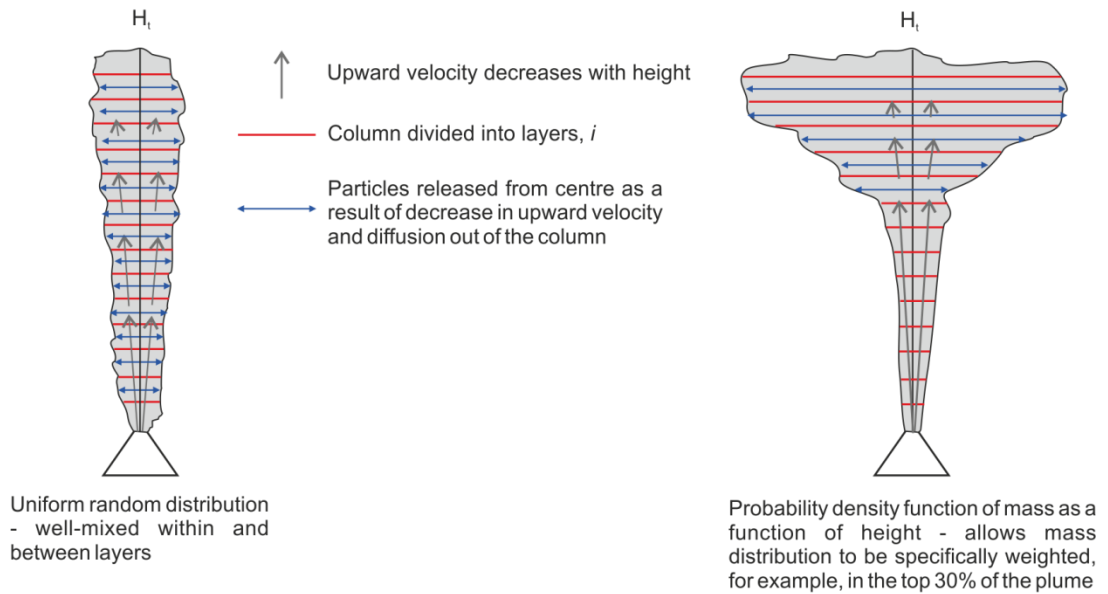


Figure 6.2 Schematic diagram describing the distribution of tephra mass within the eruption column.

The column is divided into layers from which the particles are released from a centre line as a result of the decrease in upward velocity as a function of height and diffusion out of the column. Mass can be distributed using a random uniform distribution representing a well-mixed plume, or it can be distributed using a probability density function as a function of height, which allows the mass to be distributed within a specified section of the plume, i.e. the top 30% representing the umbrella region. H_i is the maximum height of the plume which is controlled by the energy and mass flow of the eruption.

Particle fall is controlled by particle settling velocity, which is a function of particle size, shape and density (Connor et al., 2001). The size of particles is constrained by the sieve size (i.e. -4.5 to 4.5Φ , which is 22 to 0.05mm), and the particles are assumed to be spherical. Density varies with particle size, as coarse particles contain abundant vesicles and fine particles are likely to comprise predominantly crystals (Bonadonna et al. 2005). In order to account for this, *Tephra2* uses a linear model to approximate the change in density with particle size (Connor et al., In Prep.). Aggregation of fine particles is not accounted for in the *Tephra2* model.

When particles are released from a point source within a horizontal layer, i , they are transported by the wind specific for that layer until it falls into the next layer (Figure 6.3). Particles are affected by the wind speed and direction for each layer until they reach the ground. The total fall time of the particles is the sum of the fall time through the layers from the particle release point to the ground, assuming the particle settling velocity is reached instantaneously

(Bonadonna et al., 2005). The model also takes into account the Reynolds number, which describes the regime in which the particle is settling, i.e. laminar, intermediate or turbulent (Equation 6.2). The Reynolds number is calculated at every step during the particle's fall (Connor et al., In Prep.):

$$v_j = \begin{cases} \frac{\rho_j g d_j^2}{18\mu} & \text{if laminar, } Re < 6 \\ d_j \left[\frac{4g^2 \rho_j^2}{225\mu\rho_\alpha} \right]^{1/3} & \text{if intermediate, } 6 \leq Re < 500 \\ \left[\frac{3.1\rho_j g d_j}{\rho_\alpha} \right]^{1/2} & \text{if turbulent, } Re \geq 500 \end{cases}$$

Equation 6.2

where ρ_j is particle density, d_j is the diameter of particles of size j , μ is air viscosity ($\mu = 0.000018325$ Pa-s), g is gravity ($g = 9.81$), and ρ_α is air density of layer i in the atmosphere:

$$\rho_\alpha = \rho_{std} e^{-h_i/8200}$$

Equation 6.3

where $\rho_{std} = 1.293$ kg m³ at sea-level and h_i is the height above sea-level of the centre of the atmospheric layer i .

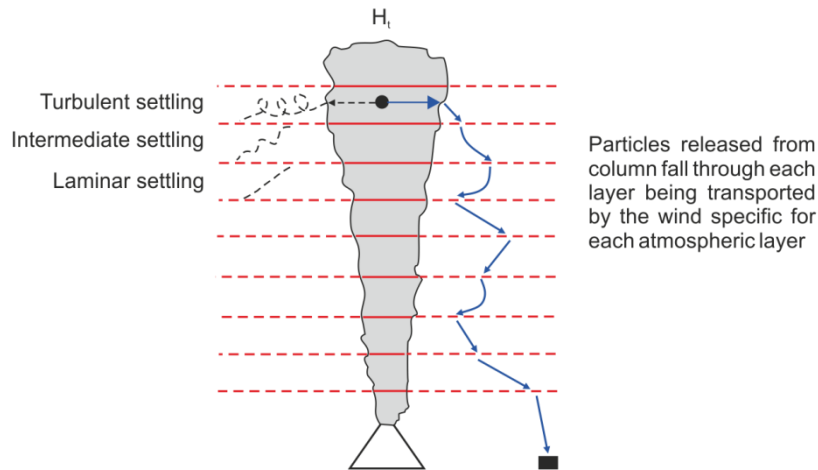


Figure 6.3 Schematic diagram showing particle fall and transport through the layers.

The particles Reynold's number is calculated for each layer, taking into account the settling regime i.e. turbulent, intermediate or laminar.

Particles are dispersed horizontally due to gravitational spreading, atmospheric diffusion and wind. The distribution of mass is assumed to be lognormal with a Gaussian distribution (Figure 6.4) in the x and y directions. During the time spent in each layer, the centre of the Gaussian distribution is shifted in the x - y plane by the wind specific for that layer. Diffusion is assumed

to be isotropic in the x,y plane, and is calculated from the total fall time, the horizontal diffusion time, a diffusion coefficient and a turbulent eddy diffusivity constant. The *Tephra2* model simplifies plume and atmospheric processes by combining them into a single parameter ($\sigma_{i,j}^2$):

$$\sigma_{i,j}^2 = \begin{cases} 4K(t_{i,j} + t'_i) & \text{if } t_{i,j} < \tau \\ \frac{8C}{5}(t_{i,j} + t'_i)^{5/2} & \text{if } t_{i,j} \geq \tau \end{cases}$$

Equation 6.4

where K is a constant diffusion coefficient, C is a turbulent eddy constant, $t_{i,j}$ is the increased horizontal diffusion time accounting for the broadening of the plume with height, and τ is the fall time threshold. The model assumes all particles are released from the plume from a vertical centre line. To account for the increase in column width, the horizontal diffusion time is increased as a function of height:

$$t'_i = [0.2h_i^2]^{2/5}$$

Equation 6.5

For coarse particles with a small fall time, the horizontal diffusion ($t_{i,j}$) is less than fall time threshold (τ), therefore the diffusion is assumed to be linear with total fall time. However, for fine particles, fall time is on the scale of hours and spread out within the umbrella region of the plume, so $t_{i,j} \geq \tau$, and diffusion is therefore non-linear with total fall time.

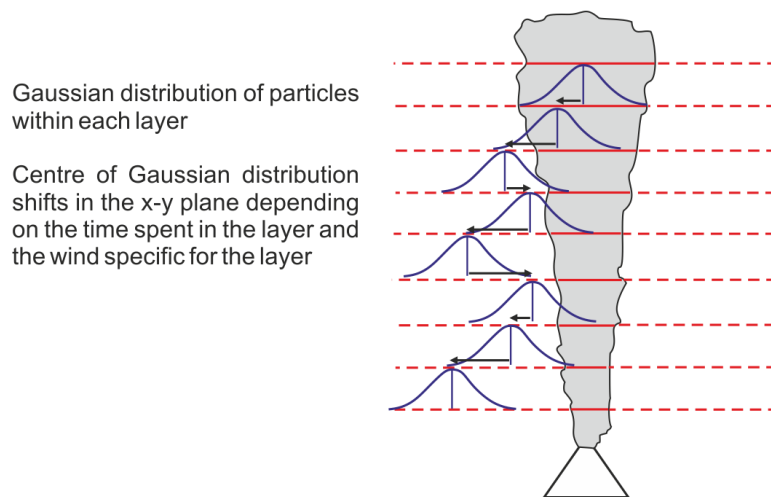


Figure 6.4 Schematic diagram showing the Gaussian distribution of particles within each layer.

The centre of the Gaussian distribution shifts depending on the time spent in each layer, and on the wind speed and direction specific to each layer

The term $f_{i,j}(x, y)$ from Equation 6.1 is a function that uses the advection-diffusion equation to estimate the fraction of mass of a given particle size (j) and release height (i) to fall to the ground at point (x, y) ; i.e. it describes the horizontal dispersion of tephra:

$$f_{i,j}(x, y) = \frac{1}{2\pi\sigma_{i,j}^2} \exp \left\{ -\frac{(x - \bar{x}_{i,j})^2 + (y - \bar{y}_{i,j})^2}{2\sigma_{i,j}^2} \right\}$$

Equation 6.6

where $\sigma_{i,j}^2$ is the variance of the Gaussian distribution (Equation 6.4), and $(x - \bar{x}_{i,j})^2 + (y - \bar{y}_{i,j})^2$ is the shift of the centre of the Gaussian distribution in the x and y directions as a result of wind speed and time spent within the layer i . The coordinates of the centre of the bivariate Gaussian distribution are:

$$\begin{aligned} \bar{x}_{i,j} &= x_i + \sum_{layers} \delta x_j \\ \bar{y}_{i,j} &= y + \sum_{layers} \delta y_j \end{aligned}$$

Equation 6.7

where δx_j and δy_j are the distances travelled on the x and y planes, respectively.

6.1.1.1 Model Inputs

In order to solve the mass-conservation equation, *Tephra2* requires a number of input parameters to be defined, which are summarised in Table 6.1. These parameters can be adjusted to observe the effects of each parameter on the outputs, i.e. the eruption column height, the erupted mass and the tephra dispersion maps; however, many combinations of input parameters can match the observed deposit thickness and grain size (Connor and Connor, 2006). The model therefore uses the downhill simplex algorithm (Nedler and Meade, 1965; Connor and Connor, 2006), a non-linear inversion model, to search for the best-fit eruption parameter set that minimises the error between the measured tephra thickness and grain size distribution, and the model outputs (Connor and Connor, 2006).

The non-linear inversion model systematically changes the parameters to find the optimal solution, or minimum. Combinations of parameters define points in a dimensional space, and each point represents a vertex of a simplex, an N-dimensional tetrahedron. The algorithm shifts each vertex towards the centre of the simplex, where they converge at the optimal set of parameters (Connor and Connor, 2006). Simulations are run in parallel on multiple processors which allows rapid implementation of the physical model and a fully probabilistic analysis of tephra fall hazard (Bonadonna et al., 2005). Input parameters are often not well constrained therefore stochastic sampling of parameter ranges is used allowing different scenarios to be

investigated (Bonadonna et al., 2005). This approach means that more simulations are undertaken giving a better understanding of the full range of outcomes (Bonadonna et al., 2005).

Input parameter	Description
Volcano location	Vent northing and easting (utm)
Plume model	Defines the plume shape (1 or 2)
Column integration steps	Number of layers within column (i)
Particle integration steps	Number of layers particle falls through (atmosphere layers)
Lithic density	-
Pumice density	-
Vent elevation	Height of the vent (m a.s.l.)
Phi range	Measured grain size range of deposit
Plume elevation	Range of the plume height (km a.s.l.)
Diffusion coefficient	Range of diffusion coefficient values - the larger the diffusion coefficient, the longer the diffusion time i.e. the larger the plume width
Eddy constant	Turbulence constant in the plume (0.04)
Total mass	Range of total erupted mass (kg)
Median phi	Range or fixed average grain size of observed deposit
Sigma phi	Range or fixed standard deviation of grain size of observed deposit
Fall time threshold	Range of particle fall times
Alpha and beta	Ranges of α and β which define the plume shape (using plume model 2)
Wind speed	Range (m/s)
Wind direction	Range from -180 to 180, where north = 0

Table 6.1 Input parameters for the *Tephra2* inversion.

The model outputs (grain size distribution and tephra thickness) are compared with the measured grain size distribution and tephra thickness; parameter ranges can be altered to find the best fit between measured and calculated. However, some eruption parameters are more difficult to constrain than others. Scollo et al. (2008) performed sensitivity tests on the *Tephra2* model, and found that the total eruption column height, particle size distribution and wind field are interdependent, and model output is non-linearly dependent on these parameters, therefore can be difficult to constrain. The model is, however, linearly dependent on, and sensitive to, the total eruption mass therefore the mass can be well-constrained through the inversion (Scollo et al., 2008).

The model inputs include physical parameters such as the volcano location and vent height, lithic and pumice density, which can be altered to represent each eruption deposit, deposit grain size (range, median and standard deviation or sigma phi estimated from measured deposit) and wind speed and direction. The wind speed and direction can be constrained using local meteorological data. The total erupted mass is generally well-constrained by the model,

therefore a narrow range can be specified after the first few runs in order to focus on finding the best fit for less-well constrained parameters.

Computational input parameters are also required, for example, the column and particle integration steps which define the number of layers the plume and atmosphere are divided into. The plume model (either 1 or 2) relates to the shape of the eruption column, and is a parameter which was used in the *Tephra* model. Model 1 is a uniform random distribution reflecting the structure of a well-mixed strong plume, and model 2 uses a probability density function of mass as a function of height (Bonadonna et al., 2005; Connor and Connor, 2006). *Tephra2* uses plume model 2, which defines the shape of the eruption column in terms of the alpha and beta parameters. If $\alpha = \beta = 1$, then the plume reflects a uniform random distribution, if $\alpha > \beta$, the particles are released at heights towards the top of the column, reflecting widening of the plume with height. If $\alpha < \beta$, particles are released towards the base of the plume (Connor et al., In Prep.).

6.1.1.2 *Some Model Assumptions and Limitations*

The distribution and transport of tephra erupted from a volcano is affected by numerous complex processes occurring within the plume, and atmospheric processes which affect the eruption column and the particles once they have left the plume. In order to model the dispersion of tephra from a volcano, models simplify the processes involved, by making a series of assumptions. This is true of all tephra dispersion models e.g. FALL3D (Folch et al., 2012), HYSPLIT (Draxler and Hess, 1998) and ASH3D (Schwaiger et al., 2012), to name a few. However, with awareness and understanding of these assumptions, tephra dispersion models are very useful tools for estimating eruption volumes and possible dispersion patterns.

The principal assumptions of *tephra2* relate to the particles themselves. It is assumed that all particles are spherical; however, volcanic ash particles are typically shards resulting from the explosive fragmentation of the magma. Angular and spherical particles will behave very differently in a flow, i.e. in the eruption column and falling through the atmosphere. To account for these differences in behaviour the settling regime according to stokes law, i.e. turbulent, intermediate or laminar, is calculated for each layer the particles fall through. Another limitation of *tephra2* is that it discounts particle aggregation – a process well documented in eruption columns (e.g. Carey and Sigurdsson, 1982). Aggregated particles will be denser and therefore have a much shorter fall time than individual particles.

Within the *Tephra2* model, eruption parameters, such as column height, are averaged for the entire eruption. In reality, however, the eruption parameters will vary throughout the eruption. Although there are a number of assumptions in the *tephra2* model, multiple inversions run in parallel, enables rapid comparison of results and evaluation of uncertainty for the modelled

eruption. Further limitations of the model are discussed in relation to the Colima eruption deposits in the next section.

6.2 Modelling Tephra Dispersion at Volcán de Colima

Tephra dispersion modelling has been carried out for units Y, W, U, S and P of the Group I eruption deposits using the *Tephra2* model. The thickness of each of the eruption deposits was measured at 8 to 30 localities and granulometry samples for grain size distribution were collected from 2 to 8 localities across the CVC compiled from data collected by Jim Luhr, and collected as part of this work (Table 6.2). The total sample was weighed, and then sieved separating the sample into fractions from -4.5 phi to 4.25 phi (22 to 0.05mm). Each size fraction was then weighed to give the grain size distribution at each locality. The grain size distribution and thicknesses for units Y, W, U, S and P at locality VF10-04, the most distal sample location at 10 km from the vent, are given in Table 6.3. The full set of data tables are given in Appendix J. Figure 6.5 shows the grain size distribution for each of the eruption units at VF10-04.

Unit Y is the thickest of the Group I eruption deposits, varying from 48 to 140cm, at 4 to 10 km from the vent. This unit is also the coarsest, with pumice clasts of up to 17cm across, 8 km from the vent. The grain size distribution at VF10-04 reveals the -3 and -2 phi fractions, which correspond to 8 and 4mm, are dominant in unit Y, which has a thickness of 48cm at this locality. Unit W is the thinnest of the Group I eruption deposits, varying from 8 to 28cm thick. At locality VF10-04, unit W has a thickness of 8cm, and the grain size distribution reveals the -1 and 0 fractions (0 and 2mm) are dominant in unit W (Figure 6.5).

Unit	Number of Localities	Thickness (cm)	Number of granulometry samples	Phi range
Y	28	48 – 140	8	-4.5 – 4.25
W	23	8 – 28	2	-4 – 4.25
U	30	15 – 27	7	-4.5 – 4.25
S	24	12 – 46	7	-4.5 – 4.25
P	21	6 – 40	8	-4.5 – 4.25

Table 6.2 Measured thickness and grain size range for units Y, W, U, S and P of the Group I eruption deposits.

Unit	Thickness (cm)	Total Weight (g)	-4.5 (g)	-4 (g)	-3 (g)	-2 (g)	-1 (g)	0 (g)	1 (g)	2 (g)	3 (g)	4 (g)	4.25 (g)
Y	48	509	9.87	20.7	114.2	118.5	77.3	54.3	39.0	26.1	17.8	25.0	5.9
W	8	340	-	3.46	17.9	61.6	85.9	83.6	58.9	23.9	2.5	2.1	0.5
U	27	418	43.8	52.1	95.2	85.0	63.3	40.7	19.4	7.4	4.5	4.3	3.0
S	42	1390	-	79.1	315.8	423.4	380.5	164.7	22.4	2.0	0.9	0.6	0.5
P	17	675	30.6	46.6	124.5	166.4	145.5	105.8	44.0	6.1	2.3	2.0	1.5

Table 6.3 Granulometry data from section VF10-04 (VF95-06 of Luhr et al., 2010), ~10km from the vent. Data from units Y and W were collected by Jim Luhr.

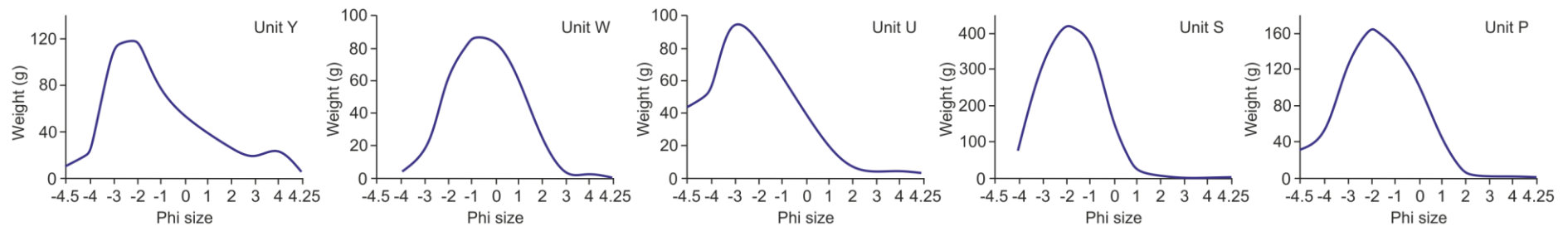


Figure 6.5 Grain size distribution for units Y, W, U, S and P at section VF10-04 using the data in Table 6.3.

In order to model the eruption deposits, a number of input parameters were constrained (see Table 6.1). Many of these parameters are fixed, such as vent location and height, while other parameter values or ranges are determined through trial and error while searching for the best fit, such as diffusion coefficient, column and particle integration steps, wind speed and direction, and eruption column height. The grain size data (range, median and standard deviation) are determined from the grain size distribution data collected in the field. Many of the eruption parameters are set as ranges, allowing the model to find a best fit. If too many parameters are fixed, the model can give spurious results. Table 6.4 gives the input parameters that yielded the best fit for units Y, W, U, S and P.

Input Parameter	Unit Y	Unit W	Unit U, S	Unit P
Vent Northing	2158088	2158088	2158088	2158088
Vent Easting	0645110	0645110	0645110	0645110
Plume Model	2	2	2	2
Column Integration Steps	60	60	60	40
Particle Integration Steps	60	60	60	40
Lithic Density (kg/m ³)	2600	2600	2600	2600
Pumice Density (kg/m ³)	1000	1000	1000	1000
Vent Elevation (m a.s.l.)	3850	3850	3850	3850
Phi Range	-4.5 to 4.5	-4.5 to 4.5	-4.5 to 4.5	-4.5 to 4.5
Maximum Plume Elevation (km a.s.l.)	10 to 30	10 to 30	10 to 30	10 to 30
Diffusion Coefficient	2000 to 5000	2000 to 10,000	2000 to 5000	2000 to 5000
Eddy Constant	0.04	0.04	0.04	0.04
Total Mass (kg)	1×10 ⁹ - 1×10 ¹¹	1×10 ⁹ - 1×10 ¹²	1×10 ⁹ to 1×10 ¹²	1×10 ⁹ to 1×10 ¹²
Median Phi	-2 to 3	-2 to 3	-2 to 3	-2 to 3
Sigma Phi	0.25 to 4	0.25 to 4	0.25 to 4	0.25 to 4
Fall Time Threshold	1×10 ⁹ to 1×10 ⁹	1×10 ⁹ to 1×10 ⁹	1×10 ⁹ to 1×10 ⁹	1×10 ⁹ to 1×10 ⁹
Alpha	0.001 to 5.0	0.001 to 5.0	0.001 to 5.0	0.001 to 5.0
Beta	0.001 to 15.0	0.001 to 15.0	0.001 to 15.0	0.001 to 15.0
Wind Speed (m/s)	10 to 30	0 to 25	10 to 30	10 to 30
Wind Direction	-20 to 70	-20 to 70	-20 to 70	-20 to 70

Table 6.4 Input parameters for units Y, W, U, S and P of the Group I eruption deposits.

The same input parameters yielded the best fit for units U and S.

The grain size data reveal that the deposits exposed on the flanks of Nevado de Colima represent the coarse fractions, which is consistent with their location close to the vent (~4 to 10 km). As a result, finer fractions are not well represented by the model, and the tephra distribution maps are not accurate representations of distal deposits. The horizontal diffusion time is less than the fall time threshold (τ) for coarse particles (Equation 6.4), therefore τ is

negligible for the coarse particles. In the *Tephra2* model, τ was set to a high value of 1×10^9 , effectively removing it from the model.

Altering the diffusion coefficient strongly affects the eruption column height, and through a series of trial and error runs, was constrained to a best fit value ranging from 2000 to 5000 for units Y, U, S and P, and 2000 to 10,000 for unit W.

The output parameters from the best fit runs are given in Table 6.5. The maximum column heights vary between the units, with the lowest column height in unit W and the highest in unit Y. This is mirrored by the total mass ejected with unit Y having the highest mass, and unit W the lowest. These results are consistent with field observations, which reveal unit Y is the thickest unit of the Group I eruption deposits, while unit W is the thinnest. The beta parameter for each of the units is consistently higher than alpha, which describes a column shape with the majority of tephra falling from the top of the column. This is consistent with the diffusion coefficient, which is high, describing more time spent in the column.

Output Parameters	Unit Y	Unit W	Unit U	Unit S	Unit P
Max Column Height	29,848	19,821	23,120	26,825	27,445
Alpha	1.01	0.73	0.04	0.001	1.15
Beta	5.46	13.36	0.21	0.29	6.90
Diffusion Coefficient	4616	6538	3959	4390	2001
Total Mass Ejected	2.39×10^{11}	1.80×10^{11}	1.17×10^{11}	1.31×10^{11}	1.24×10^{11}
Median Phi	1.01	2.93	2.43	-1.56	2.35
Std. Dev	0.25	3.99	3.98	0.32	2.29
Fit	13.50	7.66	7.04	9.80	8.70
NRMSE	0.28	0.27	0.21	0.19	0.20

Table 6.5 Results of tephra dispersion modelling for units Y, W, U, S and P of the Group I eruption deposits.

The output values are best fit values for the input parameters to match the observed deposit thickness and grain size distribution. NRMSE = Normalised Root Mean Square Error.

The model was run numerous times, varying the input parameters to find the best fit. The ranges of eruption column heights are shown in Figure 6.6. The eruption column height shows a wide variation in values for all the units, particularly unit Y. This is due to the spatial distribution of the samples. The proximity and clustering of the samples close to the vent means that the grain size distribution reflects only the coarse fractions, and does not reflect the very fine particles that are carried tens or hundreds of km from the vent. As a result, there is no unique solution, in terms of eruption column height, for the measured data. In other words, a variety of different column heights may reproduce the eruption deposit based on currently

available data. This is consistent with results from sensitivity tests carried by Scollo et al. (2008), who found eruption column height difficult to constrain.

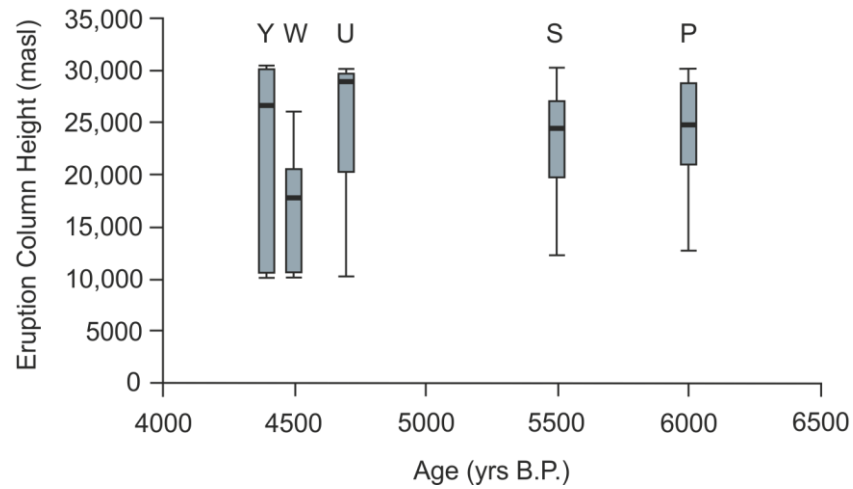


Figure 6.6 Eruption column height box plot.

The grey box is the lower and upper quartile, while the thick black line in the grey box is the median value. The whiskers are the minimum and maximum values. The eruption column heights show a wide variation in all units. This is because all samples are clustered, proximal to the vent therefore there is no unique column height value to reproduce the measured deposit thickness and grain size distribution.

Another source of this uncertainty could be with the wind profiles. Wind direction was estimated based on historical information and prevailing wind directions for the Colima area, which are from the southwest. The distribution of the samples to the northeast of Volcán de Colima, suggests a wind direction of -20 to 70° (from north); however, at least two sector collapse events have occurred which post-date the modelled eruption deposits (Cortés et al., 2010). These collapsed to the south, forming massive debris avalanche deposits which would have eroded any fallout deposits preserved to the south of Volcán de Colima. To test this, Tephra2 was run using a variety of different wind directions; however, because all the samples are located to the northeast of the vent, the best fit was with a wind direction of -20 to 70° .

The wind speed can also be a source of uncertainty in the model results, as different wind speeds can dramatically affect the eruption column height. However, as previously mentioned, due to the proximity of samples to the vent, there is no unique solution for eruption column height. Therefore, through trial and error, the best fit for wind speed was constrained to 10 to 30 m/s for units P, S, U and Y, and 0 to 25 m/s for unit W (Table 6.4).

The total erupted mass is easier to constrain as the thickness and grain size distribution of the deposit is dependant on the erupted mass. The median and ranges of total erupted mass are given in Figure 6.7. Unit Y has the highest average erupted mass, with a median of 3.3×10^{11} kg,

while unit U has the lowest with a median erupted mass of 5.5×10^{10} kg. Unit P was more difficult to constrain, with a range of 4.6×10^{10} to 1×10^{12} kg, and a median of 2.15×10^{11} kg.

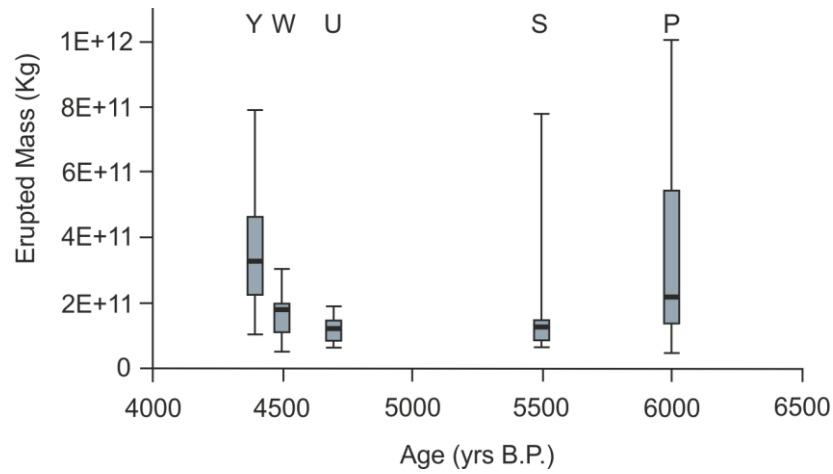


Figure 6.7 Total erupted mass (kg) boxplot of the results of modelling for units Y, W, U, S and P of the Group I eruption deposits.

The total erupted mass is better constrained than the eruption column height, with unit Y having the highest median value and unit U, the lowest.

6.2.1 Tephra Thickness Maps

The *Tephra2* model creates a contoured isopach map of the tephra fallout deposit. Figure 6.8 shows isopach maps for units Y, W and S using the output parameters in Table 6.5. Unit Y is the largest of the Holocene explosive eruptions with an estimated volume of $\sim 0.2 \text{ km}^3$. The isopach map reveals tephra dispersal to the north-northeast, with the city of Ciudad Guzman having a fallout thickness of 5 to 10 cm. Tephra dispersal for unit S is also to the north-northeast, with 5 to 10 cm thick fallout in Ciudad Guzman; however, the deposit isn't as widely dispersed as it has a much lower volume than unit Y (Figure 6.8). The isopach map for unit W reveals tephra dispersion to the northeast, and only 1 to 2 cm thick fall in Ciudad Guzman.

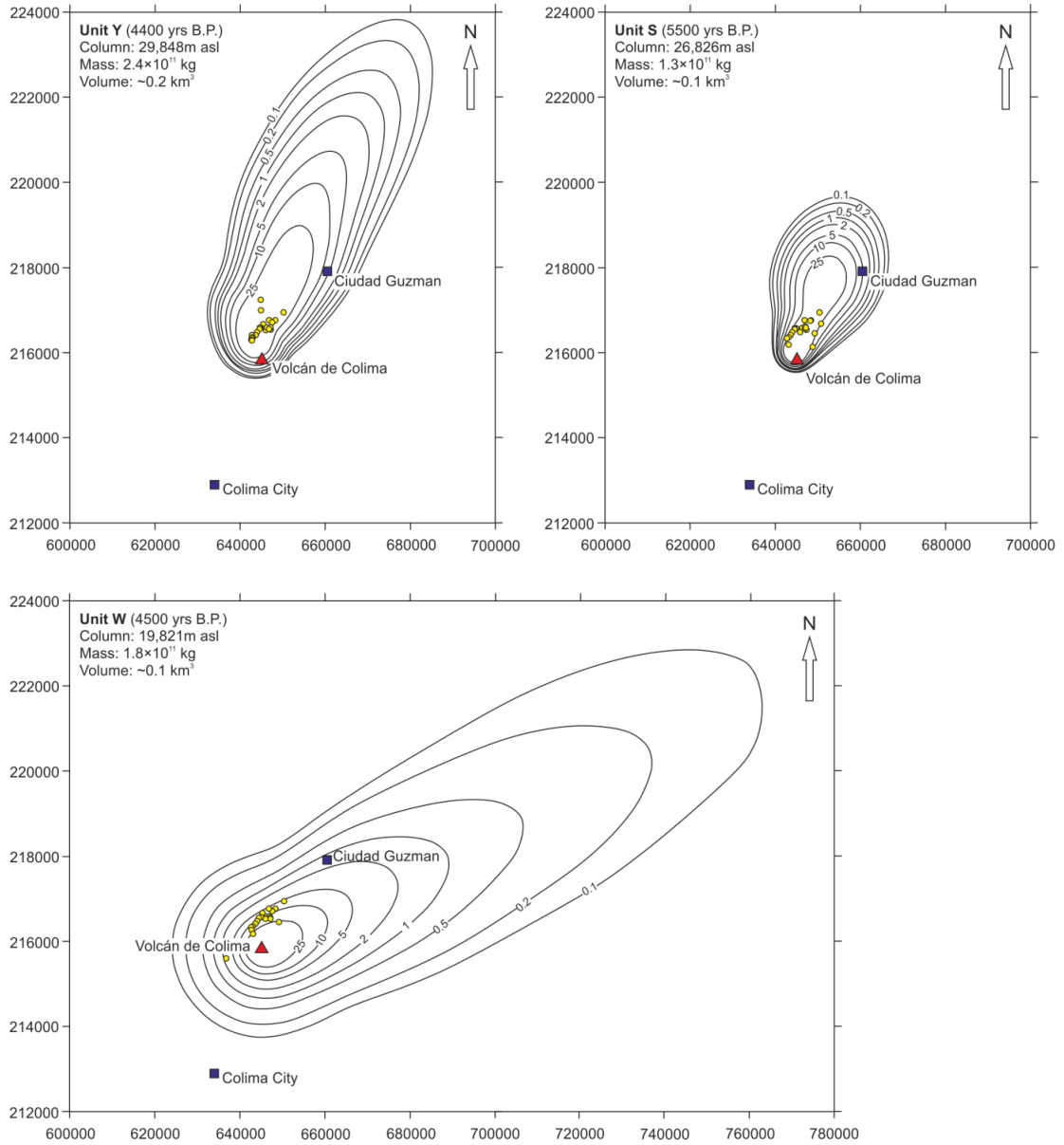


Figure 6.8 Tephra thickness maps for units Y, W and S of the Group I eruption deposits.

Although these maps are useful to compare the eruption deposits, they do not accurately reflect the dispersion of fine particles, as they are calculated based on samples collected close to the vent which represent the coarse grain size fractions. As a result, although we can draw comparisons between the modelled units, the maps are not true representations of tephra dispersal from such explosive eruptions. More detailed field work is therefore required to locate distal sections with finer particles, in order to better constrain the dispersal pattern, the erupted volume and the eruption column height.

6.3 Summary

The tephra2 model has been used to estimate the total erupted volume and tephra dispersion of units Y, U, W, S and P of the Group I deposits. Tephra2 is an advection-diffusion model which

calculates the accumulation of tephra on the ground which has been affected by processes occurring within the eruption column and atmosphere.

The tephra dispersion modelling results presented in this chapter reveal eruption deposits exposed on the flanks of Nevado de Colima were produced by sub-plinian (0.03 to 0.3 km^3 volume) explosive eruptions. The results are consistent with field observations, with the thickest unit, Y, yielding the highest erupted volume estimates. Comparisons can also be drawn between the erupted volumes and the magma compositions of the tephra fallout deposits. Unit Y is the most evolved of the Group I eruption deposits with up to 60.4 wt.% SiO_2 (see Section 2.4.1). In the field, this unit forms a distinct horizon comprising a cream pumice fallout deposit varying in thickness from 48cm to 1.4m (see Section 2.1), at distances of 4 to 12 km from the vent. The average erupted mass for unit Y, from 12 runs, is 3.3×10^{11} kg, roughly corresponding to an eruption volume of 0.3 km^3 using a pumice density of 1000 kg/m^3 .

Unit U is the least evolved unit with SiO_2 contents as low as 50.7 wt.% (see Section 2.4). Scoria from this unit is very dark in colour and the deposit has a fairly uniform thickness across the area of 15 to 20cm. The average estimated erupted mass for unit U, from 8 runs, is 5.5×10^{10} kg. Unit U scoria is denser than the unit Y pumice; therefore, the erupted volume is estimated at $\sim 0.03 \text{ km}^3$, using a density of 1800 kg/m^3 . A density of 1000 kg/m^3 would give a volume of $\sim 0.05 \text{ km}^3$. These initial results show that the more evolved deposits at the CVC resulted from higher volume eruptions, relative to the more mafic units.

Tephra dispersion maps reveal the city of Ciudad Guzman would be covered by 1 to 10cm of ash if another such explosive event were to occur at Volcán de Colima. However, granulometry and thickness data for the eruption deposits were collected from samples proximal to the vent, therefore the maps are not true representations of the ash dispersal from such explosive eruptions from Volcán de Colima. In order to assess the impact of such an explosive eruption, data needs to be collected for more distal deposits, where fine fraction sizes are preserved. To date, no distal localities have been found that can be correlated with the CVC Holocene eruption deposits presented here.

7 Conclusions

This research provides the first detailed insights into the Holocene evolution of the CVC. Tephra fallout deposits exposed on the flanks of Nevado de Colima, reveal a record of explosive activity at the CVC spanning the past ~30,000 years. Through field work carried out during this research and by Jim Luhr, Carlos Navarro-Ochoa and Ivan Savov, the tephra stratigraphy up to ~13,000 yrs B.P. is well defined across the CVC.

Petrological and geochemical analyses of the tephra fallout deposits reveal that the majority of deposits are medium-K sub-alkaline, ranging from basaltic-andesite to andesite in composition, with typical subduction-related magma trace element signatures (Group I). Three of the fallout deposits, erupted at c.7000, c.12,000 and c.13,000 yrs B.P., are mineralogically distinct, characterised by the presence of phlogopite, and geochemically distinct, with high K₂O and P₂O₅ and strongly enriched incompatible trace element abundances, relative to the Group I deposits.

The Group II magma compositions are intermediate between the Group I magmas and the alkaline magmas which formed monogenetic cinder cones on the rift floor between 450 ka and 62 ka (Allan and Carmichael, 1984; Carmichael et al., 2006). These cinder cones comprise primitive mafic magmas with mineral assemblages dominated by phlogopite, clinopyroxene and olivine (+ apatite + sanidine) with high MgO, CaO, TiO₂, K₂O and P₂O₅ (Luhr and Carmichael, 1981; Carmichael et al., 2006; Maria and Luhr, 2008; Vigouroux et al., 2008; Cai, 2009). Through two-component geochemical mixing models after Langmuir et al. (1978), we have been able to quantitatively evaluate the relationship between the alkaline and sub-alkaline CVC magmas, as proposed by Luhr and Carmichael (1981). The Group II magmas contain between 20 and 70% alkaline component, and are derived from a physical mixing between the two magma types. These units are interbedded within the CVC Group I stratigraphy, and reveal pulses of alkaline magmatism on timescales of a few thousand years.

Phenocryst phases present in the Group I and Group II pumice and scoria samples display textures, zoning patterns and core-rim compositions reflecting multiple phases of crystal growth and dissolution. Such textures have been interpreted to reflect decompression and magma replenishment events. These complex crystallisation histories are consistent with a plumbing system involving multiple magma storage regions. Using the petrological data in combination with the whole-rock geochemical and isotopic data, and recent geophysical studies, we have been able to propose a model defining magma petrogenesis at the CVC, which is shown again in Figure 7.1.

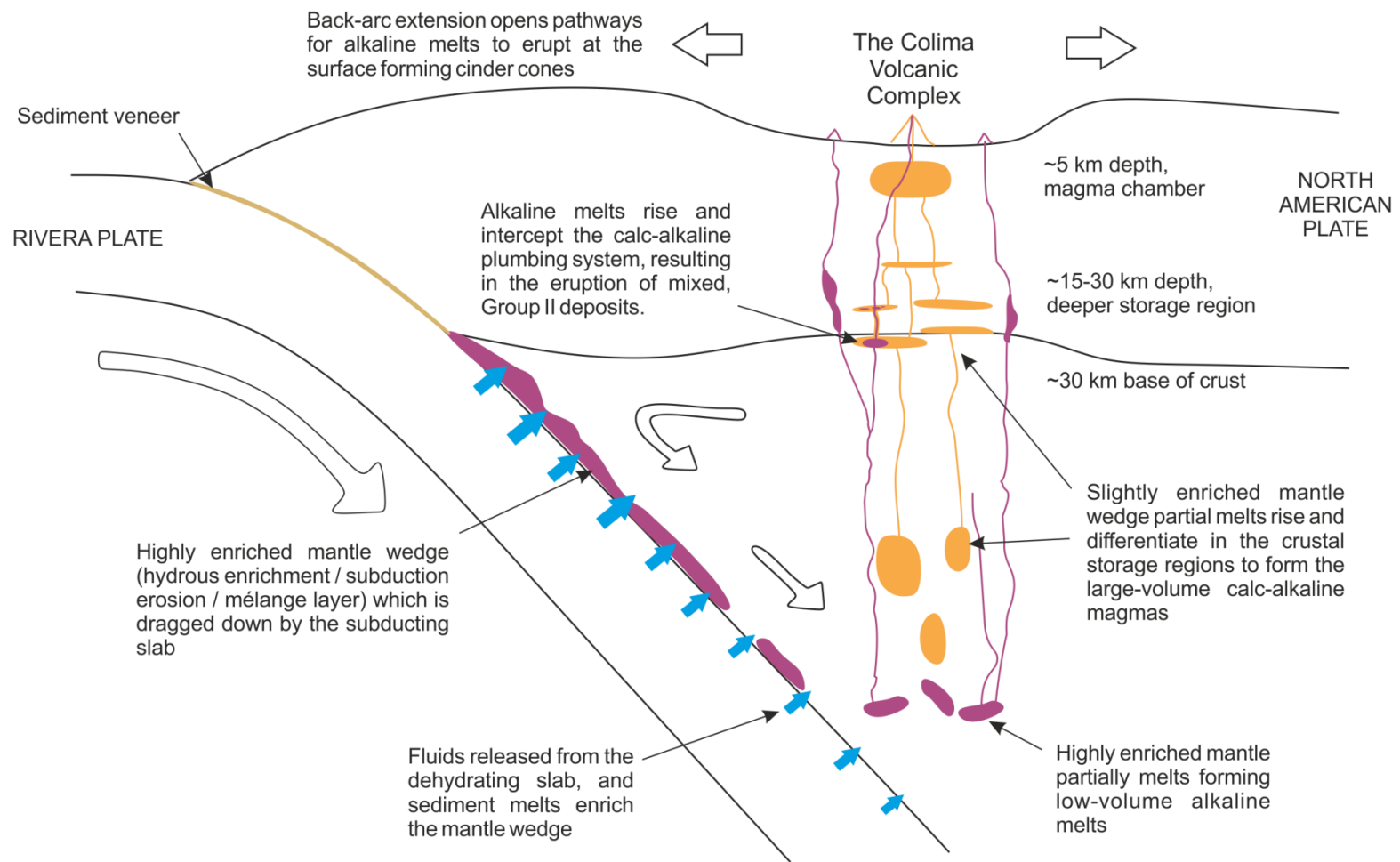


Figure 7.1 Petrogenesis of the CVC magmas.

Volcanism at the CVC is dominated by large volume sub-alkaline magmas which are derived from partial melts of the sub-arc mantle peridotite. Incompatible trace-element data reveal enrichments in the fluid- and melt-mobile elements (i.e. Rb, Ba, Th, La, Ce, Sr) which can be attributed to the addition of small amounts of slab-derived fluids and subducted sediment melts. Partial melts of the enriched peridotite mantle then evolve within the plumbing system of the CVC, undergoing magma differentiation and continued pulses of magma replenishment. The mineralogical data reveal multiple magma storage regions which is consistent with geophysical studies which reveal possible magma chambers at ~5 km depth and at 15-30 km depth (Zobin et al., 2002; Gardine, 2010; López-Loera, 2012).

Scoria and pumice samples from the Holocene eruption deposits display highly vesiculated groundmass glass textures and contain stable hornblende phenocrysts with no breakdown rims. These textures are indicative of very fast ascent rates from the storage region to the surface, supported by high water content estimates from plagioclase-melt equilibria. The majority of the Group I eruption deposits (bar units Y, U and S) contain both stable and unstable hornblende phenocrysts displaying breakdown rims of plagioclase, pyroxene and Fe-Ti oxides. This juxtaposition of stable and unstable hornblende in a single clast can result from a late stage magma mixing event, perhaps triggering explosive eruptions at the CVC.

The alkaline magmas are heterogeneous, and are strongly enriched in the incompatible trace elements relative to the sub-alkaline magmas reflecting metasomatism by slab-derived fluids and enrichments from subducted sediment melts. The alkaline magmas which formed monogenetic cinder cones on the Colima rift floor, are considered to represent direct metasomatic vein melts with little differentiation (e.g. Maria and Luhr, 2008). The presence of mixed (Group II) magmas within the CVC tephra stratigraphy indicates pulses of these alkaline magmas intersect the magmatic storage region of the CVC.

The tephra fallout deposits exposed on the flanks of Nevado de Colima show a wide range of compositions from basalt to high-silica andesite. Initial tephra modelling of units Y, W, U, S and P of the Group I fallout deposits has revealed a link between magma composition and eruption volume, with the most evolved magmas resulting from the highest volume eruptions at the CVC.

7.1 Future Work

The focus of this research has been the broader picture, with investigations into the whole-rock geochemistry and whole-rock isotopic composition of the different eruption deposits. Recommendations for future work include detailed investigations into individual eruption deposits. Whole-rock geochemical analyses of unit Y samples reveals intriguing compositional trends that we propose can be explained by the extraction (or addition) of plagioclase +

hornblende + clinopyroxene + orthopyroxene. Geochemical and isotopic analyses of mineral and glass separates from unit Y pumice samples would provide further insights into the differentiation of the unit Y magma, and its unusual composition. Unit Y is also the thickest fallout deposit exposed on the CVC, varying from 48cm to 1.4m. Detailed sampling across this deposit may reveal its geochemical and petrological evolution during the eruption.

Similar detailed investigations into the mixed (Group II) units could provide valuable insights into the relationship between the alkaline and sub-alkaline magmas. Whole-rock Sr-Nd isotopic analyses reveal two samples from unit F have isotopic compositions similar to the alkaline magmas, with up to 70% alkaline component. Other samples from unit F comprise up to 30% alkaline magma component. Further detailed analyses of the Group II samples, particularly unit F, would better constrain the percentage of alkaline component intercepting the CVC magmatic plumbing system.

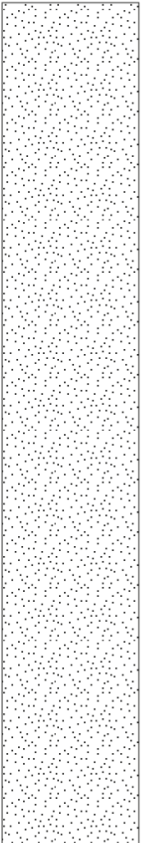


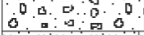

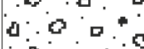
Based on mineral zoning patterns and EPMA major element analyses, the Group I and Group II magmas are interpreted to have evolved within the same magmatic plumbing system. A test for this would be to microsample phenocryst types common to both groups, for Sr isotope analysis, as phenocrysts with the same provenance will have the same Sr isotopic ratio. Another test, would be to look at the trace element concentrations in the phenocrysts. Such analyses would enable us to better understand the processes occurring within the CVC magmatic plumbing system.

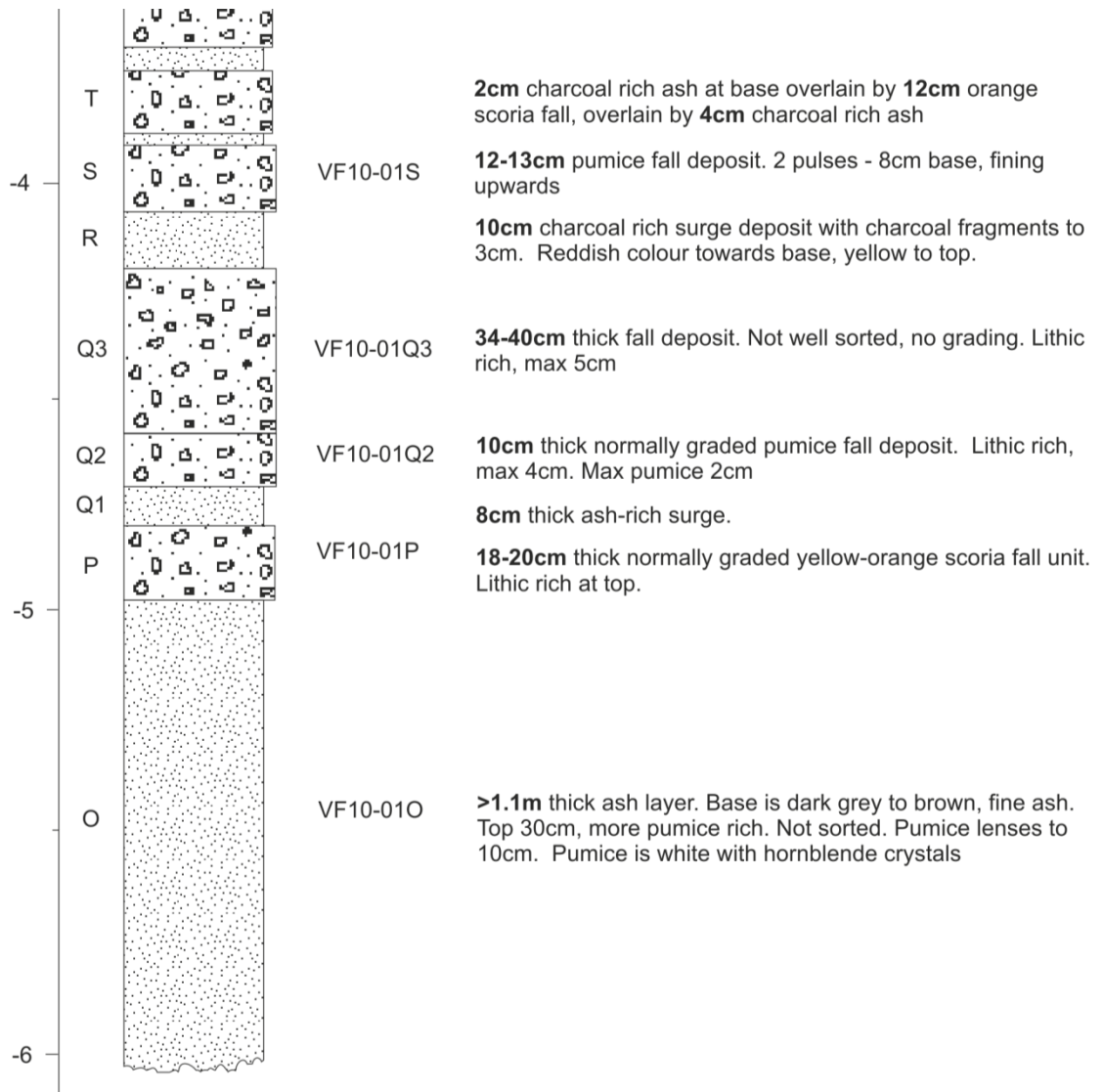
Based on the groundmass glass and hornblende phenocryst textures, the tephra fallout deposits are interpreted to have resulted from very fast ascent rates from the magmatic storage region to the surface. Diffusion modelling of olivine phenocrysts would enable the timescales of magma replenishment and eruption rate to be determined.

Further work is also needed on the tephra dispersion modelling. Due to lack of exposure, no modelling has been carried out on the mixed eruption deposits, which are the most mafic fallout deposits of the CVC. Further field work is required to find exposures of these deposits, and to find distal sections with finer fractions that can be modelled to better constrain the tephra dispersion maps presented here.

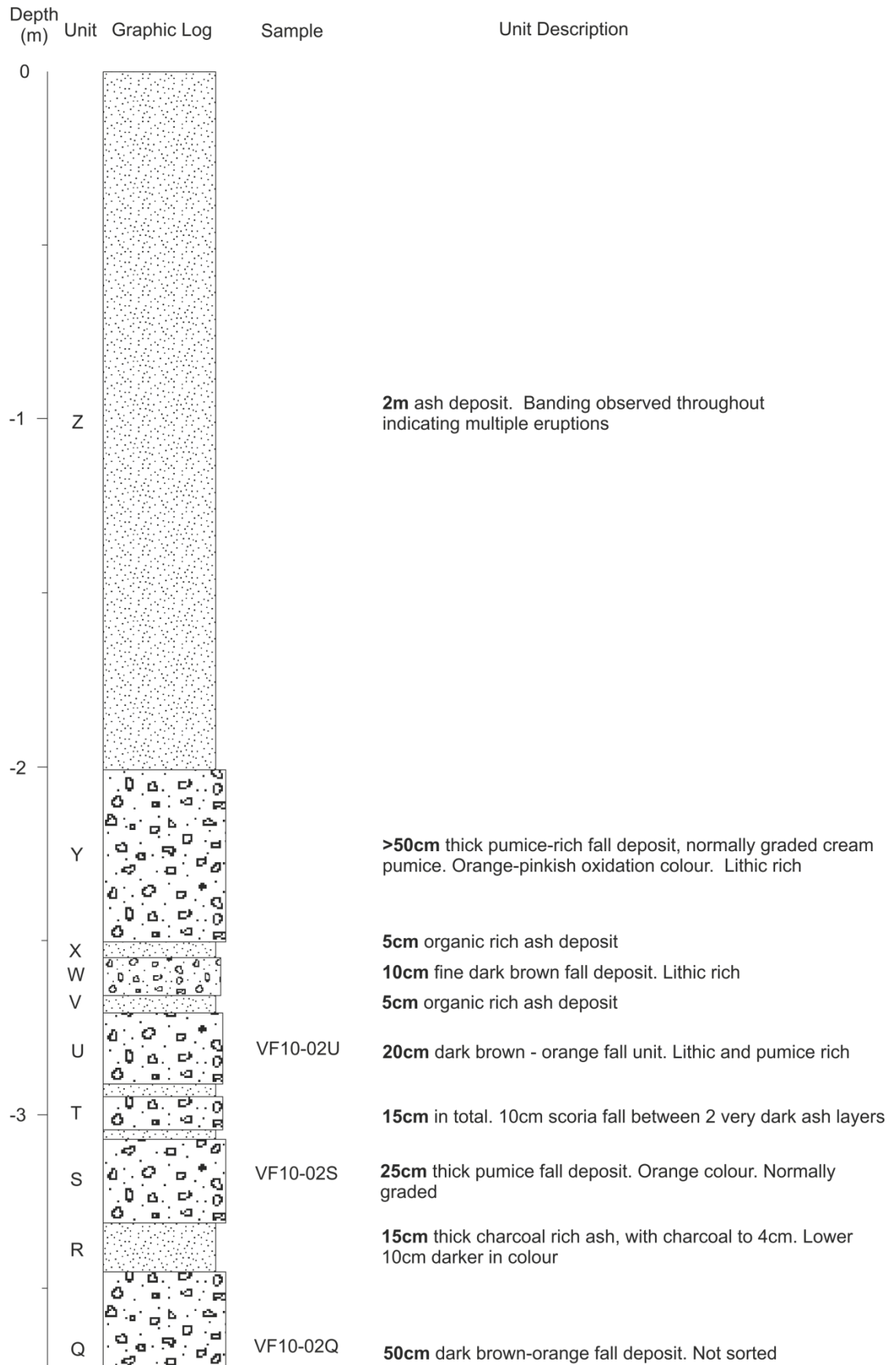
Appendix A: Stratigraphical Log

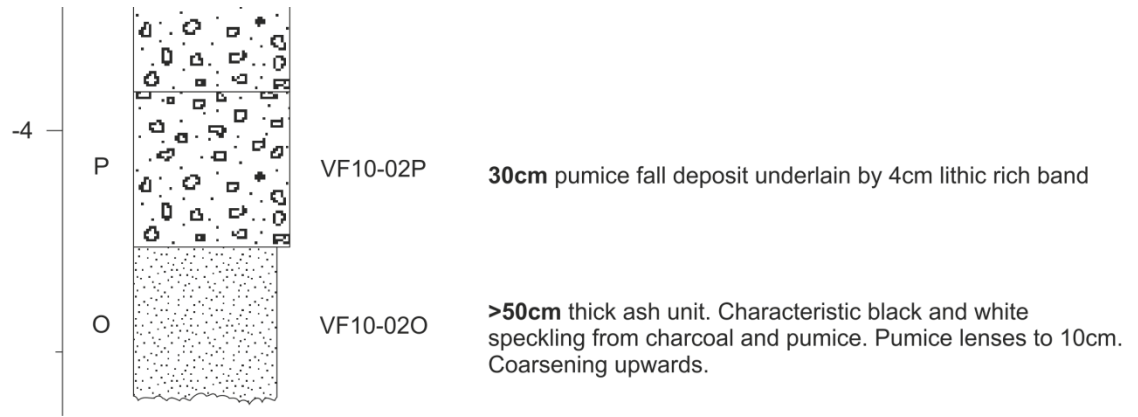
Section Name: VF10-01
 Grid Reference: 19°33.651 N; 103°38.366 W
 Altitude: 3332m a.s.l.

Depth (m)	Unit	Graphic Log	Sample	Unit Description
0				
-1	Z			>2m ash deposit. Dark grey. Banding observed throughout indicating multiple eruptions.
-2				
-3	Y			1.3m thick pumice-rich fall deposit, normally graded cream pumice. Orange-pinkish oxidation colour - very obvious at top. Lithic rich
	X			2cm organic rich ash deposit
	W			8cm fine dark brown fall deposit. Lithic rich. Undulating unit across o/c
	V			6cm organic rich ash deposit
	U		VF10-01U	16-18cm dark brown - orange fall unit. Lithic and pumice rich

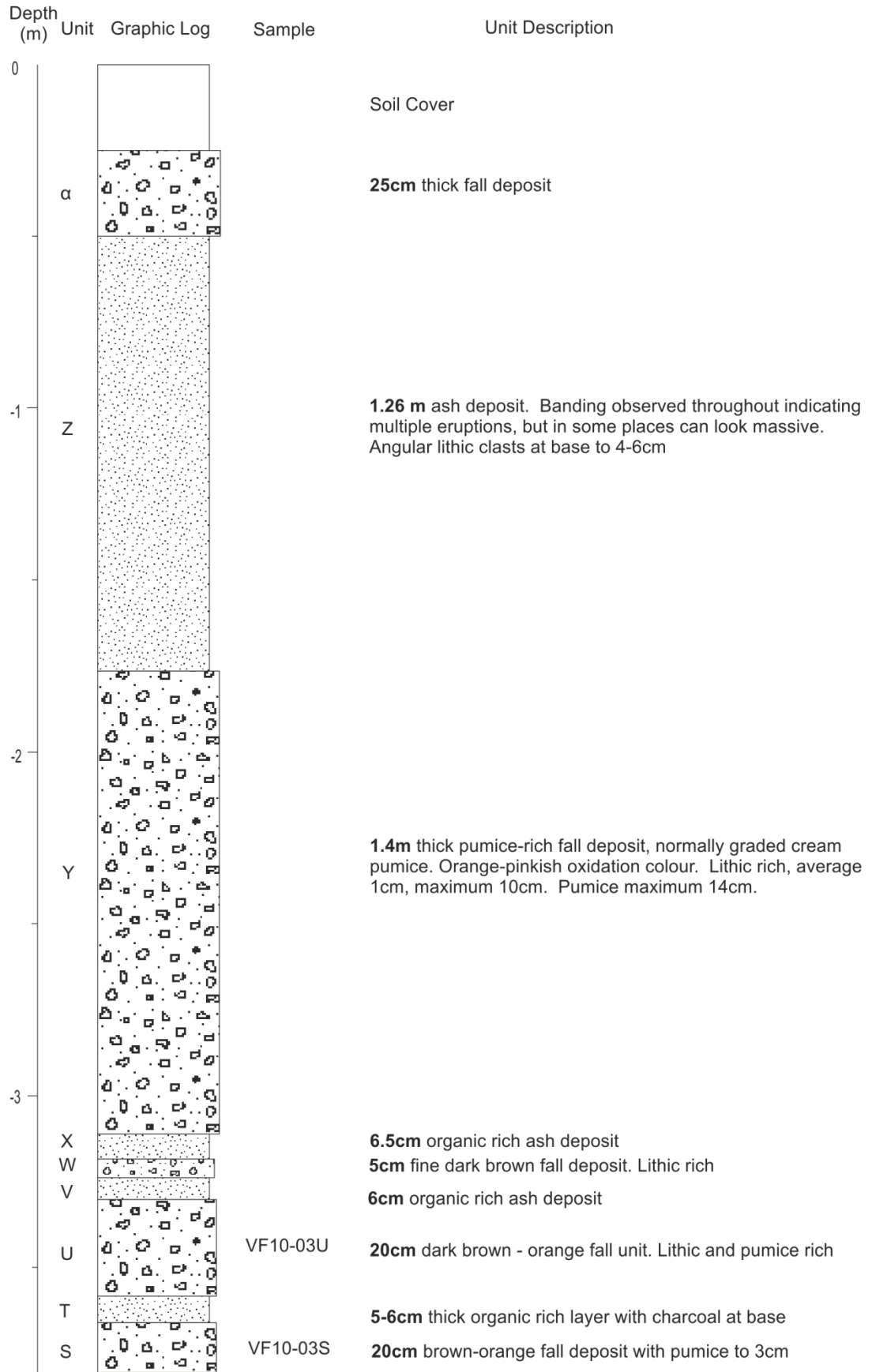


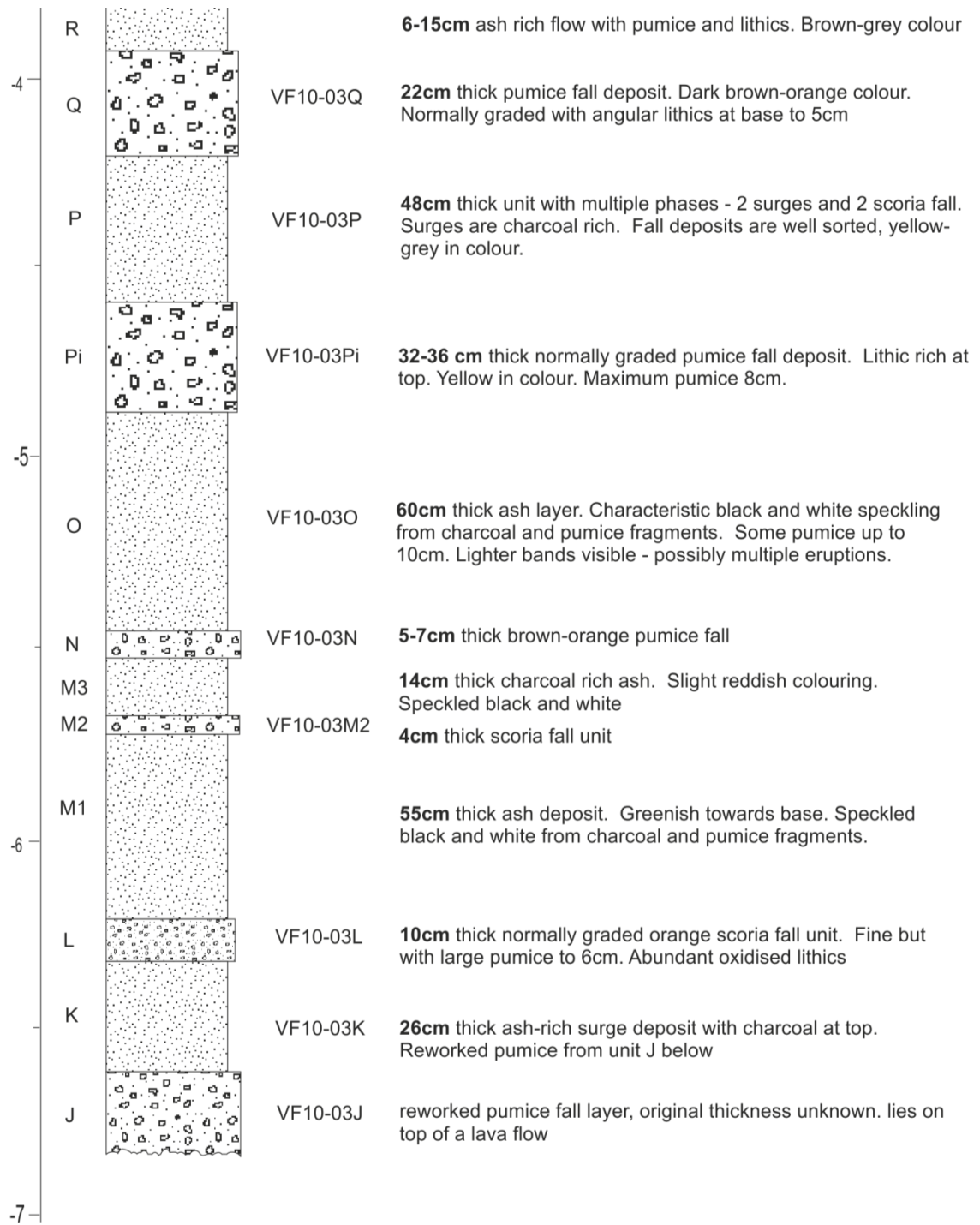
Section Name: VF10-02
 Grid Reference: 19°34.000 N; 103°37.872 W
 Altitude: 3533m a.s.l.



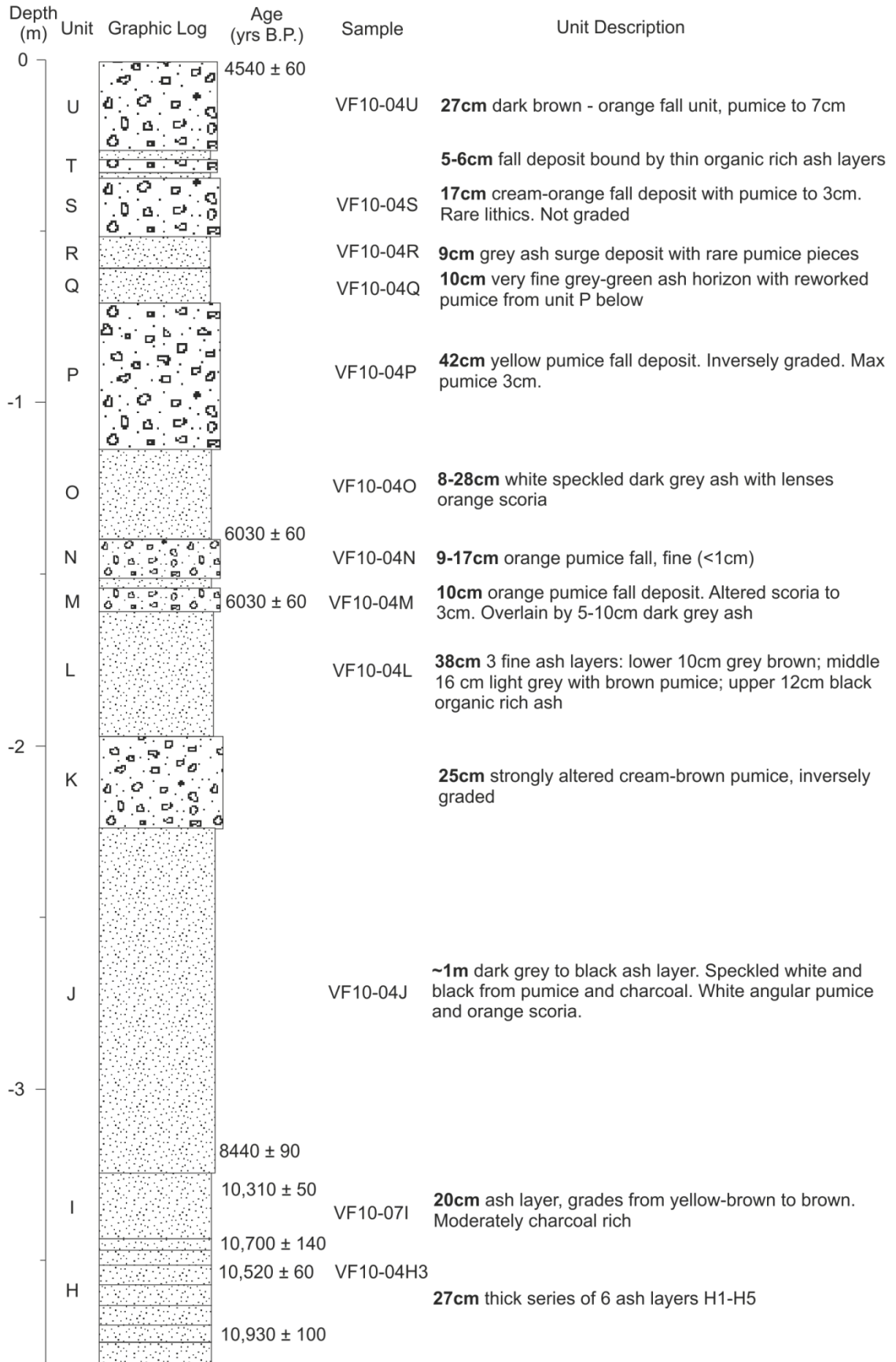


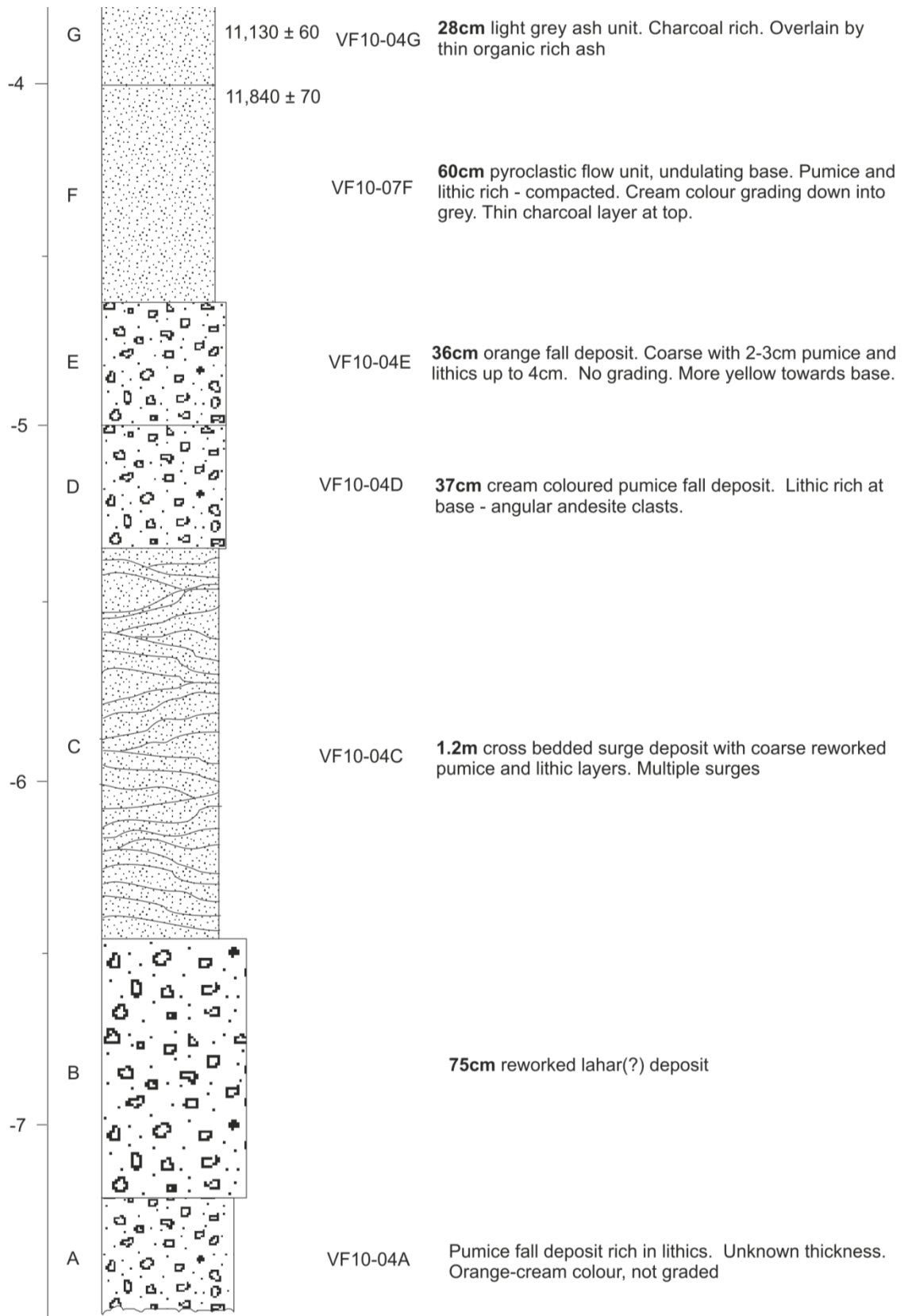
Section Name: VF10-03
 Grid Reference: 19°34.378 N; 103°37.666 W
 Altitude: 3633m a.s.l.



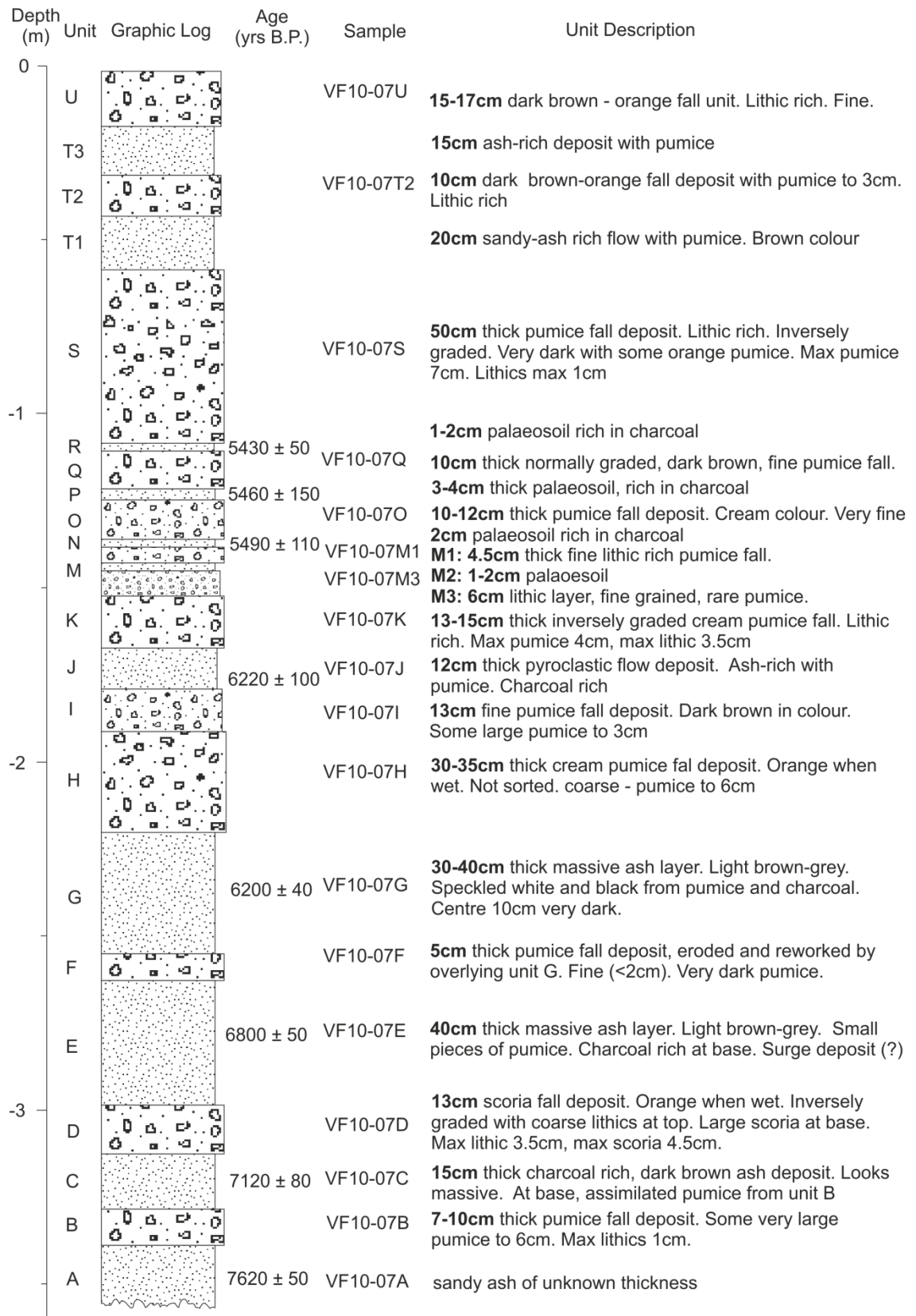


Section Name: VF10-04
 Grid Reference: 19°35.786 N; 103°35.267 W
 Altitude: 3272m a.s.l.





Section Name: VF10-07
 Grid Reference: 19°34.388 N; 103°36.609 W
 Altitude: 3581m a.s.l.



Appendix B: Group I Electron Microprobe Mineral Chemistry Data

Table 1 Plagioclase

Sample	VF95-06Y	VF95-06Y	VF95-06Y	VF95-06Y	VF95-06Y	VF95-06Y	VF95-06Y	VF95-06Y	VF95-06Y	VF95-06Y	VF95-06Y	VF95-06Y
Core/rim	plag1	plag1	plag1	plag2	plag2	plag2	plag3	plag3	plag4	plag4	plag4	plag5
Unit	Y	Y	Y	Y	Y	Y	Y	Y	Y	Y	Y	Y
Age	4400	4400	4400	4400	4400	4400	4400	4400	4400	4400	4400	4400
SiO ₂	47.98	47.76	48.02	59.06	58.79	59.41	57.38	57.58	47.91	47.85	47.97	55.10
TiO ₂	0.00	0.01	0.09	0.02	0.05	0.00	0.06	0.00	0.05	0.03	0.06	0.13
Al ₂ O ₃	32.88	32.81	32.77	25.03	24.86	25.48	26.39	25.76	32.47	32.79	32.70	28.87
Fe ₂ O ₃	0.45	0.55	0.62	0.51	0.46	0.77	0.27	0.36	0.70	0.56	0.57	0.56
MnO	0.08	0.05	0.00	0.00	0.05	0.02	0.10	0.00	0.05	0.00	0.15	0.06
MgO	0.02	0.03	0.04	0.02	0.01	0.02	0.02	0.02	0.06	0.04	0.03	0.05
CaO	16.27	16.46	16.29	7.43	7.13	7.68	9.18	8.61	16.52	16.79	16.49	11.50
Na ₂ O	2.07	2.17	2.17	7.18	7.25	7.01	6.24	6.49	2.39	1.88	2.03	5.02
K ₂ O	0.03	0.05	0.03	0.20	0.29	0.24	0.16	0.21	0.05	0.00	0.01	0.12
TOTAL	99.80	99.88	100.02	99.43	98.89	100.61	99.80	99.03	100.21	99.94	99.95	101.39
An	81	81	80	36	35	37	44	42	79	83	82	55

Sample	VF95-06Y	VF95-06Y	VF95-09X	VF95-09X	VF95-09X	VF95-09X	VF95-09X	VF95-09X	VF95-09X	VF95-09X	VF95-09X	VF95-09X
Core/rim	plag5	plag5	plag 1	plag 1	plag 1	plag 2	plag 2	plag 2	plag 3	plag 3	plag 3	plag 3
Unit	Y	Y	Y	Y	Y	Y	Y	Y	Y	Y	Y	Y
Age	4400	4400	4400	4400	4400	4400	4400	4400	4400	4400	4400	4400
SiO ₂	50.90	49.13	49.50	49.73	53.01	54.62	54.69	56.45	55.48	55.61	56.74	61.33
TiO ₂	0.00	0.07	0.04	0.00	0.03	0.12	0.09	0.14	0.04	0.09	0.15	0.05
Al ₂ O ₃	31.00	32.00	32.02	31.21	29.39	28.56	28.20	27.12	28.06	27.35	27.03	23.51
Fe ₂ O ₃	0.57	0.61	0.59	0.50	0.46	0.49	0.45	0.69	0.33	0.55	0.42	0.26
MnO	0.10	0.00	0.01	0.11	0.00	0.00	0.00	0.00	0.00	0.00	0.00	0.13
MgO	0.03	0.04	0.03	0.08	0.04	0.00	0.04	0.03	0.02	0.06	0.04	0.04
CaO	14.54	15.72	15.65	14.61	12.44	11.36	10.61	9.64	10.42	10.55	9.48	5.66
Na ₂ O	3.23	2.79	2.77	2.88	4.32	4.89	5.06	5.70	5.42	5.61	5.89	7.98
K ₂ O	0.08	0.05	0.06	0.05	0.05	0.11	0.16	0.15	0.14	0.12	0.20	0.33
TOTAL	100.45	100.43	100.67	99.16	99.72	100.15	99.30	99.91	99.90	99.92	99.94	99.30
An	71	75	76	74	61	56	53	48	51	51	47	28

Sample Core/rim Unit Age	VF95-09X plag 4 core Y 4400	VF95-09X plag 4 core Y 4400	VF95-09X plag 4 core Y 4400	VF95-09X plag 5 core Y 4400	VF95-09X plag 5 core Y 4400	VF95-09X plag 5 core Y 4400	VF97-05B plag 1 core Y 4400	VF97-05B plag 1 core Y 4400	VF97-05B plag 1 core Y 4400	VF97-05B plag 1 core Y 4400	VF97-05B plag 4 core Y 4400	VF97-05B plag 5 core Y 4400
SiO ₂	49.32	49.09	49.52	48.28	48.97	48.84	55.14	49.00	52.68	56.69	48.74	48.59
TiO ₂	0.04	0.06	0.07	0.06	0.01	0.00	0.07	0.08	0.00	0.07	0.02	0.08
Al ₂ O ₃	31.74	31.89	31.81	32.75	31.99	32.50	27.99	31.86	29.43	27.23	31.85	32.20
Fe ₂ O ₃	0.71	0.49	0.77	0.57	0.45	0.59	0.41	0.64	0.66	0.44	0.57	0.57
MnO	0.00	0.06	0.04	0.11	0.08	0.02	0.06	0.00	0.00	0.03	0.00	0.00
MgO	0.05	0.04	0.05	0.04	0.03	0.04	0.00	0.01	0.06	0.04	0.03	0.05
CaO	15.30	15.62	15.38	16.68	15.79	16.14	11.21	16.08	12.93	10.26	16.08	16.07
Na ₂ O	2.49	2.65	2.90	2.29	2.60	2.35	5.82	2.48	4.09	5.85	2.50	2.40
K ₂ O	0.04	0.07	0.05	0.01	0.02	0.04	0.13	0.02	0.06	0.17	0.02	0.04
TOTAL	99.70	99.98	100.57	100.79	99.94	100.52	100.83	100.17	99.91	100.78	99.81	99.99
An	77	76	74	80	77	79	51	78	63	49	78	79

Sample Core/rim Unit Age	VF95-06Y plag 1 rim Y 4400	VF95-06Y plag 2 rim Y 4400	VF95-06Y plag 3 rim Y 4400	VF95-06Y plag 3 rim Y 4400	VF95-06Y plag 3 rim Y 4400	VF95-06Y plag 4 rim Y 4400	VF95-06Y plag 5 rim Y 4400	VF95-09X plag 1 rim Y 4400	VF95-09X plag 2 rim Y 4400	VF95-09X plag 3 rim Y 4400	VF95-09X plag 4 rim Y 4400	VF95-09X plag 5 rim Y 4400
SiO ₂	54.18	54.91	53.63	52.40	53.88	56.13	56.04	53.96	56.22	55.94	56.34	57.75
TiO ₂	-	-	-	-	-	-	-	-	-	-	-	-
Al ₂ O ₃	28.45	28.59	29.05	30.12	28.97	28.09	27.83	28.97	27.04	27.70	26.99	25.86
Fe ₂ O ₃	0.47	0.47	0.46	0.59	0.49	0.65	0.43	0.56	0.45	0.40	0.43	0.75
MnO	0.06	0.00	0.03	0.01	0.00	0.01	0.04	0.06	0.04	0.04	0.01	0.03
MgO	0.02	0.06	0.08	0.09	0.05	0.09	0.00	0.05	0.02	0.04	0.01	0.07
CaO	11.51	11.22	12.03	13.17	11.57	10.74	10.28	12.23	9.75	10.09	9.82	9.03
Na ₂ O	5.10	5.07	4.70	3.97	4.81	5.68	5.73	4.51	5.95	5.63	5.70	5.98
K ₂ O	0.12	0.12	0.12	0.09	0.12	0.16	0.14	0.13	0.18	0.13	0.16	0.27
TOTAL	99.91	100.43	100.09	100.44	99.89	101.56	100.49	100.48	99.64	99.96	99.45	99.75
An	55	55	58	64	57	51	49	60	47	49	48	45

Sample Core/rim Unit Age	VF95-09X plag 6 rim Y 4400	VF95-09X plag 7 rim Y 4400	VF95-06Y plag 1 rim Y 4400	VF95-06Y plag 1 rim Y 4400	VF95-06Y plag 1 rim Y 4400	VF95-06Y plag 1 rim Y 4400	VF95-06Y plag 1 rim Y 4400	VF95-06Y plag 1 rim Y 4400	VF95-06Y plag 2 rim Y 4400	VF95-06Y plag 2 rim Y 4400	VF95-06Y plag 2 rim Y 4400	VF95-06Y plag 3 rim Y 4400	VF95-06Y plag 3 rim Y 4400
SiO ₂	52.90	56.77	47.33	54.37	54.09	48.56	49.28	57.03	56.20	56.91	58.17	56.06	
TiO ₂	-	-	0.00	0.03	0.03	0.01	0.07	0.07	0.09	0.01	0.01	0.00	
Al ₂ O ₃	29.40	26.97	32.67	28.41	28.62	32.53	32.03	26.78	27.39	27.27	26.25	26.86	
Fe ₂ O ₃	0.49	0.40	0.73	0.47	0.74	0.62	0.73	0.54	0.43	0.41	0.23	0.30	
MnO	0.00	0.05	0.00	0.09	0.03	0.00	0.00	0.03	0.00	0.00	0.55	0.00	
MgO	0.03	0.04	0.04	0.06	0.07	0.04	0.04	0.07	0.01	0.04	0.02	0.05	
CaO	12.35	9.24	16.38	11.36	11.62	16.20	15.74	9.51	9.77	9.91	8.51	10.01	
Na ₂ O	4.55	6.25	2.22	5.20	4.83	2.41	2.83	5.90	5.66	5.87	6.59	5.81	
K ₂ O	0.09	0.16	0.04	0.13	0.14	0.05	0.03	0.18	0.21	0.14	0.21	0.17	
TOTAL	99.82	99.87	99.41	100.10	100.16	100.43	100.75	100.11	99.75	100.55	100.53	99.26	
An	60	45	80	54	57	79	75	47	48	48	41	48	

Sample Core/rim Unit Age	VF95-06Y plag 3 rim Y 4400	VF95-06Y plag 3 rim Y 4400	VF95-06Y plag 4 rim Y 4400	VF95-06Y plag 4 rim Y 4400	VF95-06Y plag 4 rim Y 4400	VF95-06Y plag 5 rim Y 4400	VF95-06Y plag 5 rim Y 4400	VF95-06Y plag 5 rim Y 4400	VF95-09X plag 1 rim Y 4400	VF95-09X plag 1 rim Y 4400	VF95-09X plag 1 rim Y 4400	VF95-09X plag 2 rim Y 4400
SiO ₂	48.88	48.84	47.50	48.32	49.48	53.27	53.44	53.34	55.27	55.17	54.81	57.57
TiO ₂	0.04	0.04	0.09	0.05	0.00	0.04	0.00	0.09	0.02	0.06	0.00	0.06
Al ₂ O ₃	32.21	32.00	32.73	32.78	31.65	29.82	29.04	29.46	27.96	27.75	28.28	26.61
Fe ₂ O ₃	0.49	0.54	0.81	0.58	0.60	0.48	0.67	0.52	0.51	0.41	0.40	0.59
MnO	0.10	0.00	0.00	0.13	0.00	0.00	0.07	0.00	0.00	0.00	0.00	0.06
MgO	0.02	0.04	0.04	0.05	0.04	0.08	0.06	0.02	0.07	0.03	0.07	0.10
CaO	15.94	16.10	16.91	16.41	15.53	13.03	12.37	12.37	10.76	10.74	11.03	9.26
Na ₂ O	2.48	2.51	1.89	2.25	2.89	4.29	4.51	4.55	5.46	5.38	5.43	5.89
K ₂ O	0.07	0.03	0.06	0.04	0.05	0.09	0.10	0.14	0.15	0.17	0.14	0.17
TOTAL	100.23	100.09	100.04	100.61	100.24	101.08	100.26	100.50	100.20	99.71	100.16	100.30
An	78	78	83	80	75	62	60	60	52	52	52	46

Sample Core/rim	VF95-09X plag 2 rim Y 4400	VF95-09X plag 2 rim Y 4400	VF95-09X plag 2 rim Y 4400	VF95-09X plag 3 rim Y 4400	VF95-09X plag 3 rim Y 4400	VF95-09X plag 4 rim Y 4400	VF95-09X plag 4 rim Y 4400	VF95-09X plag 4 rim Y 4400	VF95-09X plag 5 rim Y 4400	VF95-09X plag 5 rim Y 4400	VF95-09X plag 5 rim Y 4400	VF97-05B plag 1 rim Y 4400
SiO ₂	55.80	54.37	56.35	61.05	60.82	51.02	51.35	50.04	57.19	59.57	56.20	55.08
TiO ₂	0.13	0.05	0.15	0.02	0.07	0.08	0.01	0.00	0.04	0.00	0.02	0.02
Al ₂ O ₃	27.57	28.51	27.48	23.97	24.46	31.09	30.95	31.68	26.35	25.51	27.88	28.36
Fe ₂ O ₃	0.65	0.53	0.57	0.35	0.29	0.60	0.46	0.55	0.41	0.30	0.53	0.54
MnO	0.18	0.02	0.00	0.00	0.00	0.00	0.08	0.00	0.00	0.11	0.00	0.00
MgO	0.06	0.03	0.03	0.02	0.00	0.07	0.04	0.06	0.06	0.03	0.06	0.05
CaO	10.20	11.35	9.76	6.00	6.17	14.51	14.18	15.02	8.87	7.60	10.22	11.66
Na ₂ O	5.55	4.91	5.66	7.73	7.82	3.54	3.49	2.92	6.19	6.94	5.68	5.20
K ₂ O	0.14	0.12	0.16	0.31	0.29	0.07	0.06	0.05	0.19	0.27	0.16	0.15
TOTAL	100.28	99.90	100.15	99.45	99.92	100.97	100.61	100.31	99.30	100.32	100.74	101.05
An	50	56	48	29	30	69	69	74	44	37	49	55

Sample Core/rim	VF97-05B plag 1 rim Y 4400	VF97-05B plag 4 rim Y 4400	VF97-05B plag 5 rim Y 4400	VF97-06B plag 1 core W 4500	VF97-06B plag 3 core W 4500	VF98-02W plag 1 core W 4500	VF98-02W plag 1 core W 4500	VF98-02W plag 2 core W 4500	VF98-02W plag 2 core W 4500	VF98-02W plag 2 core W 4500	VF98-02W plag 4 core W 4500	VF98-02W plag 4 core W 4500
SiO ₂	53.31	49.20	49.02	57.11	56.15	57.90	58.55	48.98	49.25	51.27	58.43	57.23
TiO ₂	0.00	0.01	0.04	0.16	0.14	0.00	0.02	0.03	0.00	0.12	0.01	0.00
Al ₂ O ₃	28.80	31.79	31.44	26.37	27.00	26.53	25.99	32.86	32.25	31.09	26.77	26.64
Fe ₂ O ₃	0.59	0.73	0.95	0.75	0.78	0.54	0.73	0.35	0.50	0.58	0.58	0.49
MnO	0.11	0.00	0.00	0.00	0.00	0.09	0.01	0.05	0.13	0.00	0.00	0.07
MgO	0.02	0.04	0.07	0.04	0.06	0.07	0.05	0.06	0.08	0.05	0.06	0.01
CaO	11.77	15.52	15.79	9.76	10.25	8.94	8.18	15.85	15.54	14.25	9.21	9.05
Na ₂ O	4.98	2.94	2.87	6.35	5.91	6.63	7.08	2.34	2.72	3.45	5.98	6.20
K ₂ O	0.10	0.04	0.02	0.24	0.20	0.22	0.26	0.03	0.07	0.06	0.17	0.16
TOTAL	99.69	100.29	100.18	100.77	100.48	100.93	100.88	100.56	100.55	100.86	101.19	99.84
An	56	74	75	45	48	42	38	79	76	69	46	44

Sample Core/rim Unit Age	VF99-05W plag 3 core W 4500	VF99-05W plag 4 core W 4500	VF99-05W plag 5 core W 4500	VF99-05W plag 1 core W 4500	VF99-05W plag 2 core W 4500	VF97-06B plag 1 rim W 4500	VF97-06B plag 3 rim W 4500	VF98-02W plag 1 rim W 4500	VF98-02W plag 1 rim W 4500	VF98-02W plag 2 rim W 4500	VF98-02W plag 1 rim W 4500	VF98-02W plag 2 rim W 4500
SiO ₂	57.07	49.57	53.04	55.33	46.73	53.29	54.78	58.43	58.38	52.37	52.29	52.14
TiO ₂	-	-	-	-	-	0.18	0.16	0.08	0.05	0.07	0.07	0.10
Al ₂ O ₃	26.92	32.52	29.56	27.28	33.66	28.95	28.41	26.64	26.47	29.98	30.08	30.03
Fe ₂ O ₃	0.64	0.63	0.57	0.86	0.56	0.53	0.88	0.36	0.55	0.51	0.64	0.59
MnO	0.00	0.00	0.02	0.00	0.01	0.02	0.03	0.00	0.00	0.00	0.00	0.01
MgO	0.07	0.06	0.09	0.05	0.05	0.11	0.10	0.01	0.02	0.06	0.08	0.08
CaO	9.02	15.11	12.14	10.02	17.26	12.12	11.84	8.80	8.52	13.48	13.08	13.31
Na ₂ O	6.11	2.97	4.52	5.70	1.74	4.68	4.96	6.35	7.00	4.08	4.12	4.17
K ₂ O	0.26	0.08	0.11	0.22	0.04	0.08	0.10	0.23	0.26	0.05	0.09	0.08
TOTAL	100.08	100.94	100.07	99.46	100.05	99.97	101.26	100.89	101.24	100.60	100.45	100.51
An	44	73	59	49	84	59	57	43	40	64	63	64

Sample Core/rim Unit Age	VF98-02W plag 4 rim W 4500	VF98-02W plag 4 rim W 4500	VF99-05W plag 3 rim W 4500	VF99-05W plag 4 rim W 4500	VF99-05W plag 1 rim W 4500	VF99-05W plag 2 rim W 4500	VF95-06U plag 1 core U 4700	VF95-06U plag 1 core U 4700	VF95-06U plag 1 core U 4700	VF95-06U plag 2 core U 4700	VF95-06U plag 2 core U 4700	VF95-06U plag 2 core U 4700
SiO ₂	59.07	59.26	52.72	56.14	55.23	54.86	54.29	56.01	53.58	55.81	55.15	55.48
TiO ₂	0.00	0.02	-	-	-	-	0.05	0.04	0.14	0.06	0.06	0.06
Al ₂ O ₃	25.58	25.71	28.09	27.62	27.46	28.02	28.90	26.75	29.10	27.22	27.33	27.01
Fe ₂ O ₃	0.58	0.41	0.78	0.70	1.03	0.71	0.74	0.55	0.57	0.82	0.97	0.69
MnO	0.02	0.14	0.02	0.00	0.00	0.00	0.04	0.00	0.03	0.00	0.13	0.11
MgO	0.04	0.04	0.10	0.05	0.07	0.08	0.09	0.05	0.07	0.10	0.06	0.08
CaO	8.18	8.48	10.91	9.75	9.98	10.41	12.04	9.68	12.07	10.46	10.81	10.27
Na ₂ O	6.89	6.88	5.12	6.01	5.70	5.68	4.96	5.70	4.71	5.73	5.26	5.69
K ₂ O	0.21	0.23	0.18	0.23	0.21	0.19	0.18	0.23	0.13	0.23	0.22	0.21
TOTAL	100.56	101.17	97.91	100.49	99.68	99.93	101.29	99.01	100.39	100.42	100.00	99.62
An	39	40	54	47	49	50	57	48	58	50	53	49

Sample Core/rim Unit Age	VF95-06U plag 3 core U 4700	VF95-06U plag 4 core U 4700	VF95-06U plag 5 core U 4700	VF95-06U plag 6 core U 4700	VF95-06U plag 6 core U 4700	VF95-06U plag 6 core U 4700	VF95-06U plag 7 core U 4700	VF95-06U plag 7 core U 4700	VF95-06U plag 7 core U 4700	VF98-02U plag 6 core U 4700	VF98-02U plag 7 core U 4700	VF98-02U plag 7 core U 4700
SiO ₂	54.98	54.94	55.18	51.07	51.91	51.03	49.60	48.31	51.53	52.22	56.97	54.70
TiO ₂	0.06	0.08	0.03	0.00	0.01	0.09	0.01	0.05	0.00	-	-	-
Al ₂ O ₃	28.61	28.51	27.65	31.08	30.59	30.88	31.67	32.57	30.46	29.71	26.47	28.14
Fe ₂ O ₃	0.65	1.07	0.73	0.66	0.49	0.54	0.60	0.52	0.69	0.43	0.61	0.62
MnO	0.11	0.02	0.12	0.00	0.00	0.08	0.00	0.00	0.00	0.00	0.03	0.00
MgO	0.09	0.08	0.11	0.06	0.03	0.06	0.02	0.06	0.07	0.05	0.06	0.08
CaO	11.27	11.76	10.85	14.20	13.62	13.96	15.39	16.50	13.79	12.79	8.70	10.59
Na ₂ O	5.00	5.09	5.72	3.42	3.88	3.58	2.92	2.34	3.82	4.36	6.47	5.48
K ₂ O	0.14	0.19	0.29	0.10	0.08	0.09	0.10	0.05	0.14	0.13	0.27	0.22
TOTAL	100.91	101.73	100.69	100.59	100.60	100.31	100.31	100.40	100.50	99.69	99.59	99.82
An	55	55	50	69	66	68	74	79	66	61	42	51

Sample Core/rim Unit Age	VF98-02U plag 1 core U 4700	VF98-02U plag 2 core U 4700	VF98-02U plag 3 core U 4700	VF98-02U plag 4 core U 4700	VF98-02U plag 5 core U 4700	VF95-06U plag 1 rim U 4700	VF95-06U plag 1 rim U 4700	VF95-06U plag 1 rim U 4700	VF95-06U plag 2 rim U 4700	VF95-06U plag 2 rim U 4700	VF95-06U plag 2 rim U 4700	VF95-06U plag 6 rim U 4700
SiO ₂	47.76	48.38	49.34	51.47	50.06	57.88	53.86	56.46	55.05	55.59	55.18	56.23
TiO ₂	-	-	-	-	-	0.09	0.12	0.03	0.06	0.04	0.69	0.03
Al ₂ O ₃	32.79	31.76	31.47	29.96	31.07	26.15	28.63	27.15	27.35	27.19	27.14	27.55
Fe ₂ O ₃	0.53	0.50	0.70	0.68	0.58	0.56	0.72	0.56	0.68	0.76	0.82	0.32
MnO	0.03	0.03	0.00	0.00	0.00	0.00	0.03	0.01	0.00	0.00	0.00	0.00
MgO	0.06	0.09	0.05	0.07	0.06	0.00	0.08	0.05	0.08	0.05	0.11	0.04
CaO	16.35	15.46	14.49	13.19	14.07	8.54	11.77	9.95	10.90	10.43	10.53	10.58
Na ₂ O	2.17	2.74	3.25	3.90	3.36	6.57	4.86	5.95	5.38	5.70	5.36	5.59
K ₂ O	0.06	0.05	0.08	0.11	0.08	0.29	0.15	0.24	0.19	0.22	0.22	0.17
TOTAL	99.75	99.01	99.38	99.39	99.27	100.08	100.22	100.41	99.69	99.97	100.05	100.50
An	80	76	71	65	69	41	57	47	52	50	51	51

Sample	VF95-06U	VF95-06U	VF95-06U	VF95-06U	VF95-06U	VF98-02U	VF98-02U	VF98-02U	VF98-02U	VF98-02U	VF98-02U	VF98-02U
Core/rim	plag 6	plag 6	plag 7	plag 7	plag 7	plag 6	plag 7	plag 7	plag 7	plag 1	plag 2	plag 2
Unit	rim	rim	rim	rim	rim	rim	rim	rim	rim	rim	rim	rim
Age	U	U	U	U	U	U	U	U	U	U	U	U
Age	4700	4700	4700	4700	4700	4700	4700	4700	4700	4700	4700	4700
SiO ₂	57.39	54.06	56.02	54.95	49.55	57.41	55.47	55.47	48.79	49.32	48.95	49.24
TiO ₂	0.01	0.07	0.11	0.02	0.05	-	-	-	-	-	-	-
Al ₂ O ₃	26.76	28.87	27.70	28.19	31.37	26.42	27.49	27.67	32.36	31.62	31.78	31.78
Fe ₂ O ₃	0.51	0.63	0.88	0.76	0.75	0.69	0.58	0.68	0.72	0.65	0.65	0.73
MnO	0.03	0.07	0.05	0.00	0.00	0.05	0.02	0.02	0.00	0.02	0.00	0.03
MgO	0.07	0.01	0.06	0.07	0.04	0.06	0.03	0.08	0.08	0.08	0.11	0.08
CaO	9.11	11.49	10.70	11.13	15.75	8.61	9.93	9.85	15.16	14.74	15.12	15.05
Na ₂ O	6.73	5.23	5.48	5.31	2.89	6.45	5.85	5.83	2.78	3.05	2.89	2.97
K ₂ O	0.25	0.18	0.22	0.20	0.11	0.27	0.20	0.20	0.06	0.07	0.06	0.07
TOTAL	100.88	100.60	101.24	100.62	100.51	99.95	99.58	99.79	99.95	99.55	99.57	99.94
An	42	54	51	53	75	42	48	48	75	72	74	73
Sample	VF98-02U	VF98-02U	VF98-02U	VF98-02U	VF95-09T	VF95-09T	VF95-09T	VF95-09T	VF95-09T	VF95-09T	VF95-09T	VF95-09T
Core/rim	plag 3	plag 3	plag 5	plag 5	plag 1	plag 1	plag 1	plag 2	plag 2	plag 2	plag 3	plag 3
Unit	rim	rim	rim	rim	core	core	core	core	core	core	core	core
Age	U	U	U	U	S	S	S	S	S	S	S	S
Age	4700	4700	4700	4700	5500	5500	5500	5500	5500	5500	5500	5500
SiO ₂	49.66	50.27	49.12	47.68	55.73	55.73	54.51	52.62	54.20	53.57	51.49	52.58
TiO ₂	-	-	-	-	0.11	0.09	0.04	0.11	0.05	0.00	0.02	0.03
Al ₂ O ₃	31.12	30.88	32.03	32.93	27.77	27.19	27.57	28.89	28.69	28.55	29.98	29.48
Fe ₂ O ₃	0.80	0.81	0.70	0.75	0.57	0.66	0.66	0.49	0.56	0.61	0.37	0.61
MnO	0.00	0.03	0.04	0.03	0.00	0.00	0.00	0.02	0.00	0.03	0.00	0.00
MgO	0.04	0.10	0.10	0.10	0.06	0.06	0.06	0.06	0.03	0.05	0.01	0.04
CaO	14.32	14.08	14.98	16.15	10.79	10.33	10.32	12.21	11.74	11.28	13.52	12.78
Na ₂ O	3.29	3.52	2.93	2.28	5.62	5.67	5.54	4.63	4.84	5.16	4.17	4.44
K ₂ O	0.06	0.09	0.06	0.06	0.14	0.19	0.19	0.15	0.12	0.11	0.07	0.13
TOTAL	99.30	99.78	99.96	99.99	100.78	99.92	98.88	99.16	100.23	99.38	99.63	100.09
An	70	69	74	79	51	50	50	59	57	54	64	61

Sample Core/rim Unit Age	VF95-09T plag 3 core S 5500	VF95-09T plag 4 core S 5500	VF95-09T plag 4 core S 5500	VF95-09T plag 4 core S 5500	VF95-09T plag 5 core S 5500	VF95-09T plag 5 core S 5500	VF95-09T plag 5 core S 5500	VF95-09T plag 5 core S 5500	VF95-09T plag 1 rim S 5500	VF95-09T plag 1 rim S 5500	VF95-09T plag 1 rim S 5500	VF95-09T plag 2 rim S 5500	VF95-09T plag 2 rim S 5500
SiO ₂	50.77	53.56	54.89	52.45	55.31	54.65	53.85	55.61	53.43	56.70	54.80	53.98	
TiO ₂	0.01	0.05	0.00	0.00	0.00	0.00	0.06	0.13	0.04	0.05	0.07	0.01	
Al ₂ O ₃	30.40	29.82	28.95	29.92	27.98	27.46	27.82	27.01	28.58	27.16	28.66	28.86	
Fe ₂ O ₃	0.54	0.57	0.54	0.49	0.65	0.73	0.48	0.32	0.48	0.44	0.49	0.46	
MnO	0.10	0.07	0.02	0.07	0.14	0.00	0.00	0.03	0.03	0.06	0.01	0.12	
MgO	0.03	0.02	0.05	0.08	0.07	0.07	0.06	0.07	0.05	0.07	0.03	0.07	
CaO	13.99	12.67	11.71	13.24	11.07	10.57	10.61	9.90	12.28	9.78	11.28	11.32	
Na ₂ O	3.38	4.58	5.06	4.16	5.51	5.44	5.37	5.85	4.77	6.10	5.23	4.99	
K ₂ O	0.04	0.14	0.12	0.09	0.13	0.15	0.21	0.26	0.11	0.19	0.09	0.17	
TOTAL	99.26	101.48	101.35	100.50	100.86	99.07	98.45	99.17	99.77	100.54	100.67	99.98	
An	69	60	56	63	52	51	52	48	58	46	54	55	

Sample Core/rim Unit Age	VF95-09T plag 2 rim S 5500	VF95-09T plag 3 rim S 5500	VF95-09T plag 3 rim S 5500	VF95-09T plag 3 rim S 5500	VF95-09T plag 4 rim S 5500	VF95-09T plag 4 rim S 5500	VF95-09T plag 4 rim S 5500	VF95-09T plag 5 rim S 5500	VF95-09T plag 5 rim S 5500	VF95-09T plag 5 rim S 5500	VF10-03Pi plag 1 core P 6000	VF10-03Pi plag 2 core P 6000
SiO ₂	53.95	56.50	54.01	56.41	55.26	54.54	56.13	54.74	55.20	55.58	49.91	55.66
TiO ₂	0.11	0.05	0.01	0.03	0.02	0.08	0.06	0.04	0.05	0.00	-	-
Al ₂ O ₃	28.61	26.68	28.60	26.98	28.80	28.38	27.91	28.33	29.07	28.14	31.65	27.71
Fe ₂ O ₃	0.71	0.86	0.66	0.68	0.48	0.70	0.36	0.49	0.43	0.58	0.56	0.56
MnO	0.00	0.07	0.08	0.00	0.11	0.02	0.00	0.04	0.00	0.00	0.00	0.00
MgO	0.06	0.05	0.05	0.03	0.07	0.08	0.05	0.05	0.08	0.06	0.07	0.08
CaO	11.17	9.56	11.65	10.29	11.69	11.44	10.50	11.32	11.85	11.16	14.23	10.16
Na ₂ O	4.95	5.93	5.07	5.80	4.96	5.11	5.36	4.86	5.03	5.21	3.30	5.62
K ₂ O	0.18	0.21	0.15	0.18	0.14	0.17	0.19	0.17	0.13	0.14	0.06	0.19
TOTAL	99.72	99.91	100.29	100.39	101.52	100.51	100.57	100.04	101.83	100.87	99.79	99.97
An	55	47	55	49	56	55	51	56	56	54	70	49

Sample Core/rim	VF10-03Pi plag 3 core	VF95-09L plag 1 core	VF95-09L plag 2 core	VF95-09L plag 3 core	VF95-09L plag 3 core	VF95-09L plag 3 core	VF95-09L plag 3 core	VF95-09L plag 3 core	VF95-09L plag 3 rim	VF10-03Pi plag 1 rim	VF10-03Pi plag 1 rim	VF10-03Pi plag 1 rim	VF10-03Pi plag 2 rim
Unit	P	P	P	P	P	P	P	P	P	P	P	P	P
Age	6000	6000	6000	6000	6000	6000	6000	6000	6000	6000	6000	6000	6000
SiO ₂	55.82	52.99	55.39	54.75	55.59	54.06	55.56	55.87	56.30	54.99	56.26	56.37	56.37
TiO ₂	-	0.08	0.06	0.03	0.01	0.02	0.04	-	-	-	-	-	-
Al ₂ O ₃	27.57	29.78	28.30	28.88	28.55	29.47	28.52	27.34	27.31	27.89	27.22	27.20	27.20
Fe ₂ O ₃	0.70	0.70	0.49	0.47	0.44	0.51	0.51	0.67	0.64	0.72	0.64	0.70	0.70
MnO	0.01	0.00	0.00	0.07	0.03	0.04	0.02	0.00	0.00	0.01	0.00	0.02	0.02
MgO	0.04	0.12	0.03	0.05	0.04	0.07	0.02	0.11	0.09	0.11	0.05	0.09	0.09
CaO	9.80	12.05	10.39	10.74	10.28	11.52	10.49	10.01	9.42	10.58	9.32	9.25	9.25
Na ₂ O	5.79	4.86	5.53	5.47	5.83	5.03	4.99	5.84	6.03	5.18	6.15	5.98	5.98
K ₂ O	0.18	0.11	0.18	0.21	0.21	0.14	0.16	0.20	0.23	0.22	0.21	0.24	0.24
TOTAL	99.89	100.71	100.37	100.67	100.97	100.86	100.33	100.04	100.02	99.70	99.86	99.85	99.85
An	48	57	50	51	49	55	53	48	46	52	45	45	45

Sample Core/rim	VF10-03Pi plag 2 rim	VF10-03Pi plag 2 rim	VF10-03Pi plag 2 rim	VF10-03Pi plag 3 rim	VF10-03Pi plag 3 rim	VF10-03Pi plag 3 rim	VF95-09L plag 1 rim	VF95-09L plag 1 rim	VF95-09L plag 1 rim	VF95-09L plag 2 rim	VF95-09L plag 2 rim	VF95-09L plag 2 rim	VF95-09L plag 2 rim
Unit	P	P	P	P	P	P	P	P	P	P	P	P	P
Age	6000	6000	6000	6000	6000	6000	6000	6000	6000	6000	6000	6000	6000
SiO ₂	55.97	55.07	55.96	54.92	54.71	55.46	53.42	53.62	54.18	55.46	53.98	54.57	54.57
TiO ₂	-	-	-	-	-	-	0.04	0.08	0.07	0.04	0.08	0.04	0.04
Al ₂ O ₃	27.11	27.39	27.09	28.36	28.15	28.15	28.84	29.67	29.07	28.04	29.12	29.02	29.02
Fe ₂ O ₃	0.67	0.61	0.74	0.69	0.57	0.49	0.78	0.81	0.65	0.70	0.57	0.71	0.71
MnO	0.03	0.00	0.03	0.01	0.01	0.00	0.00	0.00	0.00	0.00	0.00	0.00	0.00
MgO	0.06	0.06	0.10	0.06	0.07	0.06	0.06	0.06	0.08	0.05	0.03	0.09	0.09
CaO	9.62	9.95	9.54	10.47	10.53	10.28	11.54	11.20	11.36	10.11	11.23	10.87	10.87
Na ₂ O	5.90	6.01	5.83	5.53	5.34	5.57	5.02	5.13	5.08	5.73	5.09	5.34	5.34
K ₂ O	0.21	0.19	0.20	0.19	0.18	0.18	0.14	0.14	0.16	0.18	0.15	0.17	0.17
TOTAL	99.56	99.29	99.49	100.24	99.56	100.19	99.84	100.70	100.65	100.30	100.24	100.80	100.80
An	47	47	47	51	52	50	55	54	55	49	54	52	52

Sample Core/rim Unit Age	VF95-09L	VF95-09L	VF95-09L	VF10-03M2	VF10-03M2	VF10-03M2	VF10-03M2	VF10-03M2	VF10-03M2	VF10-03M2	VF10-03M2	VF95-09E
	plag 3	plag 3	plag 3	plag 1	plag 2	plag 2	plag 2	plag 2	plag 2	plag 2	plag 2	plag 1
	rim	rim	rim	core	core	core	core	core	core	core	core	core
	P	P	P	L	L	L	L	L	L	L	L	L
Age	6000	6000	6000	7500	7500	7500	7500	7500	7500	7500	7500	7500
SiO ₂	55.83	53.10	53.98	53.48	49.42	48.95	48.30	52.07	52.55	54.52	49.85	56.10
TiO ₂	0.05	0.04	0.03	-	-	-	-	-	-	-	-	0.03
Al ₂ O ₃	27.35	29.59	29.24	29.12	32.42	32.51	33.11	30.23	29.50	28.32	32.64	27.86
Fe ₂ O ₃	0.70	0.63	0.46	0.43	0.44	0.53	0.50	0.44	0.40	0.29	0.50	0.48
MnO	0.00	0.01	0.00	0.02	0.00	0.02	0.05	0.00	0.03	0.00	0.01	0.00
MgO	0.10	0.11	0.09	0.03	0.10	0.02	0.02	0.02	0.00	0.06	0.03	0.00
CaO	9.72	11.69	11.41	11.31	14.96	15.29	15.49	12.70	11.90	10.38	14.86	9.40
Na ₂ O	5.88	5.21	5.21	4.83	2.91	2.82	2.65	4.27	4.55	5.37	3.01	5.99
K ₂ O	0.20	0.14	0.15	0.14	0.05	0.04	0.03	0.07	0.11	0.12	0.06	0.16
TOTAL	99.84	100.52	100.57	99.37	100.30	100.17	100.15	99.79	99.03	99.07	100.95	100.03
An	47	55	54	56	74	75	76	62	59	51	73	46

Sample Core/rim Unit Age	VF95-09E	VF95-09E	VF95-09E	VF95-09E	VF95-09E	VF95-09E	VF10-03M2	VF10-03M2	VF10-03M2	VF10-03M2	VF10-03M2	VF10-03M2
	plag 1	plag 1	plag 1	plag 1	plag 2	plag 4	plag 1	plag 1	plag 1	plag 1	plag 2	plag 2
	core	core	core	core	core	core	rim	rim	rim	rim	rim	rim
	L	L	L	L	L	L	L	L	L	L	L	L
Age	7500	7500	7500	7500	7500	7500	7500	7500	7500	7500	7500	7500
SiO ₂	53.89	47.52	47.19	47.79	55.24	51.00	52.45	56.71	53.88	54.82	54.88	55.10
TiO ₂	0.01	0.01	0.00	0.00	0.03	0.03	-	-	-	-	-	-
Al ₂ O ₃	29.22	33.49	33.56	34.09	28.46	27.42	29.94	26.69	29.13	28.31	28.28	27.94
Fe ₂ O ₃	0.33	0.41	0.37	0.37	0.55	0.38	0.56	0.75	0.60	0.66	0.49	0.55
MnO	0.04	0.01	0.02	0.00	0.02	0.02	0.00	0.00	0.00	0.00	0.05	0.00
MgO	0.03	0.01	0.05	0.04	0.03	0.08	0.05	0.14	0.06	0.07	0.06	0.07
CaO	11.02	16.26	16.31	16.39	10.60	9.72	12.23	9.14	11.48	10.63	10.47	10.16
Na ₂ O	4.99	2.32	2.24	2.24	5.53	5.08	4.54	5.83	5.00	5.38	5.38	5.85
K ₂ O	0.13	0.06	0.05	0.05	0.15	0.13	0.10	0.21	0.12	0.13	0.11	0.15
TOTAL	99.68	100.09	99.79	100.97	100.60	93.87	99.88	99.46	100.25	100.00	99.72	99.82
An	55	79	80	80	51	51	59	46	56	52	51	49

Sample Core/rim	VF10-03M2 plag 3 rim	VF95-09E plag 1 rim	VF95-09E plag 1 rim	VF95-09E plag 1 rim	VF95-09E plag 2 rim	VF95-09E plag 2 rim	VF95-09E plag 2 rim	VF95-09E plag 4 rim	VF95-09E plag 4 rim	VF95-09E plag 4 rim	VF97-01F plag 1 core	VF97-01F plag 1 core
Unit	L	L	L	L	L	L	L	L	L	L	J	J
Age	7500	7500	7500	7500	7500	7500	7500	7500	7500	7500	7700	7700
SiO ₂	52.95	55.47	52.53	55.14	54.99	55.03	54.54	54.12	53.68	51.56	52.80	50.86
TiO ₂	-	0.03	0.04	0.02	0.02	0.00	0.03	0.02	0.02	0.02	0.05	0.00
Al ₂ O ₃	29.51	28.27	29.94	28.27	28.18	28.73	28.77	29.16	29.38	30.62	29.83	31.08
Fe ₂ O ₃	0.55	0.63	0.42	0.58	0.63	0.56	0.55	0.52	0.59	0.44	0.61	0.49
MnO	0.00	0.00	0.00	0.06	0.05	0.02	0.00	0.05	0.08	0.00	0.04	0.02
MgO	0.08	0.04	0.04	0.05	0.05	0.04	0.06	0.01	0.02	0.03	0.09	0.07
CaO	11.94	9.92	12.21	10.25	10.20	10.69	10.82	11.20	11.34	12.69	12.73	14.64
Na ₂ O	4.76	5.74	4.76	5.60	5.65	5.59	5.34	5.07	5.13	4.27	4.33	3.31
K ₂ O	0.10	0.22	0.13	0.17	0.18	0.16	0.16	0.16	0.14	0.11	0.12	0.06
TOTAL	99.89	100.33	100.07	100.13	99.95	100.82	100.25	100.31	100.37	99.74	100.64	100.55
An	58	48	58	50	49	51	52	54	55	62	61	71

Sample Core/rim	VF97-01F plag 1 core	VF97-01F plag 2 core	VF97-01F plag 2 core	VF97-01F plag 3 core	VF97-01F plag 3 core	VF10-03L plag 1 core	VF10-03L plag 1 core	VF10-03L plag 1 core	VF10-03L plag 2 core	VF10-03L plag 2 core	VF10-03L plag 2 core	VF10-03L plag 3 core
Unit	J	J	J	J	J	J	J	J	J	J	J	J
Age	7700	7700	7700	7700	7700	7700	7700	7700	7700	7700	7700	7700
SiO ₂	54.16	53.17	53.63	51.73	51.40	56.10	51.80	54.78	57.28	55.22	58.16	56.27
TiO ₂	0.05	0.01	0.03	0.01	0.04	0.03	0.05	0.03	0.04	0.05	0.09	0.06
Al ₂ O ₃	29.15	29.49	28.99	30.57	30.66	28.14	30.45	28.77	26.59	28.16	26.45	27.37
Fe ₂ O ₃	0.62	0.64	0.58	0.57	0.59	0.49	0.54	0.52	0.69	0.68	0.74	0.76
MnO	0.01	0.00	0.00	0.01	0.02	0.00	0.02	0.02	0.01	0.00	0.00	0.00
MgO	0.08	0.09	0.10	0.07	0.07	0.07	0.07	0.07	0.06	0.07	0.09	0.02
CaO	11.85	12.56	11.77	13.72	13.79	10.44	13.47	11.25	9.25	11.24	8.83	9.84
Na ₂ O	4.96	4.50	4.87	3.86	3.67	5.53	3.83	5.10	6.03	5.23	6.40	5.97
K ₂ O	0.13	0.10	0.11	0.07	0.08	0.16	0.09	0.17	0.25	0.14	0.26	0.23
TOTAL	101.01	100.59	100.09	100.64	100.32	100.95	100.32	100.71	100.22	100.80	101.05	100.52
An	56	60	57	66	67	51	66	54	45	54	43	47

Sample Core/rim	VF10-03L plag 3 core J Age 7700	VF97-01F plag 1 rim J Age 7700	VF97-01F plag 1 rim J Age 7700	VF97-01F plag 1 rim J Age 7700	VF97-01F plag 2 rim J Age 7700	VF97-01F plag 2 rim J Age 7700	VF97-01F plag 3 rim J Age 7700	VF97-01F plag 3 rim J Age 7700	VF10-03L plag 1 rim J Age 7700	VF10-03L plag 1 rim J Age 7700	VF10-03L plag 1 rim J Age 7700	VF10-03L plag 2 rim J Age 7700
SiO ₂	56.56	57.84	52.82	50.31	54.98	59.15	56.82	54.51	52.41	53.75	53.27	56.98
TiO ₂	0.06	0.10	0.04	0.05	0.05	0.36	0.13	0.02	0.05	0.06	0.02	0.04
Al ₂ O ₃	27.12	25.70	29.84	31.48	28.03	22.42	26.28	28.64	30.31	29.00	29.13	26.79
Fe ₂ O ₃	0.71	1.27	0.69	0.66	0.82	2.47	1.15	0.83	0.56	0.72	0.70	0.63
MnO	0.02	0.00	0.00	0.00	0.02	0.04	0.03	0.00	0.00	0.02	0.00	0.03
MgO	0.07	0.24	0.14	0.08	0.10	0.89	0.16	0.13	0.06	0.17	0.04	0.04
CaO	9.59	9.28	12.84	14.58	11.11	7.47	9.52	11.47	13.07	12.45	12.69	9.36
Na ₂ O	6.07	6.05	4.17	3.27	5.01	5.90	6.04	5.05	4.23	4.35	4.43	6.15
K ₂ O	0.22	0.30	0.12	0.09	0.14	0.78	0.31	0.12	0.11	0.18	0.11	0.23
TOTAL	100.45	100.80	100.67	100.52	100.29	99.61	100.51	100.79	100.81	100.70	100.45	100.25
An	46	45	63	71	55	39	46	55	63	61	61	45

Sample Core/rim	VF10-03L plag 2 rim J Age 7700	VF10-03L plag 3 rim J Age 7700	VF10-03L plag 3 rim J Age 7700	VF95-01F plag 1 core H Age 10,000	VF95-01F plag 1 core H Age 10,000	VF95-01F plag 1 core H Age 10,000	VF95-01F plag 1 core H Age 10,000	VF95-01F plag 2 core H Age 10,000	VF95-01F plag 2 core H Age 10,000	VF95-01F plag 3 core H Age 10,000	VF97-01Di plag 1 core H Age 10,000	VF97-01Di plag 1 core H Age 10,000
SiO ₂	56.73	56.52	58.64	55.98	52.92	53.43	57.04	54.17	57.78	51.00	56.83	57.47
TiO ₂	0.06	0.04	0.14	0.02	0.02	0.02	0.02	0.02	0.04	0.04	0.03	0.02
Al ₂ O ₃	27.14	26.88	25.43	27.01	29.32	28.92	26.80	28.52	26.19	30.74	27.04	26.58
Fe ₂ O ₃	0.79	0.69	0.81	0.54	0.62	0.54	0.47	0.51	0.33	0.58	0.50	0.50
MnO	0.00	0.03	0.02	0.03	0.00	0.00	0.00	0.01	0.01	0.00	0.00	0.03
MgO	0.12	0.07	0.12	0.05	0.07	0.08	0.07	0.08	0.02	0.10	0.07	0.02
CaO	9.72	9.60	8.56	10.08	12.48	12.11	9.25	11.40	8.83	14.10	9.94	9.10
Na ₂ O	6.02	6.08	6.42	5.66	4.55	4.51	6.27	5.05	6.61	3.47	6.09	6.40
K ₂ O	0.25	0.24	0.39	0.17	0.13	0.13	0.19	0.12	0.18	0.08	0.18	0.23
TOTAL	100.84	100.16	100.59	99.52	100.10	99.73	100.11	99.90	99.98	100.12	100.69	100.35
An	46	46	41	49	60	59	44	55	42	69	47	43

Sample Core/rim Unit Age	VF97-01Di plag 1 core H 10,000	VF97-01Di plag 2 core H 10,000	VF97-01Di plag 2 core H 10,000	VF97-01Di plag 3 core H 10,000	VF94-06E plag 1 core H 10,000	VF94-06E plag 1 core H 10,000	VF94-06E plag 1 core H 10,000	VF94-06E plag 2 core H 10,000	VF94-06E plag 2 core H 10,000	VF95-01F plag 1 rim H 10,000	VF95-01F plag 1 rim H 10,000	VF95-01F plag 2 rim H 10,000
SiO ₂	55.79	58.05	58.50	53.65	58.77	58.87	60.47	57.29	56.68	56.44	53.33	59.13
TiO ₂	0.00	0.04	0.08	0.03	0.03	0.02	0.01	0.05	0.06	0.21	0.02	0.36
Al ₂ O ₃	27.53	26.03	26.03	29.18	25.75	24.83	24.67	26.73	27.22	26.11	29.26	23.47
Fe ₂ O ₃	0.33	0.56	0.61	0.56	0.36	0.27	0.36	0.36	0.39	1.39	0.61	2.26
MnO	0.04	0.00	0.00	0.00	0.06	0.00	0.04	0.00	0.00	0.05	0.00	0.02
MgO	0.04	0.05	0.07	0.04	0.03	0.02	0.05	0.05	0.02	0.28	0.08	0.57
CaO	10.08	8.77	8.62	11.60	7.99	7.31	6.65	9.16	9.47	9.78	12.32	8.18
Na ₂ O	5.99	6.58	6.59	4.88	6.92	7.35	7.88	6.36	6.21	5.47	4.77	5.62
K ₂ O	0.16	0.21	0.24	0.10	0.31	0.31	0.34	0.24	0.25	0.33	0.13	0.60
TOTAL	99.96	100.28	100.74	100.05	100.23	98.98	100.46	100.23	100.30	100.05	100.51	100.20
An	48	42	41	56	38	35	31	44	45	49	58	43

Sample Core/rim Unit Age	VF95-01F plag 2 rim H 10,000	VF95-01F plag 3 rim H 10,000	VF95-01F plag 3 rim H 10,000	VF95-01F plag 4 rim H 10,000	VF97-01Di plag 1 rim H 10,000	VF97-01Di plag 1 rim H 10,000	VF97-01Di plag 2 rim H 10,000	VF97-01Di plag 2 rim H 10,000	VF97-01Di plag 3 rim H 10,000	VF97-01Di plag 3 rim H 10,000	VF94-06E plag 1 rim H 10,000	VF94-06E plag 1 rim H 10,000
SiO ₂	53.38	50.44	54.15	56.49	54.08	53.80	59.87	52.16	53.77	54.53	58.82	59.30
TiO ₂	0.02	0.05	0.09	0.07	0.08	0.04	0.26	0.01	0.04	0.09	0.03	0.01
Al ₂ O ₃	28.74	31.48	28.77	26.56	28.69	28.92	22.68	29.89	29.14	27.94	26.15	25.88
Fe ₂ O ₃	0.54	0.62	0.65	0.65	0.83	0.78	2.05	0.85	0.70	0.81	0.24	0.31
MnO	0.00	0.05	0.05	0.00	0.00	0.05	0.01	0.01	0.00	0.05	0.00	0.00
MgO	0.05	0.05	0.08	0.06	0.13	0.10	0.32	0.10	0.07	0.08	0.00	0.00
CaO	11.65	14.47	11.77	9.71	11.64	12.10	8.94	13.21	11.95	10.85	8.02	7.78
Na ₂ O	4.78	3.43	4.72	5.66	4.92	4.65	5.16	3.96	4.62	5.43	7.02	7.27
K ₂ O	0.13	0.08	0.13	0.24	0.15	0.13	0.53	0.11	0.11	0.13	0.26	0.30
TOTAL	99.29	100.68	100.40	99.42	100.51	100.58	99.83	100.30	100.41	99.90	100.54	100.85
An	57	70	58	48	56	59	47	64	58	52	38	37

Table 6 Plagioclase core-rim profile data

Sample Core/rim	VF99-05W plag 3 core	VF99-05W plag 3	VF99-05W plag 3	VF99-05W plag 3	VF99-05W plag 3	VF99-05W plag 3	VF99-05W plag 3	VF99-05W plag 3	VF99-05W plag 3	VF99-05W plag 3	VF99-05W plag 3	VF99-05W plag 3
Unit	W	W	W	W	W	W	W	W	W	W	W	W
Age	4500	4500	4500	4500	4500	4500	4500	4500	4500	4500	4500	4500
SiO2	55.41	56.14	54.53	56.16	56.02	55.88	55.39	55.98	55.51	55.89	55.72	55.46
TiO2	-	-	-	-	-	-	-	-	-	-	-	-
Al2O3	27.85	27.54	28.66	27.67	27.22	27.63	28.19	27.24	27.70	27.55	28.01	27.90
Fe2O3	0.56	0.56	0.64	0.65	0.64	0.67	0.55	0.52	0.67	0.63	0.63	0.59
MnO	0.01	0.00	0.01	0.01	0.00	0.00	0.00	0.03	0.02	0.00	0.00	0.01
MgO	0.07	0.11	0.07	0.07	0.07	0.06	0.09	0.11	0.05	0.08	0.09	0.07
CaO	10.10	9.75	10.67	9.71	9.37	9.93	10.46	9.47	9.93	9.57	10.12	9.92
Na2O	5.62	6.05	5.35	5.93	6.02	5.91	5.58	5.87	5.75	5.91	5.54	5.84
K2O	0.22	0.25	0.18	0.24	0.25	0.23	0.22	0.25	0.26	0.25	0.24	0.21
total	99.84	100.39	100.10	100.43	99.59	100.31	100.47	99.46	99.89	99.88	100.35	100.00
An	49	46	52	47	46	48	50	46	48	47	50	48

Sample Core/rim	VF99-05W plag 3	VF99-05W plag 3	VF99-05W plag 3	VF99-05W plag 3	VF99-05W plag 3	VF99-05W plag 3	VF99-05W plag 3	VF99-05W plag 3	VF99-05W plag 3	VF99-05W plag 3	VF99-05W plag 3	VF99-05W plag 3
Unit	W	W	W	W	W	W	W	W	W	W	W	W
Age	4500	4500	4500	4500	4500	4500	4500	4500	4500	4500	4500	4500
SiO2	56.44	55.89	55.92	55.82	56.04	56.12	57.23	56.15	57.12	56.37	57.87	57.78
TiO2	-	-	-	-	-	-	-	-	-	-	-	-
Al2O3	27.27	27.79	27.51	27.22	27.34	27.48	26.79	27.37	26.83	26.93	26.26	25.71
Fe2O3	0.59	0.61	0.70	0.59	0.60	0.63	0.67	0.64	0.64	0.54	0.49	0.59
MnO	0.00	0.00	0.03	0.00	0.02	0.03	0.00	0.04	0.01	0.01	0.03	0.04
MgO	0.04	0.05	0.08	0.07	0.05	0.05	0.06	0.05	0.04	0.07	0.04	0.06
CaO	9.33	9.80	9.83	9.77	9.36	9.77	8.79	9.56	8.93	9.24	8.10	8.00
Na2O	5.98	5.96	5.94	5.88	6.09	5.91	6.50	5.94	6.45	6.11	6.78	6.93
K2O	0.26	0.23	0.22	0.24	0.26	0.24	0.26	0.23	0.29	0.26	0.32	0.33
total	99.91	100.33	100.22	99.60	99.75	100.23	100.30	99.97	100.31	99.53	99.89	99.43
An	46	47	47	47	45	47	42	46	43	45	39	38

Sample Core/rim	VF99-05W plag 3	VF99-05W plag 3	VF99-05W plag 3	VF99-05W plag 3	VF99-05W plag 3	VF99-05W plag 3	VF99-05W plag 3	VF99-05W plag 3	VF99-05W plag 3	VF99-05W plag 3	VF99-05W plag 3	VF99-05W plag 3
Unit	W	W	W	W	W	W	W	W	W	W	W	W
Age	4500	4500	4500	4500	4500	4500	4500	4500	4500	4500	4500	4500
SiO2	59.05	54.00	56.66	57.80	53.11	53.49	53.71	55.64	55.89	53.87	54.80	56.60
TiO2	-	-	-	-	-	-	-	-	-	-	-	-
Al2O3	25.35	28.78	27.06	25.98	29.29	29.11	28.96	27.44	27.65	28.76	28.40	27.06
Fe2O3	0.58	0.63	0.66	0.58	0.48	0.49	0.54	0.63	0.58	0.65	0.68	0.62
MnO	0.00	0.00	0.00	0.04	0.03	0.01	0.00	0.02	0.02	0.00	0.00	0.04
MgO	0.06	0.07	0.05	0.04	0.06	0.08	0.05	0.09	0.06	0.06	0.05	0.08
CaO	7.29	11.03	9.36	8.05	11.67	11.45	11.30	9.82	9.76	11.04	10.65	9.29
Na2O	7.19	5.21	6.15	6.85	4.78	4.96	5.00	5.91	5.89	5.17	5.37	6.08
K2O	0.37	0.19	0.26	0.31	0.15	0.17	0.17	0.24	0.23	0.19	0.18	0.25
total	99.90	99.90	100.19	99.66	99.56	99.75	99.73	99.79	100.08	99.74	100.13	100.02
An	35	53	45	39	57	56	55	47	47	54	52	45

Sample Core/rim	VF99-05W plag 3	VF99-05W plag 3	VF99-05W plag 3	VF99-05W plag 3	VF99-05W plag 3	VF99-05W plag 3	VF99-05W plag 3	VF99-05W plag 3	VF99-05W plag 3	VF99-05W plag 3	VF99-05W plag 3	VF99-05W plag 3
Unit	W	W	W	W	W	W	W	W	W	W	W	W
Age	4500	4500	4500	4500	4500	4500	4500	4500	4500	4500	4500	4500
SiO2	54.32	52.35	50.67	51.28	51.43	53.27	52.78	55.76	56.14	56.79	52.77	52.91
TiO2	-	-	-	-	-	-	-	-	-	-	-	-
Al2O3	28.74	29.52	30.97	31.01	30.93	29.67	29.74	27.63	27.04	27.13	29.63	29.16
Fe2O3	0.57	0.69	0.61	0.61	0.64	0.65	0.72	0.74	0.72	0.65	0.68	0.71
MnO	0.02	0.00	0.02	0.04	0.00	0.00	0.01	0.00	0.00	0.03	0.01	0.03
MgO	0.04	0.09	0.04	0.08	0.05	0.07	0.10	0.06	0.08	0.05	0.06	0.07
CaO	11.17	12.25	13.86	13.55	13.30	11.77	12.16	10.00	9.24	9.38	12.23	12.14
Na2O	5.24	4.45	3.78	3.66	3.88	4.66	4.46	5.68	6.09	6.17	4.31	4.51
K2O	0.18	0.17	0.10	0.11	0.10	0.16	0.17	0.21	0.26	0.25	0.13	0.14
total	100.27	99.52	100.05	100.34	100.32	100.26	100.14	100.08	99.57	100.44	99.81	99.66
An	54	60	67	67	65	58	60	49	45	45	61	59

Sample Core/rim	VF99-05W plag 3	VF99-05W plag 3	VF99-05W plag 3	VF99-05W plag 3	VF99-05W plag 3 rim	VF98-02U plag 7 core	VF98-02U plag 7	VF98-02U plag 7 rim	VF98-02U plag 7	VF98-02U plag 7	VF98-02U plag 7	VF98-02U plag 7
Unit	W	W	W	W	W	U	U	U	U	U	U	U
Age	4500	4500	4500	4500	4500	4700	4700	4700	4700	4700	4700	4700
SiO2	53.48	53.21	55.50	54.72	54.92	56.97	56.90	55.47	53.33	50.29	50.19	51.19
TiO2												
Al2O3	28.85	29.32	28.02	28.15	27.90	26.47	27.33	27.49	28.62	31.40	31.43	30.99
Fe2O3	0.57	0.76	0.72	0.72	0.78	0.61	0.72	0.58	0.67	0.62	0.65	0.61
MnO	0.00	0.00	0.01	0.00	0.00	0.03	0.00	0.02	0.04	0.00	0.02	0.00
MgO	0.03	0.06	0.07	0.08	0.09	0.06	0.06	0.03	0.08	0.05	0.07	0.04
CaO	11.55	11.75	10.40	10.76	10.50	8.70	9.09	9.93	11.76	14.25	13.99	13.65
Na2O	4.92	4.90	5.59	5.47	5.57	6.47	6.31	5.85	4.82	3.54	3.58	3.82
K2O	0.16	0.14	0.17	0.19	0.19	0.27	0.28	0.20	0.16	0.10	0.08	0.11
total	99.57	100.14	100.47	100.09	99.94	99.59	100.70	99.58	99.48	100.26	100.03	100.41
An	56	57	50	52	50	42	44	48	57	69	68	66

Sample Core/rim	VF98-02U plag 7	VF98-02U plag 7	VF98-02U plag 7	VF98-02U plag 7	VF98-02U plag 7	VF98-02U plag 7	VF98-02U plag 7	VF98-02U plag 7	VF98-02U plag 7	VF98-02U plag 7	VF98-02U plag 7	VF98-02U plag 7
Unit	U	U	U	U	U	U	U	U	U	U	U	U
Age	4700	4700	4700	4700	4700	4700	4700	4700	4700	4700	4700	4700
SiO2	49.13	52.79	53.56	52.44	51.32	54.08	53.74	54.17	54.09	50.86	52.94	51.10
TiO2												
Al2O3	32.20	29.39	28.88	29.97	30.56	28.42	28.77	28.81	28.85	30.89	29.17	30.93
Fe2O3	0.66	0.66	0.60	0.55	0.68	0.68	0.67	0.69	0.67	0.77	0.61	0.60
MnO	0.03	0.00	0.00	0.00	0.04	0.02	0.00	0.08	0.05	0.06	0.04	0.00
MgO	0.06	0.05	0.05	0.09	0.07	0.09	0.09	0.10	0.08	0.05	0.09	0.08
CaO	15.01	11.85	11.86	12.60	13.13	11.10	11.51	11.21	11.32	13.54	11.49	13.54
Na2O	2.90	4.80	4.81	4.15	4.06	5.08	5.06	4.97	5.03	3.68	4.82	3.84
K2O	0.07	0.17	0.14	0.13	0.13	0.16	0.17	0.18	0.16	0.11	0.15	0.08
total	100.04	99.71	99.91	99.92	99.98	99.64	100.00	100.20	100.24	99.95	99.31	100.16
An	74	57	57	62	64	54	55	55	55	67	56	66

Sample Core/rim	VF98-02U plag 7	VF98-02U plag 7	VF98-02U plag 7	VF98-02U plag 7 core	VF98-02U plag 7 rim	VF98-02U plag 7	VF98-02U plag 7	VF98-02U plag 7	VF98-02U plag 7	VF98-02U plag 7	VF98-02U plag 7	VF98-02U plag 7
Unit	U	U	U	U	U	U	U	U	U	U	U	U
Age	4700	4700	4700	4700	4700	4700	4700	4700	4700	4700	4700	4700
SiO ₂	54.47	54.59	54.31	54.70	55.47	53.00	51.20	50.91	48.88	50.92	52.04	54.54
TiO ₂												
Al ₂ O ₃	28.71	28.43	28.62	28.14	27.67	29.49	30.74	30.97	31.84	30.49	29.92	28.73
Fe ₂ O ₃	0.68	0.70	0.63	0.62	0.68	0.74	0.66	0.59	0.54	0.67	0.68	0.65
MnO	0.06	0.00	0.01	0.00	0.02	0.01	0.00	0.00	0.00	0.02	0.00	0.04
MgO	0.12	0.04	0.07	0.08	0.08	0.06	0.09	0.07	0.06	0.07	0.07	0.09
CaO	11.14	10.91	11.00	10.59	9.85	11.90	13.49	14.03	15.48	13.35	12.91	11.42
Na ₂ O	5.05	5.25	5.39	5.48	5.83	4.71	3.91	3.62	2.87	3.93	4.09	5.11
K ₂ O	0.17	0.15	0.17	0.22	0.20	0.13	0.10	0.09	0.07	0.12	0.13	0.15
total	100.41	100.08	100.20	99.82	99.79	100.04	100.19	100.28	99.75	99.57	99.83	100.73
An	54	53	52	51	48	58	65	68	75	65	63	55

Table 7 Clinopyroxene

Sample Core/rim	VF99-05W cpx 1 core	VF99-05W cpx 1 core	VF99-05W cpx 2 core	VF99-05W cpx 2 core	VF99-05W cpx 3 core	VF99-05W cpx 3 core	VF99-05W cpx 4 core	VF98-02W cpx 1 core	VF98-02W cpx 1 rim	VF98-02W cpx 1 rim	VF98-02W cpx 2 rim	VF98-02W cpx 2 rim
Unit	W	W	W	W	W	W	W	W	W	W	W	W
Age	4500	4500	4500	4500	4500	4500	4500	4500	4500	4500	4500	4500
SiO ₂	49.59	50.58	51.52	49.90	50.15	49.39	50.64	51.88	50.16	50.94	50.80	51.04
TiO ₂	0.92	0.49	0.43	0.50	0.56	0.59	0.62	0.32	0.63	0.45	0.67	0.64
Al ₂ O ₃	3.45	4.13	3.06	4.70	4.47	5.10	3.43	2.40	3.06	2.85	2.42	3.97
Cr ₂ O ₃	0.22	0.52	0.20	0.49	0.65	0.37	0.20	0.11	0.11	0.08	0.06	0.08
Fe ₂ O ₃	3.71	3.48	2.94	3.15	3.32	4.34	3.02	2.48	4.39	3.72	3.50	2.84
FeO	4.57	3.04	3.75	3.02	3.08	2.50	5.57	5.28	3.60	3.45	4.99	5.05
MnO	0.23	0.14	0.18	0.14	0.23	0.18	0.17	0.21	0.14	0.15	0.25	0.10
MgO	15.00	16.16	16.47	15.57	15.53	15.55	14.68	15.13	15.50	16.12	15.61	15.69
CaO	20.31	21.02	21.09	21.42	21.63	20.97	20.78	21.56	21.33	21.37	20.83	20.78
Na ₂ O	0.56	0.43	0.37	0.38	0.37	0.50	0.55	0.48	0.39	0.34	0.43	0.41
total	98.54	99.99	100.00	99.27	99.99	99.49	99.65	99.84	99.33	99.49	99.56	100.57
Fe=FeO	7.90	6.17	6.40	5.86	6.07	6.41	8.28	7.50	7.55	6.80	8.14	7.60
Mg#	77	82	82	83	82	81	76	78	79	81	77	79

	VF99-05W	VF99-05W	VF99-05W	VF95-06U	VF95-06U	VF95-06U	VF95-06U	VF95-06U	VF95-06U	VF95-06U	VF95-06U	VF98-02U	
Sample	cpx 1	cpx 2	cpx 4	cpx 1	cpx 1	cpx 1	cpx 6	cpx 6	cpx 6	cpx 7	cpx 7	cpx 1	
Core/rim	rim	rim	rim	core	core	core	core	core	core	core	core	core	
Unit	W	W	W	U	U	U	U	U	U	U	U	U	
Age	4500	4500	4500	4700	4700	4700	4700	4700	4700	4700	4700	4700	
SiO ₂	50.71	50.97	50.42	50.90	52.38	51.55	49.41	49.80	52.06	52.23	52.41	49.93	
TiO ₂	0.68	0.51	0.74	0.46	0.30	0.48	0.83	0.83	0.34	0.40	0.34	0.48	
Al ₂ O ₃	3.24	3.70	3.82	3.22	2.98	3.37	4.16	4.00	3.10	2.62	2.37	3.47	
Cr ₂ O ₃	0.20	0.16	0.41	0.06	0.73	0.14	0.20	0.28	0.19	0.25	0.38	0.44	
Fe ₂ O ₃	3.20	2.55	2.80	2.96	1.53	2.35	2.57	1.82	0.31	0.71	0.92	4.09	
FeO	4.49	4.23	4.19	4.91	3.39	4.66	5.48	6.00	5.63	6.78	6.27	2.96	
MnO	0.22	0.12	0.16	0.23	0.12	0.06	0.24	0.21	0.07	0.25	0.21	0.27	
MgO	15.39	15.84	15.54	15.17	17.19	15.87	14.79	14.67	16.04	14.76	15.55	15.67	
CaO	21.02	21.04	21.18	21.09	21.33	21.08	20.38	20.44	20.73	21.21	20.94	21.17	
Na ₂ O	0.47	0.40	0.38	0.44	0.30	0.44	0.35	0.38	0.38	0.50	0.42	0.40	
total	99.61	99.52	99.63	99.43	100.26	100.02	98.40	98.43	98.85	99.70	99.81	98.87	
Fe=FeO	7.36	6.53	6.71	7.56	4.77	6.78	7.79	7.64	5.91	7.42	7.10	6.64	
Mg#	79	81	81	78	87	81	77	77	83	78	80	81	
	VF98-02U	VF98-02U	VF98-02U	VF98-02U	VF98-02U	VF98-02U	VF98-02U	VF98-02U	VF98-02U	VF98-02U	VF95-06U	VF95-06U	VF95-06U
Sample	cpx 1	cpx 1	cpx 1	cpx 1	cpx 5	cpx 5	cpx 5	cpx 5	cpx 5	cpx 3	cpx 1	cpx 1	cpx 1
Core/rim	core	core	core	core	core	core	core	core	core	core	rim	rim	rim
Unit	U	U	U	U	U	U	U	U	U	U	U	U	U
Age	4700	4700	4700	4700	4700	4700	4700	4700	4700	4700	4700	4700	4700
SiO ₂	48.20	49.26	48.75	49.48	51.49	49.27	50.78	49.89	51.35	52.92	51.57	51.10	
TiO ₂	0.73	0.66	0.53	0.85	0.24	0.61	0.31	0.57	0.66	0.56	0.75	0.68	
Al ₂ O ₃	4.37	3.42	5.08	3.32	2.51	4.21	3.16	1.59	2.31	1.47	2.36	2.99	
Cr ₂ O ₃	0.16	0.26	0.43	0.06	0.59	0.29	0.22	0.00	0.01	0.00	0.05	0.12	
Fe ₂ O ₃	6.14	5.01	5.09	4.70	3.70	5.10	4.64	2.21	2.00	1.75	2.93	2.88	
FeO	2.38	2.99	2.01	4.23	1.51	2.94	1.90	6.51	7.07	6.84	5.59	4.94	
MnO	0.26	0.10	0.26	0.17	0.12	0.18	0.24	0.30	0.28	0.18	0.31	0.22	
MgO	14.74	15.46	15.14	14.86	17.64	15.03	16.41	16.62	14.97	16.12	15.34	15.17	
CaO	21.16	21.27	21.43	21.00	21.22	21.11	21.60	19.62	20.16	20.50	21.03	21.19	
Na ₂ O	0.49	0.49	0.45	0.48	0.34	0.54	0.42	0.34	0.47	0.37	0.47	0.51	
total	98.62	98.93	99.15	99.14	99.37	99.28	99.68	97.64	99.28	100.71	100.39	99.79	
Fe=FeO	7.91	7.50	6.58	8.46	4.84	7.54	6.07	8.50	8.87	8.41	8.22	7.53	
Mg#	77	79	80	76	87	78	83	78	75	77	77	78	

Sample Core/rim Unit Age	VF95-06U cpx 6 rim U 4700	VF95-06U cpx 6 rim U 4700	VF95-06U cpx 6 rim U 4700	VF95-06U cpx 7 rim U 4700	VF95-06U cpx 7 rim U 4700	VF98-02U cpx 3 rim U 4700	VF10-07U cpx 1 rim U 4700	VF10-07U cpx 1 rim U 4700	VF10-07U cpx 1 rim U 4700	VF10-07U cpx 2 rim U 4700	VF10-07U cpx 2 rim U 4700	VF10-07U cpx 3 rim U 4700
SiO ₂	51.20	51.00	52.31	53.05	50.78	50.98	51.81	51.86	51.58	52.25	52.42	51.49
TiO ₂	0.57	0.61	0.36	0.30	0.52	0.51	0.37	0.36	0.35	0.30	0.27	0.38
Al ₂ O ₃	4.30	3.44	2.78	2.44	4.26	3.67	2.99	2.82	2.77	1.66	1.54	3.19
Cr ₂ O ₃	0.24	0.21	0.19	0.16	0.30	0.19	0.13	0.10	0.11	0.00	0.01	0.09
Fe ₂ O ₃	1.33	2.40	1.38	0.00	1.97	2.02	2.23	2.12	3.15	2.20	2.24	2.13
FeO	5.78	4.75	5.67	6.09	5.11	4.65	4.76	4.87	3.70	6.19	6.31	4.72
MnO	0.14	0.24	0.22	0.22	0.18	0.16	0.18	0.20	0.20	0.39	0.41	0.16
MgO	15.18	15.16	16.04	16.25	15.55	15.27	15.81	15.90	15.85	15.02	15.20	15.69
CaO	20.89	21.62	20.90	20.71	20.65	21.48	21.56	21.38	21.41	21.32	21.15	21.44
Na ₂ O	0.43	0.39	0.34	0.30	0.37	0.40	0.33	0.33	0.52	0.45	0.43	0.34
total	100.06	99.82	100.20	99.52	99.69	99.32	100.17	99.94	99.64	99.78	99.99	99.63
Fe=FeO	6.98	6.90	6.91	6.09	6.88	6.48	6.76	6.77	6.53	8.17	8.32	6.63
Mg#	80	80	81	83	80	81	81	81	81	77	77	81
Sample Core/rim Unit Age	VF10-07U cpx 3 rim U 4700	VF10-07U cpx 3 rim U 4700	VF10-07U cpx 3 rim U 4700	VF10-07U cpx 3 rim U 4700	VF10-01U cpx 1 rim U 4700	VF10-01U cpx 1 rim U 4700	VF10-01U cpx 1 rim U 4700	VF10-01U cpx 1 rim U 4700	VF10-01U cpx 1 rim U 4700	VF10-01U cpx 2 rim U 4700	VF10-01U cpx 2 rim U 4700	VF10-01U cpx 2 rim U 4700
SiO ₂	51.03	50.92	51.81	50.88	51.65	51.27	51.15	51.43	52.04	51.23	50.90	51.84
TiO ₂	0.43	0.44	0.34	0.45	0.38	0.48	0.47	0.48	0.36	0.80	0.87	0.60
Al ₂ O ₃	3.67	3.66	2.96	3.28	2.98	3.58	3.37	3.23	2.77	2.56	2.73	1.79
Cr ₂ O ₃	0.17	0.19	0.13	0.05	0.26	0.25	0.43	0.47	0.24	0.04	0.04	0.01
Fe ₂ O ₃	2.42	2.95	2.22	3.22	2.23	2.23	2.46	2.24	2.02	2.64	2.69	2.29
FeO	4.30	4.01	4.73	5.93	4.76	4.58	4.71	4.78	4.84	6.31	6.44	6.44
MnO	0.16	0.17	0.19	0.23	0.18	0.16	0.13	0.17	0.18	0.25	0.25	0.25
MgO	15.70	15.81	16.32	14.69	15.71	15.73	15.45	15.60	15.94	15.39	15.09	15.96
CaO	21.34	21.22	20.87	20.86	21.43	21.25	21.36	21.33	21.30	20.18	20.33	19.98
Na ₂ O	0.35	0.37	0.32	0.47	0.37	0.37	0.39	0.40	0.40	0.45	0.44	0.39
total	99.56	99.75	99.88	100.06	99.96	99.90	99.93	100.12	100.09	99.85	99.80	99.54
Fe=FeO	6.47	6.67	6.73	8.83	6.76	6.58	6.92	6.79	6.66	8.69	8.87	8.49
Mg#	81	81	81	75	81	81	80	80	81	76	75	77

	VF10-01U	VF10-01U	VF95-09T	VF95-09T	VF95-09T	VF95-09T	VF95-09T	VF95-09T	VF95-09T	VF10-03Pi	VF10-03Pi	VF10-03Pi	VF95-09L
Sample	cpx 2	cpx 2	cpx 1	cpx 5	cpx 5	cpx 5	cpx 5	cpx 5	cpx 5	cpx 1	cpx 1	cpx 5	cpx 1
Core/rim	rim	rim	core	core	core	rim	rim	rim	rim	core	core	core	core
Unit	U	U	S	S	S	S	S	S	S	P	P	P	P
Age	4700	4700	5500	5500	5500	5500	5500	5500	5500	6000	6000	6000	6000
SiO ₂	52.04	52.05	51.27	51.56	51.32	51.63	51.43	52.06	51.20	51.09	50.98	51.28	
TiO ₂	0.66	0.66	0.48	0.54	0.58	0.52	0.60	0.52	0.52	0.52	0.51	0.63	
Al ₂ O ₃	1.87	1.81	3.57	2.89	3.17	3.17	2.77	2.55	3.76	3.86	3.44	2.77	
Cr ₂ O ₃	0.00	0.01	0.56	0.22	0.10	0.17	0.00	0.12	0.15	0.16	0.42	0.00	
Fe ₂ O ₃	2.55	2.42	2.98	3.15	2.87	2.43	2.74	1.24	2.12	2.16	2.44	2.96	
FeO	6.60	6.95	4.05	4.88	6.12	5.59	6.29	7.31	5.50	5.38	4.83	5.64	
MnO	0.26	0.25	0.22	0.21	0.22	0.16	0.29	0.19	0.17	0.18	0.16	0.26	
MgO	15.95	15.93	15.74	15.60	14.52	15.01	14.89	14.51	15.35	15.32	15.22	15.08	
CaO	19.96	19.53	21.28	21.10	21.07	21.58	21.15	21.19	20.62	20.58	21.16	20.73	
Na ₂ O	0.42	0.48	0.46	0.47	0.57	0.44	0.40	0.48	0.48	0.51	0.47	0.55	
total	100.30	100.09	100.59	100.62	100.54	100.69	100.54	100.16	99.88	99.76	99.64	99.90	
Fe=FeO	8.89	9.13	6.73	7.71	8.71	7.78	8.75	8.43	7.42	7.33	7.02	8.30	
Mg#	76	76	81	78	75	77	75	75	79	79	79	76	

	VF95-09L	VF95-09L	VF10-03Pi	VF10-03Pi	VF10-03Pi	VF10-03Pi	VF95-09L	VF95-09L	VF95-09L	VF97-01F	VF97-01F	VF97-01F
Sample	cpx 1	cpx 2	cpx 1	cpx 5	cpx 5	cpx 5	cpx 1	cpx 1	cpx 2	cpx 1	cpx 1	cpx 1
Core/rim	core	core	rim	rim	rim	rim	rim	rim	rim	core	core	core
Unit	P	P	P	P	P	P	P	P	P	J	J	J
Age	6000	6000	6000	6000	6000	6000	6000	6000	6000	7700	7700	7700
SiO ₂	53.11	50.95	51.40	51.51	51.57	51.94	50.63	51.11	50.75	51.27	50.74	50.79
TiO ₂	0.26	0.54	0.54	0.42	0.43	0.45	0.86	0.76	0.90	0.60	0.61	0.60
Al ₂ O ₃	1.07	3.74	2.48	2.09	2.10	1.93	3.15	2.70	3.10	2.88	3.80	3.94
Cr ₂ O ₃	0.02	0.06	0.01	0.02	0.03	0.05	0.04	0.02	0.01	0.09	0.20	0.22
Fe ₂ O ₃	1.59	2.70	2.41	3.14	3.12	2.61	3.60	3.27	3.31	-	-	-
FeO	6.88	4.79	6.52	5.50	6.06	6.49	5.06	4.67	5.69	7.28	6.85	6.89
MnO	0.31	0.17	0.24	0.20	0.29	0.31	0.26	0.20	0.25	0.18	0.16	0.17
MgO	15.29	15.23	14.70	15.25	14.98	15.25	15.32	15.66	15.50	15.37	15.18	15.14
CaO	21.41	21.14	20.82	21.12	20.83	20.62	20.63	21.06	20.04	21.15	20.83	20.83
Na ₂ O	0.40	0.47	0.50	0.44	0.50	0.46	0.48	0.44	0.49	0.43	0.59	0.59
total	100.33	99.78	99.63	99.68	99.90	100.10	100.02	99.89	100.03	99.26	98.96	99.17
Fe=FeO	8.31	7.22	8.69	8.32	8.87	8.84	8.30	7.62	8.67	-	-	-
Mg#	77	79	75	77	75	75	77	79	76	79	80	80

Sample Core/rim Unit Age	VF97-01F cpx 3 core J 7700	VF97-01F cpx 3 core J 7700	VF10-03L cpx 2 core J 7700	VF10-03L cpx 2 core J 7700	VF97-01F cpx 1 rim J 7700	VF97-01F cpx 1 rim J 7700	VF97-01F cpx 1 rim J 7700	VF97-01F cpx 1 rim J 7700	VF97-01F cpx 2 rim J 7700	VF97-01F cpx 2 rim J 7700	VF97-01F cpx 3 rim J 7700	VF97-01F cpx 3 rim J 7700
SiO ₂	52.23	52.41	52.40	51.28	51.66	52.28	51.48	51.36	51.96	52.57	51.88	51.06
TiO ₂	0.47	0.44	0.35	0.55	0.57	0.45	0.48	0.60	0.43	0.58	0.56	0.65
Al ₂ O ₃	1.18	1.39	2.01	2.70	2.67	2.16	2.94	2.80	2.77	3.11	2.68	3.06
Cr ₂ O ₃	0.01	0.01	0.03	0.12	0.08	0.11	0.23	0.26	0.24	0.04	0.14	0.28
Fe ₂ O ₃	-	-	-	-	-	-	-	-	-	-	-	-
FeO	9.12	8.91	7.50	7.75	7.09	6.70	6.68	6.82	6.54	7.82	7.15	7.72
MnO	0.28	0.30	0.23	0.21	0.21	0.17	0.16	0.15	0.17	0.23	0.18	0.18
MgO	16.27	15.62	15.40	15.05	15.65	16.07	15.90	15.49	16.05	15.68	15.76	15.16
CaO	19.69	20.32	21.58	21.26	21.29	21.31	20.75	21.53	21.07	18.86	21.22	21.00
Na ₂ O	0.38	0.43	0.47	0.48	0.43	0.37	0.48	0.43	0.52	0.51	0.44	0.57
total	99.64	99.84	99.96	99.41	99.65	99.63	99.11	99.44	99.75	99.40	100.03	99.68
Fe=FeO	-	-	-	-	-	-	-	-	-	-	-	-
Mg#	76	76	79	78	80	81	81	80	81	78	80	78
Sample Core/rim Unit Age	VF10-03L cpx 1 rim J 7700	VF10-03L cpx 1 rim J 7700	VF10-03L cpx 1 rim J 7700	VF10-03L cpx 2 rim J 7700	VF10-03L cpx 2 rim J 7700	VF95-01F cpx 1 core H 10,000	VF95-01F cpx 1 core H 10,000	VF95-01F cpx 1 core H 10,000	VF95-01F cpx 2 core H 10,000	VF95-01F cpx 2 core H 10,000	VF95-01F cpx 2 core H 10,000	VF97-01Di cpx 1 core H 10,000
SiO ₂	50.77	51.87	52.19	51.57	52.76	49.08	50.97	50.29	50.80	52.37	52.31	53.57
TiO ₂	0.71	0.60	0.62	0.63	0.40	1.32	0.78	0.87	0.84	0.50	0.50	0.22
Al ₂ O ₃	2.82	2.10	1.52	1.49	2.19	6.50	4.87	5.13	4.08	2.60	2.67	2.21
Cr ₂ O ₃	0.09	0.08	0.02	0.02	0.29	0.02	0.07	0.04	0.15	0.06	0.05	0.87
Fe ₂ O ₃	-	-	-	-	-	-	-	-	-	-	-	-
FeO	8.94	8.91	8.48	8.61	5.74	7.89	7.34	7.40	7.88	7.65	7.72	4.84
MnO	0.23	0.25	0.26	0.28	0.14	0.16	0.19	0.19	0.18	0.19	0.22	0.13
MgO	14.72	15.08	15.21	15.28	16.35	14.30	15.50	14.89	15.07	16.06	16.13	17.62
CaO	20.90	20.61	20.91	20.79	21.65	20.46	20.50	21.01	20.66	20.22	20.14	20.79
Na ₂ O	0.59	0.58	0.50	0.45	0.46	0.43	0.43	0.42	0.41	0.40	0.34	0.35
total	99.76	100.07	99.70	99.11	99.96	100.17	100.64	100.23	100.06	100.05	100.07	100.60
Fe=FeO	-	-	-	-	-	-	-	-	-	-	-	-
Mg#	75	75	76	76	84	76	79	78	77	79	79	87

Sample Core/rim Unit Age	VF97-01Di	VF97-01Di	VF97-01Di	VF94-06E	VF94-06E	VF94-06E	VF94-06E	VF94-06E	VF94-06E	VF94-06E	VF95-01F	VF95-01F	VF95-01F
	cpx 1	cpx 2	cpx 2	cpx 1	cpx 1	cpx 1	cpx 2	cpx 2	cpx 2	cpx 2	cpx 1	cpx 1	cpx 1
	core	core	core	core	core	core	core	core	core	core	rim	rim	rim
	H	H	H	H	H	H	H	H	H	H	H	H	H
	10,000	10,000	10,000	10,000	10,000	10,000	10,000	10,000	10,000	10,000	10,000	10,000	10,000
SiO ₂	52.99	52.73	53.49	52.68	52.76	52.42	53.61	53.24	53.47	50.69	52.02	51.48	
TiO ₂	0.28	0.37	0.27	0.37	0.38	0.45	0.28	0.30	0.28	0.84	0.55	0.67	
Al ₂ O ₃	2.85	3.47	2.42	1.97	2.15	2.40	1.82	2.17	1.88	4.06	2.56	3.14	
Cr ₂ O ₃	0.98	0.57	0.41	0.12	0.09	0.11	0.57	0.76	0.58	0.05	0.04	0.04	
Fe ₂ O ₃	-	-	-	-	-	-	-	-	-	-	-	-	
FeO	5.18	5.47	5.23	5.58	5.63	5.53	4.08	4.31	4.28	9.10	8.73	9.37	
MnO	0.17	0.18	0.14	0.14	0.12	0.14	0.10	0.11	0.11	0.22	0.24	0.24	
MgO	17.66	17.05	17.53	16.47	16.54	16.22	17.07	17.02	17.29	14.42	15.19	14.90	
CaO	20.02	20.42	20.69	22.03	21.90	22.32	22.27	21.95	21.90	20.33	20.44	19.99	
Na ₂ O	0.39	0.42	0.36	0.32	0.29	0.32	0.33	0.37	0.34	0.53	0.42	0.47	
total	100.50	100.67	100.54	99.67	99.86	99.91	100.14	100.22	100.13	100.24	100.17	100.30	
Fe=FeO	-	-	-	-	-	-	-	-	-	-	-	-	
Mg#	86	85	86	84	84	84	88	88	88	74	76	74	

Sample Core/rim Unit Age	VF95-01F	VF95-01F	VF95-01F	VF97-01Di	VF97-01Di	VF97-01Di	VF97-01Di	VF94-06E	VF94-06E	VF94-06E	VF94-06E	VF94-06E
	cpx 2	cpx 2	cpx 2	cpx 1	cpx 1	cpx 2	cpx 2	cpx 1	cpx 1	cpx 1	cpx 2	cpx 2
	rim	rim	rim	rim	rim	rim	rim	rim	rim	rim	rim	rim
	H	H	H	H	H	H	H	H	H	H	H	H
	10,000	10,000	10,000	10,000	10,000	10,000	10,000	10,000	10,000	10,000	10,000	10,000
SiO ₂	51.33	50.68	51.03	50.98	51.52	52.45	50.48	52.34	51.57	51.78	52.94	52.08
TiO ₂	0.71	0.81	0.79	0.88	0.70	0.41	0.71	0.47	0.56	0.47	0.40	0.51
Al ₂ O ₃	2.99	3.65	3.27	3.14	3.20	2.76	5.23	2.57	3.36	2.91	2.17	2.95
Cr ₂ O ₃	0.04	0.03	0.01	0.00	0.00	0.06	0.12	0.14	0.01	0.04	0.13	0.07
Fe ₂ O ₃	-	-	-	-	-	-	-	-	-	-	-	-
FeO	9.11	9.04	9.10	9.45	8.51	6.89	7.54	6.11	7.48	6.72	5.99	6.31
MnO	0.25	0.23	0.22	0.29	0.23	0.18	0.18	0.14	0.22	0.17	0.18	0.15
MgO	15.13	14.17	14.73	15.29	15.19	16.43	14.92	16.07	15.40	15.55	16.46	15.73
CaO	19.99	20.85	20.61	19.72	20.66	20.59	20.45	21.82	21.15	21.78	21.64	21.83
Na ₂ O	0.41	0.51	0.41	0.37	0.39	0.36	0.48	0.34	0.39	0.37	0.33	0.38
total	99.96	99.96	100.16	100.11	100.40	100.13	100.11	100.00	100.13	99.78	100.23	100.00
Fe=FeO	-	-	-	-	-	-	-	-	-	-	-	-
Mg#	75	74	74	74	76	81	78	82	79	80	83	82

Table 8 Clinopyroxene core-rim profile data

	VF95-09L	VF95-09L	VF95-09L	VF95-09L	VF95-09L	VF95-09L	VF95-09L	VF95-09L	VF95-09L	VF95-09L	VF95-09L	VF95-09L
Sample	cpx 1	cpx 1	cpx 1	cpx 1	cpx 1	cpx 1	cpx 1	cpx 1	cpx 1	cpx 1	cpx 1	cpx 1
Figure	2.21b	2.21b	2.21b	2.21b	2.21b	2.21b	2.21b	2.21b	2.21b	2.21b	2.21b	2.21b
Unit	P	P	P	P	P	P	P	P	P	P	P	P
Age	6000	6000	6000	6000	6000	6000	6000	6000	6000	6000	6000	6000
SiO ₂	51.28	53.11	52.29	50.71	50.50	48.95	50.73	50.61	50.42	50.62	51.11	50.94
TiO ₂	0.63	0.26	0.46	0.78	0.60	0.87	0.59	0.67	0.75	0.69	0.77	0.74
Al ₂ O ₃	2.77	1.07	1.67	3.61	4.70	5.31	4.75	3.73	3.90	3.45	3.26	3.13
Cr ₂ O ₃	0.00	0.02	0.01	0.07	0.42	0.06	0.36	0.10	0.09	0.13	0.01	0.02
Fe ₂ O ₃	2.96	1.59	2.34	3.02	2.64	4.01	2.05	2.87	2.87	3.02	2.64	3.18
FeO	5.64	6.88	5.82	5.38	4.24	5.54	4.90	5.30	5.28	4.69	5.73	5.10
MnO	0.26	0.31	0.26	0.20	0.14	0.20	0.15	0.19	0.18	0.21	0.25	0.24
MgO	15.08	15.29	15.15	15.14	15.16	13.85	15.13	14.97	14.99	15.22	15.15	15.17
CaO	20.73	21.41	21.50	20.98	21.06	20.31	20.77	20.87	20.88	21.37	20.99	21.20
Na ₂ O	0.55	0.40	0.49	0.41	0.55	0.62	0.55	0.48	0.44	0.38	0.42	0.44
total	99.90	100.33	99.99	100.29	100.00	99.72	99.98	99.80	99.79	99.77	100.32	100.16
Fe=FeO	8.30	8.31	7.93	8.10	6.62	9.15	6.74	7.88	7.86	7.41	8.10	7.96
Mg#	76	77	77	77	80	73	80	77	77	79	77	77
	VF95-09L	VF95-09L	VF95-09L	VF95-09L	VF95-09L	VF95-09L	VF95-09L	VF95-09L	VF95-09L	VF95-09L	VF95-09L	VF95-09L
Sample	cpx 1	cpx 1	cpx 1	cpx 1	cpx 1	cpx 1	cpx 1	cpx 1	cpx 1	cpx 1	cpx 1	cpx 1
Figure	2.21b	2.21b	2.21b	2.21b	2.21b	2.21b	2.21b	2.21b	2.21b	2.21b	2.21b	2.21b
Unit	P	P	P	P	P	P	P	P	P	P	P	P
Age	6000	6000	6000	6000	6000	6000	6000	6000	6000	6000	6000	6000
SiO ₂	48.89	50.90	49.39	50.05	49.19	50.47	49.99	50.58	49.63	50.64	49.71	50.66
TiO ₂	1.01	0.70	0.93	0.78	0.95	0.81	0.91	0.85	1.03	0.91	0.99	0.83
Al ₂ O ₃	5.16	3.10	5.04	3.81	4.98	3.43	4.06	3.37	4.58	3.37	4.59	3.21
Cr ₂ O ₃	0.03	0.01	0.03	0.04	0.04	0.03	0.04	0.02	0.02	0.02	0.01	0.03
Fe ₂ O ₃	4.12	3.05	3.89	3.46	4.01	3.38	3.54	2.99	3.33	2.88	3.01	3.16
FeO	5.78	5.06	6.04	5.37	6.01	5.24	5.68	5.41	6.72	5.70	6.41	5.24
MnO	0.21	0.18	0.24	0.20	0.26	0.16	0.22	0.20	0.23	0.21	0.21	0.22
MgO	13.54	15.22	13.72	14.64	13.55	15.00	14.24	14.87	13.59	14.86	13.79	15.05
CaO	20.39	21.25	20.41	20.67	20.22	20.82	20.58	20.99	20.03	20.71	20.31	20.85
Na ₂ O	0.68	0.41	0.65	0.52	0.72	0.49	0.63	0.48	0.74	0.53	0.67	0.50
total	99.81	99.88	100.34	99.54	99.93	99.82	99.90	99.76	99.91	99.81	99.69	99.74
Fe=FeO	9.49	7.80	9.54	8.49	9.62	8.28	8.87	8.11	9.72	8.29	9.12	8.08
Mg#	72	78	72	75	72	76	74	77	71	76	73	77

Sample	VF95-09L	VF95-09L	VF95-09L	VF95-09L	VF95-09L	VF95-09L	VF95-09L	VF95-09L	VF95-09L	VF95-09L	VF95-09L	VF95-09L
Figure	cpx 1	cpx 1	cpx 2	cpx 2	cpx 2	cpx 2	cpx 2	cpx 2	cpx 2	cpx 2	cpx 2	cpx 2
Unit	2.21b	2.21b	2.21a	2.21a	2.21a	2.21a	2.21a	2.21a	2.21a	2.21a	2.21a	2.21a
Age	P	P	P	P	P	P	P	P	P	P	P	P
Age	6000	6000	6000	6000	6000	6000	6000	6000	6000	6000	6000	6000
SiO ₂	50.63	51.11	50.95	50.72	50.18	52.11	53.58	52.90	53.61	52.21	50.64	52.63
TiO ₂	0.86	0.76	0.54	0.47	0.67	0.57	0.22	0.35	0.28	0.40	0.77	0.50
Al ₂ O ₃	3.15	2.70	3.74	3.97	4.51	2.95	1.38	2.16	1.63	2.57	3.60	1.67
Cr ₂ O ₃	0.04	0.02	0.06	0.05	0.11	0.28	0.46	0.19	0.24	0.09	0.05	0.00
Fe ₂ O ₃	3.60	3.27	2.70	2.81	2.90	1.71	1.29	1.00	0.37	1.66	2.70	1.72
FeO	5.06	4.67	4.79	5.78	6.19	5.03	3.98	5.85	5.70	6.29	5.87	6.36
MnO	0.26	0.20	0.17	0.20	0.24	0.18	0.17	0.23	0.20	0.22	0.20	0.23
MgO	15.32	15.66	15.23	14.58	14.22	16.66	18.50	17.02	17.80	16.19	14.71	16.41
CaO	20.63	21.06	21.14	20.83	20.62	20.27	20.05	20.01	19.83	19.96	20.93	20.38
Na ₂ O	0.48	0.44	0.47	0.52	0.52	0.42	0.31	0.33	0.28	0.40	0.46	0.31
total	100.02	99.89	99.78	99.92	100.14	100.19	99.95	100.02	99.95	99.99	99.92	100.20
Fe=FeO	8.30	7.62	7.22	8.31	8.80	6.57	5.14	6.75	6.03	7.78	8.30	7.90
Mg#	77	79	79	76	74	82	87	82	84	79	76	79

Sample	VF95-09L	VF95-09L	VF95-09L	VF95-09L	VF95-09L	VF95-09L	VF95-09L	VF95-09L	VF95-09L	VF95-09L	VF95-09L	VF95-09L
Figure	cpx 2	cpx 2	cpx 2	cpx 2	cpx 2	cpx 2	cpx 2	cpx 2	cpx 2	cpx 2	cpx 2	cpx 2
Unit	2.21a	2.21a	2.21a	2.21a	2.21a	2.21a	2.21a	2.21a	2.21a	2.21a	2.21a	2.21a
Age	P	P	P	P	P	P	P	P	P	P	P	P
Age	6000	6000	6000	6000	6000	6000	6000	6000	6000	6000	6000	6000
SiO ₂	51.75	51.95	51.28	51.75	51.47	52.34	51.92	51.95	51.01	52.24	51.58	51.90
TiO ₂	0.54	0.49	0.58	0.55	0.58	0.42	0.55	0.57	0.68	0.59	0.62	0.61
Al ₂ O ₃	2.31	2.10	3.04	2.34	2.46	2.47	2.46	2.28	3.27	1.59	2.79	2.18
Cr ₂ O ₃	0.01	0.01	0.04	0.02	0.03	0.03	0.03	0.02	0.01	0.00	0.01	0.00
Fe ₂ O ₃	2.16	2.26	2.67	2.31	2.71	1.35	2.15	2.45	2.80	2.40	2.56	2.37
FeO	6.65	6.36	6.64	6.00	6.61	5.85	7.08	6.22	6.69	5.98	7.05	5.66
MnO	0.23	0.24	0.22	0.25	0.26	0.19	0.28	0.26	0.21	0.32	0.27	0.27
MgO	15.54	15.85	15.02	15.45	15.23	16.14	15.27	15.53	14.55	16.23	15.05	15.66
CaO	20.09	20.18	19.99	20.67	19.86	20.65	19.75	20.43	20.07	20.27	19.62	20.85
Na ₂ O	0.44	0.40	0.55	0.45	0.56	0.36	0.58	0.50	0.66	0.42	0.63	0.44
total	99.72	99.82	100.04	99.80	99.78	99.80	100.08	100.20	99.94	100.05	100.19	99.95
Fe=FeO	8.60	8.39	9.05	8.08	9.05	7.07	9.02	8.42	9.20	8.14	9.35	7.79
Mg#	76	77	75	77	75	80	75	77	74	78	74	78

Sample	VF95-09L	VF95-09L	VF95-09L	VF10-03M2	VF10-03M2	VF10-03M2	VF10-03M2	VF10-03M2	VF10-03M2	VF10-03M2	VF10-03M2	VF10-03M2
Figure	cpx 2	cpx 2	cpx 2	cpx 2	cpx 2	cpx 2	cpx 2	cpx 2	cpx 2	cpx 2	cpx 2	cpx 2
Unit	2.21a	2.21a	2.21a	2.22	2.22	2.22	2.22	2.22	2.22	2.22	2.22	2.22
Age	P	P	P	L	L	L	L	L	L	L	L	L
Age	6000	6000	6000	7500	7500	7500	7500	7500	7500	7500	7500	7500
SiO ₂	50.78	50.99	50.75	52.69	52.77	52.79	52.27	52.47	52.40	52.10	52.37	52.40
TiO ₂	0.64	0.63	0.90	0.22	0.18	0.21	0.28	0.25	0.23	0.22	0.24	0.23
Al ₂ O ₃	2.91	2.89	3.10	1.89	1.80	1.73	2.31	2.07	2.06	1.58	1.31	1.36
Cr ₂ O ₃	0.02	0.04	0.01	0.22	0.27	0.24	0.23	0.18	0.15	0.05	0.03	0.01
Fe ₂ O ₃	3.06	2.83	3.31	1.99	1.88	1.68	1.91	2.01	2.41	2.58	1.80	2.05
FeO	5.73	6.16	5.69	3.95	3.72	4.17	4.22	3.83	3.73	5.83	6.69	6.59
MnO	0.17	0.22	0.25	0.16	0.19	0.16	0.15	0.18	0.19	0.23	0.29	0.31
MgO	14.83	15.18	15.50	16.61	16.82	16.98	16.41	16.50	16.38	15.53	15.65	15.62
CaO	20.35	20.01	20.04	21.75	21.73	21.26	21.34	21.75	21.71	21.20	20.81	20.90
Na ₂ O	0.62	0.53	0.49	0.35	0.33	0.32	0.39	0.36	0.41	0.34	0.28	0.29
total	99.11	99.47	100.03	99.85	99.69	99.54	99.49	99.59	99.67	99.66	99.46	99.77
Fe=FeO	8.49	8.71	8.67	5.74	5.42	5.68	5.94	5.64	5.89	8.15	8.31	8.44
Mg#	76	76	76	84	85	84	83	84	83	77	77	77

Sample	VF10-03M2	VF10-03M2	VF10-03M2	VF10-03M2	VF10-03M2	VF10-03M2	VF10-03M2	VF10-03M2
Figure	cpx 2	cpx 2	cpx 2	cpx 2	cpx 2	cpx 2	cpx 2	cpx 2
Unit	2.22	2.22	2.22	2.22	2.22	2.22	2.22	2.22
Age	L	L	L	L	L	L	L	L
Age	7500	7500	7500	7500	7500	7500	7500	7500
SiO ₂	52.32	52.34	52.47	51.36	51.69	51.73	51.58	51.64
TiO ₂	0.27	0.26	0.25	0.42	0.38	0.38	0.44	0.42
Al ₂ O ₃	1.28	1.19	1.20	2.18	2.16	1.32	1.80	1.56
Cr ₂ O ₃	0.00	0.01	0.04	0.03	0.05	0.00	0.01	0.03
Fe ₂ O ₃	1.90	2.14	1.95	3.07	2.41	2.32	2.13	2.15
FeO	6.70	6.28	6.57	5.66	6.11	7.46	7.71	7.60
MnO	0.28	0.32	0.31	0.30	0.25	0.30	0.33	0.34
MgO	15.58	15.67	15.54	14.81	14.77	14.54	14.73	14.44
CaO	20.91	21.01	21.08	21.51	21.65	20.85	20.35	20.82
Na ₂ O	0.28	0.32	0.29	0.40	0.37	0.41	0.37	0.39
total	99.51	99.53	99.71	99.75	99.84	99.30	99.44	99.39
Fe=FeO	8.40	8.20	8.32	8.42	8.27	9.54	9.63	9.54
Mg#	77	77	77	76	76	73	73	73

Table 9 Orthopyroxene

Sample	VF98-02W	VF98-02W	VF98-02W	VF98-02W	VF98-02W	VF98-02W	VF95-06U	VF95-06U	VF95-06U	VF95-06U	VF95-06U	VF95-06U
Core/rim	opx 1	opx 1	opx 3	opx 3	opx 1	opx 1	opx 2	opx 3	opx 4	opx 5	opx 5	opx 5
Unit	core	core	core	core	rim	rim	core	core	core	core	core	core
Ages	W	W	W	W	W	W	U	U	U	U	U	U
Ages	4500	4500	4500	4500	4500	4500	4700	4700	4700	4700	4700	4700
SiO ₂	53.88	53.77	53.99	53.09	54.40	54.14	54.05	53.82	53.76	53.45	53.58	53.49
TiO ₂	0.30	0.31	0.19	0.21	0.14	0.15	0.43	0.41	0.44	0.30	0.33	0.21
Al ₂ O ₃	2.01	2.21	1.73	2.98	2.04	2.16	1.25	1.29	1.30	1.03	1.34	1.19
Cr ₂ O ₃	0.04	0.00	0.03	0.00	0.01	0.05	0.00	0.00	0.00	0.07	0.03	0.04
Fe ₂ O ₃	1.49	1.02	1.29	1.35	0.92	0.30	0.00	0.26	0.27	0.00	0.00	0.00
FeO	14.23	14.75	13.67	14.32	13.28	13.42	15.28	15.01	15.37	18.75	17.43	17.46
MnO	0.20	0.37	0.34	0.40	0.33	0.33	0.45	0.47	0.46	0.44	0.44	0.49
MgO	27.02	26.47	27.45	26.26	28.01	27.66	26.10	26.23	26.02	23.93	24.46	24.90
CaO	1.39	1.62	1.19	1.52	1.24	1.21	1.78	1.75	1.80	1.50	1.54	1.35
Na ₂ O	0.07	0.04	0.06	0.04	0.01	0.05	0.04	0.05	0.04	0.05	0.01	0.02
TOTAL	100.63	100.55	99.93	100.16	100.38	99.46	99.39	99.30	99.46	99.52	99.16	99.16
Fe=FeO	15.57	15.67	14.83	15.54	14.10	13.68	15.28	15.25	15.62	18.75	17.43	17.46
Mg#	76	75	77	75	78	78	75	75	75	69	71	72

Sample	VF98-02U	VF10-07U	VF10-07U	VF10-07U	VF10-01U	VF10-01U	VF10-01U	VF95-06U	VF95-06U	VF95-06U	VF98-02U	VF10-07U
Core/rim	opx 1	opx 1	opx 1	opx 2	opx 1	opx 2	opx 2	opx 5	opx 5	opx 5	opx 1	opx 1
Unit	core	core	core	core	core	core	core	rim	rim	rim	rim	rim
Ages	U	U	U	U	U	U	U	U	U	U	U	U
Ages	4700	4700	4700	4700	4700	4700	4700	4700	4700	4700	4700	4700
SiO ₂	54.32	53.92	53.94	54.85	54.38	54.53	54.99	52.33	52.90	53.88	53.62	54.42
TiO ₂	0.18	0.31	0.25	0.15	0.19	0.17	0.19	0.33	0.27	0.23	0.20	0.15
Al ₂ O ₃	1.98	1.63	1.58	2.10	2.48	2.09	1.29	1.01	1.35	0.75	2.85	2.01
Cr ₂ O ₃	0.14	0.00	0.00	0.07	0.08	0.04	0.05	0.02	0.00	0.00	0.08	0.05
Fe ₂ O ₃	1.44	1.98	2.02	1.43	1.42	1.21	0.89	0.91	0.00	0.00	1.40	1.24
FeO	11.47	13.70	13.97	11.42	11.80	12.21	12.90	17.34	18.76	18.52	11.68	12.53
MnO	0.26	0.42	0.41	0.31	0.26	0.30	0.32	0.63	0.46	0.36	0.26	0.32
MgO	28.89	27.16	27.13	29.35	28.87	28.68	28.52	23.97	23.68	23.80	28.15	28.33
CaO	1.17	1.65	1.47	1.24	1.22	1.25	1.37	1.52	1.35	1.52	1.41	1.29
Na ₂ O	0.08	0.03	0.03	0.02	0.02	0.03	0.03	0.05	0.02	0.07	0.08	0.04
TOTAL	99.93	100.82	100.80	100.94	100.71	100.51	100.54	98.10	98.79	99.13	99.73	100.38
Fe=FeO	12.77	15.49	15.79	12.71	13.07	13.31	13.70	18.16	18.76	18.52	12.94	13.65
Mg#	80	76	75	80	80	79	79	70	69	70	80	79

Sample	VF10-07U	VF10-07U	VF10-07U	VF10-07U	VF10-07U	VF10-01U	VF10-01U	VF10-01U	VF10-01U	VF95-09T	VF95-09T	VF95-09T
Core/rim	opx 1	opx 2	opx 2	opx 2	opx 2	opx 1	opx 2	opx 3	opx 3	opx 1	opx 1	opx 2
Unit	rim	rim	rim	rim	rim	rim	rim	rim	rim	core	core	core
Ages	U	U	U	U	U	U	U	U	U	S	S	S
SiO ₂	4700	4700	4700	4700	4700	4700	4700	4700	4700	5500	5500	5500
TiO ₂	54.83	54.50	53.76	53.97	54.55	55.00	54.23	53.92	54.05	53.55	53.70	54.38
Al ₂ O ₃	0.31	0.15	0.20	0.15	0.13	0.14	0.20	0.27	0.31	0.16	0.29	0.11
Cr ₂ O ₃	8.11	2.23	1.61	2.64	1.94	1.67	2.24	1.57	1.50	2.44	1.87	2.32
Fe ₂ O ₃	0.02	0.11	0.03	0.08	0.05	0.08	0.13	0.09	0.05	0.26	0.02	0.56
FeO	0.00	1.84	2.17	1.95	1.29	0.77	1.25	1.93	1.28	0.00	0.13	0.00
MnO	12.88	11.16	13.92	11.10	11.80	12.02	11.95	13.63	13.57	14.72	14.44	12.73
MgO	0.31	0.32	0.46	0.29	0.30	0.31	0.30	0.36	0.36	0.30	0.37	0.28
CaO	22.51	29.25	27.25	28.92	28.91	29.00	28.62	27.49	27.58	26.39	26.47	27.24
Na ₂ O	2.63	1.24	1.36	1.24	1.25	1.36	1.28	1.27	1.36	1.32	1.82	2.33
TOTAL	0.94	0.02	0.03	0.03	0.02	0.02	0.02	0.01	0.01	0.07	0.03	0.08
Fe=FeO	102.54	100.80	100.79	100.37	100.25	100.38	100.22	100.57	100.08	99.21	99.14	100.03
Mg#	12.88	12.81	15.87	12.85	12.96	12.71	13.07	15.37	14.71	14.72	14.56	12.73
	76	80	75	80	80	80	80	76	77	76	76	79

Sample	VF95-09T	VF95-09T	VF95-09T	VF95-09T	VF95-09T	VF95-09T	VF95-09T	VF95-09T	VF95-09T	VF95-09T	VF95-09T	VF95-09T
Core/rim	opx 2	opx 2	opx 3	opx 3	opx 3	opx 4	opx 4	opx 1	opx 1	opx 1	opx 2	opx 2
Unit	core	core	core	core	core	core	core	rim	rim	rim	rim	rim
Ages	S	S	S	S	S	S	S	S	S	S	S	S
SiO ₂	5500	5500	5500	5500	5500	5500	5500	5500	5500	5500	5500	5500
TiO ₂	54.87	55.09	56.29	54.27	55.12	53.79	53.67	54.34	53.92	54.70	53.85	54.33
Al ₂ O ₃	0.14	0.12	0.09	0.22	0.05	0.22	0.21	0.23	0.20	0.23	0.26	0.15
Cr ₂ O ₃	2.19	1.87	1.46	2.34	1.76	1.44	1.46	0.70	1.13	0.63	1.73	1.80
Fe ₂ O ₃	0.32	0.44	0.49	0.38	0.56	0.02	0.02	0.00	0.00	0.00	0.14	0.14
FeO	0.00	0.00	0.00	0.00	0.00	0.18	0.69	0.00	0.00	0.00	0.00	0.00
MnO	12.18	12.97	9.61	12.17	11.79	16.60	16.00	17.03	17.13	17.80	16.61	15.81
MgO	0.29	0.35	0.23	0.33	0.20	0.38	0.39	0.58	0.43	0.80	0.35	0.35
CaO	28.36	27.67	29.93	28.39	28.14	25.63	25.90	25.07	24.64	24.57	25.20	25.93
Na ₂ O	1.33	1.73	1.70	1.25	1.50	1.26	1.33	1.33	1.26	1.36	1.27	1.28
TOTAL	0.04	0.03	0.02	0.04	0.05	0.05	0.03	0.04	0.05	0.05	0.02	0.05
Fe=FeO	99.72	100.26	99.83	99.39	99.19	99.57	99.67	99.32	98.77	100.15	99.44	99.85
Mg#	12.18	12.97	9.61	12.17	11.79	16.77	16.61	17.03	17.13	17.80	16.61	15.81
	81	79	85	81	81	73	74	72	72	71	73	75

Sample	VF95-09T	VF95-09T	VF95-09T	VF95-09T	VF95-09T	VF95-09T	VF10-03Pi	VF10-03Pi	VF10-03Pi	VF10-03Pi	VF10-03Pi	VF95-09L
Core/rim	opx 2	opx 3	opx 3	opx 3	opx 4	opx 4	opx 2	opx 3	opx 3	opx 4	opx 5	opx 3
Unit	rim	rim	rim	rim	rim	rim	core	core	core	core	core	core
Ages	S	S	S	S	S	S	P	P	P	P	P	P
SiO ₂	54.18	53.53	53.51	53.56	53.72	53.75	54.23	54.08	53.97	53.80	54.16	54.67
TiO ₂	0.15	0.24	0.26	0.22	0.26	0.20	0.19	0.34	0.40	0.16	0.14	0.18
Al ₂ O ₃	1.79	1.54	2.10	1.52	1.48	1.01	1.93	1.08	1.21	1.01	0.89	1.23
Cr ₂ O ₃	0.17	0.00	0.15	0.04	0.00	0.00	0.10	0.06	0.03	0.03	0.01	0.05
Fe ₂ O ₃	0.00	0.00	0.00	0.00	0.40	0.00	1.43	1.02	1.16	1.33	1.10	1.55
FeO	16.69	16.63	16.70	16.66	16.49	16.76	11.90	13.83	13.74	16.26	15.87	12.88
MnO	0.35	0.49	0.36	0.32	0.40	0.39	0.29	0.36	0.39	0.47	0.43	0.35
MgO	25.35	24.72	24.99	25.26	25.58	25.58	28.63	27.80	27.54	26.05	26.38	28.40
CaO	1.35	1.20	1.18	1.22	1.41	1.30	1.28	1.36	1.33	0.99	1.13	1.48
Na ₂ O	0.03	0.02	0.07	0.03	0.04	0.01	0.03	0.02	0.03	0.04	0.02	0.01
TOTAL	100.06	98.36	99.32	98.83	99.77	99.00	100.01	99.96	99.79	100.13	100.12	100.78
Fe=FeO	16.69	16.63	16.70	16.66	16.85	16.76	13.19	14.76	14.78	17.45	16.86	14.27
Mg#	73	73	73	73	73	73	79	77	77	73	74	78

Sample	VF10-03Pi	VF10-03Pi	VF10-03Pi	VF10-03Pi	VF10-03Pi	VF10-03Pi	VF10-03Pi	VF10-03Pi	VF10-03Pi	VF10-03Pi	VF10-03Pi	VF95-09L	VF95-09L
Core/rim	opx 2	opx 3	opx 3	opx 3	opx 4	opx 4	opx 4	opx 5	opx 5	opx 5	opx 3	opx 3	
Unit	rim	rim	rim	rim	rim	rim	rim	rim	rim	rim	rim	rim	
Ages	P	P	P	P	P	P	P	P	P	P	P	P	
SiO ₂	53.88	53.44	53.37	52.97	53.60	52.99	53.33	53.39	53.61	53.74	54.18	54.18	
TiO ₂	0.16	0.22	0.18	0.34	0.22	0.26	0.26	0.22	0.24	0.22	0.38	0.37	
Al ₂ O ₃	0.69	0.97	0.80	0.93	1.40	1.77	1.78	1.18	0.74	0.73	1.46	1.38	
Cr ₂ O ₃	0.00	0.00	0.03	0.10	0.00	0.02	0.02	0.01	0.00	0.04	0.00	0.00	
Fe ₂ O ₃	0.76	1.17	0.95	0.76	0.99	1.61	1.44	1.43	0.68	0.74	1.27	1.49	
FeO	15.30	15.77	15.90	16.02	15.46	15.37	15.28	16.01	16.81	16.39	13.47	13.24	
MnO	0.46	0.44	0.41	0.54	0.42	0.47	0.42	0.54	0.70	0.62	0.45	0.43	
MgO	26.57	26.33	26.26	25.89	26.00	25.62	26.07	25.69	25.65	25.81	27.52	27.81	
CaO	1.29	1.15	1.08	1.22	1.50	1.49	1.33	1.35	1.22	1.31	1.58	1.62	
Na ₂ O	0.00	0.04	0.03	0.03	0.03	0.03	0.02	0.02	0.00	0.02	0.02	0.03	
TOTAL	99.12	99.52	99.01	98.81	99.61	99.64	99.95	99.84	99.65	99.61	100.33	100.55	
Fe=FeO	15.99	16.82	16.75	16.71	16.35	16.82	16.58	17.29	17.42	17.05	14.61	14.58	
Mg#	75	74	74	73	74	73	74	73	72	73	77	77	

Sample	VF10-03M2	VF10-03M2	VF10-03M2	VF10-03M2	VF10-03M2	VF10-03M2	VF97-01F	VF97-01F	VF97-01F	VF97-01F	VF97-01F	VF97-01F
Core/rim	opx 1	opx 3	opx 1	opx 3	opx 3	opx 3	opx 2	opx 2	opx 2	opx 1	opx 1	opx 2
Unit	core	core	rim	rim	rim	rim	core	core	core	rim	rim	rim
Ages	L	L	L	L	L	L	J	J	J	J	J	J
Ages	7500	7500	7500	7500	7500	7500	7700	7700	7700	7700	7700	7700
SiO ₂	53.68	55.37	53.83	52.81	53.72	54.05	55.72	55.56	54.90	54.77	55.22	54.49
TiO ₂	0.24	0.10	0.15	0.21	0.10	0.14	0.13	0.15	0.26	0.17	0.14	0.22
Al ₂ O ₃	1.22	1.26	1.26	1.78	1.04	0.81	1.64	1.90	1.05	1.90	1.42	1.78
Cr ₂ O ₃	0.05	0.15	0.02	0.01	0.01	0.00	0.17	0.17	0.03	0.16	0.10	0.08
Fe ₂ O ₃	1.41	0.89	0.77	1.26	1.32	1.07	-	-	-	-	-	-
FeO	15.39	11.26	16.16	16.40	15.65	16.01	9.92	10.14	14.10	12.38	12.57	13.44
MnO	0.37	0.29	0.47	0.46	0.47	0.49	0.21	0.23	0.31	0.24	0.26	0.28
MgO	26.27	29.78	26.01	24.61	26.15	26.28	31.31	31.17	28.58	29.32	29.51	28.83
CaO	1.45	1.20	1.11	1.94	1.11	1.21	1.35	1.32	1.20	1.26	1.31	1.18
Na ₂ O	0.01	0.02	0.02	0.03	0.04	0.03	0.03	0.02	0.03	0.02	0.02	0.02
TOTAL	100.09	100.32	99.80	99.50	99.60	100.09	100.47	100.64	100.45	100.23	100.56	100.32
Fe=FeO	16.65	12.07	16.86	17.53	16.84	16.97	-	-	-	-	-	-
Mg#	74	81	73	71	73	73	85	85	78	81	81	79

Sample	VF97-01F	VF97-01F	VF10-03L	VF10-03L	VF10-03L	VF10-03L	VF10-03L	VF10-03L	VF10-03L	VF10-03L	VF95-01F	VF95-01F	VF97-01Di
Core/rim	opx 2	opx 2	opx 1	opx 1	opx 1	opx 1	opx 2	opx 2	opx 2	opx 2	opx 1	opx 1	opx 1
Unit	rim	rim	rim	rim	rim	rim	rim	rim	rim	rim	core	core	core
Ages	J	J	J	J	J	J	J	J	J	J	H	H	H
Ages	7700	7700	7700	7700	7700	7700	7700	7700	7700	7700	10,000	10,000	10,000
SiO ₂	55.42	54.39	53.79	54.13	53.73	53.60	54.85	54.31	53.88	54.73	54.04	54.14	
TiO ₂	0.15	0.19	0.19	0.22	0.23	0.30	0.20	0.12	0.30	0.18	0.22	0.34	
Al ₂ O ₃	0.99	2.25	1.38	1.38	1.26	1.17	1.21	1.01	0.74	0.60	0.86	1.87	
Cr ₂ O ₃	0.03	0.15	0.06	0.08	0.06	0.03	0.17	0.28	0.01	0.00	0.00	0.00	
Fe ₂ O ₃	-	-	-	-	-	-	-	-	-	-	-	-	
FeO	13.00	12.66	16.37	17.09	17.14	16.93	13.68	15.45	17.31	18.77	19.53	15.68	
MnO	0.31	0.28	0.39	0.42	0.42	0.44	0.37	0.42	0.50	0.66	0.65	0.43	
MgO	29.17	29.03	26.88	26.03	26.28	25.87	28.46	27.33	25.38	25.31	24.58	26.84	
CaO	1.30	1.25	1.19	1.24	1.36	1.42	1.30	1.26	1.39	1.38	1.36	1.74	
Na ₂ O	0.05	0.03	0.03	0.04	0.03	0.03	0.02	0.02	0.03	0.04	0.03	0.04	
TOTAL	100.42	100.23	100.28	100.63	100.52	99.80	100.26	100.21	99.54	101.66	101.27	101.08	
Fe=FeO	-	-	-	-	-	-	-	-	-	-	-	-	
Mg#	80	80	75	73	73	73	79	76	72	71	69	75	

Sample	VF97-01Di	VF97-01Di	VF97-01Di	VF95-01F	VF95-01F	VF97-01Di	VF97-01Di	VF97-01Di	VF97-01Di	VF97-01Di
Core/rim	opx 1	opx 2	opx 2	opx 1	opx 1	opx 1	opx 1	opx 2	opx 2	opx 2
Unit	core	core	core	rim	rim	rim	rim	rim	rim	rim
Age	H	H	H	H	H	H	H	H	H	H
Age	10,000	10,000	10,000	10,000	10,000	10,000	10,000	10,000	10,000	10,000
SiO ₂	54.07	54.87	54.03	54.67	54.58	54.43	54.25	53.83	54.12	55.15
TiO ₂	0.22	0.14	0.25	0.32	0.36	0.22	0.20	0.36	0.33	0.19
Al ₂ O ₃	2.12	0.49	1.16	1.09	1.35	2.49	3.45	1.75	1.55	0.99
Cr ₂ O ₃	0.06	0.00	0.01	0.01	0.00	0.08	0.05	0.00	0.00	0.03
Fe ₂ O ₃	-	-	-	-	-	-	-	-	-	-
FeO	16.54	17.18	17.72	16.09	16.38	13.59	12.17	15.66	16.12	14.49
MnO	0.38	0.66	0.60	0.42	0.41	0.29	0.25	0.43	0.46	0.37
MgO	26.51	26.32	25.74	26.74	26.40	28.26	28.88	26.58	26.48	27.91
CaO	1.38	1.22	1.18	1.59	1.54	1.39	1.37	1.88	1.61	1.54
Na ₂ O	0.03	0.01	0.03	0.02	0.04	0.05	0.04	0.04	0.02	0.02
TOTAL	101.32	100.89	100.71	100.97	101.06	100.81	100.66	100.54	100.68	100.69
Fe=FeO	-	-	-	-	-	-	-	-	-	-
Mg#	74	73	72	75	74	79	81	75	75	77

Table 10 Orthopyroxene core-rim profile data

Sample	VF98-02U	VF98-02U	VF98-02U	VF98-02U	VF98-02U	VF98-02U	VF98-02U	VF98-02U	VF98-02U	VF98-02U	VF98-02U	VF98-02U
	opx 1	opx 1	opx 1	opx 1	opx 1	opx 1	opx 1	opx 1	opx 1	opx 1	opx 1	opx 1
Figure	2.25a	2.25a	2.25a	2.25a	2.25a	2.25a	2.25a	2.25a	2.25a	2.25a	2.25a	2.25a
Unit	U	U	U	U	U	U	U	U	U	U	U	U
Ages	4700	4700	4700	4700	4700	4700	4700	4700	4700	4700	4700	4700
SiO ₂	54.32	54.50	54.64	54.09	54.51	54.29	54.38	54.45	53.83	54.22	53.25	52.85
TiO ₂	0.18	0.15	0.13	0.18	0.16	0.17	0.16	0.15	0.20	0.22	0.24	0.19
Al ₂ O ₃	1.98	1.88	1.73	2.07	2.16	2.05	2.04	2.17	3.07	2.70	3.68	3.80
Cr ₂ O ₃	0.14	0.15	0.16	0.16	0.14	0.08	0.03	0.04	0.13	0.14	0.06	0.08
Fe ₂ O ₃	1.44	0.88	0.94	1.28	0.99	1.59	1.15	0.87	1.65	1.18	1.44	2.11
FeO	11.47	11.89	11.86	11.65	11.81	11.21	11.59	11.68	10.81	10.78	10.55	9.96
MnO	0.26	0.30	0.29	0.27	0.28	0.29	0.26	0.28	0.28	0.24	0.25	0.23
MgO	28.89	28.74	28.87	28.62	28.85	29.05	28.82	28.88	28.89	29.20	28.77	28.64
CaO	1.17	1.19	1.17	1.17	1.14	1.12	1.12	1.14	1.20	1.18	1.17	1.27
Na ₂ O	0.08	0.08	0.08	0.08	0.07	0.08	0.10	0.08	0.09	0.10	0.06	0.10
TOTAL	99.93	99.76	99.86	99.56	100.11	99.92	99.67	99.72	100.14	99.95	99.47	99.23
Fe=FeO	12.77	12.68	12.71	12.80	12.70	12.64	12.63	12.46	12.29	11.84	11.85	11.86
Mg#	80	80	80	80	80	80	80	81	81	81	81	81

Sample	VF98-02U	VF98-02U	VF98-02U	VF98-02U	VF98-02U	VF98-02U	VF98-02U	VF98-02U	VF98-02U	VF98-02U	VF98-02U	VF98-02U
	opx 1	opx 1	opx 1	opx 1	opx 1	opx 1	opx 1	opx 1	opx 1	opx 1	opx 1	opx 1
Figure	2.25a	2.25a	2.25a	2.25a	2.25a	2.25a	2.25a	2.25a	2.25a	2.25a	2.25a	2.25a
Unit	U	U	U	U	U	U	U	U	U	U	U	U
Ages	4700	4700	4700	4700	4700	4700	4700	4700	4700	4700	4700	4700
SiO ₂	53.24	53.18	53.20	53.28	54.17	53.55	53.67	53.43	53.72	53.71	54.49	53.51
TiO ₂	0.18	0.19	0.16	0.15	0.21	0.22	0.22	0.26	0.26	0.24	0.17	0.25
Al ₂ O ₃	3.93	3.94	3.78	3.73	2.95	2.94	2.83	3.18	2.70	2.69	1.97	2.97
Cr ₂ O ₃	0.06	0.12	0.12	0.13	0.11	0.19	0.15	0.08	0.16	0.16	0.08	0.08
Fe ₂ O ₃	1.71	1.87	1.55	1.70	0.95	1.68	1.21	1.37	1.30	1.15	0.64	1.50
FeO	10.74	10.61	10.88	10.74	10.68	10.60	11.05	11.38	11.33	11.58	11.75	11.44
MnO	0.27	0.25	0.23	0.25	0.25	0.25	0.30	0.27	0.28	0.30	0.25	0.27
MgO	28.56	28.71	28.61	28.74	29.22	28.98	28.69	28.41	28.64	28.57	28.95	28.41
CaO	1.18	1.18	1.16	1.15	1.24	1.24	1.28	1.26	1.20	1.16	1.27	1.23
Na ₂ O	0.08	0.05	0.03	0.04	0.08	0.03	0.05	0.04	0.05	0.04	0.01	0.06
TOTAL	99.95	100.09	99.72	99.90	99.86	99.66	99.45	99.68	99.64	99.60	99.58	99.71
Fe=FeO	12.28	12.30	12.27	12.27	11.54	12.11	12.14	12.62	12.50	12.61	12.32	12.79
Mg#	81	81	81	81	82	81	81	80	80	80	81	80

Sample	VF98-02U	VF98-02U	VF98-02U	VF98-02U	VF98-02U	VF98-02U	VF98-02U	VF98-02U	VF98-02U	VF98-02U	VF98-02U	VF98-02U
	opx 1	opx 1	opx 1	opx 1	opx 1	opx 1	opx 1	opx 1	opx 1	opx 1	opx 1	opx 1
Figure	2.25a	2.25a	2.25a	2.25a	2.25a	2.25a	2.25a	2.25a	2.25a	2.25a	2.25a	2.25a
Unit	U	U	U	U	U	U	U	U	U	U	U	U
Ages	4700	4700	4700	4700	4700	4700	4700	4700	4700	4700	4700	4700
SiO ₂	52.70	53.01	52.88	53.12	52.89	53.20	53.38	54.07	54.18	53.95	54.00	53.92
TiO ₂	0.31	0.30	0.28	0.30	0.29	0.24	0.23	0.18	0.18	0.22	0.22	0.19
Al ₂ O ₃	3.89	3.98	3.46	3.51	3.81	2.96	2.86	2.04	2.14	2.42	2.34	2.34
Cr ₂ O ₃	0.00	0.05	0.02	0.03	0.00	0.02	0.04	0.10	0.07	0.12	0.11	0.09
Fe ₂ O ₃	1.66	1.00	1.26	1.41	1.17	1.63	1.21	1.32	1.21	0.80	1.14	1.14
FeO	12.15	12.71	12.03	12.00	12.40	11.94	12.16	12.06	12.15	12.45	12.14	12.15
MnO	0.24	0.25	0.27	0.29	0.27	0.26	0.32	0.28	0.31	0.25	0.29	0.31
MgO	27.29	27.18	27.50	27.56	27.44	27.88	27.90	28.47	28.46	28.17	28.35	28.28
CaO	1.49	1.53	1.54	1.65	1.36	1.31	1.25	1.20	1.28	1.23	1.20	1.27
Na ₂ O	0.07	0.06	0.04	0.05	0.04	0.05	0.05	0.04	0.03	0.04	0.06	0.04
TOTAL	99.80	100.06	99.29	99.93	99.65	99.49	99.40	99.76	100.00	99.64	99.86	99.72
Fe=FeO	13.65	13.62	13.17	13.27	13.45	13.41	13.25	13.25	13.24	13.17	13.17	13.18
Mg#	78	78	79	79	78	79	79	79	79	79	79	79

Sample	VF98-02U	VF98-02U	VF98-02U	VF98-02U	VF95-09L	VF95-09L	VF95-09L	VF95-09L	VF95-09L	VF95-09L	VF95-09L	VF95-09L
	opx 1	opx 1	opx 1	opx 1	opx 3	opx 3	opx 3	opx 3	opx 3	opx 3	opx 3	opx 3
Figure	2.25a	2.25a	2.25a	2.25a	2.25b	2.25b	2.25b	2.25b	2.25b	2.25b	2.25b	2.25b
Unit	U	U	U	U	P	P	P	P	P	P	P	P
Ages	4700	4700	4700	4700	6000	6000	6000	6000	6000	6000	6000	6000
SiO ₂	53.20	53.44	53.62	53.62	54.67	53.84	54.27	52.45	54.20	53.93	54.02	54.13
TiO ₂	0.21	0.23	0.22	0.20	0.18	0.23	0.22	0.31	0.34	0.33	0.35	0.37
Al ₂ O ₃	2.98	3.11	3.01	2.85	1.23	1.91	1.92	2.75	0.84	1.23	0.94	1.01
Cr ₂ O ₃	0.14	0.05	0.07	0.08	0.05	0.02	0.01	0.04	0.01	0.00	0.01	0.01
Fe ₂ O ₃	1.69	1.07	0.85	1.40	1.55	1.82	1.09	2.38	0.71	1.26	0.79	0.87
FeO	11.45	12.05	12.32	11.68	12.88	12.79	14.21	14.70	15.64	15.50	15.83	15.17
MnO	0.31	0.28	0.27	0.26	0.35	0.42	0.37	0.47	0.50	0.49	0.51	0.53
MgO	28.11	28.01	28.07	28.15	28.40	27.69	27.05	25.76	26.44	26.08	26.11	26.56
CaO	1.28	1.26	1.28	1.41	1.48	1.55	1.61	1.45	1.56	1.63	1.68	1.68
Na ₂ O	0.06	0.05	0.01	0.08	0.01	0.01	0.05	0.01	0.04	0.05	0.01	0.01
TOTAL	99.43	99.55	99.73	99.73	100.78	100.28	100.78	100.32	100.28	100.50	100.24	100.33
Fe=FeO	12.97	13.01	13.09	12.94	14.27	14.43	15.19	16.84	16.28	16.64	16.54	15.95
Mg#	79	79	79	80	78	77	76	73	74	74	74	75

Sample	VF95-09L	VF95-09L	VF95-09L	VF95-09L	VF95-09L	VF95-09L	VF95-09L	VF95-09L	VF10-03M2	VF10-03M2	VF10-03M2	VF10-03M2
Figure	opx 3	opx 3	opx 3	opx 3	opx 3	opx 3	opx 3	opx 3	opx 1	opx 1	opx 1	opx 1
Unit	2.25b	2.25b	2.25b	2.25b	2.25b	2.25b	2.25b	2.25b	2.26a	2.26a	2.26a	2.26a
Ages	P	P	P	P	P	P	P	P	L	L	L	L
	6000	6000	6000	6000	6000	6000	6000	6000	7500	7500	7500	7500
SiO ₂	53.79	53.71	53.38	53.38	54.12	53.89	54.18	53.68	53.68	54.05	54.11	54.68
TiO ₂	0.39	0.39	0.30	0.34	0.37	0.38	0.38	0.24	0.24	0.21	0.21	0.21
Al ₂ O ₃	1.60	1.50	2.04	2.07	1.20	1.47	1.46	1.22	1.22	0.97	0.91	0.74
Cr ₂ O ₃	0.02	0.02	0.00	0.00	0.02	0.00	0.00	0.05	0.05	0.06	0.03	0.03
Fe ₂ O ₃	1.81	1.58	2.31	1.82	1.20	1.66	1.27	1.41	1.41	1.13	1.02	0.28
FeO	13.85	14.08	13.57	13.92	13.84	13.80	13.47	15.39	15.39	15.29	15.31	15.68
MnO	0.45	0.50	0.39	0.35	0.52	0.44	0.45	0.37	0.37	0.40	0.36	0.38
MgO	26.94	27.00	26.91	26.81	27.28	27.18	27.52	26.27	26.27	26.49	26.52	26.75
CaO	1.71	1.78	1.52	1.50	1.59	1.57	1.58	1.45	1.45	1.41	1.45	1.44
Na ₂ O	0.04	0.01	0.04	0.03	0.03	0.04	0.02	0.01	0.01	0.05	0.02	0.00
TOTAL	100.60	100.56	100.46	100.22	100.17	100.43	100.33	100.09	100.09	100.06	99.94	100.18
Fe=FeO	15.49	15.51	15.65	15.56	14.92	15.29	14.61	16.65	16.65	16.31	16.22	15.93
Mg#	76	76	75	75	77	76	77	74	74	74	74	75

Sample	VF10-03M2	VF10-03M2	VF10-03M2	VF10-03M2	VF10-03M2	VF10-03M2	VF10-03M2	VF10-03M2	VF10-03M2	VF10-03M2	VF10-03M2	VF10-03M2
Figure	opx 1	opx 1	opx 1	opx 1	opx 1	opx 1	opx 1	opx 1	opx 1	opx 1	opx 1	opx 1
Unit	2.26a	2.26a	2.26a	2.26a	2.26a	2.26a	2.26a	2.26a	2.26a	2.26a	2.26a	2.26a
Ages	L	L	L	L	L	L	L	L	L	L	L	L
	7500	7500	7500	7500	7500	7500	7500	7500	7500	7500	7500	7500
SiO ₂	54.04	53.72	53.59	53.40	53.19	53.58	53.61	53.88	53.88	53.81	52.74	53.80
TiO ₂	0.22	0.26	0.28	0.30	0.29	0.31	0.28	0.16	0.16	0.15	0.20	0.12
Al ₂ O ₃	1.01	1.26	1.35	1.59	1.33	1.25	1.12	2.62	2.62	2.53	3.63	1.50
Cr ₂ O ₃	0.06	0.03	0.06	0.02	0.01	0.02	0.03	0.08	0.08	0.09	0.04	0.01
Fe ₂ O ₃	1.11	1.46	1.47	1.23	1.57	0.81	1.03	1.85	1.85	1.68	1.89	1.03
FeO	14.95	14.74	14.85	15.57	15.43	16.15	15.97	10.51	10.51	10.94	11.88	14.91
MnO	0.37	0.38	0.35	0.41	0.48	0.48	0.42	0.27	0.27	0.23	0.25	0.40
MgO	26.68	26.66	26.48	25.95	25.90	25.75	25.89	29.08	29.08	29.05	27.71	26.78
CaO	1.41	1.43	1.41	1.40	1.48	1.27	1.34	1.41	1.41	1.16	1.32	1.08
Na ₂ O	0.02	0.02	0.03	0.02	0.03	0.03	0.01	0.03	0.03	0.01	0.01	0.00
TOTAL	99.88	99.95	99.87	99.89	99.71	99.66	99.71	99.90	99.90	99.64	99.67	99.63
Fe=FeO	15.95	16.05	16.18	16.68	16.84	16.88	16.89	12.17	12.17	12.45	13.58	15.83
Mg#	75	75	74	73	73	73	73	81	81	81	78	75

Sample	VF10-03M2	VF10-03M2	VF10-03M2	VF10-03M2	VF10-03M2	VF10-03M2	VF10-03M2	VF10-03M2	VF10-03M2
Figure	opx 1	opx 3	opx 3	opx 3	opx 3	opx 3	opx 3	opx 3	opx 3
Unit	2.26a	2.26b	2.26b	2.26b	2.26b	2.26b	2.26b	2.26b	2.26b
Ages	L	L	L	L	L	L	L	L	L
Ages	7500	7500	7500	7500	7500	7500	7500	7500	7500
SiO ₂	53.83	55.37	54.14	54.86	54.57	53.78	52.81	53.72	54.05
TiO ₂	0.15	0.10	0.13	0.10	0.12	0.15	0.21	0.10	0.14
Al ₂ O ₃	1.26	1.26	2.12	1.65	1.55	1.37	1.78	1.04	0.81
Cr ₂ O ₃	0.02	0.15	0.11	0.28	0.17	0.01	0.01	0.01	0.00
Fe ₂ O ₃	0.77	0.89	1.01	1.03	1.06	1.53	1.26	1.32	1.07
FeO	16.16	11.26	12.07	10.96	11.93	15.86	16.40	15.65	16.01
MnO	0.47	0.29	0.31	0.26	0.30	0.45	0.46	0.47	0.49
MgO	26.01	29.78	28.63	29.72	28.92	25.97	24.61	26.15	26.28
CaO	1.11	1.20	1.04	1.10	1.15	1.31	1.94	1.11	1.21
Na ₂ O	0.02	0.02	0.02	0.02	0.02	0.03	0.03	0.04	0.03
TOTAL	99.80	100.32	99.59	99.98	99.80	100.46	99.50	99.60	100.09
Fe=FeO	16.86	12.07	12.98	11.89	12.89	17.24	17.53	16.84	16.97
Mg#	73	81	80	82	80	73	71	73	73

Table 11 Hornblende

Sample	VF95-06Y hbd 1	VF95-06Y hbd 1	VF95-06Y hbd 2	VF95-06Y hbd 2	VF95-06Y hbd 4	VF95-06Y hbd 4	VF95-06Y hbd 5	VF95-06Y hbd 5	VF95-06Y hbd 6	VF95-06Y hbd 6
core/rim	core	core	core	core	core	core	core	core	core	core
Unit	Y	Y	Y	Y	Y	Y	Y	Y	Y	Y
Age	4400	4400	4400	4400	4400	4400	4400	4400	4400	4400
SiO ₂	41.46	43.38	43.44	42.72	43.73	43.15	42.38	43.53	42.83	42.17
TiO ₂	2.52	1.90	1.72	1.51	1.73	1.78	1.91	2.00	2.04	1.96
Al ₂ O ₃	11.17	10.90	11.57	11.14	12.98	12.69	11.74	11.96	11.36	11.34
Cr ₂ O ₃	0.01	0.05	0.00	0.00	0.13	0.23	0.04	0.00	0.06	0.13
Fe ₂ O ₃	5.91	5.90	6.70	7.51	5.26	6.23	7.05	4.96	5.56	6.37
FeO	7.83	7.30	6.43	5.70	4.43	3.37	5.67	7.46	7.12	6.22
MnO	0.26	0.32	0.27	0.22	0.07	0.18	0.20	0.18	0.18	0.24
MgO	13.50	14.27	14.69	14.71	16.03	16.34	14.78	14.37	14.29	14.42
CaO	11.17	11.33	11.31	11.07	11.40	11.45	11.14	11.32	11.02	11.03
Na ₂ O	2.55	2.40	2.52	2.40	2.62	2.67	2.58	2.63	2.59	2.51
K ₂ O	0.31	0.31	0.28	0.27	0.30	0.32	0.35	0.28	0.35	0.32
total	98.74	100.21	101.11	99.44	100.93	100.63	99.97	100.81	99.50	98.89
Fe=FeO	13.15	12.61	12.46	12.45	9.16	8.98	12.02	11.93	12.12	11.96

Sample core/rim	VF95-09X hbd 1	VF95-09X hbd 1	VF95-09X hbd 1	VF95-09X hbd 2	VF95-09X hbd 2	VF95-09X hbd 2	VF95-09X hbd 3	VF95-09X hbd 3	VF95-09X hbd 3	VF95-09X hbd 4
Unit	Y	Y	Y	Y	Y	Y	Y	Y	Y	Y
Age	4400	4400	4400	4400	4400	4400	4400	4400	4400	4400
SiO ₂	44.73	44.46	44.81	44.48	44.32	43.61	43.43	43.19	43.34	44.37
TiO ₂	1.93	2.01	1.98	1.61	2.19	1.91	1.86	1.82	1.94	1.87
Al ₂ O ₃	10.09	10.30	10.13	10.79	10.83	11.18	11.60	11.54	11.60	10.57
Cr ₂ O ₃	0.00	0.03	0.02	0.01	0.09	0.00	0.10	0.01	0.03	0.11
Fe ₂ O ₃	8.52	8.59	8.54	8.04	6.68	5.39	5.49	6.29	5.65	6.09
FeO	4.38	4.47	4.66	5.03	5.82	7.33	7.53	7.11	7.69	7.22
MnO	0.45	0.31	0.37	0.30	0.39	0.29	0.23	0.20	0.41	0.39
MgO	14.90	14.83	14.78	14.53	14.33	14.37	14.16	14.28	13.99	14.66
CaO	10.66	10.56	10.44	10.96	11.01	11.06	10.95	10.89	11.17	10.91
Na ₂ O	2.46	2.44	2.30	2.40	2.34	2.39	2.41	2.47	2.62	2.42
K ₂ O	0.33	0.33	0.36	0.32	0.33	0.35	0.29	0.31	0.30	0.35
total	100.64	100.43	100.58	100.62	100.53	100.05	100.15	100.28	100.87	101.11
Fe=FeO	12.05	12.19	12.35	12.26	11.83	12.18	12.47	12.78	12.77	12.70

Sample core/rim	VF95-09X hbd 4	VF95-09X hbd 4	VF95-09X hbd 5	VF95-09X hbd 5	VF95-09X hbd 5	VF97-06D hbd 1	VF97-06D hbd 1	VF97-06D hbd 1	VF97-06D hbd 2	VF97-06D hbd 2
Unit	Y	Y	Y	Y	Y	Y	Y	Y	Y	Y
Age	4400	4400	4400	4400	4400	4400	4400	4400	4400	4400
SiO ₂	43.98	44.10	40.78	42.96	41.68	42.77	42.37	41.90	42.28	40.84
TiO ₂	1.91	1.78	3.48	3.38	3.28	2.02	2.05	2.18	2.05	2.09
Al ₂ O ₃	10.19	10.31	11.14	11.34	11.25	12.74	12.27	12.20	11.95	12.05
Cr ₂ O ₃	0.00	0.13	0.00	0.07	0.00	0.17	0.05	0.11	0.09	0.00
Fe ₂ O ₃	5.98	5.99	4.93	5.70	4.46	4.69	4.07	4.15	4.38	5.37
FeO	6.89	6.67	7.33	6.12	7.60	5.51	5.95	6.22	7.00	6.80
MnO	0.35	0.27	0.10	0.22	0.11	0.22	0.14	0.15	0.24	0.15
MgO	14.73	14.90	14.06	14.32	14.21	15.12	15.46	15.19	14.81	14.54
CaO	10.76	10.93	11.27	11.06	11.43	11.41	11.32	11.47	11.20	11.27
Na ₂ O	2.28	2.34	2.57	2.47	2.57	2.69	2.69	2.73	2.60	2.68
K ₂ O	0.31	0.30	0.38	0.31	0.33	0.35	0.35	0.36	0.31	0.35
total	99.50	99.86	98.13	100.04	98.98	99.83	98.85	98.74	98.94	98.16
Fe=FeO	12.26	12.06	11.76	11.25	11.61	9.73	9.61	9.96	10.94	11.63

Sample core/rim	VF97-06D hbd 3	VF97-06D hbd 4	VF97-06D hbd 4	VF97-06D hbd 4	VF97-06D hbd 5	VF97-06D hbd 5	VF95-06Y hbd 1	VF95-06Y hbd 1	VF95-06Y hbd 1	VF95-06Y hbd 1
Unit	core	core	core	core	core	core	rim	rim	rim	rim
Age	Y	Y	Y	Y	Y	Y	Y	Y	Y	Y
	4400	4400	4400	4400	4400	4400	4400	4400	4400	4400
SiO ₂	43.18	43.50	43.30	43.38	43.07	43.25	41.82	42.66	43.72	43.74
TiO ₂	1.65	1.94	1.86	1.97	2.15	2.02	2.13	2.29	1.89	1.84
Al ₂ O ₃	12.56	11.55	11.49	11.60	11.65	11.73	10.85	11.01	10.69	10.52
Cr ₂ O ₃	0.00	0.05	0.03	0.00	0.04	0.00	0.05	0.00	0.02	0.00
Fe ₂ O ₃	4.40	4.53	4.13	4.36	4.07	4.28	6.85	6.32	6.71	5.27
FeO	6.65	7.94	7.85	8.24	8.09	7.84	6.18	6.86	6.60	7.42
MnO	0.19	0.18	0.30	0.24	0.20	0.28	0.30	0.27	0.37	0.21
MgO	15.21	14.82	14.64	14.54	14.57	14.69	14.34	14.41	14.72	14.45
CaO	11.26	11.32	11.23	11.16	11.13	11.25	10.96	11.12	11.03	11.17
Na ₂ O	2.65	2.60	2.66	2.53	2.61	2.51	2.48	2.48	2.27	2.48
K ₂ O	0.34	0.37	0.32	0.35	0.33	0.32	0.30	0.29	0.30	0.33
total	100.17	100.93	99.96	100.46	99.99	100.30	98.40	99.80	100.45	99.53
Fe=FeO	10.61	12.02	11.57	12.17	11.76	11.70	12.35	12.54	12.64	12.16

Sample core/rim	VF95-06Y hbd 2	VF95-06Y hbd 2	VF95-06Y hbd 2	VF95-06Y hbd 2	VF95-06Y hbd 4	VF95-06Y hbd 4	VF95-06Y hbd 4	VF95-06Y hbd 4	VF95-06Y hbd 4	VF95-06Y hbd 5
Unit	rim	rim	rim	rim	rim	rim	rim	rim	rim	rim
Age	Y	Y	Y	Y	Y	Y	Y	Y	Y	Y
	4400	4400	4400	4400	4400	4400	4400	4400	4400	4400
SiO ₂	44.32	43.16	43.36	43.97	44.02	43.22	42.77	43.85	43.39	43.21
TiO ₂	1.81	1.63	1.83	1.83	1.81	1.50	1.79	1.73	1.82	1.85
Al ₂ O ₃	11.69	11.13	11.24	11.56	12.54	12.25	11.84	11.74	11.62	11.51
Cr ₂ O ₃	0.00	0.00	0.00	0.00	0.00	0.05	0.00	0.00	0.00	0.00
Fe ₂ O ₃	4.96	6.59	5.26	5.47	5.59	6.54	5.80	7.65	5.47	6.10
FeO	7.12	6.48	7.28	7.07	6.53	4.73	6.82	5.05	6.82	6.83
MnO	0.23	0.11	0.07	0.18	0.28	0.16	0.32	0.24	0.12	0.26
MgO	14.76	14.59	14.39	14.66	14.86	15.47	14.18	14.33	14.61	14.43
CaO	11.26	11.08	11.20	10.99	11.02	11.37	10.93	10.90	11.04	11.04
Na ₂ O	2.49	2.37	2.44	2.49	2.50	2.38	2.49	2.45	2.56	2.48
K ₂ O	0.27	0.25	0.32	0.28	0.31	0.29	0.30	0.31	0.34	0.30
total	101.05	99.47	99.53	100.60	101.63	100.07	99.35	100.38	99.90	100.14
Fe=FeO	11.58	12.41	12.01	11.99	11.56	10.61	12.04	11.93	11.74	12.32

Sample core/rim	VF95-06Y hbd 5	VF95-06Y hbd 5	VF95-06Y hbd 5	VF95-06Y hbd 5	VF95-06Y hbd 6	VF95-06Y hbd 6	VF95-06Y hbd 6	VF95-09X hbd 1	VF95-09X hbd 1	VF95-09X hbd 1
Unit	Y	Y	Y	Y	Y	Y	Y	Y	Y	Y
Age	4400	4400	4400	4400	4400	4400	4400	4400	4400	4400
SiO ₂	43.56	43.27	43.75	43.25	44.10	42.34	43.64	43.69	44.73	43.22
TiO ₂	1.78	1.95	1.76	1.88	1.89	1.86	1.87	1.68	2.14	1.96
Al ₂ O ₃	11.37	12.19	11.40	11.29	11.55	11.45	11.62	11.05	10.29	10.77
Cr ₂ O ₃	0.02	0.04	0.00	0.00	0.11	0.11	0.03	0.03	0.03	0.00
Fe ₂ O ₃	5.77	5.59	6.15	5.87	7.91	6.88	5.25	6.00	7.12	6.51
FeO	7.27	6.95	7.14	7.16	4.89	6.17	7.43	6.66	5.63	6.22
MnO	0.39	0.11	0.18	0.08	0.21	0.17	0.16	0.14	0.33	0.22
MgO	14.25	14.55	14.46	14.39	14.45	14.47	14.39	14.72	14.59	14.85
CaO	11.22	11.50	10.52	10.92	10.76	10.91	11.28	11.10	10.90	10.88
Na ₂ O	2.48	2.59	2.46	2.44	2.62	2.43	2.48	2.27	2.23	2.35
K ₂ O	0.31	0.32	0.28	0.30	0.27	0.34	0.33	0.32	0.36	0.31
total	100.60	101.27	100.20	99.68	100.92	99.22	100.61	99.83	100.53	99.51
Fe=FeO	12.47	11.98	12.67	12.44	12.02	12.36	12.15	12.06	12.04	12.08

Sample core/rim	VF95-09X hbd 2	VF95-09X hbd 2	VF95-09X hbd 2	VF95-09X hbd 3	VF95-09X hbd 2	VF95-09X hbd 3	VF95-09X hbd 3	VF95-09X hbd 4	VF95-09X hbd 4	VF95-09X hbd 4
Unit	Y	Y	Y	Y	Y	Y	Y	Y	Y	Y
Age	4400	4400	4400	4400	4400	4400	4400	4400	4400	4400
SiO ₂	43.38	43.63	42.75	43.83	43.99	44.35	44.24	43.08	43.27	45.78
TiO ₂	1.80	1.84	1.75	1.96	2.03	1.96	1.93	1.97	1.88	1.63
Al ₂ O ₃	11.51	11.24	11.35	10.76	10.62	10.65	10.33	10.92	10.50	9.21
Cr ₂ O ₃	0.04	0.10	0.00	0.02	0.00	0.08	0.00	0.02	0.00	0.05
Fe ₂ O ₃	6.13	5.76	6.63	7.78	6.91	6.75	5.42	5.81	6.05	7.10
FeO	6.17	6.93	6.27	5.05	5.58	6.34	7.17	6.79	6.83	5.51
MnO	0.28	0.15	0.22	0.18	0.31	0.21	0.28	0.40	0.33	0.32
MgO	14.84	14.61	14.53	14.39	14.23	14.04	14.76	14.39	14.45	14.82
CaO	11.14	11.31	11.07	10.62	10.78	10.98	10.94	11.06	10.73	10.71
Na ₂ O	2.44	2.26	2.40	2.45	2.38	2.39	2.33	2.26	2.25	2.10
K ₂ O	0.30	0.28	0.31	0.29	0.33	0.34	0.31	0.33	0.32	0.31
total	100.25	100.26	99.33	99.43	99.31	100.31	99.83	99.12	98.80	99.79
Fe=FeO	11.69	12.12	12.23	12.05	11.80	12.41	12.04	12.02	12.27	11.90

Sample core/rim	VF95-09X hbd 5	VF95-09X hbd 5	VF95-09X hbd 5	VF97-06D hbd 1	VF97-06D hbd 1	VF97-06D hbd 1	VF97-06D hbd 2	VF97-06D hbd 2	VF97-06D hbd 3	VF97-06D hbd 4
Unit	rim	rim	rim	rim	rim	rim	rim	rim	rim	rim
Age	Y	Y	Y	Y	Y	Y	Y	Y	Y	Y
Age	4400	4400	4400	4400	4400	4400	4400	4400	4400	4400
SiO ₂	43.27	45.69	44.06	43.78	42.11	42.93	43.12	43.44	44.50	43.08
TiO ₂	1.77	1.55	1.86	1.98	1.88	1.91	1.90	1.99	1.62	1.84
Al ₂ O ₃	10.16	9.54	10.19	11.41	11.34	11.31	11.37	11.17	11.86	11.62
Cr ₂ O ₃	0.00	0.00	0.00	0.00	0.07	0.03	0.00	0.06	0.02	0.06
Fe ₂ O ₃	6.90	7.24	5.47	4.71	5.01	4.44	4.23	3.61	4.84	4.00
FeO	5.53	4.87	6.91	7.78	7.70	8.45	8.51	8.77	5.75	8.66
MnO	0.41	0.41	0.33	0.22	0.30	0.24	0.15	0.24	0.17	0.19
MgO	15.10	15.18	14.77	14.20	14.34	14.27	14.29	14.21	15.53	14.10
CaO	10.91	11.07	10.88	11.19	11.13	11.37	11.13	11.28	11.31	11.14
Na ₂ O	2.34	2.17	2.40	2.56	2.53	2.61	2.49	2.51	2.50	2.52
K ₂ O	0.31	0.28	0.30	0.32	0.31	0.39	0.32	0.31	0.28	0.35
total	98.87	100.24	99.27	100.25	98.88	100.03	99.69	99.70	100.48	99.64
Fe=FeO	11.74	11.39	11.84	12.02	12.21	12.44	12.32	12.02	10.10	12.26

Sample core/rim	VF97-06D hbd 4	VF97-06D hbd 4	VF97-06D hbd 5	VF97-06D hbd 5	VF97-06D hbd 5	VF99-05W hbd 2	VF99-05W hbd 2	VF99-05W hbd 3	VF99-05W hbd 3	VF99-05W hbd 5
Unit	rim	rim	rim	rim	rim	core	core	core	core	core
Age	Y	Y	Y	Y	Y	W	W	W	W	W
Age	4400	4400	4400	4400	4400	4500	4500	4500	4500	4500
SiO ₂	43.32	43.53	43.05	43.55	44.01	42.25	42.36	42.23	41.77	42.67
TiO ₂	1.77	1.90	1.28	1.72	1.61	2.93	3.00	2.71	2.87	2.87
Al ₂ O ₃	11.70	11.87	12.28	12.21	10.83	11.63	11.39	12.74	12.82	11.68
Cr ₂ O ₃	0.00	0.04	0.00	0.00	0.00	0.13	0.15	0.11	0.08	0.13
Fe ₂ O ₃	3.78	3.91	4.92	4.70	4.25	4.68	4.36	4.34	4.49	4.48
FeO	8.42	8.45	6.80	6.29	7.50	7.45	7.46	6.52	6.45	7.04
MnO	0.18	0.22	0.20	0.25	0.18	0.13	0.08	0.06	0.16	0.20
MgO	14.30	14.38	14.98	14.85	15.10	14.10	14.20	14.38	14.37	14.38
CaO	11.33	11.26	11.23	11.31	11.00	10.93	11.06	10.96	11.02	10.99
Na ₂ O	2.57	2.50	2.68	2.55	2.53	2.84	2.82	2.98	2.88	2.85
K ₂ O	0.31	0.29	0.29	0.29	0.27	0.38	0.36	0.36	0.41	0.35
total	99.87	100.60	99.85	99.84	99.35	99.61	99.31	99.56	99.38	99.80
Fe=FeO	11.82	11.97	11.23	10.52	11.33	11.66	11.39	10.42	10.49	11.07

Sample	VF99-05W hbd	VF98-02W hbd	VF98-02W hbd	VF98-02W hbd	VF98-02W hbd	VF98-02W hbd	VF98-02W hbd	VF99-05W hbd	VF99-05W hbd	VF99-05W hbd
core/rim	5	1	1	2	2	3	3	2	2	3
Unit	core	core	core	core	core	core	core	rim	rim	rim
Age	W	W	W	W	W	W	W	W	W	W
Age	4500	4500	4500	4500	4500	4500	4500	4500	4500	4500
SiO ₂	42.68	42.73	43.36	42.50	42.66	43.67	44.00	43.08	42.51	42.35
TiO ₂	3.00	1.79	1.74	2.47	2.54	1.84	1.63	2.38	2.54	3.12
Al ₂ O ₃	11.46	12.65	12.41	11.78	11.86	12.38	10.60	11.74	11.46	12.47
Cr ₂ O ₃	0.20	0.10	0.08	0.06	0.02	0.01	0.00	0.43	0.57	0.22
Fe ₂ O ₃	3.92	5.22	5.43	3.96	4.89	5.19	4.61	4.23	4.19	4.03
FeO	7.53	4.41	4.67	8.04	6.74	4.31	8.90	6.23	6.92	7.61
MnO	0.15	0.06	0.16	0.20	0.13	0.16	0.31	0.13	0.16	0.11
MgO	14.18	15.55	15.68	14.49	14.62	16.11	14.26	14.91	14.37	13.97
CaO	11.14	10.82	11.05	11.10	11.12	11.27	10.73	11.26	11.19	11.00
Na ₂ O	2.80	2.76	2.77	2.71	2.77	2.73	2.24	2.71	2.72	2.87
K ₂ O	0.36	0.29	0.29	0.37	0.33	0.26	0.46	0.36	0.32	0.39
total	99.56	98.45	99.72	99.82	99.81	100.09	99.94	99.57	99.03	100.24
Fe=FeO	11.06	9.11	9.56	11.60	11.14	8.98	13.05	10.03	10.70	11.23

Sample	VF99-05W hbd	VF99-05W hbd	VF99-05W hbd	VF98-02W hbd	VF98-02W hbd	VF98-02W hbd	VF98-02W hbd	VF98-02W hbd	VF98-02W hbd	VF98-02U hbd 1
core/rim	3	5	5	1	1	2	2	3	3	VF98-02U hbd 1
Unit	rim	rim	rim	rim	rim	rim	rim	rim	rim	core
Age	W	W	W	W	W	W	W	W	W	U
Age	4500	4500	4500	4500	4500	4500	4500	4500	4500	4700
SiO ₂	42.07	42.42	43.14	42.56	43.09	43.12	43.27	42.88	43.20	42.58
TiO ₂	2.94	2.65	2.09	1.71	1.73	1.88	1.82	1.53	1.74	3.01
Al ₂ O ₃	12.65	11.85	12.66	12.43	12.74	11.84	11.76	12.52	12.48	12.50
Cr ₂ O ₃	0.13	0.31	0.53	0.13	0.08	0.04	0.04	0.05	0.21	0.24
Fe ₂ O ₃	4.44	4.50	3.89	4.00	4.12	5.25	4.50	4.94	3.90	4.17
FeO	7.02	6.23	5.26	5.36	5.14	5.68	6.54	5.04	5.54	6.98
MnO	0.15	0.19	0.18	0.12	0.21	0.10	0.18	0.14	0.15	0.17
MgO	14.30	14.82	15.35	15.70	15.98	15.17	15.43	15.24	15.85	14.43
CaO	11.25	11.25	11.60	11.15	11.22	11.05	11.32	11.26	11.48	11.18
Na ₂ O	2.82	2.76	2.68	2.74	2.62	2.66	2.56	2.75	2.67	2.85
K ₂ O	0.41	0.34	0.36	0.29	0.28	0.35	0.36	0.31	0.27	0.36
total	100.25	99.45	99.92	98.31	99.38	99.32	99.91	98.76	99.67	100.55
Fe=FeO	11.01	10.27	8.76	8.95	8.84	10.40	10.59	9.49	9.05	10.73

Sample core/rim	VF98-02U hbd 1	VF98-02U hbd 4	VF98-02U hbd 4	VF98-02U hbd 6	VF98-02U hbd 6	VF97-06B hbd 1	VF97-06B hbd 1	VF97-06B hbd 2	VF97-06B hbd 2	VF97-06B hbd 3
core	core	core	core	core	core	core	core	core	core	core
Unit	U	U	U	U	U	U	U	U	U	U
Age	4700	4700	4700	4700	4700	4700	4700	4700	4700	4700
SiO ₂	43.11	43.92	42.45	40.83	40.80	41.79	42.18	42.58	42.56	41.96
TiO ₂	2.83	1.92	1.97	2.12	2.20	2.56	2.73	2.57	2.75	2.78
Al ₂ O ₃	12.24	13.24	13.45	12.64	12.37	11.98	11.63	11.50	11.62	12.58
Cr ₂ O ₃	0.09	0.21	0.03	0.10	0.13	0.01	0.06	0.00	0.05	0.30
Fe ₂ O ₃	4.64	5.06	4.87	3.67	5.19	5.33	4.81	4.96	5.05	4.64
FeO	7.02	5.16	5.22	6.02	4.80	6.20	7.15	7.50	7.59	6.03
MnO	0.25	0.30	0.13	0.21	0.12	0.10	0.18	0.15	0.20	0.15
MgO	14.56	15.47	15.90	15.84	15.66	14.53	14.28	14.24	14.19	14.81
CaO	11.21	11.15	11.38	10.67	11.10	10.61	10.97	11.21	10.96	11.13
Na ₂ O	2.87	2.82	2.78	2.83	2.77	2.73	2.60	2.78	2.60	2.71
K ₂ O	0.40	0.31	0.26	0.32	0.33	0.32	0.34	0.33	0.34	0.32
total	101.37	101.80	100.69	97.28	97.58	98.32	99.00	99.89	100.01	99.64
Fe=FeO	11.20	9.72	9.60	9.32	9.47	10.99	11.47	11.96	12.13	10.21

Sample core/rim	VF97-06B hbd 3	VF98-02U hbd 1	VF98-02U hbd 1	VF98-02U hbd 4	VF98-02U hbd 4	VF98-02U hbd 6	VF98-02U hbd 6	VF97-06B hbd 1	VF97-06B hbd 1	VF97-06B hbd 2
core	rim	rim	rim	rim	rim	rim	rim	rim	rim	rim
Unit	U	U	U	U	U	U	U	U	U	U
Age	4700	4700	4700	4700	4700	4700	4700	4700	4700	4700
SiO ₂	41.08	43.39	43.31	42.79	43.08	39.86	41.04	42.13	40.18	41.09
TiO ₂	2.77	2.47	2.42	2.25	1.81	2.22	2.11	2.78	2.85	2.95
Al ₂ O ₃	12.30	12.71	12.40	12.87	12.54	13.13	12.80	11.52	12.36	12.48
Cr ₂ O ₃	0.10	0.23	0.62	0.07	0.34	0.26	0.18	0.10	0.48	0.17
Fe ₂ O ₃	4.13	4.25	4.70	4.93	5.04	4.53	5.18	4.48	5.79	4.00
FeO	7.00	5.52	5.84	4.76	5.74	5.46	4.40	6.95	5.05	7.13
MnO	0.12	0.16	0.04	0.14	0.14	0.17	0.12	0.06	0.07	0.16
MgO	14.68	15.58	15.33	15.56	15.01	15.43	15.94	14.45	14.49	14.63
CaO	11.18	11.59	11.35	11.22	11.20	11.28	11.49	11.12	11.36	11.10
Na ₂ O	2.78	2.56	2.76	3.00	2.78	2.82	2.79	2.68	0.25	2.78
K ₂ O	0.39	0.33	0.34	0.23	0.28	0.38	0.34	0.32	0.37	0.39
total	98.63	100.94	101.32	100.04	100.10	97.58	98.50	98.62	95.37	98.92
Fe=FeO	10.72	9.35	10.07	9.20	10.28	9.54	9.06	10.98	10.27	10.72

Sample core/rim	VF97-06B hbd 2	VF97-06B hbd 3	VF97-06B hbd 3	VF95-09T hbd 1	VF95-09T hbd 1	VF95-09T hbd 2	VF95-09T hbd 2	VF95-09T hbd 3	VF95-09T hbd 3	VF95-09T hbd 1
Unit	U	U	U	S	S	S	S	S	S	S
Age	4700	4700	4700	5500	5500	5500	5500	5500	5500	5500
SiO ₂	41.96	42.54	42.07	43.88	43.89	44.26	44.35	42.26	42.93	43.51
TiO ₂	2.86	2.75	2.84	1.30	1.42	1.12	1.33	1.92	1.90	3.13
Al ₂ O ₃	12.24	12.45	12.61	11.92	11.79	11.16	11.47	12.37	11.77	11.00
Cr ₂ O ₃	0.16	0.04	0.68	0.04	0.06	1.09	0.26	0.17	0.04	0.02
Fe ₂ O ₃	4.63	4.66	4.09	9.48	9.18	8.04	8.77	10.40	10.47	11.75
FeO	5.94	6.34	6.28	0.13	0.12	0.12	0.12	0.14	0.14	0.17
MnO	0.05	0.18	0.10	16.37	16.68	17.34	17.03	15.47	15.68	13.76
MgO	14.95	14.84	14.80	11.07	11.00	10.99	10.93	10.92	10.96	10.50
CaO	11.14	11.26	11.54	0.04	0.03	0.09	0.08	0.02	0.05	0.01
Na ₂ O	2.73	2.75	2.71	2.77	2.76	2.65	2.59	2.68	2.63	2.75
K ₂ O	0.36	0.32	0.38	0.26	0.26	0.26	0.23	0.30	0.27	0.44
total	99.14	100.38	100.24	97.27	97.24	97.12	97.22	96.76	97.00	97.15
Fe=FeO	10.11	10.53	9.96	-	-	-	-	-	-	-

Sample core/rim	VF95-09T hbd 1	VF95-09T hbd 2	VF95-09T hbd 2	VF95-09T hbd 3	VF95-09T hbd 3	VF95-09T hbd 3	VF10-03M2 hbd 1	VF10-03M2 hbd 1	VF10-03M2 hbd 2	VF10-03M2 hbd 2
Unit	S	S	S	S	S	S	L	L	L	L
Age	5500	5500	5500	5500	5500	5500	7500	7500	7500	7500
SiO ₂	43.09	42.91	44.31	42.44	42.54	42.54	43.99	43.68	44.28	44.32
TiO ₂	2.57	2.69	2.88	3.11	3.22	3.21	1.89	2.00	2.78	2.75
Al ₂ O ₃	11.50	11.21	11.43	10.92	10.68	10.81	11.39	11.37	9.68	9.54
Cr ₂ O ₃	0.10	0.00	0.24	0.10	0.05	0.04	0.10	0.15	0.00	0.01
Fe ₂ O ₃	10.74	11.26	10.96	11.30	11.80	11.63	3.93	3.85	4.66	4.33
FeO	0.12	0.15	0.15	0.15	0.16	0.16	6.91	7.04	7.44	7.66
MnO	15.10	14.86	14.67	14.46	14.31	14.35	0.12	0.12	0.23	0.22
MgO	10.97	11.05	10.92	11.09	10.83	10.91	15.51	15.34	15.08	14.97
CaO	0.03	0.04	0.06	0.04	0.08	0.01	11.35	11.28	11.19	11.34
Na ₂ O	2.67	2.67	2.64	2.65	2.72	2.70	2.40	2.38	2.33	2.28
K ₂ O	0.36	0.34	0.39	0.37	0.36	0.36	0.31	0.28	0.33	0.39
total	97.33	97.34	98.75	96.78	96.85	96.90	100.04	99.62	100.11	99.91
Fe=FeO	-	-	-	-	-	-	10.44	10.51	11.63	11.55

Sample core/rim	VF95-09E hbd 1	VF95-09E hbd 1	VF95-09E hbd 3	VF10-03M2 hbd 1	VF10-03M2 hbd 1	VF10-03M2 hbd 1	VF10-03M2 hbd 1	VF10-03M2 hbd 2	VF95-09E hbd 2
Unit	L	L	L	rim	rim	rim	rim	rim	rim
Age	7500	7500	7500	7500	7500	7500	7500	7500	7500
SiO ₂	44.30	44.32	43.10	43.77	43.93	44.05	44.17	43.67	43.72
TiO ₂	1.89	1.94	2.12	1.88	1.85	1.86	1.82	2.18	2.26
Al ₂ O ₃	10.48	10.43	10.82	10.90	10.73	10.67	10.74	10.68	11.05
Cr ₂ O ₃	0.08	0.10	0.00	0.02	0.04	0.03	0.08	0.08	0.08
Fe ₂ O ₃	4.49	4.37	4.53	3.96	4.12	4.33	4.10	3.89	3.85
FeO	7.96	7.86	8.37	8.06	8.26	7.80	8.39	8.26	7.39
MnO	0.14	0.14	0.16	0.15	0.15	0.20	0.18	0.14	0.14
MgO	15.16	15.24	14.50	14.77	14.72	15.05	14.73	14.80	15.31
CaO	11.22	11.28	10.93	11.13	11.14	11.22	11.09	11.20	11.35
Na ₂ O	2.44	2.51	2.49	2.35	2.28	2.36	2.35	2.55	2.59
K ₂ O	0.27	0.29	0.32	0.31	0.26	0.28	0.31	0.31	0.30
total	100.56	100.62	99.45	99.38	99.60	99.95	100.04	99.82	100.20
Fe=FeO	12.00	11.79	12.44	11.63	11.97	11.70	12.08	11.76	10.86

Sample core/rim	VF95-09E hbd 2	VF95-09E hbd 2	VF95-01F hbd 1	VF95-01F hbd 1	VF95-01F hbd 2	VF95-01F hbd 2	VF94-06E hbd 1	VF94-06E hbd 1	VF94-06E hbd 2	VF94-06E hbd 2
Unit	L	L	core	core	core	core	core	core	core	core
Age	7500	7500	10000	10000	10000	10000	10000	10000	10000	10000
SiO ₂	44.11	43.64	42.31	42.40	43.65	42.96	42.02	42.35	42.42	42.56
TiO ₂	2.12	2.09	3.74	3.68	2.08	2.59	2.54	2.68	2.42	2.19
Al ₂ O ₃	10.85	10.84	10.79	10.94	10.37	11.20	11.49	11.66	11.57	11.61
Cr ₂ O ₃	0.04	0.15	0.02	0.02	0.03	0.00	0.00	0.00	0.06	0.05
Fe ₂ O ₃	3.86	4.30	-	-	-	-	-	-	-	-
FeO	7.04	7.29	-	-	-	-	-	-	-	-
MnO	0.15	0.14	0.17	0.16	0.20	0.22	0.17	0.21	0.10	0.12
MgO	15.60	15.32	14.10	14.31	14.29	14.31	13.59	13.87	15.62	15.61
CaO	11.27	11.29	11.05	11.11	11.01	11.05	11.05	11.09	11.51	11.46
Na ₂ O	2.43	2.58	2.78	2.79	2.52	2.72	2.66	2.69	2.49	2.52
K ₂ O	0.32	0.29	0.39	0.36	0.29	0.33	0.39	0.38	0.93	0.93
total	99.90	100.13	97.55	98.01	97.28	98.18	96.78	98.31	97.06	97.35
Fe=FeO	10.52	11.15	12.00	12.13	12.80	12.60	12.65	13.21	9.57	10.01

Sample core/rim	VF95-01F hbd 1 rim	VF95-01F hbd 1 rim	VF95-01F hbd 2 rim	VF95-01F hbd 2 rim	VF94-06E hbd 1 rim	VF94-06E hbd 1 rim	VF94-06E hbd 2 rim	VF94-06E hbd 2 rim	VF94-06E hbd 2 rim
Unit	H	H	H	H	H	H	H	H	H
Age	10000	10000	10000	10000	10000	10000	10000	10000	10000
SiO ₂	43.09	42.48	41.87	42.00	43.26	43.44	42.84	42.65	42.73
TiO ₂	3.11	3.34	4.00	3.73	2.23	2.05	2.45	2.60	2.53
Al ₂ O ₃	10.58	10.96	11.26	11.06	10.61	10.88	11.40	11.56	11.39
Cr ₂ O ₃	0.02	0.00	0.00	0.00	0.00	0.00	0.05	0.09	0.06
Fe ₂ O ₃	-	-	-	-	-	-	-	-	-
FeO	-	-	-	-	-	-	-	-	-
MnO	0.22	0.17	0.13	0.18	0.31	0.13	0.12	0.09	0.11
MgO	14.32	13.99	13.44	13.44	13.95	15.43	15.93	15.93	15.67
CaO	11.07	11.13	10.98	11.01	10.81	11.24	11.66	11.66	11.73
Na ₂ O	2.71	2.69	2.82	2.81	2.50	2.45	2.34	2.45	2.44
K ₂ O	0.35	0.31	0.36	0.38	0.42	0.82	1.20	1.10	1.11
total	97.69	97.21	97.41	97.30	97.23	97.46	97.42	97.57	97.41
Fe=FeO	12.09	12.02	12.39	12.62	12.95	10.68	9.16	9.20	9.35

Table 12 Olivine

Sample core/rim	VF97-06B ol 1 core	VF97-06B ol 1 core	VF97-06B ol 2 core	VF97-06B ol 2 core	VF97-06B ol 3 core	VF97-06B ol 3 core	VF98-02W ol 1 core	VF98-02W ol 1 core	VF98-02W ol 3 core	VF98-02W ol 3 core	VF99-05W ol 1 core	VF99-05W ol 1 core
Unit	W	W	W	W	W	W	W	W	W	W	W	W
Age	4500	4500	4500	4500	4500	4500	4500	4500	4500	4500	4500	4500
SiO ₂	39.27	39.15	39.41	39.39	38.87	39.24	39.37	39.67	39.39	39.37	38.74	38.73
TiO ₂	0.02	0.01	0.04	0.00	0.05	0.01	0.00	0.00	0.02	0.07	0.02	0.04
Al ₂ O ₃	0.02	0.00	0.00	0.05	0.01	0.02	0.00	0.00	0.00	0.00	0.00	0.02
FeO	20.30	20.18	20.26	20.24	21.60	21.79	19.13	19.20	20.06	19.79	20.76	21.23
MnO	0.23	0.28	0.39	0.30	0.32	0.40	0.29	0.28	0.34	0.29	0.31	0.36
MgO	41.03	40.75	40.88	40.50	39.72	39.86	41.84	41.28	40.97	40.98	39.35	39.35
CaO	0.09	0.17	0.10	0.11	0.10	0.16	0.15	0.06	0.09	0.10	0.12	0.08
NiO	0.19	0.08	0.05	0.10	0.20	0.17	0.14	0.18	0.08	0.10	0.07	0.18
TOTAL	101.15	100.62	101.12	100.68	100.87	101.64	100.92	100.68	100.94	100.70	99.37	99.98
Mg#	78	78	78	78	77	77	80	79	78	79	77	77

Sample core/rim Unit Age	VF99-05W ol 2 core W 4500	VF99-05W ol 2 core W 4500	VF99-05W ol 3 core W 4500	VF99-05W ol 3 core W 4500	VF99-05W ol 5 core W 4500	VF97-06B ol 1 rim W 4500	VF97-06B ol 1 rim W 4500	VF97-06B ol 2 rim W 4500	VF97-06B ol 2 rim W 4500	VF97-06B ol 3 rim W 4500	VF97-06B ol 3 rim W 4500	VF98-02W ol 1 rim W 4500
SiO ₂	38.44	38.49	38.71	38.82	39.20	39.43	38.92	39.49	39.49	38.96	39.05	39.20
TiO ₂	0.01	0.02	0.03	0.00	0.00	0.03	0.06	0.06	0.07	0.04	0.01	0.00
Al ₂ O ₃	0.01	0.01	0.01	0.01	0.00	0.00	0.00	0.00	0.01	0.00	0.05	0.00
FeO	21.66	21.25	20.71	21.20	21.49	20.21	19.68	20.37	20.63	21.60	21.68	20.28
MnO	0.34	0.35	0.29	0.30	0.34	0.32	0.44	0.28	0.17	0.26	0.24	0.36
MgO	39.09	38.92	39.50	39.29	38.92	40.71	41.01	40.30	40.29	39.47	39.50	40.11
CaO	0.12	0.12	0.08	0.12	0.09	0.11	0.13	0.10	0.11	0.13	0.08	0.10
NiO	0.12	0.07	0.12	0.14	0.21	0.11	0.12	0.08	0.07	0.01	0.19	0.00
TOTAL	99.79	99.22	99.44	99.87	100.24	100.92	100.34	100.68	100.84	100.46	100.80	100.04
Mg#	76	77	77	77	76	78	79	78	78	77	76	78

Sample core/rim Unit Age	VF98-02W ol 1 rim W 4500	VF98-02W ol 3 rim W 4500	VF98-02W ol 3 rim W 4500	VF99-05W ol 1 rim W 4500	VF99-05W ol 1 rim W 4500	VF99-05W ol 2 rim W 4500	VF99-05W ol 2 rim W 4500	VF99-05W ol 3 rim W 4500	VF99-05W ol 3 rim W 4500	VF99-05W ol 3 core U 4700	VF99-05W ol 3 core U 4700	VF98-02U ol 1 core U 4700
SiO ₂	39.38	39.40	39.34	38.80	38.59	38.54	39.17	39.34	39.43	38.4251	38.4752	38.69
TiO ₂	0.01	0.05	0.06	0.03	0.02	0.00	0.00	0.01	0.00	0.0163	0.0035	0.05
Al ₂ O ₃	0.00	0.01	0.00	0.00	0.02	0.00	0.00	0.00	0.01	0.0167	0.0284	0.00
FeO	20.72	20.81	19.38	20.28	20.63	20.35	20.51	20.29	20.95	21.9188	21.8087	20.85
MnO	0.36	0.26	0.35	0.31	0.33	0.32	0.32	0.33	0.26	0.3472	0.3472	0.37
MgO	40.01	40.11	41.14	39.38	39.59	39.65	39.63	39.47	39.67	40.0502	40.1897	39.56
CaO	0.13	0.13	0.11	0.11	0.09	0.10	0.12	0.10	0.11	0.1103	0.1180	0.08
NiO	0.01	0.08	0.15	0.16	0.18	0.04	0.16	0.11	0.06	0.1347	0.1418	0.09
TOTAL	100.63	100.85	100.52	99.06	99.44	99.00	99.91	99.66	100.48	101.0193	101.1124	99.69
Mg#	77	77	79	78	77	78	78	78	77	77	77	77

Sample core/rim	VF98-02U ol 1 core Unit Age	VF98-02U ol 3 core Unit Age	VF98-02U ol 3 core Unit Age	VF98-02U ol 3 core Unit Age	VF95-06U ol 1 core Unit Age	VF95-06U ol 1 core Unit Age	VF95-06U ol 2 core Unit Age	VF95-06U ol 2 core Unit Age	VF95-06U ol 2 core Unit Age	VF95-06U ol 3 core Unit Age	VF95-06U ol 3 core Unit Age	VF95-06U ol 3 core Unit Age
SiO ₂	38.70	39.84	39.89	40.00	38.17	38.62	37.56	37.59	37.18	37.95	38.20	37.73
TiO ₂	0.01	0.00	0.05	0.00	0.04	0.03	0.05	0.00	0.01	0.00	0.00	0.00
Al ₂ O ₃	0.00	0.00	0.00	0.00	0.00	0.00	0.01	0.00	0.00	0.03	0.00	0.01
FeO	20.80	21.42	20.76	21.33	21.15	21.16	24.88	24.99	24.86	20.45	20.64	20.68
MnO	0.37	0.38	0.35	0.21	0.34	0.34	0.37	0.54	0.49	0.24	0.25	0.33
MgO	39.31	40.03	39.97	40.41	39.55	39.60	35.99	36.60	36.42	40.11	39.71	40.11
CaO	0.12	0.20	0.12	0.16	0.10	0.13	0.12	0.12	0.14	0.12	0.12	0.11
NiO	0.15	0.11	0.21	0.25	0.16	0.11	0.08	0.06	0.07	0.17	0.10	0.06
TOTAL	99.46	101.98	101.35	102.36	99.51	99.99	99.06	99.90	99.17	99.06	99.02	99.02
Mg#	77	77	77	77	77	77	72	72	72	78	77	78

Sample core/rim	VF95-06U ol 4 core Unit Age	VF95-06U ol 4 core Unit Age	VF10-01U ol 1 rim Unit Age	VF10-01U ol 1 rim Unit Age	VF10-01U ol 1 rim Unit Age	VF10-01U ol 2 rim Unit Age	VF10-01U ol 2 rim Unit Age	VF10-01U ol 3 rim Unit Age	VF10-01U ol 3 rim Unit Age	VF10-01U ol 3 rim Unit Age	VF98-02U ol 1 rim Unit Age	VF98-02U ol 1 rim Unit Age
SiO ₂	37.77	38.00	37.9544	37.7141	52.1648	38.8557	38.3149	38.5553	38.5052	38.7656	38.73	38.95
TiO ₂	0.02	0.01	0.0228	0.0240	0.8744	0.0278	0.0310	0.0262	0.0195	0.0061	0.03	0.00
Al ₂ O ₃	0.00	0.02	0.0913	0.0618	14.6300	0.6320	0.1347	0.0630	0.0771	0.1092	0.01	0.02
FeO	20.43	20.12	24.3120	25.0229	8.0606	21.0777	21.1378	20.1365	20.7573	20.0664	20.97	20.73
MnO	0.36	0.33	0.4244	0.4339	0.1473	0.3422	0.3409	0.3246	0.3225	0.2863	0.35	0.29
MgO	40.55	40.37	37.4798	36.8322	7.1632	39.5122	39.3827	40.7974	40.4088	40.8372	39.26	39.02
CaO	0.12	0.11	0.1488	0.1682	3.8500	0.2323	0.2087	0.1534	0.1616	0.1669	0.12	0.13
NiO	0.07	0.11	0.1173	0.1066	0.0300	0.1190	0.0899	0.0999	0.1064	0.1321	0.13	0.18
TOTAL	99.32	99.06	100.5508	100.3637	86.9203	100.7989	99.6406	100.1563	100.3585	100.3698	99.60	99.32
Mg#	78	78	73	72	61	77	77	78	78	78	77	77

Sample core/rim	VF98-02U ol 3 rim U 4700	VF98-02U ol 3 rim U 4700	VF95-06U ol 1 rim U 4700	VF95-06U ol 1 rim U 4700	VF95-06U ol 1 rim U 4700	VF95-06U ol 3 rim U 4700	VF95-06U ol 3 rim U 4700	VF95-06U ol 3 rim U 4700	VF95-06U ol 3 rim U 4700	VF95-06U ol 4 rim U 4700	VF95-06U ol 4 rim U 4700	VF94-06E ol 1 core H 10000	VF94-06E ol 1 core H 10000
SiO ₂	39.80	40.00	38.75	38.66	38.73	38.45	38.79	38.63	37.80	37.59	40.42	40.17	
TiO ₂	0.00	0.00	0.00	0.04	0.04	0.02	0.02	0.03	0.01	0.06	0.00	0.01	
Al ₂ O ₃	0.01	0.00	0.02	0.01	0.00	0.00	0.02	0.00	0.00	0.02	0.01	0.02	
FeO	21.04	20.58	19.74	19.88	19.89	19.99	20.08	19.71	19.85	20.29	12.72	12.51	
MnO	0.36	0.33	0.33	0.37	0.33	0.36	0.37	0.36	0.38	0.32	0.22	0.17	
MgO	40.31	40.40	40.24	40.35	40.28	40.39	40.57	40.17	40.29	40.54	46.70	46.71	
CaO	0.11	0.12	0.12	0.13	0.13	0.12	0.14	0.12	0.14	0.13	0.15	0.15	
NiO	0.17	0.21	0.18	0.17	0.20	0.08	0.24	0.18	0.13	0.16	0.17	0.15	
TOTAL	101.78	101.64	99.39	99.61	99.60	99.42	100.22	99.18	98.59	99.10	100.39	99.88	
Mg#	77	78	78	78	78	78	78	78	78	78	87	87	

Sample core/rim	VF94-06E ol 2 core H 10000	VF94-06E ol 2 core H 10000	VF94-06E ol 3 core H 10000	VF94-06E ol 3 core H 10000	VF94-06E ol 3 core H 10000	VF94-06E ol 4 core H 10000	VF94-06E ol 4 core H 10000	VF94-06E ol 1 rim H 10000	VF94-06E ol 1 rim H 10000	VF94-06E ol 1 rim H 10000	VF94-06E ol 3 rim H 10000	VF94-06E ol 3 rim H 10000
SiO ₂	38.93	38.82	39.83	40.08	40.09	39.03	38.95	38.92	38.85	39.42	38.80	39.01
TiO ₂	0.01	0.02	0.01	0.00	0.01	0.01	0.02	0.03	0.01	0.02	0.03	0.02
Al ₂ O ₃	0.02	0.01	0.01	0.03	0.02	0.03	0.00	0.02	0.01	0.02	0.10	0.03
FeO	19.15	19.14	13.82	13.98	13.89	18.77	18.95	18.79	19.11	16.37	18.81	18.83
MnO	0.31	0.31	0.20	0.22	0.19	0.31	0.27	0.28	0.31	0.27	0.30	0.30
MgO	41.66	41.68	45.72	45.53	45.71	42.21	42.23	41.87	41.53	43.58	41.56	41.57
CaO	0.13	0.12	0.15	0.15	0.15	0.13	0.15	0.15	0.13	0.15	0.15	0.14
NiO	0.04	0.06	0.15	0.14	0.12	0.06	0.08	0.08	0.07	0.08	0.06	0.10
TOTAL	100.26	100.15	99.89	100.13	100.19	100.54	100.64	100.14	100.02	99.91	99.81	100.00
Mg#	80	80	86	85	85	80	80	80	79	83	80	80

Table 13 Glass

Sample	VF95-06Y	VF95-06Y	VF95-06Y	VF95-06Y	VF95-06Y	VF95-06Y	VF95-09X	VF95-09X	VF95-09X	VF95-09X	VF95-09X	VF95-09X
Unit	gls 1	gls 2	gls 3	gls 4	gls 5	gls 6	gls 1	gls 2	gls 3	gls 4	gls 5	gls 7
Age	Y	Y	Y	Y	Y	Y	Y	Y	Y	Y	Y	Y
Age	4400	4400	4400	4400	4400	4400	4400	4400	4400	4400	4400	4400
SiO ₂	63.96	64.82	65.13	66.00	65.89	64.43	67.53	64.87	68.09	70.04	68.56	63.82
TiO ₂	0.30	0.33	0.35	0.34	0.33	0.26	0.34	0.26	0.27	0.28	0.24	0.23
Al ₂ O ₃	19.35	16.74	16.83	19.14	16.49	18.22	17.34	16.33	16.58	16.24	16.53	16.01
FeO	3.48	4.45	4.95	3.65	4.97	4.37	3.27	3.59	2.89	2.58	2.97	2.85
MnO	0.12	0.09	0.20	0.08	0.23	0.00	0.19	0.13	0.10	0.17	0.16	0.13
MgO	1.09	1.62	1.73	0.97	1.65	1.27	1.24	1.08	1.08	0.93	1.12	0.91
CaO	5.40	4.54	3.94	5.08	3.70	5.08	3.97	3.25	3.25	2.96	3.53	2.79
Na ₂ O	5.47	4.17	4.35	5.49	4.17	4.87	3.02	3.74	4.03	4.46	4.10	3.70
K ₂ O	1.28	1.66	1.74	1.06	1.73	1.37	1.78	1.77	2.05	2.16	1.92	1.82
P ₂ O ₅	0.19	0.26	0.14	0.19	0.27	0.15	0.39	0.19	0.15	0.03	0.22	0.19
TOTAL	100.63	98.68	99.36	102.00	99.42	100.02	99.06	95.21	98.49	99.84	99.36	92.44

Sample	VF95-09X	VF97-06D	VF97-06D	VF97-06D	VF97-06D	VF97-06D	VF97-06D	VF97-06D	VF97-06D	VF97-06D	VF97-06D	VF97-06D
Unit	gls 8	gls 1	gls 2	gls 4	gls 5	gls 6	gls 7	gls 8	gls 9	gls 10	gls 11	gls 12
Age	Y	Y	Y	Y	Y	Y	Y	Y	Y	Y	Y	Y
Age	4400	4400	4400	4400	4400	4400	4400	4400	4400	4400	4400	4400
SiO ₂	73.65	67.44	63.79	64.94	63.77	62.33	62.08	66.09	72.81	62.39	73.99	72.74
TiO ₂	0.22	0.74	0.51	0.29	0.47	0.22	0.28	0.37	0.35	0.33	0.29	0.30
Al ₂ O ₃	14.71	14.13	17.84	20.02	17.12	21.96	19.88	17.69	13.91	20.03	14.37	13.81
FeO	1.70	6.34	3.86	2.37	3.95	2.21	2.94	2.56	1.27	3.55	1.59	1.38
MnO	0.14	0.11	0.03	0.03	0.12	0.07	0.03	0.07	0.05	0.01	0.00	0.00
MgO	0.47	2.04	1.24	0.64	1.29	0.53	0.82	0.33	0.22	0.96	0.23	0.19
CaO	1.76	2.65	4.52	5.04	4.61	6.14	5.80	4.10	0.85	5.97	0.73	0.74
Na ₂ O	3.68	4.39	6.64	8.31	7.48	8.85	7.02	6.84	3.61	7.38	4.52	3.63
K ₂ O	2.54	2.34	1.45	1.20	1.48	0.82	1.03	1.85	3.27	1.08	3.81	3.40
P ₂ O ₅	0.01	0.34	0.22	0.12	0.27	0.17	0.21	0.26	0.03	0.19	0.05	0.01
TOTAL	98.88	100.51	100.10	102.96	100.55	103.29	100.09	100.15	96.37	101.89	99.58	96.21

Sample	VF97-06D	VF97-06D	VF97-06D	VF97-06D	VF97-06D	VF97-06D	VF97-06D	VF97-06D	VF97-06D	VF97-05B	VF97-05B	VF97-05B	VF97-05B
	gls 13	gls 14	gls 15	gls 16	gls 17	gls 18	gls 19	gls 20	gls 1	gls 2	gls 3	gls 4	
	Y	Y	Y	Y	Y	Y	Y	Y	Y	Y	Y	Y	
Age	4400	4400	4400	4400	4400	4400	4400	4400	4400	4400	4400	4400	4400
SiO ₂	56.83	55.61	54.20	65.10	54.62	65.83	67.62	62.55	64.80	60.25	63.97	62.37	
TiO ₂	0.08	0.16	0.07	0.45	0.04	0.60	0.51	0.23	0.43	0.18	0.35	0.17	
Al ₂ O ₃	27.12	27.36	28.53	16.82	28.55	14.99	13.00	20.81	17.52	22.07	18.28	21.95	
FeO	0.44	0.53	0.77	4.02	0.69	5.79	5.34	2.28	4.14	1.86	3.49	1.81	
MnO	0.00	0.00	0.00	0.09	0.09	0.20	0.26	0.01	0.17	0.02	0.07	0.07	
MgO	0.03	0.05	0.05	1.46	0.06	1.93	1.93	0.72	1.22	0.50	1.28	0.54	
CaO	9.53	9.98	10.86	4.20	11.51	3.14	2.44	5.66	4.40	6.93	4.45	6.42	
Na ₂ O	8.98	8.79	8.08	6.86	6.91	5.26	4.67	8.28	7.54	9.03	7.79	9.34	
K ₂ O	0.34	0.26	0.23	1.61	0.14	2.29	2.95	0.96	1.34	0.67	1.26	0.73	
P ₂ O ₅	0.01	0.00	0.00	0.24	0.03	0.38	0.37	0.17	0.24	0.10	0.33	0.14	
TOTAL	103.35	102.75	102.80	100.86	102.64	100.41	99.10	101.66	101.80	101.61	101.27	103.55	

Sample	VF97-05B	VF97-05B	VF97-05B	VF97-05B	VF97-05B	VF97-05B	VF97-05B	VF97-05B	VF97-05B	VF97-05B	VF97-05B	VF97-05B
	gls 5	gls 6	gls 7	gls 10	gls 11	gls 12	gls 13	gls 14	gls 15	gls 16	gls 18	gls 19
	Y	Y	Y	Y	Y	Y	Y	Y	Y	Y	Y	Y
Age	4400	4400	4400	4400	4400	4400	4400	4400	4400	4400	4400	4400
SiO ₂	58.89	64.91	62.89	73.50	72.76	63.30	65.36	64.69	62.09	63.20	72.45	66.76
TiO ₂	0.14	0.34	0.28	0.39	0.31	0.32	0.45	0.33	0.24	0.42	0.34	0.60
Al ₂ O ₃	23.87	17.08	19.65	14.08	14.10	20.11	17.87	18.49	20.37	17.26	14.68	14.06
FeO	1.50	4.74	2.95	2.33	2.09	2.70	3.84	3.36	2.13	2.99	1.79	6.24
MnO	0.00	0.20	0.18	0.00	0.03	0.06	0.12	0.15	0.00	0.09	0.12	0.22
MgO	0.26	1.64	0.85	0.46	0.37	0.79	1.41	0.99	0.64	1.06	0.30	1.88
CaO	7.29	4.07	5.62	1.14	0.93	5.86	4.51	4.76	6.49	4.69	1.11	3.03
Na ₂ O	9.21	4.76	7.56	4.27	4.29	8.37	6.46	7.32	8.51	6.94	4.28	5.32
K ₂ O	0.52	2.25	0.95	3.09	3.16	0.92	1.45	1.33	0.97	1.48	2.98	2.05
P ₂ O ₅	0.08	0.37	0.16	0.00	0.07	0.28	0.27	0.22	0.20	0.16	0.07	0.38
TOTAL	101.75	100.34	101.07	99.25	98.10	102.71	101.74	101.64	101.64	98.29	98.12	100.54

Sample	VF97-05B	VF99-05W	VF99-05W	VF99-05W	VF99-05W	VF99-05W	VF99-05W	VF99-05W	VF99-05W	VF99-05W	VF99-05W	VF99-05W
Unit	gls 20	gls 1	gls 2	gls 3/1	gls 3/2	gls 4	gls 5	gls 6	gls 7	gls 8	gls 9	gls 10
Age	Y	W	W	W	W	W	W	W	W	W	W	W
	4400	4500	4500	4500	4500	4500	4500	4500	4500	4500	4500	4500
SiO ₂	63.74	61.27	60.01	64.39	65.07	60.76	60.16	60.61	60.93	60.77	60.95	61.01
TiO ₂	0.37	0.97	0.84	1.25	1.60	0.92	0.87	0.95	0.92	0.80	1.00	0.83
Al ₂ O ₃	18.18	15.06	19.47	16.39	15.97	17.16	16.59	17.96	17.33	17.57	17.49	17.71
FeO	3.03	6.95	4.42	5.88	5.32	5.53	5.72	4.40	4.60	4.49	4.66	4.35
MnO	0.19	0.18	0.16	0.05	0.23	0.27	0.07	0.16	0.00	0.06	0.12	0.01
MgO	1.11	2.91	2.01	1.82	1.80	3.00	2.88	3.14	2.63	3.37	3.05	2.59
CaO	4.93	5.04	6.56	3.66	3.85	5.84	6.30	4.76	5.35	5.88	5.98	6.27
Na ₂ O	8.16	4.64	5.57	4.50	1.32	3.91	4.24	3.96	5.16	4.74	4.70	5.38
K ₂ O	1.32	1.46	0.85	2.51	2.47	1.62	1.48	2.12	1.84	1.20	1.29	1.00
P ₂ O ₅	0.24	0.28	0.12	0.38	0.34	0.37	0.27	0.25	0.17	0.16	0.25	0.12
TOTAL	101.26	98.77	99.99	100.83	97.97	99.38	98.57	98.28	98.92	99.06	99.48	99.27

Sample	VF99-05W	VF99-05W	VF99-05W	VF99-05W	VF98-02W	VF98-02W	VF98-02W	VF98-02W	VF98-02W	VF98-02W	VF98-02W	VF98-02W
Unit	gls 11	gls 13	gls 14	gls 15	gls 1	gls 2	gls 3	gls 4	gls 5	gls 6	gls 7	gls 8
Age	W	W	W	W	W	W	W	W	W	W	W	W
	4500	4500	4500	4500	4500	4500	4500	4500	4500	4500	4500	4500
SiO ₂	62.26	62.45	61.01	62.61	69.83	70.87	59.79	69.36	61.69	61.55	61.50	62.10
TiO ₂	0.85	1.22	1.22	1.37	0.27	0.32	0.20	0.36	0.27	0.47	0.28	0.59
Al ₂ O ₃	17.31	17.11	16.43	16.12	15.77	15.75	24.03	16.52	21.01	18.90	20.59	18.36
FeO	4.13	4.22	5.40	4.36	2.45	3.40	1.78	3.50	2.48	4.45	3.38	4.88
MnO	0.01	0.08	0.18	0.04	0.20	0.08	0.00	0.10	0.08	0.08	0.15	0.05
MgO	2.43	2.12	3.87	2.67	0.74	0.96	0.31	0.95	0.69	1.67	0.98	1.66
CaO	4.90	4.83	5.16	4.42	2.39	2.49	7.49	2.85	6.25	5.53	6.44	4.75
Na ₂ O	4.79	5.13	4.92	4.19	4.68	3.23	5.97	4.73	5.80	5.49	5.91	5.02
K ₂ O	1.88	1.70	1.53	2.21	2.83	2.83	0.63	2.65	1.05	1.16	0.98	1.64
P ₂ O ₅	0.20	0.52	0.24	0.26	0.12	0.12	0.08	0.17	0.08	0.19	0.14	0.30
TOTAL	98.77	99.38	99.95	98.25	99.28	100.04	100.28	101.19	99.39	99.47	100.35	99.35

Sample	VF98-02W	VF98-02W	VF98-02W	VF98-02W	VF97-06B	VF97-06B	VF97-06B	VF97-06B	VF97-06B	VF97-06B	VF97-06B	VF97-06B
Unit	gls 9	gls 10	gls 11	gls 12	gls 1	gls 2	gls 3	gls 4	gls 5	gls 6	gls 7	gls 8
Age	W	W	W	W	W	W	W	W	W	W	W	W
	4500	4500	4500	4500	4500	4500	4500	4500	4500	4500	4500	4500
SiO ₂	63.52	63.76	59.29	62.80	60.13	59.62	60.72	59.03	58.39	56.72	54.10	56.29
TiO ₂	0.52	0.64	0.41	0.00	0.93	1.22	1.04	0.71	0.46	0.89	0.12	0.43
Al ₂ O ₃	16.83	16.08	21.68	16.79	18.98	15.69	17.01	20.04	23.23	17.87	29.02	21.84
FeO	4.66	6.20	3.79	5.81	5.27	8.25	5.96	4.72	2.85	5.65	1.09	3.11
MnO	0.18	0.11	0.08	0.12	0.15	0.22	0.18	0.08	0.00	0.12	0.03	0.02
MgO	1.71	2.45	1.34	2.54	1.21	2.71	1.66	1.39	0.84	2.37	0.22	0.80
CaO	4.36	4.16	7.14	4.56	5.97	4.92	5.41	6.60	7.29	5.92	11.91	7.59
Na ₂ O	5.28	4.65	5.21	5.37	5.33	4.70	5.14	5.42	6.18	4.93	4.68	5.56
K ₂ O	1.65	1.81	1.03	1.63	1.57	2.11	1.82	1.15	0.75	1.53	0.29	0.87
P ₂ O ₅	0.20	0.27	0.13	0.29	0.28	0.42	0.35	0.31	0.18	0.26	0.04	0.17
TOTAL	98.91	100.12	100.09	99.91	99.83	99.85	99.29	99.45	100.16	96.26	101.48	96.67

Sample	VF97-06B	VF97-06B	VF95-06U	VF95-06U	VF95-06U	VF95-06U	VF95-06U	VF95-06U	VF95-06U	VF95-06U	VF98-02U	VF98-02U
Unit	gls 9	gls 10	gls 1	gls 2	gls 3	gls 4	gls 5	gls 6	gls 7	gls 8	gls 1	gls 2
Age	W	W	U	U	U	U	U	U	U	U	U	U
	4500	4500	4700	4700	4700	4700	4700	4700	4700	4700	4700	4700
SiO ₂	59.50	58.28	58.90	59.76	61.55	58.22	58.81	61.39	56.46	59.16	59.98	58.79
TiO ₂	1.03	0.43	0.72	1.03	0.78	0.90	0.75	1.42	0.24	0.66	0.50	0.61
Al ₂ O ₃	17.06	22.60	18.84	16.57	19.00	17.62	17.95	15.23	23.68	18.93	21.20	20.96
FeO	6.56	3.64	4.62	5.92	4.25	7.24	4.57	6.80	2.50	5.48	2.93	3.20
MnO	0.18	0.04	0.07	0.11	0.00	0.10	0.03	0.10	0.00	0.05	0.02	0.00
MgO	1.82	0.76	2.84	3.21	0.97	1.96	3.06	2.04	0.92	1.33	1.17	0.80
CaO	5.68	7.86	6.58	5.17	5.75	6.31	5.67	4.17	9.31	6.32	7.43	6.53
Na ₂ O	5.35	5.46	5.08	4.77	5.60	5.34	5.50	4.95	5.51	5.28	5.29	5.67
K ₂ O	1.59	1.04	1.07	1.52	2.00	1.24	1.23	2.36	0.48	0.94	0.99	0.93
P ₂ O ₅	0.25	0.12	0.31	0.26	0.29	0.34	0.28	0.44	0.13	0.00	0.16	0.05
TOTAL	99.01	100.21	99.00	98.31	100.17	99.27	97.86	98.89	99.25	98.14	99.68	97.52

Sample	VF98-02U	VF98-02U	VF98-02U	VF98-02U	VF98-02U	VF98-02U	VF98-02U	VF98-02U	VF98-02U	VF98-02U	VF98-02U	VF10-07U
Unit	gls 3	gls 4	gls 6	gls 7	gls 8	gls 9	gls 10	gls 11	gls 12	gls 13	gls 14	gls 1
Age	U	U	U	U	U	U	U	U	U	U	U	U
Age	4700	4700	4700	4700	4700	4700	4700	4700	4700	4700	4700	4700
SiO ₂	60.15	57.00	60.96	60.28	62.20	60.33	62.76	62.74	61.10	63.77	59.83	60.21
TiO ₂	0.95	0.24	0.73	1.05	1.04	0.92	1.05	0.94	0.80	0.93	0.75	0.49
Al ₂ O ₃	18.02	25.27	18.35	15.20	15.71	16.58	17.06	17.54	18.20	16.29	19.96	18.57
FeO	3.07	1.27	4.24	4.99	6.37	5.73	4.47	4.35	3.64	4.76	3.72	5.51
MnO	0.00	0.03	0.07	0.18	0.20	0.12	0.22	0.09	0.14	0.07	0.03	0.12
MgO	0.90	0.26	2.37	2.51	4.56	4.28	1.32	2.04	1.43	1.81	2.02	1.92
CaO	5.76	9.22	5.88	3.97	5.09	5.03	3.60	4.88	5.47	3.85	6.82	5.27
Na ₂ O	4.95	5.81	5.23	4.58	4.80	4.61	5.32	5.15	5.48	4.87	5.06	5.21
K ₂ O	1.38	0.45	1.07	1.92	1.58	1.49	2.40	1.76	1.38	2.32	0.96	1.75
P ₂ O ₅	0.21	0.01	0.13	0.16	0.24	0.29	0.21	0.21	0.30	0.27	0.17	0.24
TOTAL	95.38	99.55	99.03	94.84	101.78	99.37	98.41	99.71	97.93	98.95	99.31	99.29

Sample	VF10-07U	VF10-07U	VF10-07U	VF10-07U	VF10-07U	VF10-07U	VF10-07U	VF10-07U	VF10-07U	VF10-07U	VF10-07U	VF10-07U
Unit	gls 2	gls 3	gls 4	gls 5	gls 6	gls 7	gls 8	gls 9	gls 10	gls 11	gls 12	gls 13
Age	U	U	U	U	U	U	U	U	U	U	U	U
Age	4700	4700	4700	4700	4700	4700	4700	4700	4700	4700	4700	4700
SiO ₂	59.43	60.57	60.71	59.85	57.94	59.81	63.80	61.74	58.40	60.64	60.38	63.07
TiO ₂	0.50	0.42	0.49	0.51	0.59	0.33	0.68	0.55	0.31	0.54	0.65	0.82
Al ₂ O ₃	20.20	20.31	19.60	18.42	19.05	21.71	15.48	17.80	22.37	16.66	14.49	13.31
FeO	3.93	3.44	4.18	4.00	4.23	2.88	5.26	4.84	2.93	5.17	8.14	6.94
MnO	0.08	0.07	0.09	0.08	0.08	0.08	0.11	0.11	0.05	0.02	0.16	0.13
MgO	1.00	0.77	0.58	1.03	1.00	0.52	1.65	1.14	1.40	2.94	5.12	3.68
CaO	5.75	6.37	6.11	5.37	4.99	7.49	4.88	5.31	8.12	7.08	3.22	2.95
Na ₂ O	5.20	6.10	5.12	5.29	5.33	5.67	4.90	5.36	5.09	4.66	4.43	4.68
K ₂ O	1.19	1.10	1.21	1.30	1.11	0.91	1.78	1.69	0.68	1.19	1.91	2.10
P ₂ O ₅	0.22	0.23	0.17	0.25	0.35	0.15	0.35	0.30	0.10	0.21	0.24	0.31
TOTAL	97.50	99.39	98.26	96.11	94.67	99.57	98.89	98.85	99.44	99.10	98.72	97.98

Sample	VF10-01U	VF10-01U	VF10-01U	VF10-01U	VF10-01U	VF10-01U	VF10-01U	VF10-01U	VF10-01U	VF10-01U	VF10-01U	VF10-01U
Unit	gls 1	gls 2	gls 3	gls 4	gls 5	gls 6	gls 7	gls 8	gls 9	gls 10	gls 11	gls 12
Age	U	U	U	U	U	U	U	U	U	U	U	U
	4700	4700	4700	4700	4700	4700	4700	4700	4700	4700	4700	4700
SiO ₂	59.11	57.54	60.02	57.52	57.87	58.30	52.83	59.51	57.83	58.79	58.41	59.99
TiO ₂	0.78	0.75	0.85	0.71	0.71	0.69	0.62	0.55	0.82	0.69	0.65	0.97
Al ₂ O ₃	17.18	17.70	17.86	18.00	17.98	17.68	16.02	17.26	16.96	17.29	17.36	13.72
FeO	6.02	5.96	5.75	4.38	6.21	6.64	5.84	4.19	4.80	4.51	4.52	5.69
MnO	0.19	0.17	0.09	0.11	0.13	0.11	0.10	0.05	0.08	0.10	0.07	0.19
MgO	2.84	2.34	2.49	1.25	2.35	2.90	2.42	1.58	2.04	1.52	1.48	4.66
CaO	5.43	6.11	5.51	5.67	6.69	5.73	4.73	4.67	5.06	4.61	4.69	7.61
Na ₂ O	3.71	5.22	4.44	4.23	5.11	4.37	3.22	4.13	3.98	4.20	3.92	4.35
K ₂ O	2.30	1.20	1.70	1.23	1.41	2.46	1.84	1.28	1.15	1.29	1.26	2.25
P ₂ O ₅	0.25	0.18	0.28	0.24	0.22	0.31	0.20	0.28	0.23	0.20	0.23	0.30
TOTAL	97.80	97.17	98.98	93.34	98.67	99.18	87.80	93.50	92.96	93.20	92.59	99.73

Sample	VF10-01U	VF10-01U	VF10-01U	VF10-01U	VF10-01U	VF10-01U	VF10-01U	VF10-01U	VF10-01U	VF10-01U	VF95-09T	VF95-09T	VF95-09T
Unit	gls 13	gls 14	gls 15	gls 16	gls 17	gls 18	gls 19	gls 20	gls 21	gls 1	gls 2	gls 3	
Age	U	U	U	U	U	U	U	U	U	S	S	S	
	4700	4700	4700	4700	4700	4700	4700	4700	4700	5500	5500	5500	
SiO ₂	60.47	60.30	60.89	59.93	60.88	61.42	58.77	57.94	60.49	64.91	57.83	57.93	
TiO ₂	1.07	1.06	1.06	0.79	1.01	0.93	0.88	0.48	0.83	0.72	0.13	0.05	
Al ₂ O ₃	16.09	16.29	16.00	12.03	16.18	16.81	16.71	22.09	17.51	16.46	25.18	25.42	
FeO	6.54	6.86	6.39	8.89	6.39	5.86	5.92	2.89	5.17	4.16	0.88	0.55	
MnO	0.06	0.16	0.10	0.20	0.11	0.15	0.14	0.00	0.11	0.04	0.00	0.00	
MgO	2.50	1.58	1.86	9.66	2.64	2.11	2.26	1.54	2.37	1.48	0.10	0.05	
CaO	4.65	4.29	4.57	3.33	5.07	4.51	5.70	7.87	5.81	4.25	8.81	8.29	
Na ₂ O	4.31	5.09	4.67	3.31	4.24	4.42	4.49	5.53	4.99	3.37	6.02	6.89	
K ₂ O	2.81	3.07	2.63	1.87	2.50	2.79	1.68	0.73	1.33	1.94	0.35	0.34	
P ₂ O ₅	0.42	0.41	0.39	0.33	0.44	0.42	0.32	0.13	0.29	0.22	0.01	0.06	
TOTAL	98.91	99.08	98.56	100.35	99.46	99.43	96.88	99.20	98.89	97.54	99.32	99.57	

Sample	VF95-09T	VF95-09T	VF95-09T	VF95-09T	VF95-09T	VF95-09T	VF10-03Pi	VF10-03Pi	VF10-03Pi	VF10-03Pi	VF10-03Pi	VF10-03Pi
Unit	gls 4	gls 5	gls 6	gls 7	gls 8	gls 9	gls 1	gls 2	gls 3	gls 4	gls 5	gls 6
Age	S	S	S	S	S	S	P	P	P	P	P	P
	5500	5500	5500	5500	5500	5500	6000	6000	6000	6000	6000	6000
SiO ₂	72.73	70.57	64.32	65.43	60.32	63.63	66.59	68.89	67.97	67.21	68.11	68.47
TiO ₂	0.44	0.43	0.61	0.76	0.43	0.63	0.62	0.63	0.66	0.63	0.62	0.66
Al ₂ O ₃	12.47	11.85	15.51	16.35	20.48	15.73	17.18	16.37	16.19	15.97	17.24	15.98
FeO	1.59	2.08	3.05	4.05	2.41	4.37	4.10	4.00	3.72	3.45	3.59	3.66
MnO	0.00	0.00	0.00	0.00	0.00	0.00	0.07	0.06	0.09	0.06	0.12	0.03
MgO	0.16	0.70	0.93	1.32	0.72	1.33	1.42	1.34	1.21	1.24	1.20	1.17
CaO	0.58	0.52	2.84	3.79	6.99	3.61	4.19	3.33	3.62	3.18	4.25	3.29
Na ₂ O	4.31	3.95	4.38	4.90	5.60	4.71	4.05	3.94	4.77	5.08	5.22	5.34
K ₂ O	4.18	4.51	2.04	2.04	0.99	2.01	1.80	2.07	2.05	2.04	1.82	2.05
P ₂ O ₅	0.10	0.06	0.22	0.27	0.17	0.16	0.24	0.21	0.24	0.22	0.22	0.23
TOTAL	96.54	94.67	93.89	98.91	98.12	96.20	100.25	100.85	100.49	99.07	102.39	100.88

Sample	VF10-03Pi	VF10-03Pi	VF10-03Pi	VF10-03Pi	VF10-03Pi	VF10-03Pi	VF10-03Pi	VF10-03Pi	VF10-03Pi	VF10-03Pi	VF10-03Pi	VF10-03Pi
Unit	gls 7	gls 8	gls 9	gls 10	gls 11	gls 12	gls 13	gls 14	gls 15	gls 16	gls 17	gls 18
Age	P	P	P	P	P	P	P	P	P	P	P	P
	6000	6000	6000	6000	6000	6000	6000	6000	6000	6000	6000	6000
SiO ₂	68.22	62.92	67.54	64.57	67.90	67.79	67.07	67.34	67.35	67.68	68.03	64.92
TiO ₂	0.66	0.60	0.63	0.31	0.69	0.61	0.60	0.66	0.60	0.67	0.68	0.63
Al ₂ O ₃	16.45	15.34	16.42	20.73	15.61	16.23	16.92	16.61	16.66	16.44	16.41	16.47
FeO	3.82	3.59	3.89	2.42	3.73	3.94	3.99	3.73	4.01	3.86	3.68	3.73
MnO	0.04	0.05	0.05	0.03	0.09	0.10	0.12	0.11	0.09	0.05	0.08	0.13
MgO	1.25	1.23	1.40	0.57	1.28	1.31	1.37	1.19	1.41	1.41	1.34	1.51
CaO	3.65	3.25	3.78	6.58	3.48	3.52	3.89	3.55	3.97	3.92	3.44	3.89
Na ₂ O	5.06	4.59	5.07	5.76	5.48	4.98	5.28	4.84	5.14	4.73	4.94	4.94
K ₂ O	1.99	1.81	1.92	1.05	2.16	1.99	1.92	1.97	1.94	1.93	2.02	1.84
P ₂ O ₅	0.28	0.19	0.21	0.10	0.24	0.17	0.16	0.21	0.21	0.23	0.21	0.29
TOTAL	101.41	93.56	100.90	102.11	100.66	100.64	101.32	100.21	101.39	100.92	100.84	98.34

Sample	VF10-03Pi	VF10-03Pi	VF10-	VF10-	VF10-	VF10-	VF10-	VF10-	VF10-	VF10-	VF10-	VF10-03M2
Unit	gls 19	gls 20	03M2 gls 1	03M2 gls 2	03M2 gls 3	03M2 gls 4	03M2 gls 5	03M2 gls 6	03M2 gls 7	03M2 gls 8	03M2 gls 9	gls 10
Age	P	P	L	L	L	L	L	L	L	L	L	L
	6000	6000	7500	7500	7500	7500	7500	7500	7500	7500	7500	7500
SiO ₂	65.66	65.97	67.05	70.47	74.15	74.80	71.36	72.12	68.21	71.96	73.64	71.77
TiO ₂	0.63	0.63	0.38	0.41	0.54	0.58	0.69	0.57	0.52	0.68	0.50	0.41
Al ₂ O ₃	16.77	16.96	14.29	13.94	13.47	13.51	13.25	14.23	16.30	13.74	12.69	15.66
FeO	3.81	4.22	3.24	3.71	3.07	3.01	3.03	3.49	3.18	4.23	2.48	2.37
MnO	0.06	0.14	0.07	0.10	0.03	0.03	0.07	0.08	0.04	0.04	0.06	0.04
MgO	1.50	1.63	0.88	1.13	0.74	0.45	0.49	0.49	0.84	0.85	0.36	0.30
CaO	4.03	4.22	2.60	2.12	1.84	1.53	1.64	1.98	3.14	1.98	1.40	3.06
Na ₂ O	5.05	4.84	5.12	4.93	4.46	4.37	4.30	4.86	5.16	4.73	4.43	4.76
K ₂ O	1.82	1.77	2.00	2.04	2.38	2.56	2.35	2.38	1.90	2.45	2.45	2.08
P ₂ O ₅	0.19	0.27	0.25	0.20	0.20	0.24	0.29	0.26	0.20	0.21	0.22	0.23
TOTAL	99.52	100.64	95.87	99.05	100.89	101.08	97.46	100.44	99.49	100.86	98.22	100.66

Sample	VF10-03M2	VF10-03M2	VF10-03M2	VF10-03M2	VF10-03M2	VF10-07B	VF10-07B	VF10-07B	VF10-07B	VF10-07B	VF10-07B	VF95-09E
Unit	gls 11	gls 12	gls 13	gls 14	gls 15	gls 1	gls 2	gls 3	gls 4	gls 5	gls 6	gls 1
Age	L	L	L	L	L	L	L	L	L	L	L	L
	7500	7500	7500	7500	7500	7500	7500	7500	7500	7500	7500	7500
SiO ₂	73.53	68.27	72.99	72.07	71.90	74.77	73.33	75.77	73.36	73.72	73.64	74.79
TiO ₂	0.53	0.41	0.42	0.43	0.55	0.56	0.48	0.53	0.46	0.52	0.48	0.35
Al ₂ O ₃	13.73	16.02	12.01	13.65	13.23	11.46	11.52	11.22	11.35	11.54	11.72	10.97
FeO	3.33	3.74	1.88	2.09	3.94	2.09	2.00	1.91	1.85	2.18	2.02	1.24
MnO	0.05	0.14	0.05	0.04	0.12	0.03	0.00	0.08	0.06	0.05	0.03	0.08
MgO	0.45	0.64	0.29	0.33	1.31	0.24	0.18	0.17	0.21	0.18	0.39	0.16
CaO	1.65	3.14	1.06	1.73	2.20	0.64	0.76	0.80	0.71	0.62	1.24	0.58
Na ₂ O	4.33	5.14	4.34	4.68	4.27	4.02	4.09	3.86	3.84	3.70	4.03	3.68
K ₂ O	2.46	2.24	2.56	2.35	2.32	3.04	3.00	3.13	3.13	3.04	2.83	2.93
P ₂ O ₅	0.26	0.19	0.09	0.14	0.25	0.06	0.05	0.05	0.07	0.03	0.31	0.01
TOTAL	100.32	99.93	95.70	97.52	100.08	96.91	95.41	97.51	95.04	95.58	96.68	94.82

Sample	VF95-09E	VF95-09E	VF95-09E	VF10-03L	VF10-03L	VF10-03L	VF10-03L	VF10-03L	VF10-03L	VF10-03L	VF10-03L	VF10-03L
Unit	gls 2	gls 3	gls 5	gls 1	gls 2	gls 3	gls 4	gls 5	gls 6	gls 7	gls 8	gls 9
Age	L	L	L	J	J	J	J	J	J	J	J	J
	7500	7500	7500	7700	7700	7700	7700	7700	7700	7700	7700	7700
SiO ₂	75.74	73.83	75.32	68.63	62.69	62.82	65.81	66.06	59.34	57.52	62.12	62.35
TiO ₂	0.35	0.35	0.36	0.90	0.70	0.69	0.90	0.79	0.93	0.80	0.72	0.72
Al ₂ O ₃	11.24	11.72	11.14	15.35	17.46	17.74	15.70	15.34	14.52	12.70	17.26	15.74
FeO	1.37	1.37	1.45	3.84	4.25	4.63	4.40	4.59	6.54	6.41	5.14	5.69
MnO	0.07	0.07	0.01	0.09	0.04	0.04	0.10	0.09	0.13	0.10	0.06	0.14
MgO	0.21	0.17	0.13	0.99	1.85	1.50	1.22	2.07	2.49	2.63	1.74	2.34
CaO	0.64	0.86	0.62	2.74	4.69	4.84	3.36	3.31	2.88	3.69	4.88	4.17
Na ₂ O	4.08	4.09	3.74	2.38	4.87	5.06	2.47	2.80	4.62	4.46	5.85	5.36
K ₂ O	2.95	2.92	2.97	2.48	1.66	1.56	2.35	2.06	1.95	1.70	1.37	1.84
P ₂ O ₅	0.01	0.05	0.01	-	-	-	-	-	0.32	0.21	0.19	0.23
TOTAL	96.66	95.42	95.76	97.40	98.21	98.88	96.31	97.11	93.71	90.22	99.33	98.59

Sample	VF10-03L	VF10-03L	VF10-03L	VF97-01F	VF97-01F	VF97-01F	VF97-01F	VF97-01F	VF97-01F	VF97-01F	VF95-01F	VF95-01F	VF95-01F
Unit	gls 10	gls 11	gls 12	gls 1	gls 2	gls 3	gls 4	gls 5	gls 6	gls 1	gls 2	gls 3	
Age	J	J	J	J	J	J	J	J	J	H	H	H	
	7700	7700	7700	7700	7700	7700	7700	7700	7700	10,000	10,000	10,000	
SiO ₂	64.65	66.59	63.44	54.48	63.61	62.14	61.59	63.71	64.61	62.37	62.34	62.57	
TiO ₂	0.80	0.84	0.76	0.06	1.13	0.90	1.00	1.10	1.11	1.10	1.06	1.07	
Al ₂ O ₃	16.23	15.45	14.70	28.19	14.55	16.95	15.01	15.15	14.33	15.19	16.41	16.58	
FeO	5.03	4.33	4.10	0.96	8.00	5.77	6.88	6.42	7.15	6.49	5.78	4.98	
MnO	0.07	0.11	0.04	0.00	0.11	0.12	0.07	0.11	0.05	0.11	0.08	0.11	
MgO	1.32	1.07	1.13	0.16	1.95	2.15	3.45	1.34	2.27	2.33	2.10	1.99	
CaO	4.05	3.08	2.59	11.65	3.37	4.60	4.09	3.47	3.12	4.46	4.46	4.39	
Na ₂ O	5.16	5.41	4.91	4.94	4.71	5.26	5.05	5.39	4.71	4.29	4.87	4.93	
K ₂ O	2.14	2.43	2.30	0.15	2.67	1.70	2.30	2.46	2.51	1.90	1.79	1.75	
P ₂ O ₅	0.28	0.26	0.26	0.00	0.31	0.32	0.32	0.39	0.37	-	-	-	
TOTAL	99.73	99.57	94.24	100.59	100.41	99.91	99.76	99.53	100.24	98.24	98.89	98.37	

Sample Unit Age	VF95-01F	VF95-01F	VF95-01F	VF95-01F	VF95-01F	VF95-01F	VF95-01F	VF97-01D	VF97-01D	VF97-01D	VF97-01D	VF97-01D
	gls 4	gls 5	gls 6	gls 7	gls 8	gls 9	gls 10	gls 1	gls 2	gls 3	gls 4	gls 5
	H	H	H	H	H	H	H	H	H	H	H	H
	10,000	10,000	10,000	10,000	10,000	10,000	10,000	10,000	10,000	10,000	10,000	10,000
SiO ₂	63.30	62.16	62.17	64.04	62.23	61.89	62.57	62.15	62.84	60.86	60.84	61.79
TiO ₂	1.08	1.05	1.01	0.99	0.97	1.01	1.06	1.17	1.09	1.06	1.03	1.19
Al ₂ O ₃	15.40	16.18	16.57	16.00	16.94	16.49	16.40	15.48	15.16	17.00	17.28	15.63
FeO	5.73	6.39	5.32	5.13	5.79	6.40	6.19	6.84	6.03	5.72	4.80	6.10
MnO	0.14	0.17	0.07	0.06	0.13	0.11	0.09	0.06	0.10	0.07	0.03	0.12
MgO	1.80	2.22	1.99	1.97	1.86	2.09	2.06	1.42	2.49	1.12	1.23	1.65
CaO	4.39	4.62	4.83	4.47	4.79	4.69	4.48	4.60	3.47	5.76	6.07	4.94
Na ₂ O	4.86	4.81	4.82	4.63	4.35	4.55	4.83	4.75	4.99	5.24	5.79	5.18
K ₂ O	1.74	1.71	1.60	1.80	1.79	1.76	1.78	1.78	2.76	1.39	1.46	1.66
P ₂ O ₅	-	-	-	-	-	-	-	-	-	-	-	-
TOTAL	98.45	99.31	98.39	99.09	98.84	98.99	99.46	98.25	98.92	98.23	98.53	98.27

Sample Unit Age	VF97-01D	VF97-01D	VF97-01D	VF97-01D	VF97-01D	VF97-01D	VF97-01D	VF97-01D	VF97-01D	VF94-06E	VF94-06E	VF94-06E	VF94-06E
	gls 6	gls 7	gls 8	gls 9	gls 10	gls 11	gls 12	gls 13	gls 1	gls 2	gls 3	gls 4	
	H	H	H	H	H	H	H	H	H	H	H	H	
	10,000	10,000	10,000	10,000	10,000	10,000	10,000	10,000	10,000	10,000	10,000	10,000	
SiO ₂	62.41	57.97	60.86	60.82	61.99	60.77	57.95	60.41	70.61	61.39	57.87	55.53	
TiO ₂	1.30	1.01	0.67	1.01	0.98	1.04	0.85	1.02	0.21	0.45	0.36	0.53	
Al ₂ O ₃	14.96	16.44	20.04	16.25	16.15	16.33	20.24	17.14	13.02	17.90	22.00	18.01	
FeO	7.40	8.08	3.67	7.00	6.91	6.27	3.88	5.83	2.17	3.50	2.50	2.61	
MnO	0.12	0.19	0.00	0.14	0.08	0.09	0.10	0.02	0.04	0.11	0.05	0.08	
MgO	2.08	2.74	0.88	1.73	2.04	2.16	1.18	1.72	0.42	0.96	0.68	0.79	
CaO	4.69	6.07	6.78	5.66	4.27	4.27	7.80	5.93	1.40	4.77	7.41	5.69	
Na ₂ O	4.68	4.02	5.95	5.21	4.48	4.80	5.20	5.46	3.73	5.04	5.21	4.19	
K ₂ O	1.82	1.99	1.06	1.28	1.90	2.81	1.27	1.43	5.67	3.64	1.97	2.71	
P ₂ O ₅	-	-	-	-	-	-	-	-	-	-	-	-	
TOTAL	99.46	98.52	99.92	99.10	98.80	98.55	98.47	98.95	97.28	97.75	98.05	90.14	

Appendix C: Sample Preparation Procedure

The freshest pumice and scoria pieces from each sample were selected for whole-rock geochemical analyses. The required sample size was 30g, therefore single pumices or scoria were selected for coarse samples; however, in many cases multiple pieces were selected. Individual pieces were cleaned with a nylon toothbrush in filtered (UHQ 18M Ω) water, and then cleaned in filtered water in an ultra-sonic bath. The samples were then dried in an oven overnight.

Once dry, samples were then crushed and powdered using a mechanical agate pestle and mortar. Pure quartz was crushed between samples and the pestle and mortar was cleaned with acetone to avoid contamination.

The powdered samples were then stored in sterile Teflon jars.

Appendix D: Geochemical Analytical Methods

Whole-rock major and trace element data for the Group I and Group II eruption deposits were analysed by Inductively Coupled Plasma Atomic Emission Spectrometry (ICP-AES) and Inductively-Coupled Plasma Mass Spectrometry (ICP-MS) at Royal Holloway University of London (RHUL).

Published data used in this study were analysed by X-Ray Fluorescence (XRF), Instrumental Neutron Activation Analysis (INAA) and ICP-MS. Although the complete database comprises a large amount of published data (Luhr and Carmichael, 1980, 1981; Luhr and Carmichael, 1982; Allan and Carmichael, 1984; Robin et al., 1991; Luhr, 1993; Robin and Potrel, 1993; Komorowski et al., 1997; Luhr, 2002; Carmichael et al., 2006; Maria and Luhr, 2008; Savov et al., 2008; Vigouroux et al., 2008; Cai, 2009; Luhr et al., 2010; Saucedo et al., 2010), only data from Luhr and Carmichael (1981; 1982), Carmichael et al. (2006), Maria and Luhr (2008), Vigouroux et al. (2008), Cai (2009) and Luhr et al. (2010) and unpublished data collected by Ivan Savov and Jim Luhr relate to the Holocene tephra fallout deposits, and alkaline cinder cone magmas.

Inductively Coupled Plasma Atomic Emission Spectrometry (ICP-AES)

Whole-rock major and select trace element (Ba, Sr, Y, Zr, Zn, Co, Cr, Cu, Li, Ni, Sc and V) data collected during this study were analysed by ICP-AES at Royal Holloway University of London (RHUL). Results were obtained by LiBO₂ flux-fusion for major elements and Ba, Sr, Y, Zr and Zn; and Hydro-Fluoric (HF) acid digestion (Co, Cr, Cu, Li, Ni, Sc and V).

ICP-AES uses inductively coupled plasma to thermally excite outer-shell electrons of the elements in the sample. As the electrons return to the ground state, the elements emit photons of light with an energy characteristic of the element. The more intense the energy, the higher the concentration in the sample.

Inductively-Coupled Plasma Mass Spectrometry (ICP-MS)

Whole-rock trace elements (Rb, Nb, Mo, Cs, Hf, Ta, Tl, Th and U) and rare earth elements (La, Ce, Pr, Nd, Sm, Eu, Gd, Tb, Dy, Ho, Er, Tm, Yb and Lu) collected during this study were analysed by ICP-MS at Royal Holloway University of London (RHUL). Results were obtained by LiBO₂ flux-fusion.

The sample solution is loaded onto the mass spectrometer and undergoes vaporisation. The vaporised sample is ionised by inductively couple plasma, and the ions are separated according to their mass-to-charge ratio by electromagnetic fields. The ions are detected and measured and the signal is proportional to the concentration. This technique has low detection limits, therefore is good for trace and REE.

X-Ray Fluorescence (XRF)

XRF analysis measures secondary (fluorescent) X-rays emitted from a sample which has been bombarded by a primary X-ray beam. The wavelengths of the secondary X-rays are characteristic to each element, and intensity of the X-rays are used to determine the concentration of the elements by reference to calibration standards.

XRF can analyse up to 80 elements with detection limits from 100% to a few parts per million (ppm), although XRF cannot analyse elements lighter than Na.

Instrumental Neutron Activation Analysis (INAA)

INAA measures the gamma rays emitted by the radioactive decay of elements within the sample. A powdered sample is bombarded with neutrons, producing radioactive isotopes or nuclides. As the nuclides decay, they emit gamma rays whose energies are characteristic of each element. The concentration of the element is measured by comparison of the intensity of the gamma rays with a standard. The gamma-ray spectrometry is measured at set intervals over several weeks in order to measure isotopes with different half-lives.

INAA has a very low detection limit and allows for analysis of a large number of elements simultaneously.

Limitations and Compatibility of Datasets

Whole-rock XRF and ICP-MS data reported by Maria and Luhr (2008), Vigouroux et al. (2008) and Luhr et al. (2010) were analysed at Washington State University. Details of the analytical techniques and precisions are reported by Luhr (2002). The published whole-rock datasets of Luhr and Carmichael (1981; 1982) were analysed by XRF, ICP-MS and INAA at Lawrence Berkeley Laboratory, University of California. The analytical precision for these data is reported by Luhr and Carmichael (1981; 1982). Cai (2009) analysed whole-rock trace element data by ICP-MS at the Lamont-Doherty Earth Observatory of Columbia University, but gives no details of the analyses.

A comparison of the analytical precision of the various techniques used is given in the graphs below (Figure 1). The majority of major element data used in this study were analysed by XRF, which is the most precise technique for major elements. ICP-MS is precise to <0.6%, while the new ICP-AES data collected in this study has errors of up to 2.2% (K₂O). The precision for the major elements with high concentrations (SiO₂, Al₂O₃, FeO, MgO and CaO) are comparable with the XRF and wet chemistry data (Figure 1).

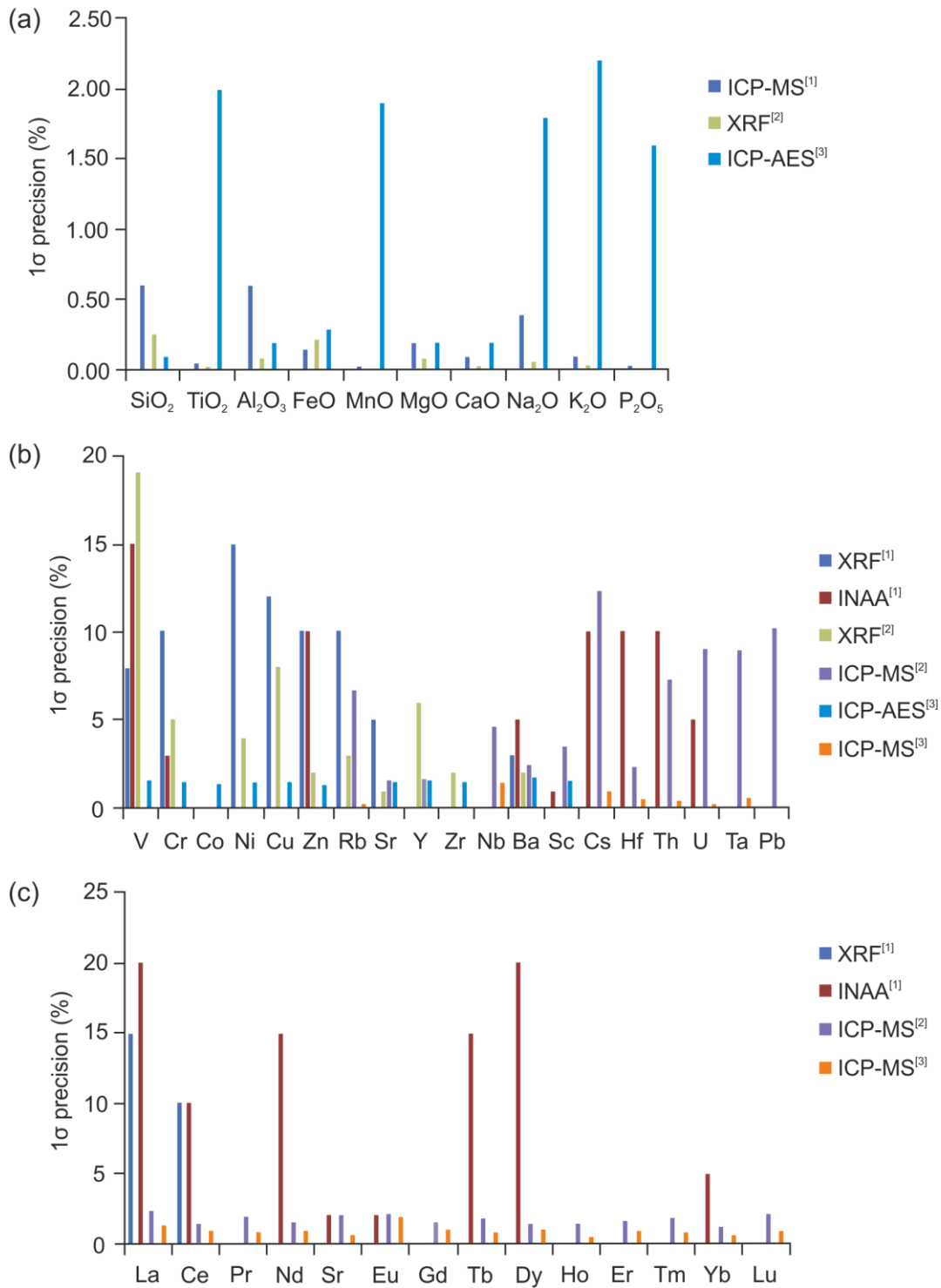


Figure 1. Comparison of the precision of the analytical techniques used to analyse the major element (a), trace element (b), and rare earth element (c) data used in this study. Analytical precision is reported as 1σ error by: [1] Luhr and Carmichael (1981; 1982); [2] Luhr (2002); and [3] this study.

Figure 1b and c show the comparison between the analytical techniques used to collect trace element data and rare earth element data. The precision varies from <1% to as much as 15% (La analysed by XRF). ICP-MS and ICP-AES are consistently the most precise

techniques, so where data has been analysed by multiple techniques, ICP-MS and ICP-AES data was used.

The variations observed within the data for the different eruption deposits may be the result of grouping together samples analysed by different techniques, therefore this is taken into account when interpreting the data. However, the variations are relatively small, and any trends interpreted in the data are out with analytical error.

Appendix E: Group I Whole-rock Major and Trace Element Data

Table 1 Whole-rock major and trace element XRF data

Sample:	VF97-13B	VF95-06Y	VF95-09X	VF97-06D	VF98-02Y	Vf99-05Yi	VF99-05Ys	VF01-01X	VF97-05B	VF95-06W	VF01-01V	VF97-06B
Unit:	Y	Y	Y	Y	Y	Y	Y	Y	Y	W	W	W
Age (yrs B.P.)	4400	4400	4400	4400	4400	4400	4400	4400	4400	4500	4500	4500
SiO ₂	59.6	56.1	58.7	59.5	55.6	56.6	56.0	53.9	60.4	55.9	56.5	56.0
TiO ₂	0.7	0.5	0.5	0.5	0.5	0.5	0.5	0.5	0.4	0.7	0.7	0.8
Al ₂ O ₃	17.9	20.4	19.4	19.1	21.4	20.6	21.3	21.5	18.1	18.7	17.7	18.4
FeOt	5.4	5.3	4.7	5.1	5.5	4.9	5.5	5.7	4.7	5.8	6.2	6.4
MnO	0.11	0.10	0.10	0.11	0.11	0.10	0.10	0.11	0.10	0.11	0.11	0.12
MgO	2.8	2.3	1.8	2.3	2.2	1.9	2.4	2.2	2.1	4.3	5.2	4.8
CaO	5.9	5.6	5.1	5.7	5.5	5.0	5.6	5.4	5.6	6.7	6.7	7.5
Na ₂ O	4.3	4.2	4.5	4.6	4.2	4.3	4.2	3.8	4.9	4.2	4.0	4.1
K ₂ O	1.2	1.0	1.3	1.3	1.1	1.2	1.0	1.0	1.5	1.0	1.0	1.0
P ₂ O ₅	0.17	0.26	0.27	0.30	0.31	0.30	0.29	0.32	0.24	0.20	0.20	0.21
L.O.I.	1.9	4.1	2.5	1.6	3.7	3.2	3.1	4.8	0.8	1.5	1.1	0.8
Total	99.94	99.77	98.79	100.05	99.96	98.65	100.11	99.15	98.78	98.97	99.44	100.03
V	128	91	70	82	93	70	92	69	77	142	111	160
Cr	12	17	11	12	16	<3	21	18	12	82	173	92
Co	15	12	11	10	14	10	12	18	10	21	22	23
Ni	15	11	7	11	14	12	15	10	10	37	62	42
Cu	18	11	11	14	16	13	15	21	13	28	29	29
Zn	65	64	59	66	65	60	64	66	67	63	70	70
Rb	18	16	19	16	13	14	13	13	17	16	10	12
Sr	629	664	625	682	673	601	653	638	685	628	592	666
Y	17	15	16	15	16	15	15	17	14	16	18	17
Zr	128	148	158	140	165	159	160	188	146	124	152	125
Nb	4	4	7	2	4	6	2	3	5	5	5	4
Ba	485	468	566	471	446	466	436	386	495	409	353	391

Sample Unit: Age (yrs B.P.)	VF98-02W W 4500	VF99-05W W 4500	VF98-02U U 4700	VF95-06U U 4700	VF10-04U U 4700	VF95-09V U 4700	VF97-20Q U 4700	VF10-01U U 4700	VF10-02U U 4700	VF10-03U U 4700	VF10-07U U 4700	VF01-01T U 4700
SiO ₂	57.1	54.7	55.3	54.2	50.7	56.8	57.8	55.7	53.9	55.1	54.5	52.8
TiO ₂	0.6	0.8	0.7	0.8	0.5	0.6	0.8	0.8	0.7	0.7	0.7	0.8
Al ₂ O ₃	18.9	18.2	18.3	18.0	21.4	18.4	17.5	18.4	17.8	17.4	18.5	18.9
FeOt	5.7	6.6	6.4	6.6	-	5.6	6.1	-	-	-	-	7.1
MnO	0.11	0.12	0.12	0.12	0.10	0.11	0.12	0.11	0.11	0.11	0.11	0.12
MgO	3.9	5.9	5.6	5.8	2.3	4.0	4.1	4.6	5.9	6.1	5.1	5.9
CaO	6.4	7.5	7.5	7.4	5.5	6.6	6.9	7.1	7.5	7.1	7.2	7.2
Na ₂ O	4.4	3.8	4.0	3.8	3.9	4.2	4.4	4.1	3.8	4.0	3.9	3.3
K ₂ O	1.1	0.8	1.2	0.8	0.9	1.1	1.3	1.0	0.8	0.9	0.9	0.7
P ₂ O ₅	0.21	0.20	0.20	0.19	0.35	0.22	0.21	0.21	0.23	0.22	0.22	0.23
L.O.I.	1.1	1.0	0.9	1.3	-	1.3	0.1	-	-	-	-	2.2
Total	99.56	99.92	100.10	99.00	92.07	99.01	99.19	98.90	97.99	98.76	97.98	99.14
V	132	163	164	171	89	133	143	155	148	149	153	127
Cr	93	190	178	156	22	77	57	102	198	177	157	199
Co	21	28	27	26	12	19	19	21	22	23	21	27
Ni	41	74	67	63	15	35	24	44	69	75	58	79
Cu	32	37	30	37	17	27	22	35	39	42	41	43
Zn	66	64	66	62	68	64	69	69	61	69	59	70
Rb	12	10	12	13	-	16	16	-	-	-	-	7
Sr	629	617	639	627	653	612	586	658	618	575	624	627
Y	15	16	16	16	18	15	18	18	17	18	18	18
Zr	140	117	126	114	151	122	133	109	109	101	110	158
Nb	5	4	7	8	-	7	3	-	-	-	-	9
Ba	418	318	360	342	-	446	438	-	-	-	-	280

Sample	VF01-10J	VF10-07S	VF95-09T	VF10.07Q	VF97-03BR	VF01-10H	VF95-06P	VF98-10S	VF99-03T	VF10-01S	VF10-02S	VF10-03S
Unit:	U	S	S	S	S	S	S	S	S	S	S	S
Age (yrs B.P.)	4700	5500	5500	5500	5500	5500	5500	5500	5500	5500	5500	5500
SiO ₂	54.7	55.4	55.8	56.9	57.6	55.4	55.0	55.7	55.5	56.0	58.6	59.7
TiO ₂	0.8	0.8	0.8	0.8	0.7	0.8	0.8	0.8	0.8	0.7	0.6	0.5
Al ₂ O ₃	18.3	18.1	17.4	17.1	18.8	18.6	18.3	18.3	18.6	17.5	17.2	17.2
FeO _t	6.6	-	6.3	-	5.7	6.5	6.4	6.4	6.4	-	-	-
MnO	0.11	0.11	0.12	0.12	0.10	0.11	0.12	0.11	0.12	0.11	0.10	0.09
MgO	5.6	5.0	5.8	5.4	4.1	4.9	5.0	5.1	4.9	5.7	5.0	4.1
CaO	7.4	7.4	7.5	6.8	6.7	7.4	7.5	7.4	7.5	7.4	6.5	5.7
Na ₂ O	3.7	4.1	4.1	4.4	4.5	4.0	4.1	4.1	4.1	4.1	4.4	4.3
K ₂ O	0.8	1.0	1.0	1.1	1.0	0.9	0.9	1.0	0.9	1.0	1.1	1.3
P ₂ O ₅	0.22	0.21	0.20	0.21	0.17	0.20	0.20	0.20	0.19	0.22	0.20	0.25
L.O.I.	1.7	-	0.3	-	0.6	1.0	0.6	0.6	0.7	-	-	-
Total	99.74	99.48	99.21	99.71	99.97	99.80	98.90	99.73	99.80	99.72	100.05	98.98
V	125	142	169	148	151	129	173	164	161	156	129	119
Cr	191	112	170	122	83	121	108	143	113	172	143	126
Co	25	21	26	19	18	23	25	26	24	21	17	16
Ni	75	54	61	42	39	50	47	57	49	68	44	49
Cu	40	36	40	27	28	31	31	32	31	42	22	20
Zn	61	73	60	75	67	74	69	74	67	63	71	85
Rb	9	-	14	-	13	10	14	13	11	-	-	-
Sr	630	666	613	593	646	655	654	657	639	615	604	564
Y	18	19	16	18	16	19	17	16	17	17	17	16
Zr	157	109	112	115	123	155	113	121	125	104	109	111
Nb	5	-	5	-	6	6	7	4	5	-	-	-
Ba	309	-	386	-	442	323	385	389	368	-	-	-

Sample Unit: Age (yrs B.P.)	VF97-20O S 5500	VF10-07M1 S 5500	VF95-09L P 6000	VF97-03BP P 6000	VF97-20M P 6000	VF98-10Q P 6000	VF99-03Ti P 6000	VF99-05O P 6000	VF99-05P P 6000	VF10-02P P 6000	VF10-01P P 6000	VF95-06M P 6000
SiO ₂	54.9	58.1	57.1	57.7	57.2	57.6	57.5	59.7	57.2	57.2	55.4	57.4
TiO ₂	0.8	0.6	0.7	0.6	0.7	0.7	0.6	0.5	0.7	0.7	0.8	0.6
Al ₂ O ₃	18.0	19.6	18.8	17.2	18.7	18.5	18.9	18.7	19.3	17.6	18.3	18.9
FeO _t	6.4	-	5.6	5.8	5.6	5.8	4.9	4.7	5.7	-	-	5.0
MnO	0.11	0.09	0.10	0.11	0.10	0.10	0.09	0.09	0.10	0.11	0.11	0.09
MgO	5.0	2.6	3.7	6.2	3.8	4.2	3.7	3.3	4.0	4.5	4.9	3.6
CaO	7.3	6.6	6.7	6.8	6.6	6.6	5.7	5.6	6.6	6.5	7.1	5.8
Na ₂ O	4.1	4.7	4.4	4.2	4.2	4.3	4.1	4.4	4.3	4.2	4.2	4.0
K ₂ O	1.0	1.1	1.0	1.0	1.0	1.0	1.1	1.3	1.0	1.1	1.0	1.0
P ₂ O ₅	0.22	0.22	0.18	0.16	0.18	0.18	0.20	0.20	0.19	0.19	0.20	0.18
L.O.I.	1.4	-	0.7	0.6	1.7	0.8	2.4	1.6	0.9	-	-	2.8
Total	99.13	99.14	99.04	100.29	99.65	99.82	99.33	100.26	100.28	98.62	98.79	99.31
V	170	113	150	145	136	150	105	102	146	145	156	114
Cr	128	22	70	303	68	100	90	87	87	107	116	87
Co	25	13	20	25	19	23	15	15	20	19	21	15
Ni	51	13	33	90	35	44	35	34	39	38	49	30
Cu	31	18	28	30	27	27	23	25	27	31	32	23
Zn	73	66	63	67	65	69	53	58	62	70	66	51
Rb	12	-	15	11	13	14	15	16	13	-	-	17
Sr	669	679	635	594	640	621	540	563	614	558	627	559
Y	18	17	16	14	17	16	14	15	14	18	17	14
Zr	129	112	111	122	123	130	137	138	127	117	105	134
Nb	5	-	7	2	5	4	5	3	6	-	-	7
Ba	375	-	431	399	436	422	460	509	411	-	-	484

Sample Unit: Age (yrs B.P.)	VF10-04M Pi 6000	VF10-04N Ps 6000	VF95-06N P 6000	VF10-07M3 P 6000	VF10-07B L 7500	VF98-07B L 7500	VF97-01G L 7500	VF10-03M2 L 7500	VF95-09E L 7500	VF00-06T1 J 7700	VF00-06T3 J 7700	VF97-01F J 7700
SiO ₂	58.0	55.5	56.6	57.9	59.7	59.5	59.4	59.9	58.0	59.5	59.0	59.5
TiO ₂	0.5	0.7	0.7	0.7	0.6	0.6	0.7	0.6	0.6	0.6	0.7	0.7
Al ₂ O ₃	18.5	19.0	18.7	19.0	17.3	17.5	16.9	17.4	17.8	16.4	16.7	17.5
FeO _t	-	-	5.7	-	-	4.9	5.4	-	5.0	5.2	5.6	5.4
MnO	0.08	0.10	0.10	0.10	0.10	0.09	0.10	0.09	0.09	0.10	0.10	0.10
MgO	3.8	4.1	3.9	3.3	4.2	3.9	5.1	4.1	4.1	5.2	5.1	4.6
CaO	5.8	6.4	6.7	6.5	5.9	5.9	6.3	6.0	6.2	5.9	6.4	6.2
Na ₂ O	4.2	4.2	4.3	4.7	4.2	4.2	4.7	4.5	4.1	5.2	5.1	4.6
K ₂ O	1.2	1.0	1.0	1.1	1.1	1.1	1.2	1.2	1.0	1.1	1.1	1.3
P ₂ O ₅	0.16	0.19	0.19	0.20	0.18	0.15	0.17	0.15	0.17	0.16	0.16	0.20
L.O.I.	-	-	1.0	-	-	1.0	0.3	-	2.0	0.8	0.7	0.5
Total	97.48	97.49	98.83	99.74	98.71	98.96	100.21	99.18	99.14	99.22	99.75	100.70
V	102	137	154	133	108	111	140	111	116	91	105	134
Cr	105	71	72	39	157	105	126	125	101	165	135	77
Co	14	17	20	15	15	16	20	16	17	18	20	20
Ni	37	33	33	21	49	44	58	49	38	72	56	43
Cu	25	29	26	27	22	18	30	22	16	28	36	31
Zn	53	68	61	70	60	57	62	70	58	60	61	59
Rb	-	-	15	-	-	14	14	-	16	13	12	15
Sr	539	615	622	654	636	595	661	628	611	618	615	679
Y	14	16	16	18	14	14	16	13	12	17	17	16
Zr	122	111	117	113	108	116	128	101	101	140	138	133
Nb	-	-	7	-	-	7	10	-	6	2	4	4
Ba	-	-	431	-	-	547	482	-	603	426	383	483

Sample Unit: Age (yrs B.P.)	VF98-07ZZ J 7700	VF10-03L J 7700	VF97-03AE J 7700	VF97-01Ds H 10,000	Vf97-01Di H 10,000	Vf00-06R H 10,000	VF95-01F H 10,000	VF97-20G H 10,000	VF97-03AC H 10,000
SiO ₂	57.8	57.3	58.7	58.0	56.9	54.5	58.7	54.7	58.2
TiO ₂	0.7	0.7	0.7	0.8	0.7	0.8	0.8	0.9	0.7
Al ₂ O ₃	17.3	17.3	16.6	18.0	17.2	16.1	17.6	17.2	17.2
FeOt	5.8	-	5.6	6.3	6.3	7.0	5.7	7.2	5.8
MnO	0.10	0.10	0.10	0.12	0.12	0.12	0.11	0.13	0.11
MgO	5.4	5.4	5.2	4.0	5.2	7.3	4.2	6.4	5.4
CaO	6.5	6.4	6.5	6.8	7.7	7.5	6.8	8.0	6.7
Na ₂ O	5.4	5.4	5.2	4.0	5.2	7.3	4.3	3.7	4.2
K ₂ O	1.1	1.2	1.1	1.1	0.9	0.8	1.1	0.8	1.1
P ₂ O ₅	0.18	0.19	0.15	0.19	0.16	0.17	0.19	0.9	1.0
L.O.I.	0.7	-	1.2	0.7	0.4	2.0	0.7	0.9	1.0
Total	99.82	99.16	99.82	100.23	99.66	99.19	100.17	100.06	100.44
V	139	123	145	158	169	131	145	198	145
Cr	140	121	144	25	104	322	75	194	234
Co	23	19	21	18	23	28	21	29	20
Ni	62	62	56	15	15	86	41	57	76
Cu	29	38	35	17	13	49	40	36	22
Zn	61	94	62	65	69	64	63	77	65
Rb	11	-	12	13	11	7	16	11	12
Sr	648	658	648	561	512	563	551	676	627
Y	14	16	14	18	17	18	17	21	15
Zr	124	110	120	131	107	144	138	134	120
Nb	3	-	5	3	5	3	5	4	5
Ba	463	-	428	438	352	223	494	382	418

Table 14 Whole-rock trace element ICP-MS data

Sample: Unit: Age (yrs B.P.)	VF97-13B Y 4400	VF95-06Y Y 4400	VF95-09X Y 4400	VF97-06D Y 4400	VF98-02Y Y 4400	Vf99-05Yi Y 4400	VF99-05Ys Y 4400	VF01-01X Y 4400	VF97-05B Y 4400	VF95-06W W 4500	VF01-01V W 4500
Sc	15.8	8.1	6.6	9.6	9.7	8.2	9.9	10.0	8.4	17.5	21.9
Rb	19.1	13.5	17.3	16.5	14.4	15.8	13.5	12.9	19.2	12.5	11.7
Sr	630	663	631	702	673	644	665	663	695	611	600
Y	17.22	14.93	15.85	15.32	16.09	17.11	16.22	17.19	14.25	15.31	16.07
Zr	-	-	-	-	-	-	-	144	-	-	104
Nb	3.14	3.36	3.67	3.21	3.53	3.70	3.58	3.56	3.09	3.06	2.90
Cs	0.50	0.43	0.52	0.54	0.45	0.52	0.44	0.40	0.55	0.37	0.48
Ba	516	434	548	526	458	521	461	419	542	414	399
La	12.42	14.13	15.63	14.22	15.49	16.54	14.34	15.60	14.09	11.23	10.77
Ce	24.90	28.69	30.19	28.50	30.29	32.26	28.95	31.45	27.48	23.20	22.58
Pr	3.15	3.65	3.80	3.54	3.82	4.15	3.76	4.10	3.35	2.89	2.97
Nd	14.17	14.60	15.96	15.28	16.29	17.26	15.85	16.97	14.39	12.68	12.89
Sm	3.44	3.21	3.36	3.25	3.64	3.71	3.56	3.92	3.10	3.14	3.13
Eu	1.11	0.99	1.06	1.01	1.08	1.10	1.13	1.11	0.99	1.03	1.02
Gd	3.29	2.78	3.06	2.79	3.12	3.24	3.21	3.40	2.64	2.85	3.07
Tb	0.52	0.45	0.47	0.45	0.50	0.52	0.51	0.52	0.42	0.46	0.49
Dy	3.25	2.74	2.83	2.61	2.89	3.08	3.04	3.11	2.54	2.92	2.92
Ho	0.66	0.56	0.56	0.55	0.61	0.62	0.62	0.63	0.51	0.60	0.59
Er	1.82	1.56	1.62	1.56	1.69	1.72	1.70	1.75	1.45	1.57	1.65
Tm	0.27	0.23	0.25	0.24	0.25	0.26	0.25	0.26	0.22	0.24	0.23
Yb	1.67	1.50	1.57	1.46	1.59	1.73	1.64	1.71	1.43	1.50	1.54
Lu	0.26	0.25	0.26	0.24	0.26	0.28	0.27	0.27	0.23	0.24	0.24
Hf	3.11	3.47	3.88	3.42	3.76	4.10	3.82	3.84	3.25	3.10	2.89
Ta	0.24	0.24	0.26	0.23	0.25	0.28	0.25	0.25	0.23	0.22	0.20
Pb	5.80	7.22	8.19	7.03	7.78	7.62	7.19	8.34	6.98	6.20	5.26
Th	1.81	2.10	2.37	1.95	2.21	2.45	2.23	2.20	2.03	1.67	1.54
U	0.64	0.73	0.83	0.71	0.77	0.82	0.76	0.82	0.71	0.57	0.52

Sample:	VF97-06B	VF98-02W	VF99-05W	VF98-02U	VF95-06U	VF10-04U	VF95-09V	VF97-20Q	VF10-01U	VF10-02U	VF10-03U
Unit:	W	W	W	U	U	U	U	U	U	U	U
Age (yrs B.P.)	4500	4500	4500	4700	4700	4700	4700	4700	4700	4700	4700
Sc	22.1	15.5	26.3	25.0	24.5	-	16.1	20.4	-	-	-
Rb	13.0	13.2	10.3	11.3	10.1	9.9	13.4	17.0	12.7	9.1	10.1
Sr	663	621	626	636	630	-	608	594	-	-	-
Y	16.62	14.88	16.69	16.66	16.65	-	15.60	16.83	-	-	-
Zr	-	-	-	-	-	-	-	-	-	-	-
Nb	3.33	2.91	3.98	3.85	4.06	8.57	2.92	3.31	3.91	4.66	4.40
Cs	0.35	0.41	0.30	0.31	0.28	0.37	0.41	0.50	0.48	0.44	0.38
Ba	408	412	351	356	335	-	428	433	-	-	-
La	12.00	10.61	10.23	9.96	9.83	15.10	11.17	11.49	11.82	10.74	10.58
Ce	24.73	23.06	22.61	20.89	21.47	29.91	23.93	24.40	25.16	22.36	22.82
Pr	3.24	3.00	2.90	2.81	2.83	4.26	3.09	3.06	3.56	3.10	3.15
Nd	14.52	12.23	12.99	12.85	12.69	18.51	13.12	13.03	15.99	14.20	14.07
Sm	3.73	2.89	3.34	3.10	3.12	3.94	3.14	3.39	3.66	3.42	3.42
Eu	1.20	0.90	1.11	1.03	1.04	1.07	0.96	1.08	1.14	1.04	1.00
Gd	3.37	2.78	3.23	2.96	3.09	3.16	2.96	3.08	3.28	2.92	2.91
Tb	0.54	0.46	0.52	0.49	0.50	0.53	0.48	0.51	0.54	0.51	0.53
Dy	3.28	2.66	3.11	2.82	2.92	2.72	2.90	3.23	2.78	2.73	2.66
Ho	0.67	0.58	0.64	0.59	0.61	0.55	0.60	0.68	0.56	0.56	0.55
Er	1.73	1.63	1.69	1.66	1.65	1.49	1.65	1.83	1.52	1.52	1.49
Tm	0.24	0.23	0.25	0.24	0.24	0.24	0.24	0.25	0.23	0.24	0.23
Yb	1.56	1.47	1.56	1.43	1.51	1.74	1.51	1.70	1.54	1.59	1.62
Lu	0.25	0.23	0.25	0.24	0.24	0.24	0.24	0.26	0.22	0.22	0.24
Hf	2.84	2.77	2.86	2.69	2.88	4.08	3.05	2.93	2.72	3.00	2.62
Ta	0.23	0.19	0.28	0.25	0.27	0.28	0.21	0.24	0.24	0.30	0.28
Pb	5.47	5.57	4.57	4.49	4.66	-	5.86	5.64	-	-	-
Th	1.47	1.61	1.43	1.25	1.40	2.12	1.70	1.52	1.72	1.38	1.30
U	0.54	0.59	0.51	0.47	0.49	0.55	0.62	0.56	0.39	0.38	0.41

Sample:	VF10-07U	VF01-01T	VF01-10J	VF95-09T	VF97-03BR	VF01-10H	VF95-06P	VF98-10S	VF10-01S	VF10-02S	VF10-03S
Unit:	U	U	U	S	S	S	S	S	S	S	S
Age (yrs B.P.)	4700	4700	4700	5500	5500	5500	5500	5500	5500	5500	5500
Sc	-	27.0	25.8	24.8	18.9	21.7	19.5	20.1	-	-	-
Rb	10.3	7.1	9.7	12.0	12.7	11.6	11.4	12.4	11.4	12.8	15.5
Sr	-	602	628	602	629	661	639	662	-	-	-
Y	-	17.19	16.71	16.13	16.03	17.44	15.97	16.24	-	-	-
Zr	-	104	101	-	-	105	-	-	-	-	-
Nb	5.21	4.14	4.06	4.09	2.94	3.92	3.16	2.99	4.40	13.29	3.58
Cs	0.35	0.23	0.33	0.32	0.43	0.31	0.30	0.33	0.43	0.68	0.61
Ba	-	290	335	385	456	360	359	371	-	-	-
La	10.76	11.16	10.97	11.07	9.83	11.82	10.89	10.40	10.41	10.48	11.61
Ce	23.11	22.94	21.53	23.66	20.61	24.50	24.23	22.74	22.57	21.37	23.96
Pr	3.25	3.06	3.00	2.90	2.66	3.23	3.16	3.20	3.02	3.08	3.17
Nd	14.47	13.85	13.29	12.87	11.55	14.61	13.66	13.46	13.64	13.61	13.64
Sm	3.37	3.51	3.34	3.33	2.96	3.71	3.44	3.22	3.31	3.26	3.10
Eu	1.00	1.15	1.07	1.08	1.00	1.18	1.13	1.05	0.96	0.96	0.88
Gd	2.98	3.29	3.20	3.26	2.91	3.56	3.11	2.97	2.89	2.83	2.67
Tb	0.50	0.53	0.51	0.50	0.48	0.55	0.52	0.52	0.49	0.48	0.45
Dy	2.59	3.20	3.11	3.23	2.90	3.24	2.97	2.81	2.55	2.48	2.38
Ho	0.60	0.66	0.62	0.65	0.59	0.64	0.62	0.61	0.54	0.53	0.49
Er	1.49	1.78	1.70	1.70	1.61	1.72	1.65	1.67	1.45	1.44	1.34
Tm	0.24	0.26	0.25	0.25	0.23	0.25	0.23	0.23	0.22	0.21	0.21
Yb	1.59	1.60	1.57	1.62	1.46	1.58	1.51	1.43	1.61	1.53	1.47
Lu	0.22	0.26	0.25	0.25	0.22	0.24	0.23	0.23	0.22	0.22	0.21
Hf	1.98	2.93	2.83	2.85	2.80	2.91	2.59	2.47	2.56	2.73	3.13
Ta	0.29	0.28	0.26	0.29	0.21	0.26	0.21	0.20	0.29	0.58	0.28
Pb	-	50.9	5.06	4.52	4.83	5.30	4.93	4.66	-	-	-
Th	1.36	1.35	1.33	1.35	1.30	1.41	1.47	1.20	1.42	1.67	1.78
U	0.31	0.49	0.50	0.49	0.49	0.53	0.55	0.49	0.53	0.41	0.54

Sample:	VF97-200	VF97-03BP	VF98-10Q	VF10-02P	VF10-01P	VF95-06M	VF10-04M	VF10-04N	VF95-06N	VF10-07B	VF97-01G
Unit:	S	P	P	P	P	P	P	P	P	L	L
Age (yrs B.P.)	5500	6000	6000	6000	6000	6000	6000	6000	6000	7500	7500
Sc	20.7	20.8	19.5	-	-	14.7	-	-	17.5	-	18.5
Rb	11.6	12.2	14.5	14.3	11.3	14.3	15.5	11.4	12.2	13.9	14.9
Sr	636	582	635	-	-	585	-	-	628	-	607
Y	15.88	14.21	16.13	-	-	13.78	-	-	15.66	-	14.75
Zr	-	-	-	-	-	-	-	-	-	-	-
Nb	3.20	2.44	2.96	3.19	3.42	2.92	2.97	3.27	2.90	2.74	2.86
Cs	0.32	0.40	0.47	0.58	0.44	0.49	0.54	0.43	0.41	0.51	0.47
Ba	374	411	463	-	-	434	-	-	397	-	483
La	11.52	8.91	9.39	10.78	11.18	10.32	10.95	8.93	9.33	8.82	9.73
Ce	24.03	19.14	20.12	23.01	23.34	21.76	21.97	19.71	19.75	18.29	20.50
Pr	3.27	2.44	2.62	3.17	3.26	2.74	2.81	2.67	2.54	2.51	2.58
Nd	13.93	10.80	11.70	14.32	14.75	11.68	11.96	11.93	11.37	11.09	11.50
Sm	3.63	2.69	2.90	3.40	3.50	2.67	2.74	2.92	2.81	2.69	2.91
Eu	1.11	0.95	0.99	1.75	1.03	0.83	0.79	0.87	0.92	0.81	0.94
Gd	3.10	2.73	2.91	2.93	3.01	2.47	2.26	2.64	2.72	2.38	2.77
Tb	0.52	0.43	0.47	0.51	0.50	0.40	0.40	0.44	0.46	0.41	0.47
Dy	3.08	2.60	2.83	2.73	2.69	2.43	2.10	2.40	2.75	2.12	2.84
Ho	0.65	0.52	0.57	0.57	0.54	0.50	0.42	0.51	0.59	0.43	0.58
Er	1.69	1.41	1.63	1.51	1.43	1.39	1.18	1.35	1.59	1.15	1.51
Tm	0.23	0.20	0.24	0.2	0.23	0.20	0.18	0.21	0.22	0.18	0.22
Yb	1.54	1.28	1.41	1.70	1.49	1.32	1.29	1.53	1.40	1.30	1.37
Lu	0.23	0.20	0.23	0.24	0.22	0.22	0.21	0.20	0.23	0.18	0.22
Hf	2.61	2.73	2.81	2.97	2.57	3.33	3.08	2.71	2.75	2.70	2.89
Ta	0.22	0.17	0.20	0.23	0.30	0.21	0.23	0.23	0.20	0.22	0.20
Pb	4.94	5.01	5.31	-	-	6.95	-	-	5.25	-	5.39
Th	1.34	1.29	1.25	1.66	1.33	2.11	1.86	1.22	1.44	1.15	1.53
U	0.50	0.47	0.48	0.50	0.67	0.73	0.54	0.53	0.55	0.39	0.65

Sample:	VF10-03M2	VF95-09E	VF00-06T1	VF00-06T3	VF97-01F	VF10-03L	VF97-03AE	VF97-01Ds	VF97-01Di	VF00-06R	VF97-03AC
Unit:	L	L	J	J	J	J	J	H	H	H	H
Age (yrs B.P.)	7500	7500	7700	7700	7700	7700	7700	10,000	10,000	10,000	10,000
Sc	-	17.1	18.3	21.0	16.9	-	21.6	21.6	27.3	29.5	19.1
Rb	13.9	12.6	13.9	13.1	15.5	12.6	12.7	12.9	11.9	7.7	12.7
Sr	-	612	646	658	627	-	651	563	519	561	594
Y	-	12.81	13.97	14.85	15.35	-	15.00	19.08	16.89	17.69	14.20
Zr	-	-	98	97	-	-	-	-	-	101	-
Nb	2.88	2.67	2.67	2.65	3.29	3.27	2.62	3.35	2.63	2.15	2.64
Cs	0.60	0.45	0.48	0.42	0.46	0.63	0.42	0.43	0.34	0.21	0.38
Ba	-	570	481	444	485	-	432	436	353	251	411
La	8.46	8.58	10.02	9.79	11.15	10.25	9.35	11.17	8.74	10.12	9.99
Ce	18.12	17.50	20.27	20.03	23.14	21.62	18.70	23.33	18.73	20.92	19.60
Pr	2.41	2.28	2.58	2.64	2.93	2.98	2.53	3.04	2.51	3.06	2.60
Nd	10.64	10.03	11.21	11.74	12.73	13.16	11.12	13.65	11.12	14.21	11.38
Sm	2.56	2.60	2.80	3.03	3.10	3.28	2.90	3.53	3.11	3.67	2.91
Eu	0.85	0.85	0.90	0.96	0.98	0.92	0.94	1.08	1.00	1.19	1.01
Gd	2.24	2.50	2.68	2.91	2.85	2.78	2.76	3.54	3.10	3.59	2.80
Tb	0.40	0.40	0.42	0.47	0.47	0.48	0.45	0.57	0.52	0.57	0.46
Dy	1.97	2.37	2.58	2.73	2.85	2.54	2.58	3.56	3.20	3.40	2.82
Ho	0.40	0.49	0.51	0.55	0.59	0.51	0.54	0.74	0.66	0.68	0.57
Er	1.14	1.29	1.39	1.51	1.57	1.38	1.41	1.97	1.81	1.81	1.53
Tm	0.17	0.19	0.20	0.22	0.23	0.21	0.20	0.28	0.26	0.26	0.22
Yb	1.13	1.16	1.25	1.37	1.42	1.44	1.32	1.78	1.67	1.63	1.41
Lu	0.17	0.18	0.20	0.21	0.23	0.21	0.21	0.29	0.26	0.25	0.22
Hf	2.57	2.77	2.64	2.74	2.97	2.73	2.60	2.96	2.62	2.85	2.78
Ta	0.20	0.20	0.19	0.20	0.23	0.23	0.18	0.23	0.19	0.14	0.19
Pb	-	5.91	6.04	5.92	5.09	-	5.16	5.54	5.29	4.84	6.29
Th	1.0	1.19	1.24	1.17	1.67	0.97	1.19	1.32	0.99	1.33	1.22
U	0.28	0.51	0.48	0.48	0.65	0.44	0.47	0.56	0.38	0.49	0.46

Table 15 Whole-rock trace element INAA data

Sample: Unit: Age (yrs B.P.)	VF97-13B Y 4400	VF95-06Y Y 4400	VF95-09X Y 4400	VF97-06D Y 4400	VF98-02Y Y 4400	VF97-05B Y 4400	VF95-06W W 4500	VF97-06B W 4500	VF98-02W W 4500	VF98-02U U 4700	VF95-06U U 4700
Sc	13.0	7.5	6.0	7.3	7.8	6.5	15.5	18.4	14.6	21.9	21.3
Cr	60	20	10	18	19	14	94	122	86	184	176
Co	15.4	11.5	9.1	11.7	12.5	10.9	20.1	24.0	19.0	25.7	26.3
Ni	18	12	5	8	3	13	50	40	40	90	70
Zn	67	62	63	65	65	70	65	57	67	53	48
As	1.0	1.5	1.4	0.8	1.7	1.3	1.5	0.7	0.7	0.8	0.9
Se	0.0	0.0	0.1	0.0	0.1	0.0	0.0	0.0	0.0	0.5	0.5
Br	2.0	9.1	3.1	2.8	5.4	2.0	3.4	1.7	3.7	1.6	4.0
Rb	20	15	18	18	13	18	14	15	14	13	10
Sr	660	660	638	710	700	710	630	640	630	630	630
Zr	129	160	173	129	146	127	110	90	100	130	130
Ag	0.0	0.0	0.0	0.0	0.0	0.0	0.0	0.0	0.0	0.0	0.0
Sb	0.19	0.21	0.20	0.20	0.19	0.21	0.15	0.12	0.18	0.11	0.14
Cs	0.44	0.43	0.53	0.49	0.40	0.54	0.39	0.34	0.41	0.32	0.25
Ba	480	439	533	494	425	542	411	398	441	372	329
La	11.9	14.0	15.4	13.9	14.6	14.0	10.7	11.3	11.1	10.2	10.2
Ce	25.8	29.5	31.5	29.9	30.6	29.3	23.5	25.7	24.4	23.6	22.9
Nd	14	14	18	13	17	16	11	14	15	15	11
Sm	3.31	3.28	3.42	3.14	3.45	3.06	2.99	3.51	3.05	3.17	3.12
Eu	0.98	0.94	0.96	0.90	0.96	0.92	0.95	1.10	0.91	0.96	0.98
Tb	0.47	0.41	0.43	0.39	0.42	0.39	0.42	0.51	0.42	0.45	0.44
Yb	1.66	1.53	1.61	1.47	1.58	1.42	1.45	1.48	1.51	1.49	1.50
Lu	0.259	0.236	0.249	0.226	0.245	0.228	0.221	0.230	0.226	0.231	0.236
Hf	3.18	3.75	3.92	3.43	3.75	3.38	3.17	2.92	3.21	2.85	2.94
Ta	0.21	0.23	0.25	0.21	0.22	0.19	0.20	0.20	0.21	0.25	0.26
W	0.0	0.1	0.1	0.0	0.0	0.0	0.0	0.3	0.4	0.4	1.0
Au	39.0	1.4	1.9	0.0	1.2	1.0	0.0	55.0	1.4	2.0	106.0
Th	1.59	2.01	2.12	1.80	2.00	1.79	1.50	1.28	1.54	1.23	1.33
U	0.58	0.71	0.73	0.77	0.83	0.76	0.62	0.61	0.67	0.47	0.60

Sample:	VF95-09V	97-20Q	VF95-09T	VF95-06P	VF98-10S	VF97-20O	VF98-10Q	VF95-06M	VF95-06N
Unit:	U	U	S	S	S	S	P	P	P
Age (yrs B.P.)	4700	4700	5500	5500	5500	5500	6000	6000	6000
Sc	14.9	17.8	21.4	18.7	19.0	19.0	16.7	13.0	15.8
Cr	90	67	187	121	138	130	96	104	82
Co	19.0	20.1	26.0	24.6	25.0	24.5	20.9	15.8	19.4
Ni	28	30	90	50	60	50	30	40	20
Zn	73	69	51	60	59	74	71	55	60
As	0.8	1.3	1.0	0.8	0.8	0.7	1.2	1.7	1.3
Se	0.0	0.0	0.0	0.0	0.0	0.0	0.0	0.0	0.0
Br	2.6	2.1	1.9	2.2	1.4	1.8	2.0	3.6	2.2
Rb	14	17	12	11	14	13	14	15	14
Sr	630	570	620	680	630	630	590	580	650
Zr	110	130	110	120	100	90	100	130	102
Ag	0.0	0.0	0.0	0.0	0.0	0.0	0.0	0.0	0.0
Sb	0.17	0.17	0.19	0.14	0.13	0.11	0.19	10.25	0.20
Cs	0.42	0.51	0.31	0.29	0.30	0.29	0.43	0.51	0.40
Ba	417	408	366	380	392	370	452	449	421
La	11.4	11.0	10.3	11.2	11.1	11.2	9.5	10.5	9.7
Ce	25.0	24.5	23.5	25.1	24.5	25.3	21.6	22.4	21.1
Nd	16	14	14	16	13	13	14	14	12
Sm	3.16	3.16	3.13	3.55	3.47	3.74	2.91	2.74	2.90
Eu	0.95	0.99	0.97	1.07	1.06	1.09	0.91	0.79	0.94
Tb	0.44	0.49	0.42	0.49	0.48	0.50	0.43	0.37	0.41
Yb	1.56	1.60	1.49	1.49	1.48	1.50	1.47	1.32	1.47
Lu	0.241	0.249	0.223	0.232	0.222	0.223	0.230	0.199	0.225
Hf	3.26	3.15	2.86	2.86	2.86	2.81	2.94	3.50	2.99
Ta	0.20	0.22	0.27	0.21	0.18	0.19	0.19	0.19	0.19
W	0.0	0.0	4.0	0.2	0.0	0.0	0.0	0.0	0.4
Au	0.5	3.0	0.0	0.0	0.0	1.6	3.0	1.4	0.0
Th	1.56	1.38	1.28	1.27	1.24	1.32	1.19	1.77	1.21
U	0.66	0.60	0.57	0.51	0.58	0.50	0.53	0.74	0.50

Appendix F: Sr and Nd Analytical Procedure

A total of 55 $^{87}\text{Sr}/^{86}\text{Sr}$ and 31 $^{143}\text{Nd}/^{144}\text{Nd}$ ratio analyses were carried out for the Group I and II CVC eruption deposits on the Thermo Scientific TRITON thermal ionisation mass spectrometer (TIMS) at the University of Leeds. Powdered samples were digested in a mixture of Hydrofluoric acid (HF) and Nitric acid (HNO_3) before chemical separation in cation-exchange columns. The Sr fraction was collected first, and evaporated ready for loading onto a metal (W) filament for analysis on the TIMS. Nd together with the REE were then collected, and Nd was separated through two further sets of cation-exchange columns. The Nd fraction was then evaporated, and the residue loaded onto a metal (Re) filament ready for TIMS analysis. The procedure is outlined below.

Sample Preparation

Samples were prepared by dissolving 0.05g whole-rock powder (see Appendix C for powdering procedure) in a 3:1 HF: HNO_3 mixture of 1.5ml concentrated HF and 0.5 ml concentrated HNO_3 in 15ml Teflon jars to digest the silicates in the samples. The lids of the beaker were tightly screwed on and the beakers left on a hot plate in a fume cupboard overnight to dissolve.

Once dissolved, the beakers were opened and put back on the hot plate to evaporate the solution. Once evaporated, 1ml HNO_3 was added and evaporated, which was repeated with 0.5ml HNO_3 . The next step was to add 1ml of 6M HCl to the sample and evaporate to convert the sample cack to chloride. Finally, the samples were dissolved in 2ml of 2.5M HCl ready for chemical separation. The cation exchange columns are conditioned with 2.5M HCl, therefore the samples need to be loaded in an HCl solution.

Sr-Rb Chemical Separation

The samples were divided, and 1ml of the samples in 2.5M HCl were passed through ion exchange columns containing BioRad AG50-X12 resin. The other half of the samples were kept for re-run. Once loaded, two rinses of 1ml of 2.5M HCl elutant were passed through the columns to wash the sample into the resin bed. Further rinses with increasing volumes of 2.5M HCl elute elements according to their partition coefficient in the resin, with the order: Fe, Na, Mg, K, Rb, Sr, Ba and REE (Dickin, 2005). Rb was stripped out by passing 27-30 ml of 2.5M HCl through the columns, with the amount depending on the column calibration. The Sr fraction from each of the samples was then collected in 11ml of 2.5M HCl and the solution was evaporated to dryness, ready for loading onto metal filaments. Finally, Nd and the rare earth elements (REE) were collected in 18 ml of 4.24M HCl.

Nd Chemical Separation

In order to separate Nd from the other REE, the samples were passed through another two sets of columns: REE anion exchange columns and LN-spec resin columns. The REE anion

exchange column is pre-conditioned with a 90/10 Acetic/Nitric mixture; therefore the samples must be loaded in an Acetic/Nitric mixture.

The HCl solution collected from the first set of columns was dried on the hotplate, and 1ml of concentrated HNO₃ was added and evaporated to convert the sample to nitrate. 5mls of 75/25 Acetic/Nitric mixture was added to the sample, and the whole lot was loaded on to the resin bed in the REE anion exchange columns. Once loaded, two rinses of 1ml of 90/10 Acetic/Nitric mixture were passed through the columns to wash the sample into the resin bed. 15mls of 90/10 Acetic/Nitric mixture was eluted, followed by 10mls of MeOH cocktail comprising 75% methanol, 10% acetic acid, 5% concentrated HNO₃ and 10% filtered water. The sample was then collected in 30mls of the MeOH cocktail.

The final set of columns separated Nd from the other REE. These are pre-conditioned in 0.25M HCl. The sample was dried on the hotplate and 1ml 6M HCl was added and evaporated to just dryness to convert back into chloride. Another 1ml 6M HCl was added and evaporated to a tiny drop which was then taken up in 250 microlites of 0.25M HCl and loaded onto the pre-conditioned LN-resin column. The columns are all calibrated individually; therefore different amounts of 0.25M HCl were eluted according to the calibrations. The Nd sample was collected in 2.5 mls 0.25M HCl and evaporated to dryness, ready for loading.

Sample Loading

The Sr samples were loaded onto to single Tungsten (W) wire filaments with a TaCl chloride solution. The TaCl solution was prepared at the start of lab work in 2009, and the same solution was used throughout for all the CVC samples.

The TaCl solution was added on to the filament incrementally and evaporated off. A drop of 2.5M HCl was added to the Sr samples, a third of which was then loaded directly onto the evaporated salt. The sample was also loaded incrementally, and evaporated between each layer, at ~1 amp of current. Once evaporated the sample was heated slowly by increasing the current up to 3.5 amps, followed by flashing the sample to ~4.2 amps twice before turning off the current.

The Nd samples were loaded on Rhenium (Re) wire double filaments in a drop of 10% HNO₃. Again the samples were loaded in increments and dried in between. The samples were slowly heated until they glowed red (up to ~3.5 A) for 10 seconds, before turning off the current. The Re filaments were loaded as doubles; the evaporation filament with the sample, and the ionisation filament with no sample.

Analytical Precision

Samples were run on the Thermo Scientific TRITON TIMS at the University of Leeds. For $^{87}\text{Sr}/^{86}\text{Sr}$ analysis, the TIMS was run at between 3 and 5V on ^{87}Sr , and ratios were recorded to 2σ error on 200 ratios. The analytical precision for the 200 runs was 10^{-6} .

For $^{143}\text{Nd}/^{144}\text{Nd}$ analysis, the TIMS was run at 0.2 to 0.9 V on ^{144}Nd , and 240 ratios were recorded at 2σ error. The analytical precision was 10^{-6} .

The external precision was checked by analysing NBS-987 and La Jolla standards, for Sr and Nd, respectively, with every run on the TIMS throughout the duration of the project. The literature value for NBS-987 is 0.710248 (Thirlwall, 1991), and the La Jolla value is 0.51185 (Thirlwall, 1991). The NBS-987 standard analyses averaged 0.710262 ± 5 over 58 runs between September 2010, and the La Jolla standard analyses averaged 0.511842 ± 6 over 23 runs between August 2011 and July 2012. The values are shown in the Figure 1 below. The analyses for the CVC samples were corrected accordingly.

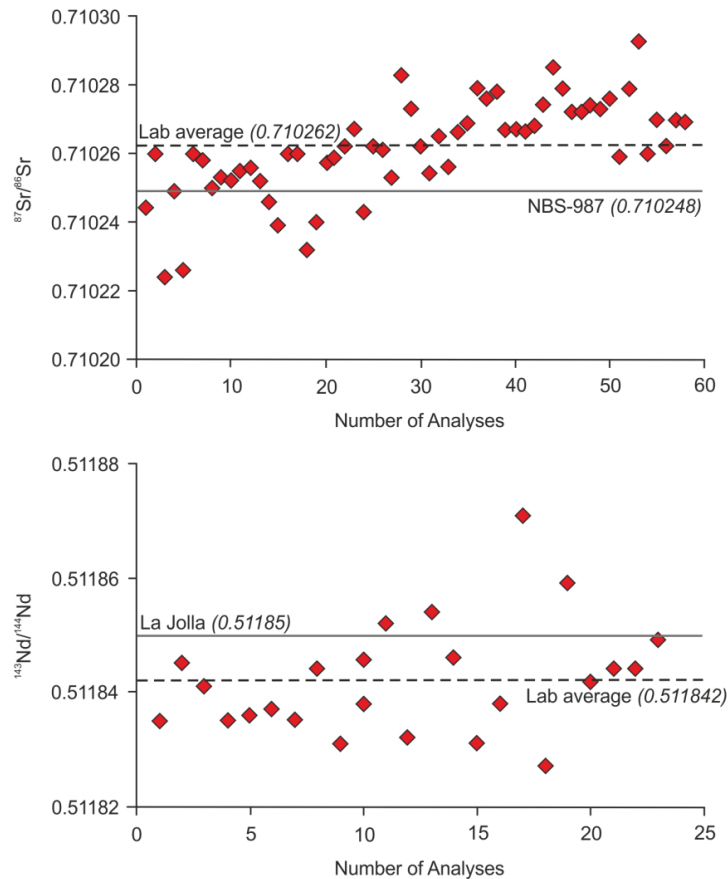


Figure 1. Results of NBS-987 and La Jolla standards run between September 2010 and July 2012. Internal error is within symbol size. Also shown are the lab average and literature values after Thirlwall (1991).

Appendix G: Group II Electron Microprobe Mineral Chemistry Data

Table 16 Plagioclase

Sample	VF10-03N	VF10-03N	VF10-03N	VF10-07D	VF10-07D	VF10-07D	VF10-07D	VF10-07D	VF10-07D	VF10-07D	VF95-09G	VF95-09G	VF95-09G
Core/rim	plag 1	plag 2	plag 3	plag 1	plag 1	plag 2	plag 2	plag 3	plag 3	plag 3	plag 1	plag 2	plag 3
Unit	N	N	N	N	N	N	N	N	N	N	N	N	N
Age	7000	7000	7000	7000	7000	7000	7000	7000	7000	7000	7000	7000	7000
SiO ₂	53.11	52.54	53.83	51.91	52.70	54.31	54.80	52.99	54.81	53.77	53.88	52.19	
TiO ₂	-	-	-	0.02	0.03	0.05	0.09	0.05	0.08	0.07	0.09	0.08	
Al ₂ O ₃	29.42	29.50	28.52	30.13	29.76	28.33	28.05	29.18	28.04	29.16	29.25	30.12	
Fe ₂ O ₃	0.78	0.94	0.87	0.60	0.63	0.95	1.00	0.90	0.92	0.84	0.91	0.86	
MnO	0.05	0.02	0.00	0.04	0.00	0.00	0.00	0.04	0.04	0.05	0.01	0.00	
MgO	0.06	0.11	0.05	0.08	0.09	0.05	0.10	0.10	0.07	0.06	0.10	0.08	
CaO	11.42	11.89	10.87	13.24	12.63	11.22	10.58	11.75	10.73	11.26	11.56	12.64	
Na ₂ O	4.72	4.44	5.06	4.03	4.30	4.96	5.24	4.66	5.12	5.04	4.96	4.48	
K ₂ O	0.26	0.23	0.32	0.12	0.15	0.30	0.36	0.25	0.31	0.30	0.27	0.23	
TOTAL	99.81	99.67	99.52	100.17	100.28	100.20	100.24	99.91	100.14	100.54	101.02	100.67	
An	56	59	53	64	61	55	52	57	53	54	55	60	

Sample	VF10-03N	VF10-03N	VF10-03N	VF10-03N	VF10-03N	VF10-03N	VF10-03N	VF10-03N	VF10-03N	VF10-03N	VF10-03N	VF10-03N	VF10-03N
Core/rim	plag 1	plag 1	plag 1	plag 1	plag 2	plag 2	plag 2	plag 2	plag 2	plag 3	plag 3	plag 3	plag 3
Unit	N	N	N	N	N	N	N	N	N	N	N	N	N
Age	7000	7000	7000	7000	7000	7000	7000	7000	7000	7000	7000	7000	7000
SiO ₂	51.68	52.56	52.55	51.68	51.39	53.68	54.49	53.72	54.38	55.42	54.77	53.36	
TiO ₂	-	-	-	-	-	-	-	-	-	-	-	-	
Al ₂ O ₃	30.29	29.45	29.96	29.71	29.42	29.00	28.49	28.39	28.45	27.28	28.09	28.63	
Fe ₂ O ₃	0.69	0.67	0.71	0.71	1.05	0.64	0.79	0.73	0.85	0.84	0.76	0.81	
MnO	0.00	0.00	0.00	0.00	0.00	0.00	0.02	0.00	0.00	0.00	0.00	0.04	
MgO	0.11	0.06	0.08	0.07	0.12	0.10	0.04	0.09	0.10	0.15	0.06	0.04	
CaO	12.67	11.85	12.04	12.38	11.84	11.21	10.70	10.46	10.65	9.82	10.26	11.15	
Na ₂ O	4.19	4.33	4.22	4.14	4.16	4.79	5.20	5.32	5.15	5.74	5.54	5.07	
K ₂ O	0.22	0.28	0.28	0.27	0.25	0.29	0.32	0.32	0.30	0.46	0.35	0.29	
TOTAL	99.85	99.21	99.83	98.96	98.25	99.69	100.05	99.03	99.88	99.70	99.82	99.40	
An	62	59	60	61	60	55	52	51	52	47	50	54	

Sample Core/rim	VF10-07D	VF10-07D	VF10-07D	VF10-07D	VF10-07D	VF10-07D	VF95-09G	VF95-09G	VF95-09G	VF95-09G	VF95-09G	VF95-09G
	plag 1	plag 1	plag 2	plag 2	plag 3	plag 3	plag 1	plag 1	plag 1	plag 1	plag 3	plag 3
	rim	rim	rim	rim	rim	rim	rim	rim	rim	rim	rim	rim
	Unit	N	N	N	N	N	N	N	N	N	N	N
Age	7000	7000	7000	7000	7000	7000	7000	7000	7000	7000	7000	7000
SiO ₂	51.53	52.11	54.47	54.90	53.96	52.00	53.95	54.48	54.24	54.67	53.92	54.04
TiO ₂	0.03	0.00	0.17	0.14	0.28	0.06	0.06	0.08	0.09	0.06	0.05	0.06
Al ₂ O ₃	30.14	30.25	27.29	27.36	26.46	30.06	28.50	29.06	28.72	28.53	28.79	28.59
Fe ₂ O ₃	0.79	0.71	1.28	1.26	1.84	0.86	0.75	0.81	0.82	0.76	0.70	0.82
MnO	0.00	0.00	0.05	0.02	0.00	0.00	0.00	0.03	0.00	0.02	0.02	0.00
MgO	0.07	0.06	0.36	0.22	0.36	0.12	0.07	0.12	0.06	0.09	0.13	0.06
CaO	13.32	13.27	10.75	10.55	10.96	12.91	10.67	10.77	10.82	10.55	11.00	11.02
Na ₂ O	3.89	3.84	4.93	4.91	4.04	3.98	5.22	5.26	5.11	5.40	5.10	4.98
K ₂ O	0.20	0.22	0.61	0.49	0.61	0.29	0.31	0.30	0.31	0.33	0.29	0.29
TOTAL	100.02	100.48	100.01	99.95	98.64	100.32	99.54	100.90	100.18	100.41	100.00	99.85
An	65	65	53	53	58	63	52	52	53	51	53	54

Sample Core/rim	VF95-09G	VF00-06P	VF00-06P	VF00-06P	VF01-02Ps	VF01-02Ps	VF01-02Ps	VF01-02Ps	VF02-01G	VF02-01G	VF02-01G	VF02-01G
	plag 3	plag 1	plag 2	plag 3	plag 1	plag 2	plag 4	plag 4	plag 1	plag 1	plag 2	plag 3
	rim	core	core	core	core	core	core	core	core	core	core	core
	Unit	N	F	F	F	F	F	F	F	F	F	F
Age	7000	12,000	12,000	12,000	12,000	12,000	12,000	12,000	12,000	12,000	12,000	12,000
SiO ₂	54.09	52.99	52.97	55.55	53.96	51.36	53.96	55.33	57.25	57.17	55.11	54.21
TiO ₂	0.09	0.04	0.05	0.07	0.06	0.03	0.03	0.00	0.01	0.02	0.07	0.07
Al ₂ O ₃	28.57	29.36	28.79	26.51	27.98	29.56	29.32	27.95	26.85	26.66	28.25	27.68
Fe ₂ O ₃	0.76	0.70	1.02	0.90	1.18	1.04	0.32	0.33	0.24	0.21	0.52	1.06
MnO	0.02	0.02	0.01	0.00	0.00	0.00	0.01	0.00	0.02	0.00	0.00	0.00
MgO	0.06	0.05	0.09	0.12	0.10	0.09	0.00	0.04	0.01	0.01	0.03	0.09
CaO	10.67	12.16	11.69	9.22	10.65	12.45	12.01	10.33	8.91	8.85	10.95	10.13
Na ₂ O	5.21	4.50	4.34	5.52	4.62	3.87	4.88	5.48	6.68	6.54	5.36	5.04
K ₂ O	0.31	0.43	0.59	0.84	0.61	0.47	0.29	0.48	0.17	0.17	0.22	0.84
TOTAL	99.79	100.26	99.55	98.73	99.16	98.87	100.82	99.95	100.14	99.62	100.51	99.13
An	52	58	58	46	54	62	57	50	42	42	52	50

Sample Core/rim Unit Age	VF00-06P plag 1 rim F 12,000	VF00-06P plag 2 rim F 12,000	VF00-06P plag 2 rim F 12,000	VF00-06P plag 2 rim F 12,000	VF00-06P plag 3 rim F 12,000	VF01-02Ps plag 1 rim F 12,000	VF01-02Ps plag 2 rim F 12,000	VF01-02Ps plag 4 rim F 12,000	VF02-01G plag 2 rim F 12,000	VF02-01G plag 3 rim F 12,000	VF00-06O plag 1 core D 13,000	VF00-06O plag 1 core D 13,000
SiO ₂	53.52	52.55	52.96	53.52	54.41	52.59	52.00	52.92	55.42	54.78	55.61	55.62
TiO ₂	0.08	0.06	0.11	0.07	0.13	0.30	0.06	0.07	0.05	0.10	0.04	0.04
Al ₂ O ₃	28.20	28.55	28.86	28.07	27.79	23.82	29.20	28.78	27.29	26.97	26.92	26.99
Fe ₂ O ₃	0.93	1.01	0.94	0.97	0.99	2.68	1.05	0.88	0.74	1.35	0.59	0.55
MnO	0.02	0.03	0.01	0.03	0.02	0.05	0.00	0.03	0.01	0.00	0.03	0.00
MgO	0.07	0.09	0.12	0.09	0.12	0.70	0.11	0.10	0.07	0.12	0.06	0.04
CaO	10.82	11.40	11.53	10.53	10.15	8.32	11.84	11.00	9.91	9.59	10.30	10.38
Na ₂ O	4.61	4.53	4.38	4.70	5.01	5.30	4.23	4.68	5.37	5.16	5.50	5.62
K ₂ O	0.61	0.61	0.64	0.70	0.76	1.01	0.49	0.59	0.69	0.91	0.25	0.23
TOTAL	98.85	98.84	99.57	98.68	99.38	94.77	98.99	99.04	99.55	98.98	99.29	99.46
An	54	56	57	53	50	44	59	55	48	48	50	50

Sample Core/rim Unit Age	VF00-06O plag 2 core D 13,000	VF00-06O plag 3 core D 13,000	VF00-06O plag 3 core D 13,000	VF00-06O plag 3 core D 13,000	VF00-06O plag 3 core D 13,000	VF00-06O plag 3 core D 13,000	VF00-06O plag 3 core D 13,000	VF01-02Ns plag 1 core D 13,000	VF01-02Ns plag 1 core D 13,000	VF01-02Ns plag 1 core D 13,000	VF01-02Ns plag 1 core D 13,000	VF01-02Ns plag 1 core D 13,000
SiO ₂	54.81	55.71	55.45	55.33	56.74	57.24	54.65	50.29	51.23	59.99	59.72	59.76
TiO ₂	0.03	0.04	0.02	0.03	0.01	0.02	0.01	0.05	0.04	0.05	0.07	0.07
Al ₂ O ₃	27.76	27.33	27.51	27.80	26.53	26.41	27.86	30.70	30.54	24.69	24.85	25.02
Fe ₂ O ₃	0.52	0.21	0.30	0.24	0.20	0.23	0.22	0.57	0.47	0.53	0.44	0.56
MnO	0.00	0.00	0.01	0.00	0.00	0.02	0.00	0.04	0.01	0.00	0.00	0.05
MgO	0.01	0.00	0.02	0.00	0.02	0.02	0.03	0.06	0.00	0.03	0.02	0.02
CaO	11.14	10.51	10.43	10.93	9.37	9.23	11.10	14.52	13.88	7.31	7.41	7.17
Na ₂ O	5.21	5.66	5.66	5.39	6.15	6.21	5.08	3.28	3.66	7.29	6.99	7.33
K ₂ O	0.18	0.18	0.18	0.16	0.22	0.27	0.26	0.12	0.14	0.49	0.49	0.48
TOTAL	99.66	99.63	99.57	99.87	99.25	99.66	99.20	99.62	99.98	100.37	99.99	100.45
An	54	50	50	52	45	44	54	70	67	35	36	34

Sample Core/rim Unit Age	VF01-02Ns plag 1 core D 13,000	VF01-02Ns plag 1 core D 13,000	VF01-02Ns plag 1 core D 13,000	VF01-02Ns plag 2 core D 13,000	VF01-02Ns plag 3 core D 13,000	VF01-02Ns plag 4 core D 13,000	VF01-05N plag 1 core D 13,000	VF01-05N plag 2 core D 13,000	VF01-05N plag 2 core D 13,000	VF01-05N plag 2 core D 13,000	VF01-05N plag 2 core D 13,000	VF01-05N plag 3 core D 13,000
SiO ₂	57.09	57.84	56.78	54.44	56.05	53.68	58.91	53.92	55.03	51.45	52.82	58.88
TiO ₂	0.06	0.08	0.08	0.04	0.04	0.06	0.03	0.04	0.01	0.00	0.04	0.00
Al ₂ O ₃	26.46	26.21	26.35	28.04	27.16	28.99	25.67	28.84	28.11	30.18	29.20	25.09
Fe ₂ O ₃	0.67	0.60	0.53	0.36	0.45	0.56	0.22	0.64	0.45	0.65	0.59	0.54
MnO	0.00	0.01	0.00	0.02	0.00	0.04	0.02	0.05	0.04	0.02	0.00	0.00
MgO	0.02	0.07	0.06	0.02	0.04	0.06	0.00	0.07	0.06	0.05	0.06	0.03
CaO	9.52	8.93	9.45	10.92	10.18	12.18	7.92	12.01	10.99	13.45	12.21	7.96
Na ₂ O	6.02	6.46	6.07	4.92	5.66	4.59	6.81	4.70	5.19	3.76	4.50	6.92
K ₂ O	0.34	0.38	0.34	0.25	0.21	0.15	0.33	0.24	0.24	0.19	0.22	0.23
TOTAL	100.20	100.57	99.65	99.01	99.77	100.30	99.92	100.50	100.12	99.75	99.64	99.64
An	46	42	45	54	49	59	38	58	53	66	59	38

Sample Core/rim Unit Age	VF01-05N plag 4 core D 13,000	VF01-05N plag 4 core D 13,000	VF01-05N plag 4 core D 13,000	VF01-05N plag 4 core D 13,000	VF01-05N plag 4 core D 13,000	VF01-05N plag 4 core D 13,000	VF01-05N plag 5 core D 13,000	VF00-06O plag 1 rim D 13,000	VF00-06O plag 1 rim D 13,000	VF00-06O plag 1 rim D 13,000	VF00-06O plag 1 rim D 13,000	VF00-06O plag 2 rim D 13,000
SiO ₂	52.79	52.73	53.94	49.67	49.29	48.44	54.33	57.93	58.38	59.47	56.25	56.49
TiO ₂	0.02	0.04	0.03	0.03	0.02	0.02	0.02	0.06	0.05	0.05	0.02	0.02
Al ₂ O ₃	29.56	29.61	28.84	31.81	31.45	32.09	28.47	26.02	25.19	24.59	26.65	26.67
Fe ₂ O ₃	0.55	0.52	0.54	0.49	0.50	0.61	0.35	0.46	0.67	0.57	0.62	0.47
MnO	0.03	0.02	0.00	0.02	0.03	0.03	0.00	0.01	0.00	0.06	0.00	0.03
MgO	0.04	0.04	0.06	0.00	0.05	0.02	0.04	0.03	0.07	0.05	0.05	0.03
CaO	12.60	13.13	11.77	15.51	15.48	16.03	11.16	8.63	7.90	7.08	9.95	9.63
Na ₂ O	4.35	3.99	4.75	2.76	2.73	2.42	5.00	6.54	6.53	7.13	5.81	5.99
K ₂ O	0.19	0.17	0.22	0.09	0.08	0.07	0.17	0.40	0.67	0.65	0.35	0.30
TOTAL	100.13	100.25	100.14	100.38	99.63	99.73	99.53	100.08	99.45	99.65	99.69	99.62
An	61	64	57	75	75	78	55	41	39	34	48	46

Sample Core/rim Unit Age	VF00-06O plag 3 rim D 13,000	VF00-06O plag 3 rim D 13,000	VF00-06O plag 3 rim D 13,000	VF01-02Ns plag 1 rim D 13,000	VF01-02Ns plag 1 rim D 13,000	VF01-02Ns plag 1 rim D 13,000	VF01-02Ns plag 2 rim D 13,000	VF01-02Ns plag 3 rim D 13,000	VF01-02Ns plag 3 rim D 13,000	VF01-02Ns plag 3 rim D 13,000	VF01-02Ns plag 4 rim D 13,000	VF01-05N plag 1 rim D 13,000
SiO ₂	52.99	52.87	53.00	60.27	60.99	59.04	54.32	59.42	60.86	60.45	62.22	55.53
TiO ₂	0.01	0.02	0.00	0.08	0.05	0.05	0.00	0.01	0.04	0.01	0.01	0.03
Al ₂ O ₃	28.84	28.73	28.69	24.80	23.96	24.99	27.90	24.97	23.92	24.53	22.79	27.53
Fe ₂ O ₃	0.64	0.67	0.53	0.68	0.53	0.66	0.61	0.35	0.41	0.57	0.28	0.47
MnO	0.04	0.04	0.00	0.02	0.00	0.00	0.02	0.01	0.04	0.01	0.00	0.04
MgO	0.09	0.04	0.06	0.05	0.05	0.05	0.07	0.02	0.01	0.04	0.01	0.05
CaO	12.34	12.40	12.16	7.06	6.42	7.68	10.97	7.48	6.54	6.86	5.11	10.33
Na ₂ O	4.36	4.41	4.28	7.20	7.60	6.86	5.12	7.17	7.64	7.42	8.36	5.56
K ₂ O	0.23	0.21	0.20	0.47	0.52	0.44	0.29	0.37	0.44	0.48	0.64	0.24
TOTAL	99.54	99.40	98.92	100.64	100.12	99.76	99.29	99.81	99.90	100.37	99.42	99.78
An	60	60	60	34	31	37	53	36	31	33	24	50

Sample Core/rim Unit Age	VF01-05N plag 2 rim D 13,000	VF01-05N plag 2 rim D 13,000	VF01-05N plag 3 rim D 13,000	VF01-05N plag 4 rim D 13,000	VF01-05N plag 5 rim D 13,000
SiO ₂	49.24	52.53	55.04	55.59	57.42
TiO ₂	0.05	0.01	0.00	0.01	0.01
Al ₂ O ₃	31.65	29.66	27.82	27.34	26.14
Fe ₂ O ₃	0.67	0.75	0.61	0.56	0.51
MnO	0.04	0.00	0.00	0.03	0.05
MgO	0.04	0.08	0.03	0.07	0.05
CaO	15.16	12.98	10.86	10.20	8.74
Na ₂ O	2.80	4.03	5.13	5.49	6.22
K ₂ O	0.13	0.22	0.28	0.28	0.38
TOTAL	99.78	100.26	99.76	99.56	99.52
An	74	63	53	50	43

Table 17 Plagioclase core-rim profile data

Sample Core/rim Unit Age	VF00-06O plag 1 core D 13,000	VF00-06O plag 1 core D 13,000	VF00-06O plag 1 D 13,000	VF00-06O plag 1 D 13,000	VF00-06O plag 1 D 13,000	VF00-06O plag 1 D 13,000	VF00-06O plag 1 D 13,000	VF00-06O plag 1 D 13,000	VF00-06O plag 1 D 13,000	VF00-06O plag 1 D 13,000	VF00-06O plag 1 D 13,000	VF00-06O plag 1 D 13,000
SiO2	55.61	55.62	55.84	55.15	55.14	55.12	56.99	56.50	54.64	55.08	52.83	56.42
TiO2	0.04	0.04	0.04	0.05	0.04	0.00	0.05	0.05	0.03	0.04	0.05	0.04
Al2O3	26.92	26.99	26.57	27.03	27.01	26.95	26.33	26.19	27.19	27.46	26.10	26.19
Fe2O3	0.59	0.55	0.57	0.74	0.78	0.66	0.59	0.59	0.65	0.67	0.60	0.72
MnO	0.03	0.00	0.04	0.05	0.03	0.00	0.00	0.03	0.00	0.01	0.03	0.04
MgO	0.06	0.04	0.06	0.11	0.06	0.07	0.02	0.07	0.07	0.06	0.06	0.05
CaO	10.30	10.38	10.14	10.53	10.71	10.73	9.27	9.71	10.82	10.82	10.51	9.82
Na2O	5.50	5.62	5.88	5.60	5.38	5.32	6.24	6.01	5.35	5.30	5.03	6.00
K2O	0.25	0.23	0.21	0.22	0.20	0.18	0.26	0.23	0.18	0.18	0.18	0.22
total	99.29	99.46	99.35	99.47	99.34	99.04	99.75	99.38	98.93	99.62	95.38	99.51
An	50	50	48	50	52	52	44	47	52	52	53	47

Sample Core/rim Unit Age	VF00-06O plag 1 D 13,000	VF00-06O plag 1 D 13,000	VF00-06O plag 1 D 13,000	VF00-06O plag 1 D 13,000	VF00-06O plag 1 D 13,000	VF00-06O plag 1 D 13,000	VF00-06O plag 1 D 13,000	VF00-06O plag 1 D 13,000	VF00-06O plag 1 D 13,000	VF00-06O plag 1 D 13,000	VF00-06O plag 1 D 13,000	VF00-06O plag 1 D 13,000
SiO2	56.66	55.40	55.77	55.87	55.51	55.66	55.28	55.40	55.47	55.17	54.63	54.71
TiO2	0.04	0.02	0.04	0.04	0.06	0.05	0.05	0.04	0.04	0.03	0.07	0.05
Al2O3	26.59	27.09	26.96	27.02	27.41	27.04	26.96	27.10	27.18	27.31	27.61	27.60
Fe2O3	0.52	0.65	0.63	0.66	0.71	0.66	0.57	0.69	0.63	0.72	0.68	0.66
MnO	0.00	0.00	0.00	0.03	0.00	0.02	0.03	0.04	0.00	0.02	0.00	0.00
MgO	0.08	0.07	0.11	0.03	0.10	0.06	0.09	0.03	0.01	0.06	0.02	0.07
CaO	9.60	10.88	10.13	10.44	10.93	10.40	10.71	10.43	10.81	10.74	11.03	11.23
Na2O	5.96	5.41	5.74	5.70	5.34	5.62	5.47	5.52	5.36	5.29	5.46	5.16
K2O	0.24	0.18	0.21	0.21	0.19	0.19	0.19	0.20	0.17	0.20	0.17	0.18
total	99.70	99.69	99.57	99.99	100.25	99.69	99.35	99.44	99.68	99.54	99.66	99.65
An	46	52	49	50	53	50	51	50	52	52	52	54

Sample Core/rim	VF00-06O plag 1	VF00-06O plag 1	VF00-06O plag 1	VF00-06O plag 1	VF00-06O plag 1	VF00-06O plag 1	VF00-06O plag 1	VF00-06O plag 1	VF00-06O plag 1	VF00-06O plag 1	VF00-06O plag 1	VF00-06O plag 1
Unit	D	D	D	D	D	D	D	D	D	D	D	D
Age	13,000	13,000	13,000	13,000	13,000	13,000	13,000	13,000	13,000	13,000	13,000	13,000
SiO2	55.97	55.26	55.75	55.51	55.17	55.48	55.37	55.82	55.25	55.27	55.34	54.94
TiO2	0.05	0.05	0.07	0.03	0.04	0.05	0.03	0.08	0.05	0.06	0.00	0.05
Al2O3	26.55	26.94	26.49	26.87	27.44	27.45	27.18	27.11	27.10	27.08	27.17	27.57
Fe2O3	0.60	0.67	0.61	0.57	0.55	0.58	0.61	0.61	0.56	0.64	0.58	0.56
MnO	0.03	0.00	0.03	0.00	0.00	0.01	0.00	0.02	0.03	0.02	0.02	0.05
MgO	0.07	0.05	0.02	0.07	0.00	0.04	0.04	0.01	0.07	0.02	0.05	0.06
CaO	10.05	10.56	10.28	10.46	10.91	10.71	10.67	10.30	10.43	10.41	10.78	11.20
Na2O	5.75	5.57	5.74	5.63	5.27	5.38	5.53	5.70	5.48	5.57	5.52	5.35
K2O	0.19	0.20	0.21	0.21	0.19	0.20	0.19	0.23	0.21	0.18	0.20	0.17
total	99.25	99.29	99.19	99.35	99.57	99.90	99.63	99.86	99.17	99.24	99.67	99.96
An	49	51	49	50	53	52	51	49	51	50	51	53

Sample Core/rim	VF00-06O plag 1	VF00-06O plag 1	VF00-06O plag 1	VF00-06O plag 1 rim	VF01-02Ns plag 4 core	VF01-02Ns plag 4	VF01-02Ns plag 4	VF01-02Ns plag 4	VF01-02Ns plag 4	VF01-02Ns plag 4	VF01-02Ns plag 4	VF01-02Ns plag 4
Unit	D	D	D	D	D	D	D	D	D	D	D	D
Age	13,000	13,000	13,000	13,000	13,000	13,000	13,000	13,000	13,000	13,000	13,000	13,000
SiO2	54.87	55.75	57.07	57.93	53.68	54.24	54.11	53.51	55.25	55.45	56.18	54.46
TiO2	0.06	0.04	0.04	0.06	0.06	0.04	0.07	0.05	0.04	0.06	0.07	0.04
Al2O3	27.94	27.09	25.67	26.02	28.99	28.12	28.40	28.70	27.48	27.45	26.81	27.95
Fe2O3	0.56	0.53	0.44	0.46	0.56	0.49	0.52	0.45	0.54	0.62	0.55	0.50
MnO	0.00	0.00	0.01	0.01	0.04	0.00	0.00	0.00	0.00	0.02	0.03	0.00
MgO	0.02	0.09	0.03	0.03	0.06	0.04	0.06	0.06	0.04	0.01	0.03	0.01
CaO	11.34	10.24	8.99	8.63	12.18	11.59	11.67	11.90	10.54	10.36	9.52	11.25
Na2O	5.26	5.76	6.31	6.54	4.59	5.00	4.84	4.80	5.49	5.52	6.02	5.24
K2O	0.16	0.21	0.31	0.40	0.15	0.16	0.13	0.15	0.19	0.19	0.24	0.18
total	100.21	99.71	98.88	100.08	100.30	99.68	99.80	99.62	99.56	99.68	99.45	99.62
An	54	49	43	41	59	56	57	57	51	50	46	54

Sample Core/rim	VF01-02Ns plag 4	VF01-02Ns plag 4	VF01-02Ns plag 4	VF01-02Ns plag 4	VF01-02Ns plag 4	VF01-02Ns plag 4	VF01-02Ns plag 4	VF01-02Ns plag 4	VF01-02Ns plag 4	VF01-02Ns plag 4	VF01-02Ns plag 4	VF01-02Ns plag 4
Unit	D	D	D	D	D	D	D	D	D	D	D	D
Age	13,000	13,000	13,000	13,000	13,000	13,000	13,000	13,000	13,000	13,000	13,000	13,000
SiO2	54.16	55.29	54.58	54.43	53.75	53.80	55.08	57.48	58.19	58.83	59.27	59.51
TiO2	0.07	0.07	0.05	0.06	0.06	0.08	0.07	0.03	0.05	0.02	0.02	0.03
Al2O3	28.46	27.24	27.64	28.01	28.42	28.32	26.95	26.52	26.06	25.21	25.18	24.27
Fe2O3	0.49	0.54	0.42	0.49	0.44	0.52	0.46	0.46	0.45	0.36	0.44	0.37
MnO	0.00	0.00	0.00	0.00	0.00	0.02	0.00	0.03	0.00	0.01	0.00	0.00
MgO	0.04	0.04	0.00	0.01	0.02	0.00	0.02	0.03	0.00	0.02	0.04	0.01
CaO	11.51	10.86	10.93	11.22	11.39	11.61	10.27	9.04	8.58	8.10	7.77	7.23
Na2O	5.02	5.35	5.26	5.08	4.90	5.03	5.79	6.41	6.51	6.86	6.98	7.59
K2O	0.16	0.20	0.18	0.18	0.16	0.17	0.21	0.26	0.30	0.33	0.37	0.42
total	99.90	99.58	99.06	99.49	99.13	99.54	98.84	100.28	100.13	99.73	100.06	99.42
An	55	52	53	54	56	56	49	43	41	39	37	34

Sample Core/rim	VF01-02Ns plag 4	VF01-02Ns plag 4	VF01-02Ns plag 4	VF01-02Ns plag 4 rim	VF01-05N plag 1 core	VF01-05N plag 2	VF01-05N plag 3	VF01-05N plag 4	VF01-05N plag 5	VF01-05N plag 6	VF01-05N plag 7	VF01-05N plag 8
Unit	D	D	D	D	D	D	D	D	D	D	D	D
Age	13,000	13,000	13,000	13,000	13,000	13,000	13,000	13,000	13,000	13,000	13,000	13,000
SiO2	60.48	60.90	61.41	62.22	58.91	55.86	56.93	57.68	55.96	56.46	55.77	55.73
TiO2	0.02	0.03	0.02	0.01	0.03	0.02	0.02	0.00	0.03	0.01	0.03	0.01
Al2O3	24.22	24.01	23.98	22.79	25.67	27.51	27.12	26.52	27.37	27.24	27.48	26.37
Fe2O3	0.28	0.38	0.24	0.28	0.22	0.47	0.41	0.41	0.42	0.40	0.44	0.38
MnO	0.00	0.00	0.08	0.00	0.02	0.01	0.00	0.01	0.00	0.00	0.04	0.00
MgO	0.00	0.01	0.04	0.01	0.00	0.03	0.05	0.02	0.05	0.04	0.04	0.06
CaO	6.78	6.47	6.01	5.11	7.92	10.20	9.63	9.12	10.28	10.02	10.39	9.06
Na2O	7.66	7.59	7.90	8.36	6.81	5.48	6.18	6.21	5.79	5.70	5.68	5.88
K2O	0.41	0.48	0.53	0.64	0.33	0.20	0.19	0.21	0.16	0.19	0.19	0.18
total	99.86	99.87	100.21	99.42	99.92	99.77	100.53	100.18	100.05	100.05	100.06	97.67
An	32	31	29	24	38	50	46	44	49	49	50	46

Sample Core/rim	VF01-05N plag 9	VF01-05N plag 10	VF01-05N plag 11	VF01-05N plag 12	VF01-05N plag 13	VF01-05N plag 14	VF01-05N plag 15	VF01-05N plag 16	VF01-05N plag 17	VF01-05N plag 18	VF01-05N plag 19	VF01-05N plag 20
Unit	D	D	D	D	D	D	D	D	D	D	D	D
Age	13,000	13,000	13,000	13,000	13,000	13,000	13,000	13,000	13,000	13,000	13,000	13,000
SiO2	58.24	56.85	55.54	57.05	56.47	55.88	53.31	55.34	54.77	54.89	54.77	54.48
TiO2	0.02	0.01	0.05	0.02	0.01	0.00	0.00	0.04	0.02	0.02	0.01	0.03
Al2O3	26.18	27.13	27.87	26.86	27.05	27.61	28.81	27.95	28.30	28.03	28.23	28.43
Fe2O3	0.39	0.41	0.43	0.40	0.39	0.49	0.47	0.48	0.47	0.45	0.52	0.47
MnO	0.01	0.00	0.00	0.00	0.00	0.02	0.00	0.04	0.04	0.02	0.02	0.03
MgO	0.02	0.00	0.05	0.02	0.04	0.03	0.04	0.08	0.07	0.05	0.07	0.09
CaO	8.64	9.77	10.41	9.34	9.72	10.22	12.12	10.83	11.21	10.87	11.06	11.58
Na2O	6.59	6.16	5.69	6.09	5.91	5.70	4.71	5.30	4.99	5.08	5.15	5.00
K2O	0.25	0.18	0.16	0.18	0.22	0.23	0.15	0.19	0.19	0.18	0.22	0.22
total	100.33	100.51	100.19	99.97	99.81	100.17	99.61	100.25	100.06	99.59	100.05	100.33
An	41	46	50	45	47	49	58	52	55	54	54	55

Sample Core/rim	VF01-05N plag 21	VF01-05N plag 22	VF01-05N plag 23	VF01-05N plag 24 rim
Unit	D	D	D	D
Age	13,000	13,000	13,000	13,000
SiO2	54.42	53.06	54.22	55.53
TiO2	0.03	0.01	0.02	0.03
Al2O3	28.44	29.02	28.41	27.53
Fe2O3	0.57	0.57	0.58	0.47
MnO	0.07	0.00	0.00	0.04
MgO	0.03	0.05	0.09	0.05
CaO	11.09	12.43	11.53	10.33
Na2O	4.99	4.27	5.07	5.56
K2O	0.22	0.22	0.22	0.24
total	99.85	99.63	100.13	99.78
An	54	61	55	50

Table 18 Clinopyroxene

Sample Core/rim	VF10-07D	VF10-07D	VF10-07D	VF10-07D	VF10-03N	VF10-03N	VF10-03N	VF95-09G	VF95-09G	VF95-09G	VF95-09G	VF95-09G
	cpx 1 core	cpx 1 core	cpx 2 core	cpx 2 core	cpx 1 core	cpx 2 core	cpx 2 core	cpx 1 core	cpx 1 core	cpx 3 core	cpx 3 core	cpx 3 core
Unit	N	N	N	N	N	N	N	N	N	N	N	N
Age	7000	7000	7000	7000	7000	7000	7000	7000	7000	7000	7000	7000
SiO ₂	51.54	52.55	50.76	51.73	51.10	52.07	51.38	52.57	52.36	53.40	53.21	52.22
TiO ₂	0.56	0.32	0.86	0.69	0.56	0.36	0.45	0.38	0.42	0.30	0.33	0.39
Al ₂ O ₃	2.32	1.42	2.78	2.16	3.07	1.90	2.27	1.34	1.42	1.19	1.30	2.16
Cr ₂ O ₃	0.07	0.03	0.02	0.01	0.17	0.02	0.03	0.04	0.03	0.52	0.13	0.87
Fe ₂ O ₃	-	-	-	-	2.70	1.92	2.55	2.30	2.16	1.34	1.74	2.32
FeO	7.45	8.37	6.96	6.52	4.89	6.79	6.48	5.51	5.60	2.48	2.61	1.96
MnO	0.22	0.26	0.22	0.21	0.18	0.22	0.25	0.22	0.16	0.05	0.11	0.11
MgO	15.69	16.33	15.55	16.14	15.78	14.71	14.37	15.61	15.58	17.59	17.22	16.97
CaO	21.41	20.12	21.76	21.74	20.27	21.35	21.33	21.27	21.35	22.64	22.94	22.42
Na ₂ O	0.40	0.33	0.47	0.42	0.53	0.43	0.47	0.52	0.46	0.26	0.24	0.38
total	99.66	99.73	99.37	99.61	99.26	99.79	99.57	99.75	99.53	99.77	99.83	99.80
Fe=FeO	-	-	-	-	7.32	8.53	8.77	7.58	7.54	3.69	4.18	4.06
Mg#	79	78	80	82	79	75	74	79	79	89	88	88

Sample Core/rim	VF10-07D	VF10-07D	VF10-07D	VF10-07D	VF10-07D	VF10-07D	VF10-07D	VF10-07D	VF10-07D	VF10-03N	VF10-03N	VF10-03N	VF10-03N
	cpx 1 rim	cpx 1 rim	cpx 2 rim	cpx 3 rim	cpx 3 rim	cpx 3 rim	cpx 3 rim	cpx 3 rim	cpx 3 rim	cpx 1 rim	cpx 2 rim	cpx 2 rim	cpx 2 rim
Unit	N	N	N	N	N	N	N	N	N	N	N	N	N
Age	7000	7000	7000	7000	7000	7000	7000	7000	7000	7000	7000	7000	7000
SiO ₂	52.05	51.83	52.02	51.75	51.28	50.97	50.82	49.65	51.96	51.70	51.80	51.80	51.28
TiO ₂	0.62	0.79	1.00	0.44	0.47	0.53	0.79	0.97	0.71	0.72	0.70	0.70	0.78
Al ₂ O ₃	1.82	2.11	8.26	2.80	2.92	2.95	2.93	3.65	2.21	2.29	2.17	2.17	2.46
Cr ₂ O ₃	0.01	0.01	0.00	0.27	0.38	0.44	0.13	0.02	0.03	0.02	0.00	0.00	0.02
Fe ₂ O ₃	-	-	-	-	-	-	-	-	2.41	3.03	2.52	3.15	3.15
FeO	6.78	6.85	7.41	6.96	7.02	7.01	7.70	8.06	4.13	3.74	4.04	3.65	3.65
MnO	0.21	0.22	0.20	0.19	0.16	0.18	0.21	0.22	0.29	0.24	0.29	0.22	0.22
MgO	16.22	16.02	10.74	15.80	15.49	15.32	15.57	14.77	16.25	16.27	16.30	15.98	15.98
CaO	21.21	21.25	16.82	21.12	21.21	21.22	20.86	21.29	21.39	21.39	21.31	21.44	21.44
Na ₂ O	0.43	0.51	1.16	0.50	0.50	0.53	0.48	0.50	0.43	0.45	0.41	0.47	0.47
total	99.35	99.59	97.60	99.85	99.43	99.16	99.49	99.13	99.80	99.86	99.54	99.46	99.46
Fe=FeO	-	-	-	-	-	-	-	-	6.30	6.46	6.31	6.48	6.48
Mg#	81	81	72	80	80	80	78	77	82	82	82	81	81

Sample	VF95-09G	VF95-09G	VF95-09G	VF95-09G	VF95-09G	VF95-09G	VF95-09G	VF95-09G	VF95-09G	VF95-09G	VF00-06P	VF00-06P	VF00-06P
Core/rim	cpx 1	cpx 1	cpx 1	cpx 3	cpx 3	cpx 3	cpx 3	cpx 3	cpx 3	cpx 3	cpx 2	cpx 2	cpx 2
Unit	rim	rim	rim	rim	rim	rim	rim	rim	rim	rim	core	core	core
Age	N	N	N	N	N	N	N	N	N	N	F	F	F
Age	7000	7000	7000	7000	7000	7000	7000	7000	7000	7000	12,000	12,000	12,000
SiO ₂	52.19	52.08	51.52	51.75	51.81	51.77	51.93	51.38	51.38	50.96	49.99	53.50	53.50
TiO ₂	0.65	0.51	0.78	0.72	0.71	0.77	0.64	0.69	0.64	0.81	0.71	0.32	0.29
Al ₂ O ₃	2.23	1.98	2.65	2.37	2.26	2.52	2.27	2.33	2.27	2.84	4.21	1.27	1.26
Cr ₂ O ₃	0.03	0.02	0.02	0.01	0.04	0.03	0.02	0.01	0.02	0.02	0.07	0.46	0.39
Fe ₂ O ₃	2.54	2.58	3.10	2.84	2.94	3.16	2.19	2.95	2.95	3.39	4.33	1.49	1.48
FeO	4.08	4.58	3.94	3.86	3.81	3.77	4.67	4.15	4.15	3.99	3.03	2.74	2.64
MnO	0.22	0.22	0.27	0.22	0.24	0.26	0.23	0.22	0.22	0.28	0.19	0.12	0.10
MgO	16.36	16.39	16.01	16.19	16.32	16.20	16.16	15.98	15.98	15.87	15.15	17.35	17.45
CaO	21.37	21.38	21.16	21.48	21.30	21.48	21.00	20.97	20.97	20.77	21.88	22.71	22.74
Na ₂ O	0.46	0.29	0.53	0.45	0.47	0.47	0.44	0.51	0.51	0.54	0.46	0.29	0.27
total	100.13	100.02	99.99	99.90	99.90	100.42	99.55	99.19	99.19	99.46	100.03	100.25	100.13
Fe=FeO	6.37	6.90	6.73	6.42	6.46	6.61	6.64	6.81	6.81	7.04	6.92	4.08	3.98
Mg#	82	81	81	82	82	81	81	81	81	80	80	88	89
Sample	VF00-06P	VF00-06P	VF00-06P	VF00-06P	VF00-06P	VF02-01G	VF02-01G	VF02-01G	VF02-01G	VF02-01G	VF02-01G	VF02-01G	VF02-01G
Core/rim	cpx 3	cpx 2	cpx 3	cpx 6	cpx 6	cpx 1	cpx 1	cpx 2	cpx 2	cpx 3	cpx 3	cpx 4	
Unit	core	core	core	core	core	core	core	core	core	core	core	core	
Age	F	F	F	F	F	F	F	F	F	F	F	F	
Age	12,000	12,000	12,000	12,000	12,000	12,000	12,000	12,000	12,000	12,000	12,000	12,000	
SiO ₂	50.91	51.55	53.76	50.83	52.20	52.27	52.39	50.56	50.26	51.57	51.46	52.04	
TiO ₂	0.52	0.47	0.29	0.50	0.24	0.33	0.31	0.64	0.76	0.37	0.39	0.60	
Al ₂ O ₃	3.61	2.91	1.21	2.60	1.40	2.91	2.82	3.97	3.82	3.47	3.67	2.42	
Cr ₂ O ₃	0.13	0.21	0.49	0.00	0.03	0.85	0.86	0.35	0.00	0.76	0.80	0.10	
Fe ₂ O ₃	3.81	2.83	1.17	3.37	2.37	1.41	1.30	2.93	3.78	2.55	2.32	2.57	
FeO	3.12	3.60	3.44	6.79	7.97	3.66	3.65	3.50	3.73	3.15	3.36	4.74	
MnO	0.15	0.15	0.14	0.30	0.32	0.16	0.13	0.15	0.20	0.20	0.18	0.18	
MgO	15.78	15.91	17.78	13.98	13.96	17.04	16.99	15.61	15.19	16.44	16.76	16.15	
CaO	21.45	21.69	21.94	20.75	21.15	20.91	21.17	21.87	21.51	21.00	20.59	21.04	
Na ₂ O	0.53	0.46	0.25	0.56	0.50	0.39	0.37	0.33	0.47	0.52	0.45	0.45	
total	100.02	99.79	100.46	99.69	100.14	99.92	99.99	99.91	99.73	100.03	99.98	100.29	
Fe=FeO	6.55	6.15	4.49	9.82	10.11	4.93	4.82	6.13	7.13	5.45	5.45	7.05	
Mg#	81	82	88	72	71	86	86	82	79	84	85	80	

Sample	VF02-01G	VF02-01G	VF01-02Ps	VF01-02Ps	VF01-02Ps	VF01-02Ps	VF01-02Ps	VF01-02Ps	VF01-02Ps	VF01-02Ps	VF01-02Ps	VF00-06P	VF00-06P
Core/rim	cpx 5	cpx 6	cpx 1	cpx 1	cpx 2	cpx 3	cpx 3	cpx 3	cpx 3	cpx 3	cpx 3	cpx 2	cpx 2
Unit	core	core	core	core	core	core	core	core	core	core	core	rim	rim
Age	F	F	F	F	F	F	F	F	F	F	F	F	F
Age	12,000	12,000	12,000	12,000	12,000	12,000	12,000	12,000	12,000	12,000	12,000	12,000	12,000
SiO ₂	51.39	52.14	53.42	53.53	53.72	51.99	52.12	53.55	53.42	53.45	48.52	49.80	
TiO ₂	0.66	0.40	0.31	0.30	0.26	0.20	0.25	0.28	0.27	0.27	0.91	1.22	
Al ₂ O ₃	2.72	2.86	1.39	1.35	1.11	1.54	2.17	1.24	1.45	1.33	3.64	3.93	
Cr ₂ O ₃	0.00	0.18	0.62	0.64	0.67	0.08	0.06	0.60	0.73	0.61	0.01	0.00	
Fe ₂ O ₃	2.48	2.35	1.71	1.21	1.35	1.87	1.95	1.57	1.35	1.28	5.17	3.40	
FeO	3.98	3.09	2.11	2.57	2.41	8.57	7.21	2.20	2.49	2.54	1.82	3.70	
MnO	0.14	0.12	0.11	0.12	0.11	0.41	0.34	0.13	0.12	0.11	0.21	0.23	
MgO	16.02	16.24	17.28	17.16	17.81	13.68	13.68	17.52	17.27	17.38	16.98	14.65	
CaO	21.83	22.46	23.00	23.01	22.49	21.00	21.73	22.82	22.77	22.68	22.00	21.95	
Na ₂ O	0.30	0.37	0.35	0.32	0.32	0.45	0.59	0.32	0.34	0.31	0.51	0.53	
total	99.54	100.23	100.31	100.21	100.25	99.79	100.10	100.23	100.21	99.98	99.78	99.43	
Fe=FeO	6.22	5.21	3.66	3.66	3.63	10.26	8.96	3.61	3.71	3.70	6.47	6.76	
Mg#	82	85	89	89	90	70	73	90	89	89	82	79	
Sample	VF00-06P	VF00-06P	VF00-06P	VF00-06P	VF00-06P	VF02-01G	VF02-01G	VF02-01G	VF02-01G	VF02-01G	VF02-01G	VF02-01G	VF02-01G
Core/rim	cpx 2	cpx 3	cpx 3	cpx 6	cpx 6	cpx 1	cpx 1	cpx 2	cpx 2	cpx 3	cpx 3	cpx 4	
Unit	rim	rim	rim	rim	rim	rim	rim	rim	rim	rim	rim	rim	
Age	F	F	F	F	F	F	F	F	F	F	F	F	
Age	12,000	12,000	12,000	12,000	12,000	12,000	12,000	12,000	12,000	12,000	12,000	12,000	
SiO ₂	50.27	51.43	47.85	52.06	51.23	50.37	52.51	52.47	52.41	50.96	49.09	51.30	
TiO ₂	1.40	0.78	1.51	0.53	0.81	0.57	0.44	0.50	0.48	0.73	0.68	0.56	
Al ₂ O ₃	4.77	2.84	5.54	2.62	3.09	4.00	2.17	1.87	2.31	2.85	3.34	3.02	
Cr ₂ O ₃	0.03	0.01	0.00	0.09	0.00	0.39	0.18	0.13	0.04	0.04	0.01	0.09	
Fe ₂ O ₃	0.00	1.81	5.40	2.66	3.61	3.03	2.63	2.37	1.59	4.03	5.01	3.96	
FeO	7.63	4.51	3.22	3.61	3.05	5.21	3.05	4.07	4.48	2.40	1.53	2.60	
MnO	0.20	0.19	0.21	0.15	0.17	0.19	0.15	0.20	0.11	0.21	0.16	0.18	
MgO	12.99	15.27	14.11	16.15	15.93	14.70	16.65	17.02	15.79	16.30	16.56	16.18	
CaO	21.87	22.22	21.69	22.19	21.94	20.85	22.47	21.59	22.58	21.81	21.74	21.99	
Na ₂ O	0.42	0.39	0.47	0.37	0.49	0.51	0.33	0.22	0.31	0.43	0.45	0.44	
total	99.58	99.46	99.99	100.45	100.33	99.83	100.59	100.45	100.10	99.77	98.57	100.33	
Fe=FeO	7.63	6.14	8.07	6.01	6.30	7.94	5.42	6.20	5.91	6.03	6.04	6.16	
Mg#	75	82	76	83	82	77	85	83	83	83	83	82	

Sample	VF02-01G	VF01-02Ps	VF01-02Ps	VF01-02Ps	VF01-02Ps	VF01-02Ps	VF01-02Ps	VF02-01G	VF01-05N	VF01-05N	VF01-05N	VF01-05N	
Core/rim	cpx 6	cpx 1	cpx 1	cpx 2	cpx 3	cpx 3	cpx 3	cpx 2	cpx 1	cpx 1	cpx 2	cpx 2	
Unit	rim	rim	rim	rim	rim	rim	rim	rim	core	core	core	core	
Age	F	F	F	F	F	F	F	F	D	D	D	D	
	12,000	12,000	12,000	12,000	12,000	12,000	12,000	12,000	13,000	13,000	13,000	13,000	
SiO ₂	48.93	51.71	47.03	51.52	52.49	52.60	52.57	50.98	52.67	52.62	51.41	51.63	
TiO ₂	1.14	0.55	1.40	0.61	0.42	0.40	0.42	0.95	0.30	0.32	0.46	0.45	
Al ₂ O ₃	4.76	2.53	5.94	2.38	1.85	1.89	2.00	2.91	2.02	2.05	3.02	2.85	
Cr ₂ O ₃	0.12	0.07	0.02	0.05	0.04	0.14	0.03	0.01	0.89	0.80	0.10	0.16	
Fe ₂ O ₃	4.22	2.88	4.79	2.93	1.92	2.23	1.69	3.39	1.95	1.82	2.78	2.24	
FeO	3.68	3.55	4.31	4.40	4.26	3.84	4.38	3.05	2.56	2.64	3.90	4.28	
MnO	0.16	0.15	0.16	0.19	0.14	0.20	0.13	0.19	0.10	0.16	0.15	0.15	
MgO	14.32	16.13	13.33	16.45	16.60	16.70	16.31	15.91	16.91	17.03	15.71	15.75	
CaO	22.01	21.96	21.23	20.95	21.74	21.85	21.90	21.81	22.49	22.20	21.84	21.89	
Na ₂ O	0.42	0.37	0.44	0.30	0.28	0.31	0.34	0.49	0.35	0.35	0.40	0.34	
total	99.75	99.92	98.67	99.80	99.73	100.16	99.78	99.69	100.25	99.98	99.77	99.73	
Fe=FeO	7.48	6.15	8.62	7.04	5.99	5.85	5.90	6.10	4.32	4.28	6.40	6.29	
Mg#	77	82	73	81	83	84	83	82	87	88	81	82	
Sample	VF01-05N	VF01-05N	VF01-05N	VF01-05N	VF01-05N	VF01-05N	VF01-05N	VF01-05N	VF01-05N	VF01-05N	VF01-02Ns	VF01-02Ns	VF01-02Ns
Core/rim	cpx 2	cpx 2	cpx 3	cpx 3	cpx 4	cpx 4	cpx 4	cpx 4	cpx 4	cpx 4	cpx 1	cpx 1	cpx 1
Unit	core	core	core	core	core	core	core	core	core	core	core	core	core
Age	D	D	D	D	D	D	D	D	D	D	D	D	D
	13,000	13,000	13,000	13,000	13,000	13,000	13,000	13,000	13,000	13,000	13,000	13,000	13,000
SiO ₂	51.63	52.82	53.07	52.03	51.10	52.08	51.62	51.78	51.37	51.28	51.64	51.78	
TiO ₂	0.49	0.24	0.24	0.40	0.44	0.46	0.38	0.35	0.47	0.49	0.47	0.46	
Al ₂ O ₃	3.06	1.64	1.30	2.16	2.82	1.80	1.77	2.12	2.93	2.90	2.91	2.74	
Cr ₂ O ₃	0.13	0.48	0.30	0.51	0.43	0.03	0.00	0.06	0.09	0.36	0.32	0.32	
Fe ₂ O ₃	2.70	2.18	1.88	2.31	2.86	2.48	3.40	2.89	2.97	2.55	2.47	2.42	
FeO	3.92	2.69	2.82	2.75	6.83	7.44	6.73	5.33	3.54	3.58	3.97	3.75	
MnO	0.14	0.08	0.15	0.10	0.27	0.37	0.32	0.24	0.14	0.13	0.17	0.18	
MgO	15.82	17.13	17.58	16.85	13.83	14.86	14.13	15.85	15.80	15.63	15.96	15.77	
CaO	21.94	22.25	22.13	21.97	20.82	20.12	21.05	20.81	22.08	22.12	21.76	22.31	
Na ₂ O	0.39	0.34	0.25	0.33	0.67	0.56	0.62	0.37	0.37	0.39	0.36	0.36	
total	100.21	99.85	99.71	99.40	100.06	100.19	100.02	99.80	99.76	99.42	100.04	100.10	
Fe=FeO	6.35	4.66	4.51	4.83	9.40	9.67	9.79	7.93	6.21	5.87	6.19	5.93	
Mg#	82	87	87	86	72	73	72	78	82	83	82	83	

Sample Core/rim Unit Age	VF01-02Ns	VF01-02Ns	VF01-02Ns	VF01-02Ns	VF01-02Ns	VF01-02Ns	VF01-02Ns	VF00-06O	VF00-06O	VF00-06O	VF00-06O	VF00-06O
	cpx 1 core D	cpx 1 core D	cpx 1 core D	cpx 2 core D	cpx 2 core D	cpx 3 core D	cpx 3 core D	cpx 1 core D	cpx 1 core D	cpx 1 core D	cpx 2 core D	cpx 2 core D
Age	13,000	13,000	13,000	13,000	13,000	13,000	13,000	13,000	13,000	13,000	13,000	13,000
SiO ₂	52.87	53.09	52.81	52.32	51.98	52.77	52.00	51.04	51.72	51.06	51.49	51.46
TiO ₂	0.26	0.26	0.28	0.36	0.48	0.26	0.28	0.54	0.45	0.46	0.41	0.46
Al ₂ O ₃	1.83	1.79	1.84	1.95	2.15	1.94	2.26	3.58	2.92	3.08	2.73	2.92
Cr ₂ O ₃	0.43	0.46	0.37	0.06	0.14	0.78	0.82	0.09	0.02	0.02	0.02	0.01
Fe ₂ O ₃	1.74	1.88	1.77	2.16	2.42	1.65	2.38	2.72	1.70	2.68	2.64	3.12
FeO	2.69	2.72	2.75	5.38	5.36	2.83	2.21	5.59	6.31	6.41	6.07	5.86
MnO	0.05	0.11	0.13	0.20	0.24	0.13	0.13	0.23	0.23	0.22	0.21	0.23
MgO	17.10	17.30	17.23	16.21	16.34	17.33	17.09	14.91	16.15	15.96	14.98	14.91
CaO	22.45	22.33	22.17	20.74	20.33	21.83	21.82	21.14	19.81	19.33	20.89	20.93
Na ₂ O	0.32	0.31	0.31	0.40	0.39	0.33	0.36	0.44	0.33	0.35	0.47	0.53
total	99.74	100.25	99.64	99.78	99.80	99.84	99.35	100.28	99.63	99.58	99.91	100.42
Fe=FeO	4.26	4.41	4.34	7.32	7.53	4.32	4.36	8.05	7.84	8.83	8.45	8.67
Mg#	88	87	88	80	79	88	87	77	79	76	76	75

Sample Core/rim Unit Age	VF00-06O	VF00-06O	VF00-06O	VF00-06O	VF00-06O	VF00-06O	VF00-06O	VF00-06O	VF00-06O	VF00-06O	VF01-05N	VF01-05N	VF01-05N
	cpx 3 core D	cpx 3 core D	cpx 3 core D	cpx 3 core D	cpx 4 core D	cpx 4 core D	cpx 4 core D	cpx 4 core D	cpx 4 core D	cpx 4 core D	cpx 1 rim D	cpx 2 rim D	cpx 2 rim D
Age	13,000	13,000	13,000	13,000	13,000	13,000	13,000	13,000	13,000	13,000	13,000	13,000	13,000
SiO ₂	53.11	52.74	52.50	52.47	50.69	51.52	50.90	51.38	51.66	50.59	51.70	51.70	51.59
TiO ₂	0.27	0.25	0.29	0.31	0.56	0.43	0.45	0.57	0.35	0.63	0.41	0.41	0.41
Al ₂ O ₃	1.96	2.01	2.22	2.17	3.82	2.28	3.53	2.87	2.28	4.06	2.47	2.47	2.57
Cr ₂ O ₃	0.91	0.89	0.96	0.96	0.33	0.19	0.59	0.20	0.14	0.07	0.04	0.04	0.08
Fe ₂ O ₃	1.49	1.67	1.53	1.57	2.38	2.85	2.37	2.42	2.35	2.91	2.67	2.67	2.72
FeO	2.74	2.50	2.72	2.70	5.36	5.85	5.56	6.54	6.34	4.51	3.74	3.74	3.95
MnO	0.12	0.08	0.08	0.12	0.16	0.25	0.15	0.19	0.22	0.19	0.15	0.15	0.23
MgO	17.27	17.04	17.02	16.97	14.85	14.90	14.93	14.76	14.62	15.10	16.03	16.03	16.03
CaO	22.20	22.41	21.96	22.15	21.26	20.95	20.82	20.36	21.06	21.34	21.96	21.96	21.63
Na ₂ O	0.36	0.35	0.38	0.34	0.40	0.54	0.48	0.61	0.54	0.45	0.34	0.34	0.34
total	100.41	99.94	99.67	99.77	99.82	99.75	99.79	99.90	99.54	99.85	99.51	99.51	99.55
Fe=FeO	4.08	4.00	4.10	4.11	7.49	8.41	7.70	8.72	8.45	7.13	6.14	6.14	6.40
Mg#	88	88	88	88	78	76	78	75	76	79	82	82	82

Sample Core/rim Unit Age	VF01-05N	VF01-05N	VF01-05N	VF01-05N	VF01-05N	VF01-02Ns	VF01-02Ns	VF01-02Ns	VF01-02Ns	VF01-02Ns	VF00-06O	VF00-06O
	cpx 2 rim D 13,000	cpx 3 rim D 13,000	cpx 4 rim D 13,000	cpx 4 rim D 13,000	cpx 4 rim D 13,000	cpx 1 rim D 13,000	cpx 2 rim D 13,000	cpx 3 rim D 13,000	cpx 3 rim D 13,000	cpx 3 rim D 13,000	cpx 4 rim D 13,000	cpx 1 rim D 13,000
SiO ₂	51.83	51.46	51.77	52.05	51.55	50.83	52.30	50.26	51.27	51.42	52.27	51.88
TiO ₂	0.44	0.38	0.42	0.43	0.46	0.56	0.37	0.78	0.53	0.51	0.39	0.42
Al ₂ O ₃	2.91	2.35	2.55	2.46	2.84	3.37	2.07	4.04	3.12	3.01	2.34	2.98
Cr ₂ O ₃	0.00	0.01	0.13	0.16	0.01	0.16	0.07	0.10	0.07	0.07	0.03	0.05
Fe ₂ O ₃	2.21	3.30	3.10	2.06	3.01	2.69	2.21	3.08	3.02	2.40	1.71	2.11
FeO	4.71	5.86	3.26	4.08	3.71	3.66	4.07	3.92	3.72	4.58	4.81	4.50
MnO	0.14	0.52	0.18	0.16	0.15	0.13	0.18	0.13	0.19	0.15	0.18	0.16
MgO	15.70	14.97	16.22	16.13	16.02	15.76	16.58	15.44	15.76	15.65	16.11	15.78
CaO	21.70	20.67	22.06	21.93	21.73	21.73	21.68	21.36	21.82	21.63	21.62	21.33
Na ₂ O	0.37	0.50	0.36	0.33	0.39	0.33	0.29	0.41	0.40	0.35	0.31	0.49
total	100.00	100.01	100.05	99.80	99.87	99.22	99.80	99.52	99.89	99.74	99.78	99.71
Fe=FeO	6.69	8.83	6.05	5.94	6.41	6.08	6.05	6.68	6.44	6.73	6.35	6.40
Mg#	81	75	83	83	82	82	83	80	81	81	82	81

Sample Core/rim Unit Age	VF00-06O	VF00-06O	VF00-06O	VF00-06O	VF00-06O	VF00-06O	VF00-06O	VF00-06O	VF00-06O	VF00-06O
	cpx 3 rim D 13,000	cpx 3 rim D 13,000	cpx 4 rim D 13,000	cpx 4 rim D 13,000	cpx 4 rim D 13,000	cpx 4 rim D 13,000	cpx 4 rim D 13,000	cpx 4 rim D 13,000	cpx 1 rim D 13,000	cpx 3 rim D 13,000
SiO ₂	51.40	50.64	52.02	49.56	51.57	52.29	50.75	50.84	51.35	51.58
TiO ₂	0.48	0.64	0.37	0.41	0.51	0.41	0.67	0.62	0.49	0.43
Al ₂ O ₃	3.05	4.01	2.26	2.59	2.83	2.37	3.75	3.40	3.09	2.63
Cr ₂ O ₃	0.12	0.04	0.01	0.06	0.11	0.06	0.15	0.11	0.07	0.04
Fe ₂ O ₃	2.24	2.65	2.82	3.19	2.34	2.25	1.92	2.81	2.43	3.22
FeO	4.59	5.44	3.96	3.81	4.02	3.87	4.98	4.07	4.80	3.50
MnO	0.17	0.23	0.16	0.19	0.16	0.13	0.18	0.15	0.18	0.16
MgO	15.32	14.75	16.43	15.64	15.80	16.26	15.36	15.50	15.44	16.12
CaO	21.93	21.28	21.46	20.43	21.92	22.11	21.06	21.55	21.48	21.71
Na ₂ O	0.37	0.40	0.35	0.34	0.37	0.34	0.38	0.41	0.39	0.40
total	99.66	100.09	99.83	96.22	99.62	100.11	99.20	99.46	99.71	99.79
Fe=FeO	6.60	7.83	6.50	6.68	6.12	5.90	6.70	6.60	6.99	6.40
Mg#	81	77	82	81	82	83	80	81	80	82

Table 19 Clinopyroxene core-rim profile data

Sample	VF00-06O	VF00-06O	VF00-06O	VF00-06O	VF00-06O	VF00-06O	VF00-06O	VF00-06O	VF00-06O	VF00-06O	VF00-06O	VF00-06O
Figure	cpx 1	cpx 1	cpx 1	cpx 1	cpx 1	cpx 1	cpx 1	cpx 1	cpx 1	cpx 1	cpx 1	cpx 1
Unit	3.21b	3.21b	3.21b	3.21b	3.21b	3.21b	3.21b	3.21b	3.21b	3.21b	3.21b	3.21b
Age	D	D	D	D	D	D	D	D	D	D	D	D
Age	13,000	13,000	13,000	13,000	13,000	13,000	13,000	13,000	13,000	13,000	13,000	13,000
SiO ₂	51.06	50.88	51.19	51.46	51.66	51.85	51.88	51.78	51.38	51.71	51.54	52.48
TiO ₂	0.46	0.57	0.45	0.42	0.41	0.43	0.41	0.42	0.43	0.40	0.41	0.39
Al ₂ O ₃	3.08	2.94	2.66	2.46	2.06	2.23	2.12	2.03	2.14	1.96	2.12	1.68
Cr ₂ O ₃	0.02	0.05	0.00	0.00	0.04	0.02	0.01	0.01	0.02	0.00	0.01	0.02
Fe ₂ O ₃	2.68	2.99	3.19	2.65	2.23	2.44	1.96	2.24	2.73	2.83	2.70	2.05
FeO	6.41	6.25	5.88	6.59	7.00	6.87	7.10	6.87	6.53	6.26	6.46	5.30
MnO	0.22	0.19	0.28	0.30	0.37	0.39	0.34	0.28	0.34	0.35	0.31	0.16
MgO	15.96	14.84	14.89	14.71	14.75	14.60	14.58	14.62	14.64	14.97	14.53	16.34
CaO	19.33	20.46	20.79	20.71	20.61	20.94	20.96	20.93	20.81	20.89	21.18	21.09
Na ₂ O	0.35	0.48	0.48	0.49	0.44	0.49	0.46	0.48	0.47	0.45	0.47	0.32
total	99.58	99.65	99.81	99.79	99.57	100.25	99.81	99.65	99.48	99.82	99.72	99.83
Fe=FeO	8.83	8.94	8.75	8.98	9.01	9.07	8.87	8.89	8.99	8.81	8.89	7.14
Mg#	76	75	75	75	74	74	75	75	74	75	74	80

Sample	VF00-06O	VF00-06O	VF00-06O	VF00-06O	VF00-06O	VF00-06O	VF00-06O	VF00-06O	VF00-06O	VF00-06O	VF00-06O	VF00-06O
Figure	cpx 1	cpx 1	cpx 1	cpx 1	cpx 1	cpx 1	cpx 1	cpx 3	cpx 3	cpx 3	cpx 3	cpx 3
Unit	3.21b	3.21b	3.21b	3.21b	3.21b	3.21b	3.20	3.20	3.20	3.20	3.20	3.20
Age	D	D	D	D	D	D	D	D	D	D	D	D
Age	13,000	13,000	13,000	13,000	13,000	13,000	13,000	13,000	13,000	13,000	13,000	13,000
SiO ₂	52.10	52.21	52.15	51.86	52.18	52.12	52.27	53.11	52.74	52.50	52.47	52.62
TiO ₂	0.40	0.40	0.41	0.43	0.36	0.43	0.39	0.27	0.25	0.29	0.31	0.31
Al ₂ O ₃	2.33	2.37	2.30	2.18	2.13	2.35	2.34	1.96	2.01	2.22	2.17	2.25
Cr ₂ O ₃	0.12	0.13	0.08	0.11	0.08	0.06	0.03	0.91	0.89	0.96	0.96	1.05
Fe ₂ O ₃	1.79	2.39	2.10	2.66	2.09	1.77	1.71	1.49	1.67	1.53	1.57	1.38
FeO	4.44	3.97	4.15	3.50	4.13	4.40	4.81	2.74	2.50	2.72	2.70	2.94
MnO	0.17	0.16	0.20	0.14	0.17	0.13	0.18	0.12	0.08	0.08	0.12	0.08
MgO	16.00	16.23	16.20	16.43	16.45	16.29	16.11	17.27	17.04	17.02	16.97	16.95
CaO	21.86	22.00	21.92	21.96	21.68	21.72	21.62	22.20	22.41	21.96	22.15	22.02
Na ₂ O	0.32	0.33	0.30	0.29	0.28	0.29	0.31	0.36	0.35	0.38	0.34	0.38
total	99.53	100.18	99.81	99.56	99.54	99.54	99.78	100.41	99.94	99.67	99.77	99.97
Fe=FeO	6.05	6.12	6.04	5.90	6.01	5.99	6.35	4.08	4.00	4.10	4.11	4.18
Mg#	82	83	83	83	83	83	82	88	88	88	88	88

Sample	VF00-06O	VF00-06O	VF00-06O	VF00-06O	VF00-06O	VF00-06O	VF00-06O	VF00-06O	VF00-06O	VF00-06O	VF00-06O	VF00-06O
Figure	cpx 3	cpx 3	cpx 3	cpx 3	cpx 3	cpx 3	cpx 3	cpx 3	cpx 3	cpx 3	cpx 3	cpx 3
Unit	D	D	D	D	D	D	D	D	D	D	D	D
Age	13,000	13,000	13,000	13,000	13,000	13,000	13,000	13,000	13,000	13,000	13,000	13,000
SiO ₂	52.74	52.50	52.92	52.58	52.38	50.58	50.80	51.78	50.65	50.71	50.90	50.87
TiO ₂	0.30	0.29	0.34	0.34	0.42	0.74	0.57	0.43	0.51	0.54	0.52	0.52
Al ₂ O ₃	2.16	2.24	2.23	2.43	2.62	3.97	3.74	2.68	3.77	3.77	3.38	3.54
Cr ₂ O ₃	0.85	0.77	0.75	0.61	0.51	0.09	0.01	0.00	0.00	0.08	0.04	0.04
Fe ₂ O ₃	1.20	1.91	1.35	2.00	1.42	3.10	2.90	2.65	2.84	2.89	3.25	2.95
FeO	3.25	2.78	3.23	3.10	3.84	3.95	5.35	4.55	5.04	4.96	4.27	4.73
MnO	0.11	0.08	0.13	0.11	0.09	0.13	0.22	0.18	0.20	0.20	0.24	0.18
MgO	17.13	17.07	17.04	17.06	16.52	15.80	15.26	15.57	14.86	14.82	15.11	14.91
CaO	21.78	21.91	22.00	21.69	21.85	21.27	20.81	21.93	21.47	21.60	22.08	21.90
Na ₂ O	0.34	0.37	0.36	0.39	0.35	0.36	0.40	0.37	0.38	0.40	0.35	0.37
total	99.84	99.92	100.35	100.31	99.99	99.98	100.05	100.13	99.72	99.97	100.13	100.00
Fe=FeO	4.33	4.50	4.45	4.90	5.12	6.73	7.96	6.93	7.60	7.56	7.19	7.38
Mg#	88	87	87	86	85	81	77	80	78	78	79	78

Sample	VF00-06O	VF00-06O	VF00-06O	VF00-06O	VF00-06O	VF00-06O	VF00-06O	VF01-05N	VF01-05N	VF01-05N	VF01-05N	VF01-05N
Figure	cpx 3	cpx 3	cpx 3	cpx 3	cpx 3	cpx 3	cpx 3	cpx 4	cpx 4	cpx 4	cpx 4	cpx 4
Unit	D	D	D	D	D	D	D	D	D	D	D	D
Age	13,000	13,000	13,000	13,000	13,000	13,000	13,000	13,000	13,000	13,000	13,000	13,000
SiO ₂	51.03	50.79	50.89	50.92	50.97	51.40	50.64	51.10	52.08	51.62	51.78	51.37
TiO ₂	0.48	0.51	0.54	0.51	0.53	0.48	0.64	0.44	0.46	0.38	0.35	0.47
Al ₂ O ₃	3.33	3.44	3.58	3.50	3.59	3.05	4.01	2.82	1.80	1.77	2.12	2.93
Cr ₂ O ₃	0.12	0.18	0.07	0.07	0.05	0.12	0.04	0.04	0.03	0.00	0.06	0.09
Fe ₂ O ₃	2.74	3.19	2.79	2.84	2.63	2.24	2.65	2.86	2.48	3.40	2.89	2.97
FeO	4.63	4.48	4.96	4.71	5.01	4.59	5.44	6.83	7.44	6.73	5.33	3.54
MnO	0.18	0.18	0.19	0.19	0.17	0.17	0.23	0.27	0.37	0.32	0.24	0.14
MgO	15.12	15.03	14.93	14.95	14.88	15.32	14.75	13.83	14.86	14.13	15.85	15.80
CaO	21.89	21.80	21.75	21.86	21.86	21.93	21.28	20.82	20.12	21.05	20.81	22.08
Na ₂ O	0.35	0.39	0.36	0.38	0.37	0.37	0.40	0.67	0.56	0.62	0.37	0.37
total	99.88	99.99	100.05	99.93	100.06	99.66	100.09	100.06	100.19	100.02	99.80	99.76
Fe=FeO	7.10	7.35	7.46	7.26	7.37	6.60	7.83	9.40	9.67	9.79	7.93	6.21
Mg#	79	78	78	79	78	81	77	72	73	72	78	82

Sample Figure Unit Age	VF01-05N cpx 4 3.21a D 13,000	VF01-05N cpx 4 3.21a D 13,000	VF01-05N cpx 4 3.21a D 13,000	VF01-05N cpx 4 3.21a D 13,000	VF01-05N cpx 4 3.21a D 13,000	VF01-05N cpx 4 3.21a D 13,000	VF01-05N cpx 4 3.21a D 13,000
SiO ₂	52.81	52.54	53.13	52.74	51.77	52.05	51.55
TiO ₂	0.31	0.31	0.28	0.32	0.42	0.43	0.46
Al ₂ O ₃	1.44	1.97	1.38	1.32	2.55	2.46	2.84
Cr ₂ O ₃	0.25	0.17	0.23	0.22	0.13	0.16	0.01
Fe ₂ O ₃	1.85	1.88	2.05	1.74	3.10	2.06	3.01
FeO	3.95	3.87	3.08	3.44	3.26	4.08	3.71
MnO	0.15	0.12	0.16	0.12	0.18	0.16	0.15
MgO	17.59	16.96	17.56	17.49	16.22	16.13	16.02
CaO	21.04	21.52	21.96	21.78	22.06	21.93	21.73
Na ₂ O	0.21	0.28	0.27	0.20	0.36	0.33	0.39
total	99.62	99.61	100.11	99.38	100.05	99.80	99.87
Fe=FeO	5.61	5.56	4.93	5.00	6.05	5.94	6.41
Mg#	85	84	86	86	83	83	82

Table 20 Orthopyroxene

Sample Core/rim Unit Ages	VF95-09G opx 2 core N 7000	VF10-07D opx 1 rim N 7000	VF10-07D opx 1 rim N 7000	VF10-07D opx 1 rim N 7000	VF95-09G opx 2 rim N 7000	VF95-09G opx 2 rim N 7000	VF95-09G opx 2 rim N 7000
SiO ₂	56.12	54.49	54.78	55.01	54.22	54.17	54.24
TiO ₂	0.06	0.15	0.15	0.14	0.32	0.30	0.30
Al ₂ O ₃	1.03	1.59	1.49	1.34	1.20	1.15	0.96
Cr ₂ O ₃	0.43	0.23	0.19	0.21	0.01	0.01	0.01
Fe ₂ O ₃	0.57	-	-	-	0.98	1.24	0.99
FeO	7.63	13.20	12.95	12.77	14.13	13.96	14.25
MnO	0.19	0.29	0.28	0.31	0.42	0.41	0.41
MgO	31.88	28.65	28.78	28.91	27.28	27.43	27.48
CaO	1.80	1.39	1.39	1.40	1.40	1.32	1.30
Na ₂ O	0.05	0.04	0.03	0.04	0.03	0.02	0.04
TOTAL	99.76	100.02	100.04	100.14	99.97	100.01	99.96
Fe=FeO	8.14	-	-	-	15.01	15.08	15.14
Mg#	87	79	80	80	76	76	76

Sample	VF95-09G opx 2	VF95-09G opx 1	VF95-09G opx 1	VF95-09G opx 4	VF95-09G opx 4	VF95-09G opx 5	VF95-09G opx 5
Core/rim	rim	rim	rim	rim	rim	rim	rim
Unit	N	N	N	N	N	N	N
Ages	7000	7000	7000	7000	7000	7000	7000
SiO ₂	53.87	53.99	54.16	54.22	53.95	55.05	54.65
TiO ₂	0.30	0.23	0.24	0.24	0.27	0.33	0.39
Al ₂ O ₃	1.17	2.45	2.73	2.28	2.44	1.31	1.56
Cr ₂ O ₃	0.02	0.11	0.12	0.10	0.07	0.00	0.01
Fe ₂ O ₃	1.25	1.27	0.89	1.23	1.33	0.97	1.12
FeO	14.01	11.01	11.22	11.78	11.53	11.55	11.30
MnO	0.40	0.25	0.26	0.29	0.26	0.38	0.39
MgO	27.36	28.95	29.04	28.68	28.57	29.40	29.25
CaO	1.35	1.32	1.26	1.28	1.44	1.27	1.32
Na ₂ O	0.01	0.04	0.02	0.04	0.04	0.04	0.03
TOTAL	99.74	99.62	99.95	100.15	99.89	100.31	100.02
Fe=FeO	15.13	12.15	12.02	12.89	12.72	12.42	12.31
Mg#	76	81	81	80	80	81	81

Table 21 Hornblende

Sample	VF95-09G hbd 2	VF95-09G hbd 2	VF95-09G hbd 1	VF95-09G hbd 1	VF95-09G hbd 2	VF95-09G hbd 2	VF01-05N hbd 1	VF01-05N hbd 1	VF01-05N hbd 1	VF01-05N hbd 1
core/rim	core	core	rim	rim	rim	rim	core	core	core	core
Unit	N	N	N	N	N	N	D	D	D	D
Age	7000	7000	7000	7000	7000	7000	13,000	13,000	13,000	13,000
SiO ₂	40.38	40.29	41.94	41.26	40.72	40.62	41.54	41.53	41.31	41.16
TiO ₂	2.62	2.72	2.45	2.65	2.69	2.75	1.99	2.17	1.95	2.08
Al ₂ O ₃	13.16	13.22	12.14	12.38	12.77	13.16	12.05	12.44	12.37	12.43
Cr ₂ O ₃	0.00	0.00	0.00	0.02	0.02	0.00	0.00	0.02	0.00	0.00
Fe ₂ O ₃	4.36	4.10	3.58	3.71	3.82	4.13	4.68	4.74	4.92	4.94
FeO	7.65	8.64	8.05	8.08	7.90	7.95	9.13	9.67	9.61	9.66
MnO	0.14	0.16	0.19	0.17	0.13	0.17	0.20	0.23	0.25	0.22
MgO	13.99	13.38	14.24	14.07	13.98	13.94	13.37	13.11	12.98	12.94
CaO	11.81	11.72	11.59	11.62	11.83	11.85	11.39	11.34	11.43	11.42
Na ₂ O	2.50	2.49	2.52	2.64	2.50	2.54	2.61	2.62	2.70	2.55
K ₂ O	0.96	0.94	0.81	0.82	0.93	0.97	0.43	0.41	0.43	0.40
total	99.77	99.87	99.71	99.66	99.48	100.25	99.53	100.39	100.08	99.95
Fe=FeO	11.58	12.33	11.27	11.42	11.34	11.66	13.34	13.93	14.04	14.10

Sample core/rim	VF01-05N hbd 1	VF01-05N hbd 2	VF01-05N hbd 2	VF01-05N hbd 2	VF01-05N hbd 2	VF01-05N hbd 2	VF01-05N hbd 2	VF01-05N hbd 2	VF01-05N hbd 3	VF01-05N hbd 3	VF01-05N hbd 3
Unit	core	core	core	core	core	core	core	core	core	core	core
Age	D	D	D	D	D	D	D	D	D	D	D
	13,000	13,000	13,000	13,000	13,000	13,000	13,000	13,000	13,000	13,000	13,000
SiO ₂	41.20	41.62	41.33	41.35	41.19	41.80	41.86	42.59	42.43	41.32	41.32
TiO ₂	2.05	2.06	2.17	2.08	2.13	2.09	2.26	2.38	2.27	2.00	2.00
Al ₂ O ₃	12.48	12.67	12.72	12.78	12.70	12.74	12.44	12.01	11.89	12.53	12.53
Cr ₂ O ₃	0.01	0.00	0.03	0.04	0.00	0.00	0.03	0.02	0.03	0.04	0.04
Fe ₂ O ₃	4.75	5.04	5.13	4.81	5.03	4.92	4.65	4.23	4.37	4.76	4.76
FeO	9.72	8.27	8.41	8.51	8.33	8.40	8.32	6.30	5.82	8.67	8.67
MnO	0.25	0.19	0.14	0.17	0.18	0.12	0.23	0.10	0.09	0.19	0.19
MgO	12.86	13.89	13.78	13.65	13.74	13.95	14.00	15.59	15.77	13.54	13.54
CaO	11.31	11.07	11.09	11.22	11.33	11.25	11.22	11.45	11.68	11.53	11.53
Na ₂ O	2.54	2.58	2.57	2.60	2.59	2.67	2.57	2.60	2.41	2.41	2.41
K ₂ O	0.42	0.38	0.36	0.34	0.35	0.37	0.38	0.73	0.89	0.76	0.76
total	99.75	99.95	99.87	99.65	99.71	100.47	100.08	100.18	99.81	99.91	99.91
Fe=FeO	13.99	12.81	13.03	12.84	12.86	12.83	12.51	10.10	9.76	12.95	12.95

Sample core/rim	VF01-05N hbd	VF01-02Ns hbd	VF01-02Ns hbd	VF01-02Ns hbd	VF01-02Ns hbd	VF01-02Ns hbd	VF01-02Ns hbd	VF01-02Ns hbd	VF00-06O hbd 1	VF00-06O hbd 1	VF00-06O hbd 2
Unit	3	1	1	2	2	3	3	3	core	core	core
Age	D	D	D	D	D	D	D	D	D	D	D
	13,000	13,000	13,000	13,000	13,000	13,000	13,000	13,000	13,000	13,000	13,000
SiO ₂	42.52	42.54	42.57	42.33	42.34	42.10	42.03	41.76	42.02	42.47	42.47
TiO ₂	1.80	2.54	2.64	2.21	2.27	2.02	2.56	1.72	1.63	2.21	2.21
Al ₂ O ₃	11.66	11.09	10.97	11.42	11.93	12.50	12.47	12.57	13.04	11.89	11.89
Cr ₂ O ₃	0.03	0.06	0.03	0.00	0.07	0.00	0.02	0.01	0.00	0.05	0.05
Fe ₂ O ₃	5.09	4.32	3.96	4.63	4.38	4.53	4.01	4.57	5.31	4.67	4.67
FeO	8.80	8.70	9.10	8.12	5.92	8.26	7.54	8.55	6.29	5.55	5.55
MnO	0.27	0.18	0.18	0.24	0.12	0.17	0.09	0.18	0.11	0.10	0.10
MgO	13.87	14.24	14.05	14.35	15.65	14.03	14.65	13.65	15.07	15.94	15.94
CaO	11.43	11.26	11.30	11.23	11.55	11.15	11.45	11.55	11.25	11.53	11.53
Na ₂ O	2.43	2.29	2.33	2.58	2.44	2.53	2.63	2.58	2.68	2.51	2.51
K ₂ O	0.37	0.61	0.69	0.52	0.83	0.39	0.35	0.60	0.56	0.80	0.80
total	100.42	99.98	100.01	99.85	99.68	99.78	99.96	99.88	100.10	99.94	99.94
Fe=FeO	13.38	12.59	12.66	12.29	9.86	12.34	11.15	12.67	11.07	9.75	9.75

Sample core/rim	VF00-06O hbd 2	VF01-05N hbd 1	VF01-05N hbd 1	VF01-05N hbd 2	VF01-05N hbd 2	VF01-05N hbd 2	VF01-05N hbd 3	VF01-05N hbd 3	VF01-02Ns hbd 1
Unit	core	rim	rim	rim	rim	rim	rim	rim	rim
Age	D	D	D	D	D	D	D	D	D
	13,000	13,000	13,000	13,000	13,000	13,000	13,000	13,000	13,000
SiO ₂	42.47	40.92	41.52	42.41	42.88	43.09	42.59	42.68	42.61
TiO ₂	2.31	2.05	1.98	1.78	2.13	2.09	2.28	2.29	2.36
Al ₂ O ₃	11.82	12.49	11.38	11.55	11.17	11.44	11.00	11.39	11.66
Cr ₂ O ₃	0.06	0.04	0.01	0.01	0.02	0.04	0.00	0.00	0.15
Fe ₂ O ₃	4.51	5.06	5.00	4.92	4.31	4.30	4.95	4.44	4.17
FeO	5.64	8.04	7.80	7.54	5.69	5.38	5.79	6.10	5.35
MnO	0.11	0.19	0.18	0.18	0.10	0.11	0.16	0.17	0.08
MgO	15.92	13.82	14.19	14.61	16.00	16.21	15.94	15.70	16.16
CaO	11.60	11.76	11.51	11.38	11.61	11.63	11.55	11.53	11.68
Na ₂ O	2.51	2.47	2.32	2.45	2.33	2.36	2.44	2.36	2.41
K ₂ O	0.82	0.88	0.81	0.87	1.07	1.02	0.90	0.84	1.15
H ₂ O	1.94	1.98	1.94	1.93	1.91	1.91	1.90	1.88	1.92
F	0.25	0.09	0.14	0.21	0.30	0.31	0.30	0.37	0.30
Cl	0.03	0.05	0.04	0.04	0.02	0.03	0.03	0.02	0.02
total	99.99	99.84	98.81	99.88	99.54	99.91	99.84	99.78	100.02
Fe=FeO	9.70	12.60	12.30	11.97	9.57	9.25	10.24	10.10	9.10

Sample core/rim	VF01-02Ns hbd 1	VF01-02Ns hbd 2	VF01-02Ns hbd 3	VF01-02Ns hbd 3	VF00-06O hbd 1	VF00-06O hbd 1	VF00-06O hbd 2
Unit	rim	rim	rim	rim	rim	rim	rim
Age	D	D	D	D	D	D	D
	13,000	13,000	13,000	13,000	13,000	13,000	13,000
SiO ₂	42.87	42.64	42.08	41.41	42.83	42.55	42.77
TiO ₂	2.30	2.12	2.14	2.31	2.40	2.18	2.22
Al ₂ O ₃	11.65	11.63	12.37	12.20	11.27	11.33	11.62
Cr ₂ O ₃	0.10	0.07	0.01	0.03	0.02	0.00	0.04
Fe ₂ O ₃	4.11	4.19	4.46	4.48	4.59	4.64	4.55
FeO	5.48	5.51	8.31	7.38	5.82	5.76	5.52
MnO	0.13	0.07	0.16	0.15	0.06	0.13	0.13
MgO	16.12	15.98	14.07	14.47	16.05	15.85	16.08
CaO	11.70	11.64	11.13	11.60	11.47	11.72	11.63
Na ₂ O	2.31	2.33	2.63	2.49	2.39	2.29	2.45
K ₂ O	1.07	1.11	0.38	0.91	0.81	0.94	0.97
total	100.10	99.51	99.89	99.62	99.93	99.61	100.36
Fe=FeO	9.18	9.28	12.32	11.41	9.95	9.94	9.62

Table 22 Olivine

Sample	VF10-07D	VF10-07D	VF10-07D	VF10-07D	VF10-07D	VF10-07D	VF10-07D	VF10-07D	VF10-07D	VF10-07D	VF10-07D	VF10-07D
core/rim	ol 1	ol 1	ol 2	ol 3	ol 3	ol 4	ol 5	ol 5	ol 1	ol 1	ol 2	ol 2
Unit	core	core	core	core	core	core	core	core	rim	rim	rim	rim
Age	N	N	N	N	N	N	N	N	N	N	N	N
	7000	7000	7000	7000	7000	7000	7000	7000	7000	7000	7000	7000
SiO ₂	39.07	39.06	38.97	38.78	38.95	38.40	38.82	38.83	39.04	38.83	41.58	39.14
TiO ₂	0.02	0.02	0.01	0.02	0.01	0.02	0.01	0.00	0.02	0.09	0.08	0.00
Al ₂ O ₃	0.02	0.02	0.02	0.02	0.02	0.03	0.02	0.01	0.03	0.04	1.83	0.04
FeO	18.76	18.77	18.25	19.02	18.95	21.14	18.90	18.83	18.81	19.49	18.36	18.34
MnO	0.36	0.39	0.37	0.38	0.39	0.48	0.43	0.39	0.40	0.40	0.41	0.38
MgO	41.71	41.75	42.13	41.78	41.76	39.71	41.89	41.71	41.77	41.25	41.65	41.98
CaO	0.13	0.13	0.14	0.13	0.13	0.15	0.13	0.11	0.14	0.14	0.40	0.17
NiO	0.18	0.16	0.12	0.16	0.20	0.06	0.10	0.11	0.15	0.13	0.11	0.15
TOTAL	100.26	100.30	100.01	100.30	100.42	99.99	100.30	100.00	100.37	100.36	104.43	100.20
Mg#	80	80	80	80	80	77	80	80	80	79	80	80

Sample	VF10-07D	VF10-07D	VF10-07D	VF10-07D	VF10-07D	VF10-07D	VF01-02Ps	VF01-02Ps	VF01-02Ps	VF01-02Ps	VF01-02Ps	VF01-02Ps
core/rim	ol 3	ol 3	ol 3	ol 4	ol 5	ol 5	ol 1	ol 2	ol 2	ol 3	ol 4	ol 4
Unit	rim	rim	rim	rim	rim	rim	core	core	core	core	core	core
Age	N	N	N	N	N	N	F	F	F	F	F	F
	7000	7000	7000	7000	7000	7000	12,000	12,000	12,000	12,000	12,000	12,000
SiO ₂	38.41	39.02	38.94	37.99	38.58	39.29	40.10	40.13	40.04	39.19	40.29	40.36
TiO ₂	0.02	0.03	0.03	0.03	0.01	0.02	0.01	0.00	0.01	0.00	0.01	0.01
Al ₂ O ₃	0.06	0.79	0.02	0.05	0.03	0.10	0.03	0.03	0.02	0.00	0.03	0.01
FeO	20.58	21.39	19.62	20.91	18.88	18.95	11.50	12.96	12.66	17.71	12.12	12.23
MnO	0.43	0.45	0.40	0.43	0.42	0.40	0.14	0.20	0.21	0.30	0.18	0.19
MgO	40.25	40.48	40.99	40.13	41.84	41.43	47.74	46.23	46.76	42.84	47.57	47.38
CaO	0.16	0.26	0.16	0.16	0.14	0.17	0.16	0.14	0.15	0.11	0.15	0.17
NiO	0.08	0.06	0.14	0.07	0.13	0.13	0.23	0.17	0.21	0.13	0.18	0.14
TOTAL	99.99	102.48	100.30	99.77	100.01	100.48	99.91	99.86	100.05	100.29	100.53	100.50
Mg#	78	77	79	77	80	80	88	86	87	81	87	87

Sample core/rim	VF02-01G ol 1 core	VF02-01G ol 2 core	VF01-02Ps ol 1 rim	VF01-02Ps ol 2 rim	VF01-02Ps ol 2 rim	VF01-02Ps ol 2 rim	VF01-02Ps ol 3 rim	VF01-02Ps ol 4 rim	VF01-02Ps ol 4 rim	VF02-01G ol 1 rim	VF02-01G ol 2 rim	VF00-06O ol 1 core
Unit	F	F	F	F	F	F	F	F	F	F	F	D
Age	12,000	12,000	12,000	12,000	12,000	12,000	12,000	12,000	12,000	12,000	12,000	13,000
SiO ₂	40.62	40.56	40.57	39.26	39.51	39.45	39.19	38.97	38.34	39.33	38.75	40.15
TiO ₂	0.01	0.02	0.25	0.01	0.01	0.02	0.02	0.03	0.03	0.03	0.02	0.00
Al ₂ O ₃	0.01	0.04	3.45	0.02	0.01	0.04	0.05	0.04	0.07	0.04	0.03	0.03
FeO	11.30	11.22	16.94	18.27	18.17	17.88	17.94	17.37	17.58	16.72	17.00	12.21
MnO	0.18	0.21	0.35	0.32	0.30	0.30	0.30	0.30	0.33	0.26	0.30	0.18
MgO	48.10	47.57	36.38	42.23	42.29	42.33	42.38	43.04	42.82	43.15	42.98	47.13
CaO	0.14	0.13	1.17	0.15	0.17	0.17	0.16	0.16	0.21	0.15	0.19	0.15
NiO	0.22	0.21	0.04	0.09	0.11	0.13	0.10	0.13	0.08	0.14	0.10	0.17
TOTAL	100.58	99.96	99.16	100.35	100.57	100.31	100.14	100.03	99.47	99.83	99.37	100.02
Mg#	88	88	79	80	81	81	81	82	81	82	82	87

Sample core/rim	VF00-06O ol 1 core	VF00-06O ol 1 core	VF00-06O ol 2 core	VF00-06O ol 3 core	VF00-06O ol 3 core	VF00-06O ol 3 core	VF00-06O ol 4 core	VF01-02Ns ol 1 core	VF01-02Ns ol 2 core	VF01-05N ol 1 core	VF01-05N ol 2 core	VF01-05N ol 2 core
Unit	D	D	D	D	D	D	D	D	D	D	D	D
Age	13,000	13,000	13,000	13,000	13,000	13,000	13,000	13,000	13,000	13,000	13,000	13,000
SiO ₂	40.24	40.29	40.05	40.19	40.20	40.26	40.01	39.89	39.83	40.01	40.18	39.97
TiO ₂	0.00	0.00	0.01	0.00	0.00	0.00	0.01	0.00	0.01	0.00	0.00	0.00
Al ₂ O ₃	0.02	0.03	0.02	0.02	0.03	0.03	0.02	0.02	0.03	0.00	0.01	0.03
FeO	12.21	12.09	13.38	12.27	12.16	13.11	13.37	13.95	14.56	12.83	13.61	13.40
MnO	0.17	0.13	0.13	0.17	0.20	0.19	0.23	0.26	0.20	0.17	0.23	0.18
MgO	47.00	46.95	46.00	47.03	47.12	46.43	46.33	45.80	45.37	46.70	45.95	46.26
CaO	0.13	0.14	0.14	0.14	0.14	0.14	0.14	0.15	0.15	0.14	0.14	0.16
NiO	0.18	0.21	0.15	0.15	0.16	0.16	0.16	0.11	0.10	0.18	0.12	0.16
TOTAL	99.96	99.84	99.88	99.97	100.02	100.31	100.26	100.17	100.25	100.03	100.24	100.16
Mg#	87	87	86	87	87	86	86	85	85	87	86	86

Sample core/rim	VF01-05N ol 2 core Unit Age	VF00-06O ol 1 rim D 13,000	VF00-06O ol 1 rim D 13,000	VF00-06O ol 2 rim D 13,000	VF00-06O ol 3 rim D 13,000	VF00-06O ol 3 rim D 13,000	VF00-06O ol 3 rim D 13,000	VF00-06O ol 4 rim D 13,000	VF01-02Ns ol 1 rim D 13,000	VF01-02Ns ol 2 rim D 13,000	VF01-05N ol 1 rim D 13,000	VF01-05N ol 2 rim D 13,000
SiO ₂	40.04	39.08	38.38	39.18	38.76	38.53	38.76	38.62	38.68	38.98	38.84	38.95
TiO ₂	0.01	0.02	0.04	0.02	0.02	0.03	0.00	0.01	0.00	0.02	0.03	0.02
Al ₂ O ₃	0.02	0.00	0.04	0.06	0.03	0.05	0.04	0.04	0.06	0.03	0.04	0.05
FeO	14.29	17.67	19.93	19.82	19.19	19.79	19.67	19.76	19.70	19.61	19.64	19.42
MnO	0.21	0.23	0.33	0.37	0.29	0.27	0.31	0.32	0.34	0.31	0.29	0.30
MgO	45.59	43.21	41.35	40.34	41.61	41.05	40.98	41.37	41.20	41.31	41.28	41.44
CaO	0.15	0.13	0.14	0.15	0.15	0.14	0.23	0.17	0.14	0.15	0.15	0.14
NiO	0.08	0.09	0.08	0.10	0.07	0.07	0.05	0.07	0.07	0.07	0.05	0.03
TOTAL	100.38	100.44	100.28	100.03	100.12	99.93	100.03	100.36	100.20	100.48	100.32	100.35
Mg#	85	81	79	78	79	79	79	79	79	79	79	79

Sample core/rim	VF01-05N ol 2 rim Unit Age	VF01-05N ol 2 rim D 13,000
SiO ₂	38.74	38.95
TiO ₂	0.02	0.01
Al ₂ O ₃	0.04	0.04
FeO	19.57	19.61
MnO	0.36	0.34
MgO	41.32	41.44
CaO	0.14	0.13
NiO	0.05	0.11
TOTAL	100.24	100.63
Mg#	79	79

Table 23 Glass

Sample	VF10-03N	VF10-03N	VF10-03N	VF10-03N	VF10-03N	VF10-03N	VF10-03N	VF10-03N	VF10-03N	VF10-03N	VF10-03N	VF10-03N
Unit	gls 1	gls 2	gls 3	gls 4	gls 5	gls 6	gls 7	gls 8	gls 9	gls 10	gls 11	gls 12
Age	N	N	N	N	N	N	N	N	N	N	N	N
Age	7000	7000	7000	7000	7000	7000	7000	7000	7000	7000	7000	7000
SiO ₂	59.12	59.84	58.30	59.51	59.05	64.85	63.99	59.26	60.85	59.01	59.26	59.50
TiO ₂	0.83	0.76	0.80	0.85	0.82	1.04	0.96	0.76	0.78	0.79	0.77	0.80
Al ₂ O ₃	18.59	18.40	17.41	16.51	18.19	16.73	16.86	18.32	18.29	18.05	18.41	18.37
FeO	5.83	5.45	6.02	6.19	4.94	3.78	3.78	5.74	5.28	5.91	5.55	4.93
MnO	0.06	0.09	0.16	0.11	0.13	0.08	0.12	0.09	0.06	0.16	0.13	0.14
MgO	2.47	2.48	2.75	3.02	2.20	1.65	1.61	2.46	2.46	2.79	2.55	2.46
CaO	5.44	5.36	5.53	6.09	4.79	3.35	3.57	5.46	5.56	5.98	5.48	5.26
Na ₂ O	4.49	4.55	5.32	4.18	4.26	5.49	5.03	4.63	4.68	4.52	4.35	4.38
K ₂ O	3.52	3.50	3.76	3.18	4.05	3.89	3.93	3.37	3.35	3.34	3.81	4.02
P ₂ O ₅	0.53	0.61	0.50	0.46	0.48	0.33	0.25	0.47	0.46	0.49	0.57	0.46
TOTAL	100.87	101.04	100.55	100.11	98.92	101.18	100.09	100.55	101.76	101.02	100.86	100.32

Sample	VF10-03N	VF10-03N	VF10-03N	VF10-04N	VF10-04N	VF10-04N	VF10-04N	VF10-04N	VF10-04N	VF10-04N	VF10-04N	VF10-04N
Unit	gls 13	gls 14	gls 15	gls 1	gls 2	gls 3	gls 4	gls 5	gls 6	gls 7	gls 8	gls 9
Age	N	N	N	N	N	N	N	N	N	N	N	N
Age	7000	7000	7000	7000	7000	7000	7000	7000	7000	7000	7000	7000
SiO ₂	61.58	60.06	59.23	64.55	60.40	61.38	59.62	62.47	58.48	59.12	59.46	62.36
TiO ₂	0.65	0.81	0.80	0.92	0.77	0.90	0.76	0.84	0.70	0.86	1.05	0.63
Al ₂ O ₃	18.45	18.29	18.13	15.21	15.39	15.00	15.37	16.70	15.25	13.93	11.20	15.78
FeO	2.32	4.91	5.26	5.02	6.42	6.92	6.79	5.78	6.12	8.07	9.31	5.86
MnO	0.10	0.09	0.11	0.09	0.08	0.10	0.14	0.10	0.12	0.19	0.13	0.15
MgO	0.47	2.23	2.39	1.53	2.67	2.66	2.68	1.41	2.69	3.54	3.96	2.28
CaO	3.56	5.11	5.17	3.47	4.58	3.71	5.07	4.00	3.29	3.61	3.36	4.04
Na ₂ O	5.56	4.63	5.15	4.99	5.10	4.35	5.04	5.29	6.22	5.32	4.98	5.31
K ₂ O	4.05	4.08	4.29	2.70	2.30	2.22	1.89	2.09	2.71	2.44	3.08	1.96
P ₂ O ₅	0.64	0.52	0.47	0.37	0.27	0.28	0.26	0.27	0.26	0.31	0.22	0.19
TOTAL	97.38	100.72	100.98	99.12	98.21	97.60	98.02	99.12	96.28	97.89	97.33	98.73

Sample	VF10-04N	VF95-09G	VF95-09G	VF95-09G	VF95-09G	VF95-09G	VF95-09G	VF95-09G	VF95-09G	VF95-09G	VF95-09G	VF95-09G
Unit	gls 10	gls 1	gls 2	gls 3	gls 4	gls 5	gls 6	gls 7	gls 8	gls 9	gls 10	gls 11
Age	N	N	N	N	N	N	N	N	N	N	N	N
	7000	7000	7000	7000	7000	7000	7000	7000	7000	7000	7000	7000
SiO ₂	60.66	56.85	57.67	62.65	54.63	59.70	57.53	60.54	60.91	60.23	59.69	59.91
TiO ₂	0.75	0.83	0.89	0.77	0.24	0.93	0.91	0.82	0.94	0.92	0.92	0.96
Al ₂ O ₃	14.08	16.77	17.46	15.89	1.81	16.06	17.49	17.20	17.65	17.01	17.32	17.70
FeO	6.92	5.91	5.81	4.66	11.49	6.27	5.85	4.35	4.72	5.43	4.60	4.47
MnO	0.12	0.20	0.09	0.02	0.36	0.16	0.15	0.13	0.09	0.10	0.16	0.07
MgO	3.26	2.81	2.70	1.15	29.98	2.26	2.05	1.85	2.12	2.50	1.99	2.11
CaO	3.10	6.12	5.86	3.53	1.64	4.01	4.97	4.12	5.29	5.05	4.59	4.40
Na ₂ O	5.56	5.25	4.79	4.62	0.05	4.33	4.91	4.56	5.44	5.30	4.91	4.82
K ₂ O	2.43	3.00	3.16	1.65	0.00	4.17	3.83	4.49	2.11	2.37	4.06	3.87
P ₂ O ₅	0.25	-	-	-	-	-	-	-	-	-	-	-
TOTAL	97.48	97.75	98.43	94.93	100.19	97.89	97.68	98.06	99.28	98.91	98.23	98.32

Sample	VF95-09G	VF10-07D	VF10-07D	VF10-07D	VF10-07D	VF10-07D	VF10-07D	VF02-01G	VF02-01G	VF02-01G	VF02-01G	VF02-01G
Unit	gls 12	gls 1	gls 2	gls 3	gls 4	gls 5	gls 6	gls 2	gls 3	gls 4	gls 5	gls 6
Age	N	N	N	N	N	N	N	F	F	F	F	F
	7000	7000	7000	7000	7000	7000	7000	12,000	12,000	12,000	12,000	12,000
SiO ₂	58.49	56.14	56.48	56.84	49.47	57.50	57.43	58.64	58.71	59.09	59.10	56.81
TiO ₂	0.83	0.88	0.69	0.81	0.74	0.89	1.06	0.79	0.80	0.67	0.88	0.73
Al ₂ O ₃	17.63	16.37	19.86	17.58	14.09	15.71	15.54	17.37	17.16	18.03	18.16	17.00
FeO	5.40	6.59	5.57	6.32	5.19	7.39	7.41	4.06	3.84	2.63	2.34	1.85
MnO	0.11	0.11	0.11	0.14	0.12	0.17	0.11	0.12	0.10	0.06	0.16	0.06
MgO	2.32	2.78	2.14	2.24	2.10	3.00	2.52	2.00	1.53	1.20	0.46	0.71
CaO	5.18	5.53	7.20	5.53	4.27	5.61	5.10	3.63	3.23	2.38	4.50	4.07
Na ₂ O	4.74	4.54	4.34	4.90	3.96	5.09	4.87	4.84	5.14	5.49	4.79	4.16
K ₂ O	3.64	4.34	2.78	3.09	2.58	3.29	2.84	3.81	4.40	5.32	3.04	3.67
P ₂ O ₅	-	0.53	0.43	0.53	0.49	0.49	0.47	-	-	-	-	-
TOTAL	98.34	97.80	99.60	97.98	83.01	99.14	97.35	95.24	94.91	94.88	93.44	89.06

Sample	VF01-05N	VF01-05N	VF01-05N	VF01-05N	VF01-05N	VF01-05N	VF01-05N	VF01-05N	VF01-05N	VF01-05N	VF01-05N	VF01-05N
Unit	gls 1	gls 2	gls 3	gls 4	gls 5	gls 6	gls 7	gls 8	gls 9	gls 10	gls 11	gls 12
Age	D	D	D	D	D	D	D	D	D	D	D	D
	13,000	13,000	13,000	13,000	13,000	13,000	13,000	13,000	13,000	13,000	13,000	13,000
SiO ₂	58.61	58.72	56.84	55.84	58.93	59.35	56.59	57.92	60.44	58.84	54.81	55.04
TiO ₂	0.42	0.37	0.19	0.14	0.58	0.58	0.13	0.40	0.58	0.39	0.81	0.87
Al ₂ O ₃	19.90	21.24	23.72	24.20	18.20	18.19	25.68	21.71	16.95	21.37	17.73	17.65
FeO	2.54	2.11	1.63	1.79	3.44	3.34	1.07	2.26	3.65	2.39	6.01	6.28
MnO	0.09	0.09	0.04	0.01	0.06	0.09	0.00	0.10	0.09	0.06	0.17	0.09
MgO	0.74	0.55	0.36	0.77	1.82	1.23	0.26	0.56	1.84	0.63	2.31	2.56
CaO	6.57	6.77	8.62	8.96	6.22	5.25	9.72	6.84	6.04	7.09	5.51	5.73
Na ₂ O	4.74	5.29	5.21	4.99	4.42	4.54	5.69	5.09	4.63	5.17	4.61	4.55
K ₂ O	2.87	2.64	1.39	1.25	3.20	3.69	0.53	2.40	3.55	2.40	3.29	3.20
P ₂ O ₅	0.40	0.23	0.14	0.18	0.42	0.49	0.03	0.33	0.37	0.37	0.76	0.69
TOTAL	96.89	98.01	98.15	98.14	97.30	96.75	99.70	97.59	98.15	98.70	96.00	96.66

Sample	VF01-05N	VF01-05N	VF01-02Ns	VF01-02Ns	VF01-02Ns	VF01-02Ns	VF01-02Ns	VF01-02Ns	VF01-02Ns	VF01-02Ns	VF01-02Ns	VF01-02Ns
Unit	gls 13	gls 15	gls 1	gls 2	gls 3	gls 4	gls 5	gls 6	gls 7	gls 8	gls 9	gls 10
Age	D	D	D	D	D	D	D	D	D	D	D	D
	13,000	13,000	13,000	13,000	13,000	13,000	13,000	13,000	13,000	13,000	13,000	13,000
SiO ₂	57.47	60.57	60.78	62.38	60.57	54.37	64.67	63.64	60.50	56.78	59.86	60.78
TiO ₂	0.25	0.71	0.46	0.41	0.56	0.15	0.44	0.33	0.67	0.39	0.32	0.40
Al ₂ O ₃	23.11	17.76	19.04	18.76	17.62	25.95	15.02	16.85	16.49	19.37	21.48	20.01
FeO	2.25	4.29	2.85	2.52	3.14	1.12	3.29	2.58	3.77	2.49	1.97	2.53
MnO	0.01	0.10	0.04	0.04	0.10	0.02	0.02	0.06	0.09	0.04	0.04	0.05
MgO	0.64	1.46	0.87	0.65	0.97	0.26	1.54	0.79	1.38	0.84	0.53	0.69
CaO	8.27	4.99	5.25	4.69	4.79	10.72	2.31	3.36	4.33	6.30	6.72	5.59
Na ₂ O	5.30	4.92	5.17	5.38	4.93	4.61	4.45	4.82	4.61	4.66	5.58	5.28
K ₂ O	1.67	3.57	3.45	3.52	3.85	0.90	5.02	4.47	3.89	2.55	2.31	3.04
P ₂ O ₅	0.29	0.57	0.26	0.12	0.44	0.12	0.20	0.20	0.51	0.44	0.33	0.35
TOTAL	99.25	98.94	98.16	98.47	96.98	98.22	96.97	97.09	96.25	93.86	99.14	98.72

Sample	VF01-02Ns gls 11	VF01-02Ns gls 12	VF01-02Ns gls 13	VF01-02Ns gls 14	VF01-02Ns gls 15	VF01-02Ns gls 16	VF01-02Ns gls 17	VF00-06O gls 1	VF00-06O gls 2	VF00-06O gls 5
Unit	D	D	D	D	D	D	D	D	D	D
Age	13,000	13,000	13,000	13,000	13,000	13,000	13,000	13,000	13,000	13,000
SiO ₂	60.40	58.69	58.70	55.18	55.11	54.72	59.53	65.60	66.92	61.60
TiO ₂	0.79	0.46	0.50	0.45	0.85	0.83	0.48	0.31	0.48	0.46
Al ₂ O ₃	17.35	21.18	18.82	20.43	17.18	17.88	14.86	16.03	13.73	17.94
FeO	4.32	2.86	2.99	2.97	6.54	7.01	6.02	2.30	2.56	1.71
MnO	0.13	0.01	0.07	0.10	0.14	0.17	0.08	0.09	0.06	0.00
MgO	1.38	0.87	0.90	0.92	2.80	2.97	2.72	0.45	0.51	0.58
CaO	4.60	6.40	4.94	6.26	5.47	6.16	3.73	2.39	1.38	4.58
Na ₂ O	5.06	5.31	4.88	4.65	4.57	4.18	4.45	4.40	3.96	4.83
K ₂ O	3.68	2.40	3.55	2.59	3.10	2.92	4.98	5.22	5.74	4.01
P ₂ O ₅	0.73	0.39	0.56	0.30	0.73	0.85	0.15	0.03	0.09	0.35
TOTAL	98.44	98.58	95.92	93.85	96.48	97.69	97.00	96.81	95.44	96.05

Table 24 Phlogopite

Sample	VF10-03N phlog_1	VF01-02Ps phlog_1	VF01-02Ps phlog_2	VF01-02Ps phlog_3	VF01-02Ps phlog_4	VF01-02Ps phlog_2_1	VF01-02Ps phlog_2_2	VF01-02Ps phlog_2_3	VF01-02Ps phlog_2_4	VF01-02Ps phlog_2_5
Unit	N	F	F	F	F	F	F	F	F	F
Age	7000	12,000	12,000	12,000	12,000	12,000	12,000	12,000	12,000	12,000
SiO ₂	38.01	37.74	37.79	36.96	36.62	37.56	39.50	40.54	36.43	37.36
TiO ₂	5.99	3.68	3.66	3.57	3.73	3.50	3.65	3.61	3.41	3.50
Al ₂ O ₃	12.88	14.85	14.91	16.36	15.02	15.37	15.29	14.55	14.99	14.83
Cr ₂ O ₃	0.03	0.07	0.15	0.12	0.14	0.09	0.10	0.11	0.10	0.12
FeO	10.27	8.49	8.66	8.53	9.14	8.48	8.44	8.32	8.43	8.59
MnO	0.05	0.04	0.06	0.03	0.05	0.06	0.06	0.04	0.03	0.06
MgO	18.16	20.15	19.80	18.85	21.13	20.19	20.90	21.84	19.63	19.71
CaO	0.00	0.03	0.05	0.21	0.03	0.37	0.66	0.98	0.46	0.28
Na ₂ O	1.02	0.78	0.80	0.77	1.06	0.68	0.30	0.04	0.77	0.77
K ₂ O	8.27	8.52	8.57	8.43	8.58	7.10	3.16	0.73	8.09	8.37
H ₂ O	4.08	4.11	4.11	4.09	4.12	4.10	4.17	4.18	4.02	4.07
TOTAL	98.78	98.46	98.55	97.90	99.63	97.50	96.23	94.95	96.36	97.65

Sample	VF01-02Ps	VF01-02Ps	VF01-02Ps	VF01-02Ps	VF01-02Ps	VF01-02Ps	VF01-02Ps	VF01-02Ps	VF01-02Ps	VF01-02Ps
Unit	phlog 3_1	phlog 3_2	phlog 3_3	phlog 3_4	phlog 4_1	phlog 4_2	phlog 4_3	phlog 4_4	phlog 4_5	phlog 4_6
Age	F	F	F	F	F	F	F	F	F	F
	12,000	12,000	12,000	12,000	12,000	12,000	12,000	12,000	12,000	12,000
SiO ₂	38.26	38.18	36.12	36.36	39.60	39.39	40.06	37.77	39.85	38.15
TiO ₂	3.64	3.65	3.65	3.71	3.61	2.44	3.54	3.61	3.55	3.56
Al ₂ O ₃	14.80	15.07	14.33	15.05	14.43	18.79	14.19	14.62	14.56	14.72
Cr ₂ O ₃	0.11	0.15	0.13	0.15	0.08	0.12	0.16	0.10	0.12	0.09
FeO	8.24	8.44	8.45	8.69	8.20	6.44	7.87	8.39	8.25	8.41
MnO	0.07	0.08	0.02	0.02	0.00	0.03	0.02	0.02	0.00	0.09
MgO	19.71	19.83	18.72	19.07	19.28	15.26	19.15	20.10	19.31	20.13
CaO	0.33	0.22	0.47	0.45	0.33	0.63	0.40	0.25	0.26	0.10
Na ₂ O	0.60	0.62	0.12	0.06	0.02	0.02	0.01	0.69	0.33	0.90
K ₂ O	7.01	7.47	1.13	0.66	0.14	0.07	0.11	6.90	5.05	8.61
H ₂ O	4.09	4.11	3.80	3.86	3.99	3.94	3.99	4.07	4.10	4.13
TOTAL	96.86	97.82	86.95	88.09	89.68	87.13	89.52	96.54	95.38	98.89

Sample	VF02-01G	VF02-01G	VF02-01G	VF02-01G	VF02-01G	VF02-01G	VF02-01G	VF02-01G	VF02-01G	VF02-01G
Unit	phlog 1_1	phlog 1_2	phlog 1_3	phlog 1_4	phlog 2_1	phlog 2_2	phlog 2_3	phlog 3_1	phlog 3_2	phlog 3_3
Age	F	F	F	F	F	F	F	F	F	F
	12,000	12,000	12,000	12,000	12,000	12,000	12,000	12,000	12,000	12,000
SiO ₂	36.78	36.02	37.03	36.54	37.47	37.59	37.77	36.56	37.29	35.85
TiO ₂	3.21	3.45	3.05	2.80	2.92	2.75	2.82	3.83	3.17	3.48
Al ₂ O ₃	18.61	18.25	20.57	20.98	17.95	20.02	19.67	17.88	16.87	19.03
Cr ₂ O ₃	0.19	0.15	0.15	0.12	0.26	0.19	0.14	0.24	0.26	0.33
FeO	7.08	7.28	6.89	6.34	7.16	7.36	7.20	7.09	7.11	6.90
MnO	0.04	0.04	0.03	0.02	0.06	0.06	0.06	0.08	0.05	0.02
MgO	18.23	17.55	17.78	16.11	17.52	17.59	18.85	17.78	16.58	15.95
CaO	0.91	0.92	0.88	0.98	0.59	0.73	0.70	0.75	0.81	0.82
Na ₂ O	0.03	0.04	0.05	0.03	0.03	0.04	0.04	0.03	0.08	0.04
K ₂ O	0.04	0.05	0.08	0.09	0.04	0.05	0.06	0.06	0.42	0.05
H ₂ O	3.97	3.90	4.05	3.95	3.93	4.04	4.08	3.93	3.85	3.86
TOTAL	89.08	87.65	90.55	87.97	87.93	90.42	91.39	88.23	86.49	86.32

Sample	VF02-01G	VF02-01G	VF02-01G	VF02-01G	VF02-01G	VF02-01G	VF00-06P	VF00-06P	VF00-06P	VF00-06P
Unit	phlog 3_4	phlog 3_5	phlog 4_1	phlog 4_2	phlog 4_3	phlog 4_4	phlog 1_1	phlog 1_2	phlog 1_3	phlog 2_1
Age	F	F	F	F	F	F	F	F	F	F
	12,000	12,000	12,000	12,000	12,000	12,000	12,000	12,000	12,000	12,000
SiO ₂	37.49	36.93	37.55	36.99	36.91	38.87	37.67	36.83	37.40	38.04
TiO ₂	2.70	2.34	3.59	3.59	4.82	3.53	3.12	3.60	3.67	3.41
Al ₂ O ₃	21.48	20.96	17.17	18.06	15.43	15.65	14.79	15.15	15.67	14.93
Cr ₂ O ₃	0.20	0.17	0.08	0.24	0.24	0.09	0.25	0.19	0.15	0.27
FeO	6.64	6.84	7.55	7.92	8.54	7.71	8.09	8.40	8.35	8.38
MnO	0.04	0.02	0.09	0.03	0.00	0.02	0.03	0.03	0.03	0.02
MgO	14.80	14.99	17.01	16.57	18.29	20.10	20.20	20.22	16.40	20.18
CaO	0.55	0.53	1.42	1.05	0.68	0.90	0.04	0.08	1.02	0.02
Na ₂ O	0.06	0.04	0.07	0.06	0.54	0.51	0.88	0.94	0.14	0.92
K ₂ O	0.07	0.07	0.04	0.07	6.02	5.41	8.74	8.58	4.88	8.89
H ₂ O	3.97	3.91	3.93	3.93	4.04	4.15	4.08	4.08	3.92	4.13
TOTAL	87.99	86.80	88.50	88.51	95.49	96.93	97.90	98.10	91.62	99.21

Appendix H: Group II Whole-rock Major Element and Trace Element Geochemical Data

Table 25 XRF

Sample:	VF01-10D	VF95-09G	VF98-07D	VF98-10O	VF99-03R	VF10-07D	VF97-03BJ	VF10-03N	VF10-04F	VF00-06Pi	VF00-06Ps	VF01-02Pi
Unit:	N	N	N	N	N	N	N	N	F	F	F	F
Age (yrs B.P.)	7000	7000	7000	7000	7000	7000	7000	7000	12,000	12,000	12,000	12,000
SiO ₂	56.4	56.2	56.1	56.5	55.6	55.2	56.4	52.8	50.5	52.1	53.3	51.8
TiO ₂	0.80	0.84	0.85	0.82	0.83	0.79	0.79	0.86	0.84	0.98	0.85	0.99
Al ₂ O ₃	17.2	17.6	18.3	17.8	17.9	18.1	16.3	18.8	17.2	14.4	17.4	14.9
FeOt	6.0	6.0	6.1	5.9	6.1	-	6.0	-	-	6.9	7.0	7.0
MnO	0.11	0.11	0.11	0.11	0.11	0.12	0.11	0.11	0.11	0.11	0.13	0.12
MgO	4.4	4.3	3.4	3.5	4.2	3.8	6.2	3.3	7.3	7.3	6.4	7.5
CaO	6.6	6.7	6.2	6.2	6.4	6.3	7.2	5.7	7.8	8.0	7.6	7.7
Na ₂ O	4.0	4.2	4.1	4.1	3.9	4.0	4.2	3.5	3.3	2.8	3.5	2.4
K ₂ O	2.1	2.1	2.5	2.5	2.1	2.4	1.6	2.1	0.7	2.3	1.0	1.9
P ₂ O ₅	0.41	0.46	0.48	0.51	0.43	0.54	0.28	0.56	0.27	0.60	0.27	0.64
L.O.I.	1.4	1.0	0.9	1.0	2.2	-	0.6	-	-	2.7	1.6	4.1
Total	99.38	99.63	99.41	99.23	100.06	98.10	94.69	96.20	98.15	99.14	99.09	98.44
V	122	163	165	162	149	150	157	141	177	149	142	146
Cr	131	102	68	67	111	71	279	80	205	299	209	292
Co	21	20	18	18	20	17	26	17	27	29	29	28
Ni	54	44	35	36	48	36	100	34	69	98	98	109
Cu	42	45	47	44	44	49	36	52	42	85	54	89
Zn	85	75	80	81	76	78	67	102	73	82	80	111
Rb	26	30	28	30	24	-	21	-	-	19	8	16
Sr	1247	1318	1466	1422	1282	1423	962	1308	578	2540	1033	2296
Y	21	20	20	19	20	22	18	22	20	19	17	19
Zr	281	212	248	241	227	222	177	234	125	304	153	384
Nb	2	6	4	3	8	-	5	-	-	9	4	6
Ba	916	989	1036	1103	977	-	677	-	-	1844	539	1769

Sample Unit: Age (yrs B.P.)	VF01-02Ps F 12,000	VF02-01G F 12,000	VF01-05PA F 12,000	VF95-01B D 13,000	VF95-01C D 13,000	VF01-02Ni D 13,000	VF00-06Os D 13,000	VF01-05N D 13,000	VF97-20D D 13,000	VF00-06Oi D 13,000	VF01-02Ns D 13,000
SiO ₂	49.6	43.9	48.4	57.5	57.2	55.5	53.7	54.2	56.8	54.1	54.4
TiO ₂	1.1	1.3	1.1	0.8	0.8	0.9	0.9	0.9	0.8	0.9	0.9
Al ₂ O ₃	16.0	19.2	16.2	18.6	18.8	16.3	16.2	15.9	18.4	16.1	16.0
FeO _t	7.7	9.1	7.8	6.3	6.2	6.6	7.0	6.8	6.2	6.8	6.8
MnO	0.12	0.11	0.09	0.13	0.12	0.12	0.13	0.12	0.11	0.13	0.12
MgO	7.5	8.1	7.7	2.9	2.8	5.1	6.0	6.1	4.9	5.8	5.8
CaO	7.6	6.9	7.1	6.4	6.4	7.2	8.0	7.9	6.9	7.6	7.7
Na ₂ O	2.1	1.2	1.6	4.4	4.3	3.6	3.7	3.4	4.0	3.7	3.5
K ₂ O	1.0	0.4	1.0	1.1	1.0	2.1	2.1	2.2	1.0	2.1	2.2
P ₂ O ₅	0.60	0.41	0.68	0.26	0.24	0.44	0.51	0.49	0.21	0.48	0.48
L.O.I.	5.1	8.1	7.5	1.7	1.9	1.5	1.2	1.3	1.1	1.3	1.3
Total	98.44	98.70	98.92	100.08	99.95	99.29	99.36	99.26	100.38	99.04	99.15
V	157	194	163	137	141	132	144	142	151	138	140
Cr	344	375	311	12	<3	101	146	159	92	143	148
Co	33	42	30	20	21	24	25	26	21	25	25
Ni	121	137	123	17	17	29	41	42	51	41	40
Cu	92	75	92	39	36	48	66	54	36	61	54
Zn	71	64	70	76	71	84	85	84	69	86	84
Rb	3	2	7	15	12	21	23	24	12	22	21
Sr	2507	1674	1922	680	624	1288	1398	1395	619	1346	1381
Y	20	20	21	20	21	22	22	21	17	22	21
Zr	433	361	395	158	150	276	285	288	137	280	278
Nb	6	9	2	3	7	5	5	5	<2	6	5
Ba	1700	892	1354	430	395	812	842	808	461	812	820

Table 26 ICP-MS Trace Element Data

Sample:	VF01-10D	VF95-09G	VF10-07D	VF97-03BJ	VF10-03N	VF10-04F	VF00-06Pi	VF00-06Ps	VF01-02Pi	VF01-02Ps	VF01-05PA
Unit:	N	N	N	N	N	F	F	F	F	F	F
Age (yrs B.P.)	7000	7000	7000	7000	7000	12,000	12,000	12,000	12,000	12,000	12,000
Sc	14.7	15.3	-	21.0	-	-	26.3	25.4	27.0	30.8	29.8
Rb	26.4	27.0	26.7	20.6	26.0	6.9	20.6	9.0	17.1	6.1	8.9
Sr	1257	1333	-	933	-	-	2548	990	2171	2544	1798
Y	20.94	20.29	-	18.68	-	-	18.25	17.62	20.13	20.63	22.30
Zr	194	-	-	-	-	-	207	112	211	244	241
Nb	4.26	4.46	4.39	3.62	4.55	3.63	4.94	3.23	4.98	5.94	5.64
Cs	0.60	0.61	0.57	0.51	1.17	0.29	0.34	0.22	0.39	0.20	0.22
Ba	969	969	-	685	-	-	1826	571	1667	1606	1270
La	33.12	33.35	36.70	21.06	35.38	19.35	54.86	18.51	61.01	61.44	67.64
Ce	68.55	70.25	81.25	45.25	73.13	38.14	110.58	36.96	116.48	134.72	107.04
Pr	8.80	9.01	10.68	5.82	10.64	5.97	13.84	5.03	15.34	16.14	17.70
Nd	36.11	37.30	45.19	25.17	44.84	25.48	57.11	21.58	62.84	64.96	70.71
Sm	7.19	7.07	8.18	5.43	8.03	5.36	10.19	4.63	10.98	11.17	12.27
Eu	1.96	1.98	2.07	1.64	2.08	1.41	2.64	1.44	2.86	2.91	3.12
Gd	5.37	5.17	5.69	4.39	5.71	4.20	6.63	3.89	7.16	7.51	7.59
Tb	0.72	0.74	0.82	0.63	0.80	0.68	0.77	0.59	0.82	0.91	0.93
Dy	3.96	3.91	3.39	3.44	3.54	3.24	3.81	3.39	4.17	4.66	4.62
Ho	0.74	0.73	0.65	0.66	0.68	0.64	0.68	0.66	0.73	0.82	0.80
Er	1.97	1.90	1.76	1.76	1.84	1.77	1.66	1.79	1.84	2.05	2.00
Tm	0.28	0.28	0.26	0.25	0.27	0.26	0.23	0.25	0.25	0.28	0.28
Yb	1.77	1.68	1.88	1.58	1.86	1.79	1.35	1.59	1.47	1.70	1.68
Lu	0.28	0.26	0.28	0.25	0.26	0.25	0.21	0.25	0.23	0.26	0.25
Hf	5.34	5.23	5.60	3.89	5.58	3.18	5.98	3.24	6.30	7.15	7.10
Ta	0.26	0.26	0.29	0.24	0.33	0.22	0.25	0.19	0.25	0.31	0.29
Pb	9.51	9.77	-	7.17	-	-	21.17	7.71	21.76	23.15	23.64
Th	3.61	3.96	4.50	2.53	4.24	1.66	4.98	1.55	5.21	5.50	5.70
U	1.11	1.26	1.28	0.88	1.55	0.55	1.41	0.58	1.44	1.69	1.46

Sample: Unit: Age (yrs B.P.)	VF01-02Ni D 13,000	VF00-06Os D 13,000	VF01-05N D 13,000	VF00-06Oi D 13,000	VF01-02Ns D 13,000
Sc	22.0	25.1	24.5	24.2	23.9
Rb	22.5	22.2	22.8	22.2	23.2
Sr	1229	1478	1346	1360	1320
Y	21.24	21.70	21.29	21.01	20.98
Zr	173	185	182	179	179
Nb	4.09	3.96	3.89	3.93	3.88
Cs	0.45	0.40	0.42	0.40	0.43
Ba	803	865	803	800	810
La	35.37	37.29	37.42	37.02	36.53
Ce	73.85	81.13	79.48	78.21	77.84
Pr	9.72	10.70	10.47	10.32	10.33
Nd	42.31	46.78	45.43	44.63	44.06
Sm	8.65	9.57	9.34	9.04	8.94
Eu	2.42	2.54	2.54	2.47	2.39
Gd	6.38	6.95	6.85	6.47	6.45
Tb	0.81	0.86	0.86	0.83	0.82
Dy	4.10	4.44	4.27	4.24	4.12
Ho	0.77	0.80	0.77	0.76	0.77
Er	1.99	2.07	1.93	1.97	1.94
Tm	0.27	0.28	0.28	0.26	0.27
Yb	1.67	1.69	1.65	1.63	1.64
Lu	0.26	0.26	0.26	0.25	0.25
Hf	4.73	5.09	5.02	5.04	4.93
Ta	0.24	0.23	0.23	0.23	0.22
Pb	9.76	10.02	10.15	9.73	9.52
Th	3.79	4.24	4.31	4.11	4.09
U	1.22	1.27	1.33	1.28	1.27

Appendix I: Cinder Cone Whole-rock Major and Trace Element Data

Table 27 Whole-rock major and trace element XRF data.

Ref:	1	1	1	1	1	1	1	1	1	1	1
Sample:	17B	SAY-22E	500	501	507	508	510	511	5A	6A	6D
Composition:	Basaltic	Basaltic	Basanite	Basanite	Basanite	Basanite	Basanite	Minette	Leucite Basanite	Minette	Minette
Cinder cone:	Usmajac	Tezontal	Apaxtepec	Apaxtepec	Telcampana	Telcampana	Cuauhatemoc	Le Erita	Le Erita	San Isidro	San Isidro
SiO₂	55.40	49.42	50.27	49.48	47.78	48.45	47.96	47.60	48.30	47.96	48.32
TiO₂	1.50	0.77	1.75	1.60	1.10	1.01	1.14	1.61	1.16	1.53	1.61
Al₂O₃	17.08	16.92	14.76	13.51	12.26	11.85	14.50	11.14	11.98	11.44	11.39
Fe₂O₃	1.71	4.40	3.07	2.84	4.86	4.10	4.90	5.42	6.29	5.61	5.92
FeO	5.86	5.30	5.84	5.36	2.98	3.78	3.82	2.34	1.72	2.45	2.15
MnO	0.16	0.15	0.15	0.15	0.14	0.14	0.16	0.13	0.13	0.13	0.13
MgO	4.90	9.27	7.41	9.80	13.40	15.25	10.44	12.35	13.27	12.21	11.65
CaO	7.02	10.12	9.39	9.07	9.11	8.86	10.29	8.78	9.25	8.57	8.64
Na₂O	4.31	2.49	3.20	2.97	2.60	2.12	2.63	3.83	3.85	3.45	3.51
K₂O	1.59	0.65	3.02	3.69	3.69	3.05	2.64	2.48	2.55	3.01	3.11
P₂O₅	0.47	0.20	0.76	0.99	0.91	0.71	0.74	1.31	1.02	1.23	1.27
L.O.I.	0.28	0.19	0.39	0.74	0.87	0.55	0.75	2.23	0.29	1.99	1.84
SUM	100.28	99.88	100.01	100.20	99.70	99.87	99.97	99.22	99.81	99.58	99.54
XRF (ppm)											
V	-	-	-	-	-	-	-	-	-	-	-
Cr	121	196	313	535	844	1280	580	805	755	655	658
Co	-	-	-	-	-	-	-	-	-	-	-
Ni	93	221	82	212	449	506	192	506	392	344	406
Cu	16	24	50	68	62	39	74	50	71	82	100
Zn	75	66	84	74	81	74	69	83	72	84	85
Rb	23	7	38	52	32	21	16	62	37	51	49
Sr	856	444	1220	1566	2142	1715	1464	1670	2308	2342	2456
Y	24	18	27	25	18	16	18	19	23	22	23
Zr	187	92	346	420	251	215	188	411	312	404	413
Nb	22	4	11	14	6	6	10	14	11	14	15
Ba	-	-	-	-	-	-	-	-	2009	2425	-

Ref:	1	1	1	1	2	2	2	2	2	2	2
Sample:	6E	7E	8G	8H	1001B	1003B	1005A	1006B	1007A	1007B	1008B
Composition:	Minette	Minette El Carpintero	Minette	Minette	Basanite	Basanite	Basanite	Basanite	Minette	Minette	Basanite
Cinder cone:	San Isidro	Norte	Comal Chico	Comal Chico	Apaxtepec	La Erita	Telcampana	Comal Chico	El Carpintero	El Carpintero	Comal Grande
SiO₂	49.01	48.20	48.49	48.24	50.06	48.66	49.18	48.52	48.48	48.41	49.90
TiO₂	1.48	1.64	1.32	1.36	1.65	1.12	1.04	1.37	1.62	1.63	1.34
Al₂O₃	12.41	11.62	12.46	12.43	15.99	11.72	12.42	12.38	11.57	11.66	14.42
Fe₂O₃	5.36	4.22	4.60	4.60	2.87	5.25	5.29	4.30	4.07	4.63	3.54
FeO	2.58	3.27	3.53	3.60	7.11	2.73	2.79	3.92	3.41	2.91	4.96
MnO	0.11	0.11	0.15	0.15	0.15	0.12	0.13	0.13	0.12	0.12	0.14
MgO	10.05	11.81	11.07	11.54	6.15	13.09	13.43	11.54	11.67	11.74	9.08
CaO	8.81	8.32	8.84	8.83	9.15	9.01	9.02	8.52	8.01	8.07	9.04
Na₂O	4.16	3.28	3.23	2.55	3.35	2.93	2.56	3.06	3.52	3.76	2.55
K₂O	2.77	3.58	2.98	4.38	2.20	2.95	3.38	3.35	3.38	2.94	3.55
P₂O₅	1.13	1.32	1.05	1.13	0.52	1.01	0.83	1.13	1.32	1.31	0.86
L.O.I.	1.76	1.96	1.46	0.76	-	-	-	-	-	-	-
SUM	99.63	99.33	99.18	99.57	99.20	98.59	100.07	98.22	97.17	97.18	99.38
XRF (ppm)											
V	-	-	-	-	-	-	-	-	-	-	-
Cr	470	265	700	600	99	809	884	606	613	542	424
Co	-	-	-	-	-	-	-	-	-	-	-
Ni	194	436	272	282	52	453	430	324	390	358	137
Cu	49	90	41	56	-	-	-	-	-	-	-
Zn	76	80	83	81	-	-	-	-	-	-	-
Rb	51	73	31	35	23	32	20	21	74	74	28
Sr	2372	3079	2273	2189	1060	2330	2030	2350	3180	3270	1745
Y	22	29	22	21	26	20	20	20	29	28	22
Zr	390	554	347	359	300	315	256	388	590	590	360
Nb	10	16	9	14	-	-	-	-	-	-	-
Ba	2287	-	2162	-	1180	2240	1995	2480	4940	5180	1970

Ref:	2	2	2	2	2	3	3	3	3	3	3
Sample:	1013	1015	1016	22E (new)	1002	LE-02	LE-03	AP-01	AP-03	CU-01	CU-02
Composition:	Minette	Basanite	Basanite	Basalt	Basalt-andesite	Minette	Minette	Minette	Basanite	Basalt-andesite	Basalt-andesite
Cinder cone:	San Isidro	La Erita	Cuauhtemoc	Tezontal	Usmajac	La Erita	La Erita	Apaxtepec	Apaxtepec	Usmajac	Usmajac
SiO₂	48.44	48.77	48.46	49.44	55.18	46.74	48.30	48.47	49.35	54.45	54.95
TiO₂	1.52	1.30	1.10	0.82	1.40	1.42	1.26	1.35	1.47	1.36	1.37
Al₂O₃	11.03	11.39	14.13	16.55	16.87	10.72	10.72	12.07	13.05	16.46	16.74
Fe₂O₃	5.21	4.47	5.08	2.82	2.75	-	-	-	-	-	-
FeO	2.94	3.56	3.82	6.71	4.86	-	-	-	-	-	-
MnO	0.12	0.13	0.15	0.15	0.12	0.12	0.13	0.14	0.14	0.13	0.13
MgO	12.73	13.42	10.57	9.15	4.88	11.97	14.24	13.55	10.88	5.86	5.50
CaO	8.37	9.35	10.22	10.05	6.95	8.57	8.21	8.09	8.82	6.68	6.75
Na₂O	2.34	2.28	2.43	2.43	4.03	2.46	1.94	1.73	1.95	3.84	3.82
K₂O	4.64	3.91	2.58	0.64	1.64	4.77	3.76	3.24	3.55	1.48	1.49
P₂O₅	1.18	0.95	0.70	0.19	0.44	1.29	0.97	0.82	0.89	0.43	0.43
L.O.I.	-	-	-	-	-	1.50	1.90			0.60	0.90
SUM	98.52	99.53	99.24	98.95	99.12	96.56	98.78	97.54	98.01	99.07	99.80
XRF (ppm)											
V	-	-	-	-	-	198	185	215	229	145	148
Cr	741	945	572	345	117	591	941	746	600	152	146
Co	-	-	-	-	-	-	-	-	-	-	-
Ni	468	401	227	168	76	353	487	437	266	114	103
Cu	-	-	-	-	-	73	34	70	79	30	27
Zn	-	-	-	-	-	96	92	75	77	83	81
Rb	35	29	7	6	18	-	-	-	-	-	-
Sr	2430	1850	1570	496	910	-	-	-	-	-	-
Y	21	19	18	21	21	-	-	-	-	-	-
Zr	404	329	207	111	192	-	-	-	-	-	-
Nb	-	-	-	-	-	-	-	-	-	-	-
Ba	2540	1950	1255	227	552	2342	1881	1548	1672	475	490

Ref:	4	4	4	4	4	4	5	5	5
Sample:	SAY-22F	VF99-01A	VF99-01B	VF99-09A	VF99.08	VF99-07A	SAY-7E	SAY-8H	1004-500
Composition:	Basalt-andesite	Basanite	Basanite	Basanite	Minette	Minette	Minette	Minette	Basanite
Cinder cone:	Tezontal	Apaxtepec	Apaxtepec	Telcampana	La Erita	San Isidro	El Carpintero Norte	Comal Chico	Apaxtepec
SiO₂	50.18	49.02	50.54	46.63	48.05	47.20	48.20	48.24	50.27
TiO₂	0.85	1.43	1.67	0.97	1.21	1.53	1.64	1.36	1.75
Al₂O₃	17.19	12.72	15.31	12.07	10.89	10.99	11.62	12.43	14.76
Fe₂O₃	3.61	4.00	3.16	4.53	4.45	5.24	-	-	-
FeO	5.76	4.46	5.96	3.13	3.34	2.68	-	-	-
MnO	0.15	0.14	0.14	0.13	0.13	0.12	0.11	0.15	0.15
MgO	7.99	12.23	7.09	13.02	13.80	12.00	11.81	11.54	7.41
CaO	9.67	8.45	9.07	8.53	8.39	8.00	8.32	8.83	9.40
Na₂O	2.60	1.69	2.84	2.33	1.93	2.39	3.28	2.55	3.20
K₂O	0.69	3.39	2.80	3.03	3.67	4.70	3.58	4.38	3.02
P₂O₅	0.20	0.87	0.70	0.80	0.90	1.23	1.32	1.13	0.80
L.O.I.	0.91	0.57	0.46	3.40	1.94	1.75	-	-	-
SUM	99.80	98.97	99.74	98.57	98.70	97.83	89.88	90.61	90.76

XRF (ppm)

V	161	209	225	181	180	212	-	-	-
Cr	960	735	297	1134	1133	766	-	-	-
Co	38	41	40	38	39	37	-	-	-
Ni	477	349	82	492	488	427	-	-	-
Cu	64	69	59	85	86	61	-	-	-
Zn	90	88	120	110	107	110	-	-	-
Rb	-	-	-	-	-	-	-	-	-
Sr	-	-	-	-	-	-	-	-	-
Y	-	-	-	-	-	-	-	-	-
Zr	-	-	-	-	-	-	-	-	-
Nb	-	-	-	-	-	-	-	-	-
Ba	-	-	-	-	-	-	-	-	-

Table 28 Whole-rock trace element ICP-MS data

Ref:	3	3	3	3	3	3	4	4	4	4	4
Sample:	LE-02	LE-03	AP-01	AP-03	CU-01	CU-02	SAY-22F	VF99-01A	VF99-01B	VF99-09A	VF99-08
Composition:	Minette	Minette	Minette	Basanite	Basalt-andesite	Basalt-andesite	Basalt-andesite	Basanite	Basanite	Basanite	Minette
Cinder cone:	La Erita	La Erita	Apaxtepec	Apaxtepec	Cerro Usmajac	Cerro Usmajac	Tezontal	Apaxtepec	Apaxtepec	Telcampana	La Erita
Sc	24.0	25.0	27.0	29.0	17.0	18.0	36.8	30.2	31.6	29.9	28.9
Rb	55.0	37.0	47.0	51.0	21.0	21.0	7.7	46.5	36.8	25.7	35.5
Sr	2579	1896	1429	1574	890	921	511	1576	1332	2142	1887
Y	19.00	17.00	19.00	21.00	20.00	20.00	20.60	21.20	26.70	17.60	18.10
Zr	413	333	387	421	179	181	104	400	360	236	317
Nb	7.50	6.80	7.70	9.20	19.00	18.00	3.55	9.18	10.54	6.49	7.55
Cs	-	-	-	-	-	-	0.15	0.40	0.32	0.36	0.34
Ba	2342	1881	1548	1672	475	490	225	1616	1266	1589	1801
La	64.00	50.00	25.00	26.00	24.00	23.00	10.77	25.97	27.14	38.19	46
Ce	142.00	110.00	55.00	62.00	55.00	52.00	23.72	55.4	57.7	77.7	95.1
Pr	-	-	-	-	-	-	3.03	7.18	7.51	10.23	12.08
Nd	73.00	56.00	32.00	36.00	27.00	28.00	13.60	31.20	32.80	43.30	49.70
Sm	13.00	10.00	6.50	7.20	5.40	5.60	3.41	6.97	7.53	8.54	9.22
Eu	3.40	2.60	1.90	2.10	1.70	1.80	1.10	2.03	2.25	2.30	2.48
Gd	-	-	-	-	-	-	3.35	5.64	6.39	5.89	6.24
Tb	1.00	0.80	0.70	0.80	0.70	0.70	0.57	0.77	0.93	0.71	0.75
Dy	4.50	3.70	3.90	4.40	4.00	4.10	3.63	4.18	5.13	3.52	3.68
Ho	-	-	-	-	-	-	0.76	0.77	0.96	0.61	0.65
Er	-	-	-	-	-	-	2.15	1.98	2.48	1.55	1.55
Tm	-	-	-	-	-	-	0.32	0.26	0.35	0.21	0.21
Yb	1.20	1.20	1.50	1.70	1.80	1.80	2.06	1.63	2.12	1.32	1.23
Lu	0.20	0.20	0.20	0.30	0.30	0.30	0.33	0.26	0.33	0.20	0.19
Hf	12.00	10.00	11.00	12.00	4.20	4.30	2.66	11.61	10.18	6.82	9.25
Ta	-	-	-	-	-	-	0.23	0.46	0.56	0.30	0.31
Pb	24.00	19.00	11.00	12.00	8.00	6.00	2.63	14.07	11.15	14.20	16.21
Th	6.60	4.70	0.70	1.60	2.50	2.50	1.54	2.90	2.94	4.58	4.19
U	1.90	1.30	0.90	1.00	0.70	0.70	0.42	0.95	0.96	1.23	1.26

Ref:	4	5	5	5	5	5
Sample:	VF99-07A	SAY-7E	SAY-101B	SAY-8H	1004-500	A60
Composition:	Minette	Minette	Lamprophyre	Minette	Basanite	Lamprophyre
Cinder cone:	San Isidro	El Carpintero Norte	Unknown	Comal Chico	Apaxtepec	
Sc	26.0	-	-	-	-	-
Rb	48.3	82.2	51.0	35.0	42.0	25.0
Sr	2532	3327	1961	2334	1349	1705
Y	20.90	26.88	18.00	20.00	25.00	17.00
Zr	410	682	352	412	427	241
Nb	11.17	14.18	13.00	12.29	12.00	12.00
Cs	0.38	0.50	0.35	0.30	0.36	0.47
Ba	2198	4657	1963	2098	1430	1364
La	61.01	84.21	47	42	26	47
Ce	130.4	194.4	105	91	62	98
Pr	16.32	24.58	13.00	12.00	9.00	13.00
Nd	67.00	94.75	54.00	49.24	35.00	51.00
Sm	12.26	15.83	9.00	9.00	7.00	9.00
Eu	3.30	4.43	3.00	2.55	2.00	2.00
Gd	8.20	14.01	6.00	6.29	7.00	6.00
Tb	0.94	1.33	0.78	0.81	0.90	0.82
Dy	4.48	5.55	3.00	3.64	5.00	4.00
Ho	0.74	-	-	-	-	-
Er	1.76	-	-	-	-	-
Tm	0.23	-	-	-	-	-
Yb	1.35	1.79	1.40	1.50	2.20	1.30
Lu	0.21	0.27	0.21	0.22	0.33	0.20
Hf	11.93	17.13	10.00	11.43	11.00	6.00
Ta	0.47	0.58	-	0.46	0.59	0.55
Pb	21.33	43.98	16.00	18.09	12.50	47.00
Th	5.98	7.00	4.00	5.00	3.00	4.00
U	1.76	2.45	1.00	1.39	1.00	2.00

Table 29 Whole-rock trace element INAA data

Ref:	1	1	1	1	1	1	1	1	1	1
Sample:	17B	SAY-22E	500	501	507	508	511	6D	7E	8H
Composition:	Basaltic	Basaltic	Basanite	Basanite	Basanite	Basanite	Minette	Minette	Minette	Minette
Cinder cone:	Usmajac	Tezontal	Apaxtepec	Apaxtepec	Telcampana	Telcampana	Le Erita	Sani Isidro	El Carpintero Norte	Comal Chico
Na₂O	3.26	1.91	2.15	1.73	1.87	1.54	2.79	2.58	2.45	1.89
Sc	18.2	35.5	30.4	29.3	26.5	28.2	25.2	25.5	26.7	27.5
Cr	121	196	313	535	844	1280	805	658	265	600
FeO	6.07	7.45	6.7	6.12	5.89	6.02	5.97	5.97	5.78	6.1
Ni	93	221	82	212	449	506	506	406	436	282
Cs	0.8	0.6	0.6	0.8	0.8	0.9	1.4	0.9	1	0.8
Ba	460	161	1430	1710	1800	1590	2130	2360	4230	2060
La	27.2	9.3	27.8	28.4	44.2	30.9	67.9	62.3	82.3	40.1
Ce	57	22	65	63	98	68	151	143	188	91
Nd	22	12	30	36	55	36	75	72	93	46
Sm	5.48	2.96	7.34	7.07	9.45	6.78	12.05	11.59	15.24	8.31
Eu	1.97	1.13	2.38	1.55	2.92	2.08	3.59	3.5	4.5	2.64
Tb	0.78	0.61	0.9	0.92	3.6	0.83	0.84	0.97	1.2	3.8
Yb	1.9	2.08	2.09	1.57	1.39	1.3	1.39	4.2	5.5	1.46
Lu	0.15	0.26	0.2	0.13	0.16	0.14	0.16	0.19	1.18	0.16
Hf	5	2.6	11.6	13.2	8.1	7.1	13.3	13.3	17.9	12.1
Th	2.66	0.44	2.28	1.45	3.93	1.24	6.16	5.61	7.13	3.23
U	0.57	0.33	0.91	0.9	1.48	1.03	1.94	1.77	2.41	1.13

References are:

1. Luhr and Carmichael (1981);
2. Carmichael et al. (2006);
3. Vigouroux et al. (2008);
4. Maria et al. (2008);
5. Cai (2009).

Appendix J: Granulometry Data

Table 30 Unit Y Thickness and Grain Size Analysis Data

Sample	Thickness (cm)	Total Weight (g)	-4.5 phi (g)	-4 phi (g)	-3 phi (g)	-2 phi (g)	-1 phi (g)	0 phi (g)	1 phi (g)	2 phi (g)	3 phi (g)	4 phi (g)	4.25 phi (g)
VF95-06Y	48	508.66	9.87	20.65	114.22	118.49	77.33	54.32	39.03	26.06	17.84	24.99	5.87
VF95-09X	56	596.43	9.45	60.09	150.99	135.30	109.17	68.35	34.38	12.68	6.89	6.80	2.33
VF97-05B	68	457.81	-	14.97	126.72	116.99	89.60	63.10	31.06	10.35	1.99	1.23	1.81
VF97-06D	72	869.30	-	83.33	240.47	199.36	150.89	105.58	59.50	21.23	4.29	3.09	1.57
VF97-13B	50	720.57	-	19.26	104.65	166.17	201.95	147.02	58.97	15.92	2.93	2.32	1.39
VF98-02Y	60	616.60	80.40	33.30	153.91	139.03	85.60	53.54	32.48	15.94	11.24	9.24	1.91
VF99-05Y	65	639.83	5.05	61.75	224.84	149.00	97.04	55.65	25.96	9.58	4.90	4.82	1.23
VF01-01X	45	868.83	52.98	95.29	239.14	178.47	138.68	92.83	45.25	13.48	6.31	4.86	1.53

Table 31 Unit W Thickness and Grain Size Analysis Data

Sample	Thickness (cm)	Total Weight (g)	-4.5 phi (g)	-4 phi (g)	-3 phi (g)	-2 phi (g)	-1 phi (g)	0 phi (g)	1 phi (g)	2 phi (g)	3 phi (g)	4 phi (g)	4.25 phi (g)
VF95-06W	8	340.36	-	3.46	17.95	61.58	85.90	83.61	58.87	23.94	2.47	2.13	0.45
VF97-06B	35	981.64	-	-	57.01	183.48	352.80	326.27	54.74	2.71	1.72	2.17	0.74

Table 32 Unit U Thickness and Grain Size Analysis Data

Sample	Thickness (cm)	Total Weight (g)	-4.5 phi (g)	-4 phi (g)	-3 phi (g)	-2 phi (g)	-1 phi (g)	0 phi (g)	1 phi (g)	2 phi (g)	3 phi (g)	4 phi (g)	4.25 phi (g)
VF10-01U	18	1442.90	55.5	114.4	271.2	284.6	290.5	239.8	131.3	37.8	6.3	5.9	5.6
VF10-02U	20	1228.11	23.5	49.2	222.9	267.6	234.5	218.2	145.1	50.1	7.7	4.4	4.9
VF10-03U	20	1465.70	162.3	178.5	262.9	275.7	239.0	201.5	106.0	24.6	4.6	5.7	4.9
VF10-04U	27	418.70	43.8	52.1	95.2	85.0	63.3	40.7	19.4	7.4	4.5	4.3	3.0
VF10-07U	17	952.50	-	5.9	17.4	114.3	278.8	278.4	169.6	54.9	12.7	10.4	10.1
VF95-09V	15	834.24	-	6.78	82.68	144.74	185.14	218.15	144.82	44.40	4.24	2.52	0.79
VF95-06U	27	413.73	-	3.82	60.02	94.47	95.06	87.21	53.31	12.52	3.65	3.00	0.68

Table 33 Unit S Thickness and Grain Size Analysis Data

Sample	Thickness (cm)	Total Weight (g)	-4.5 phi (g)	-4 phi (g)	-3 phi (g)	-2 phi (g)	-1 phi (g)	0 phi (g)	1 phi (g)	2 phi (g)	3 phi (g)	4 phi (g)	4.25 phi (g)
VF10-01S	13	747.70	61.3	93.1	77.0	93.3	106.9	132.1	115.7	34.2	7.5	9.5	17.1
VF10-02S	25	1384.10	98.0	69.0	248.9	233.5	233.7	213.1	173.9	74.9	10.7	15.8	12.6
VF10-03S	20	1229.90	39.8	43.8	194.5	225.8	214.3	199.2	164.4	78.1	17.0	29.5	23.5
VF10-04P	42	1389.94	-	79.1	315.8	423.4	380.5	164.7	22.4	2.0	0.9	0.6	0.5
VF10-07Q	10	304.50	-	-	11.3	60.8	94.1	86.2	31.4	5.4	4.4	5.4	5.5
VF10-07S	50	1557.00	182.9	108.0	362.2	482.5	318.4	81.2	9.8	3.0	2.7	3.6	2.7
VF95-09T	20	1051.45	-	90.68	182.53	222.56	216.20	202.75	108.55	22.41	2.61	1.99	1.17

Table 34 Unit P Thickness and Grain Size Analysis Data

Sample	Thickness (cm)	Total Weight (g)	-4.5 phi (g)	-4 phi (g)	-3 phi (g)	-2 phi (g)	-1 phi (g)	0 phi (g)	1 phi (g)	2 phi (g)	3 phi (g)	4 phi (g)	4.25 phi (g)
VF10-01P	20	974.80	-	13.1	70.7	181.1	263.9	289.3	131.6	17.1	2.7	3.4	1.9
VF10-02P	30	1206.80	-	3.9	160.8	292.7	303.4	301.1	124.9	12.3	2.0	3.3	2.4
VF10-03Pi	36	752.00	84.7	102.2	153.8	136.1	100.4	85.0	67.4	18.4	1.6	1.5	0.9
VF10-04M	10	380.60	31.4	58.4	75.9	78.1	60.5	46.9	22.0	2.5	1.9	1.7	1.3
VF10-04N	17	675.30	30.6	46.6	124.5	166.4	145.5	105.8	44.0	6.1	2.3	2.0	1.5
VF10-01Q2	10	610.30	52.9	53.1	123.1	96.1	95.6	97.2	64.3	24.0	2.3	0.8	0.9
VF10-07M3	6	354.60	-	-	5.9	19.0	60.5	141.0	114.8	9.0	1.6	1.6	1.2
VF10-07M1	5	317.90	-	6.6	28.3	46.0	71.6	90.2	51.5	15.6	3.4	2.2	2.5

References

- Allan, J., 1986, Geology of the Colima and Zacoalco grabens, SW Mexico: Late Cenozoic rifting in the Mexican Volcanic Belt: *Geological Society of America Bulletin*, v. 97, p. 473-485.
- Allan, J.F., and Carmichael, I.S.E., 1984, Lamprophyric lavas in the Colima graben, SW Mexico: *Contributions to Mineralogy and Petrology*, v. 88, p. 203-216.
- Allegre, C.J., and Turcotte, D.L., 1986, Implications of a two-component marble-cake mantle: *Nature*, v. 323, p. 123-127.
- Annen, C., Blundy, J.D., and Sparks, R.S.J., 2006, The genesis of intermediate and silicic magmas in deep crustal hot zones: *Journal of Petrology*, v. 47, p. 505-539.
- Arámbula-Mendoza, R., Lesage, P., Valdes-González, C., Varley, N.R., Reyes-Dávila, G., and Navarro, C., 2011, Seismic activity that accompanied the effusive and explosive eruptions during the 2004-2005 period at Volcán de Colima, Mexico: *Journal of Volcanology and Geothermal Research*, v. 205, p. 30-46.
- Atlas, Z.D., Dixon, J.E., Sen, G., Finny, M., Lillian, A., and Pozzo, M.D., 2006, Melt inclusions from Volcan Popocatepetl and Volcan de Colima, Mexico: Melt evolution due to vapor-saturated crystallization during: *Journal of Volcanology and Geothermal Research*, v. 153, p. 221-240.
- Bebout, G.E., and Barton, M.D., 1989, Fluid-flow and Metasomatism in a Subduction Zone Hydrothermal System: Catalina Schist Terrane, California: *Geology*, v. 17, p. 976-980.
- Blundy, J., and Cashman, K., 2001, Ascent-driven crystallisation of dacite magmas at Mount St Helens, 1980-1986: *Contributions to Mineralogy and Petrology*, v. 140, p. 631-650.
- Bonadonna, C., Connor, C.B., Houghton, B.F., Connor, L., Byrne, M., Laing, A., and Hincks, T.K., 2005, Probabilistic modelling of tephra dispersal: Hazard assessment of a multiphase rhyolitic eruption at Tarawera, New Zealand: *J. Geophys. Res.*, v. 110.
- Bonadonna, C., and Houghton, B.F., 2005, Total Grain-Size Distribution and Volume of Tephra-fall Deposits: *Bulletin of Volcanology*, v. 67, p. 441-456.
- Bretón González, M., Ramírez, J.J., and Navarro-Ochoa, C., 2002, Summary of the historical eruptive activity of Volcan de Colima, México, 1519-2000: *Journal of Volcanology and Geothermal Research*, v. 117, p. 21-46.
- Browne, B.L., and Gardner, J.E., 2006, The influence of magma ascent path on the texture, mineralogy, and formation of hornblende reaction rims: *Earth and Planetary Science Letters*, v. 246, p. 161-176.
- Cabrera-Gutiérrez, R., and Espindola, J.-M., 2010, The 1998-1999 Eruption of Volcán de Colima, México: An Application of Maeda's Viscoelastic Model: *Geofísica Internacional*, v. 49, p. 83-96.
- Cai, Y., 2009, Tracing Upper Mantle Heterogeneities with Radiogenic Isotopes at the Mexican Volcanic Belt and the Arctic Gakkel Ridge [PhD thesis], Columbia University.
- Cameron, K., and Robinson, J., 1990, Comments on "Sr isotopic compositions of lower crustal xenoliths-Evidence for the origin of mid-Tertiary felsic volcanics in Mexico" by J. Ruiz, P.J. Patchett, and R.J. Arculus: *Contributions to Mineralogy and Petrology*, v. 104, p. 609-614.
- Cameron, K.L., Robinson, J.V., Niemeyer, S., Nimz, G.J., Kuentz, D.C., Harmon, R.S., Bohlen, S.R., and Collerson, K.D., 1992, Contrasting Styles of Pre-Cenozoic and Mid-Tertiary Crustal Evolution in Northern Mexico: Evidence From Deep Crustal Xenoliths From La Olivina: *J. Geophys. Res.*, v. 97, p. 17353-17376.
- Campa, M.F., and Coney, P.J., 1983, Tectono-stratigraphic terranes and mineral-resource distributions in Mexico: *Canadian Journal of Earth Sciences*, v. 20, p. 1040-1051.
- Capra, L., and Macias, J.L., 2002, The cohesive Naranjo debris-flow deposit (10 km³): A dam breakout flow derived from the Pleistocene debris-avalanche deposit of Nevado de Colima Volcano (Mexico): *Journal of Volcanology and Geothermal Research*, v. 117, p. 213-235.
- Carey, S., and Sparks, R.S.J., 1986, Quantitative models of the fallout and dispersal of tephra from volcanic eruption columns: *Bulletin of Volcanology*, v. 48, p. 109-125.

- Carey, S.N., and Sigurdsson, H., 1982, Influence of particle aggregation on deposition of distal tephra from the M_Ay 18, 1980, eruption of Mount St. Helens volcano: *Journal of Geophysical Research: Solid Earth*, v. 87, p. 7061-7072.
- Carmichael, I., Frey, H., Lange, R., and Hall, C., 2006, The Pleistocene cinder cones surrounding Volcán Colima, Mexico re-visited: eruption ages and volumes, oxidation states, and sulfur content: *Bulletin of Volcanology*, v. 68, p. 407-419.
- Castillo, P.R., Janney, P.E., and Solidum, R.U., 1999, Petrology and geochemistry of Camiguin Island, southern Philippines: insights to the source of adakites and other lavas in a complex arc setting: *Contributions to Mineralogy and Petrology*, v. 134, p. 33-51.
- Centeno-García, E., Ruiz, J., Coney, P.J., Patchett, P.J., and Ortégutierrez, F., 1993, Guerrero terrane of Mexico - Its role in the Southern Cordillera from new geochemical data: *Geology*, v. 21, p. 419-422.
- Chauvel, C., Marini, J.C., Plank, T., and Ludden, J.N., 2009, Hf-Nd input flux in the Izu-Mariana subduction zone and recycling of subducted material in the mantle: *Geochemistry Geophysics Geosystems*, v. 10, p. 23.
- Cloos, M., and Shreve, R., 1988, Subduction Channel Model of Prism Accretion, Mélange Formation, Sediment Subduction, and Subduction Erosions at Convergent Plate Margins: 2. Implications and Discussion: *Pure and Applied Geophysics*, v. 128, p. 501-545.
- Connor, C.B., Connor, L.J., Bonadonna, C., Luhr, J.F., Savov, I.P., and Navarro-Ochoa, C., In Prep., Modelling tephra thickness and particle size distribution of the 1913 eruption of Volcán Colima, Mexico, *in* Varley, N.R., and Komorowski, J.C., eds., *Volcán Colima: Managing the Threat*, Springer.
- Connor, C.B., Hill, B.E., Winfrey, B., Franklin, N.M., and La Femina, P.C., 2001, Estimation of volcanic hazards from tephra fallout: *Natural Hazards Review*, v. 2, p. 33-42.
- Connor, L.J., and Connor, C.B., 2006, Inversion is the key to dispersion: Understanding eruption dynamics by inverting tephra fallout, *in* Mader, H.M., Coles, S.G., Connor, C.B., and Connor, L.J., eds., *Statistics in Volcanology: Special publications of IAVCEI*, London Geological Society, p. 231-242.
- Cortés, A., Garduño, V.H., Macías, J.L., Navarro-Ochoa, C., Komorowski, J.C., Saucedo, R., and Gavilanes, J.C., 2010, Geologic mapping of the Colima volcanic complex (Mexico) and implications for hazard assessment, *in* Groppelli, G., and Viereck-Goette, L., eds., *Stratigraphy and Geology of Volcanic Areas: Geological Society of America Special Paper 464*, p. 249-264.
- Cortés, A., Garduño, V.H., Navarro-Ochoa, C., Komorowski, J.C., Saucedo, R., Macías, J.L., and Gavilanes, J.C., 2005, Carta Geológica del Complejo Volcánico de Colima, con Geología del Complejo Volcánico de Colima, Volume 10, Universidad Nacional Autónoma de México, Instituto de Geología, *Cartas Geológicas y Mineras*.
- Cortés, A., Macías, J.L., Capra, L., and Garduño-Monroy, V.H., 2009, Sector collapse of the SW flank of Volcán de Colima, México: The 3600 yr BP La Lumbre-Los Ganchos debris avalanche and associated debris flows: *Journal of Volcanology and Geothermal Research*, v. 197, p. 52-66.
- Cox, K.G., Bell, J.D., and Pankhurst, R.J., 1979, *The interpretation of igneous rocks*: London, Allen and Unwin.
- Crabtree, S.M., and Lange, R.A., 2011, Complex phenocryst textures and zoning patterns in andesites and dacites: Evidence of degassing-induced rapid crystallisation?: *Journal of Petrology*, v. 52, p. 3-38.
- Davidson, J.P., Morgan, D.J., Charlier, B.L.A., Harlou, R., and Hora, J.M., 2007, Microsampling and isotopic analysis of igneous rocks: Implications for the study of magmatic systems, *Annual Review of Earth and Planetary Sciences*, Volume 35: *Annual Review of Earth and Planetary Sciences: Palo Alto, Annual Reviews*, p. 273-311.
- De Barros, L., Martini, F., Bean, C.J., Garcia-Yeguas, A., and Ibanez, J., 2012, Imaging magma storage below Teide volcano (Tenerife) using scattered seismic wavefields: *Geophysical Journal International*, v. 191, p. 695-706.

- De la Cruz-Reyna, S., 1993, Random patterns of activity at Colima volcano, Mexico: *Journal of Volcanology and Geothermal Research*, v. 55, p. 51-68.
- Deer, W.A., Howie, R.A., and Zussman, J., 1992, *An Introduction to the Rock-Forming Minerals*, Pearson
- Deer, W.A., Howie, R.A., and Zussman, J., 1997, *Rock Forming Minerals: Orthosilicates*, Geological Society of London.
- Defant, M.J., and Drummond, M.S., 1990, Derivation of some Modern Arc Magmas by Melting of Young Subducted Lithosphere: *Nature*, v. 347, p. 662-665.
- Defant, M.J., and Drummond, M.S., 1993, Mount St. Helens: Potential example of the partial melting of the subducted lithosphere in a volcanic arc: *Geology*, v. 21, p. 547-550.
- DePaolo, D.J., and Wasserburg, G.J., 1976, Nd isotopic variations and petrogenetic models: *Geophysical Research Letters*, v. 3, p. 249-252.
- Dickin, A.P., 2005, *Radiogenic Isotope Geology*, Cambridge University Press, 492 p.
- Dickinson, W.R., and Lawton, T.F., 2001, Carboniferous to Cretaceous assembly and fragmentation of Mexico: *Geological Society of America Bulletin*, v. 113, p. 1142-1160.
- Draxler, R.R., and Hess, G.D., 1998, An Overview of the HYSPLIT_4 Modeling System of Trajectories, Dispersion, and Deposition: *Australian Meteorological Magazine*, v. 47, p. 295-308.
- Duzgoren-Aydin, N.S., Aydin, A., and Malpas, J., 2002, Re-assessment of chemical weathering indices: case study on pyroclastic rocks of Hong Kong: *Engineering Geology*, v. 63, p. 99-119.
- Ego, F., and Ansan, V., 2002, Why is the Central Trans-Mexican Volcanic Belt (102 degrees-99 degrees W) in transtensive deformation?: *Tectonophysics*, v. 359, p. 189-208.
- Evans, J.R., Huntoon, J.E., Rose, W.I., Varley, N.R., and Stevenson, J.A., 2009, Particle sizes of andesitic ash fallout from vertical eruptions and co-pyroclastic flow clouds, Volcan de Colima, Mexico: *Geology*, v. 37, p. 935-938.
- Ferrari, L., 2004, Slab detachment control on mafic volcanic pulse and mantle heterogeneity in central Mexico: *Geology*, v. 32, p. 77-80.
- Ferrari, L., Orozco-Esquivel, T., Manea, V., and Manea, M., 2012, The dynamic history of the Trans-Mexican Volcanic Belt and the Mexico subduction zone: *Tectonophysics*, v. 522, p. 122-149.
- Ferrari, L., Petrone, C.M., and Francalanci, L., 2001, Generation of ocean-island basalt-type volcanism in the western Trans-Mexican volcanic belt by slab rollback, asthenosphere infiltration, and variable flux melting: *Geology*, v. 29, p. 507-510.
- Ferrari, L., and Rosas-Elguera, J., 2000, Late Miocene to Quaternary extension at the northern boundary of the Jalisco block, western Mexico: the Tepic-Zacoalca rift revisited, *in* Aguirre-Diaz, G., Delgado-Granados, H., and Stock, J., eds., *Cenozoic tectonics and volcanism of Mexico: Geological Society of America Special Paper*, 334, p. 42-64.
- Fierstein, J., and Nathenson, M., 1992, Another Look at the Calculation of Fallout Tephra Volumes: *Bulletin of Volcanology*, v. 54, p. 156-167.
- Folch, A., Costa, A., and Basart, S., 2012, Validation of the FALL3D ash dispersion model using observations of the 2010 Eyjafjallajökull volcanic ash clouds: *Atmospheric Environment*, v. 48, p. 165-183.
- Foley, S., 1992, Vein-plus-wall-rock melting mechanisms in the lithosphere and the origin of potassic alkaline magmas: *Lithos*, v. 28, p. 435-453.
- Gardine, M.D., 2010, *Tracing the movement and storage of magma in the crust through seismology: Examples from Alaska and western Mexico [Dissertation thesis]*, University of Alaska Fairbanks.
- Garduño, V.H., Saucedo, R., Jimenez, S., Gavilanes, J.C., Cortes, A., and Uribe, R.M., 1998, La Falla Tamazula, limite suroriental del bloque Jalisco, y sus relaciones cone el Complejo Volcanico de Colima, Mexico: *Revista Mexicana de Ciencias Geologicas*, v. 15, p. 132-144.
- Ghiorso, M.S., and Evans, B.W., 2008, Thermodynamics of Rhombohedral Oxide Solid Solutions and a Revision of the FE-TI Two-Oxide Geothermometer and Oxygen-Barometer: *American Journal of Science*, v. 308, p. 957-1039.

- Ghiorso, M.S., and Sack, O., 1991, Fe-Ti oxide geothermometry: thermodynamic formulation and the estimation of intensive variables in silicic magmas: *Contributions to Mineralogy and Petrology*, v. 108, p. 485-510.
- Ginibre, C., Kronz, A., and Wörner, G., 2002a, High-resolution quantitative imaging of plagioclase composition using accumulated backscattered electron images: new constraints on oscillatory zoning: *Contributions to Mineralogy and Petrology*, v. 142, p. 436-448.
- Ginibre, C., and Wörner, G., 2007, Variable parent magmas and recharge regimes of the Parinacota magma system (N. Chile) revealed by Fe, Mg and Sr zoning in plagioclase: *Lithos*, v. 98, p. 118-140.
- Ginibre, C., Wörner, G., and Kronz, A., 2002b, Minor- and trace-element zoning in plagioclase: implications for magma chamber processes at Parinacota volcano, northern Chile: *Contributions to Mineralogy and Petrology*, v. 143, p. 300-315.
- Gómez-Tuena, A., LaGatta, A., Langmuir, C.H., Goldstein, S.L., Ortega-Gutiérrez, F., and Carrasco-Nuñez, G., 2003, Temporal Control of Subduction Magmatism in the Eastern Trans-Mexican Volcanic Belt: Mantle Sources, Slab Contributions and Crustal Contamination: *Geochemistry Geophysics Geosystems*, v. 4, p. 8912.
- Gómez-Tuena, A., Langmuir, C.H., Goldstein, S.L., Straub, S.M., and Ortega-Gutiérrez, F., 2007a, Geochemical Evidence for Slab Melting in the Trans-Mexican Volcanic Belt: *Journal of Petrology*, v. 48, p. 537-562.
- Gómez-Tuena, A., Mori, L., Goldstein, S.L., and Perez-Arvizu, O., 2011, Magmatic Diversity of Western Mexico as a Function of Metamorphic Transformations in the Subducted Oceanic Plate: *Geochimica Et Cosmochimica Acta*, v. 75, p. 213-241.
- Gómez-Tuena, A., Orozco-Esquivel, M.T., and Ferrari, L., 2007b, Igneous petrogenesis of the Trans-Mexican Volcanic Belt, *in* America, G.S.o., ed., *Geology of Mexico: Celebrating the Centenary of the Geological Society of Mexico*, Volume 422, p. 129-181.
- Gómez-Tuena, A., Orozco-Esquivel, M.T., and Ferrari, L., 2007, Igneous petrogenesis of the Trans-Mexican Volcanic Belt, *in* America, G.S.o., ed., *Geology of Mexico: Celebrating the Centenary of the Geological Society of Mexico*, Volume 422, p. 129-181.
- Hammer, J.E., Cashman, K.V., Hoblitt, R.P., and Newman, S., 1999, Degassing and microlite crystallization during pre-climactic events of the 1991 eruption of Mt. Pinatubo, Philippines: *Bulletin of Volcanology*, v. 60, p. 355-380.
- Hammond, W.C., and Humphreys, E.D., 2000, Upper mantle seismic wave velocity: Effects of realistic partial melt geometries: *Journal of Geophysical Research-Solid Earth*, v. 105, p. 10975-10986.
- Hanson, G.N., 1980, Rare Earth Elements in Petrogenetic Studies of Igneous Systems: *Annual Review of Earth and Planetary Sciences*, v. 8, p. 371-406.
- Hastie, A.R., Kerr, A.C., Pearce, J.A., and Mitchell, S.F., 2007, Classification of altered volcanic island arc rocks using immobile trace elements: Development of the Th-Co discrimination diagram: *Journal of Petrology*, v. 48, p. 2341-2357.
- Hawkesworth, C.J., and van Calsteren, P.W.C., 1984, Radiogenic isotopes - some geological applications, *in* Henderson, P., ed., *Rare earth element geochemistry*: Amsterdam, Elsevier, p. 375-421.
- Hofmann, A.W., 1997, Mantle geochemistry: the message from oceanic volcanism: *Nature*, v. 385, p. 219-229.
- Humphreys, M.C.S., Blundy, J.D., and Sparks, R.S.J., 2006, Magma evolution and open-system processes at Shiveluch volcano: Insights from phenocryst zoning: *Journal of Petrology*, v. 47, p. 2303-2334.
- Husen, S., Smith, R.B., and Waite, G.P., 2004, Evidence for gas and magmatic sources beneath the Yellowstone volcanic field from seismic tomographic imaging: *Journal of Volcanology and Geothermal Research*, v. 131, p. 397-410.
- Isaak, D.G., 1992, High-Temperature Elasticity of Iron-Bearing Olivines *Journal of Geophysical Research-Solid Earth*, v. 97, p. 1871-1885.
- Jerram, D.A., and Kent, A.J.R., 2006, An overview of modern trends in petrography: Textural and microanalysis of igneous rocks: *Journal of Volcanology and Geothermal Research*, v. 154, p. VII-IX.

- Kelemen, P.B., Hanghøj, K., and Greene, A.R., 2004, One View of the Geochemistry of Subduction-related Magmaic Arcs, with an Emphasis on Primitive Andeiste and Lower Crust, *in* Rudnick, R., ed., *The Crust, Volume 3: Treatise on Geochemistry*: Oxford, Elsevier-Pergamon, p. 593-660.
- Kelley, K.A., and Cottrell, E., 2009, Water and the Oxidation State of Subduction Zone Magmas: *Science*, v. 325, p. 605-607.
- Kempton, P.D., Fitton, J.G., Hawkesworth, C.J., and Ormerod, D.S., 1991, Isotopic and trace-element constraints on the composition and evolution of the lithosphere beneath the southwestern United States: *Journal of Geophysical Research - Solid Earth and Planets*, v. 96, p. 13713-13735.
- Kent, A.J.R., Darr, C., Koleszar, A.M., Salisbury, M.J., and Cooper, K.M., 2010, Preferential eruption of andesitic magmas through recharge filtering: *Nature Geosci.*, v. 3, p. 631-636.
- Kirchenbaur, M., Munker, C., Schuth, S., Garbe-Schnonberg, D., and Marchev, P., 2012, Tectonomagmatic Constraints on the Sources of Eastern Mediterranean K-rich Lavas: *Journal of Petrology*, v. 53, p. 27-65.
- Komorowski, J.C., Navarro-Ochoa, C., Cortes, A., Saucedo, R., Gavilanes, J.C., Siebe, C., Espindola, J.-M., and Rodriguez, S., 1997, The Colima Volcanic Complex, part I: Quaternary multiple debris-avalanche deposits: Puerto Vallarta, Mexico.
- LaGatta, A., 2003, *Arc Magma Genesis in the Eastern Mexican Volcanic Belt [PhD thesis]*: New York, Columbia University.
- Lange, R.A., and Carmichael, I.S.E., 1990, Hydrous Basaltic Andesites Associated with Minette and Related Lavas in Western Mexico: *Journal of Petrology*, v. 31, p. 1225-1259.
- Lange, R.A., Frey, H.M., and Hector, J., 2009, A thermodynamic model for the plagioclase-liquid hygrometer/thermometer: *American Mineralogist*, v. 94, p. 494-506.
- Langmuir, C.H., Vocke Jr, R.D., Hanson, G.N., and Hart, S.R., 1978, A general mixing equation with applications to Icelandic basalts: *Earth and Planetary Science Letters*, v. 37, p. 380-392.
- Le Maitre, R.W., Streckeisen, A., Zanettin, B., Le Bas, M.J., Bonin, B., Bateman, P., Bellieni, G., Dudek, A., Efremova, S., Keller, J., Lameyre, J., Sabine, P.A., Schmid, R., Sorenson, H., and Wooley, A.R., 2002, *Igneous Rocks A Classification and Glossary of Terms*, Cambridge University Press.
- Leake, B.E., Woolley, A.R., Arps, C.E.S., Birch, W.D., Gilbert, M.C., Grice, J.D., Hawthorne, F.C., Kato, A., Kisch, H.J., Krivovichiev, V.G., Linthout, K., Laird, J., Mandarino, J.A., Maresch, W.V., Nickel, E.H., Rock, N.M.S., Schumacher, J.C., Smith, D.C., Stephenson, N.C.N., Ungarretti, L., Whittaker, E.J.W., and Youzhi, G., 1997, Nomenclature of amphiboles: Report of the subcommittee on amphiboles of the International Mineralogical Association, commission on new minerals and mineral names: *The Canadian Mineralogist*, v. 35, p. 219-246.
- Lees, J.M., 1992, The magma system of Mount St. Helens: non-linear high-resolution P-wave tomography: *Journal of Volcanology and Geothermal Research*, v. 53, p. 103-116.
- Liang, Y., and Elthon, D., 1990, Geochemistry and Petrology of Spinel Lherzolite Xenoliths from Xalapasco de La Joya, San Luis Potosi, Mexico: Partial Melting and Mantle Metasomatism: *J. Geophys. Res.*, v. 95, p. 15,859-15,877.
- López-Loera, H., 2012, 2 3/4 Dimension Modelling of the Aeromagnetic Anomaly of Volcán de Colima, Western Mexico: *Geofísica Internacional*, v. 51, p. 129-42.
- Luhr, J., and Carmichael, I.E., 1985, Jorullo Volcano, Michoacan, Mexico (1759-1774): The earliest stages of fractionation in calc-alkaline magmas: *Contributions to Mineralogy and Petrology*, v. 90, p. 142-161.
- Luhr, J.F., 1993, Petrology and geochemistry of stage-I andesites and dacites from the caldera wall of Volcán Colima, Mexico: *Geofísica Internacional*, v. 32, p. 591-603.
- Luhr, J.F., 1997, Extensional tectonics and the diverse primitive volcanic rocks in the Western Mexican Volcanic Belt: *The Canadian Mineralogist*, v. 35, p. 473-500.
- Luhr, J.F., 2002, Petrology and geochemistry of the 1991 and 1998-1999 lava flows from Volcán de Colima, Mexico: implications for the end of the current eruptive cycle: *Journal of Volcanology and Geothermal Research*, v. 117, p. 169-194.

- Luhr, J.F., and Carmichael, I.S.E., 1980, The Colima Volcanic Complex, Mexico: Part I. Post-caldera andesites from Volcán Colima: *Contributions to Mineralogy and Petrology*, v. 71, p. 343-372.
- Luhr, J.F., and Carmichael, I.S.E., 1981, The Colima Volcanic Complex, Mexico: Part II. Late-Quaternary cinder cones: *Contributions to Mineralogy and Petrology*, v. 76, p. 127-147.
- Luhr, J.F., and Carmichael, I.S.E., 1982, The Colima Volcanic Complex, Mexico: Part III. Ash and scoria fall deposits from upper slopes of Volcán Colima: *Contributions to Mineralogy and Petrology*, v. 42, p. 235-260.
- Luhr, J.F., and Carmichael, I.S.E., 1990a, Geology of Volcán de Colima, Universidad Nacional Autónoma de México, Instituto de Geología.
- Luhr, J.F., and Carmichael, I.S.E., 1990b, Petrological Monitoring of Cyclical Eruptive Activity at Volcán de Colima, Mexico: *Journal of Volcanology and Geothermal Research*, v. 42, p. 235-260.
- Luhr, J.F., Navarro-Ochoa, C., Connor, C.B., and Connor, L., 2006, The 1913 VEI-4 Plinian eruption of Volcan de Colima (Mexico): tephrochronology, petrology and plume modelling: *Eos Transaction AGU* 87, v. 52, p. 1786.
- Luhr, J.F., Navarro-Ochoa, C., and Savov, I.P., 2010, Tephrochronology, petrology and geochemistry of Late-Holocene pyroclastic deposits from Volcán de Colima, Mexico: *Journal of Volcanology and Geothermal Research*, v. 197, p. 1-32.
- Luhr, J.F., Nelson, S., Allan, J., and Carmichael, I.S.E., 1985, Active rifting in southwestern Mexico: Manifestations of an incipient eastward spreading-ridge jump: *Geology*, v. 13, p. 54-57.
- Luhr, J.F., and Prestegard, K.L., 1988, Caldera formation at Volcán Colima, Mexico, by a large Holocene volcanic debris avalanche: *Journal of Volcanology and Geothermal Research*, v. 35, p. 335-348.
- Macpherson, C.G., Dreher, S.C., and Thirlwall, M.F., 2006, Adakites without Slab Melting: High Pressure Differentiation of Island Arc Magma, Mindanao, the Philippines: *Earth and Planetary Science Letters*, v. 243, p. 581-593.
- Maria, A.H., and Luhr, J.F., 2008, Lamprophyres, basanites, and basalts of the western Mexican volcanic belt: Volatile contents and a vein-wallrock melting relationship: *Journal of Petrology*, v. 49, p. 2123-2156.
- Marschall, H.R., and Schumacher, J.C., 2012, Arc Magmas Sourced from Mèlange Diapirs in Subduction Zones: *Nature Geoscience*, v. 5, p. 862-867.
- Medina-Martínez, F., 1983, Analysis of the eruptive history of the Volcán de Colima, México (1560-1980): *Geofísica Internacional*, v. 22, p. 157-178.
- Mendoza, O.T., and Suastegui, M.G., 2000, Geochemistry and isotopic composition of the Guerrero Terrane (western Mexico): implications for the tectono-magmatic evolution of southwestern North America during the Late Mesozoic: *Journal of South American Earth Sciences*, v. 13, p. 297-324.
- Miller, D.P., Marschall, H.R., and Schumacher, J.C., 2009, Metasomatic Formation and Petrology of Blueschist-facies Hybrid Rocks from Syros (Greece): Implications for Reactions at the Slab-Mantle Interface: *Lithos*, v. 107, p. 53-67.
- Moore, G., and Carmichael, I.S.E., 1998, The hydrous phase equilibria (to 3 kbar) of an andesite and basaltic andesite from western Mexico: Constraints on water content and conditions of phenocryst growth: *Contributions to Mineralogy and Petrology*, v. 130, p. 304-319.
- Mooser, F., 1961, Los volcanes de Colima: Universidad Nacional Autonoma de Mexico, Boletín del Instituto de Geología, v. 61.
- Morimoto, N., 1988, Nomenclature of pyroxenes: *American Mineralogist*, v. 73, p. 1123-1133.
- Moyen, J.F., 2009, High Sr/Y and La/Yb Ratios: The Meaning of the "Adakitic Signature": *Lithos*, v. 112, p. 556-574.
- Mukasa, S.B., Blatter, D.L., and Andronikov, A.V., 2007, Mantle peridotite xenoliths in andesite lava at El Penon, central Mexican Volcanic Belt: Isotopic and trace element evidence for melting and metasomatism in the mantle wedge beneath an active arc: *Earth and Planetary Science Letters*, v. 260, p. 37-55.
- Nakamura, N., 1974, Determination of REE, Ba, Fe, Mg, Na and K in carbonaceous and ordinary chondrites: *Geochimica Et Cosmochimica Acta*, v. 38, p. 757-775.

- Navarro-Ochoa, C., Gavilanes, J.C., and Cortés, A., 2002, Movement and emplacement of lava flows at Volcán de Colima, México: Nov. 1998 - Feb. 1999: *Journal of Volcanology and Geothermal Research*, v. 117, p. 155-167.
- Nedler, J.A., and Meade, R., 1965, A Simplex Method for Function Minimisation: *Computing Journal*, v. 7, p. 308-313.
- Nelson, S.T., and Montana, A., 1992, Sieve-textured plagioclases in volcanic rocks produced by rapid decompression: *American Mineralogist*, v. 77, p. 1242-1249.
- Newhall, C.G., and Self, S., 1982, The volcanic explosivity index (VEI): an estimate of explosive magnitude for historical volcanism: *Journal of Geophysical Research*, v. 87, p. 1231-1238.
- Nimz, G.J., Cameron, K.L., and Niemeyer, S., 1995, Formation of Mantle Lithosphere Beneath Northern Mexico: Chemical and Sr-Nd-Pb Isotopic Systematics of Peridotite Xenoliths from La Olivina: *Journal of Geophysical Research*, v. 100, p. 4181-4196.
- Niu, Y., Regelous, M., Wendt, I.J., Batiza, R., and O'Hara, M.J., 2002, Geochemistry of near-EPR seamounts: importance of source vs. process and the origin of enriched mantle component: *Earth and Planetary Science Letters*, v. 199, p. 327-345.
- Noll, P.D., Newsom, H.E., Leeman, W.P., and Ryan, J.G., 1996, The role of hydrothermal fluids in the production of subduction zone magmas: Evidence from siderophile and chalcophile trace elements and boron: *Geochimica Et Cosmochimica Acta*, v. 60, p. 587-611.
- Norini, G., Capra, L., Gropelli, G., Agliardi, F., Pola, A., and Cortes, A., 2010, Structural architecture of the Colima Volcanic Complex: *J. Geophys. Res.*, v. 115, p. B12209.
- Núñez-Cornú, F., Nava, F.A., De la Cruz-Reyna, S., Jimenez, Z., Valencia, C., and Garcia-Arthur, R., 1994, Seismic Activity Related to the 1991 Eruption of Colima Volcano, Mexico: *Bulletin of Volcanology*, v. 56, p. 228-237.
- Pabst, S., Zack, T., Savov, I.P., Ludwig, T., Rost, D., Tonarini, S., and Vicenzi, E.P., 2012, The fate of subducted oceanic slabs in the shallow mantle: Insights from boron isotopes and light element composition of metasomatized blueschists from the Mariana forearc: *Lithos*, v. 132-133, p. 162-179.
- Pallister, J.S., Hoblitt, R.P., Meeker, G.P., Knight, R.J., and Siems, D.F., 1996, Magma Mixing at Mount Pinatubo: Petrographic and chemical evidence from the 1991 deposits, *in* Newhall, C.G., and R.S., P., eds., *Fire and Mud: Eruptions and Lahars of Mount Pinatubo, Philippines*: Quezon City, Philippines, Univ Wash Press, p. 687-731.
- Pallister, J.S., Hoblitt, R.P., and Reyes, A.G., 1992, A basalt trigger for the 1991 eruptions of Pinatubo volcano?: *Nature*, v. 356, p. 426-428.
- Parai, R., Mukhopadhyay, S., and Lassiter, J.C., 2009, New constraints on the HIMU mantle from neon and helium isotopic compositions of basalts from the Cook-Austral Islands: *Earth and Planetary Science Letters*, v. 277, p. 253-261.
- Pardo, M., and Suarez, G., 1993, Steep subduction geometry of the Rivera plate beneath the Jalisco Block in western Mexico: *Geophysical Research Letters*, v. 20, p. 2391-2394.
- Pardo, M., and Suarez, G., 1995, Shape of the subducted Rivera and Cocos plate in southern Mexico: Seismic and tectonic implications: *Journal of Geophysical Research*, v. 100, p. 12357-12373.
- Paulatto, M., Annen, C., Henstock, T.J., Kiddle, E., Minshull, T.A., Sparks, R.S.J., and Voight, B., 2012, Magma chamber properties from integrated seismic tomography and thermal modeling at Montserrat: *Geochemistry, Geophysics, Geosystems*, v. 13, p. Q01014.
- Pearce, J.A., 1982, Trace element characteristics of lavas from destructive plate boundaries, *in* Thorpe, R.S., ed., *Andesites: orogenic andesites and related rocks*: Chichester, Wiley, p. 525-548.
- Perez-Campos, X., Kim, Y., Husker, A., Davis, P.M., Clayton, R.W., Iglesias, A., Pacheco, J.F., Singh, S.K., Manea, V.C., and Gurnis, M., 2008, Horizontal subduction and truncation of the Cocos Plate beneath central Mexico: *Geophysical Research Letters*, v. 35, p. 6.
- Petrone, C.M., Francalanci, L., Ferrari, L., Schaaf, P., and Conticelli, S., 2006, The San Pedro-Cerro Grande Volcanic Complex (Nayarit, Mexico): Inferences on Volcanology and Magma Evolution, *in* Siebe, C., Macias, J.L., and Aguirre-Diaz, G., eds., *Neogene-*

- Quaternary Continental Margin Volcanism: A Perspective from Mexico, Volume 402, Geological Society of America Special Paper, p. 65-98.
- Phipps Morgan, J., and Morgan, W.J., 1999, Two-stage melting and the geochemical evolution of the mantle: A recipe for mantle plum-pudding: *Earth and Planetary Science Letters*, v. 170, p. 215-239.
- Plank, T., and Langmuir, C.H., 1998, The chemical composition of subducting sediment and its consequences for the crust and mantle: *Chemical Geology*, v. 145, p. 325-394.
- Putirka, K.D., 2008, Thermometers and Barometers for Volcanic Systems, *in* Putirka, K.D., and Tepley III, F.J., eds., *Minerals, Inclusions and Volcanic Processes, Volume 69: Reviews in Mineralogy & Geochemistry*, Mineralogical Society of America Geochemical Society, p. 61-120.
- Pyle, D.M., 1989, The Thickness, Volume and Grainsize of Tephra Fall Deposits: *Bulletin of Volcanology*, v. 51, p. 1-15.
- Reubi, O., and Blundy, J., 2008, Assimilation of Plutonic Roots, Formation of High-K Exotic Melt Inclusions and Genesis of Andesitic Magmas at Volcán De Colima, Mexico: *Journal of Petrology*, v. 49, p. 2221-2243.
- Rhodes, J.M., Dungan, M.A., Blanchard, D.P., and Long, P.E., 1979, Magma mixing at mid-ocean ridges: evidence from basalts drilled near 22N on the mid-Atlantic Ridge: *Tectonophysics*, v. 55, p. 35-61.
- Richard, P., Shimizu, N., and Allegre, C.J., 1976, $^{143}\text{Nd}/^{144}\text{Nd}$, a natural tracer: an application to oceanic basalts: *Earth and Planetary Science Letters*, v. 31, p. 269-278.
- Ridolfi, F., Renzulli, A., and Puerini, M., 2010, Stability and chemical equilibrium of amphibole in calc-alkaline magmas: an overview, new thermobarometric formulations and application to subduction-related volcanoes: *Contributions to Mineralogy and Petrology*, v. 160, p. 45-66.
- Righter, K., 2000, A comparison of basaltic volcanism in the Cascades and western Mexico: compositional diversity in continental arcs: *Tectonophysics*, v. 318, p. 99-117.
- Righter, K., Carmichael, I.S.E., Becker, T.A., and Renne, P.R., 1995, Pliocene-Quaternary Volcanism and Faulting at the Intersection of the Gulf of California and the Mexican Volcanic Belt: *Geological Society of America Bulletin*, v. 107, p. 612-626.
- Righter, K., and Rosas-Elguera, J., 2001, Alkaline Lavas in the Volcanic Front of the Western Mexican Volcanic Belt: *Geology and Petrology of the Ayutla and Tapalpa Volcanic Fields: Journal of Petrology*, v. 42, p. 2333-2361.
- Robin, C., Camus, G., and Gourgaud, A., 1991, Eruptive and magmatic cycles at Fuego de Colima volcano (Mexico): *Journal of Volcanology and Geothermal Research*, v. 45, p. 209-225.
- Robin, C., Mossand, P., Camus, G., Cantagrel, J.M., Gourgaud, A., and Vincent, P.M., 1987, Eruptive History of the Colima Volcanic Complex (Mexico): *Journal of Volcanology and Geothermal Research*, v. 31, p. 99-113.
- Robin, C., and Potrel, A., 1993, Multi-stage magma mixing in the pre-caldera series of Fuego de Colima volcano: *Geofisica Internacional*, v. 32, p. 605-615.
- Rollinson, H.R., 1993, *Using geochemical data: evaluation, presentation, interpretation*, Pearson.
- Ruiz, J., Patchett, P.J., and Arculus, R.J., 1988, Nd-Sr isotope composition of lower crustal xenoliths - evidence for the origin of mid-Tertiary felsic volcanics in Mexico *Contributions to Mineralogy and Petrology*, v. 99, p. 36-43.
- Rutherford, M.J., 2008, Magma Ascent Rates, *in* Putirka, K.D., and Tepley III, F.J., eds., *Minerals, Inclusions and Volcanic Processes, Volume 69: Reviews in Mineralogy and Geochemistry*, Mineralogical Society of America, p. 241-271.
- Rutherford, M.J., and Devine, J.D., 2003, Magmatic Conditions and Magma Ascent as Indicated by Hornblende Phase Equilibria and Reactions in the 1995-2002 Soufriere Hills Magma: *Journal of Petrology*, v. 44, p. 1433-1453.
- Rutherford, M.J., and Hill, P.M., 1993, Magma ascent rates from amphibole breakdown: an experimental study applied to the 1980-1986 Mount St. Helens eruptions: *Journal of Geophysical Research*, v. 98, p. 19667-19685.

- Saucedo, R., Macias, J.L., Gavilanes, J.C., Arce, J.L., Komorowski, J.C., Gardner, J.E., and Valdez-Moreno, G., 2010, Eyewitness, stratigraphy, chemistry, and eruptive dynamics of the 1913 Plinian eruption of Volcan de Colima, Mexico: *Journal of Volcanology and Geothermal Research*, v. 191, p. 149-166.
- Saucedo, R., Macias, J.L., Sheridan, M.F., Bursik, M.I., and Komorowski, J.C., 2005, Modeling of pyroclastic flows of Colima Volcano, Mexico: implications for hazard assessment: *Journal of Volcanology and Geothermal Research*, v. 139, p. 103-115.
- Saunders, A.D., Norry, M.J., and Tarney, J., 1991, Fluid Influence on the Trace Element Compositions of Subduction Zone Magmas: *Philosophical Transactions of the Royal Society of London. Series A: Physical and Engineering Sciences*, v. 335, p. 377-392.
- Savov, I.P., Luhr, J.F., and Navarro-Ochoa, C., 2008, Petrology and geochemistry of lava and ash erupted from Volcán Colima, Mexico, during 1998-2005: *Journal of Volcanology and Geothermal Research*, v. 174, p. 241-256.
- Savov, I.P., Ryan, J.G., D'Antonio, M., and Fryer, P., 2007, Shallow slab fluid release across and along the Mariana arc-basin system: Insights from geochemistry of serpentinized peridotites from the Mariana fore arc: *J. Geophys. Res.*, v. 112, p. B09205.
- Savov, I.P., Ryan, J.G., D'Antonio, M., Kelley, K., and Mattie, P., 2005, Geochemistry of serpentinized peridotites from the Mariana Forearc Conical Seamount, ODP Leg 125: Implications for the elemental recycling at subduction zones: *Geochemistry, Geophysics, Geosystems*, v. 6, p. Q04J15.
- Scaillet, B., and Evans, B.W., 1999, The 15 June 1991 eruption of Mount Pinatubo. I. Phase equilibria and pre-eruption P-T-fO₂-fH₂O conditions of the dacite magma: *Journal of Petrology*, v. 40, p. 381-411.
- Schmidt, M.E., and Grunder, A.L., 2011, Deep mafic roots to arc volcanoes: Mafic recharge and differentiation of basaltic andesite at North Sister Volcano, Oregon Cascades: *Journal of Petrology*, v. 52, p. 306-341.
- Schmidt, M.W., and Poli, S., 2004, Generation of Mobile Components during Subduction of Oceanic Crust, *in* Rudnick, R., ed., *The Crust, Volume 3: Treatise on Geochemistry*: Oxford, Elsevier-Pergamon, p. 567-592.
- Schwaiger, H.F., Denlinger, R.P., and Mastin, L.G., 2012, Ash3d: A finite-volume, conservative numerical model for ash transport and tephra deposition: *Journal of Geophysical Research: Solid Earth*, v. 117, p. B04204.
- Scollo, S., Tarantola, S., Bonadonna, C., Coltelli, M., and Saltelli, A., 2008, Sensitivity analysis and uncertainty estimation for tephra dispersal models: *J. Geophys. Res.*, v. 113, p. B06202.
- Selvans, M., Stock, J., DeMets, C., Sanchez, O., and Marquez-Azua, B., 2011, Constraints on Jalisco Block Motion and Tectonics of the Guadalajara Triple Junction from 1998–2001 Campaign GPS Data: *Pure and Applied Geophysics*, v. 168, p. 1435-1447.
- Sisson, T.W., and Grove, T.L., 1993, Experimental investigations of the role of H₂O in calc-alkaline differentiation and subduction zone magmatism *Contributions to Mineralogy and Petrology*, v. 113, p. 143-166.
- Sorenson, H., and Barton, M.D., 1987, Metasomatism and Partial Melting in a Subduction Complex: Catalina Schist, Southern California: *Geology*, v. 15, p. 115-118.
- Sorenson, H., and Grossman, J.N., 1993, Accessory Minerals and Subduction Zone Metasomatism: A Geochemical Comparison of two Melanges (Washington and California, U.S.A.): *Chemical Geology*, v. 110, p. 269-297.
- Soto, G.L., Ni, J.F., Grand, S.P., Sandvol, E., Valenzuela, R.W., Speziale, M.G., Gonzalez, J.M.G., and Reyes, T.D., 2009, Mantle flow in the Rivera-Cocos subduction zone: *Geophysical Journal International*, v. 179, p. 1004-1012.
- Sparks, R.S.J., 1986, The dimensions and dynamics of volcanic eruption columns: *Bulletin of Volcanology*, v. 48, p. 3-15.
- Sparks, S.R.J., and Sigurdsson, H., 1977, Magma mixing: a mechanism for triggering acid explosive eruptions: *Nature*, v. 267, p. 315-318.
- Stoopes, G.R., and Sheridan, M.F., 1992, Giant debris avalanches from the Colima volcanic complex, Mexico: Implications for long-runout landslides (<100km) and hazard assessment: *Geology*, v. 20, p. 299-302.

- Stracke, A., Hofmann, A.W., and Hart, S.R., 2005, FOZO, HIMU, and the rest of the mantle zoo: *Geochemistry Geophysics Geosystems*, v. 6, p. Q05007.
- Straub, S.M., Goldstein, S.L., Class, C., Schmidt, A., and Gomez-Tuenca, A., 2010, Slab and Mantle Controls on the Sr-Nd-Pb-Hf Isotope Evolution of the Post 42 Ma Izu-Bonin Volcanic Arc: *Journal of Petrology*, v. 51, p. 993-1026.
- Streck, M.J., 2008, Mineral Textures and Zoning as Evidence for Open System Processes, *in* Putirka, K.D., and Tepley III, F.J., eds., *Minerals, Inclusions and Volcanic Processes*, Volume 69: *Reviews in Mineralogy and Geochemistry*, Mineralogical Society of America, p. 595-622.
- Sun, S.S., and McDonough, W.F., 1989, Chemical and isotopic systematics of ocean basalts: implications for mantle composition and processes, *in* Saunders, A.D., and Norry, M.H., eds., *Magmatism in the Ocean Basins*, Volume 42, Geological Society Special Publication, p. 313-345.
- Suzuki, T., 1983, A theoretical model for the dispersion of tephra, *in* Shimozuru, D., and Yokoyama, I., eds., *Arc Volcanism, Physics and Tectonics*: Tokyo, Terra Scientific Publishing, p. 95-113.
- Szramek, L., Gardner, J.E., and Larsen, J., 2006, Degassing and microlite crystallization of basaltic-andesite magma erupting at Arenal Volcano, Costa Rica: *Journal of Volcanology and Geothermal Research*, v. 157, p. 182-201.
- Tatsumi, Y., and Kogiso, T., 1997, Trace element transport during dehydration processes in the subducted oceanic crust: 2. Origin of chemical and physical characteristics in arc magmatism: *Earth and Planetary Science Letters*, v. 148, p. 207-221.
- Tatsumi, Y., Murasaki, M., and Nohda, S., 1992, Across-arc variation of lava chemistry in the Izu-Bonin Arc - identification of subduction components: *Journal of Volcanology and Geothermal Research*, v. 49, p. 179-190.
- Thirlwall, M.F., 1991, Long-term Reproducibility of Multicollector Sr and Nd Isotope Ratio Analysis: *Chemical Geology*, v. 94, p. 85-104.
- Thorpe, R.S., Gibson, I.L., and Viscaino, J.S., 1977, Andesitic pyroclastic flows from Colima Volcano: *Nature*, v. 265, p. 724-725.
- Ulrich, M., Hémond, C., Nonnotte, P., and Jochum, K.P., 2012, OIB/seamount recycling as a possible process for E-MORB genesis: *Geochemistry, Geophysics, Geosystems*, v. 13, p. Q0AC19.
- Urrutia-Fucugauchi, J., and Uribe-Cifuentes, R.M., 1999, Lower-crustal xenoliths from the Valle de Santiago maar field, Michoacan-Guanajuato volcanic field, central Mexico: *International Geology Review*, v. 41, p. 1067-1081.
- Varley, N., Arámbula-Mendoza, R., Reyes-Dávila, G., Stevenson, J., and Harwood, R., 2010, Long-period seismicity during magma movement at Volcán de Colima: *Bulletin of Volcanology*, v. 72, p. 1093-1107.
- Venzke, E., Wunderman, R.W., McClelland, L., Simkin, T., Luhr, J.F., Siebert, L., Mayberry, G., and Sennert, S., 2002-, *Global Volcanism, 1968 to the Present*, Smithsonian Institution, Global Volcanism Program Digital Information Series, GVP-4 (<http://www.volcano.si.edu/reports/>).
- Verma, S.P., and Gomez-Arias, E., 2013, Three-dimensional temperature field simulation of magma chamber in the Los Humeros geothermal field, Puebla, Mexico: *Applied Thermal Engineering*, v. 52, p. 512-515.
- Verma, S.P., and Luhr, J.F., 2010, Sr, Nd, and Pb isotopic evidence for the origin and evolution of the Cántaro-Colima volcanic chain, Western Mexican Volcanic Belt: *Journal of Volcanology and Geothermal Research*, v. 197, p. 33-51.
- Vigouroux, N., Wallace, P.J., and Kent, A.J.R., 2008, Volatiles in High-K Magmas from the Western Trans-Mexican Volcanic Belt: Evidence for Fluid Fluxing and Extreme Enrichment of the Mantle Wedge by Subduction Processes: *Journal of Petrology*, v. 49, p. 1589-1618.
- von Huene, R., Ranero, C.s.R., and Vannucchi, P., 2004, Generic model of subduction erosion: *Geology*, v. 32, p. 913-916.

- Waite, G.P., and Moran, S.C., 2009, VP Structure of Mount St. Helens, Washington, USA, imaged with local earthquake tomography: *Journal of Volcanology and Geothermal Research*, v. 182, p. 113-122.
- Waitz, P., 1906, *Le Volcan de Colima*, X Congreso Geologico Internacional, Libreto-Guia: Mexico, Volume 13, p. 27.
- Waitz, P., 1915, El estado actual de los volcanes de Mexico y la ultima erupcion del Volcán de Colima (1913): *Revista Volcanologica*, p. 259-268.
- Waitz, P., 1935, Datos historicos y bibliograficos acerca del Volcán de Colima: *Memorias de la Sociedad Cientifica Antonio Alzate*, v. 53, p. 349-383.
- Wallace, P., and Carmichael, I.S.E., 1989, Minette lavas and associated leucitites from the western front of the Mexican Volcanic Belt: petrology, chemistry, and origin: *Contributions to Mineralogy and Petrology*, v. 103, p. 470-492.
- Wells, P.R.A., 1977, Pyroxene thermometry in simple and complex systems: *Contributions to Mineralogy and Petrology*, v. 62, p. 129-139.
- White, W.M., and Bryan, W.B., 1977, Sr-Isotope, K, Rb, Cs, Sr, Ba, and Rare-Earth Geochemistry of Basalts from Famous Area: *Geological Society of America Bulletin*, v. 88, p. 571-576.
- Wilcox, R.E., 1954, *Petrology of Paricutin Volcano, Mexico*: United States Geological Survey Bulletin, v. 965C, p. 281-353.
- Willbold, M., and Stracke, A., 2010, Formation of enriched mantle components by recycling of upper and lower continental crust: *Chemical Geology*, v. 276, p. 188-197.
- Wilson, M., 1989, *Igneous Petrogenesis*: London, Chapman & Hall.
- Wood, B.J., and Banno, S., 1973, Garnet-orthopyroxene and orthopyroxene-clinopyroxene relationships in simple and complex systems: *Contributions to Mineralogy and Petrology*, v. 42, p. 109-124.
- Woodhead, J., Stern, R.J., Pearce, J., Hergt, J., and Vervoort, J., 2012, Hf-Nd isotope variation in Mariana Trough basalts: The importance of “ambient mantle” in the interpretation of subduction zone magmas: *Geology*, v. 40, p. 539-542.
- Yang, T., Grand, S.P., Wilson, D., Guzman-Speziale, M., Gomez-Gonzalez, J.M., Dominguez-Reyes, T., and Ni, J., 2009, Seismic structure beneath the Rivera subduction zone from finite-frequency seismic tomography: *Journal of Geophysical Research-Solid Earth*, v. 114, p. 12.
- Zindler, A., and Hart, S.R., 1986, Chemical geodynamics: *Annual Review of Earth and Planetary Sciences*, v. 14, p. 493-571.
- Zindler, A., Staudigel, H., and Batiza, R., 1984, Isotope and trace element geochemistry of young Pacific seamounts: implications for the scale of upper mantle heterogeneity: *Earth and Planetary Science Letters*, v. 70, p. 175-195.
- Zobin, V.M., Luhr, J.F., Taran, Y.A., Breton Gonzalez, M., Cortes, A., De la Cruz-Reyna, S., Dominguez-Reyes, T., Galindo, L., Gavilanes, J.C., Munez, J.J., Navarro-Ochoa, C., Ramirez, J.J., Reyes, G.A., Ursua, M., Velasco, J., Alatorre, E., and Satiago, H., 2002, Overview of the 1997-2000 activity of Volcan de Colima, Mexico: *Journal of Volcanology and Geothermal Research*, v. 117, p. 1-19.
- Zobin, V.M., Varley, N.R., Gonzalez, J.M.G., J., O., Reyes, G.A., Navarro-Ochoa, C., and Breton Gonzalez, M., 2008, Monitoring the 2004 andesitic block-lava extrusion at Volcan de Colima, Mexico from seismic activity and SO₂ emission: *Journal of Volcanology and Geothermal Research*, v. 177, p. 367-377.